GAS-PHASE EPOXIDATION OF HEXAFLUOROPROPYLENE

David Lokhat

[MSc. (Eng.) and BSc. (Eng.), UKZN]

A thesis submitted in the School of Chemical Engineering
University of KwaZulu-Natal
Durban

In fulfilment of the requirements for the degree
Doctor of Philosophy in Engineering, Chemical Engineering

April 2012

Supervisors: Professor Maciej Starzak and Professor Deresh Ramjugernath

As the candidate's Supervisor I agree to the submission of this thesis

……..

Professor Maciej Starzak

As the candidate's Supervisor I agree to the submission of this thesis

……..

Professor Deresh Ramjugernath

DECLARATION

I ..... declare that

(i) The research reported in this dissertation/thesis, except where otherwise indicated, is my original work.

(ii) This dissertation/thesis has not been submitted for any degree or examination at any other university.

(iii) This dissertation/thesis does not contain other persons' data, pictures, graphs or other information, unless specifically acknowledged as being sourced from other persons.

(iv) This dissertation/thesis does not contain other persons' writing, unless specifically acknowledged as being sourced from other researchers. Where other written sources have been quoted, then:

a) their words have been re-written but the general information attributed to them has been referenced;

b) where their exact words have been used, their writing has been placed inside quotation marks, and referenced.

(v) Where I have reproduced a publication of which I am an author, co-author or editor, I have indicated in detail which part of the publication was actually written by myself alone and have fully referenced such publications.

(vi) This dissertation/thesis does not contain text, graphics or tables copied and pasted from the Internet, unless specifically acknowledged, and the source being detailed in the dissertation/thesis and in the References sections.

Signed: Date:

Acknowledgements

This research formed part of the Fluorochemical Expansion Initiative of the Department of Science and Technology. It was supported by the South African Research Chairs Initiative, the National Research Foundation and in part by the South African Nuclear Energy Corporation.

I would like to express my most sincere gratitude to the many people who made the completion of this work possible. Special thanks must go to Professor M. Starzak whose supervision of the project was superlative. I would also like to thank my co-supervisor Professor D. Ramjugernath for providing the opportunity and platform to carry out this research. I am indebted to the technical staff of the School of Chemical Engineering at the University of KwaZulu-Natal for their generous advice and assistance, in particular Rekha Maharaj, Sadha Naidoo, Danny Singh, Ken Jack, Rajen Krishna, Patrick Mlambo, Elliot Mlambo, Preyothen Nayager, Dudley Naidoo, Frik Van de Merwe, Leon Augustyne, Lindinkosi Mkize and Ayanda Kanyele. I also acknowledge the assistance of former University employees Kelly Robertson and Les Henwood.

Personal thanks go to my postgraduate colleagues Shalendra Subramoney, Suren Moodley, Sudhir Pillay and Rasmika Prithipal. Lastly I would like to thank my sister, Sarah, my mother and aunt for their support and encouragement.

Abstract

A process was developed for the production of hexafluoropropylene oxide via the gas-phase oxidation of hexafluoropropylene with molecular oxygen. The non-catalytic oxidation reaction was investigated in an isothermal, laminar flow reactor at a total pressure of 4.5 bar and over the temperature range of 453 to 503 K. Feed mixtures comprising 20 to 67% HFP in oxygen were used at total flow-rates between 150 and 550 cm^3 min^{-1}. The reactor was fabricated from $^1/_8$ inch nominal sized, copper refrigeration tubing and was 114.3 m long. The reactor was used in the form of a helical coil. Gas-chromatographic analysis was used for reactant and stable product quantification. The reaction gave hexafluoropropylene oxide, trifluoroacetyl fluoride and carbonyl fluoride as major products. Minor products included tetrafluoroethylene and hexafluorocyclopropane. The oxidation reaction also produced high molecular weight oligomers that were retained on the inner surface of the reactor tube. The operating conditions for the non-catalytic oxidation were optimized independently for HFPO selectivity and yield using quadratic response surface methodology. A maximum HFPO selectivity of 55.81% was identified at 478.2 K, a HFP/O_2 molar feed ratio of 1.34 mol mol^{-1} and a space time of 113 seconds. An optimum HFPO yield of 40.10% was identified at 483.2 K, a HFP/O_2 molar feed ratio of 1.16 mol mol^{-1} and a space time of 121 seconds. Using the weighted-sum-of-squared-objective-functions (WSSOF) multi-response optimization technique, a combined optimum HFPO selectivity and yield of 56% and 40%, respectively, was obtained at 480 K, with a HFP/O_2 molar feed ratio of 1.21 and a space time of 118 seconds. This represented the best trade-off between these two performance criteria.

A kinetic reaction scheme involving 8 species and 7 reactions was developed, based on the results of the experimental study, and was used to model the non-catalytic oxidation of HFP. The initial steps in this scheme encompassed the addition of oxygen to the double bond of the fluoro-olefin and transformation of the resultant dioxetane intermediate to form HFPO and the haloacetyl fluorides. Subsequent steps included the thermal decomposition of HFPO to yield CF_3COF, C_2F_4 and *c*-C_3F_6, as well as elimination of C_2F_4, and to a lesser extent CF_3COF, through oxidation. Rate parameters for the oxidation reactions were determined through a least-squares minimization procedure.

The investigation was extended by considering the catalyzed synthesis of HFPO. Four different catalysts were studied *viz*., 1wt% Au/Al_2O3, 1wt% Au/ZnO, 10wt% CuO/SiO_2 as well as 10wt% CuO/SiO_2 doped with caesium. The gold-based catalysts were found to be completely inactive for the oxidation reaction. The caesium promoted, copper-based catalyst appeared to be the most stable

and active, with no observable decomposition to copper fluoride. At 453 K, a HFP/O_2 molar feed ratio of 0.86 and a weight-hourly-space-velocity of 0.337 h^{-1}, a HFPO selectivity of 85.88% was obtained. This was significantly greater than what was achieved in the non-catalytic system.

List of publications and conference contributions

- Lokhat, D., Starzak, M. and Ramjugernath, D., "Gas-phase epoxidation of hexafluoropropylene", South African Chemical Engineering Conference (SACEC 2009), Somerset West, Cape Town, South Africa, 20th-23rd September 2009.

- Lokhat, D., Starzak, M. and Ramjugernath, D., "Gas-phase epoxidation of hexafluoropropylene", 19th International Congress of Chemical and Process Engineering (CHISA 2010), 7th European Congress of Chemical Engineering (ECCE-7), Prague, Czech Republic, 28th-1st September 2010.

- Lokhat, D., Starzak, M. and Ramjugernath, D., "Epoxidation of hexafluoropropylene", AIChE Annual Meeting, Salt Lake City, Utah, USA, 7th-12th November 2010.

- Lokhat,D., Starzak, M. and Ramjugernath, D., "Gas-phase epoxidation of hexafluoropropylene: optimization of reaction conditions", 11th International Conference on Frontiers of Polymers and Advanced Materials, Pretoria, South Africa, 26th May 2011.

Table of contents

List of figures

Chapter 3

Chapter 4

Appendix A

Appendix C

Appendix D

Appendix I

List of tables

Chapter 2

Chapter 3

Chapter 4

Appendix D

Appendix F

Appendix G

Appendix I

List of photographs

Chapter 3

List of schemes

Chapter 2

List of drawings

Chapter 3

Appendix B

List of symbols

Latin capital and lowercase letters (boldface symbols are vectors or tensors)

Symbol	Description	Units
a	activity	
A	gas chromatogram peak area	μV min
A	pre-exponential factor	
A	Helmholtz free energy	J mol^{-1}
b	vector of model parameters or parameter estimates	
c	intercept coefficient for gas chromatograph detector calibration	
C	concentration	mol m^{-3}
$\overline{C}$	mixed-cup average concentration	mol m^{-3}
C_j	atomic group contribution increment, gas viscosity correlation	
C_V	ideal gas heat capacity, constant volume	J mol^{-1} K^{-1}
C_P	ideal gas heat capacity, constant pressure	J mol^{-1} K^{-1}
C_P°	standard-state heat capacity, constant pressure	J mol^{-1} K^{-1}
C	centre point of the central composite design	
d_c	coil diameter	m
d_t	tube diameter	m
D_{AB}	binary diffusion coefficient	m^2 s^{-1}
D_{im}	multicomponent diffusion coefficient	m^2 s^{-1}
Dn	Dean number	
E_a	activation energy	J mol^{-1}
E	quantum mechanical energy	J mol^{-1}
f	fugacity	
F	molar flow-rate	mol s^{-1}
F	Fischer test statistic	
F	independently optimized response	
$\hat{F}$	normalized independently optimized response	
F	orthogonal factorial design point of the central composite design	
F	Jacobian matrix	

Symbol	Description	Units
g_{ik}	k-th dependent variable in the i-th experiment predicted by model	
G	Gibbs free energy	J mol^{-1}
g	gravitational acceleration vector	m^2 s^{-1}
ΔG°_{rxn}	standard Gibbs energy change of reaction	J mol^{-1}
h	Planck's constant	
H	enthalpy	J mol^{-1}
ΔH°_{f}	standard enthalpy change of formation	J mol^{-1}
ΔH°_{rxn}	standard enthalpy change of reaction	J mol^{-1}
I	moment of inertia	
j	mass flux vector	kg m^{-2} s^{-1}
k	gas chromatograph detector coefficient of proportionality	
k	reaction rate constant	
κ	Boltzmann's constant	
K_a	activity-based equilibrium constant	
K_c	concentration-based equilibrium constant	
l_e	entrance length	m
m	mass	kg
$\bar{M}$	average molar mass	g mol^{-1}
n	number of moles	mol
n_D	number of dependent variables	
n_E	number of experimental points	
N	number of replicate data points	
N_i^j	number of atoms of element j in molecule i	
P	pressure	bar
P_c	critical pressure	bar
P_r	reduced pressure	
q, Q	canonical partition function	
Q_{ij}	mixture viscosity interaction parameter	
r	radial dimension	
r_j	molar rate of production of species j by chemical reaction	mol m^{-3} s^{-1}
R	universal gas constant	

Symbol	Description	Units
R^2	coefficient of multiple determination	
Re	Reynolds number	
$Re_{critical}$	critical transitional Reynolds number	
R_i	net rate of production of mass of species i per unit volume by reaction	kg m^{-3} s^{-1}
R_p	gas chromatogram peak resolution	
R_t	tube radius	m
S	reaction selectivity	%
S	objective function	
S	entropy	J mol^{-1} K^{-1}
S	axial design point of the central composite design	
t	time	s
t_R	gas chromatogram retention time	min
T	temperature	K
T_c	critical temperature	K
T_r	reduced temperature	
U	internal energy	J mol^{-1}
v	velocity	m s^{-1}
$(\sum v)_i$	summation of atomic and structural diffusion volumes	
v_r	radial velocity component	m s^{-1}
v_z	axial velocity component	m s^{-1}
v_θ	angular velocity component	m s^{-1}
V	volume	m^3
V°	molar volume	m^3 mol^{-1}
v	mass average velocity vector	m s^{-1}
w	gas chromatogram peak width at the base	min
w	mass fraction	
w_{ik}	weighting factor of the k-th dependent variable in the i-th experiment	
W	weighting factor for multi-response optimization	
x	mole fraction	
X	reaction conversion	%
X_i	technological independent variable of the central composite design	
X_i^s	statistical independent variable of the central composite design	

Symbol	Description	Units
$\mathbf{X}$	vector of independent variables	
y	mole fraction	
y_{ik}	measured value of the k-th dependent variable in the i-th experiment	
Y	reaction yield	%
Y^s	response predicted by statistical quadratic response model	
Y^t	response predicted by technological quadratic response model	
z	axial dimension	
Z	compressibility factor	
Z^0, Z^l	functions of the generalized compressibility factor correlation	

Greek letters (boldface symbols are vectors or tensors)

Symbol	Description	Units
α	spacing for axial design point of central composite design	
β	quadratic model coefficient	
ε	energy level	
Θ	rotational temperature	
Θ_v	vibrational temperature	
ϕ	fugacity coefficient	
Ω_u	collision integral	
ρ	density	kg m^{-3}
σ	collision diameter	
σ	rotational symmetry number	
σ^2_{ik}	variance of the k-th dependent variable in the i-th experiment	
σ_j	uncertainty in j	
τ	space time	s
$\boldsymbol{\tau}$	viscous stress tensor	kg m^{-1} s^{-2}
μ	viscosity	Pa s
υ	stoichiometric coefficient	
ω	degeneracy of an energy level	

Subscripts/ superscripts

Symbol	Description
0	inlet, reference
a	atom
ele	electronic ground state
exit	reactor exit
i	species *i*
m	mixture, molecule
max	maximum
mode	energy mode
nuc	nuclear
rot	rotational
s	standard
sample	gas chromatograph sample
tot	total
tra	translational
vib	vibrational
ZPE	zero-point energy

List of abbreviations

BET	Brunauer, Emmet and Teller
$ECAN_i$	effective carbon number for component *i*
HFA	hexafluoroacetone
HFP	hexafluoropropylene
HFPO	hexafluoropropylene oxide
LFR	laminar flow reactor
OVAT	one-variable-at-a-time
PFPP	perfluoropolyether polyperoxide
PFR	plug flow reactor
PLOT	porous-layer-open-tubular
RSM	response surface methodology
WHSV	weight hourly space velocity

Chapter 1
Introduction

South African reserves of fluorspar, a naturally occurring mineral that is the precursor to almost all industrial fluorochemicals, exceed 41 million tons and production capacity is approximately 5% of the total world output, yet only a fraction of this is converted to higher value products (Simandl, 2009). The beneficiation of domestic fluorspar and the development of the local fluorochemical technology base are the main objectives of the Fluorochemical Expansion Initiative (FEI), a priority South African government strategy within the departments of Minerals and Energy, Trade and Industry and Science and Technology. To this end, the South African Nuclear Energy Corporation (NECSA) commissioned the South African research chair in fluorine process engineering and separation technology at the University of KwaZulu-Natal to develop a process for the production of 2,2,3-trifluoro-3-(trifluoromethyl)-oxirane (commonly known as hexafluoropropylene oxide, HFPO), a valuable fluorochemical intermediate that can be converted to inert oils, high performance fluids, elastomers and membranes. The traditional methods of preparation, as described in the literature, include nucleophilic and radical-based syntheses from hexafluoropropylene (HFP) using different oxidizers such as hypohalites, hydrogen peroxide, organic peroxides and molecular oxygen (Millauer et al., 1985). These processes are often carried out batch-wise, in the presence of inert liquid solvents and at elevated pressures (Furin, 2006). In most cases, the materials used are expensive and the processes themselves are either complicated, dangerous in operation or produce a lot of waste by way of used solvents (Huang et al., 2006).

To date, no viable continuous process has been found for the direct, gas-phase, thermally-initiated epoxidation of HFP that offers high selectivity and yield towards HFPO. This route offers several advantages, though, including being easier to operate, inherently safer due to the absence of large amounts of organic solvents, such as carbon tetrachloride, and is suitable for large-scale operations.

The literature is practically devoid of kinetic information regarding the thermally-initiated, gas-phase oxidation of perfluoro-olefins. Even basic data, relating to the effect of operating conditions on reaction performance, appears to be lacking. The purpose of the current investigation was then to generate fundamental information on the application of this reaction type for the beneficiation of perfluoro-olefins. The reaction between HFP and O_2 in particular was selected, since this system offered the definite possibility for the formation of a useful epoxide product. The overall objective of this study was the development of a useable process for the preparation of HFPO from HFP,

preferentially via the gas-phase epoxidation of HFP using molecular oxygen. In order to achieve this objective, the following tasks were defined:

- Optimization of reaction conditions for the non-catalytic reaction with regard to maximizing the selectivity and yield towards HFPO.
- Development of a kinetic model for the non-catalytic route using proposed mechanisms and identification of the kinetic parameters.
- Attempt to find materials which would serve as catalysts for the gas-phase epoxidation of HFP, to further improve the selectivity and yield towards HFPO.

A formal strategy was adopted to accomplish each of these proposed tasks. First a two-level experimental design was used to investigate the fundamental behaviour of the non-catalytic reaction system and to identify the key operating parameters. The purpose of these experiments was to study how the combined effects of reaction temperature, HFP/O_2 molar feed ratio and space time influenced selected performance parameters, viz. HFP conversion, selectivity and yield towards HFPO. A more sophisticated, statistical experimental design was subsequently used to probe for optimal reaction conditions. Kinetic data was collected for the non-catalytic process and a reaction model was constructed to fit the observations. It was believed that the development of a feasible and competitive process for the production of HFPO and an adequate non-catalytic reaction model would constitute novel work and contribute to the knowledge in the field.

The study was extended by considering the solid catalyzed epoxidation of HFP. A number of classical oxidation catalysts were selected as potential candidate materials for the epoxidation of HFP, based on a comprehensive literature review. These were screened in a quantitative fashion for their ability to produce HFPO, using a low-level experimental design.

This thesis consists of six chapters and nine appendices. The first chapter is a general introduction to the topic, including the rationale and motivation for the project. The objectives and methodology of the investigation are also succinctly described.

In chapter 2, an overview of the current knowledge regarding the oxidation of HFP is presented within the framework of a comprehensive literature review. Catalytic and non-catalytic processes for the production of HFPO are discussed in detail. Important aspects of the reaction chemistry and

kinetics are also considered. The chapter closes with a brief look at the development strategy for solid epoxidation catalysts and a summary of the technologies available for the epoxidation of HFP.

The experimental apparatus, materials, procedures and analytical techniques that were used for both the non-catalytic and catalytic studies are described in detail in Chapter 3. The methodological approach and experimental results are presented in Chapter 4. For the non-catalytic study, this included the results of preliminary experiments, the optimization of operating conditions, the development of a reaction model and the identification of kinetic parameters. The experimental results of the catalytic study are thereafter analyzed and compared to the non-catalytic study. The salient points of both investigations are discussed at length in Chapter 5.

Concluding remarks for this work, as well as recommendations for improving the research, are given in the final chapter. The appendices contain information on instrument calibrations, calculation procedures, raw experimental data as well as equipment drawings and software programming files.

Chapter 2
Literature review

2.1. Industrial applications of HFPO

HFPO plays a significant role in the manufacture of many high-grade organofluorine products. The perfluorinated epoxide can be converted by anionic polymerization into oligomers, under the action of various catalysts and in the presence of a number of different solvents (Millauer et al., 1985). The oligomerization is preceded by the isomerisation of HFPO to perfluoroproprionic acid fluoride. Perfluoropropoxide ions, in equilibrium with the latter, attack molecules of HFPO, giving rise to an alkoxide intermediate that forms the oligomer after the elimination of a fluoride ion (cf. Scheme 2.1).

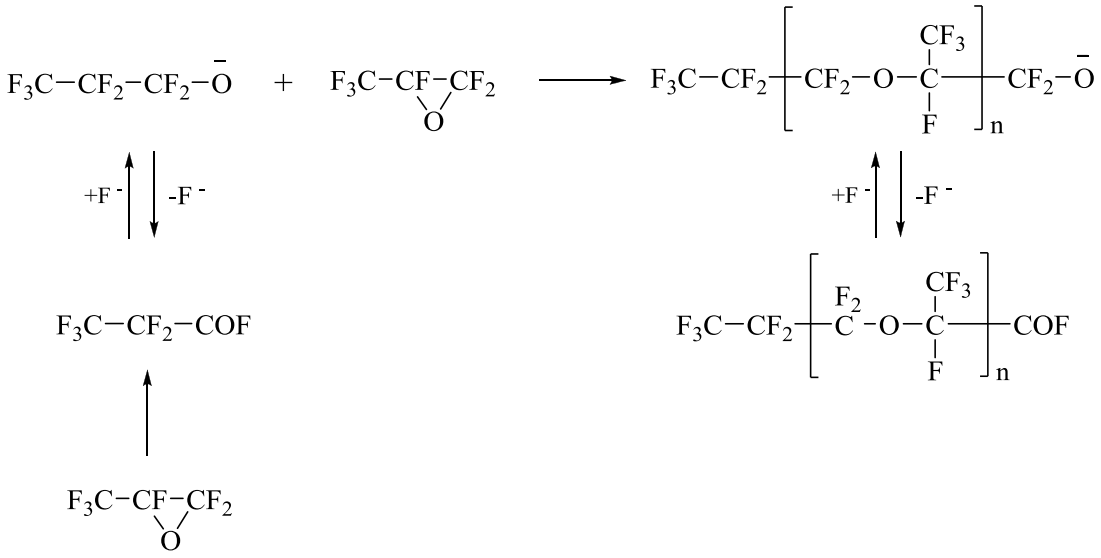

Scheme 2.1. Anionic polymerization of HFPO.

The degree of polymerization is strongly dependent on the type of catalyst system and the aprotic solvent that is used, such that the process can be tailored to produce a variety of different oligomers. Oligomeric HFPO, after treatment with fluorinating agents such as elemental fluorine, AlF_3 or SbF_3, produces chemically and thermally stable liquids that are used extensively in the chemical industry, in air liquefaction plants (e.g. Krytox) and, importantly, in nuclear engineering (Sokolov et al., 1984).

Perfluoroakylvinylethers are produced commercially in a two-stage process involving HFPO and the acid fluoride by-products of fluoro-olefin oxidation (Ebnesajjad, 2006):

1. HFPO is reacted with a perfluorinated acyl fluoride to produce perfluoro-2-alkoxy-propionyl fluoride:

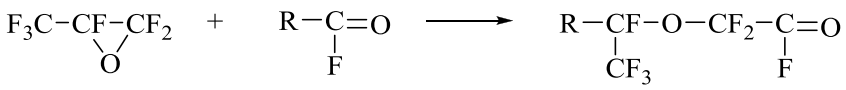

2. Perfluoro-2-alkoxy-propionyl fluoride is reacted with the oxygen containing salt of an alkali or alkaline earth metal at an elevated temperature. An example of the salt used for this purpose is sodium carbonate:

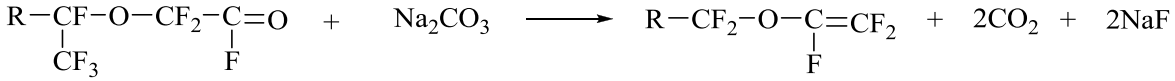

Perfluoropropylvinylether lowers the melt viscosity of the co-polymer with tetrafluoroethylene sufficiently to make injection moulding and extrusion possible (Millauer et al., 1985). The copolymer is manufactured under the proprietary names Teflon PFA (du Pont) and Hostaflon TFA (Hoechst AG). Perfluoromethylvinylether copolymerizes with tetrafluoroethylene to produce a perfluorinated elastomer commonly known as Kalrez (du Pont).

More recently, HFPO has been used as a material for generating difluorocarbene (CF_2), which is very useful in difluorocarbene insertion reactions (Huang et al., 2006; Banks, 1976). HFPO was also shown to be a good reagent for the nucleophilic formation of the elemental-fluorine bond in organo-elemental compounds (Lermontov et al., 1999), as a starting material for the production of hexafluoroacetone (Millauer et al., 1985) and as a component of fluorinated surfactants (Lawson, 1991).

2.2. Non-catalytic oxidation of HFP

2.2.1. Liquid-phase non-catalytic oxidation of HFP

The liquid-phase non-catalytic oxidation of HFP may be classified further according to the type of oxidizer that is used as well as the nature of the reaction conditions. There exist nucleophilic processes, carried out at or below room temperature, employing inorganic peroxides or hypohalites as the oxidizing agents (Furin, 2006; Millauer et al., 1985). These are the traditional "wet" oxidation processes that are frequently used in industry. Alternatively, the oxidation may be carried out via a radical-based synthesis in the condensed phase, at very low temperatures using molecular oxygen, or under high pressure and temperature in an inert solvent, also in the presence of molecular oxygen (Furin, 2006).

The earliest reported nucleophilic synthesis of HFPO involved the batch reaction of HFP with 30% hydrogen peroxide in an aqueous potassium hydroxide/methanol solution at 233 K (Eleuterio, 1967). The reaction produced a 35% yield of HFPO. A higher yield of the epoxide was obtained using an aqueous hydrogen peroxide solution in the presence of acetonitrile (Millauer et al., 1985). HFPO can also be produced by the action of hypohalites, in particular sodium hypochlorite. The reaction is usually carried out between 288 and 293 K (Millauer et al., 1985). More recently, Ikeda et al. (1990) proposed a refinement of the hypohalite method using a two-liquid-phase process. The two-phase batch system consisted of an aqueous hypohalite solution and a reaction phase comprising an organic liquid and HFP. The reaction only proceeded in the presence of a phase-transfer catalyst. Quaternary ammonium salts, phosphium and assonium salts as well as lipophilic complexing agents in the presence of an inorganic base were all found to be suitable catalysts (Millauer et al., 1985). In one example, 18 ml of 1,1,2-trichloro-1,1,2-trifluoroethane (F113) solvent, 20 ml of aqueous sodium hypochlorite and 1.8 g of HFP were combined with trioctylmethylammonium chloride to produce HFPO with a selectivity of 84% at a HFP conversion of 96%. Various other catalyst-solvent combinations were tried but with no further increase in HFPO selectivity. Lawson (1991) modified the two-liquid-phase method of Ikeda (1990) to maximize the selectivity towards HFPO. The batch process used a pH 7.5-9.6 aqueous phase containing hypohalite ions and a reaction phase comprising an organic liquid in which a phase transfer catalyst was soluble and in which there was a higher affinity for the HFP rather than its epoxide. Toluene was selected as the most appropriate solvent. The best selectivity towards HFPO achieved was 86% at a conversion of 43% when the reaction was carried out at 273.95 K. Lawson

(1990) also presented a three-liquid-phase batch process which included agitation to maintain an aqueous phase comprising hypohalite ions, an epoxide phase comprising the bulk of the epoxide and virtually no phase transfer catalysts and a reaction phase comprising an organic liquid in which a phase transfer catalyst was dissolved and which has a higher affinity for the perfluoro-olefin than for the epoxide. The maximum selectivity towards HFPO that was obtained was 80.5% at a conversion of 55%. Lee et al (2001) showed that the addition of ferric chloride to two-liquid-phase mixtures of sodium hypochlorite or hydrogen peroxide, HFP, tetrabutyl ammonium chloride and F113 enhanced the yield of HFPO. An epoxide yield of 66.3% was obtained at a reaction temperature of 273.15 K.

The oxidation of HFP with molecular oxygen requires some form of activation, either through the use of high energy radiation, the addition of radical generating species (chemical initiators) or thermal initiation (Millauer et al., 1985).

The low temperature, liquid-phase oxidation of HFP with molecular oxygen is often carried out using photo-initiation (Millauer et al., 1985; Shapovalov et al., 1984). Sianessi et al. (1965) reacted HFP with oxygen under the action of ultraviolet light in a closed system. The photo-oxidation of the liquid perfluoro-olefin was carried out at 203 K and 243 K. At the lower temperature, the primary product was a polyperoxide, $(C_3F_6O_2)_n$, that decomposed violently when exposed to temperatures above 333 K. At 243 K, a polymer having the average formula $(C_3F_6O_{1.35})_n$ was formed that was thermally stable up to 393 K. The low temperature photo-initiated oxidation of HFP is now often used for the production of similar oligomeric peroxidic polyethers that are thermally, stable, chemically resistant, non-flammable, non-toxic and possess high dielectric properties (Faucitano et al., 1991; Maksimov et al., 2009). The by-products of the low temperature process include COF_2, CF_3COF and HFPO (Shapovalov et al., 1984; Maksimov et al., 2009). The oxidation proceeds under the influence of ultra-violet light of wavelengths shorter than 320 nm, usually obtained using low and medium pressure mercury lamps (Maksimov et al., 2009).

A frequently employed industrial method of producing HFPO is the batch-wise oxidation of HFP with molecular oxygen in an inert solvent under high pressure (40 bar). The process requires thermal initiation at temperatures between 373 and 473 K (Millauer et al., 1985; Furin, 2006). The conversion of HFP under these conditions is about 70%, while the yield of the epoxide can also reach 70% (Millauer et al., 1985). The reaction phase is usually diluted with a perfluorinated of chlorofluoroalkane solvent (Furin, 2006). The difficulty associated with the synthesis of

perfluorinated epoxides using this method can be attributed to the propensity for the oxirane structure to decompose under the temperatures necessary for initiation, or temperatures attained within the reactor due to localized exothermic heat effects, leading to deeper oxidation products (Meissner and Wróblewska, 2007). The oxidation of HFP under high pressure can often proceed explosively, even when carried out in the presence of a solvent (Meissner and Wróblewska, 2007; Huang et al., 2006). Carlson (1970) was one of the first to report that partial and fully fluorinated epoxides could be prepared from halogenated olefins using the former method. These epoxides were prepared by heating the halo-olefin with oxygen at super-atmospheric pressures in the presence of various inert diluents (e.g. perfluoropropane, nitrogen, carbon dioxide, argon, neon, carbon tetrafluoride, C_6F_{16}, etc.) at temperatures between 323 and 523 K, in a closed vessel. Metals from which the reactor or its wall lining could be constructed and which did not catalyze the epoxide rearrangement to the corresponding haloacetyl fluorides were copper, nickel and its alloys, chromium, titanium, silver and platinum. The use of high HFP:O_2 ratios led to high selectivity towards HFPO. HFP, being less active than chlorotrifluoroethylene, required a reaction temperature between 403 and 523 K. The use of higher reaction temperatures, however, facilitated the decomposition of the epoxide. In a batch stainless-steel vessel, maintained at approximately 423 K with an initial total pressure of 26 bar, using HFP and O_2 in the ratio of 9:1 and CCl_4 as the diluent, a conversion of 72% and selectivity towards HFPO of 76% was obtained (Carlson, 1970). The reaction was also carried out in a continuous stainless-steel tubular reactor, lined with polytetrafluoroethylene (Teflon), at a temperature of 473 K and a pressure of 88.7 bar. The results of these experiments are shown in Table 2.1.

Table 2.1. Results of HFP oxidation experiments conducted in a Teflon-lined, stainless-steel tubular reactor (Carlson, 1970).

Diluent	**Diluent flow-rate [cm^3 min^{-1}]**	**HFP flow-rate [cm^3 min^{-1}]**	**Oxygen flow-rate [cm^3 min^{-1}]**	**HFPO selectivity [%]**
Nitrogen	850	0.89	65	20.48
Helium	930	0.88	65	28.21
Carbon dioxide	600	0.89	65	1.22

Octafluorocyclobutane was also tested as a liquid diluent for the synthesis of HFPO using a stainless-steel tubular reactor. At a total pressure of 82.7 bar, a reaction temperature of 473 K and using 6.5 cm^3 min^{-1} of a mixture of 15 wt% HFP in octafluorocyclobutane as well as 75 cm^3 min^{-1}

of oxygen, a conversion of 15% was obtained with selectivity towards HFPO of 76.1%. Stainless-steel has been found to catalyze the rearrangement of HFPO to hexafluoroacetone, however, as well as the isomerisation and decomposition of alkylperoxy radicals to the low molecular weight acid fluorides COF_2 and CF_3COF, in the liquid-phase oxidation of HFP (Kartsov et al., 1978). Experiments conducted with a Teflon-lined reactor showed that higher selectivity towards HFPO could be obtained at the same reaction conditions (Kartsov et al., 1978).

The synthesis of HFPO was also carried out by Shapovalov and Poluéktov (1994 a) in a sealed 1litre glass vessel maintained at a temperature of 413 K using a liquid fluorocarbon solvent and a reactant feed rate of 5 cm^3 min^{-1} for both HFP and O_2. The product mixture contained 24.5 mol% HFP, 61.5 mol% HFPO, 7 mol% CF_3COF and 7 mol% COF_2. In order to accelerate the reaction, the synthesis was performed at an elevated temperature using the same solvent (Shapovalov and Poluéktov, 1998 a) but lower yields of HFPO were obtained. A product mixture of 13.5 mol% HFP, 68.4 mol% HFPO, 9.1 mol% CF_3COF and 9 mol% COF_2 was obtained when using HFP oligomers as the liquid solvent at a reaction temperature of 428 K (Shapovalov and Poluéktov, 1998 a).

Meissner and Wróblewska (2007) prepared HFPO using molecular oxygen and HFP dissolved in excess CCl_4 contained within a 0.5 litre chromium-nickel-molybdenum steel autoclave, at temperatures between 393 and 443 K and molar ratios of HFP to O_2 between 4 and 14. The use of greater amounts of oxygen resulted in an increase in the conversion of HFP but a decrease in the selectivity towards HFPO from 77% to 67%. Within the temperature range 393-413 K, the selectivity towards HFPO remained virtually unchanged, yet was observed to decrease rapidly above 413 K. The total pressure of the system was varied by addition of an inert gas (nitrogen). Higher total pressure appeared to be beneficial to both conversion and selectivity and was ascribed to the fact that better solubility of oxygen in the liquid HFP/CCl_4 mixture was obtained at higher total pressure. Reaction conditions for the high pressure (>35 bar) oxidation of HFP were later optimized for the yield of HFPO (Wróblewska et al., 2010). At 438 K, with an initial molar ratio of HFP/O_2 of 2.2 and after a reaction time of 3.1 hours, a HFPO yield of 43% was obtained. Łągiewczyk and Czech (2010) found that the type of the solvent used in the high pressure, thermally-initiated HFP oxidation process had a dramatic effect on the yield of HFPO. The experiments of Wróblewska et al. (2010) were repeated using three different solvents and a new 1.31 litre reactor. The best results were obtained with F113 as the solvent, with a HFPO yield of approximately 83% reported.

The liquid-phase oxidation of HFP with molecular oxygen can also be carried out using a suitable chemical initiator. An 85% yield of HFPO was obtained by reacting HFP and O_2 in a stainless-steel vessel, using F113 as a solvent and elemental fluorine as an initiator. The conversion of HFP was greater than 95% (Furin, 2006). Elemental fluorine can promote an explosive chain reaction in this system and its use requires strict control of all technological process parameters (Furin, 2006). In particular, the concentration of fluorine in the mixture should be maintained between 0.5-1.4% (Maksimov et al., 2009).

An alternative to elemental fluorine is trifluoromethyl hypofluorite (CF_3OF), which also undergoes homolytic dissociation at low temperatures and can be used as an initiator for the radical-based synthesis of HFPO. Shoshin et al. (1999) produced HFPO in a 600 mm long glass bubble column filled with 12F chlorofluorocarbon liquid solvent, using various chemical initiators. The concentration of the initiator was between 1.5-2% by volume. The results are given in Table 2.2.

Table 2.2. Results of the liquid-phase, chemically-initiated oxidation of HFP (Shoshin et al., 1999)

Initiator	Temperature [K]	HFP conversion [%]	HFPO selectivity [%]
F_2	353	76.5	70.2
Cl_2	353	72.9	62.2
Br_2	363	70.0	59.6
CF_3OF	363	78.3	77.2

The effect of the reactor material on the yield of the epoxide was also studied, by substituting the glass column for a stainless-steel one (Shoshin et al., 1999). Experiments were conducted at 353 K using an equimolar feed ratio of HFP/O_2 and a CF_3OF concentration in oxygen of 1.6% by volume. A higher epoxide yield was observed in the glass reactor, confirming the inappropriateness of stainless-steel as a material for reactor fabrication (Kartsov et al., 1978).

2.2.2. Gas-phase non-catalytic oxidation of HFP

Initial examinations of the gas-phase non-catalytic oxidation of HFP were focused on the photo-initiated reaction occurring at room temperature. In one of the earliest reported studies, Saunders and Heicklen (1965) investigated the gas-phase reaction of oxygen atoms with HFP at 297 K in a cylindrical Pyrex cell. The oxygen atoms were generated by in situ mercury-photosensitized decomposition of N_2O. The major advantages for this method of generating oxygen atoms were that the only oxygen specie produced was atomic oxygen having a triplet electronic spin state and that N_2O was non-reactive with this specie and most radicals. Appreciable amounts of CO_2, COF_2 and CF_3COF were formed, together with small quantaties of C_4F_8 (as perfluorinated methyl-cylcopropane) and a C_5 fluorocarbon, which was most likely perfluoro-1,2-dimethylcyclopropane. Heicklen and Knight (1965) studied the same system at 486 K. They found that CO_2, COF_2, CF_3COF, C_2F_4 and C_4F_8 were produced when the reaction was carried out in the presence of molecular oxygen.

The gas-phase batch reaction of equimolar mixtures of HFP and O_2 under the action of ultraviolet light was studied by Sianessi et al. (1965). The main products from these experiments were found to be COF_2, CF_3COF, CF_3CF_2COF, HFPO and a high molecular weight viscous liquid that was thermally stable up to 473 K. Quantitative details of the actual product distribution were not disclosed. Further experimentation showed that the greater the molecular weight of the starting olefin, the greater was the epoxide content of the product mixture. In particular, the only product of the reaction of 1-perfluoroheptene with oxygen was the epoxide.

The photo-initiated gas-phase oxidation of HFP was also studied by Kuricheva et al. (1999), between 680 and 840 K. The reaction was initiated using a CO_2 IR laser source and was carried out batch-wise in a 12 or 24 cm^3 glass reactor equipped with BaF_2 windows for spectrophotometric analysis. At the conditions that were employed, only deeper oxidation products such as COF_2 and CF_3COF were formed together with trace amounts of C_2F_4 and C_4F_8.

Sianessi et al. (1973) reacted HFP and O_2 in a 270 mm long, copper, tubular reactor operating at atmospheric pressure. The reaction was thermally initiated at 623 K. COF_2, CF_3COF and a number of different perfluoropolyethers were produced.

Trifluoromethyl hypofluorite was used as a chemical initiator for the gas-phase oxidation of HFP with molecular oxygen at 303, 313 and 323.4 K (Dos Santos Afonso, 2000). The partial pressures of the initiator and the reactants were varied simultaneously in the 19 experiments that were conducted. The use of chemical initiators, instead of ultraviolet light, for the oxidation of fluoro-olefins can result in better control over the structure and relative molecular mass of the perfluoropolyethers that are formed (Romano, 2003). The major products included COF_2, CF_3COF and $CF_3OCF_2OCF_3COF$. Small amounts of CF_3OCF_2COF were also formed. Under the temperatures that were studied, no HFPO was formed.

An important recent investigation of the gas-phase epoxidation of HFP was conducted by Romano and Czarnowski (2004). The thermal gas-phase reaction between NO_2 and HFP was carried out using a 270 cm^3 quartz bulb reactor at temperatures of 413.1, 421.0 and 432.8 K. The reaction was allowed to proceed until all the HFP had been consumed. It is known that in reactions between NO_2 and halogenated olefins, the NO_2 can act as a nitrating or oxidizing agent and the products of these reactions include nitrohaloacetyl halides, dinitro compounds and nitrohaloketones (Arce et al., 2005). Only four compounds were observed in the work of Romano and Czarnowski (2004) viz., NO, HFPO, $CF_3CFNO_2CF_2NO$ and $CF_3COCF_2NO_2$. A HFPO yield of 63-89% was obtained across the set of 15 experiments that were conducted.

2.2.3. Reaction mechanisms

All known methods of producing HFPO were shown to be based on the reaction of HFP with an appropriate oxidizing agent. Syntheses that proceed in the presence of hydrogen peroxide are nucleophilic in nature (Millauer et al., 1985). The hydroperoxide anion, a strong nucleophile, attacks the electron-deficient double bond of the fluoro-olefin. Subsequent hydroxide ion elimination and ring closure gives the epoxide (cf. Scheme 2.2).

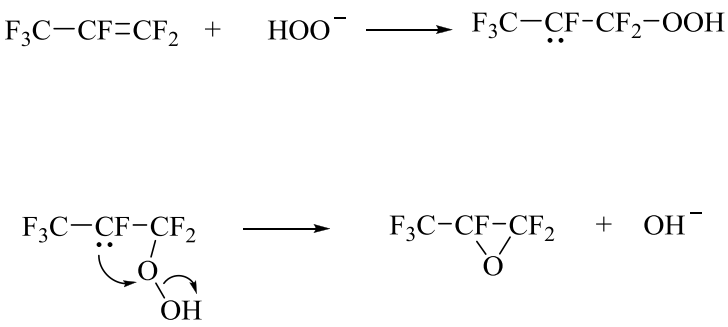

Scheme 2.2. Nucleophilic reaction of hydrogen peroxide with HFP.

For the liquid-phase reaction of HFP and hydrogen peroxide in the presence of acetonitrile, oxygen transfer is perpetuated by an acetoperoxyimidic acid intermediate (cf. Scheme 2.3). Acetamide is formed as a by-product.

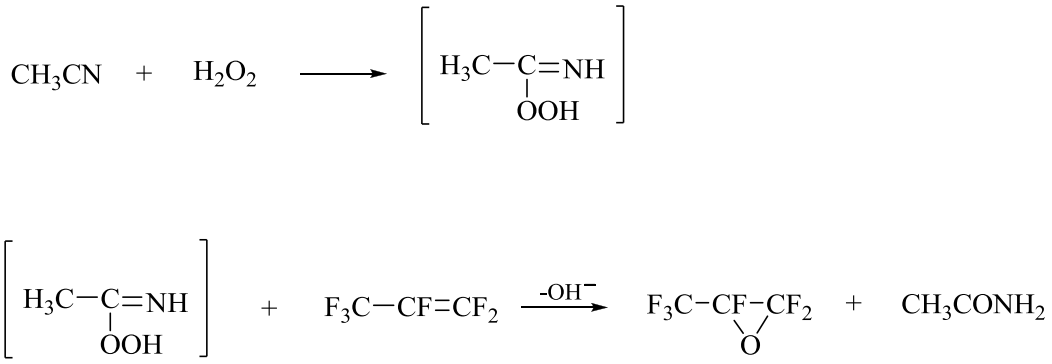

Scheme 2.3. Expoxidation of HFP with hydrogen peroxide in the presence of acetonitrile.

All processes for the production of HFPO using oxygen may be described in terms of a radical-based mechanism and therefore require some form of initiation (Millauer et al., 1985).

The kinetics of the low temperature, photo-initiated oxidation of HFP was investigated by Faucitano et al. (1991). They conceded that a complex free radical process was extant and proposed a thirteen step short-chain reaction scheme for the oxidation at 233 K, in the liquid state under an oxygen atmosphere, using a high-pressure mercury lamp (cf. Table 2.3).

Table 2.3. Reaction scheme for the low-temperature photo-oxidation of HFP.[a]

No.	Reaction	Rate constant [l mol^{-1} s^{-1}][b]
1	$C_3F_6 + O_2 \rightarrow CF_3\bullet + CFO\bullet + CF_2O$	
2	$ROOR \rightarrow 2RO\bullet$	
3	$R\bullet + O_2 \rightarrow RO_2\bullet$	10^8
4	$RO_2\bullet + C_3F_6 \rightarrow ROOCF_2\dot{C}FCF_3$ $\rightarrow ROOCFCF_3\dot{C}F_2$	0.3 ± 0.05
5	$RO\bullet + C_3F_6 \rightarrow ROCF_2\dot{C}FCF_3$ $\rightarrow ROCFCF_3\dot{C}F_2$	95 ± 4 (s^{-1})
6	$ROCF_2CFCF_3O\bullet \rightarrow RO\dot{C}F_2 + CF_3COF$ $\rightarrow RO\dot{C}F_2CFO + CF_3\bullet$	57 ± 5 (s^{-1})
7	$ROCFCF_3CF_2O\bullet \rightarrow RO\dot{C}FCF_3 + COF_2$	57 ± 5 (s^{-1})
8	$RO_2\bullet + RO_2\bullet \rightarrow 2RO\bullet + O_2$	$(2.8 \pm 0.4)\times10^6$
9	$RO_2\bullet + RO_2\bullet \rightarrow ROOR + O_2$	$(6.7 \pm 1.2)\times10^4$
10	$RO_2\bullet + R\bullet \rightarrow ROOR$	10^7
11	$RO\bullet + R \rightarrow ROR$	10^7
12	$RO\bullet + RO\bullet \rightarrow ROOR$	10^7
13	$R\bullet + R\bullet \rightarrow RR$	10^7

[a] $R\bullet$, $RO\bullet$ and $RO_2\bullet$ represent all types of carbon-centred radicals, alkoxy radicals and peroxy radicals, respectively.

[b] The rates of initiation and photo-scission of peroxides (reaction 1 and 2, respectively) are functions of the intensity of radiation as well as the molar absorption coefficients of the monomer and peroxides.

Under the action of the ultraviolet light initiator, CF_3• and CFO• radicals, as well as COF_2, were formed by the reaction of HFP with oxygen. Subsequent reaction of these perfluoroalkyl species with O_2 gave perfluroperoxyl, or peroxy, radicals. The major reaction path for the formation of peroxides was assumed to be the addition of peroxy radicals to HFP. The chain mechanism for the generation of ether bonds in the oligomeric peroxidic perfluoroethers that were formed was based on the non-terminative disproportionation of peroxy radicals followed by addition of the subsequent alkoxy radicals to HFP, which was found to be faster than the addition of peroxy radicals. Under the conditions used for that particular study, the epoxide product was not formed. The formation of COF_2 and CF_3COF were proposed to be due to β-scission of alkoxy radicals, with the former being present in greater amounts. The same reaction scheme was adopted by Maksimov et al. (2009) in a study relating to the synthesis of perfluoropolyethers through photo-oxidation of HFP.

Perfluoropolyether polyperoxide (PFPP), the major oligomeric product of the low-temperature, liquid-phase, photo-oxidation of HFP with molecular oxygen was also suggested to form through the following chain mechanism (Shapovalov, 2000 a):

$$R\bullet + O_2 \rightarrow RO_2\bullet \quad (2.1)$$

$$RO_2\bullet + C_3F_6 \rightarrow RO_2C_3F_6\bullet \quad (2.2)$$

$$RO_2\bullet + RO_2\bullet \rightarrow 2RO\bullet + O_2 \quad (2.3)$$

$$RO\bullet + C_3F_6 \rightarrow ROC_3F_6\bullet \quad (2.4)$$

Below room temperature, thermal initiation did not occur and the non-catalytic oxidation reaction required chemical or photo-initiation. In photo-initiation, HFP absorbed light quanta and was postulated to decompose into two perfluorocarbenes, i.e. CF_3CF• and CF_2• which initiated the chain by reacting with oxygen (Shapovalov et al., 1984). The $-C_3F_6O-$, $-CF_2O-$ and $-CF(CF_3)O-$ ether units predominated in the structure of PFPP, with peroxy units accounting for less than 10% of the total units (Shapovalov, 2000 a). The following general formula for PFPP was proposed (Shapovalov et al., 1984):

$$CF_3\text{-}O\text{-}(C_3F_6\text{-}O)_P\text{-}(CF_2\text{-}O)_Q\text{-}[CF(CF3)\text{-}O]_R\text{-}(\text{-}O\text{-})\text{-}C$$

where P, Q and R were numbers ranging from 1-50, (-O-) denoted a peroxy group which could be (C_3F_6-O-O), (CF_2-O-O) or [$CF(CF_3)$-O-O], and C was the end group, which could be (-COF), (-CF_2-COF) or [-$CF(CF_3)$-COF]. Importantly, low molecular weight compounds (COF_2 and CF_3COF) were suggested to form via the non-terminative interaction of peroxy radicals, rather than alkoxy radical fragmentation (Shapovalov and Poluéktov, 1995):

$$RO_2\bullet + ROCF_2(CF_3)CFO_2\bullet \rightarrow RO\bullet + O_2 + CF_3COF + ROCF_2\bullet \quad (2.5)$$

$$RO_2\bullet + ROCF(CF_3)CF_2O_2\bullet \rightarrow RO\bullet + O_2 + COF_2 + ROCF(CF_3)\bullet \quad (2.6)$$

HFPO was produced by fragmentation of alkyl radicals in which the last oxygen link was an ether bond:

$$ROC_3F_6\bullet \rightarrow R\bullet + C_3F_6O \quad (2.7)$$

Chain termination occurred via the bimolecular coupling of alkoxy radicals (Shapovalov and Poluéktov, 1993 a):

$$RO\bullet + RO\bullet \rightarrow ROOR \quad (2.8)$$

Other recombination reactions were also possible and in fact, the various self and cross coupling termination reactions were all thermodynamically favoured and very fast (Sianessi et al., 1999). Provided that there was enough HFP and O_2 present, these reactions were not expected to play a significant role, since the concentration of these reactive species would be limited due to their tendency toward other scavenging reactions in the sequence (Sianessi et al., 1999).

In summary, the oxidation of HFP at low temperatures and in the liquid phase involved the formation of a peroxidic polymer and the decomposition of this moiety gave low molecular weight products. The basic steps in the mechanism included initiation, propagation, chain transfer and termination.

The effect of reaction temperature and oxygen partial pressure on the molecular mass of PFPP was investigated by Shapovalov (2000 b). It was discovered that with decreasing temperature (in the range 303-213 K) and increasing oxygen partial pressure (in the range 1-15 bar), the molecular

mass of PFPP increased. In a separate study (Shapovalov, 2002), the rate of PFPP formation was also found to increase with an increase in oxygen partial pressure. The proportions of $-CF_2-$ and $-CF(CF_3)-$ units in the structure of PFPP increase with increasing reaction temperature, due to the fact that the activation energy of the steps for the formation of low molecular weight acid fluorides is higher than the activation energy for the formation of PFPP (Shapovalov, 2000 a). The activation energies for the formation of the four major products of the low-temperature oxidation of HFP were reported by Shapovalov et al. (1984) and are given in Table 2.4. Interestingly, the rate of formation of both HFPO and PFPP were found to be linearly dependent on the concentration of HFP, whereas the rate of formation of CF_3COF and COF_2 were found to be independent of HFP concentration (Shapovalov et al., 1984). The formation rates of the acyl fluorides were found to be independent of oxygen partial pressure, above 2-3 bar (Shapovalov and Poluéktov, 1993 b). The rate of HFP consumption was also found to be independent of O_2 pressure, indicative of chain termination that involved oxygen-centred peroxy and alkoxy radicals (Shapovalov and Poluéktov, 1993 a).

Table 2.4. Activation energies for the formation of products in the low-temperature oxidation of HFP (Shapovalov et al., 1984).

Product	Activation energy [kJ mol^{-1}]
PFPP	19.3
HFPO	17.2
CF_3COF	26.4
COF_2	26

The dependence of the molecular mass of PFPP on the oxygen partial pressure was found to be due to the mechanism of formation of HFPO (Shapovalov and Poluéktov, 1994 b). The epoxide was formed by the fragmentation of alkyl radicals containing the ether link in the β position (Shapovalov and Poluéktov, 1993 a). The epoxidation of HFP was suppressed by competitive reaction of the alkyl radical with oxygen, producing a radical that added to the polyether chain:

$$ROC_3F_6\bullet + O_2 \rightarrow ROC_3F_6O_2\bullet \qquad (2.9)$$

An increase in the pressure of O_2 favoured reaction 2.9 and resulted in an increase in the unit number and molecular mass of PFPP as well as a decrease in the HFPO formation rate. Epoxidation could not be completely suppressed, however, even at very high oxygen partial pressures

(Shapovalov and Poluéktov, 1998 b). The inhibitory effect of high levels of oxygen on the epoxidation of HFP was investigated further by Shapovalov and Poluéktov (1992; 1994 c). They found that the rate of formation of HFPO was indeed inversely proportional to the oxygen partial pressure that was utilized.

The kinetics of the gas-phase reaction of HFP with oxygen atoms, the latter generated by in situ mercury photosensitized decomposition of N_2O, was investigated by Saunders and Heicklen (1965). At room temperature it was suggested that HFP quantitatively scavenges the oxygen atoms to form products:

$$O + C_3F_6 \rightarrow COF_2 + CF_3CF\cdot \quad (2.10)$$

$$O + C_3F_6 \rightarrow CF_2\cdot + CF_3COF \quad (2.11)$$

The radical fragments formed in reactions 2.10 and 2.11 can disappear by one or a combination of the following processes:

$$2CF_2\cdot \rightarrow C_2F_4 \quad (2.12)$$

$$2CF_3CF\cdot \rightarrow 2C_4F_8 \quad (2.13)$$

$$CF_3CF\cdot \rightarrow C_2F_4 \quad (2.14)$$

$$CF_3CF\cdot + CF_2\cdot \rightarrow C_3F_6 \quad (2.15)$$

$$CF_2\cdot + C_3F_6 \rightarrow F_3C{-}CF(-CF_2-)CF_2 \quad (2.16)$$

$$CF_3CF\cdot + C_3F_6 \rightarrow F_3C{-}CF(-CF_2-)CF{-}CF_3 \quad (2.17)$$

In the presence of molecular oxygen, the amounts of COF_2 and CF_3COF produced were found to fall rapidly as the oxygen partial pressure was increased. A competing radical chain mechanism was suggested to account for this observation (shown here in a simpler form):

$$R\cdot + O_2 \rightarrow RO_2\cdot \quad (2.18)$$

$$2RO_2\bullet \rightarrow 2RO + O_2 \quad (2.19)$$

$$RO_2\bullet + C_3F_6 \rightarrow 2RO + R\bullet \quad (2.20)$$

where R• is either CF_2• or CF_3CF•. The molecular oxygen can also react with O atoms and a C_3F_6O• intermediate (if formed):

$$O + O_2 \xrightarrow{C_3F_6} O_3 \quad (2.21)$$

$$C_3F_6O\bullet + O_2 \rightarrow COF_2 + C_2F_4O_2 \quad (2.22)$$

Saunders and Heicklen (1965) were among the first to propose a link between oxygen partial pressure and the propensity for low-molecular-weight acid anhydride formation. Heicklen and Knight (1965) reiterated that a long chain mechanism was most probably involved, but no definite attempt was made in their investigation at elucidating the sequence of steps. The system was later examined at a higher reaction temperature of 398 K (Saunders and Heicklen, 1966). The rate of formation of COF_2 and CF_3COF was found in that study to be unaffected by changes in initial HFP partial pressure.

The kinetics of the high temperature oxidation of HFP by oxygen radicals were studied by Hynes et al (1999) using a single-pulse shock tube. The oxygen atoms were generated by thermal decomposition of N_2O. Mixtures of 0.6 mol% HFP in 1.5 mol% N_2O, 6.2 mol% HFP in 0.6 mol% N_2O and 0.7 mol% in 6.3 mol% N_2O, all diluted in argon , were used. The reactions were carried out in the temperature range 1300-1600 K and at pressures between 16 and 20 bar. Under all conditions, the most significant products were C_2F_6, C_2F_4, COF_2, CO, CO_2 and CF_4. Under oxidizer-rich conditions, ignition of the HFP was observed along with the production of significant quantities of CF_4 and O_2. Under fuel-rich conditions, pyrolysis of HFP occurred resulting in a protracted product distribution. Detectable amounts of heavier fluorocarbons were also found, including iso-C_4F_8 and perfluoro-2-butene as well as octafluoropropane, hexafluoro-2-butyne, perfluorinated cyclobutenes, hexafluorobenzene, pentafluorocyclopentadiene and pentafluoro (trifluoromethyl) benzene. A 77-step reaction model with 38 species was proposed to model the oxidation of HFP, emphasizing the complexity of the free-radical reaction scheme for thermal gas-phase oxidation of fluoro-olefins. In the concluding remarks of their study, the authors noted that HFP decomposes

primarily by O addition to both carbons of the double bond. When CFO• radicals form, they undergo unimolecular F loss and these F atoms are able to attack HFP to cause a radical chain that includes CF_2• carbenes. At the severe thermal conditions employed, no epoxide product was found.

The mechanism of the oxidation of HFP by molecular oxygen under IR laser excitation was studied by Kuricheva et al. (1999). The formation of reaction products was explained using a two-stage mechanism. First, interaction of HFP with O_2 led to the formation of a dioxetane intermediate. Decomposition of this intermediate resulted in the formation of the two acyl fluorides, COF_2 and CF_3COF. HFPO may have also formed from the dioxetane, but under the conditions of the experiments, decomposed to CF_3COF and CF_2•. Difluorocarbene recombination gave rise to C_2F_4 and CF_3COF decomposition to COF_2 was also suggested.

Dos Santos Afonso et al. (2000) proposed a 33-step free-radical chain mechanism to explain the results of a study regarding the gas-phase oxidation of HFP with molecular oxygen in the presence of CF_3OF. Under the conditions that were used in the study, the reaction was found to be pseudo-zero-order with respect to O_2. The chain was initiated by reaction of CF_3OF with HFP to produce CF_3CFCF_3• and CF_3O• radicals. CF_3O• then adds to the fluoro-olefin to form haloalkoxy radicals, which decompose to give low molecular weight acid fluorides. In the presence of molecular oxygen, the perfluoroalkoxyl radicals also react rapidly with O_2 leading to perfluoroperoxy radicals. The lack of formation of HFPO was attributed to the fact that perfluoroperoxy radicals do not add to the double bond of HFP at the reaction conditions used, disappearing preferentially via self reaction to form perfluoroalkoxy radicals.

Shoshin et al. (1999) proposed a much simpler scheme for the CF_3OF-initiated oxidation of HFP. First, the dissociation of CF_3OF resulted in the formation of CF_3O• and F• radicals that subsequently attacked the double bond of HFP. This gave rise to a chain process with intermediate formation of peroxides and polyperoxides. The final products were dependent on the oxidation conditions and formed directly from the intermediates (cf. Scheme 2.4).

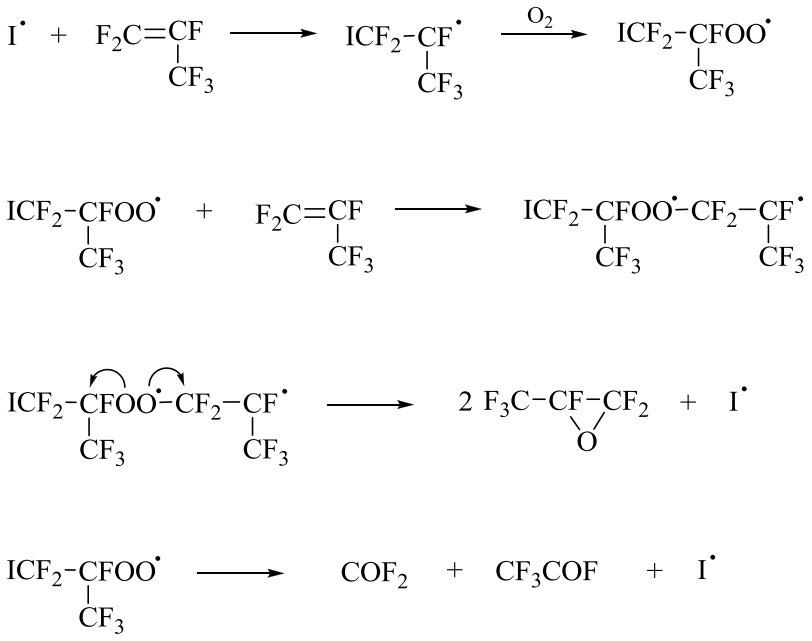

Scheme 2.4. CF_3OF-initiated oxidation of HFP, I• is CF_3O• or F• (Shoshin et al., 1999).

A short radical chain mechanism was also proposed for the thermal gas-phase reaction between NO_2 and HFP at temperatures between 413 and 433 K (Romano and Czarnowski, 2004):

$$CF_3CF{=}CF_2 + NO_2 \rightarrow CF_3\dot{C}FCF_2NO_2 \qquad (2.23)$$

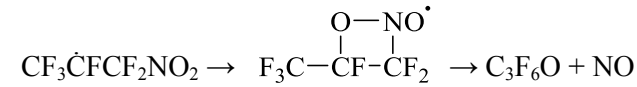

(2.24)

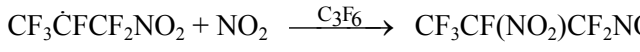

(2.25)

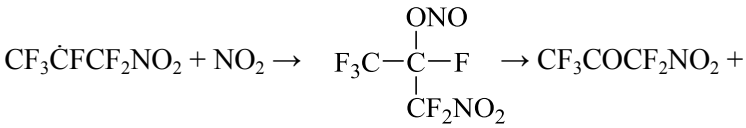

(2.26)

The oxidation of HFP was initiated by addition of NO_2 to the double bond of the olefin. Interestingly, a four-member ring intermediate was proposed to be involved in reaction 2.24. The

interaction of FNO with the quartz reactor walls resulted in the formation of volatile SiF_4 according to the reaction:

$$SiO_2 + 4FNO \rightarrow SiF_4 + 2NO + 2NO_2 \quad (2.27)$$

The lack of formation of CF_3COF indicated that within the temperature range explored, HFPO did not decompose.

The results of the high-pressure, thermally-initiated oxidation experiments performed by Wróblewska et al. (2010) as well as Łągiewczyk and Czech (2010) were explained in terms of a biradical reaction mechanism (cf. Table 2.5). This particular scheme was based on the reactive routes proposed by Gilbert et al. (1976) for the reaction of oxygen atoms with fluoroethylenes. The initial steps in the high-temperature oxidation of HFP are represented by the first two reactions in Table 2.5, with subsequent reactions accounting only for the thermal decomposition and rearrangement of the epoxide.

Table 2.5. Biradical mechanism for the oxidation of HFP at high temperature, including decomposition steps (Wróblewska et al., 2010; Łągiewczyk and Czech, 2010).

No.	Reaction
1	$C_3F_6 + ½\ O_2 \rightarrow C_3F_6O$
2	$C_3F_6 + O_2 \rightarrow COF_2 + CF_3COF$
3	$C_3F_6O \rightarrow CF_3COF + CF_2\bullet$
4	$C_3F_6 + CF_2\bullet \rightarrow CF_3\text{-}C_3F_5$
5	$CF_2\bullet + CF_2\bullet \rightarrow C_2F_4$
6	$CF_2\bullet + C_2F_4 \rightarrow c\text{-}C_3F_6$

The oxidation was postulated to occur through three steps, shown in greater detail in Scheme 2.5. Neither oxygen nor HFP dissociates under the reaction temperatures that were considered. The sequence was initiated via a C_3F_6-O_2 encounter which involved the electrophilic addition of oxygen to the double bond of the fluoro-olefin to form an excited biradical intermediate. A similar initiating step was reported by Liu and Davis (1992) in a matrix isolation spectroscopic study of tetrafluoroethylene oxidation. The formation of a cyclic peroxide and its subsequent decomposition resulted in the formation of COF_2 as well as CF_3COF. Alternatively, the elimination of an oxygen

atom from the original biradical adduct and subsequent ring closure produced the epoxide. HFPO, however, decomposed at temperatures above 423 K to yield CF_2• and CF_3COF (Millauer et al., 1985). CF_2• recombination finally gave rise to C_2F_4 and *c*-C_3F_6.

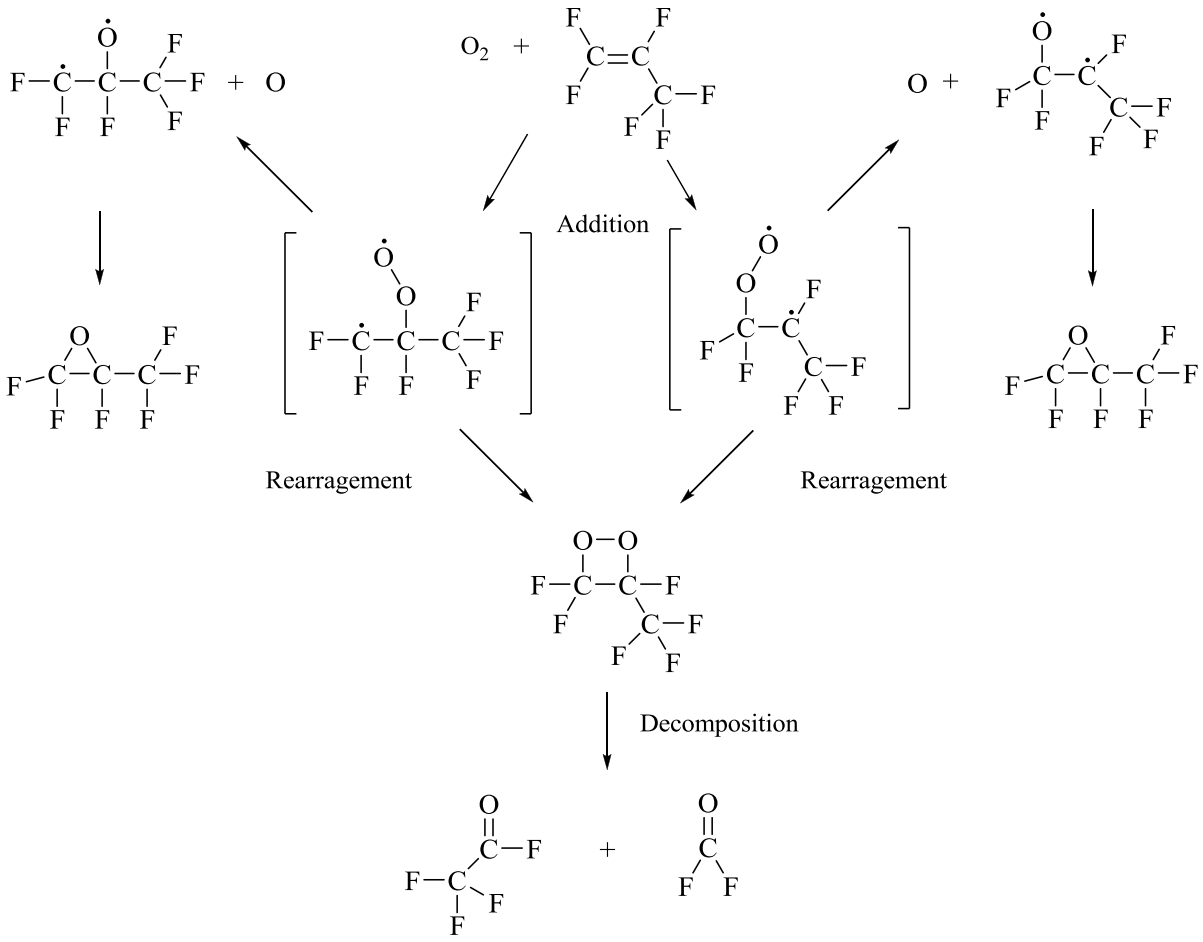

Scheme 2.5. Mechanism for the reaction of molecular oxygen with HFP at high temperatures, modified from Gilbert et al. (1976).

Apart from the set of free-radical reactions that are postulated to occur during the gas-phase oxidation of HFP, other reactions have been suggested to arise under high reaction temperatures. The thermal dimerization of HFP was considered by Hauptschein et al. (1957). They reported cyclic dimerization of the fluoroalkene at 623 K under a pressure of several hundred bar, with a 72% conversion to dimers after 5 hours. Under these conditions, three of the possible four dimers (cis and trans-perfluoro-[1,2-dimethylcyclobutane] and cis and trans-perfluoro-[1,3-

dimethylcyclobutane]) were produced. At 723 K under similar pressures, the highly toxic perfluoroisobutylene (PFIB) was formed. The lowest practicable temperature for dimer formation was found to be 523 K at high pressures but the reaction proceeded very slowly. The formation of cyclic dimers was also reported by Brown (1957), who investigated the thermal reaction of HFP at 673 K and pressures between 75 and 145 bar. It does not seem probable that thermal dimerization should affect the gas-phase epoxidation of HFP, which is normally carried out at much milder conditions that are favourable for partial oxidation. Thermal decomposition of HFP is also unlikely to occur below about 820 K (Matula, 1968).

2.3. Catalytic oxidation of HFP

2.3.1. Patented processes

The solid catalyzed, selective oxidation of HFP remains a largely unexploited route towards the higher valued epoxide product, HFPO. Much of the available information regarding the process is contained within the patent literature. None of the proposed patented methods, however, have achieved commercialization.

Cavanaugh (1973) described in an early patent a continuous process for the epoxidation of HFP with molecular oxygen over a heterogeneous silica catalyst. The silica gel required activation with a mixture of O_2 and HFP or with HFPO at temperatures between 473 and 553 K, for approximately two to five hours, before use. Pure silica gel was preferred (80 $m^2 g^{-1}$ to 200 $m^2 g^{-1}$) but other grades of glass were also tested. The catalyst was found to be suitable for epoxidation for a period of between 10-80 hours, after which HFPO was found to undergo rearrangement to hexafluoroacetone. The results of selected experiments conducted using a packed, stainless-steel tube with a bed volume of 90 cm^3, are presented in Table 2.6. Inlet volumetric flow-rates of HFP and O_2 were 20 and 10 $cm^3 min^{-1}$, respectively.

Table 2.6. Results of experiments using silica-based catalysts for the epoxidation of HFP (Cavanaugh, 1973).

Catalyst	Temperature [K]	HFP conversion [%]	HFPO selectivity [%]	Selectivity towards significant other product
Silica gel (Davison grade 02)	475	7	79	COF_2 - 21%
Silica gel (Davison grade 45)	518	20	45	COF_2 - 55%
Pyrex glass	448	52	37	CO_2 - 25%
Silica sand	473	43	42	CF_3COF - 42%

Atkins (1973) sought to improve on the work of Cavanaugh (1973). He included several new steps to the catalyst activation procedure previously described. The silica gel was first contacted with dilute hydrochloric acid, followed by water washing prior to treatment with HFP and O_2 as before.

A significantly greater selectivity towards HFPO was obtained from experiments conducted using a similar packed tube containing 90 cm^3 of catalyst (cf. Table 2.7). Inlet volumetric flow-rates of HFP and O_2 were once again 20 and 10 cm^3 min^{-1}, respectively.

Table 2.7. Results of experiments using pre-treated silica-based catalysts for the epoxidation of HFP (Atkins, 1973).

Catalyst	Temperature [K]	HFP conversion [%]	HFPO selectivity [%]	Selectivity towards significant other product
Silica gel (Davison grade 45)	473	15	80	CO_2 - 20%
Silica gel (Davison grade 05)	483	7	84	CO_2 - 16%

Oda et al. (1977 a) produced HFPO from HFP and O_2 in the presence of a silica-supported CuO catalyst. The synthesis was carried out continuously at 573 K in a fixed-bed reactor containing approximately 110 g of catalyst. The inlet volumetric flow-rates of HFP and O_2 were 30 cm^3 and 10 cm^3, respectively. A HFP conversion of 15% was achieved together with a HFPO selectivity of 30%. COF_2 was obtained as a by-product, at 60% selectivity. Oda et al. (1977 b) later used CuO supported on SiO_2-Al_2O_3 to synthesize HFPO. A HFP conversion of 29.1% and HFPO selectivity of 45.7% was obtained at the same set of experimental conditions. Selectivity towards COF_2 was 47.3%.

Ohsaka and Tohzuka (1981) described a continuous process for preparing HFPO by reacting HFP and O_2 in the presence of a barium compound that was pre-treated with nitrogen between 673 and 773 K. The results are presented in Table 2.8. All catalysts were tested at a HFP/O_2 molar feed ratio of 2.

Ratcliffe (1981) showed that halogenated epoxides could be prepared from the corresponding halo-olefins by interaction with an alkali or alkaline earth metal carbonate, an effective amount of moisture and elemental chlorine:

$$M_2CO_3 + Cl_2 + CF_3CF{=}CF_2 \rightarrow C_3F_6O + CO_2 + 2MCl \qquad (2.28)$$

where M=Na, K, Cs or Rb. Cs_2CO_3 was used for the synthesis with HFP. An elaborate experimental procedure was indicated. This included condensing Cl_2 and HFP into a glass vessel containing Cs_2CO_3 at 77 K and 4.1 bar gauge and then warming to room temperature. A conversion of HFP of 30-50% was obtained, together with a very high selectivity of 95.8% towards HFPO.

Table 2.8. Results of experiments using barium-based catalysts for the epoxidation of HFP (Ohsaka and Tohzuka, 1981).

Catalyst	Pretreatment	Temp. [K]	Catalyst charge [g]	Space velocity [h^{-1}]	HFP conversion [%]	HFPO selectivity [%]
Barium oxide	N_2 at 773 K	523	7.8	100	24.2	67.4
Barium sulphate	N_2 at 673 K	523	5.6	100	28.6	60.3
Barium carbonate	N_2 at 673 K	473	40	60	26.1	64.3
Barium oxide + barium fluoride	N_2 at 673 K	473	7.8	80	34.1	70.7

Castellan et al. (1992) described the reaction of HFP and O_2 over various silica-supported metal oxide catalysts. Each catalyst was activated using a mixture of 0.5% HF in N_2. Experiments were conducted using a conventional fixed-bed reactor fabricated from Incoloy, operating slightly above atmospheric pressure. The most significant by-product was COF_2. The results are presented in Table 2.9. Strong acid sites on the surface of the CuO/SiO_2-Al_2O_3 catalyst may catalyze the isomerisation and decomposition of HFPO, resulting in a much lower yield of the epoxide.

Table 2.9. Results of experiments using silica-supported metal oxide catalysts for the epoxidation of HFP.

Catalyst	HFP/O_2 ratio	WHSV [h^{-1}]	Temperature [K]	HFP conversion [%]	HFPO selectivity [%]
CuO/SiO_2	9:7	1.287	433	41.3	75.6
CuO/SiO_2	9:7	2.573	418	30	77
CuO/SiO_2	9:7	11.029	473	19.2	75.9
CoO/SiO_2	9:7	3.860	453	31	74.7
CeO/SiO_2	9:7	11.029	468	27.9	61.2
CuO/SiO_2-Al_2O_3	9:2	28.899	473	30	0.15

A comprehensive patent application was made by Zang et al. (2007) regarding the continuous, catalytic, gas-phase epoxidation of HFP. SiO_2, Al_2O_3, ZnO_2, TiO_2 and $CaCO_3$-supported Ag catalysts were tested, doped with various promoters, viz., potassium, caesium, calcium and barium. Experiments were carried out using a packed tube in the form of a coil. A catalyst comprising 30% Ag, 10% $BaCl_2$ and 60% SiO_2 gave a HFP conversion of 51.3% and the best selectivity of 70.2% at 393 K, with a HFP/O_2 molar feed ratio of 2 and at a total pressure of 2.5 bar.

Most of the methods proposed in the patents utilized a crystalline form of a porous silicon dioxide, often carrying a well dispersed metal oxide, as the catalyst. These required some form of pre-treatment, in the simplest case heating under N_2. Exposure to HCl and mixtures of HFP and O_2 were also recommended. The pure silica catalyst of Cavanaugh (1973) and Atkins (1973) suffered from rapid deactivation, a problem that was alleviated to some extent by the addition of the transition metal oxide (Oda et al., 1977 a; Castellan, 1992). The preferred metals were copper, cobalt, cerium and chromium (Castellan, 1992). Operating temperatures close to and beyond the epoxide decomposition temperature were still required, however, resulting in low HFPO yields.

2.3.2. Non-patented processes

There are a small number of non-patented catalytic processes discussed in the open literature, relating to the oxidation of HFP. These are focused primarily on the complete oxidation of HFP as well as production of hexafluoroacetone. The noble metals (Pd, Pt, Rh, Ru and Ir) supported by activated carbon, have been found to be highly active and selective catalysts for the preparation of HFA via the gas-phase oxidation of HFP (Kurosaki and Okazaki, 1988). The reaction also proceeds over the oxides of tin, iron and indium or fluorinated aluminium oxide as well as alkali metal fluorides NaF, KF, CsF or RbF supported by activated carbon (Igumnov et al., 2001).

Faris et al. (1992) investigated the deactivation of a Pt/Al_2O_3 catalyst used for the complete oxidation of HFP in humid air, at temperatures between 573 and 673 K. The concentration of HFP in the feed gas was between 500 and 4500 ppm. Surprisingly, the only product detected in the reactor effluent was CO_2 and no fluorine containing products were found. Several important conclusions were drawn from a thorough examination of reactivity data, catalyst surface area and X-ray photo-electron spectroscopy (XPS) spectra. Irreversible poisoning of the platinum metal via fluorine adsorption was suggested. The loss of platinum surface was also reported. This was

proposed to be due to migration of the platinum metal resulting in sintering or support degradation. Most importantly, decomposition of the alumina support by hydrofluoric acid, formed during the reaction, was observed and the detrimental effect of the presence of water in the system was highlighted.

Fan and Yates (1994) studied the complete oxidation of HFP over TiO_2 in a static cell equipped with CaF_2 windows for in-situ infrared spectroscopy, with particular emphasis being placed on the role of the solid. No transition metals were displaced on the TiO_2. The complete oxidation of HFP over TiO_2 was found to occur at 673 K to yield CO_2 and CO. HF was also produced from residual surface hydroxyl groups on the catalyst. The role of TiO_2 in the oxidation of HFP was postulated to to be one, or a combination of the following three: (1) as a catalyst that lowers the activation energy of the reaction so that it may proceed easily, (2) as a reactant, supplying lattice oxygen or (3) as a medium facilitating heat transfer to the gaseous reactants, promoting oxidation in the gas-phase. In the latter case, TiO_2 would provide a large surface area to increase thermal contact between the gaseous reactants and the heated surface. This increases the average gas temperature and hence the fraction of molecules with sufficient energy for the homogeneous reaction. The last possibility would imply that any porous solid could be used. The oxidation of HFP over TiO_2 was ultimately found to follow the conventional Mars-van-Krevelen redox cycle which involves both lattice and gaseous oxygen. The overall reaction can be written as:

$$C_3F_{6\,(g)} + O_{2\,(g)} + 2TiO_{2\,(s)} \xrightarrow{673\ K} 2CO_{2\,(g)} + CO_{(g)} + TiF_{4\,(g)} + TiOF_{2\,(s)} \qquad (2.29)$$

The fluoroacetate $CF_3COO\bullet$ was found to be an important reaction intermediate on the TiO_2 surface. The formation of TiF_4 resulting from the interaction of HF with the surface of the solid TiO_2, was suggested to be responsible for the consumption of titanium.

The use of silver, supported on γ-Al_2O_3, as an epoxidation catalyst for HFP was studied by Huang et al. (2006). Using air as the oxygen source, an air to HFP ratio of 2 and a total inlet flow-rate of 2.5 $cm^3\ min^{-1}$, it was found that an optimum metal loading of 10 wt% Ag on γ-Al_2O_3 gave a HFPO selectivity of 41.1% and a HFP conversion of 12.3%, in a fixed-bed reactor containing 10 g of catalyst. When a caesium doped Ag/Al_2O_3 catalyst (100 ppm Cs) was used, it was observed that the activity (in terms of the conversion of HFP) and selectivity towards HFPO improved to 16.5% and 47.8% respectively. Increasing the ratio of air to HFP to 10 resulted in an increase in conversion but a decrease in selectivity.

2.3.3. Development of catalysts for epoxidation

A partial oxidation catalyst is designed to promote oxygen insertion within a reactant molecule, yet inhibit further oxidation that would give complete oxidation products (Gates et al., 1979). In non-catalytic systems, the O=O bond is generally stronger than most other bonds that are present in the reactant to be oxidized and oxidation reactions are initiated with the scission of a bond in the reactant molecule, resulting in radical formation. These radicals then attack molecular oxygen.

Catalytic oxidation reactions, however, proceed through a number of different mechanisms. The most important for hydrocarbon olefins involves the abstraction of a hydrogen atom resulting in an allylic surface-bound intermediate, which is a reactive radical stabilized by resonance (Gates et al., 1979). Alternatively, proton acceptance can lead to the formation of oxidizable carbonium ions. The transfer of electrons and protons are facilitated by surface species, which may include electrophilic metal ions. Occasionally, two different metal ions are employed, one to attack the molecule to be oxidized and the other to interact with O_2 and facilitate electron transfer between cations (Gates et al., 1979).

The oxygen that is introduced into the molecule is not necessarily derived directly from the O_2 in the system, but may come from a surface intermediate or the lattice structure of the catalyst (Gates et al., 1979). Often, the Mars-van-Krevelen redox mechanism is used to explain partial oxidation reactions catalyzed by surface oxides. The Mars-van-Krevelen mechanism of catalytic oxidations over metal oxides is a redox mechanism involving both gas-phase and lattice oxygen:

$$MO + R \rightarrow RO + M \tag{2.30}$$

$$2M + O_2 \rightarrow MO \tag{2.31}$$

where M is a metal cation and R is a reactant (Spivey, 1987). The reactant is first oxidized via reaction with the oxide, which in turn is reduced. Thereafter, the reduced oxide reacts with O_2 to restore its initial state. Thus, in the Mars-van-Krevelan mechanism, the oxidizing agent is presumably O^{2-} from the lattice. The tendency of the oxide to donate its' oxygen is of major importance in determining whether it is a selective partial oxidation catalyst. If reduction of the oxide is easy, then the catalyst will be active and non-selective. On the other hand, difficult

dissociation of O_2 because of a strong metal-oxide bond would be indicative of a catalyst exhibiting low activity and possibly high selectivity (Gates et al., 1979).

Two types of conventional catalysts are used for oxidation reactions i.e. metal oxides and noble metals, both supported and unsupported. Metal oxide catalysts, including single and mixed metal oxides (i.e. the oxides of metals occurring in groups three to twelve of the periodic table) are characterized by high electron mobility and positive oxidation states (Spivey, 1987). They are generally less active than noble metals but more resistant to poisoning. These oxides can be further classified by the stability of the oxide. Those forming the most stable oxides are the alkali and alkali earth metals such as Sc, Ti, V, Cr and Mn together with the rare earth metals as well as the actinides Ge, In, Sn, Zn, Al (Spivey, 1987). The oxides with intermediate stability include Fe, Co, Ni, Cd, Sb and Pb. Unstable oxides are formed from the noble metals Ru, Rh, Pd, Pt, Ir, Au and Ag. The metals that do not form stable bulk oxides remain as reduced metals during oxidation reactions at moderate temperatures. The mechanism of oxidation over these metals involves only molecular O_2, whereas for metals forming stable oxides lattice oxygen can also be involved in the oxidation reaction (Spivey, 1987). There also exists some optimum level of metal-oxygen content in an oxide catalyst. For metal oxide catalysts, the catalytic activity has been found to be inversely related to the strength of the chemisorption of the reactant and O_2 (Spivey, 1987), as was pointed out earlier.

The metal oxide catalysts are generally divided into three groups with respect to their activity, *viz*. n-type semiconductors, p-type semiconductors and insulators (based on electrical conductivity). The n-type materials are not generally active oxidation catalysts, with the exception of V_2O_5 (Spivey, 1987). P-type semiconductors are generally active and insulators are often used as catalyst supports. Due to the different electrical and chemical properties of n-type and p-type oxides, n-type oxides lose oxygen upon heating in air, whereas p-type oxides gain oxygen. Also, the less stable the metal oxide is, the more easily the surface is reduced to form oxygen adsorption sites (Spivey, 1987). The difference in reaction conditions is a direct result of the interaction with oxygen at reaction conditions. Oxygen adsorption occurs far more readily on p-type oxides. On n-type oxides, oxygen adsorption occurs only on a pre-reduced surface (Spivey, 1987).

The activity of a catalyst for complete oxidation may be related to the type of oxygen available on the surface of the metal. The existence of O_2^-, atomic O^- and regular O^{2-} ions in the oxide lattice is

well known (Spivey, 1987). It has been shown that the interaction of gaseous diatomic oxygen with an oxide surface proceeds through the following steps:

$$O_{2\,(g)} + e^- \rightarrow O_2^- \tag{2.32}$$

$$O_2^- + e^- \rightarrow 2O^- \tag{2.33}$$

$$O^- + e^- \rightarrow O^{2-} \tag{2.34}$$

where O^{2-} is directly incorporated into the oxide lattice (Spivey, 1987). Bond (1974) suggests that for partial oxidation reactions, selective oxidation is dependent only on the lattice oxygen. Weak metal-oxygen bonds i.e. low energies of oxygen binding to the oxide surface are necessary for catalysts that completely oxidize reactants. Oxidation on n-type oxides is thought to involve lattice oxygen, while on p-type oxides the reaction involves adsorbed oxygen. Concluding, it may be stated that some of the n-type oxides can be used for partial oxidation reactions (Spivey, 1987).

Oxidation over noble metals may follow either a Langmuir-Hinshelwood type mechanism (reaction between adsorbed oxygen and adsorbed reactant) or an Eley-Rideal mechanism (reaction between adsorbed oxygen and a gas-phase reactant molecule). However, on Ag, oxygen chemisorption is relatively strong, with a transfer of electrons to the oxygen taking place. This implies that the reaction mechanism on Ag involves a redox mechanism similar to that for metal oxides. By comparison, oxygen adsorption on Pd is relatively weak and anionic surface oxygen species do not exist. In this case the metal surface may provide an energy modifying function (Spivey, 1987). The most commonly applied catalysts and catalyst components for selective oxidation reactions include V_2O_5, MoO_3, Bi_2O_3, WO_3, PbO and CuO (Gates et al., 1979). These catalysts have been employed for various hydrocarbon partial oxidation processes but have not been tested for fluorocarbon systems. Other possible catalysts are Cr_2O_3, as well as the pure metals Co, Mo, Ni and Ag.

A more recent review of heterogeneous alkene epoxidation by Lambert et al. (2005) considered the most successful candidates for epoxidation catalysts in the context of commercial applications. The technical process of ethylene epoxidation employs a catalyst consisting of silver particles supported on α-Al_2O_3 with the addition of ppm levels of a gaseous chloro-carbon that acts to moderate activity and enhance selectivity. A small amount of alkali is also added to the catalyst to enhance selectivity. Even though the process has been used extensively, the reaction mechanism is still not

fully resolved. The two opposing views are that a) adsorbed diatomic oxygen is the epoxidizing agent whereas dissociatively adsorbed oxygen atoms (O_a) are responsible for combustion and b) all chemistry is due to O_a, thought to undergo either Eley-Rideal or Langmuir-Hinshelwood reactions with ethylene, resulting in epoxidation or combustion, respectively. The general consensus now is that dissociatively adsorbed oxygen atoms are responsible for selective oxidation. The selectivity promotion by Cl is primarily an electronic effect and not just a steric or geometric effect (e.g. Cl adsorbed atoms simply blocking the dissociative chemisorption of oxygen, inhibiting formation of O_a which was erroneously suggested to be an unselective oxidant. In fact, the halogen depletes the valence charge density on O_a rendering it more electrophilic and thus favouring oxygen insertion into the C=C bond (epoxidation) over C-H bond cleavage (combustion). An important observation was that the higher the oxygen coverage on the surface of the catalyst, the lower was the valence charge density on any given O_a, favouring epoxidation.

Gold on titanium trioxide (Au/TiO_3) has been shown to catalyze propylene epoxidation. The titanium containing oxide appears to play an important role in the reaction mechanism, possibly as a source of oxygen species for the selective oxidation. The minimum necessary conditions for epoxidation appear to be the formation of two surface species: π-adsorbed alkene and O_a. Copper should thus be an effective epoxidation catalyst, since these conditions are achieved, unlike other transition metals where the alkene undergoes strong rehybridization of the C=C bond upon adsorption (Cropley et al., 2005). The usefulness of copper as a selective oxidation catalyst has only recently been studied. It has been deduced from the minimal work that has been conducted that copper generally delivers higher epoxidation selectivities than silver for a number of alkenes (Cropley et al., 2005). However, at sufficiently high oxygen coverages, nucleation and growth of copper oxide occurs which results in a drop in selectivity and increased combustion.

The suitability of copper as a selective catalyst for the epoxidation of propylene was also investigated by Vaughan et al. (2005). They reported that metallic copper was also selective in inducing epoxidation of styrene. Low adsorption enthalpies for both ethylene and propylene were found. Interestingly, they also found that at the reaction temperatures used in their study (i.e. below 523 K), Cu^0 was the predominant surface species. Between 523 and 623 K, Cu_2O forms and 623 K represents the temperature for the onset of CuO formation. Earlier studies concluded that CuO catalyzes the combustion of propylene, whereas Cu_2O favours partial oxidation to acrolein but these results appeared to indicate that Cu^0 is associated with propylene epoxidation.

Jankowiak and Barteau (2005) found that Cu-Ag bimetallic catalysts were approximately 1.5 times more selective than pure silver catalysts at optimal copper loadings for the epoxidation of ethylene. The bimetallic catalyst was also more active for the reaction. The major effect of copper, as concluded by the authors, was to further lower the activation barrier for dissociative oxygen adsorption, which is beneficial to epoxidation.

Choudhary et al. (2007) reported that unsupported simple CuO and supported CuO, particularly CuO/Ga_2O_3, CuO/SiO_2 and CuO/In_2O_3 are highly active and selective heterogeneous catalysts for the epoxidation of styrene. Monnier and Hartley (2001) have, however, found that Cu is not capable of functioning as an epoxidation catalyst for the selective oxidation of butadiene, possibly due to readsorption of the epoxide product on the surface and subsequent decomposition.

Wang et al. (2008) showed that a K^+-doped CuO_x/SBA-15 catalyst exhibited outstanding catalytic performances in the epoxidation of propylene by oxygen. They found that copper was unique for this reaction among the many transition metals that were investigated and that K^+ was the best modifier for propylene oxide formation among the various alkali and alkaline earth metal ions that were tested.

The main characteristic differentiating perfluorinated compounds from hydrocarbons is the higher bond dissociation energy of C-F bonds relative to C-H bonds (Zachariah et al., 1995; Cordishi et al., 1964). The intrinsic C-C bond strength is also weaker for the former. Consequently, the surface chemistry for the oxidation of perfluorinated compounds can be very different to that of hydrocarbon analogues. The difficulty associated with fluorine atom abstraction makes non-insertion reactions, with oxygen derived from the lattice structure, likely to be responsible for the oxidation of perfluoroolefins over solid oxide catalysts.

The active components of partial oxidation catalysts are often accompanied by various promoters and inhibitors that improve the catalyst activity and selectivity. Small amounts of alkali metals doped on the surface of partial oxidation catalysts have been found to dramatically improve their performance and lifetime (Doskocil and Mueller, 2005).

Caesium is the preferred promoter for the epoxidation of ethylene and butadiene over Ag/Al_2O_3 (Monnier et al., 2004). The role of electropositive promoters in the selective oxidation of hydrocarbons such as these is not fully understood, although a number of different mechanisms

have been proposed. For the synthesis of ethylene oxide over Ag/Al_2O_3, Caesium was proposed to act as a binder between Al_2O_3 and Ag crystallites, resulting in less exposed Al_2O_3. The rate of Al_2O_3-catalyzed isomerisation to acetaldehyde and combustion to CO and H_2O is thus lowered (Monnier et al., 2004). Carter et al. (1989) presented an opposing view, suggesting that the promotion effect of caesium is not due to site blockage, but is electronic in nature. Caesium was proposed to increase activity by improving adsorption of ethylene as well as render the adsorbed molecule more readily accessible for interaction with nearby oxygen radicals. An increase in selectivity was thought to be brought about by the manner in which caesium modifies the bonding of ethylene to the catalyst surface, inhibiting the direct combustion pathway. Alternatively, caesium may lower the desorption energy of the olefin epoxide when doped to the catalyst surface, thereby reducing the possibility that the molecule would undergo further oxidation (Doskocil and Mueller, 2005).

The effect of alkali metal ions, including caesium, on the epoxidation of propylene has also been investigated (Jin et al., 2003). The addition of these electron-donating components to the catalyst surface reduced the electrophilicity of the oxygen species adsorbed on the metal, which were originally active in complete oxidation (Bulushev et al., 2000). An improvement in both activity and selectivity has also been reported or the epoxidation of HFP over caesium promoted Ag/γ-Al_2O_3 (Huang et al., 2006).

An important mechanism to consider in the alkali metal doping of supported metal-oxide catalysts is the possible ion-exchange of alkali metal ions with hydroxyl groups on the support surface (Millar and Rochester, 1996). The neutralization of the acidic support may result in improved selectivity due to the reduction in the rates of isomerisation and combustion reactions that were likely catalyzed by strong acid sites that were prevalent in the un-doped catalyst (Lambert, 2005). In cases were epoxidation proceeds through an oxidation-reduction mechanism, which is likely for perfluoroolefins (Fan and Yates, 1994), alkali metal ions may still play a role as a promoter. Traces of potassium have been found to improve the redox ability of cobalt-cerium composite oxide catalyst and thus catalytic activity (Xue et al., 2009).

2.4. Summary of available technologies for the epoxidation of HFP

Table 2.10 lists the most popular commercial processes for the epoxidation of HFP. All currently utilized methods are non-catalytic and are carried out batch-wise. Note that none of the proposed continuous catalytic processes presented in section 2.3 have achieved commercialization due to limited through-put and rapid catalyst degradation.

Table 2.10. Currently utilized commercial processes for the production of HFPO.

Type	Oxidizer	Temperature [K]	Pressure [bar]	X_{HFP} [%]	S_{HFPO} [%]	Y_{HFPO} [%]	Operating costs	reference
Nucleophilic synthesis, batch single liquid phase	Hydrogen peroxide	233	20-40	100	35-52	35-52	Moderate	Millauer et al., 1985
Nucleophilic synthesis, batch two-liquid phase	Aqueous sodium hypochlorite	273-293	20-40	100	70-86	70-86	Very high	Millauer et al., 1985; Ikeda et al., 1990
Radical synthesis, batch single liquid phase[a]	Oxygen	373-473	40-100	100	50-70	50-70	High	Furin, 2006
Radical synthesis, batch single liquid phase[b]	Oxygen	353-363	1-20	67-77	60-78	40-60	High	Furin, 2006; Shoshin et al., 1999

[a] Thermally initiated, carbon tetrachloride solvent.

[b] Chemical initiated (CF_3OF), F113 solvent.

Chapter 3
Experimental

3.1. Equipment

3.1.1. Non-catalytic oxidation of HFP.

The gas-phase, non-catalytic oxidation of HFP using molecular oxygen was carried out in a tubular reactor operating under laminar-flow conditions. The reactor was fabricated from $^{1}/_{8}$ inch, nominal size, copper refrigeration tubing. The total length of the reactor tube was 150 m. The reactor was used in the form of a helical coil. Such a coil was formed from straight 37.5 m lengths of tubing, by bending into the coil shape and joining the coiled tubes end-to-end to form the helix. Standard Swagelok compression unions were used to join the individual lengths of tubing. The entire reactor tube consisted of four such helices, with a coil radius of 25 mm each (cf. Photographs 3.1 and 3.2).

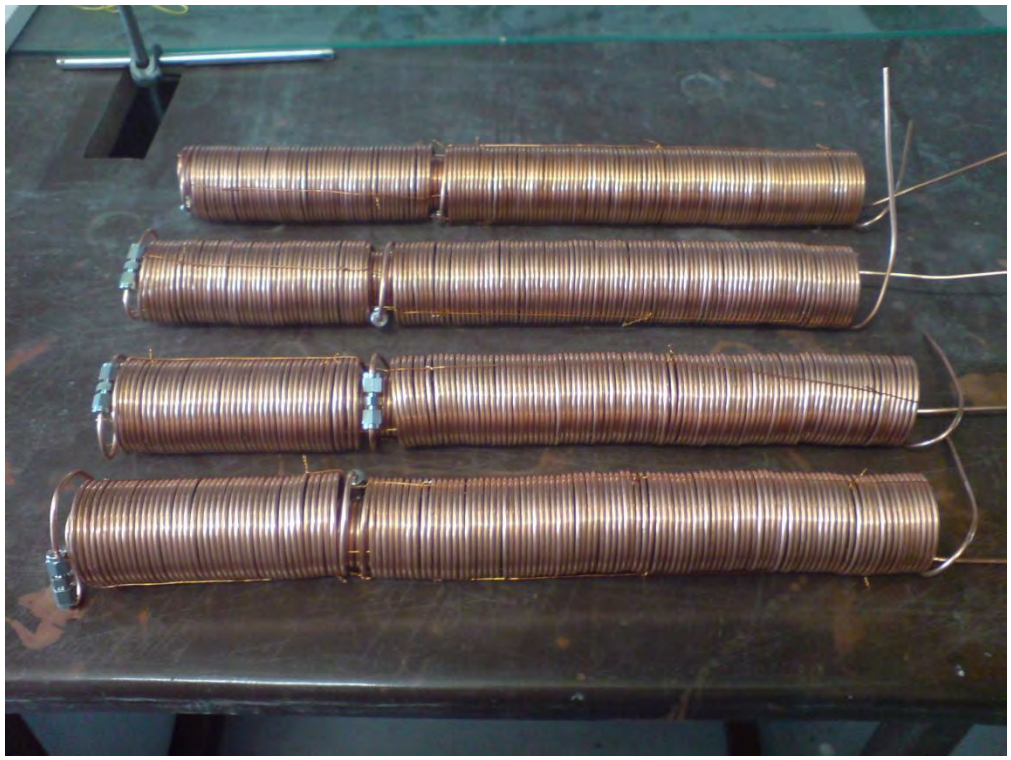

Photograph 3.1. Hand-wound copper reactor coils prior to installation.

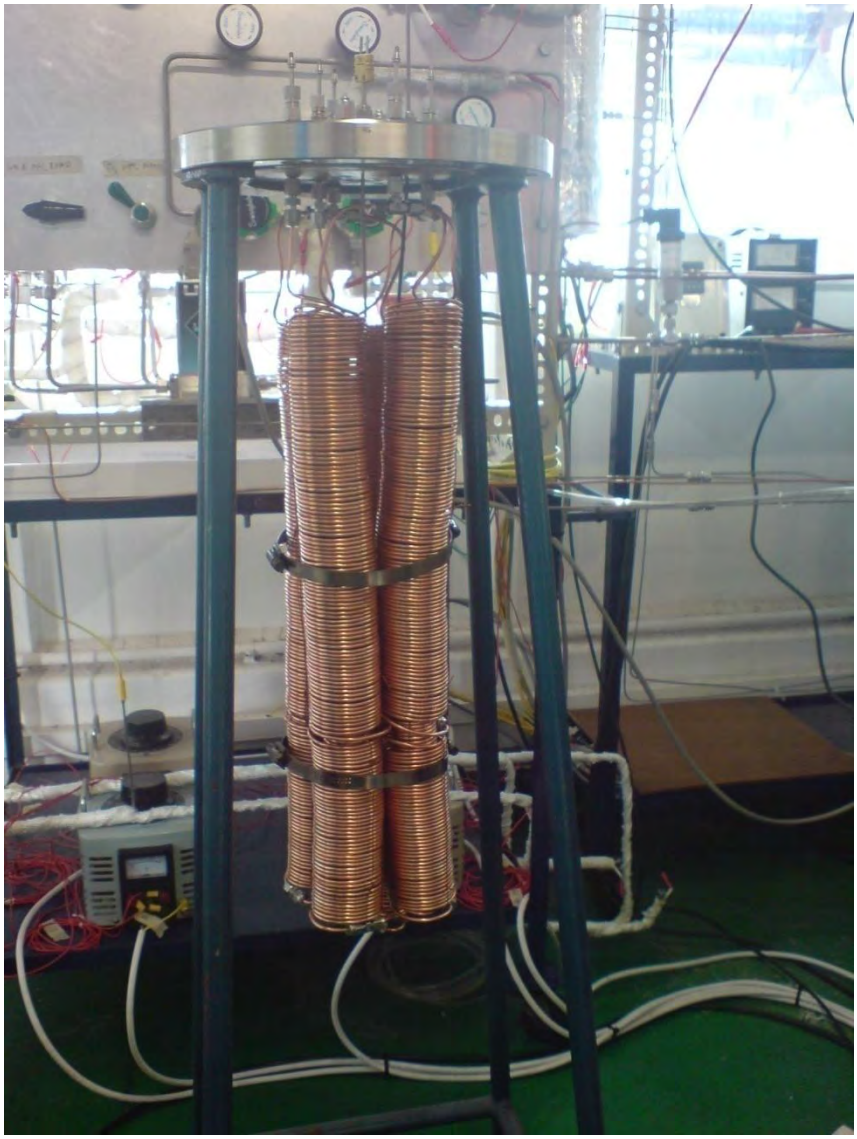

Photograph 3.2. Copper reactor coils fixed to the top blind-flange of the stainless steel heating jacket.

A Swagelok 5-way switching valve was connected to the end of each of the coiled sections and was used to vary the effective length of the reactor tube. The total length of copper tubing used in the experiments was 114.3 m, which represented 3 of the 4 installed coils. The set of reactor coils was immersed in a sealed, stainless steel jacket containing a eutectic heat transfer fluid (Julabo Thermal HS). The jacket was insulated with layers of glass fibre and mineral wool, secured by a sheet of insulation foil. The heating jacket was fabricated from a length of 6-inch, schedule 40, 304L stainless steel pipe, equipped with a welded dished end and a top blind-flange. The flange was drilled and tapped and secured with six M30 bolts. Each of the coiled sections had a compact vertical height of 60 cm once mounted to the top blind flange of the stainless steel heating jacket.

An external oil-bath heater/circulator was used to raise and maintain the temperature of the reactor coils. Type K thermocouples were inserted 200 mm into the reactor tube at the inlet and exit, as well as at the centre of the reactor coils along the outer wall, to monitor the reaction temperature. The measurement probes were calibrated using a Fluke 9103 dry-well calibrator (cf. Appendix A). The reactor had an internal surface-to volume ratio of 2667 m^{-1} and the volume of the reaction zone was 2.019×10^{-4} m^3. The fully commissioned reactor is shown in Photograph 3.3.

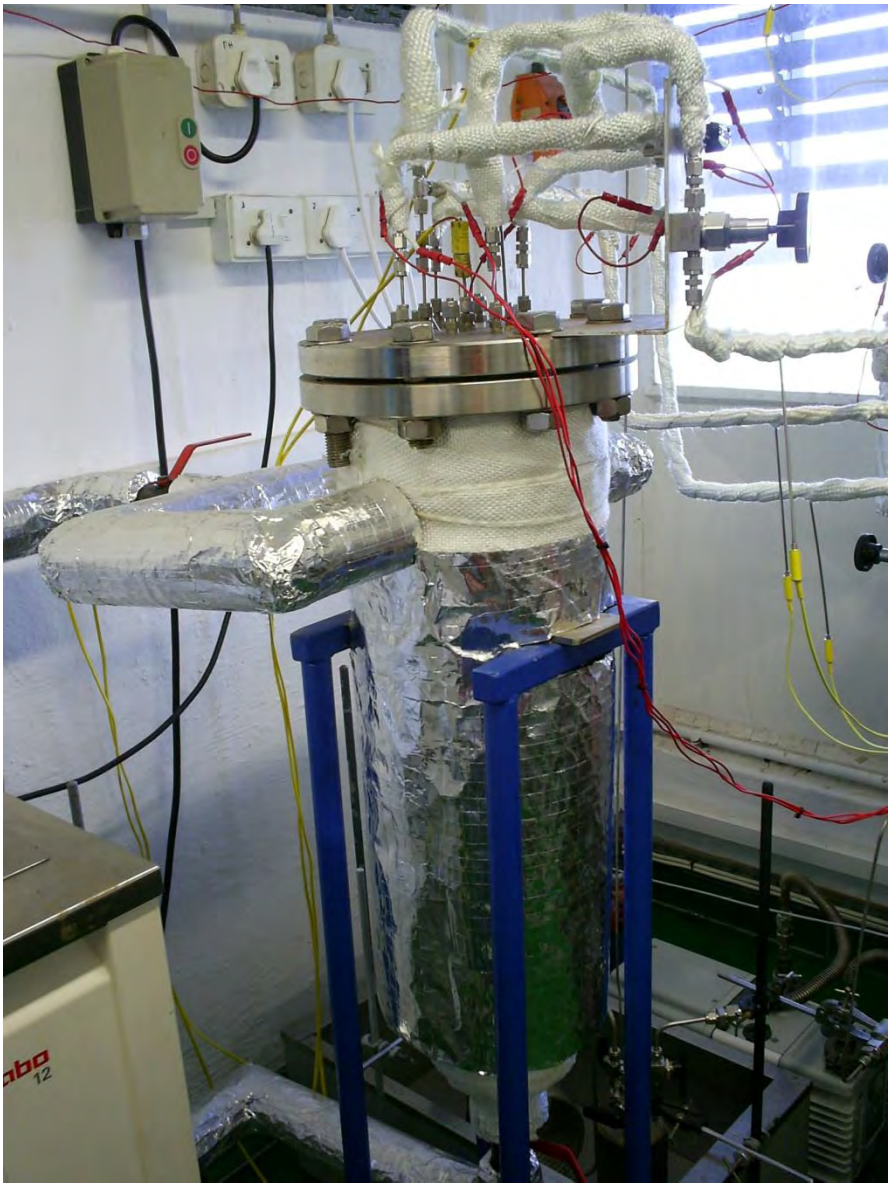

Photograph 3.3. Fully commissioned laminar flow HFP oxidation reactor.

A simplified schematic of the pilot-scale HFP oxidation apparatus is presented in Figure 3.1, showing the most important components of the system. A detailed piping and instrumentation diagram is given on the next page. All process piping was either $^1/_4$ or $^1/_8$ inch stainless steel instrumentation grade tubing. The reactants were continuously fed via separate lines into one end of the reactor tube and the reaction products were withdrawn continuously from the exit end. The oxidation in the reaction zone was executed under isothermal conditions and at an average total pressure between 1 and 4.5 bar. The pressure drop over the reactor tube was generally less than 10% of the total operating pressure. A stainless steel catch-pot was placed at the exit of the reactor to collect possible oligomeric liquid products. The catch-pot had an internal volume of 500 ml, was maintained at a temperature of 100 °C using a band-heater and was equipped with a drain valve. A back pressure regulator (GO Regulators, USA) was installed on the exit line to maintain a constant pressure in the reactor. This pressure was measured using a Wika P10 precision pressure transmitter.

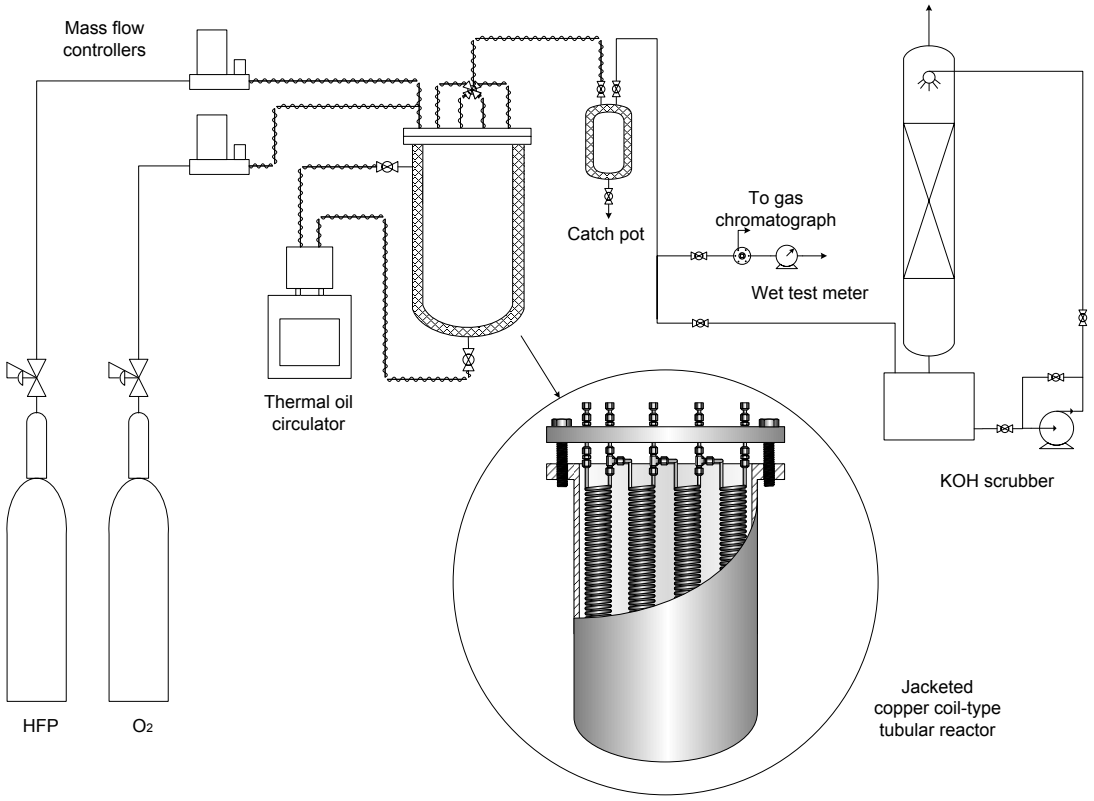

Figure 3.1. Schematic of the non-catalytic HFP oxidation apparatus, showing detail of the coil-type reactor (inset).

The flow-rate of HFP was controlled using a Celerity 1660 thermal mass-flow controller (accuracy: ± 1% of full-scale, 1 l min^{-1} at STP). The flow-rate of oxygen was controlled by means of a Bronkhorst El-flow thermal mass-flow controller (accuracy: ± 0.5% of reading ± 0.2% of full scale, 1 l min^{-1} at STP). The pressure at the inlet for both controllers was maintained at 6 bar. The feed gas flow-rate was checked using a drum-type wet-test meter from Ritter GmBH (model TG05), containing an inert perfluorinated packing liquid (Galden, Solvay Solexis). The same instrument was used for product gas flow-rate measurements. The calibration plot for the oxygen flow controller appeared to follow closely the manufacturer's specifications (cf. Appendix A). The HFP controller provided constant flow at higher than expected values, possibly due to the higher than recommended inlet pressure, which is a source of zero error on mass-flow controllers operating with high density, low viscosity gases. This was not a major concern since the flow-rates were measured independently using the wet-test meter. No manufacturer's calibration was available for the HFP controller. A helium or nitrogen sweep was admitted on the oxygen feed line from standard cylinders equipped with multistage forward pressure regulators. This flow was not controlled. A controlled flow of nitrogen was provided via a switching valve on the HFP feed line, using the HFP mass-flow controller. The total pressure on the combined feed line was measured using a Wika S10 pressure transmitter (0-40 bar).

A Coriflow coriolis mass-flow controller (Bronkhorst B.V.) was also installed on the HFP inlet line together with an electrically heated vaporization tube. These two items were intended for use with liquid HFP under a pressure of 30 bar, enabling system operating pressures in excess of 6.5 bar which is the vapour pressure of HFP at room temperature and the available gas bottle pressure. An appropriate feed vessel, rated at 214 bar and equipped with a dip-tube and helium padding-gas inlet line, was constructed but was not used. The vaporization tube was fabricated from a 500 mm length of 2 inch nominal size stainless steel pipe equipped with internal fins. The tube could be maintained at 100 °C using a series of band heaters and was insulated with preformed sections of mineral wool and covered by insulation foil. By installing a back-pressure regulator (GO Regulators, USA) on the vaporization tube, any pulsations due to uneven vaporization, which are common at low flow-rates, were eliminated (Harrison et al., 1965).

The reactor effluent was directed through a system of parallel, heat-traced tubes, all terminating at the entrance of an off-gas scrubber. The path of the exit gas was altered by switching different pairs of air-actuated, bellows-sealed valves (Swagelok SS-4BG-3C). On the first line the Ritter wet test meter was installed, together with a pressure reducing valve, a Wika S10 pressure transmitter (0-1

bar) and a pressure relief valve (0.5 bar gauge) connected to a vent line. Accurate temperature and pressure measurements were made using a Pt-100 temperature probe and an absolute pressure transducer (Sensotec TGE 0-25 psia) mounted at ports provided on the meter (cf. Photograph 3.4).

Photograph 3.4. Ritter drum-type wet-test meter (model TG05) used for the measurement of feed and product-gas volumetric flow-rates.

The second line contained another pressure reducing valve, a Shimadzu 6-port, pneumatically-driven sample valve that was used to direct a portion of the reactor effluent to a gas chromatograph for analysis. This line was also equipped with a Pt-100 probe and an absolute pressure transducer (Sensotec Super TGE 0-100 psia). A vacuum pump was installed on the third line, which was used to evacuate the system during the pressure/vacuum purge cycle undertaken, before and after each experiment. The fourth line led directly to the off-gas scrubber and was the one usually open during the course of an experiment. All inlet and outlet piping was heat traced using nichrome wire covered by a glass-fibre sheath and further insulated using woven glass cloth. Power to the heating

wires was provided by four 250V/3A variable voltage transformers. The various pressure regulating valves, isolation valves, switching valves and mass flow-controllers were all mounted on a Dexion instrument frame furnished with an aluminium valve panel, shown in Photograph 3.5.

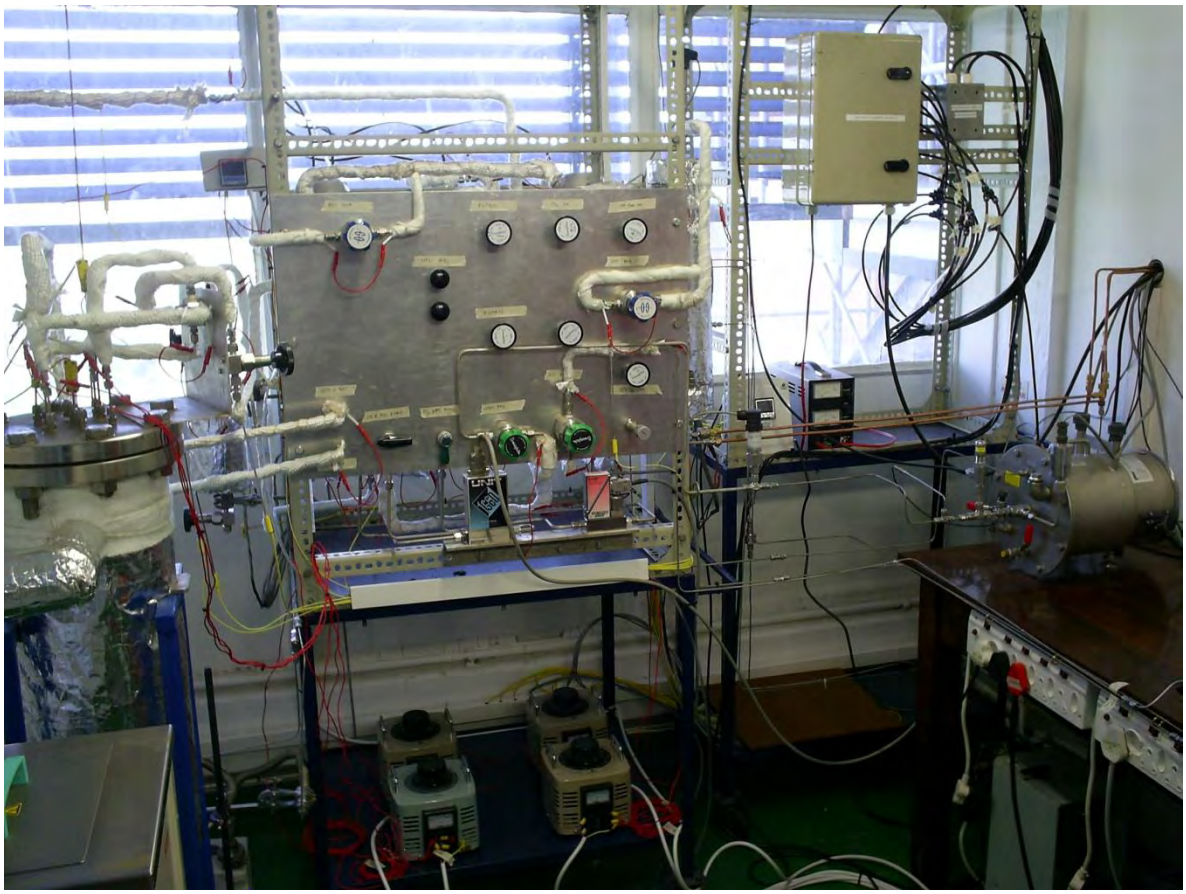

Photograph 3.5. Reaction system valve panel (centre), bank of variable voltage transformers (bottom), coil type reactor (left) and wet-test meter (right).

All measurements obtained from the Wika pressure transmitters and the type K thermocouples mounted on the reactor were displayed on Shinko JCS 33A controller units. The Pt-100 probes were connected to a Toho TTM4 controller via a selector switch and the Sensotec pressure transducers were linked to Sensotec GM signal conditioning-indicating units. The various display units and controllers were mounted in a Siemans electrical enclosure. Photograph 3.6 shows a view of the experimental apparatus from inside the control room, where data logging was performed. Photograph 3.7 shows the various display units and controllers that were used to control the oxidation process and monitor critical system parameters.

Photograph 3.6. View of the non-catalytic HFP oxidation apparatus, from the control room.

The Pt-100 probes were calibrated using a Wika CTB 9100 oil-bath and a standard Pt-100 probe connected to a Wika CTH 6500 display unit (cf. Appendix A). The transducers/transmitters responsible for critical pressure measurements (reactor inlet/outlet transmitters, wet-test meter transducer and gas chromatograph sample loop transducer) were calibrated using a combination of a Wika PCS-H 250 hand-pump pressure calibrator and a Wika CPP 1000 M/L hydraulic test pump (cf. Appendix A).

The off-gas scrubber that was used to scrub the reactor effluent, prior to venting, consisted of a packed column, a liquid reservoir and a scrubber solution circulating pump. The column, fabricated from polypropylene, was 2 m high and was packed with 20 mm nylon Pall rings. The liquid reservoir at the bottom of the column had a capacity of 25 litres and was usually maintained 75% full, charged with a 20 wt% aqueous solution of potassium hydroxide. This solution was circulated through the column via a high flow-rate centrifugal pump.

Photograph 3.7. HFP oxidation apparatus display and control units.

The normal operation of the caustic scrubber was often hindered by excessive foaming, which was typically observed at least 27 hours after replacing the potassium hydroxide solution with a fresh charge (in terms of experimental run time). The liquid in the reservoir was still found to be highly alkaline at that stage. In an aqueous solution of potassium hydroxide, CF_3COF and COF_2, the major by-products from the oxidation of HFP, first undergo hydrolysis to yield HF as well as CF_3COOH and CO_2, respectively (Wallington and Nielsen, 2002; Igumnov et al., 2001):

$$CF_3COF + H_2O \rightarrow CF_3COOH + HF \quad (3.1)$$

$$COF_2 + H_2O \rightarrow 2HF + CO_2 \quad (3.2)$$

Each of these hydrolysis products are expected to interact with KOH in the following manner:

$$KOH + HF \rightarrow KF + H_2O \quad (3.3)$$

$$KOH + CF_3COOH \rightarrow CF_3COOK + H_2O \quad (3.4)$$

$$2KOH + CO_2 \rightarrow K_2CO_3 + H_2O \quad (3.5)$$

The hydrolysis of HFP is not expected to be strong, due to the lack of hydrolyzable functional groups (Meylan and Howard, 1993). Both trifluoroacetic acid and potassium trifluoroacetate are able to modify the surface tension of aqueous solutions. These surfactants were thus judged to be responsible for the observed foaming. The addition of small quantities of a thermally stable and alkali-resistant anti-foaming agent (SE-30, Sigma-Aldrich) did not resolve the issue. Of major concern was the presence of aqueous potassium hydroxide solution in the stainless-steel scrubber inlet piping, which was due to back-flow caused by the build-up of foam inside the scrubber column. Rapid corrosion of the inner walls of the inlet tube was observed. Photograph 3.8 shows the extent of corrosion on a stainless steel fitting that was originally connected directly to the head of the scrubber reservoir.

Photograph 3.8. Corrosion of stainless-steel tubing connected directly to the caustic scrubber unit.

A transparent, polypropylene guard-column was installed (cf. Photograph 3.9), to protect the metal line from the possible back-flow of caustic solution and to serve as a visual indication of excessive foaming in the scrubber unit.

Photograph 3.9. Installation of a transparent, polypropylene guard column at the inlet of the caustic scrubber unit.

3.1.2. Catalytic oxidation of HFP

The gas-phase catalytic oxidation of HFP was carried out using a laboratory-scale, fixed-bed reactor, operating under isothermal conditions. The reactor was a 430 mm long, thick-walled, copper tube with an internal diameter of 9 mm. A similarly sized tube was used successfully by Huang et al. (2006) for the catalytic oxidation of HFP. The reactor tube used in this work was surrounded by an oil-jacket fabricated from a length of 4-inch carbon steel pipe equipped with two 150(PN20) steel flanges. The top and bottom blind flanges were drilled and tapped and secured with six M22 bolts. The reactor tube and heating jacket were fixed to a steel frame equipped with castors for mobility (cf. Photograph 3.10). A sheathed, $^{1}/_{16}$-inch, type K thermocouple was mounted through the centre of the reactor tube, from the bottom. A circular stainless steel grid was attached to the thermocouple using a set of grubb screws. The particles of catalyst were held in place by this grid such that the tip of the temperature probe was at the centre of the bed. The position of the grid could be adjusted to accommodate a larger catalyst charge. The unit was linked to the same feed preparation and product-gas sampling system described in section 3.1.1. The thermal mass-flow controllers used for the non-catalytic study were initially replaced by two, 0-90 cm^3 min^{-1} (STP), quartz glass rotameters, in order to obtain lower total inlet flow-rates (cf. Photograph 3.11). The control over the inlet flow-rates was found to be unsatisfactory, however, and it was decided to revert to the use of the mass-flow controllers for delivery of the feed gases to the reactor module.

Further catalytic performance tests were carried out using a pilot-scale reactor tube fabricated from a 2.5 m length of ½ inch nominal diameter copper tubing, shown in Photograph 3.12. The tube was used in the form of a coil, having a coil radius of approximately 120 mm, and was placed directly within the coil bath-circulator reservoir (cf. Photograph 3.13).

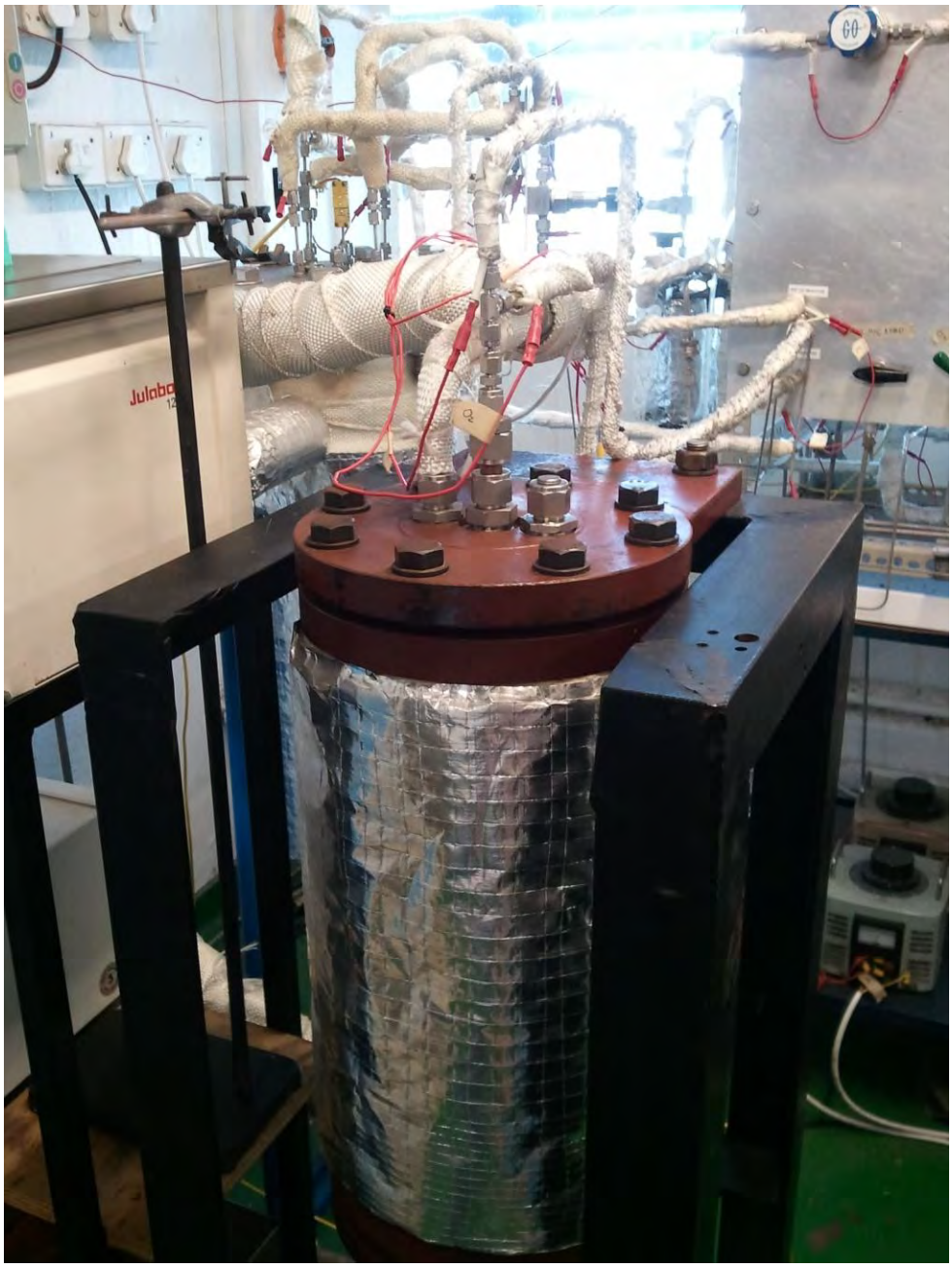

Photograph 3.10. Laboratory-scale fixed-bed reactor used for the study of the catalytic oxidation of HFP.

Photograph 3.11. Platon quartz glass rotameter for low feed-gas flow-rates.

Photograph 3.12. Coil-type fixed-bed reactor used for the study of the catalytic oxidation of HFP.

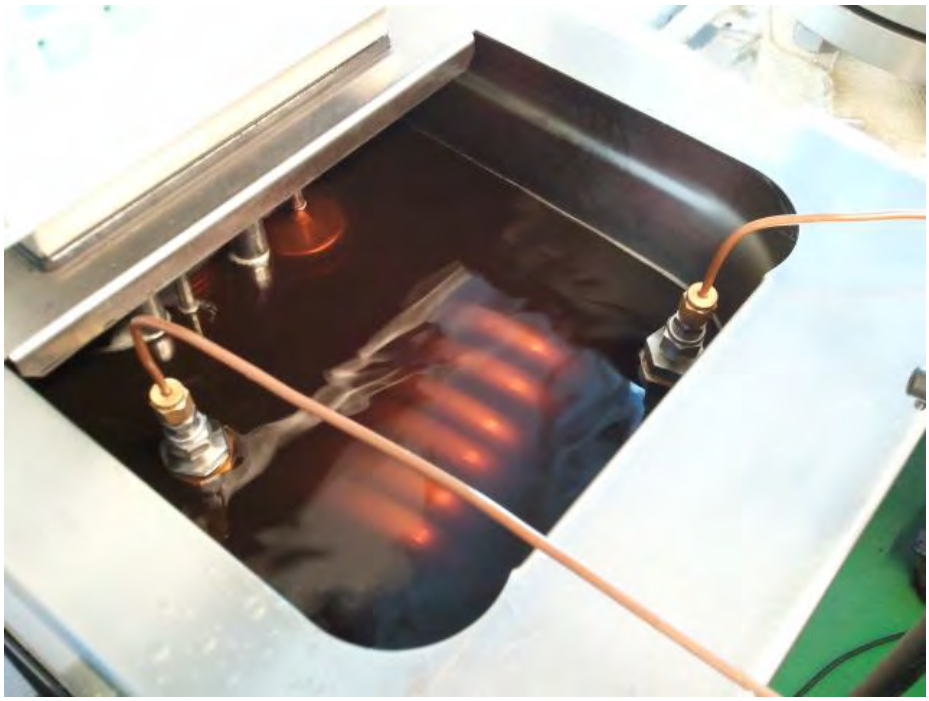

Photograph 3.13. Coil-type fixed-bed reactor immersed in a constant temperature oil bath.

3.2. Materials

Hexafluoropropylene was obtained from the South African Nuclear Energy Corporation (NECSA) and was used without further purification. The feed gas was found to be 99.8% pure via gas-chromatography, with trace amounts of hexafluorocyclopropane and octafluoropropane as impurities. Technical grade oxygen (99.5%) was obtained from Afrox (Linde Group). Carbonyl fluoride (97%), trifluoroacetyl fluoride (99.5%), hexafluorocyclopropane (97%), tetrafluoroethylene (99.9%) and hexafluoroacetone (98%) calibration standards were purchased from ABCR GmbH and Co. KG research chemicals. HFPO (99.5%) and carbon tetrafluoride (99.9%) were obtained from NECSA. Lecture bottles containing octafluoropropane (98%, Air Products) and hexafluoroethane (99.9%, Fedgas) were available in the laboratory.

3.3. Procedures

3.3.1. Experimental procedures for the non-catalytic oxidation of HFP

The reactor coil and inlet piping were heated to 393 K by activating the Julabo oil bath/circulator and the bank of variable voltage transformers. To allow for thermal expansion of the oil, a small quantity was pumped out of the reservoir during heating. PPBV-1 was opened and the scrubber reservoir pump was switched on.

BV-4 and BV-6 were opened and 3V-1 was directed to the helium line. PV-4, PV-8 and the helium cylinder were opened and the system was purged with helium prior to start-up to ensure that all traces of moisture were removed. After terminating the flow of helium by closing BV-4 and BV-6, the reactor was brought to the required operating temperature. BPR-2 was adjusted to roughly provide an operating pressure of 4.5 bar. 3V-1 was directed to the HFP line. The HFP cylinder was opened and the appropriate flow-rate of HFP was set on the Celerity mass-flow controller. The oxygen cylinder was then opened. PV-1 and PV-3 were opened to admit oxygen and HFP to the inlet of the reactor coil. The appropriate flow-rate of oxygen was set on the Bronkhorst mass-flow controller. Fine adjustments to BPR-2 were made to give an operating pressure as close to 4.5 bar as possible.

The reaction was allowed to proceed for a period of one hour, after which the system was deemed to have reached steady state (this was checked independently by assessing the stability of the reactor exit gas flow-rate and composition at regular time intervals after start-up). During normal

operation there was no significant deviation from the temperature set-point. After the prescribed period of stabilization, samples of the product gas were withdrawn for composition analysis and measurements of the product gas flow-rates were made according to the following procedure. Firstly, PV-8 was closed and the GC line was opened by activating the pneumatic valves PV-6 and PV-10. After sweeping the sample loop for a few minutes whilst recording the loop temperature and pressure, the G.C. valve was activated and a sample was withdrawn. A sample was also withdrawn manually from the septum-sealed sample point for analysis on a second gas chromatograph. PV-6 and PV-10 were then closed and PV-8 was opened again. PV-8 was then closed and the wet-test meter line was opened by activating the pneumatic valves PV-5 and PV-9. The wet-test meter temperature, pressure and flow-rate were recorded and reactor exit gas flow was once again directed through PV-8. The reactor operating conditions were then adjusted and the prescribed period of stabilization was once again observed before repeating the sampling procedure. Three to four settings were investigated during one full day of operation.

The experiment was terminated by closing PV-3 and PV-1 and adjusting BPR-2 to atmospheric pressure. The system was then allowed to bleed. PV-2 was opened and the system was purged for a few minutes with nitrogen. PV-2 was then closed. After a few minutes, PV-8 was closed and the vacuum line was opened by activating the pneumatic valves PV-7 and PV-11. The vacuum pump was then turned on. This pressure/vacuum purge cycle was repeated three times. The oil bath/circulator temperature was lowered and the oil that was previously removed was returned to the reservoir. The reactor system was then allowed to cool to room temperature. All instruments and process equipment were switched off. Finally PV-8 was closed.

3.3.2. Experimental procedures for the catalytic oxidation of HFP

A 10 wt% CuO/SiO_2 catalyst was prepared by wet impregnation of silica gel (Davisil grade 646, 35-60 mesh, Sigma-Aldrich) with a calculated amount of copper nitrate trihydrate (99%, Sigma-Aldrich) in distilled water. Approximately 20 g of silica was dried in an oven at 353 K before use. After cooling to room temperature, 6.7490 g of $Cu(NO_3)_2 \cdot 3H_2O$ was added as an aqueous solution to the silica support. More distilled water was added until the slurry had obtained the necessary consistency. The mixture was allowed to age overnight, whilst stirring under the action of a decommissioned rotary evaporator (cf. Photograph 3.14).

Photograph 3.14. Silica gel and copper nitrate trihydrate agitated and aged for 18 hours.

The surfaces of inorganic oxides such as SiO_2 tend to become polarized once they are suspended in an aqueous solution (Perego and Villa, 1997; Pinna, 1998). The surface charge is usually controlled by the pH of the surrounding medium. In acidic media, adsorption sites are positively charged and attract anions whereas in basic media, surface sites are negatively charged and attract cations (Pinna, 1998). For each support material, a particular pH exists at which the surface carries no charge. The point of zero charge or isoelectric point of SiO_2 lies between a pH of 1-2 (Pinna, 1998). Once suspended in an aqueous solution with a pH close to 7, the surface of the SiO_2 support was expected to be negatively polarized, favouring adsorption of the copper cations. No adjustment of the solution pH was therefore necessary.

The slurry was carefully dried the following day, under vacuum using a rotary evaporator, to remove the imbibed liquid. The drying temperature had to be maintained below 333 K to prevent premature thermal decomposition of the metal precursor. The catalyst was thereafter packed into a

special calcination tube, fabricated from a 200 mm length of ½ inch stainless steel pipe, and subsequently placed within a tube furnace (cf. Photograph 3.15). The catalyst was calcined at 773 K for 12 hours under a stream of dry air (100 cm^3 min^{-1}), following a 1 K min^{-1} ramp from room temperature to the final calcination temperature. During this period the metal precursor was decomposed to form the appropriate metal oxide and gaseous products were removed (Pinna, 1998; Alouche, 2008):

$$2Cu(NO_3)_2 \rightarrow 2CuO + 4NO_2 + O_2 \qquad (5.1)$$

The caesium promoted CuO/SiO_2 catalyst was prepared by simultaneous impregnation of the silica support with aqueous solutions of copper nitrate trihydrate and caesium nitrate (99.999%, Sigma-Aldrich). 6.7490 g of $Cu(NO_3)_2 \cdot 3H_2O$ and 0.0326g of $CsNO_3$ mixed with distilled water were added to a aqueous mixture containing 20 g of silica gel. The loading of caesium was approximately 0.1 wt%. The aging, drying and calcination procedures were as before. Both catalysts were stored in sealed amber bottles in a dark cupboard until use.

Photograph 3.15. Tube furnace used for the calcination of the copper-based, silica-supported HFP oxidation catalysts.

The BET specific surface area of each of the prepared catalysts was determined using a Micrometrics ASAP 2020 gas adsorption analyzer. Nitrogen adsorption measurements were performed at 77 K, after degassing the samples at 473 K under nitrogen for 18 hours.

A fresh catalyst charge of between 5 and 10 grams was loaded into the fixed bed reactor. The bed was consolidated by tapping the tube gently. The coiled reactor tube was filled by applying a vacuum at the exit end and introducing the catalyst in small batches at the opposite end. A circular stainless steel mesh was placed at the exit end for this purpose. The particles were once again consolidated by tapping, after each addition. The reactor was sealed and heated to the desired operating temperature (along with the feed and product lines) as before. 3V-1 was directed to the nitrogen line, BV-3 was opened, the Celerity mass-flow controller was switched on and the catalyst was pre-treated under a 100 cm^3 min^{-1} stream of nitrogen for 2 hours, following recommendations given by Ohsaka and Tohsuka (1981). After closing BV-3 and directing 3V-1 to the HFP line, the oxidation experiment was conducted in the same manner as described in the preceding section. However, the reaction in this case was allowed to proceed for a minimum period of 2 hours before samples of the product gas were withdrawn for composition analysis and measurements of the product gas flow-rates were made. Four to five sets of operating conditions were investigated during one full day of operation. After terminating the experiment and allowing the system to cool to room temperature, the reactor was opened and the spent catalyst charge was removed and discarded.

3.4. Analytical techniques

Quantitative composition analyses of feed and product gas mixtures were performed using gas chromatography. The technique remains the most widely used procedure for analyzing multi-component gas and liquid hydrocarbon mixtures (Raal and Mühlbauer, 1998). The application of gas-chromatography to systems containing perfluorocarbons is generally more difficult, however, due to varying degrees of polarity and vast differences in physical properties, even amongst analogues (O'Mahony et al., 1993). The development of a suitable method for the analysis of the HFP oxidation products consisted of two critical tasks. First, a suitable detector and chromatographic column capable of effectively separating all components needed to be selected. Thereafter, the quantitative response of the detector for each species needed to be obtained.

Among the available detectors, the electron-capture detector (ECD) is the most sensitive and selective for halogenated compounds (O'Mahony et al., 1993). High cost, as well as difficult and expensive maintenance routines made this detector an unattractive choice. The flame-ionization detector (FID) has also been found to be suitable for the analysis of perfluorocarbons (Fikry et al., 1980; O'Mahony et al., 1993). The FID exhibits high sensitivity and stability as well as a wide linear dynamic range (Blades, 1973 a). For hydrocarbon molecules, the response of the FID is proportional to the number of constitutional carbon atoms (Kállai et al., 2003). However, certain functional groups attached to the carbon chain can decrease the detector response. Sternberg et al. (1962) showed how different atoms present in a molecule contribute to the overall detector response. Their work ultimately led to the development of the effective carbon number concept (Kállai et al., 2003; Guiochon and Guillemin, 1988). The relationship between the detector response (peak area) and the number of moles of the analyte is given by the equation:

$$n_i = k_i \times A_i \tag{3.6}$$

where k_i is the coefficient of proportionality or response factor for component i (Lebbe, 1969). For a mixture of two components the following is also applicable (Raal and Mühlbauer, 1998):

$$\frac{n_1}{n_2} = \frac{k_1}{k_2} \times \frac{A_1}{A_2} \tag{3.7}$$

The ratio of response factors may also be written as k_{12}. The effective carbon number for component *i* can be calculated from the sum of the effective carbon number atomic increments of the different constituents present in the molecule (Kállai et al., 2003):

$$ECAN_i = \sum ECAN_{inc} \tag{3.8}$$

Lists of values of the atomic increments for hydrocarbons are available in the literature (Kállai et al., 2003; Guiochon and Guillemin, 1988). The response factor ratio can then be obtained by taking the inverse ratio of the effective carbon numbers:

$$k_{12} = \frac{ECAN_2}{ECAN_1} \tag{3.9}$$

In this way the relative response of analytes can be obtained a priori. The method must be employed with reservation, however, since it has been shown that changes in the chromatographic conditions can result in some variation in the value of the atomic increments and hence the computed relative response ratio (Kállai et al., 2003; Guiochon and Guillemin, 1988; Blades, 1973 b).

For perfluorocarbons, the response of the FID is not as easily rationalized. This is due to the operational nature of the detector itself. The response of the detector arises from conductivity imparted by ions that are generated from analyte molecules destroyed in a flame (Blades, 1973 b). The strength of the C-F bond is greater than the C-C bond so destruction of perflurocarbon compounds is likely to be initiated by C-C bond rupture, whereas hydrogen atom abstraction is far easier in hydrocarbons. The atomic increment of a carbonyl functional group to the overall FID response is zero for both hydrocarbons and perfluorocarbon molecules. Fluorine atoms attached to aliphatic and olefinic carbons have a near zero contribution, as well (Guiochon and Guillemin, 1988). This explains the high response of the FID to high molecular weight perfluorocarbons with a large number of C-C bonds (Fikry et al., 1980), insensitivity to components such as carbon tetrafluoride, COF_2 and CF_3COF and a generally disproportionate relationship between carbon number and detector response. It was essential then, to utilize two parallel detectors for the analysis of the HFP oxidation products. The FID was used for the analysis of C_2F_4, *c*-C_3F_6, C_3F_6 and C_3F_6O, whereas a thermal conductivity detector (TCD) was used to quantify the amounts of COF_2, CF_3COF and un-reacted O_2.

Conventional packed columns and specialized variants equipped with fluorinated stationary phases as well as a limited number of capillary columns have all been exploited for the analysis of perfluorocarbons (O'Mahony et al., 1993). The simultaneous separation of low-to-high molecular weight perfluorocarbons on a single column has been found to be difficult, however. The chromatographic analysis of the gaseous products of HFP oxidation, in particular, requires special treatment due to the presence of highly reactive carbonyl compounds and the closeness in boiling points of the two main components, 243.75 K and 245.75 K for HFP and HFPO, respectively. The separation of selected species involved in the oxidation of HFP has previously been reported in the literature. Arito and Soda (1977) separated the pyrolysis products of polytetrafluoroethylene and polyfluoroethylenepropylene on a 3m long column packed with Porapak Q (80-100 mesh), using a 4 K min^{-1} temperature ramp from 323 to 503 K. COF_2, CF_3COF, C_2F_4 and C_3F_6 were all resolved under these conditions. Bright and Matula (1968) used a composite packed column consisting of Porapak T and Porapak N at 296 K to separate C_2F_4 oxidation products, *viz*. CF_4, CO_2, COF_2 and C_2F_4 as well as O_2. Zenkavich (2003) demonstrated that *c*-C_3F_6 and C_3F_6 could also be separated using Porapak Q. Shapovalov and Mezentsev (1996) performed a separation of COF_2, CO_2, CF_3COF, HFP and HFPO on a 2m long stainless steel column packed with polysorb-1 (100-300µm grain size) between 308-343 K. The analysis had to be carried out in two stages at different chromatographic conditions, first separating CO_2, COF_2 and CF_3COF and thereafter the high-molecular-weight compounds.

Fluorinated stationary phases in packed columns allow for the analysis of thermally labile compounds at lower temperatures than on conventional non-fluorinated phases (O'Mahony et al., 1993). The more popular fluorinated phases such as Kel-F No. 90, Krytox and Fomblin YR have been used primarily for the separation of high-molecular weight perfluorocarbons, however. In one distinct example, the gas-chromatographic analysis of the low-molecular-weight pyrolysis products of HFPO was performed by Kennedy and Levy (1976) using a 3.66m column packed with 30% Fluorolube on Chromosorb W.

Only a few examples of the use of capillary columns for the separation of perfluorocarbons are found in the literature, in particular the separation of C_5 and C_6 perfluoroalkanes (O'Mahony et al., 1993). Fused silica and alumina porous-layer-open-tubular (PLOT) capillary columns generally offer greater resolution and efficiency than packed columns. The GS-GasPro PLOT column from Agilent Technologies is the preferred column for high performance gas chromatography/mass spectrometry of fluorine containing compounds in air (Culbertson et al., 2000). For exceedingly

volatile compounds the column provides better peak shape and signal-to-noise responses. The column is fabricated from a proprietary, bonded silica-based phase that is inert and specifically prepared for reactive compounds. Moreover, good separation of multi-component gas mixtures containing low-to-high molecular weight species, including O_2, CO, CO_2 and various perfluoroalkanes, is reported in the literature (Laurens et al., 2001; Culbertson et al., 2000). The GS-GasPro column was believed to be suitable for the separation of the HFP oxidation products in this study.

A Shimadzu G.C. 2010 gas chromatograph equipped with an Agilent GS-GasPro PLOT column (30m×0.32mm ID) as well as both a TCD and a FID was thus commissioned, in the dual channel configuration shown in Figure 3.2, to undertake composition analyses of the product gas samples obtained in this investigation. The gas chromatograph was also furnished with a CO_2 driven cooling unit to enable operation at below ambient temperature. Samples were withdrawn from the reactor exit stream via an automated, pneumatically-driven, 6-port sample valve equipped with a 300 µl sample loop. Photograph 3.16 shows the installed gas chromatograph.

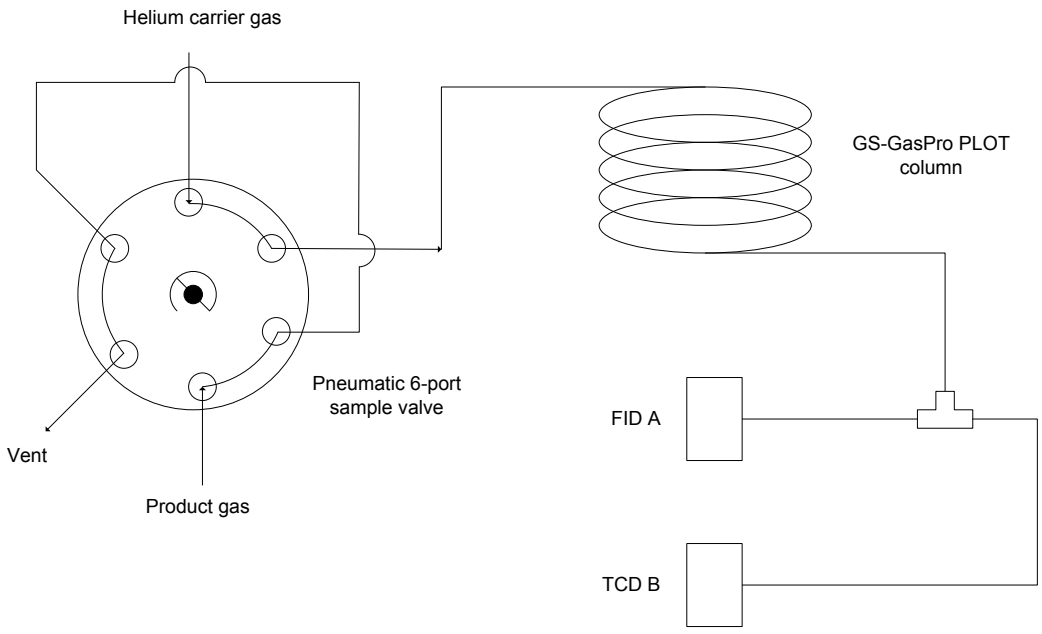

Figure 3.2. Gas chromatograph configuration for dual channel analysis of HFP oxidation products.

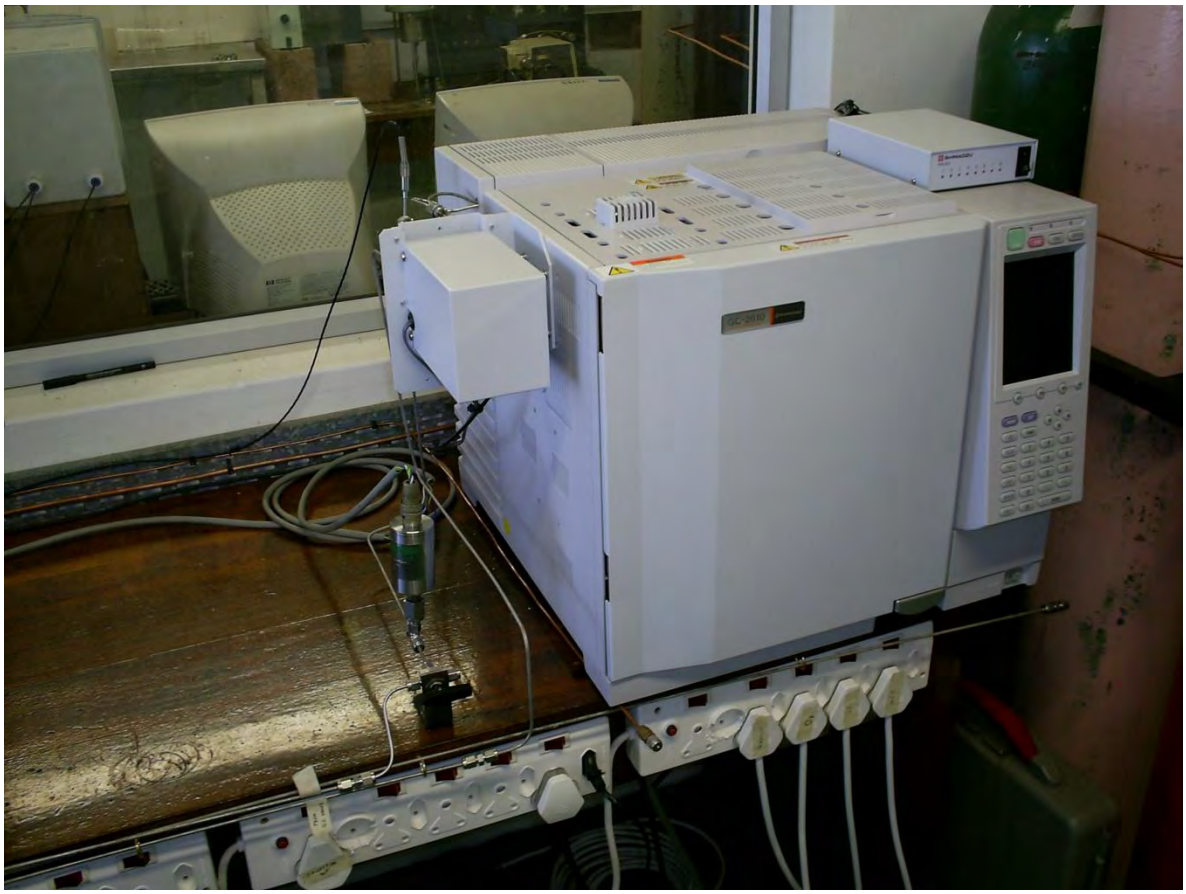

Photograph 3.16. Shimadzu G.C. 2010 gas chromatograph, equipped with a pneumatically-actuated 6-port sample valve (mounted on left).

The column oven was operated isothermally at 303 K for 25 minutes. Due to the sensitivity of the FID to HFP and HFPO, a relatively high injection split ratio of 175:1 had to be used to prevent detector overloading. This also resulted in a lower than satisfactory signal-to-noise ratio for the less sensitive TCD. Figures 3.3 and 3.4 show sample G.C traces obtained on the FID and TCD, respectively.

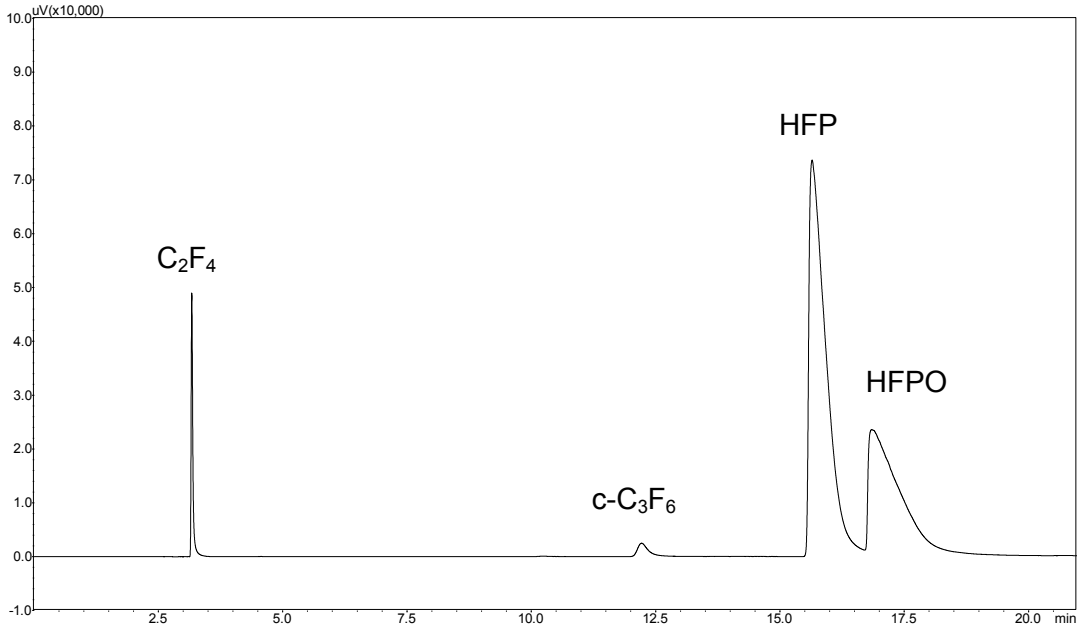

Figure 3.3. FID trace showing typical HFP oxidation products separated on a 30m GS-GasPro PLOT column at 303 K.

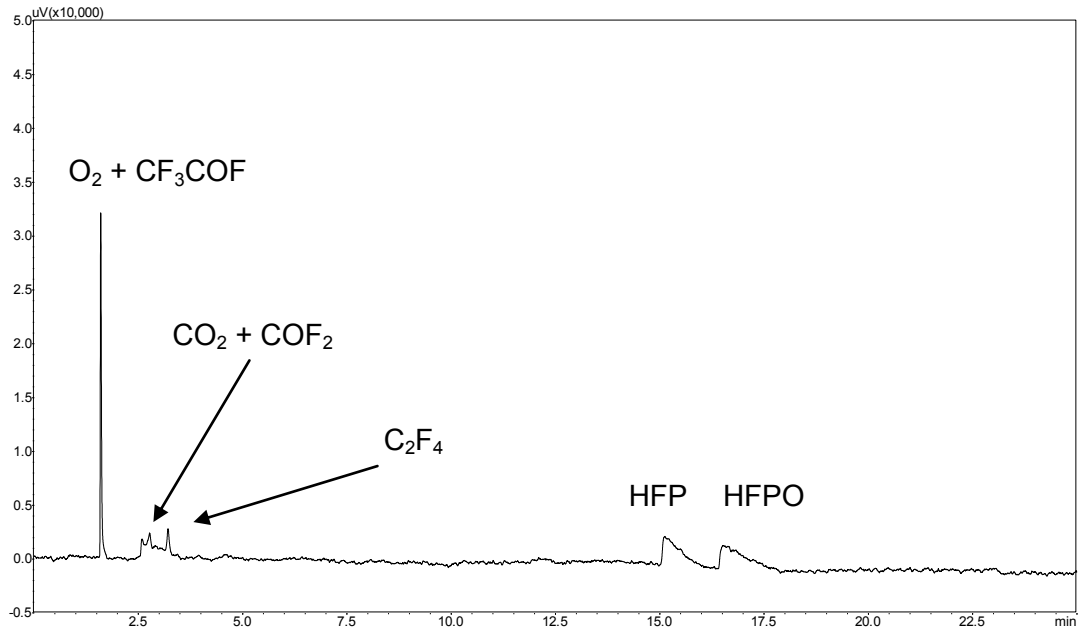

Figure 3.4. TCD trace showing typical HFP oxidation products separated on a 30m GS-GasPro PLOT column at 303 K.

The resolution between consecutive peaks is given by Equation 3.10 (Guiochon and Guillemin, 1988):

$$R_p = 2\frac{t_{R1} - t_{R2}}{w_1 + w_2} \tag{3.10}$$

where R_p is the peak resolution, t_R is the retention time and w is the width at the base of the peak. The average resolution between peaks of HFP and HFPO, obtained on the FID chromatogram, was calculated to be 0.85, which, although not the most satisfactory, was greater than the theoretical limit resolution of 0.75 given by Tranchant (1969) for quantitative analysis.

Gas chromatographic detector calibration was undertaken, utilizing a direct injection technique (Guiochon and Guillemin, 1988; Panday and Kim, 2008; Hunter et al., 1999). Fixed volumes of each of the standard gases were introduced into the instrument using a gas-tight sample syringe and the peak area was recorded via data acquisition on Shimadzu GCsolution software. The number of moles injected was calculated based on the measured sample temperature and pressure, according to the ideal gas equation of state:

$$n_i = \frac{PV}{RT} \tag{3.11}$$

The data were correlated according to two linear functions (Cuadros-Rodríguez, 2007):

$$n_i = k_i A_i \tag{3.12}$$

$$n_i = c_i + k_i A_i \tag{3.13}$$

Calibration plots for each of the species, together with the estimated relative measurement uncertainties, are presented in Appendix C. The measurement uncertainties were similar for both functions. Special arrangements had to be made for the extremely toxic and aggressive gases COF_2, CF_3COF and HFA. A gas-tight, full-body, hazardous materials suit and self-contained breathing apparatus were required (cf. Photograph 3.17). Each calibration period was restricted to 15 minutes, during which a number of injections were performed. The injections were made using robust Hamilton gas-tight syringes equipped with chaney adapters that improved reproducibility. The

stainless steel regulators fitted to the outlet of each toxic gas cylinder had to be equipped with a nitrogen purge line (cf. Photograph 3.18). This line was connected to the reactor system vent line and ultimately to the scrubber unit, which was operated during each calibration sequence.

Photograph 3.17. Gas-chromatograph detector calibration for a toxic gas, undertaken using a full-body hazardous materials suit and self-contained breathing apparatus.

Two problems regarding the analysis of the carbonyl compounds were encountered. CF_3COF was found to co-elute with oxygen on the GS GasPro column, even at temperatures as low as 233 K. The decomposition of COF_2 to CO_2 on the silica-based column was also observed, resulting in a pair of partially resolved peaks after 2.5 minutes on the TCD trace (cf Figure 4.4). HFP and HFA could also not be resolved under the chromatographic conditions that were used.

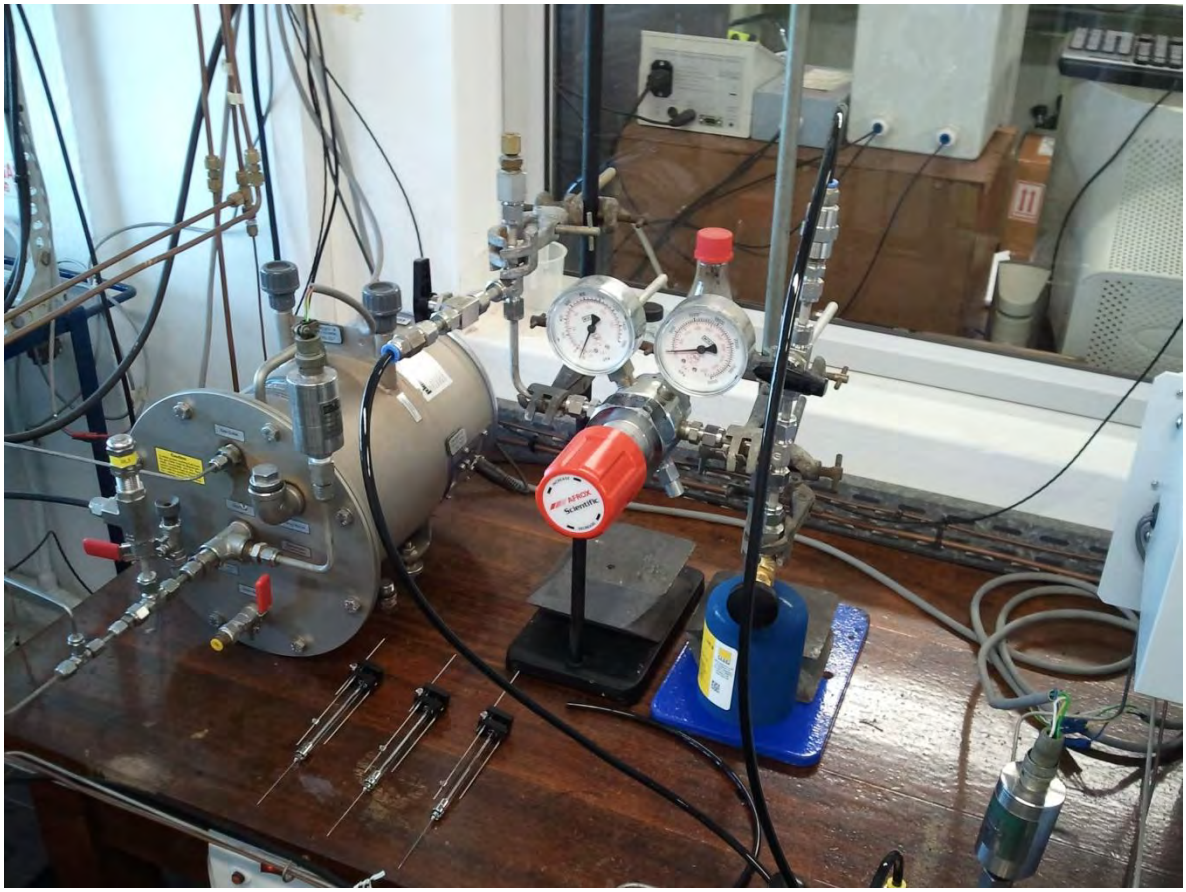

Photograph 3.18. Toxic gas sampling system equipped with a nitrogen purge (black polypropylene tubing) and septum-sealed sample point.

It was proposed that by analyzing the scrubber exit gas and making a measurement of the flow-rate, the amount of un-reacted oxygen in the product gas could be estimated, provided that all of the CF_3COF was destroyed in the scrubber. The unknown quantity of CF_3COF could then be obtained through a mass balance. In order to validate this method, the time required to completely displace the volume of gas in the scrubber had to be determined. It was also necessary to show that the analysis of a sample of gas taken from the scrubber exit after the appropriate amount of time was representative of the reactor product gas entering the scrubber at that time, but without the presence of the carbonyl compounds. The gas hold-up in the scrubber was estimated to be 43.95 litres based on a void fraction of 0.6 for the packed section and a 75% full reservoir. At normal operating flow-rates of about 200 $cm^3\ min^{-1}$, the theoretical displacement time was 3.7 hours. A test was conducted by first admitting a stream of air into the scrubber at a flow-rate of 500 $cm^3\ min^{-1}$ for 3 hours, followed by a helium purge at 1500 $cm^3\ min^{-1}$ for another 3 hours. A composite G.C. trace is

presented in Figure 3.5, representing the amount of air in the scrubber exit gas 1, 30 and 45 minutes after the start of the helium purge. At least 45 minutes was clearly required, at an inlet flow-rate of 1500 cm^3 min^{-1} to completely displace the gas present in the scrubber. It was thus estimated that under normal operating flow-rates, 5.7 hours would be required, which was regarded as impractical. This method was subsequently abandoned. Nevertheless, a 6 hour experiment at 463 K was conducted, employing an equimolar feed mixture of HFP and O_2 and a space time of 120 seconds, which translated into a volumetric feed flow-rate of 250 cm^{-3} min^{-1}. Samples of the reactor exit gas as well as the scrubber effluent were analyzed. The composite chromatograms are presented in Figures 3.6 and 3.7, showing FID and TCD traces, respectively. The COF_2 present in the reactor exit gas appeared to be completely destroyed in the scrubber. Approximately half of the HFP and HFPO originally present in the reactor product gas was unaffected. Due to the co-elution of CF_3COF and O_2, the fate of the former could not be determined. A small amount of C_2F_6, a possible decomposition product, was also observed in the scrubber effluent.

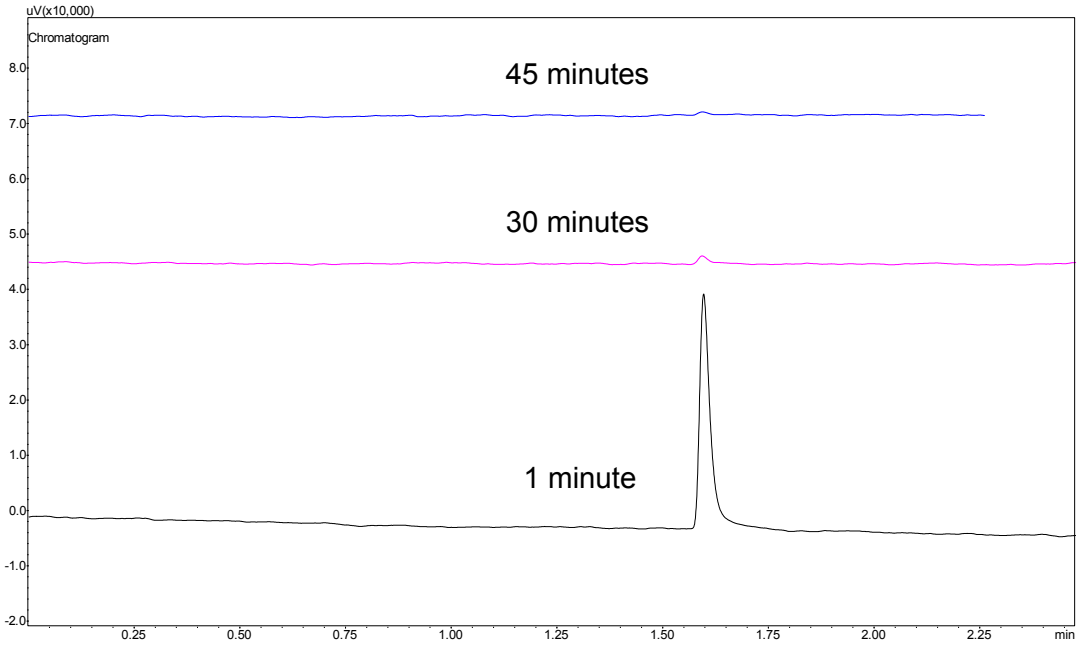

Figure 3.5. TCD gas chromatogram of the scrubber exit gas 1, 30 and 45 minutes after the start of the helium purge.

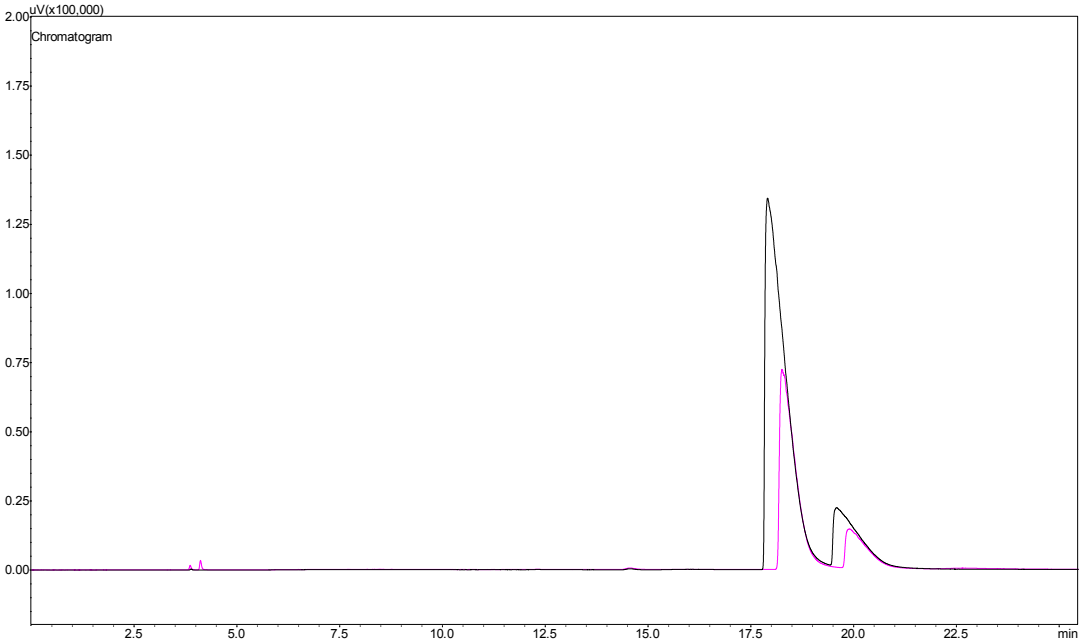

Figure 3.6. FID chromatogram overlay, showing reactor product gas (black) and scrubber exit gas (pink) traces. The sample of the scrubber exit gas was drawn 6 hours after the product gas sample. Products were separated on a 30m GS-GasPro PLOT column operating at 293 K.

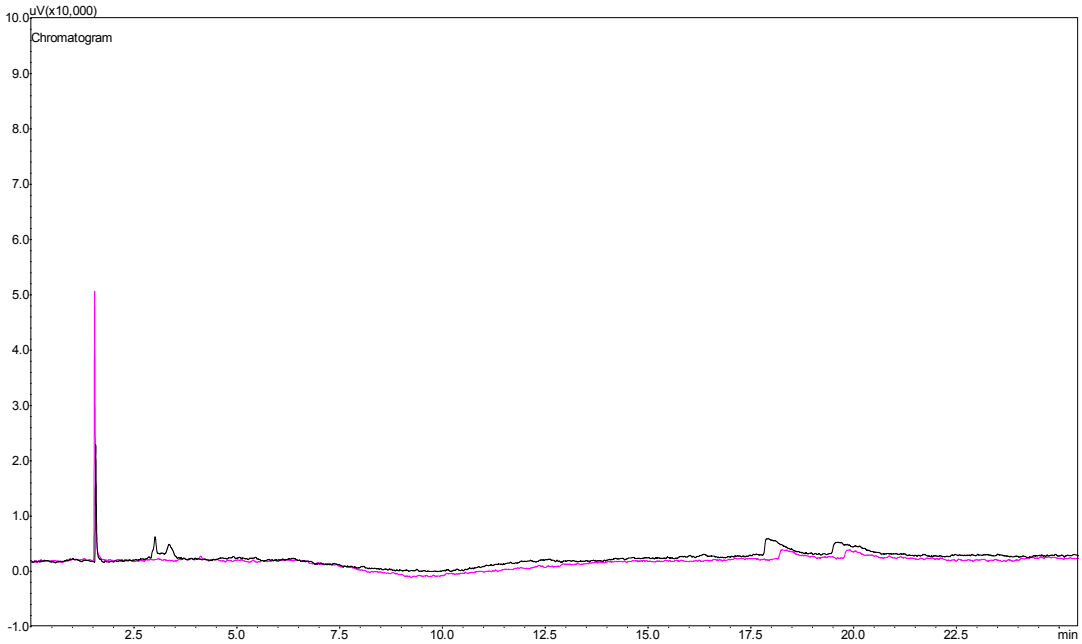

Figure 3.7. TCD chromatogram overlay, showing reactor product gas (black) and scrubber exit gas (pink) traces. The sample of the scrubber exit gas was drawn 6 hours after the product gas sample. Products were separated on a 30m GS-GasPro PLOT column operating at 293 K.

The use of a second gas chromatograph for the analysis of the low-molecular-weight products was finally explored. A Shimadzu G.C. 2014 gas chromatograph equipped with a TCD was made available for testing. Several packed columns were installed and chromatographic analyses of gas mixtures containing O_2, COF_2 and CF_3COF were performed. The retention times for the carbonyl compounds were found to be unsatisfactory on 2m long molecular sieve 3A and Restek ShinCarbon packed columns operating as high as 523 K. These columns were initially regarded as good candidates since they are used frequently for permanent gas analysis. A 3m long stainless steel column packed with Haysep D was eventually used to separate O_2, COF_2, CF_3COF, HFP and HFA. HFP and HFPO could not be resolved on this column. Figure 3.8 shows a sample chromatogram obtained from the Shimadzu G.C. 2014 gas chromatograph using the Haysep D column.

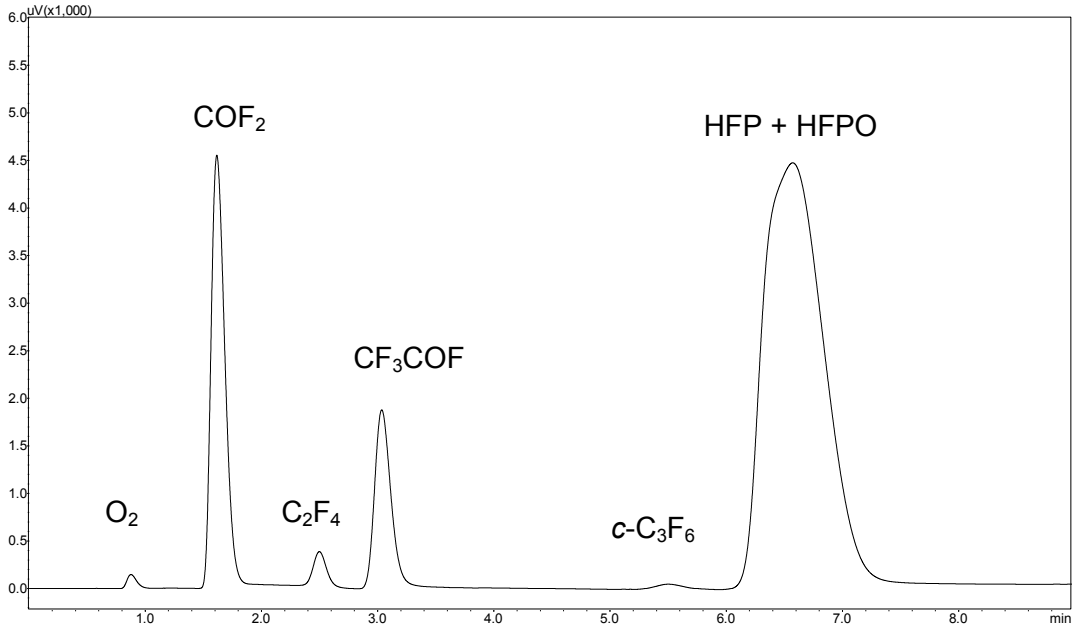

Figure 3.8. TCD trace showing typical HFP oxidation products separated on a 3m Haysep D packed column at 368 K.

Ultimately, the mole fractions of HFPO, HFP, *c*-C_3F_6 and C_2F_4 in the product gas were established using the Shimadzu G.C. 2010 gas chromatograph equipped with the GS-GasPro column, based on samples withdrawn from the reactor exit line via the 6-port sample valve. Unreacted oxygen and the acid fluoride by-products were separated on the Shimadzu G.C. 2014 gas chromatograph equipped with the Haysep D packed column. A septum-sealed sample point was installed in-line with the sample valve and was used to withdraw 100-200µl samples for manual injection into the second G.C. using a gas-tight syringe. The specifications for each machine are presented in Tables 3.1 and

3.2. TCD calibration for the necessary components were undertaken on the Shimadzu G.C. 2014 using the same direct injection technique discussed earlier. The full calibration results are given in Appendix C.

The mole fractions of each species in a sample were determined as follows:

$$x_i = \frac{n_i}{n_{total}} \tag{3.14}$$

The number of moles of the species in the sample, n_i, was obtained from the peak area on the chromatogram and the absolute response factor, according to Equation 3.13. The total number of moles of the sample, n_{total}, was calculated according to:

$$n_{total} = \frac{P_{sample} V_{sample}}{R T_{sample}} \tag{3.15}$$

where P_{sample}, V_{sample} and T_{sample} are the sample point pressure, volume and temperature, respectively.

Table 3.1. Shimadzu G.C. 2010 gas chromatograph specifications.

Item	Specification
Column	GS-GasPro PLOT (30m×0.32mm ID)
Injector temperature [K]	473
Oven temperature [K]	303
FID temperature [K]	523
TCD temperature [K]	523
TCD current [mA]	80
Split ratio	175:1
Carrier gas	Helium
Carrier gas total flow-rate [ml min^{-1}]	424.1
Linear velocity	36.7

Table 3.2. Shimadzu G.C. 2014 gas chromatograph specifications.

Item	Specification
Column	Haysep D packed column (3m×80-100 mesh)
Injector temperature [K]	393
Oven temperature [K]	368
TCD temperature [K]	473
TCD current [mA]	80
Carrier gas	Helium
Carrier gas total flow-rate [ml min^{-1}]	25
Reference gas total flow-rate [ml min^{-1}]	25

There were a number of additional difficulties associated with the manual withdrawal and injection of pure COF_2 and CF_3COF samples for calibration. Even after evacuation and filling under pressure, the sample point at the exit of the toxic gas regulator still contained a small amount of air. This amount had to be subtracted from the total number of injected moles before correlating against the measured peak area. The Teflon lined silicone septa and Teflon syringe plunger also experienced severe swelling and decomposition upon exposure to these gases. This was found to be unavoidable. Tables 3.3 and 3.4 show the retention times and relative response ratios obtained for the components analyzed on the Shimadzu G.C. 2010 and 2014 gas chromatographs, respectively.

Table 3.3. Retention times and FID relative response ratios for components separated on a 30m GS-GasPro PLOT column.

Component	Retention time [min][a]	Relative response ratio[b]
C_2F_4	3.2	2.53
C_2F_6	2.5	400.47
C_3F_8	8.0	8.87
c-C_3F_6	12.2	2.84
HFP	15.6	1
HFA	15.6	96.5
HFPO	17.0	5.26

[a] Analyses were carried out at 303 K.

[b] Response factors are normalized relative to HFP.

Table 3.4. Retention times and TCD relative response ratios for components separated on a 3m Haysep D packed column.

Component	Retention time [min][a]	Relative response ratio[b]
O_2	0.89	2.32
Air	0.89	2.21
COF_2	1.60	3.45
C_2F_4	2.49	Not measured
CF_3COF	3.02	3.31
c-C_3F_6	5.48	1.46
HFP	6.50	1
HFA	7.50	2.76

[a] Analyses were carried out at 368 K.

[b] Response factors are normalized relative to HFP.

Unlike the hydrocarbon analogues, there were vast differences in the relative response ratios for components detected on the FID. An attempt was made to fit effective carbon number atomic increments using the obtained relative response ratio data, similar to those postulated by Sternberg et al., (1962) for hydrocarbons, but the results were unsatisfactory. Perfluorocarbons may not be amenable to this sort of treatment.

The actual volume of the sample delivered by the 6-port rotary valve to the Shimadzu G.C. 2010 gas chromatograph had to be determined. This value was required for the calculation of the total number of injected moles and hence the mole fractions of the constituent species of the gas sample withdrawn. The Peyron acidimetric method is recommended in the literature for the precise determination of the sample-loop volume (Guiochon and Guillemin, 1988). In this method, the sample loop is filled with a 1 N acetic acid solution. The volume of acid that is transferred to a stream of distilled water passing through the carrier gas line, upon switching the valve, is collected in a beaker and titrated with a 0.1 N solution of sodium hydroxide. A precision of at least 0.5% of the measured volume can be achieved through multiple determinations. The presence of organics and moisture in the analytical lines were to be avoided, however, so an alternative method had to be used. Pure components (CO, CO_2, O_2 and C_2F_4) were introduced into the gas chromatograph via the sample loop and the peak areas were recorded. The total number of moles injected for each sample was obtained from direct calibration plots that were prepared previously. The sample loop volume was then calculated using the ideal gas equation of state as well as the measured sample pressure and temperature. The average calculated sample loop volume was 295 µl. This value was 5 µl lower

than the manufacturers' specification and was likely brought about during assembly and installation of the valve and loop.

3.5. Laboratory safety

The physical and toxicological properties of the various species involved in the oxidation of HFP are summarized in Table 3.5. HFP, HFPO and tetrafluoroethylene may be regarded as practically non-toxic, except in the event of a very large release (Clayton, 1977). The low-molecular-weight acid fluorides, on the other hand, are very toxic and aggressive even at small concentrations (Scheel at al., 1968). Most of the perfluorocarbons hydrolyze rapidly to HF in the presence of water and react readily with almost any organic hydrocarbon medium that may be present in the system (Millauer et al., 1985). Owing to the toxic nature of the by-products, as well as the reactivity of all of the species concerned, the entire experimental apparatus was isolated in a sealed equipment room. The room was equipped with an industrial-grade extractor hood with petrol-driven generator back-up. A viewing window was placed between the equipment room and the control room to allow safe monitoring of the process. The operator could make adjustments to the gas flow-rates and temperatures remotely from a central control panel as well as institute emergency shut-down procedures, if required. A half-mask respirator, composite filter (Dräeger A2B2E2K1P2), dust coat and butyl gloves were used when direct adjustments to the equipment were required during an experimental run.

Table 3.5. Physical and toxicological properties of the fluorocarbon products from the oxidation of HFP.

Property	**HFP**[a]	**HFPO**[a]	**HFA**[a]	**COF_2**[a]	**CF_3COF**[b]	**C_2F_4**[b]	***c*-C_3F_6**[b]
CAS Number	116-15-4	428-59-1	684-16-2	353-50-4	354-34-7	116-14-3	931-91-9
Molecular formula	C_3F_6	C_3F_6O	CF_3OCF_3	COF_2	CF_3COF	C_2F_4	$(CF_2)_3$
Molecular mass [g mol^{-1}]	150.02	166.02	150.02	66.01	116.02	100.02	150.02
Boiling point [K]	243.55	245.75	245.88	188.58	214.15	197.51	243.55
Vapour pressure at 298 K [bar]	6.5	6.6	5.9	-	1.7	33.22	9.6
Critical temperature [K]	367.15	359.15	357.15	297	-	306.15	-
Critical pressure [bar]	29	28.96	28.37	57.6	-	39.41	-
Appearance	Colourless gas	Colourless gas	Colourless gas	Colourless gas	Colourless gas	Colourless gas	Colourless gas
Flash point [K]	Non flammable	Non flammable	Non flammable	Non flammable	Non flammable	131.15	Non flammable
LC_{50} [ppm]	3060	Not available	460	360	Not available	40 000	Not available

[a] Yaws, 2001; Clayton, 1977.

[b] Moore, 2006.

Chapter 4
Methodological approach and experimental results

4.1. Non-catalytic oxidation of HFP

4.1.1. Preliminary experiments

The optimum range of operating conditions for the non-catalytic, gas-phase oxidation of HFP at low pressures was not clearly defined in the literature. Therefore, a series of exploratory experiments were performed at temperatures ranging between 373 K and 473 K, employing equimolar feed mixtures of HFP and oxygen and space time values between 60 and 120 seconds. Quantitative data concerning the yields of acid fluoride by-products was lacking at this stage. The performance criteria, *viz*. conversion of HFP, selectivity and yield of HFPO, were defined as follows:

$$X_{HFP} = \frac{F^0_{HFP} - F_{HFP}}{F^0_{HFP}} \times 100\% \tag{4.1}$$

$$S_{HFPO} = \frac{F_{HFPO}}{F^0_{HFP} - F_{HFP}} \times 100\% \tag{4.2}$$

$$Y_{HFPO} = \frac{X_{HFP} \times S_{HFPO}}{100} = \frac{F_{HFPO}}{F^0_{HFP}} \times 100\% \tag{4.3}$$

where F_i^0 and F_i refer to the inlet and exit molar flow-rates of species *i*, respectively. Note that due to the complex nature of the reaction chemistry, a stoichiometric selectivity and yield could not be defined. No reaction was observed at a total operating pressure of 1 bar (cf. Table 4.1). Jones et al. (1969) found that the system pressure dramatically affected the initiation temperatures for the oxidation of various hydrocarbon olefins (cf. Table 4.2). It was suggested that systems containing perfluorinated compounds may exhibit similar behaviour.

Table 4.1. HFP oxidation experiments carried out at 1 bar total operating pressure in which no reaction was observed.

Temperature [K]	HFP/O_2 molar feed ratio [mol mol^{-1}]	Space time [seconds]
373	1	60
423	1	60
473	1	120
473	1	120

Table 4.2. Minimum initiation temperatures for the oxidation of light olefins (Jones et al., 1969).

	Pressure [bar]			
	1	**4.5**	**7.9**	**11.3**
	Minimum reaction temperature [K]			
Ethylene	> 773	653	643	628
Propylene	733	633	613	-
1-Butene	< 663	< 633	613	-
2-Butene	703	613	< 573	-

The total operating pressure was gradually increased until an acceptable HFP conversion and yield of HFPO was achieved (cf. Table 4.3). The oxidation of the fluoro-olefin was first observed at a temperature of 473 K, a space time of 120 seconds and a total pressure of 2 bar. At 4.5 bar the conversion and yield had risen to 42% and 36%, respectively. Further increments in the reaction pressure were not warranted, however, since operation of the system closer to the HFP bottle pressure of 6.5 bar resulted in less stable feed flow-rates and an increased risk of explosion (Meissner and Wróblewska, 2007). 4.5 bar was deemed to be the minimum effective reaction pressure and was used throughout the rest of this work.

Table 4.3. Results of HFP oxidation experiments carried out at 473 K and different total operating pressures.

Pressure [bar]	Temperature [K]	HFP/O_2 molar feed ratio [mol mol^{-1}]	Space time [seconds]	HFP conversion [%]	HFPO selectivity [%]
1	473	1	120	0.00	0.00
2	473	1	120	2.30	0.10
2.5	473	1	120	2.70	0.12
3	473	1	120	3.80	17.50
4.5	473	1	120	42.00	36.00

Researchers at NECSA who were originally involved in the study of the high pressure (> 20 bar), gas-phase, thermal oxidation of HFP indicated that pre-treatment of the reactor walls with HFPO or mixtures of HFP and O_2 at > 473 K was essential. Apparently, a film of high molecular weight products, resulting from the high temperature decomposition of HFPO or oxidation of HFP, gradually covered the inner walls of the reactor, altering the overall reaction chemistry and reactor performance. The same phenomenon was observed by Kartsov et al. (1978). The conversion of HFP, selectivity and yield of HFPO at 478 K, using an equimolar feed mixture of HFP and O_2 and a space time of 120 seconds, was measured several times after the initial installation of the reactor coils, to determine whether the total operating time had any effect on the performance of the system. All three parameters were found to stabilize after approximately 80 hours (cf. Figure 4.1), which was probably due to the gradual build-up of reaction products on the inner surface of the reactor tube with a subsequent change in the reaction chemistry. The latter is discussed further in Chapter 5. All subsequent measurements were made after the observed stabilization.

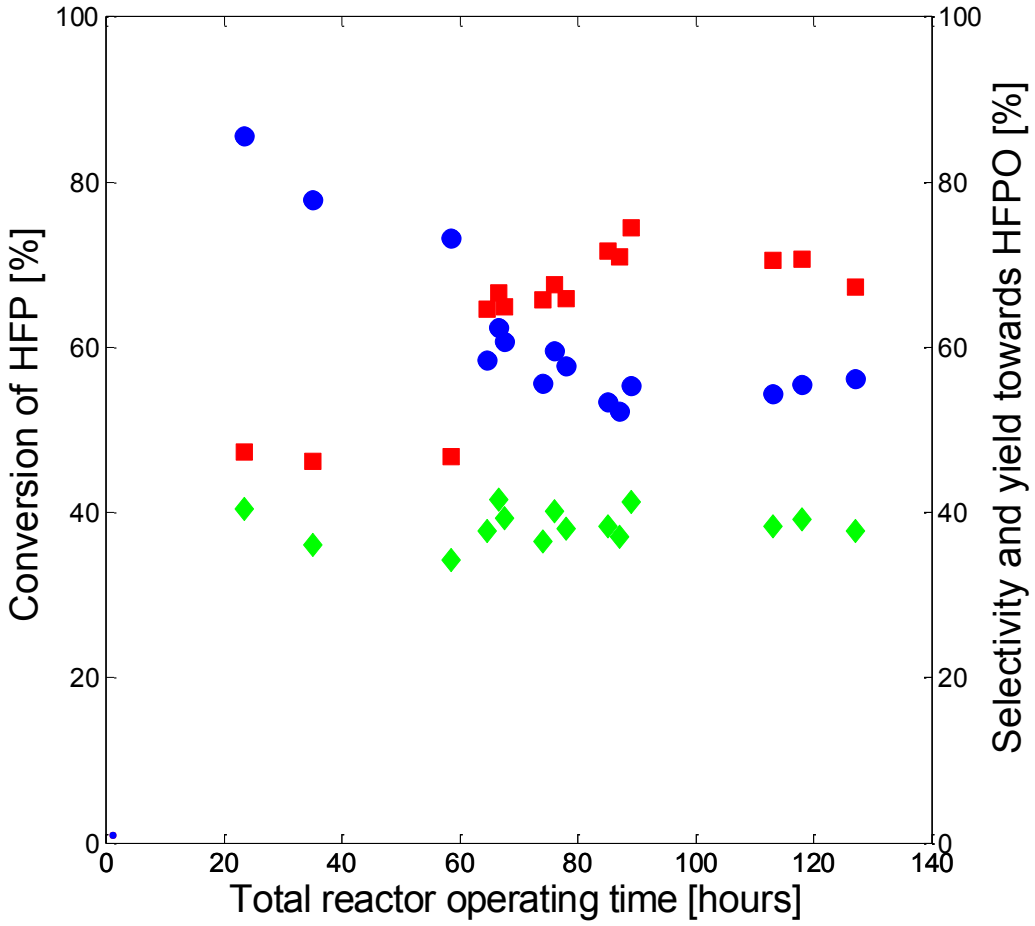

Figure 4.1. Conversion of HFP (■), selectivity (●) and yield (◆) towards of HFPO as a function of total reactor operating time. Reaction conditions were 478 K, HFP/O_2 molar feed ratio 1 mol mol^{-1} and space time 120 seconds.

4.1.2. Experimental design

4.1.2.1. Single factor effects

In order to assess the effect of operating conditions on the performance of the oxidation reaction and to gain a better understanding of the fundamental behaviour of this system, a classical experimental design or one-variable-at-a-time (OVAT) approach was adopted (Antony, 2003; Lazić, 2004). Three variables were considered, viz. reaction temperature, HFP/O_2 molar feed ratio and space time. The experimental design was accomplished by varying only a single factor at a time, whilst holding the other two independent variables constant. The method required that two excursions were made for each variable from a set of reference conditions (478 K, 1 mol mol^{-1} and 120 seconds). The selection of test limits for each variable was based on the results of the preliminary experimentation (cf. Table 4.4).

Table 4.4. Classical experimental design for qualitative single factor effects.

Experiment	Temperature [K]	HFP/O_2 molar feed ratio [mol mol^{-1}]	Space time [seconds]
1[a]	478	1	120
2	463	1	120
3	493	1	120
4	478	0.5	120
5	478	1.5	120
6	478	1	100
7	478	1	140

[a] Reference conditions.

4.1.2.2. Central composite design

The classical or OVAT approach to experimental design was sufficient only for a preliminary probe of the single factor effects and to identify the key operating parameters. The method, however, has been found to be inefficient and the results can often be misleading, especially if there are interactions between variables (Antony, 2003). The exploration of a limited domain of operating conditions was more effectively handled by employing a multifactor design. To allow for the elucidation of possible interaction between variables, the latter were varied simultaneously (Montgomery and Runger, 2007). In this work, a central composite experimental design was used. Reaction temperature (X_1), HFP/O_2 molar feed ratio (X_2) and space time (X_3) were once again chosen as the variables to be considered. The central composite design consisted of 20 experiments, composed of a two-level full factorial design, 4 axial design points and 6 centre points. A three-dimensional representation of the design is given in Figure 4.2. The selected test limits of the design matrix are presented in Table 4.5. The low axial design point for HFP/O_2 molar feed ratio was found to be unrealizable in this system and was replaced with a point 10% closer to the design centre.

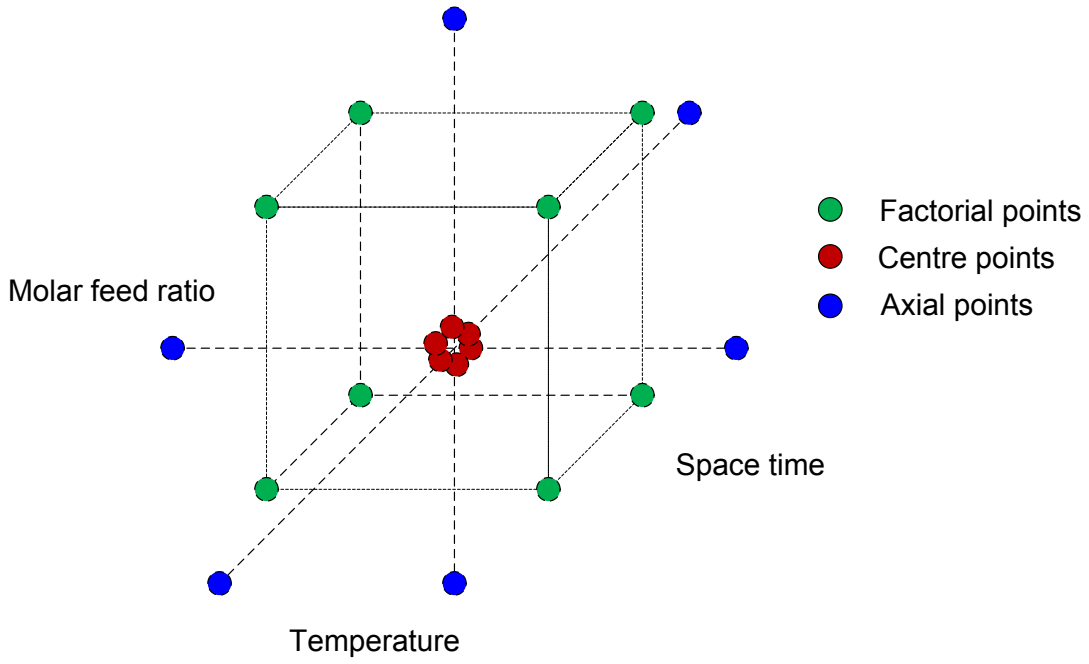

Figure 4.2. Central composite experimental design for three factors.

Table 4.5. Selected test limits of the central composite experimental design.

Run[a]	Manipulated variables					
	X_1 Temperature [K]	Level[b]	X_2 HFP/O_2 feed ratio [mol/mol]	Level[b]	X_3 Space time [seconds]	Level[b]
F1	463	-1	0.5	-1	100	-1
F2	493	+1	0.5	-1	100	-1
F3	463	-1	1.5	+1	100	-1
F4	493	+1	1.5	+1	100	-1
F5	463	-1	0.5	-1	140	+1
F6	493	+1	0.5	-1	140	+1
F7	493	+1	1.5	+1	140	+1
F8	463	-1	1.5	+1	140	+1
S1	478	0	1	0	86	$-\alpha$
S2	478	0	1	0	154	$+\alpha$
S3	478	0	0.25	$-\alpha$	120	0
S4	478	0	1.841	$+\alpha$	120	0
S5	453	$-\alpha$	1	0	120	0
S6	503	$+\alpha$	1	0	120	0
C1	478	0	1	0	120	0
C2	478	0	1	0	120	0
C3	478	0	1	0	120	0
C4	478	0	1	0	120	0
C5	478	0	1	0	120	0
C6	478	0	1	0	120	0

[a] F = orthogonal factorial design points, S = axial design points, C = centre points

[b] -1 = low value, 0 = centre point value, +1 = high value, $-\alpha$ = low axial value, $+\alpha$ = high axial value

A statistical experimental design of this nature allowed for the prediction of optimal reaction conditions through the use of response surface methodology. The relationships between the independent variables and the response functions (HFPO selectivity and yield) were approximated by quadratic regression models. A Nelder-Mead simplex optimization algorithm was subsequently applied to each of these second-order response surfaces. In order to ensure that the variance of the predicted responses were independent of direction and constant at all points that were the same distance from the centre of the design, the latter was made rotable by proper selection of the spacing for the axial design points (Montgomery and Runger, 2007). For a rotable design, the axial spacing is given by:

$$\alpha = N^{1/4} \tag{4.4}$$

where N is the number of points in the factorial portion of the design ($N = 2^k$, where k is the number of factors). Since there are three factors, $\alpha = 1.6817$. Such an arrangement ensured that there was an unbiased representation of the response and that the response was predicted with equal precision at all of the design points (Montgomery and Runger, 2007).

4.1.2.3. Hybridized factorial design of experiments for kinetic data generation

In the literature, various optimal strategies of experimental design for kinetic parameter assessment are given (Box and Lucas, 1959; Kitrell et al., 1966; Froment, 1975, Buzzi-Ferraris and Manenti, 2009). One of the more popular methods involves the minimization of the confidence volume of the current parameters to determine the next set of experimental conditions (Box and Lucas, 1959). The new point has to maximize the determinant of the matrix $\mathbf{F}_{n+1}^{T}\mathbf{F}_{n+1}$ where $\mathbf{F}_{n+1}$ is given, for each dependent variable, by:

$$\mathbf{F}_{n+1} = \begin{pmatrix} f_1(\mathbf{x}_1) & f_2(\mathbf{x}_1) & \cdots & f_p(\mathbf{x}_1) \\ f_1(\mathbf{x}_2) & f_2(\mathbf{x}_2) & \cdots & f_p(\mathbf{x}_2) \\ \vdots & \vdots & \ddots & \vdots \\ f_1(\mathbf{x}_{n+1}) & f_2(\mathbf{x}_{n+1}) & \cdots & f_p(\mathbf{x}_{n+1}) \end{pmatrix}$$

where $f_k(\mathbf{x}_i)$ are the partial derivatives of the predicted response with respect to the k-th parameter b_k, evaluated at the measurement conditions $\mathbf{x}_i$ and for an optimized $\mathbf{b}$ based on $\mathbf{F}_n$. This is known as the D-optimality criterion (Box and Lucas, 1959).

In practice, a preliminary set of kinetic data is generated using a lower-level experimental design, such as the central composite design discussed in the preceding section. These measurements are used to obtain first estimates of the kinetic parameters. The confidence volume criterion is then checked and new experimental conditions are proposed. This sequential procedure is stopped once the determinant $\left|\mathbf{F}_{n+1}^{T}\mathbf{F}_{n+1}\right|$ has reached an asymptotic value.

One drawback of the aforementioned method is that the proposed new set of experimental conditions, given by the D-optimality criterion, may not be physically attainable in the apparatus, a result that was observed in this work. Therefore an alternative, explicitly defined experimental

design was adopted for the kinetic data generation. Measurements were made at three temperatures, *viz*. 463, 478 and 493 K. As shown schematically in Figure 4.3, a transformation of the molar feed ratio-space time plane from the original full factorial design was performed, for each of the three temperatures, resulting in an expanded, hybridized factorial design. Thus for each reaction temperature, there were a total of 56 potential experimental points.

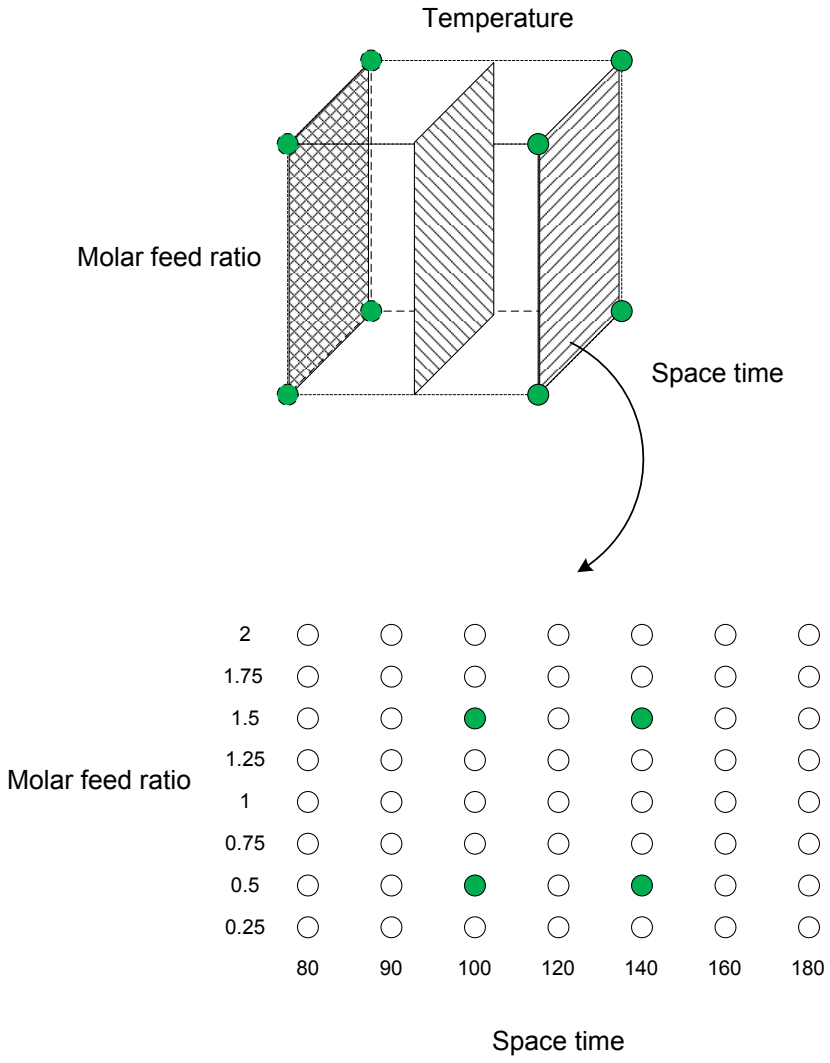

Figure 4.3. Generation of hybridized factorial design points from the original full factorial experimental design, for kinetic data collection. Filled circles represent the original factorial design points.

4.1.3. Main experimental results

4.1.3.1. Single factor effects

Figure 4.4 shows the effect of reaction temperature on the conversion of HFP as well as the selectivity and yield towards HFPO, at a fixed HFP/O_2 molar feed ratio and space time. The reaction also gave CF_3COF, COF_2, C_2F_4 and *c*-C_3F_6 as products. These components were identified according to their relative retention times in the chromatographic system (cf. Tables 3.3 and 3.4 in section 3.4). Over the narrow temperature range that was investigated, the conversion of HFP was observed to increase from 30% to almost 100%. The higher reaction temperatures, however, resulted in lower selectivity towards HFPO, favouring the formation of CF_3COF and COF_2.

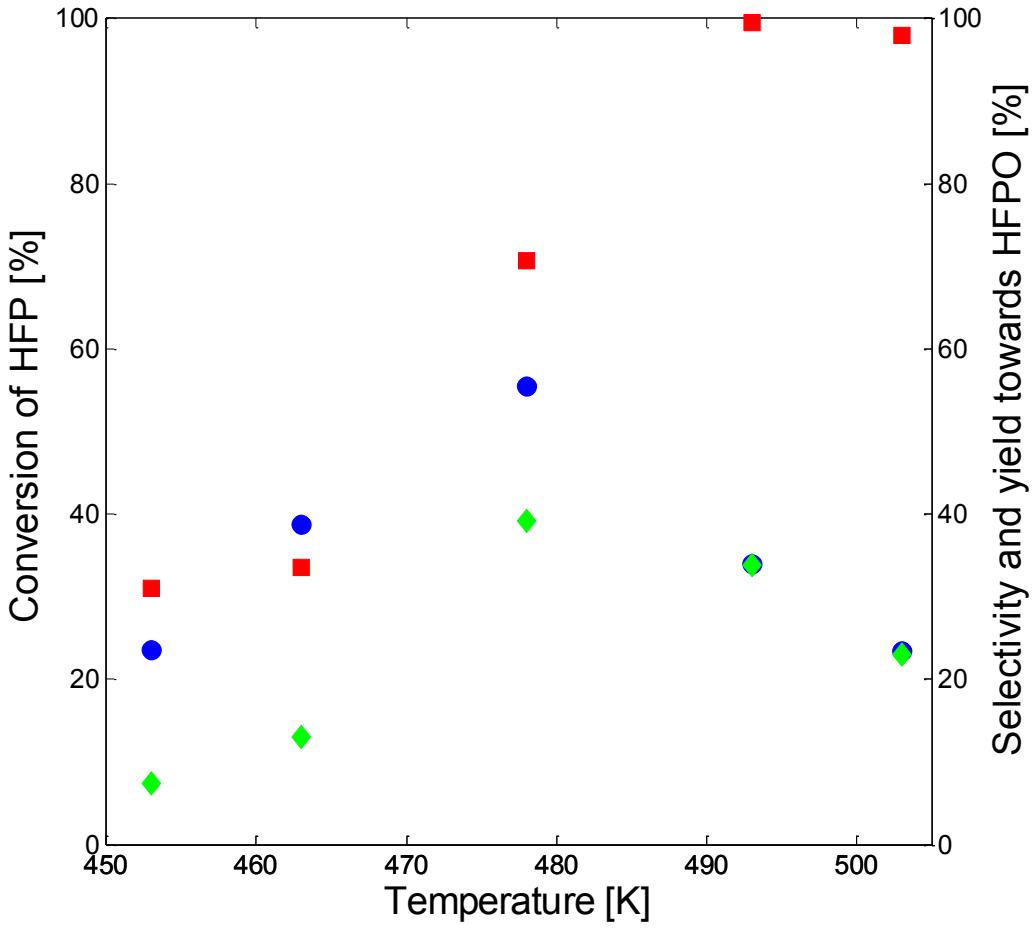

Figure 4.4. The effect of reaction temperature on the conversion of HFP (■), selectivity (●) and yield (◆) towards HFPO at a fixed HFP/O_2 molar feed ratio (1 mol mol^{-1}) and space time (120 s).

Note that extra data points were added to the original three-level OVAT experimental design for the study of the single factor effects. Figure 4.5 shows the effect of the HFP/O_2 molar feed ratio on the conversion of HFP as well as the selectivity and yield towards HFPO, at a fixed reaction temperature and space time. All three values were found to increase in the range 0.2-0.6 mol mol^{-1} HFP/O_2 and declined very slowly thereafter.

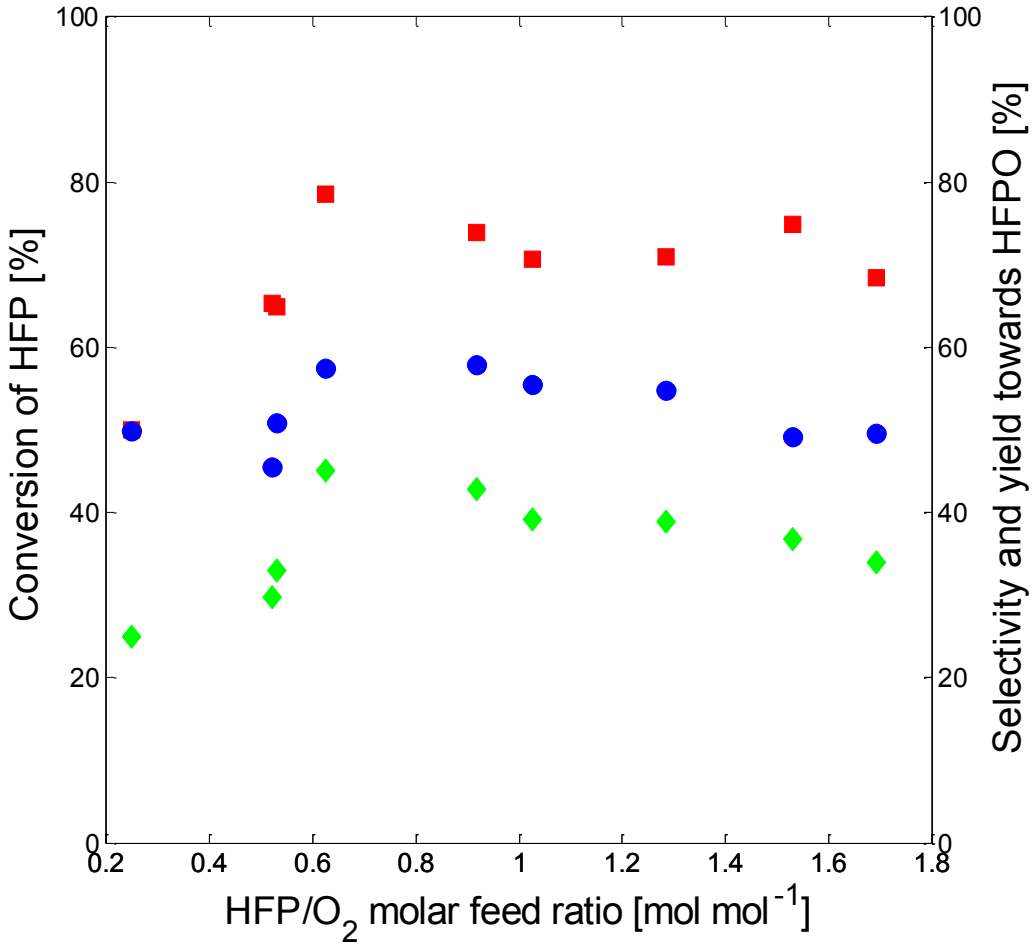

Figure 4.5. The effect of HFP/O_2 molar feed ratio on the conversion of HFP (■), selectivity (●) and yield (◆) towards HFPO at a fixed reaction temperature (478 K) and space time (120 s).

An examination of the effect of space time on the reactor performance at a fixed temperature and HFP/O_2 molar feed ratio revealed that the reaction had not reached equilibrium under the conditions that were considered, since the conversion of HFP was still found to be increasing (cf. Figure 4.6). The selectivity and yield towards HFPO also increased up to approximately 120 seconds then began to decrease.

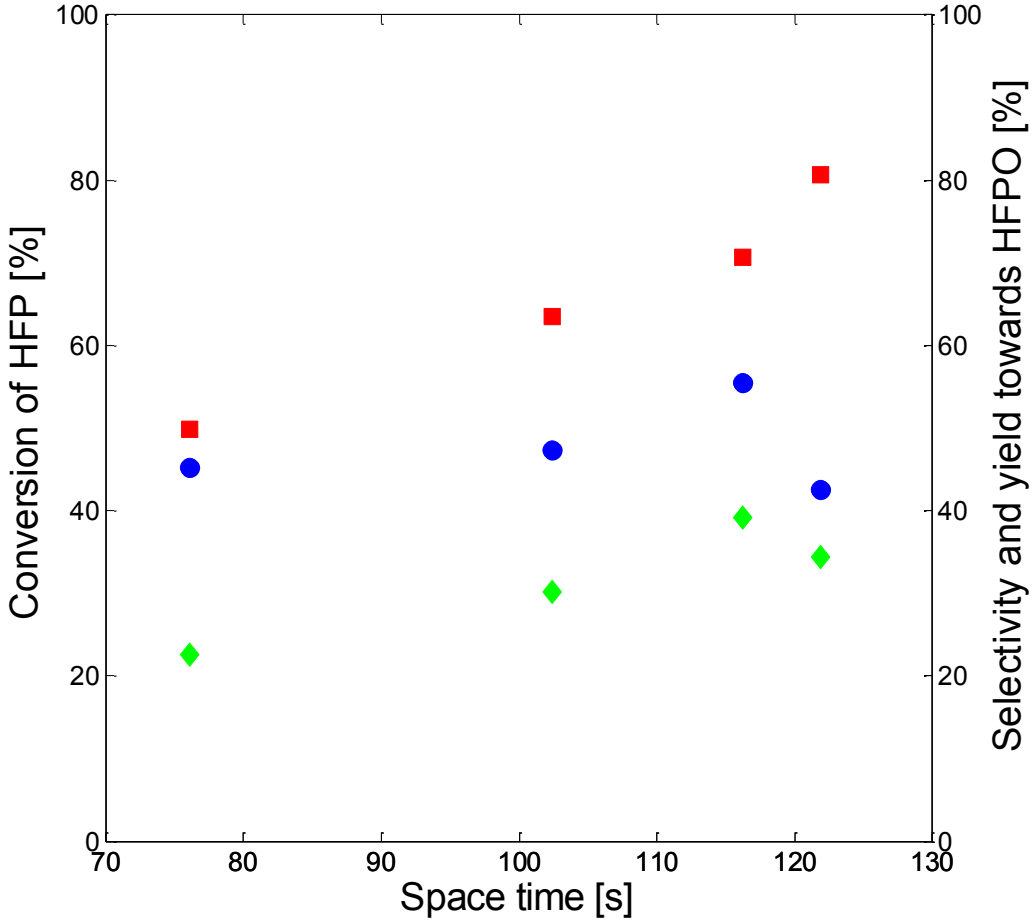

Figure 4.6. The effect of space time on the conversion of HFP (■), selectivity (●) and yield (◆) towards HFPO at a fixed reaction temperature (478 K) and HFP/O_2 molar feed ratio (1 mol mol^{-1}).

The effect of reaction temperature on the exit concentration of the HFP oxidation products, at a fixed HFP/O_2 molar feed ratio and space time, is shown in Figure 4.7. The gas-phase concentration of each species at the reactor exit was calculated according to the ideal gas law:

$$C_i^{exit} = \frac{x_i^{exit} P}{RT} \tag{4.5}$$

where x_i^{exit} is the exit mole fraction of species i, obtained by chromatographic analysis, and P and T are the reaction pressure and temperature, respectively.

COF_2 was the main reaction product, followed by HFPO and CF_3COF, at all the temperatures that were considered. The selectivity towards the acid fluorides increased at higher reaction temperatures.

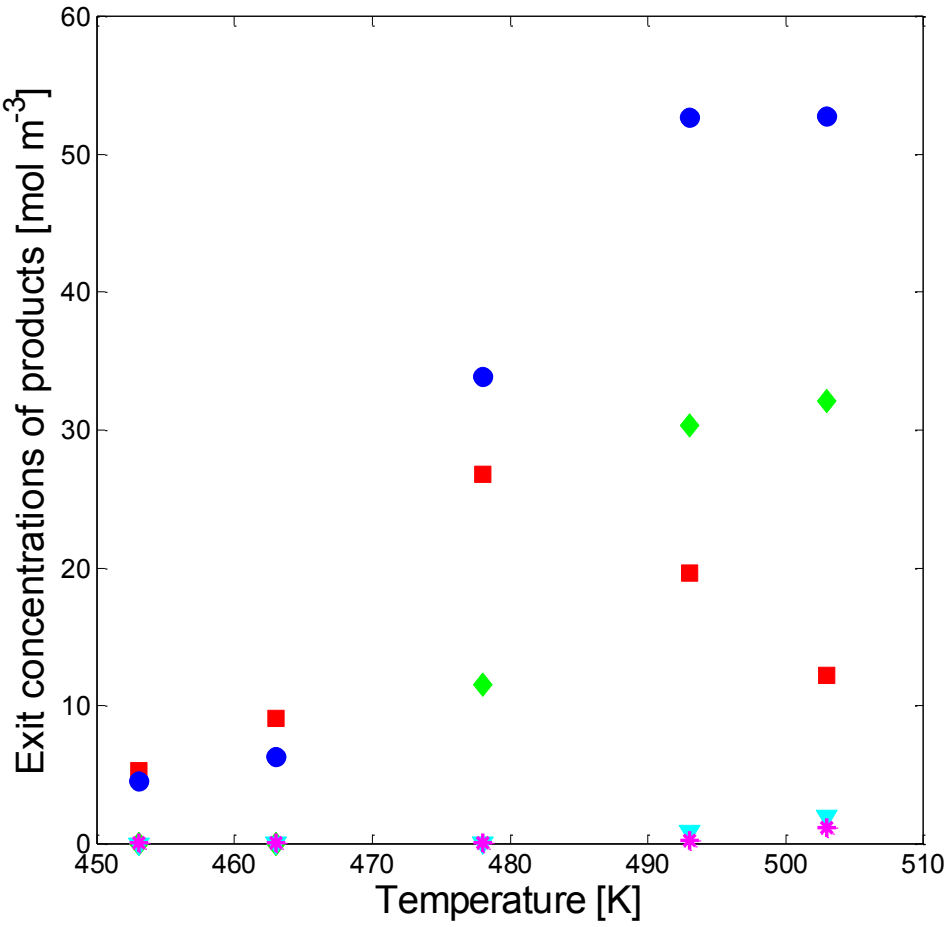

Figure 4.7. The effect of reaction temperature on the exit concentration of HFPO (■), COF_2 (●), CF_3COF (◆), C_2F_4 (▼) and *c*-C_3F_6 (✱), at a fixed HFP/O_2 molar feed ratio (1 mol mol^{-1}) and space time (120 s).

Figure 4.8 shows the effect of space time on the exit concentration of the HFP oxidation products, at a fixed reaction temperature and HFP/O_2 molar feed ratio. The exit concentrations of all the major products were found to increase with space time.

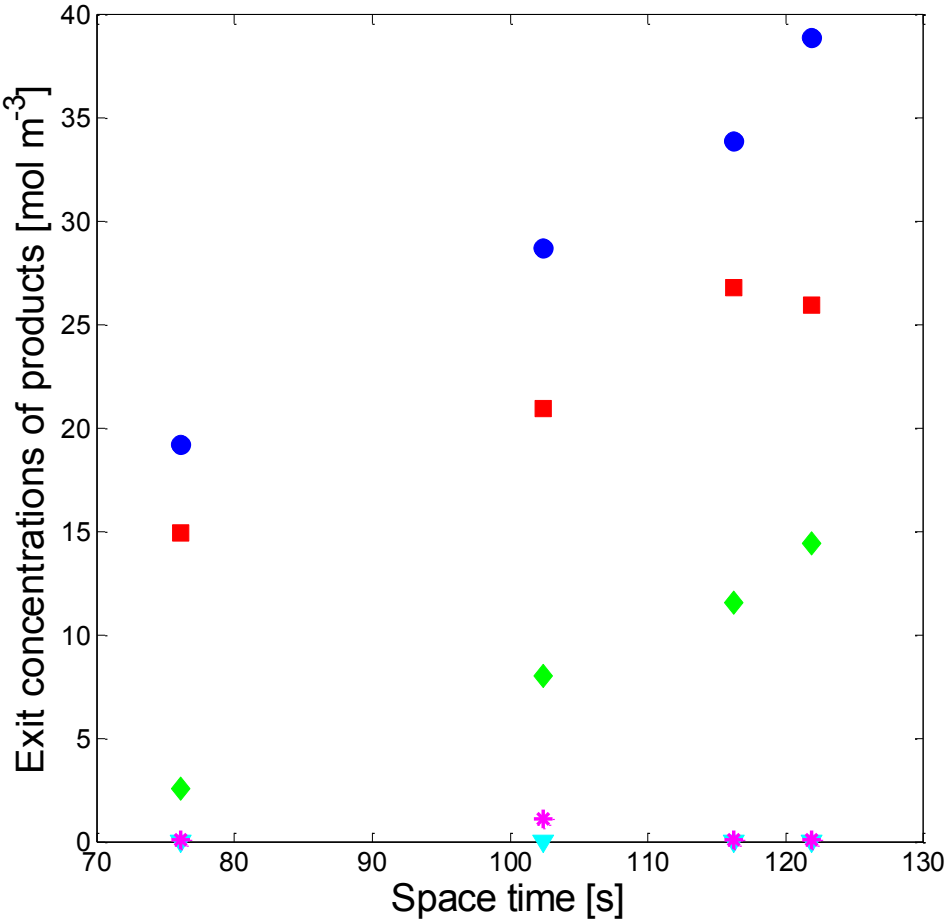

Figure 4.8. The effect of space time on the exit concentration of HFPO (■), COF_2 (●), CF_3COF (◆), C_2F_4 (▼) and *c*-C_3F_6 (✱), at a fixed reaction temperature (478 K) and HFP/O_2 molar feed ratio (1 mol mol^{-1}).

Figures 4.9 to 4.13 illustrate the effect of the HFP/O_2 molar feed ratio on the exit concentrations of HFPO, CF_3COF, COF_2, C_2F_4 and *c*-C_3F_6, respectively, at three different reaction temperatures and a fixed space time of 120 seconds. The exit concentration of HFPO was found to increase with the molar feed ratio, at all the temperatures that were considered. Similar behaviour was observed for both C_2F_4 and *c*-C_3F_6. The exit concentrations of the latter were considerably lower than that of the epoxide and exhibited maxima at a HFP/O_2 molar feed ratio of 1.5 mol mol^{-1} when the reaction temperature was 493 K. Maximum exit concentrations of COF_2 and CF_3COF were obtained at HFP/O_2 molar feed ratios between 1 and 1.2 mol mol^{-1}. The exit concentrations of the acid fluorides dropped dramatically in the oxygen-rich and HFP-rich regions.

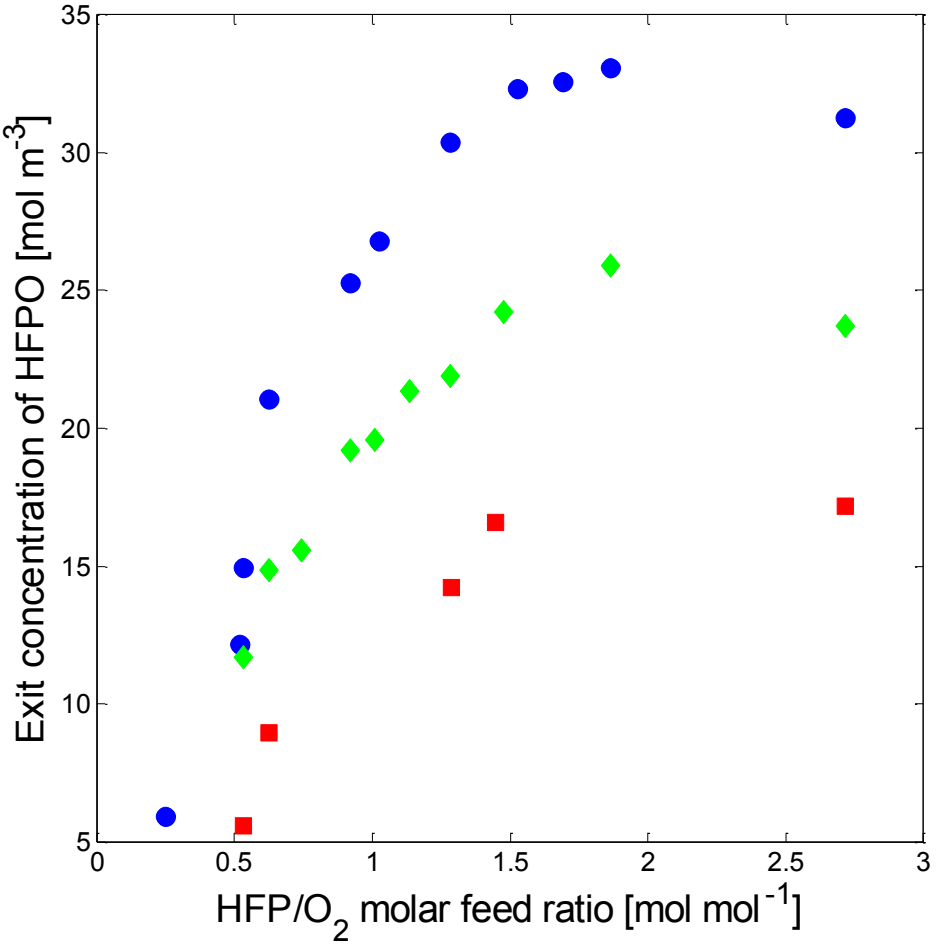

Figure 4.9. The effect of HFP/O_2 molar feed ratio on the exit concentration of HFPO at 463 K (■), 478 K (●) and 493 K (◆), at a fixed space time (120 s).

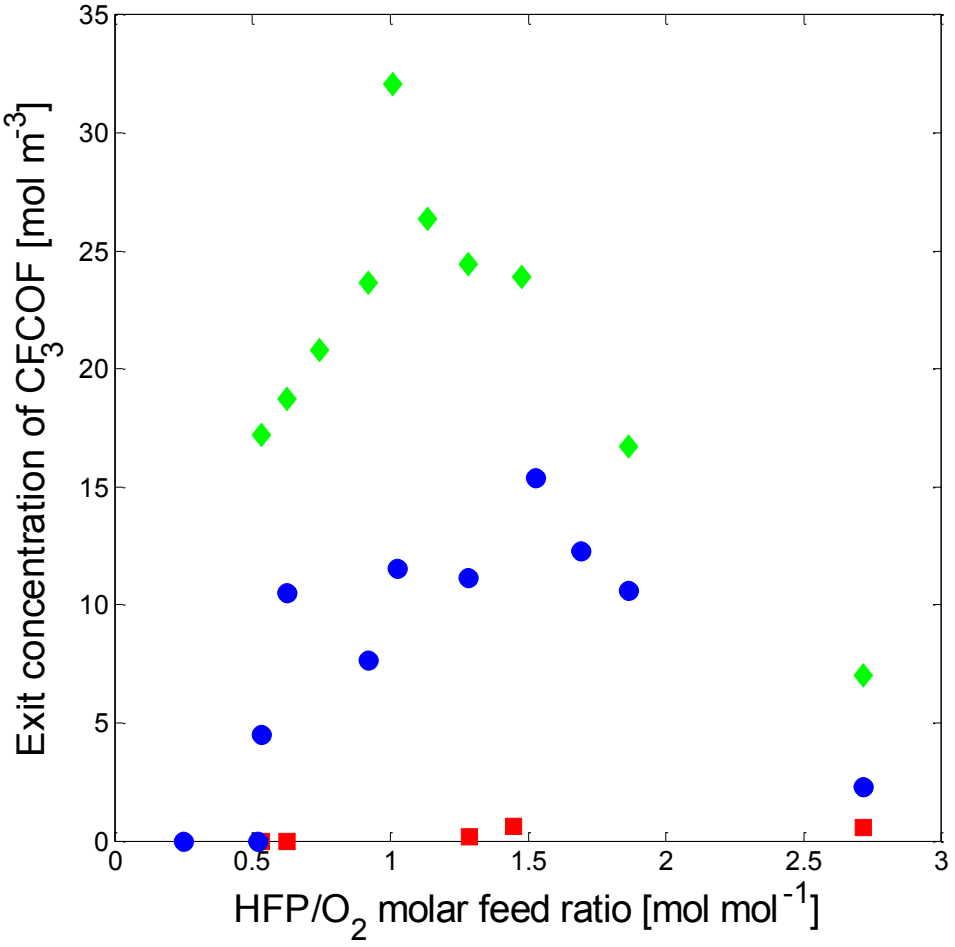

Figure 4.10. The effect of HFP/O_2 molar feed ratio on the exit concentration of CF_3COF at 463 K (■), 478 K (●) and 493 K (◆), at a fixed space time (120 s).

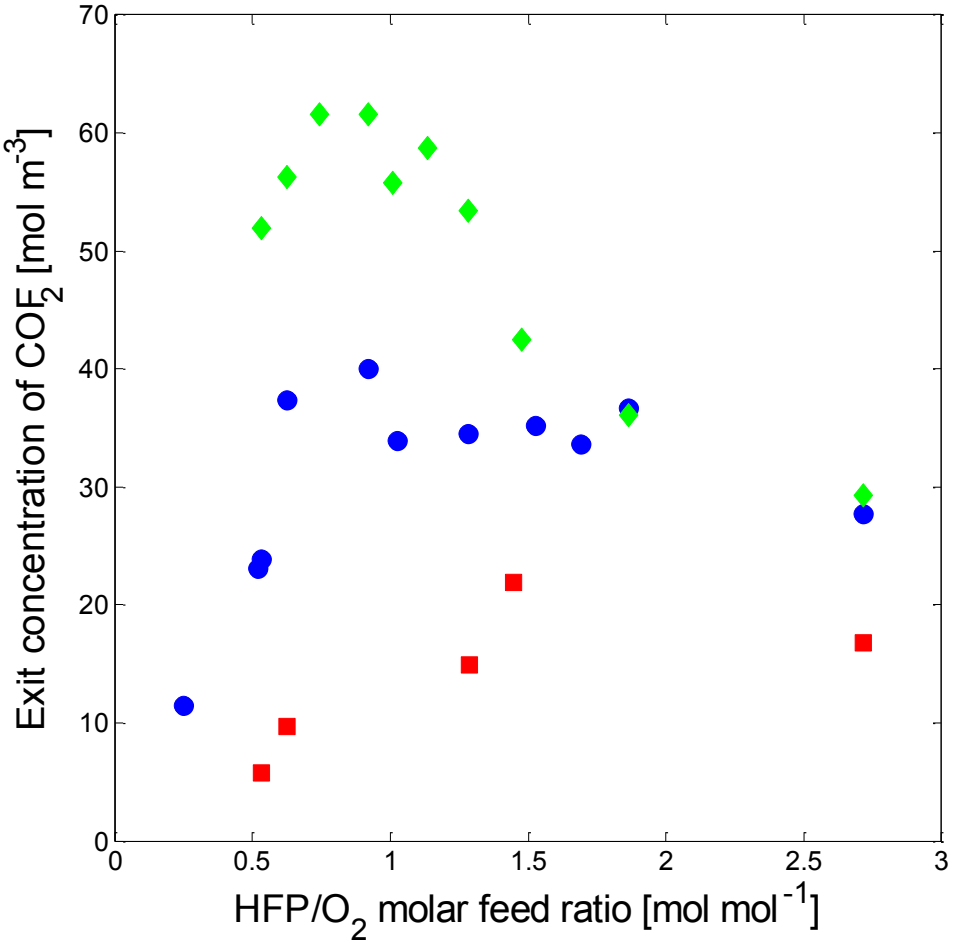

Figure 4.11. The effect of HFP/O_2 molar feed ratio on the exit concentration of COF_2 at 463 K (■), 478 K (●) and 493 K (◆), at a fixed space time (120 s).

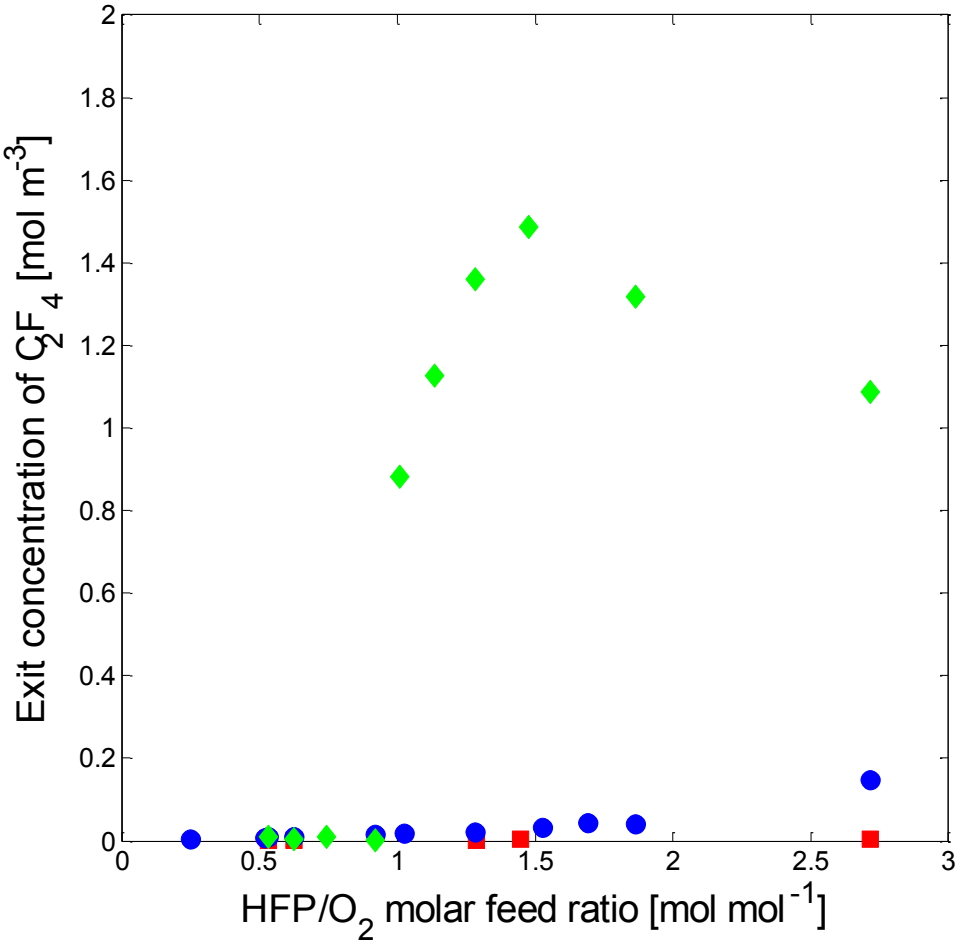

Figure 4.12. The effect of HFP/O_2 molar feed ratio on the exit concentration of C_2F_4 at 463 K (■), 478 K (●) and 493 K (◆), at a fixed space time (120 s).

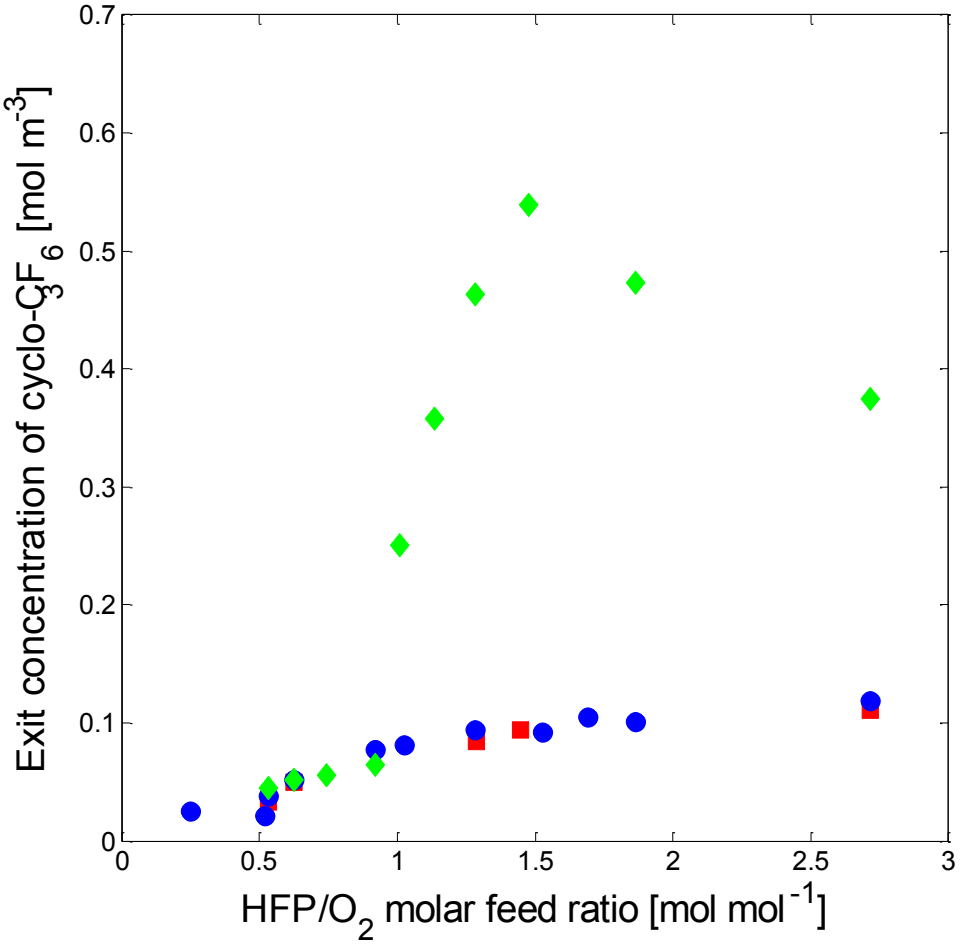

Figure 4.13. The effect of HFP/O_2 molar feed ratio on the exit concentration of *c*-C_3F_6 at 463 K (■), 478 K (●) and 493 K (◆), at a fixed space time (120 s).

Figure 4.14 shows the effect of the HFP/O_2 molar feed ratio on the ratio of CF_3COF/COF_2. There was always a greater amount of COF_2 in the product gas compared to CF_3COF. At 463 K, practically no CF_3COF was formed. Though there was a fair amount of scatter in the experimental data, a maximum could be identified at around 1.5 mol mol^{-1}.

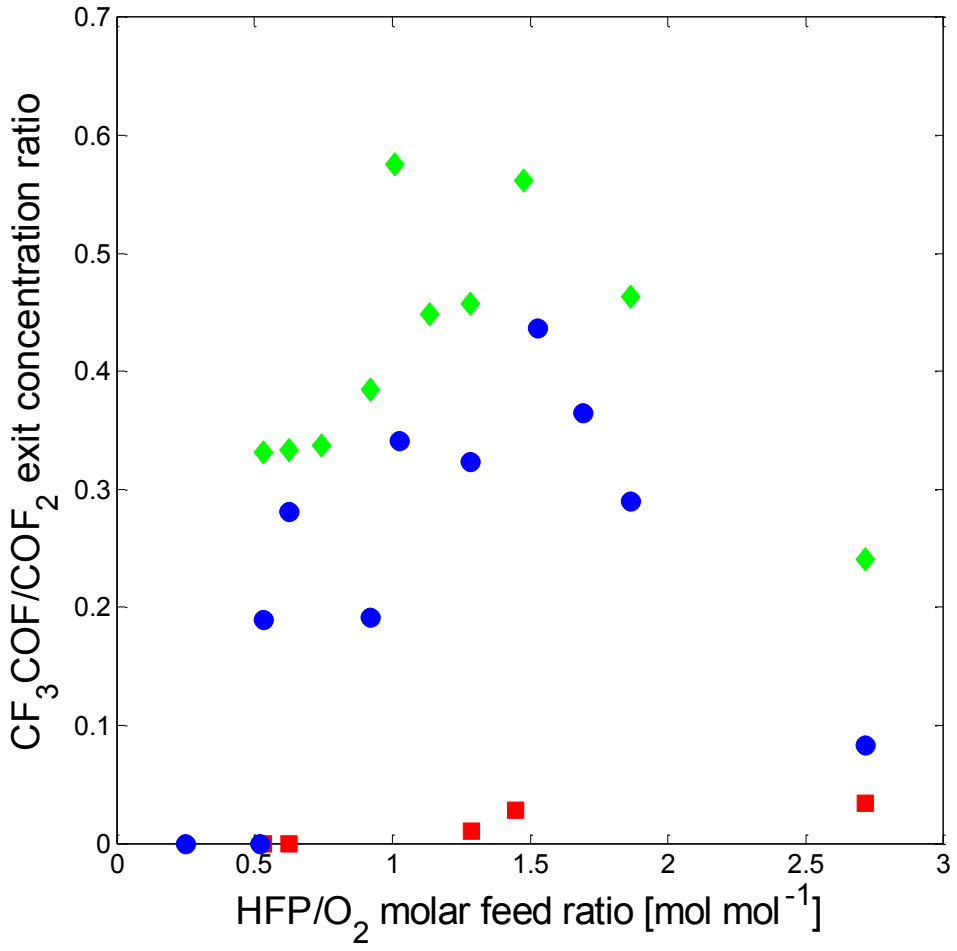

Figure 4.14. The effect of HFP/O_2 molar feed ratio on the CF_3COF/COF_2 exit concentration ratio at 463 K (■), 478 K (●) and 493 K (◆), at a fixed space time (120 s).

The variation in the consumption ratio of HFP/O_2 with the molar feed ratio, at a fixed temperature and space time, should be the same at different temperatures if a single reaction mechanism is extant. This parameter was found to follow the same decay curve for all three temperatures that were studied (cf. Figure 4.15), which appeared to confirm the hypothesis.

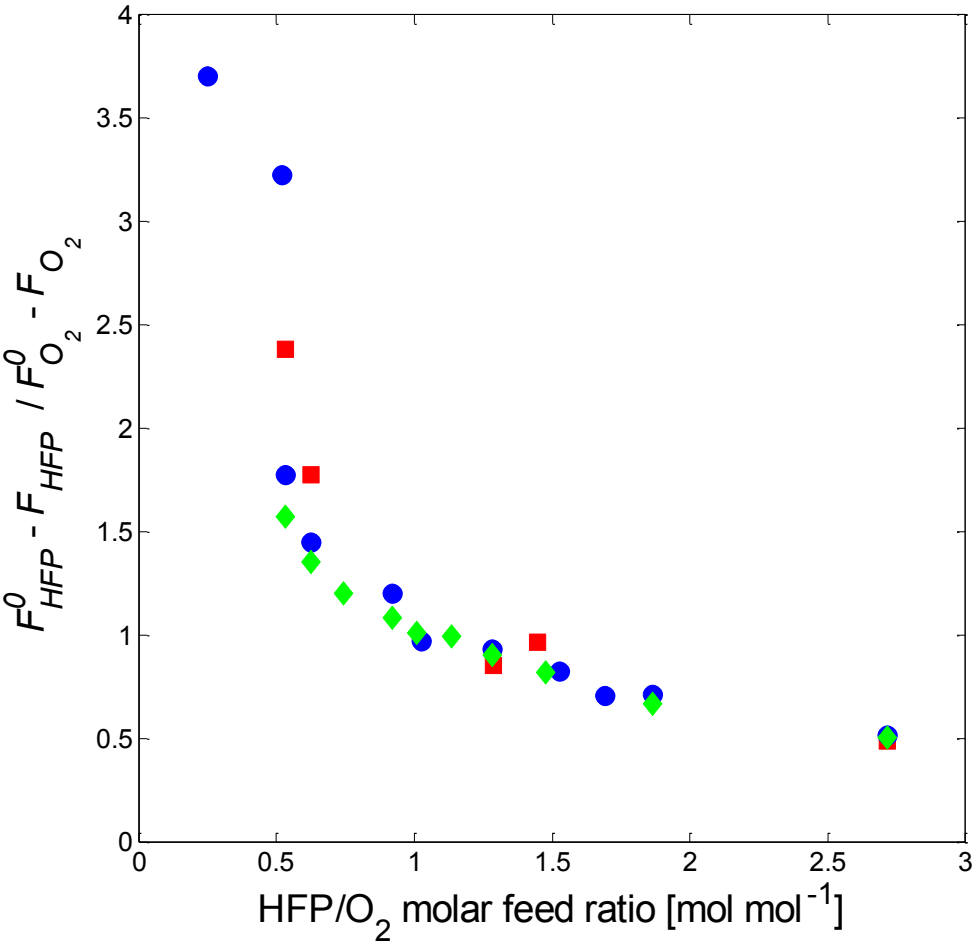

Figure 4.15. The effect of HFP/O_2 molar feed ratio on the HFP/O_2 consumption ratio at 463 K (■), 478 K (●) and 493 K (◆), at a fixed space time (120 s).

4.1.3.2. Central composite experimental design

The results of the central composite experimental design are presented in Table 4.6. The runs were conducted in a random order in order to minimize the experimental bias in the measurements (Antony, 2003).

Table 4.6. Results of the central composite experimental design.

Run[a]	Manipulated variables						Observed responses		
	X_1 Temperature [K]	Level[b]	X_2 HFP/O_2 feed ratio [mol mol^{-1}]	Level[b]	X_3 Space time [seconds]	Level[b]	Conversion of HFP [%]	HFPO selectivity [%]	HFPO yield [%]
F1	463	-1	0.5	-1	100	-1	25.29	28.44	7.19
F2	493	+1	0.5	-1	100	-1	99.51	28.30	28.16
F3	463	-1	1.5	+1	100	-1	27.40	44.36	12.16
F4	493	+1	1.5	+1	100	-1	80.35	41.70	33.51
F5	463	-1	0.5	-1	140	+1	45.33	43.95	19.92
F6	493	+1	0.5	-1	140	+1	99.90	23.14	23.11
F7	493	+1	1.5	+1	140	+1	81.32	33.31	27.09
F8	463	-1	1.5	+1	140	+1	48.60	37.62	18.28
S1	478	0	1	0	86	$-\alpha$	71.64	53.42	38.27
S2	478	0	1	0	154	$+\alpha$	49.88	45.28	22.59
S3	478	0	0.25	$-\alpha$	120	0	80.61	42.59	34.33
S4	478	0	1.841	$+\alpha$	120	0	50.00	49.85	24.92
S5	453	$-\alpha$	1	0	120	0	68.46	49.55	33.92
S6	503	$+\alpha$	1	0	120	0	30.99	23.62	7.32
C1	478	0	1	0	120	0	97.98	23.40	22.93
C2	478	0	1	0	120	0	70.95	52.23	37.05
C3	478	0	1	0	120	0	74.52	55.37	41.26
C4	478	0	1	0	120	0	70.48	54.42	38.35
C5	478	0	1	0	120	0	70.67	55.50	39.22
C6	478	0	1	0	120	0	67.32	56.15	37.80

[a] F = orthogonal factorial design points, S = axial design points, C = centre points

[b] -1 = low value, 0 = centre point value, +1 = high value, $-\alpha$ = low axial value, $+\alpha$ = high axial value

4.1.3.3. Hybridized factorial experimental design

A comprehensive list of experimental results generated using the hybridized factorial design is presented in Table 4.7. Some experimental points do not contain quantitative data on the acid fluoride by-products and unreacted oxygen, due to problems associated with the Shimadzu G.C. 2014 gas chromatograph at the time. The quantitative analyses of HFP, HFPO, C_2F_4 and *c*-C_3F_6 were still performed on the Shimadzu G.C. 2010 in these cases. Over the course of the experimentation no liquid products were observed at the collection point maintained at 373 K. However, an unknown, highly viscous, black deposit was found on the inner walls of the reactor exit piping and catch-pot. Under all reaction conditions that were investigated no detonations were observed. To check internal data consistency, atomic carbon, fluorine and oxygen mass balances were evaluated as follows:

$$\text{Carbon balance deviation} = \frac{\text{Total C flow in - Total C flow out}}{\text{Total C flow in}} \times 100\% \tag{4.6}$$

$$\text{Fluorine balance deviation} = \frac{\text{Total F flow in - Total F flow out}}{\text{Total F flow in}} \times 100\% \tag{4.7}$$

$$\text{Oxygen balance deviation} = \frac{\text{Total O flow in - Total O flow out}}{\text{Total O flow in}} \times 100\% \tag{4.8}$$

where the total carbon, fluorine and oxygen mass flow-rate into or out of the system was determined using the following expressions:

$$\text{Total carbon flow in/out} = \sum_i N_i^C \times F_i \tag{4.9}$$

$$\text{Total fluorine flow in/out} = \sum_i N_i^F \times F_i \tag{4.10}$$

$$\text{Total oxygen flow in/out} = \sum_i N_i^O \times F_i \tag{4.11}$$

where F_i is the molar flow-rate of component *i* and N_i^C, N_i^F and N_i^O are the number of carbon, fluorine and oxygen atoms in component *i*.

Table 4.7. Results of the hybridized factorial experimental design for kinetic data generation.

Temp [K]	HFP/O_2 [mol mol^{-1}]	Space time [s]	X_{HFP} [%]	S_{HFPO} [%]	Y_{HFPO} [%]	Exit concentrations of oxidation products					C balance consistency [%]	O balance consistency [%]
						C_{HFPO} [mol m^{-3}]	C_{CF3COF} [mol m^{-3}]	C_{COF2} [mol m^{-3}]	C_{C2F4} [mmol m^{-3}]	$C_{c\text{-}C3F6}$ [mmol m^{-3}]		
478	1.03	116.31	48.30	60.59	29.26	21.08	-	-	11.45	96.57	-	-
478	0.52	118.66	75.50	46.91	35.42	16.73	-	-	7.79	55.24	-	-
478	1.53	130.24	61.36	58.29	35.76	28.51	-	-	18.43	100.23	-	-
478	2.06	125.03	64.14	49.60	31.82	31.92	-	-	24.46	120.57	-	-
478	0.25	126.98	64.71	44.30	28.67	8.47	-	-	7.61	49.80	-	-
493	1.01	123.82	99.12	31.19	30.92	20.76	-	-	902.82	271.55	-	-
478	1.03	116.31	65.71	55.65	36.56	25.32	-	-	16.60	95.12	-	-
463	1.09	126.02	28.72	60.59	17.40	10.97	-	-	1.80	75.72	-	-
478	1.03	116.31	67.58	59.51	40.22	26.84	-	-	17.59	97.75	-	-
478	0.99	200.42	99.60	43.68	43.50	27.03	-	-	1.05	90.11	-	-
478	1.03	116.31	65.91	57.77	38.07	25.57	-	-	13.21	79.97	-	-
459	1.12	116.99	26.47	38.24	10.12	6.83	-	-	0.00	81.33	-	-
478	2.06	125.03	59.27	58.04	34.40	28.75	-	-	42.51	143.20	-	-
478	0.25	126.98	49.35	62.59	30.89	6.86	-	-	4.41	28.48	-	-
463	0.56	108.40	28.64	35.24	10.09	4.64	-	-	0.00	46.71	-	-
463	1.09	126.02	39.52	26.03	10.29	7.29	0.00	6.10	2.51	83.12	26.35	-2.90
463	1.12	115.90	38.39	26.29	10.09	7.39	0.00	8.79	3.75	84.16	24.28	2.69
478	1.03	116.25	71.64	53.42	38.27	25.41	13.71	34.85	15.98	94.60	2.05	11.53
478	1.53	129.73	74.89	49.17	36.82	32.30	16.27	37.26	31.05	91.84	11.54	16.09
478	1.03	116.25	70.95	52.23	37.05	24.87	15.33	35.62	16.77	75.73	0.95	14.87
493	1.01	123.65	99.44	33.99	33.80	19.59	32.09	55.80	881.94	250.38	-4.64	4.98
478	1.03	116.25	74.52	55.37	41.26	27.72	15.58	36.92	21.50	81.47	-0.56	14.67
478	0.52	118.61	65.31	45.57	29.76	12.16	0.00	24.43	6.15	21.45	15.66	-3.16
478	0.25	126.94	62.02	38.35	23.78	5.49	0.00	12.73	3.09	25.02	19.85	-2.01
463	0.56	87.72	25.29	28.44	7.19	3.24	0.00	4.23	1.36	53.99	14.94	1.20
453	1.01	99.40	30.99	23.62	7.32	5.26	0.00	4.74	0.00	71.44	21.49	9.11
478	1.69	115.94	68.46	49.55	33.92	32.57	12.97	35.60	44.61	104.96	13.14	25.68
493	1.48	117.31	81.32	33.31	27.09	24.20	23.87	42.52	1485.83	539.40	18.96	24.29
478	1.10	102.39	63.57	47.39	30.12	20.94	8.49	30.40	15.85	1088.16	9.27	9.91
478	1.05	121.89	80.61	42.59	34.33	25.94	15.26	41.18	14.83	88.38	14.63	20.21
478	1.01	76.05	49.88	45.28	22.59	14.96	2.72	20.31	7.57	66.85	14.36	6.81
463	1.48	91.40	27.40	44.36	12.16	9.06	0.00	8.76	0.59	82.82	11.37	-6.58
493	1.45	90.59	80.35	41.70	33.51	25.88	18.94	48.02	895.95	236.93	8.83	11.71
463	1.45	121.86	48.60	37.62	18.28	16.57	0.62	21.87	4.21	94.12	21.82	19.15
493	0.51	99.77	99.51	28.30	28.16	11.95	18.14	46.81	0.00	45.79	6.09	15.25

Table 4.7. (*continued*)

Temp [K]	HFP/O_2 [mol mol^{-1}]	Space time [s]	X_{HFP} [%]	S_{HFPO} [%]	Y_{HFPO} [%]	Exit concentrations of oxidation products					C balance consistency [%]	O balance consistency [%]
						C_{HFPO} [mol m^{-3}]	C_{CF3COF} [mol m^{-3}]	C_{COF2} [mol m^{-3}]	C_{C2F4} [mmol m^{-3}]	$C_{c\text{-}C3F6}$ [mmol m^{-3}]		
493	0.57	136.92	99.90	23.14	23.11	10.52	20.37	48.54	0.00	39.37	11.46	12.16
463	0.52	140.72	45.33	43.95	19.92	8.76	0.38	14.98	1.90	48.35	13.50	4.99
463	1.08	125.92	33.89	50.43	17.09	11.17	0.23	13.88	2.80	80.82	9.49	-1.10
478	0.25	126.94	50.00	49.85	24.92	5.91	0.20	12.18	3.78	25.21	7.41	3.97
503	0.99	123.88	97.98	23.40	22.93	12.23	34.00	55.85	1951.28	1118.97	-6.70	2.85
463	1.06	120.35	33.61	38.73	13.02	9.03	0.00	6.25	2.09	73.49	17.58	3.55
478	1.06	116.57	70.55	42.94	30.29	23.84	0.00	34.26	14.10	62.65	25.74	17.86
493	1.06	113.03	99.75	30.40	30.33	21.08	23.12	63.97	563.53	144.80	15.92	16.33
493	1.14	126.81	98.54	26.47	26.09	21.35	26.37	58.74	1127.59	358.06	25.77	25.23
463	1.14	135.02	41.51	60.41	25.08	17.45	0.00	24.45	5.43	72.94	-0.16	-10.74
478	1.03	116.25	70.48	54.42	38.35	26.12	10.59	37.45	17.91	87.16	3.38	15.78
478	1.14	130.78	86.73	41.49	35.99	29.86	15.97	45.08	19.58	76.48	19.80	22.45
463	1.86	131.28	31.78	44.69	14.20	12.69	0.00	8.75	2.29	89.55	14.33	6.07
478	1.86	127.16	68.80	48.29	33.22	33.08	10.62	36.64	41.96	100.80	16.19	21.73
493	1.86	123.29	65.94	46.65	30.76	25.89	16.73	36.12	1317.03	473.34	6.13	11.57
478	1.03	116.25	70.67	55.50	39.22	26.79	12.21	35.85	19.50	80.84	2.00	16.45
463	0.78	114.09	32.35	57.32	18.54	10.28	0.00	10.25	1.25	60.55	7.64	3.19
478	0.78	110.51	66.10	51.33	33.93	20.00	6.45	27.05	12.19	61.31	9.56	12.47
463	0.61	113.97	32.73	28.55	9.35	4.71	0.00	3.33	0.82	42.17	21.19	3.69
463	0.61	143.17	34.73	42.32	14.70	7.29	0.00	8.40	2.16	50.31	14.37	5.80
478	0.61	110.40	67.50	43.88	29.62	15.25	2.48	23.87	8.00	40.49	19.22	9.80
493	0.61	107.04	99.90	26.94	26.91	13.33	18.75	49.35	0.00	42.95	14.56	14.46
493	0.78	107.15	99.97	29.73	29.72	17.08	23.26	56.02	0.00	49.03	10.77	16.82
478	1.33	106.86	58.41	55.22	32.25	24.13	8.10	28.38	15.70	78.48	6.30	8.21
478	1.03	116.25	67.32	56.15	37.80	26.55	9.76	33.41	19.34	77.35	4.36	19.21
463	1.33	110.32	26.32	53.23	14.01	9.94	0.00	8.66	1.50	67.07	8.27	-3.43
463	1.48	140.42	44.92	42.43	19.06	16.89	0.00	16.07	2.40	81.48	19.83	14.23
478	1.48	136.01	80.08	47.05	37.67	35.10	2.97	54.17	58.91	93.62	20.86	23.41
478	0.61	138.68	86.13	44.07	37.96	21.03	5.01	45.73	20.86	55.88	14.59	23.38
493	0.61	134.46	99.85	25.87	25.83	12.87	16.68	56.52	2.14	57.76	13.86	18.42
493	1.48	131.87	77.40	41.83	32.38	24.40	18.84	45.92	1531.21	606.93	6.01	9.94
463	0.82	93.59	21.17	57.80	12.24	7.04	0.00	4.72	1.06	57.37	6.21	6.63
493	0.82	87.90	99.21	34.08	33.81	20.47	20.93	59.79	1.32	63.29	9.44	20.78
493	1.33	103.61	85.37	45.05	38.46	26.46	20.56	50.89	868.05	207.11	1.32	4.10
478	0.82	90.66	51.63	59.65	30.80	17.95	1.66	24.38	10.77	57.67	4.98	11.60

Table 4.7. (*continued*)

Temp [K]	HFP/O_2 [mol mol^{-1}]	Space time [s]	X_{HFP} [%]	S_{HFPO} [%]	Y_{HFPO} [%]	Exit concentrations of oxidation products					C balance consistency [%]	O balance consistency [%]
						C_{HFPO} [mol m^{-3}]	C_{CF3COF} [mol m^{-3}]	C_{COF2} [mol m^{-3}]	C_{C2F4} [mmol m^{-3}]	$C_{c\text{-}C3F6}$ [mmol m^{-3}]		
463	1.55	111.65	38.29	34.97	13.39	12.08	0.00	7.89	2.50	86.67	21.99	12.12
478	1.55	108.15	72.01	45.86	33.02	31.70	0.44	45.44	23.10	92.97	22.90	23.43
493	1.55	104.86	77.36	40.96	31.69	27.33	12.32	48.23	1216.19	385.34	16.24	19.67
493	0.88	132.27	99.86	23.25	23.22	16.32	24.49	63.34	4.52	76.14	23.34	28.19
478	0.88	136.42	95.38	36.92	35.21	25.29	18.09	53.99	10.41	67.26	18.31	25.33
463	0.88	140.84	49.16	52.33	25.72	17.17	0.22	20.99	3.83	63.30	12.74	16.26
463	0.92	128.69	34.39	59.27	20.38	12.51	0.00	13.25	1.93	67.55	6.82	4.84
478	0.92	124.65	73.90	57.87	42.77	25.27	7.65	40.04	15.85	76.82	-0.10	4.90
463	0.76	102.63	22.05	46.58	10.27	5.68	0.00	3.65	1.03	57.60	9.57	4.66
478	0.76	99.41	52.61	52.65	27.70	15.87	0.38	20.20	10.29	56.11	12.70	9.77
493	0.76	96.38	99.71	34.15	34.06	18.24	20.78	57.83	1.02	58.11	3.81	12.96
493	0.92	120.86	99.93	31.48	31.45	19.21	23.65	61.57	0.69	64.37	9.06	13.67
478	1.29	111.08	73.84	53.78	39.71	32.98	11.91	40.52	23.77	94.66	8.29	24.68
463	1.29	114.68	28.88	60.97	17.61	14.23	0.15	14.92	1.97	84.40	1.87	7.62
478	1.68	140.66	65.80	58.44	38.45	32.43	11.07	37.55	35.46	98.82	3.74	13.02
493	1.29	107.70	81.81	39.15	32.03	25.84	20.56	46.53	1327.42	450.83	12.03	25.37
463	1.68	145.22	24.70	66.57	16.44	12.80	0.00	9.48	2.31	85.50	4.21	-1.41
463	0.65	103.42	25.04	43.14	10.80	5.68	0.00	4.22	0.88	52.03	11.57	10.24
478	0.65	100.17	61.13	49.78	30.43	16.73	2.05	23.42	9.19	50.65	14.03	16.39
493	0.65	97.13	99.86	31.29	31.25	16.24	19.47	54.71	0.65	47.88	8.58	19.35
493	1.68	136.38	68.18	48.72	33.22	25.47	18.09	39.12	1493.41	761.64	0.07	8.51
463	1.28	130.89	37.96	56.10	21.30	15.64	1.47	17.27	6.65	85.17	7.48	5.52
478	1.28	126.79	70.99	54.80	38.91	30.39	11.15	34.47	22.40	94.40	7.83	13.81
493	1.28	122.93	89.30	33.61	30.01	21.88	24.42	53.38	1359.50	462.85	10.78	11.38
463	0.83	107.38	23.88	45.80	10.94	6.51	0.00	4.52	1.18	59.88	10.42	8.08
478	0.83	104.01	55.57	54.22	30.13	18.89	1.07	22.83	10.90	62.02	12.16	15.46
493	0.83	100.84	99.81	33.98	33.91	19.79	22.60	61.21	0.80	69.73	5.12	17.86
493	0.69	86.24	99.91	33.32	33.29	17.64	19.44	55.26	1.05	62.11	7.39	17.62
478	0.69	88.94	55.58	53.46	29.71	15.34	4.06	23.58	9.22	54.50	5.40	8.49
463	0.69	91.82	25.04	51.60	12.92	6.64	0.00	6.08	0.52	49.35	8.19	3.79
463	1.21	98.36	25.34	45.17	11.45	7.79	0.00	6.26	0.93	66.46	10.84	-5.15
478	1.21	95.28	54.49	49.16	26.79	20.01	4.26	23.29	11.79	73.95	13.50	10.03
493	1.21	92.38	94.26	36.69	34.58	23.82	22.90	57.87	576.80	140.18	8.87	6.97
463	2.27	143.26	31.59	43.51	13.74	13.14	0.00	10.03	2.24	98.96	14.36	5.74
478	2.27	138.77	61.49	52.54	32.31	33.32	7.16	31.46	89.27	107.40	14.34	17.91

Table 4.7. (*continued*)

Temp [K]	HFP/O_2 [mol mol^{-1}]	Space time [s]	X_{HFP} [%]	S_{HFPO} [%]	Y_{HFPO} [%]	Exit concentrations of oxidation products					C balance consistency [%]	O balance consistency [%]
						C_{HFPO} [mol m^{-3}]	C_{CF3COF} [mol m^{-3}]	C_{COF2} [mol m^{-3}]	C_{C2F4} [mmol m^{-3}]	$C_{c\text{-}C3F6}$ [mmol m^{-3}]		
493	2.27	134.55	61.53	41.75	25.69	24.67	13.44	32.32	1402.88	588.17	13.82	15.85
493	2.57	134.40	48.78	68.67	33.50	28.05	10.89	25.93	1278.99	513.56	-5.21	-0.24
478	2.57	138.62	52.29	61.97	32.40	30.54	8.63	28.58	236.04	97.55	3.52	7.12
463	2.57	143.11	35.31	64.50	22.78	20.72	3.57	21.24	8.55	100.58	2.14	0.68
463	1.14	110.96	14.52	60.60	8.80	9.34	0.00	6.90	1.20	76.28	-3.69	3.87
478	1.14	107.48	47.41	61.71	29.26	24.59	6.58	26.89	15.01	79.66	-12.37	9.21
493	1.14	104.21	83.31	46.24	38.52	26.22	20.32	50.24	1035.35	291.78	-1.04	18.70
463	0.99	89.93	21.52	41.02	8.83	5.56	0.00	3.11	0.54	63.36	11.06	1.05
478	0.99	87.11	37.08	57.22	21.21	13.30	0.00	11.78	8.15	63.34	9.60	3.39
493	0.99	84.46	99.70	34.58	34.48	22.98	22.34	62.91	1.16	73.80	11.42	17.75
493	1.26	87.37	87.16	46.09	40.17	28.60	19.69	51.19	667.02	166.59	3.84	11.40
478	1.26	90.11	59.78	51.58	30.83	22.80	9.17	30.66	15.83	77.30	6.84	11.23
463	1.26	93.03	22.78	55.25	12.59	8.73	0.00	5.98	1.01	72.30	7.32	-1.48
463	1.74	105.83	23.54	60.37	14.21	11.20	0.00	8.37	1.44	84.05	5.79	-3.19
478	1.74	102.51	54.66	51.50	28.15	25.00	6.23	27.77	17.82	94.07	11.39	15.09
493	1.74	99.39	71.82	43.53	31.26	27.68	15.88	39.40	1145.50	359.12	12.60	17.80
463	0.51	97.60	26.59	37.73	10.03	4.54	0.00	2.39	0.00	37.92	14.80	9.87
478	0.51	94.54	45.36	52.45	23.79	10.42	0.00	10.56	7.63	43.25	13.52	8.52
493	0.51	91.66	99.74	27.91	27.84	12.48	14.02	49.62	2.31	36.65	14.13	18.75
493	0.63	117.51	99.89	31.27	31.24	14.84	18.74	56.27	3.46	51.33	2.91	14.77
478	0.63	121.20	78.50	57.48	45.12	21.06	10.52	37.38	10.22	51.73	-8.32	7.97
463	0.63	125.12	24.82	78.15	19.39	8.95	0.00	9.75	1.02	50.12	-1.59	1.32
463	0.53	125.10	24.39	52.86	12.89	5.56	0.00	5.79	1.17	32.93	7.03	3.24
478	0.53	121.18	64.93	50.86	33.02	14.94	4.51	23.83	8.67	37.55	7.69	11.23
493	0.53	117.49	99.61	28.22	28.11	11.70	17.18	51.92	9.30	45.10	2.39	11.87
463	1.29	142.49	36.50	42.07	15.36	12.63	-	-	2.31	81.26	-	-
478	1.29	138.02	77.75	48.55	37.75	32.83	-	-	19.43	92.24	-	-
493	1.29	133.82	85.33	33.33	28.44	22.27	-	-	1622.84	785.57	-	-
493	1.08	151.63	-	-	-	-	31.14	82.72	-	-	-	-
478	1.08	156.39	90.49	47.73	43.19	32.15	16.65	53.28	51.05	95.66	8.45	20.04
463	1.08	161.46	44.37	68.42	30.36	19.94	2.96	24.95	6.83	80.25	-1.67	7.12
463	0.74	135.48	19.88	62.00	12.32	10.00	0.17	10.05	1.81	52.21	-7.41	-1.20
478	0.74	131.23	68.75	60.39	41.52	21.61	7.98	35.22	13.64	58.78	-5.57	7.95
493	0.74	127.24	99.62	31.29	31.17	15.56	20.78	61.60	8.50	55.59	-0.44	9.87
463	1.03	99.84	21.03	45.07	9.48	6.10	0.00	3.82	1.35	64.10	9.59	2.30

Table 4.7. (*continued*)

Temp [K]	HFP/O_2 [mol mol^{-1}]	Space time [s]	X_{HFP} [%]	S_{HFPO} [%]	Y_{HFPO} [%]	Exit concentrations of oxidation products					C balance consistency [%]	O balance consistency [%]
						C_{HFPO} [mol m^{-3}]	C_{CF3COF} [mol m^{-3}]	C_{COF2} [mol m^{-3}]	C_{C2F4} [mmol m^{-3}]	$C_{c\text{-}C3F6}$ [mmol m^{-3}]		
478	1.03	96.70	45.27	59.75	27.05	17.95	8.61	15.11	10.02	69.34	1.99	13.09
493	1.03	93.76	98.99	35.76	35.40	23.09	19.82	65.11	374.93	98.46	9.63	13.67
493	1.49	164.51	67.25	45.06	30.31	22.02	17.59	43.21	1693.22	872.54	-1.66	13.65
478	1.49	169.67	59.99	61.69	37.01	33.50	12.38	38.96	436.07	153.72	-20.58	6.41
463	1.49	175.17	42.06	63.20	26.58	27.21	5.01	26.01	9.03	103.34	-8.38	18.18
463	1.82	150.55	34.46	64.08	22.72	21.97	-	-	4.74	107.36	-	-
478	1.82	145.83	60.16	69.36	41.72	36.80	0.95	19.81	171.31	111.33	10.08	-1.34
493	1.82	141.39	63.66	41.01	26.10	23.87	14.60	35.59	1555.79	692.66	12.15	25.68
463	2.26	116.46	22.41	48.70	10.91	9.72	0.00	4.81	1.41	100.17	9.69	-2.26
478	2.26	112.81	49.30	56.00	27.61	26.81	0.00	19.64	17.50	100.54	14.93	5.62
493	2.26	109.37	59.72	48.00	28.67	25.76	11.26	34.56	1164.29	398.84	8.69	9.08
493	2.72	120.10	49.86	49.84	24.85	23.72	7.03	29.26	1087.55	374.22	8.85	13.33
478	2.72	123.87	50.97	58.69	29.91	31.26	2.29	27.68	146.40	118.62	10.68	19.20
463	2.72	127.88	26.87	69.63	18.71	17.17	0.57	16.79	4.19	110.42	1.65	4.15
463	0.71	157.48	26.21	64.53	16.91	11.84	0.14	10.39	2.81	53.86	-2.59	11.97
478	0.71	152.54	79.25	56.74	44.97	23.45	10.61	38.24	14.21	70.61	-3.76	9.81
493	0.71	147.90	99.64	30.12	30.02	13.75	21.14	62.33	38.63	56.53	-6.57	5.48
463	1.40	101.69	16.47	71.11	11.71	8.26	-	-	0.00	77.65	-	-
478	1.40	98.50	38.62	61.31	23.67	17.92	-	-	10.05	77.79	-	-
493	1.40	95.51	78.64	44.80	35.23	27.37	-	-	896.36	246.89	-	-
493	1.43	168.09	82.85	27.19	22.53	19.09	-	-	1829.23	1079.98	-	-
478	1.43	173.36	78.89	52.42	41.36	31.84	-	-	667.28	221.58	-	-
463	1.43	178.98	67.12	53.15	35.67	30.59	-	-	23.89	92.23	-	-
463	0.94	169.93	55.57	61.54	34.20	21.39	-	-	8.23	72.44	-	-
478	0.94	164.60	95.83	36.82	35.28	23.39	-	-	4.61	76.55	-	-
493	0.94	159.59	99.62	25.48	25.38	15.58	-	-	17.57	67.55	-	-
463	1.10	85.43	19.34	42.62	8.24	5.32	-	-	0.00	59.08	-	-
478	1.10	82.75	33.63	51.95	17.47	11.86	-	-	6.48	66.40	-	-
493	1.10	80.23	92.14	42.14	38.83	27.38	-	-	39.17	83.65	-	-
493	0.61	107.04	98.99	29.04	28.75	12.78	-	-	17.06	51.86	-	-
478	0.61	110.40	81.01	42.54	34.46	16.90	-	-	6.45	46.35	-	-
463	0.61	113.97	31.91	48.54	15.49	7.19	-	-	1.30	40.06	-	-
463	1.20	207.25	57.11	58.71	33.53	24.76	-	-	4.45	75.29	-	-
478	1.20	200.75	92.90	42.92	39.87	28.50	-	-	310.12	100.74	-	-
493	1.20	194.64	92.50	26.36	24.38	17.20	-	-	1680.24	1004.54	-	-

The ratio of the number of carbon atoms to fluorine atoms in all of the species contributing to the atomic balances was 1:2. The balances for carbon and fluorine as defined in Equations 4.6 and 4.7 were therefore numerically equivalent. Only the carbon balance deviation is reported here for brevity. Figures 4.16 to 4.23 show plots of the carbon and oxygen balance deviation against the experiment number, reaction temperature, HFP/O_2 molar feed ratio and space time, respectively. In most cases, deficiencies in carbon, fluorine and oxygen were found in the gaseous products. The deficiencies in the atomic balances were likely due to the retention of some heavy reaction products inside the reactor system. The reaction pathways leading to the formation of such products and the possible molecular structure of the latter are discussed further in Chapter 5.

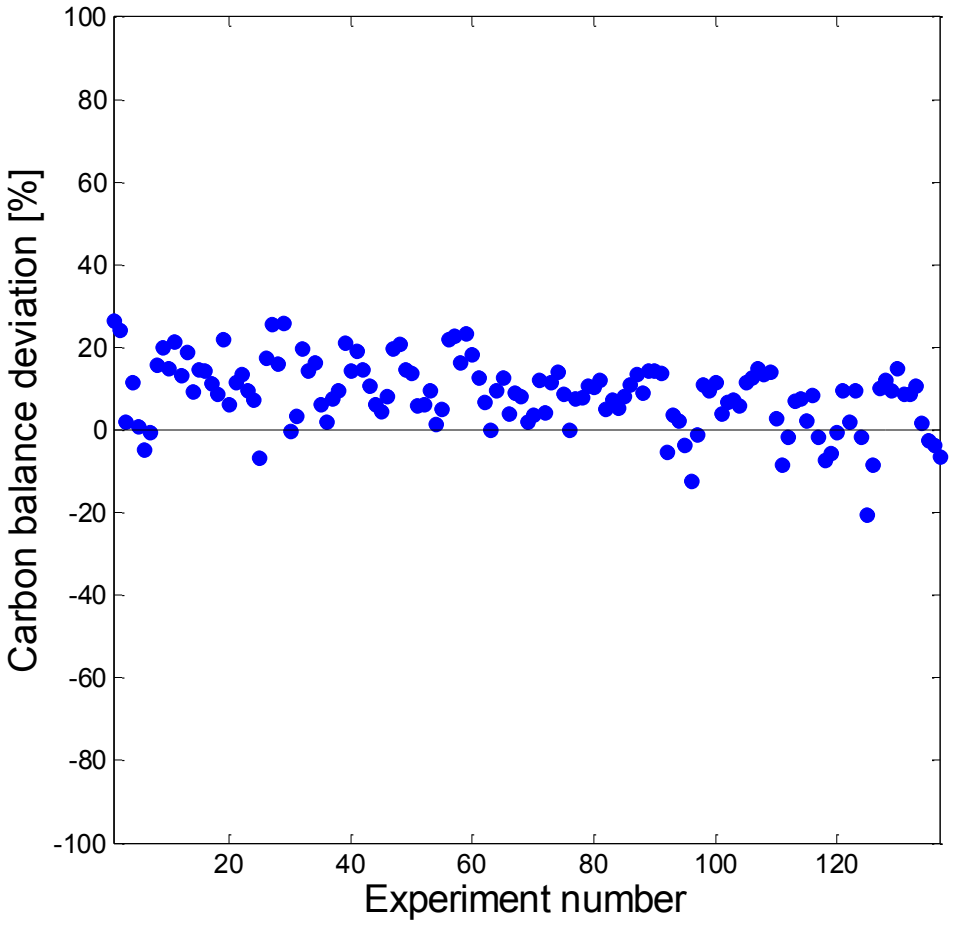

Figure 4.16. Plot of carbon balance deviation against experiment number.

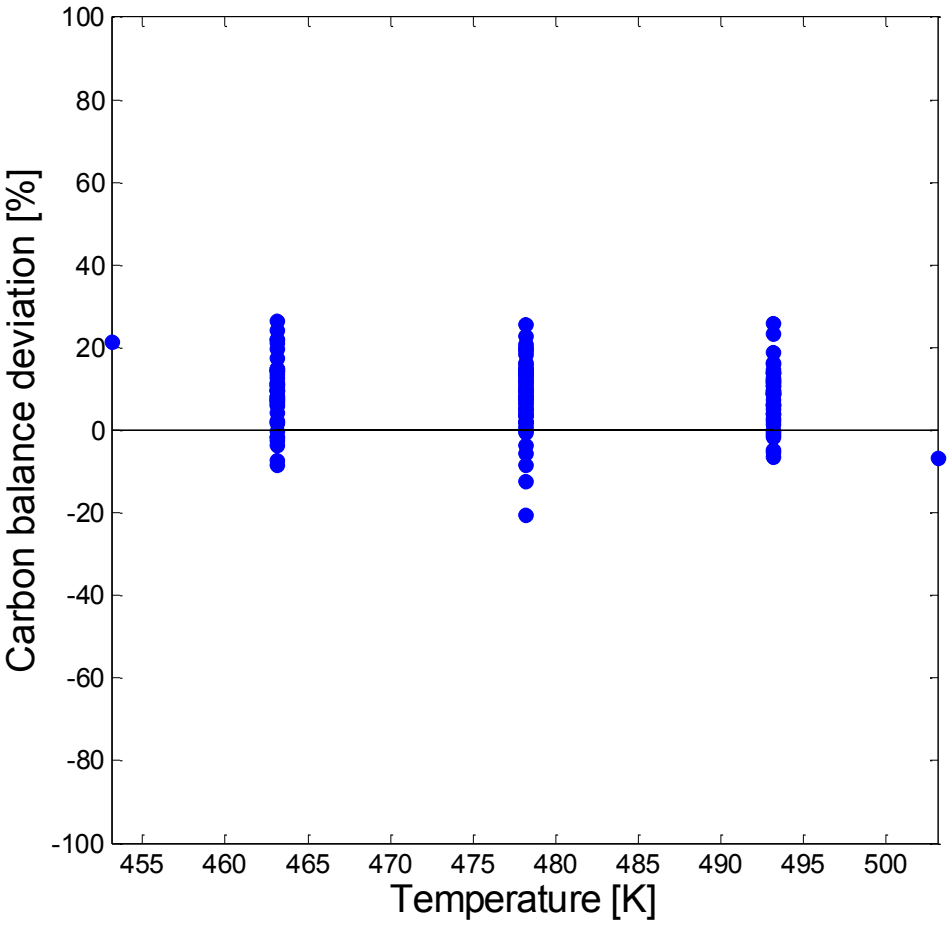

Figure 4.17. Plot of carbon balance deviation against reaction temperature.

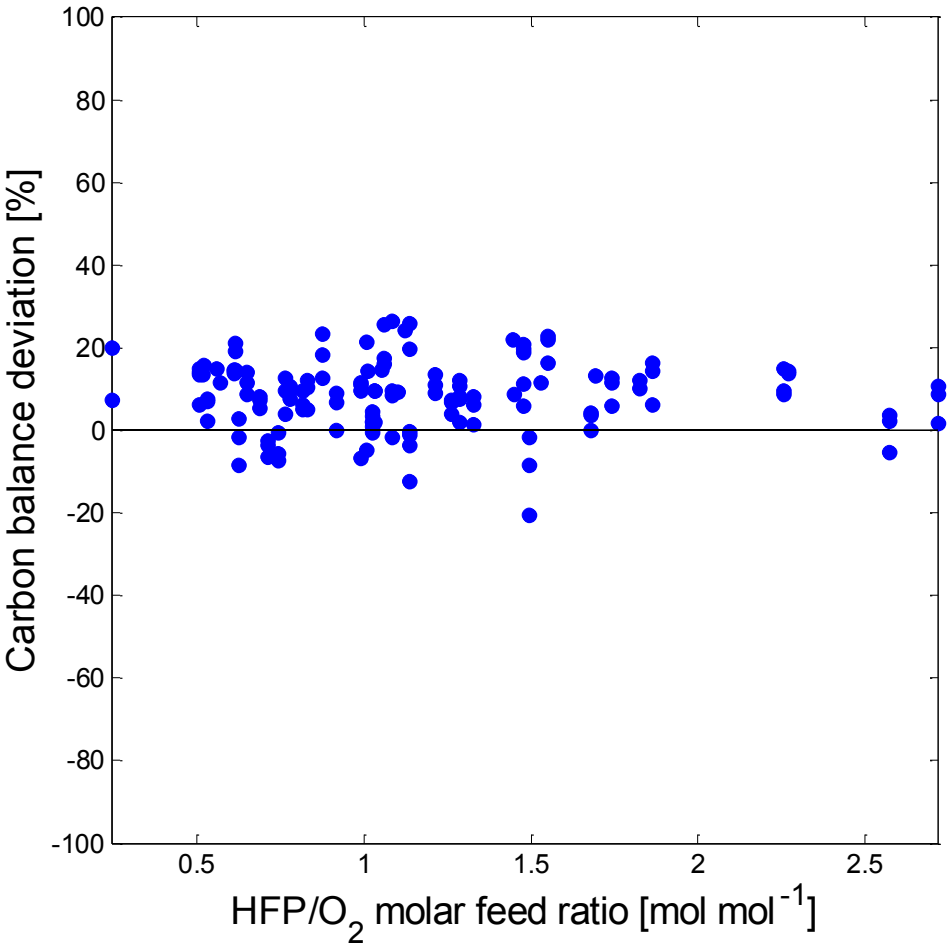

Figure 4.18. Plot of carbon balance deviation against HFP/O_2 molar feed ratio.

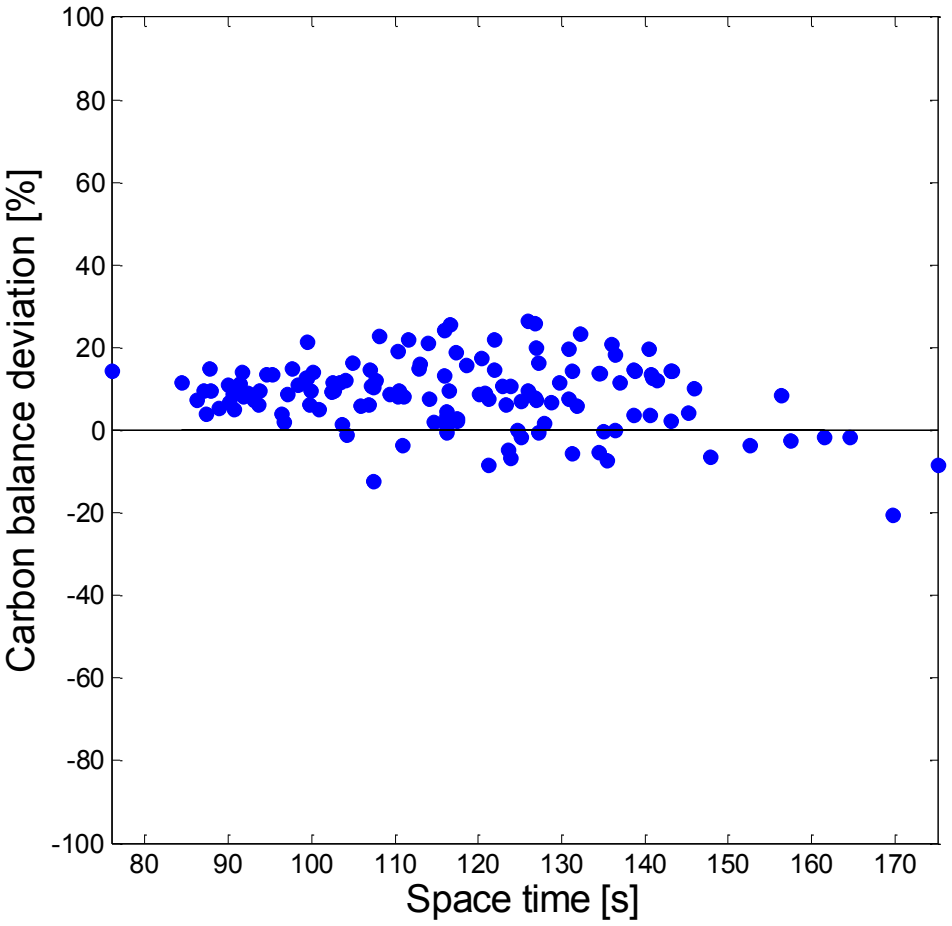

Figure 4.19. Plot of carbon balance deviation against space time.

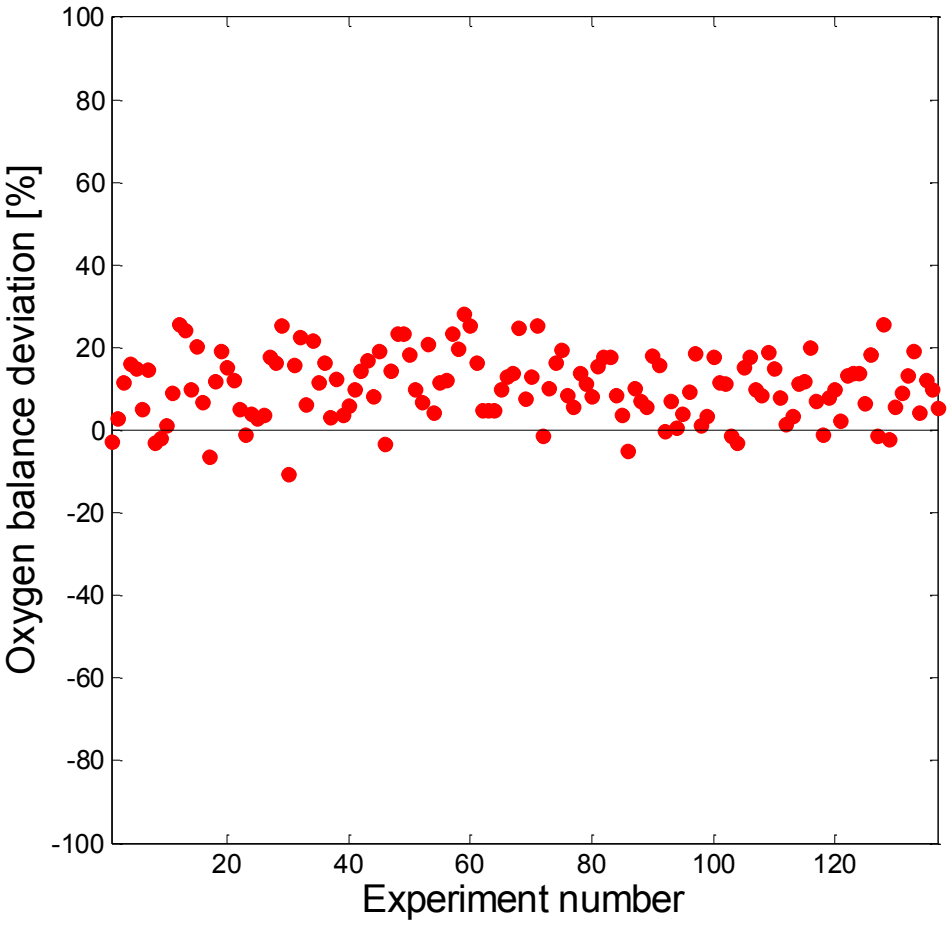

Figure 4.20. Plot of oxygen balance consistency against experiment number.

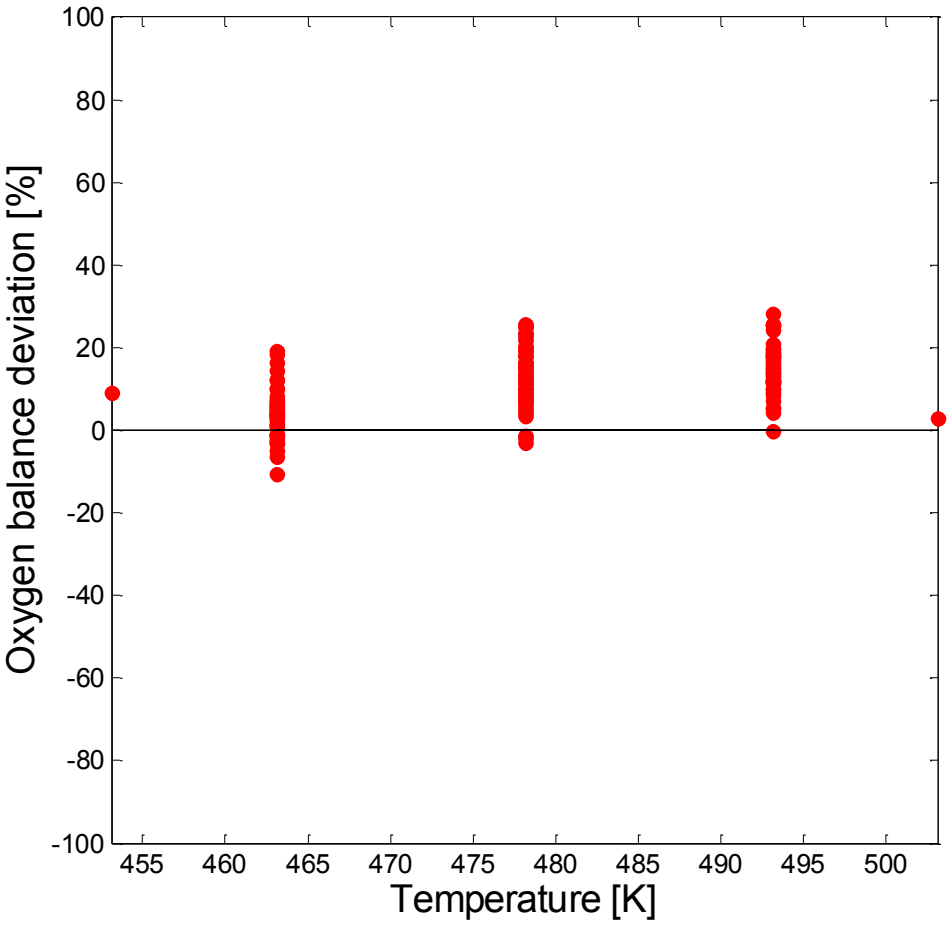

Figure 4.21. Plot of oxygen balance consistency against reaction temperature.

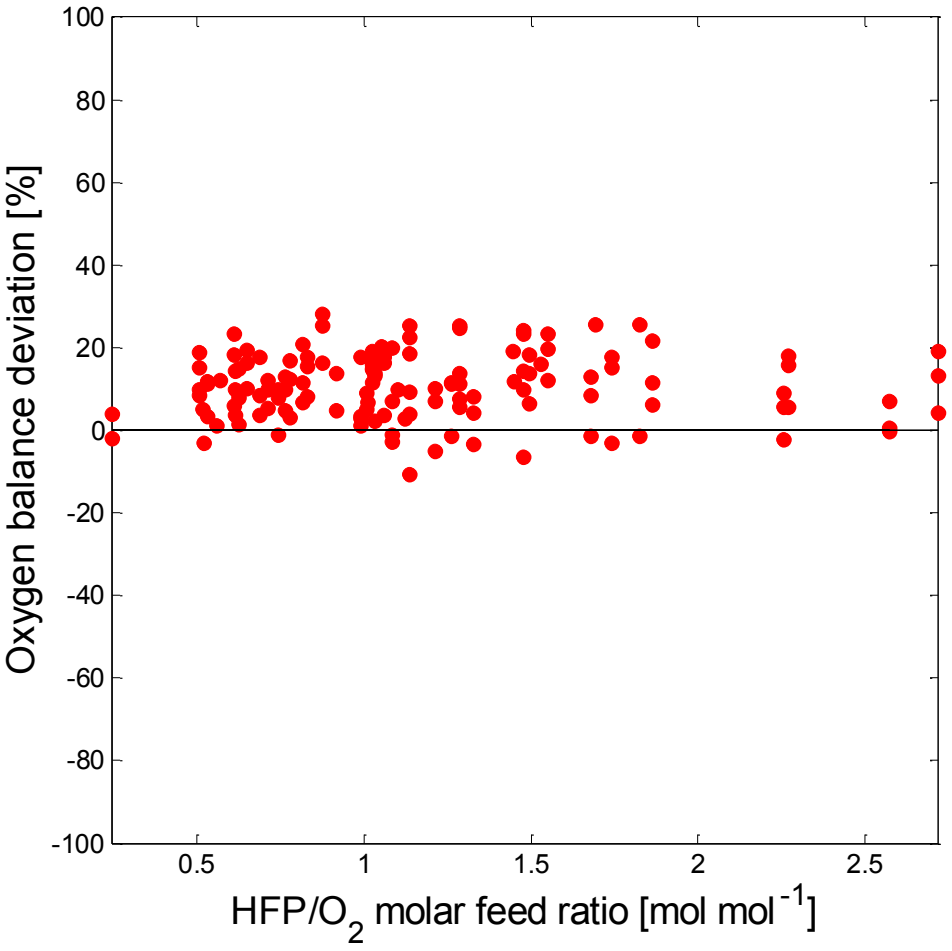

Figure 4.22. Plot of oxygen balance consistency against HFP/O_2 molar feed ratio.

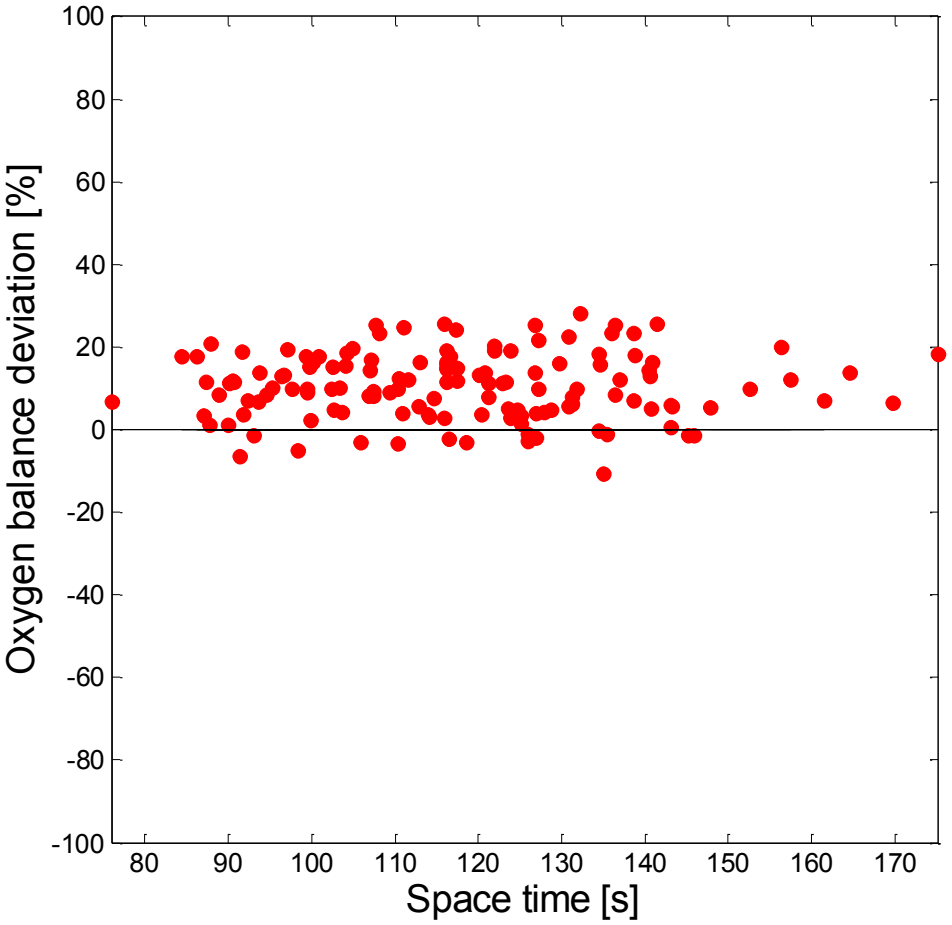

Figure 4.23. Plot of oxygen balance consistency against space time.

4.1.4. Prediction of optimal reaction conditions

4.1.4.1. Single response optimization

The search for optimal reaction conditions was carried out using response surface methodology (RSM). Each of the dependent responses considered in the optimization (HFPO selectivity and yield) was approximated by a quadratic regression model, which in general form was given as:

$$Y = \beta_0 + \sum_{i=1}^{3} \beta_i X_i + \sum_{i=1}^{3} \beta_{ii} X_i^2 + \sum_{i<j} \sum_{j} \beta_{ij} X_i X_j \tag{4.12}$$

where Y was the predicted response, β_0 was the intercept coefficient, β_i were the coefficients of the linear terms, β_{ii} were the coefficients of the squared terms, β_{ij} were the coefficients of the interaction terms and X_i and X_j were the independent variables (reaction temperature X_1, HFP/O_2 molar feed ratio X_2 and space time X_3). The RSM technique was first applied to the yield of HFPO. The coefficients of the full quadratic polynomial expression for two models, one employing the actual values of the process variables (technological model, Y^t_{HFPO}) and the other the normalized levels for each factor given by the central composite design in Table 4.5 (statistical model, Y^s_{HFPO}) were established using the method of least-squares:

$$\begin{aligned} Y^t_{HFPO} &= -9999.4915 + 39.4045X_1 + 1.5623X_2 + 8.5665X_3 + 9.9894\times10^{-2}X_1X_2 \\ &-1.2639\times10^{-2}X_1X_3 - 9.9674\times10^{-2}X_2X_3 - 3.9311\times10^{-2}X_1^2 - 16.3186X_2^2 - 9.6843\times10^{-3}X_3^2 \end{aligned} \tag{4.13}$$

$$\begin{aligned} Y^s_{HFPO} &= 38.6849 + 5.8991X_1^s + 2.3656X_2^s + 1.9868X_3^s + 7.4921\times10^{-1}X_1^sX_2^s - 3.7913X_1^sX_3^s \\ &-9.9674\times10^{-1}X_2^sX_3^s - 8.6961X_1^{s^2} - 4.0991X_2^{s^2} - 3.9811X_3^{s^2} \end{aligned} \tag{4.14}$$

The average response at the centre of the design was 38.66% and did not equal the average response for the points that constituted the factorial portion of the design, which was 21.17%. This indicated that some pure quadratic curvature existed in the response of interest. The adequacy of each model was checked with an analysis of variance test (ANOVA). The results are presented in Table 4.8. The coefficient of multiple determination, adjusted R^2 value and the Fischer test statistic of the technological model were marginally superior to those of the statistical model. Further analysis of the statistical model was not undertaken. The full technological model coefficients were estimated

with a satisfactory R^2 value of 0.967 and an adjusted R^2 value of 0.937. A parity plot of the observed and predicted HFPO yields for the full technological model is presented in Figure 4.24.

Table 4.8. ANOVA results and regression statistics for the quadratic HFPO yield response models.

Statistics	Technological model	Statistical model	Reduced model
R^2	0.967	0.966	0.961
Adjusted R^2	0.937	0.935	0.938
Standard error	2.681	2.716	2.651
F-statistic	32.135	31.269	42.012
p-value	3.228×10^{-6}	3.673×10^{-6}	1.662×10^{-7}
Regression Mean Square	230.949	230.736	295.158
Residual Mean Square	7.188	7.379	7.025

The computed value of the Fischer test statistic was greater than the tabulated value, $F_{(p\text{-}1,\ N\text{-}p,\ \alpha)}$ (p is the number of parameters in the model, N is the number of experiments and α in this case represents the significance level, of 4.94 at the 99% level of significance. The F-value and the corresponding p-value of 3.228×10^{-6} show a statistically significant regression.

The regression statistics related to the individual estimated model coefficients are presented in Table 4.9. Reaction temperature had the largest effect on the HFPO yield, followed by the space time and HFP/O_2 molar feed ratio, respectively, based on the magnitude of the p-value and absolute t-value of the individual regression coefficients. The linear term of the molar feed ratio, the reaction temperature-molar feed ratio interaction term and the molar feed ratio-space time interaction term were not found to be statistically significant. Consequently, a reduction in the full quadratic technological HFPO yield model to include only significant terms resulted in:

$$Y^t_{HFPO} = -10035.2948 + 39.5044X_1 + 37.3656X_2 + 8.4668X_3 - 1.2639\times10^{-2}X_1X_3 \\ -3.9311\times10^{-2}X_1^2 - 16.3186X_2^2 - 9.6843\times10^{-3}X_3^2 \quad (4.15)$$

In order to maintain the model hierarchy, the HFP/O_2 molar feed ratio (X_2) term was retained.

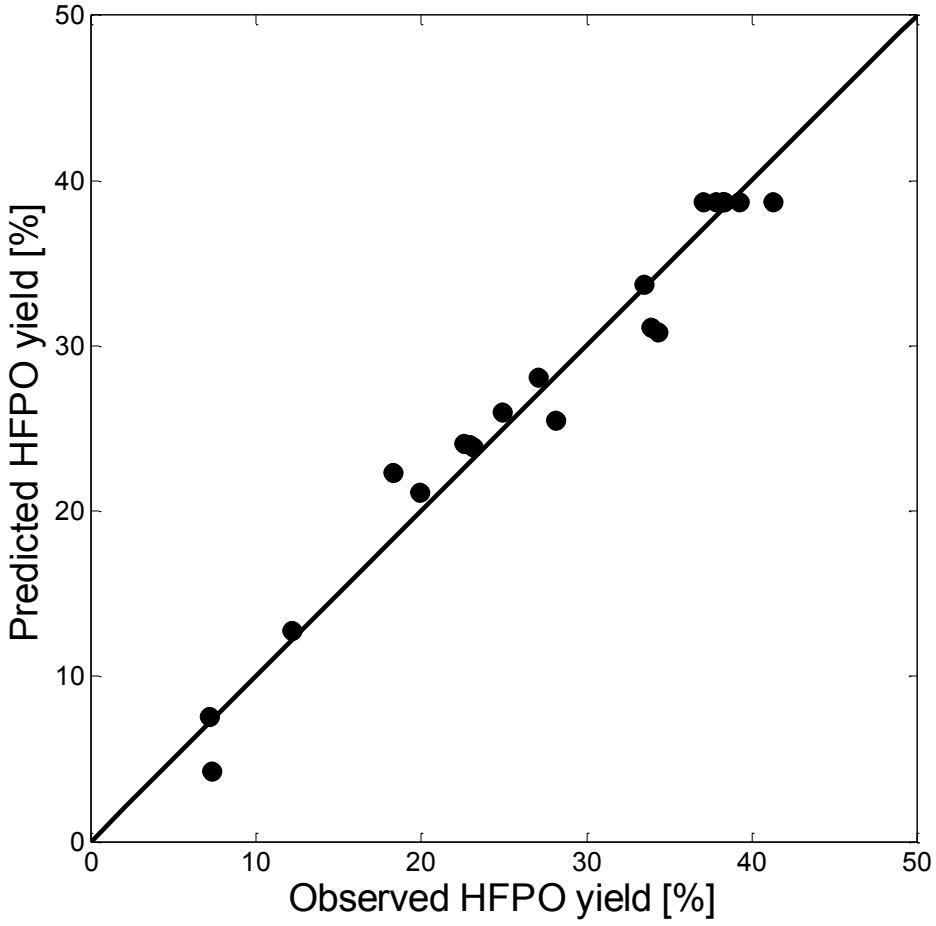

Figure 4.24. Parity plot of the observed and predicted responses for the full technological HFPO yield model.

Table 4.9. Least squares regression results and significance effects of the regression coefficients for the full technological HFPO yield model.

Parameter	Term	Coefficient	*t*-value	*p*-value
β_0	intercept	-9999.4914	-13.258	1.137×10^{-7}
β_1	X_1	39.4045	13.852	1.528×10^{-7}
β_2	X_2	1.5623	2.527×10^{-2}	9.803×10^{-1}
β_3	X_3	8.5665	5.456	2.783×10^{-4}
β_{12}	X_1X_2	9.9894×10^{-2}	7.904×10^{-1}	4.476×10^{-1}
β_{13}	X_1X_3	-1.2639×10^{-2}	-4.001	2.516×10^{-3}
β_{23}	X_2X_3	-9.9674×10^{-2}	-1.051	3.177×10^{-1}
β_{11}	X_1^2	-3.9311×10^{-2}	-12.368	2.197×10^{-7}
β_{22}	X_2^2	-16.3186	-5.329	3.334×10^{-4}
β_{33}	X_3^2	-9.6843×10^{-3}	-5.594	2.295×10^{-4}

Global regression statistics for the reduced technological HFPO yield model are presented in Table 4.8 and the results of statistical tests on individual regression coefficients are presented in Table 4.10. All terms in the reduced model were found to be significant. A parity plot of the observed and predicted HFPO yields for the reduced technological model is presented in Figure 4.25. Although the calculated *F*-statistic and *p*-value were better, the overall fit was approximately the same as the full technological model.

Table 4.10. Least squares regression results and significance effects of the regression coefficients for the reduced technological HFPO yield model.

Parameter	Term	Coefficient	*t*-value	*p*-value
β_0	intercept	-10035.2948	-13.502	1.285×10^{-8}
β_1	X_1	39.5044	13.043	1.901×10^{-8}
β_2	X_2	37.3656	5.865	7.654×10^{-5}
β_3	X_3	8.4668	5.464	1.443×10^{-4}
β_{13}	X_1X_3	-1.239×10^{-2}	-4.046	1.621×10^{-3}
β_{11}	X_1^2	-3.9311×10^{-2}	-12.509	3.038×10^{-8}
β_{22}	X_2^2	-16.3186	-5.389	1.627×10^{-4}
β_{33}	X_3^2	-9.6843×10^{-3}	-5.657	1.059×10^{-4}

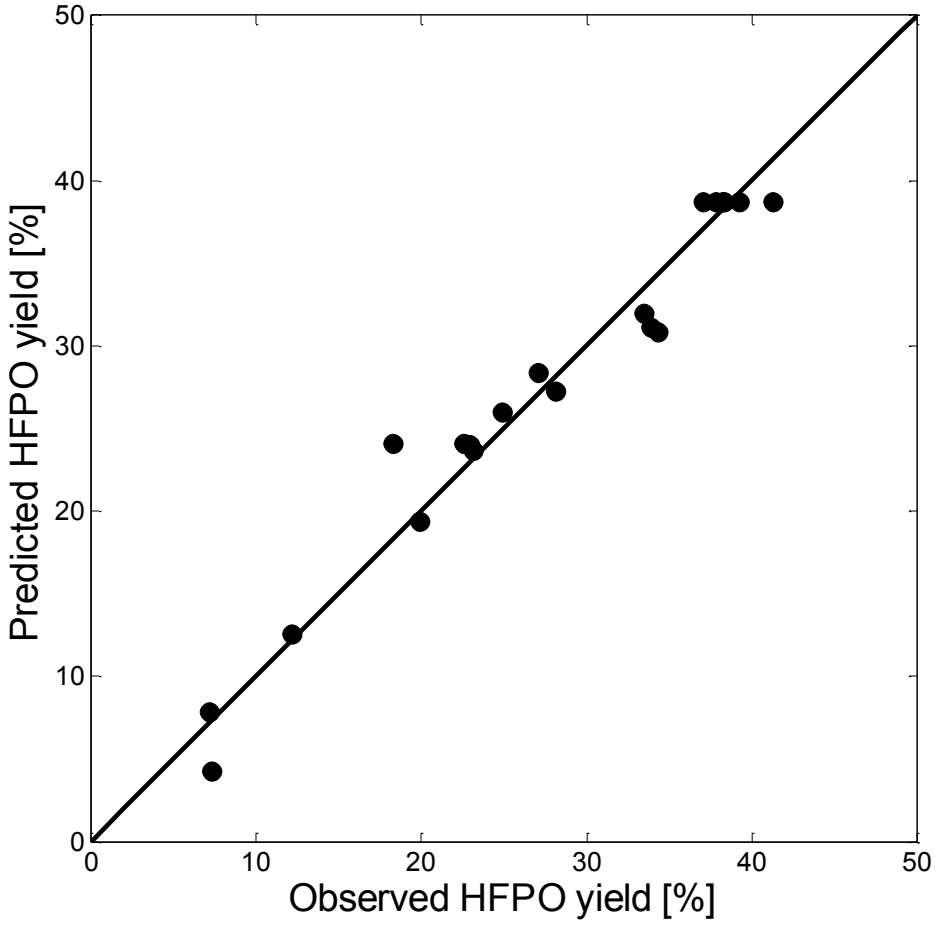

Figure 4.25. Parity plot of the observed and predicted responses for the reduced technological HFPO yield model.

Contour and surface plots for each combination of operating variables were generated using the full technological HFPO yield model (cf. Figures 4.26-4.28) and were used in assessing the combined effect of any two of the independent variables on the yield of HFPO. Interaction between two variables exists when the effect of one variable on the response is different at different levels of the other variable. It determines whether variables can be optimized independently of one another. Generally, interaction between variables is evident if the shape of the contours is elliptical and inclined (Montgomery and Runger, 2007). The strongest interaction was thus found between reaction temperature and space time (cf. Figure 4.28). In each of the plots a distinct maximum was observed within the experimental region. By setting the partial differential expressions with respect to each independent variable equal to zero and solving the system of linear equations, an optimum HFPO yield of 40.10% was identified at 483.2 K, a HFP/O_2 molar feed ratio of 1.16 mol mol^{-1} and a space time of 121 seconds.

A complete understanding of the effect of operating conditions on the performance of this system could not be gleaned without first examining the variation in the selectivity towards HFPO. Data obtained from the central composite experimental design was again fitted to full quadratic models, both technological and statistical, for the selectivity response:

$$S^t_{HFPO} = -12424.4866 + 50.6093X_1 - 45.0703X_2 + 7.2491X_3 + 2.3299\times10^{-1}X_1X_2 \\ -9.3064\times10^{-3}X_1X_3 - 3.1858\times10^{-1}X_2X_3 - 5.2143\times10^{-2}X_1^2 - 11.3225X_2^2 - 1.0478\times10^{-2}X_3^2 \quad (4.16)$$

$$S^s_{HFPO} = 54.7824 - 2.0719X_1^s + 2.7314X_2^s - 6.8162\times10^{-1}X_3^s + 1.7473X_1^sX_2^s - 2.7919X_1^sX_3^s \\ -3.1857X_2^sX_3^s - 11.5394X_1^{s^2} - 2.8607X_2^{s^2} - 4.3169X_3^{s^2} \quad (4.17)$$

There was little difference in the global regression statistics between the two models (cf. Table 4.11), and the technological model was retained for further analysis. The model coefficients were estimated with a satisfactory R^2 value of 0.939 and an adjusted R^2 value of 0.884. The computed value of the Fischer test statistic and the *p*-value also showed a statistically significant fit. A parity plot of the observed and predicted HFPO selectivities for the full technological model is presented in Figure 4.29.

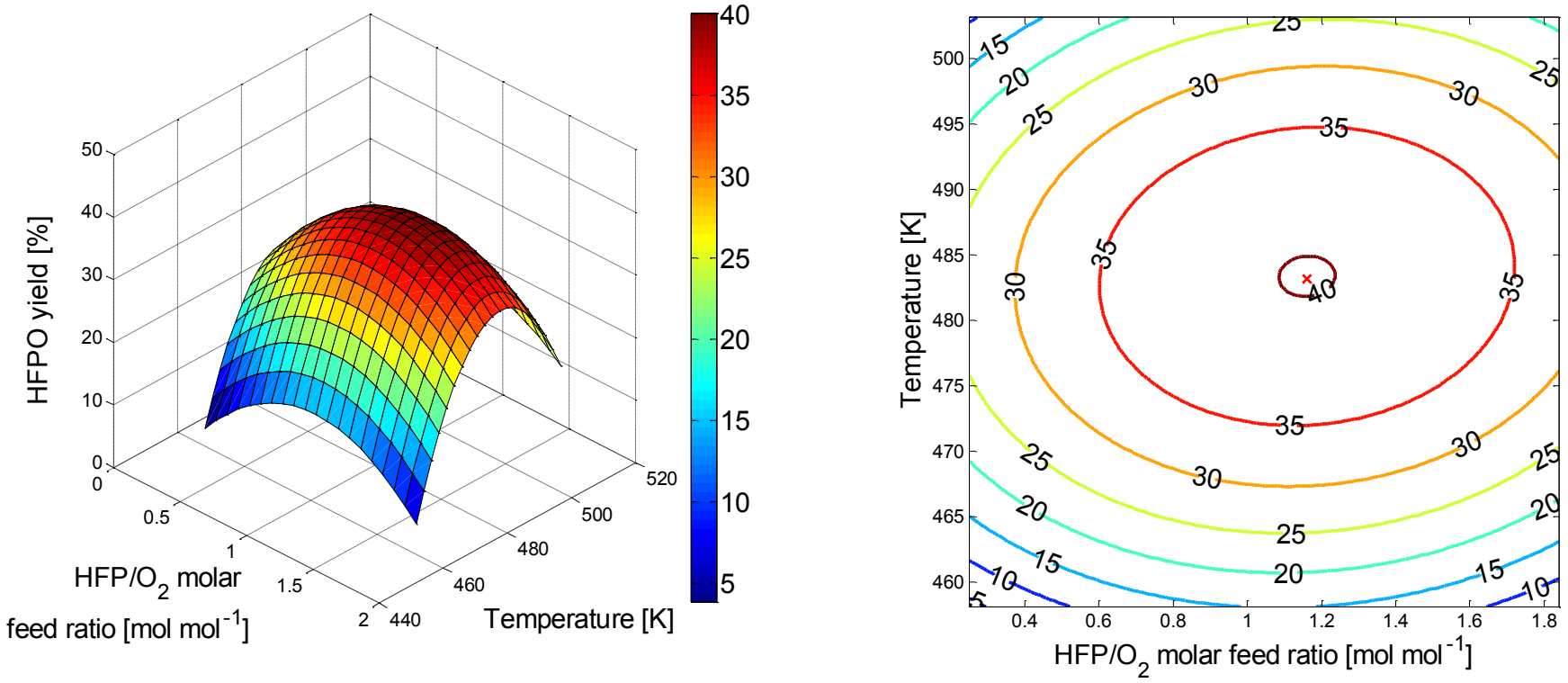

Figure 4.26. Surface and contour plot of HFPO yield (%) for reaction temperature and HFP/O_2 molar feed ratio at a fixed space time (120 s).

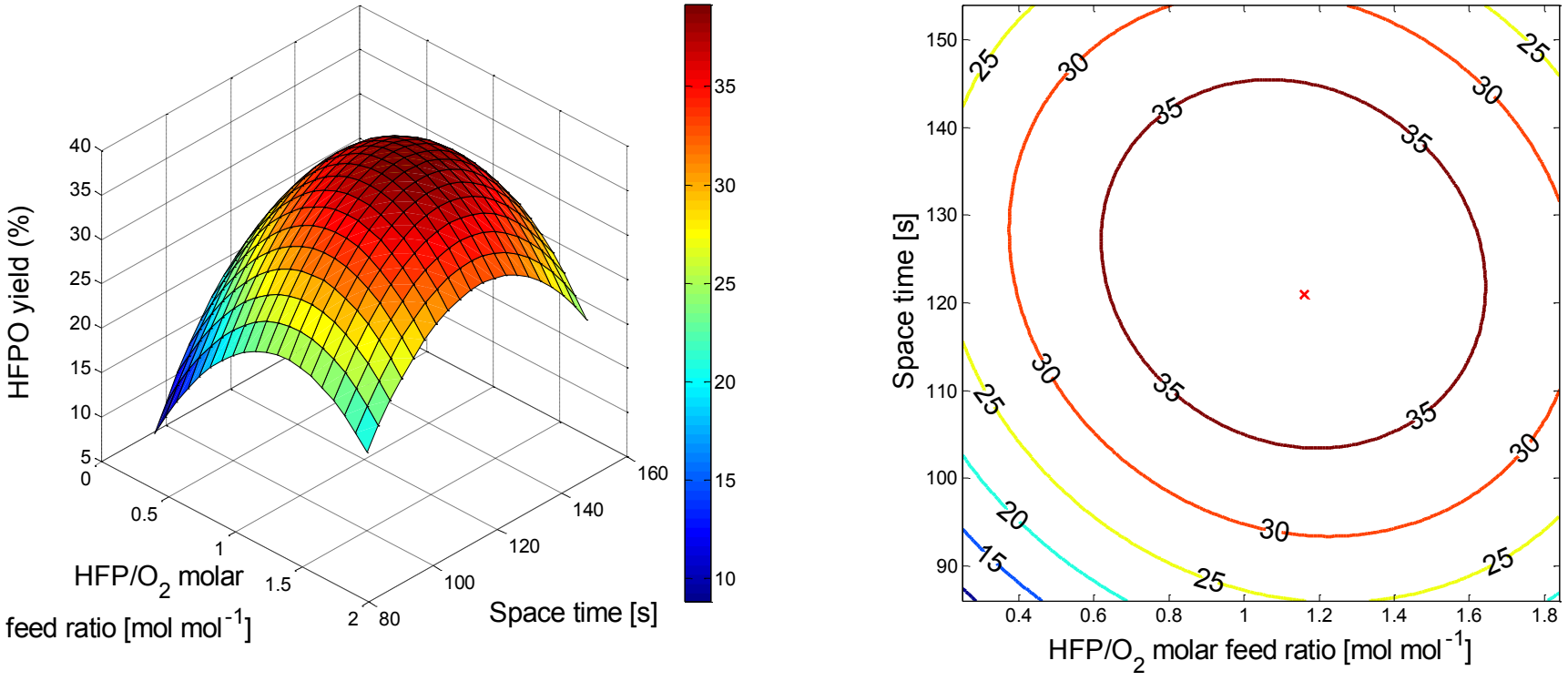

Figure 4.27. Surface and contour plot of HFPO yield (%) for space time and HFP/O_2 molar feed ratio at a fixed reaction temperature (478 K).

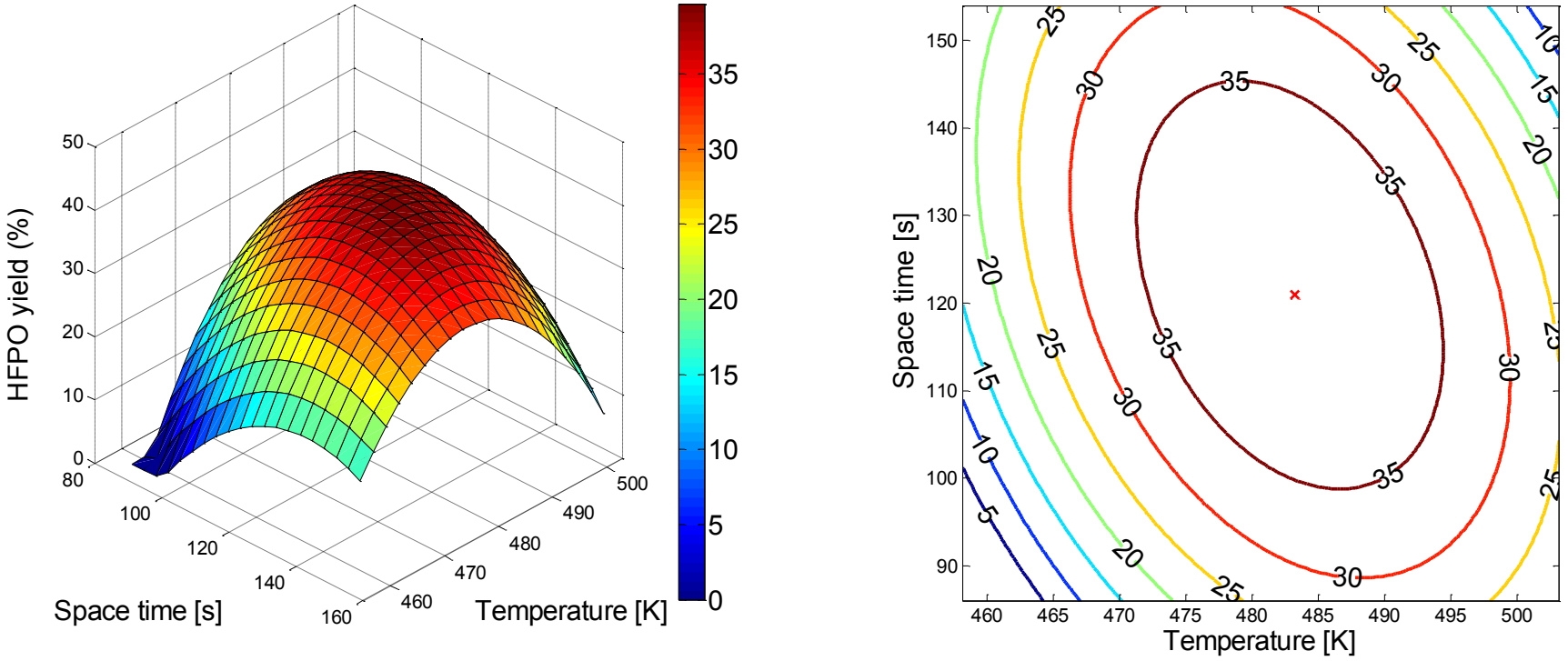

Figure 4.28. Surface and contour plot of HFPO yield (%) for space time and reaction temperature at a fixed HFP/O_2 molar feed ratio (1 mol mol^{-1})

Table 4.11. ANOVA results and regression statistics for the quadratic HFPO selectivity response models.

Statistics	Technological model	Statistical model	Reduced model
R^2	0.939	0.938	0.905
Adjusted R^2	0.884	0.882	0.850
Standard error	3.981	4.009	4.521
F-statistic	17.077	16.829	16.421
p-value	6.057×10^{-5}	6.472×10^{-5}	2.879×10^{-5}
Regression Mean Square	270.766	270.522	335.730
Residual Mean Square	15.854	16.074	20.445

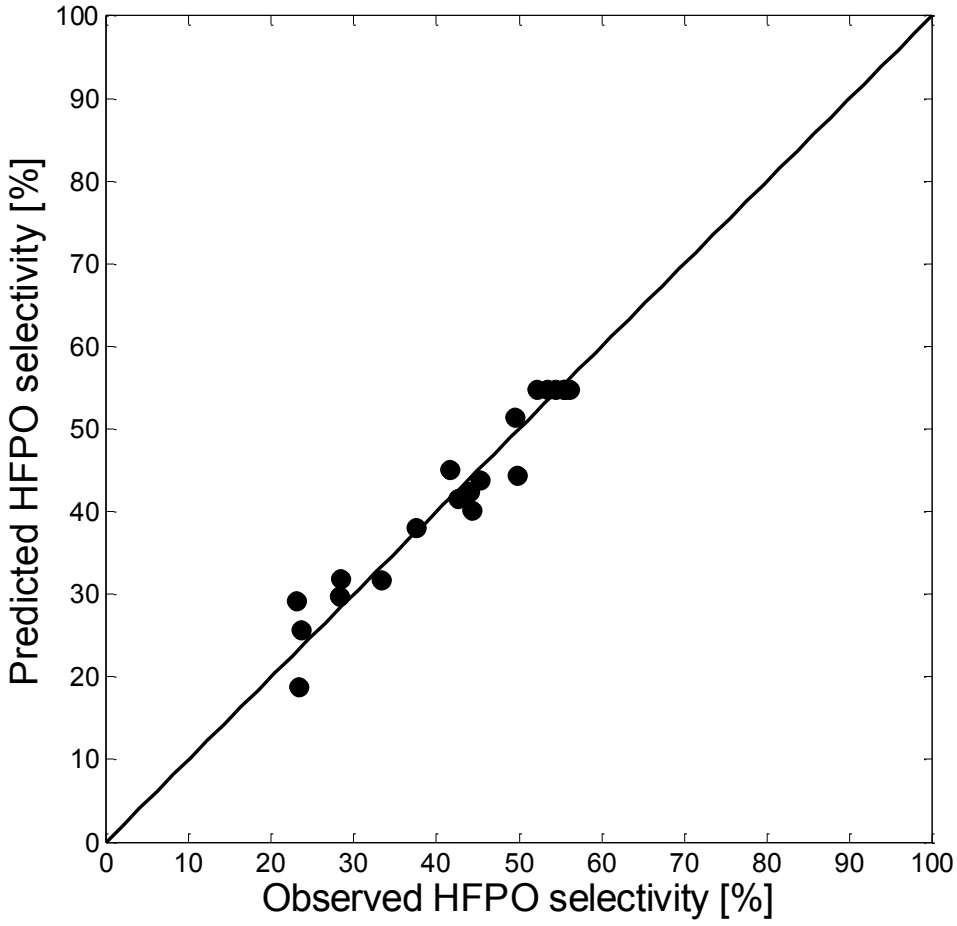

Figure 4.29. Parity plot of the observed and predicted responses for the full technological HFPO selectivity model.

Least squares regression results and significance effects of the regression coefficients for the full technological HFPO selectivity model are presented in Table 4.12. The reaction temperature had the largest effect on the selectivity towards HFPO, followed by the space time and HFP/O_2 molar feed ratio, respectively. The linear term of the molar feed ratio, the reaction temperature-molar feed ratio interaction term and the reaction temperature-space time interaction term were not found to be statistically significant. Consequently, a reduction in the full quadratic technological HFPO selectivity model to include only significant terms resulted in:

$$S^t_{HFPO} = -12001.9077 + 49.7255X_1 + 66.3316X_2 + 2.7992X_3 - 3.1858\times10^{-1}X_2X_3 \\ -5.2143\times10^{-2}X_1^2 - 11.3225X_2^2 - 1.0478\times10^{-2}X_3^2 \quad (4.18)$$

Global regression statistics for the reduced technological HFPO selectivity model are presented in Table 4.11 and the results of statistical tests on individual regression coefficients are presented in Table 4.13. A parity plot of the observed and predicted HFPO selectivities for the reduced technological model is presented in Figure 4.37. The fit of the experimental data to the reduced model was worse than the full technological model in all respects.

Table 4.12. Least squares regression results and significance effects of the regression coefficients for the full technological HFPO selectivity model.

Parameter	**Term**	**Coefficient**	***t*-value**	***p*-value**
β_0	intercept	-12424	-11.091	6.104×10^{-7}
β_1	X_1	50.6093	11.113	5.992×10^{-7}
β_2	X_2	-45.0703	-4.908×10^{-1}	6.341×10^{-1}
β_3	X_3	7.2491	3.108	1.108×10^{-2}
β_{12}	X_1X_2	2.3299×10^{-1}	1.241	2.428×10^{-1}
β_{13}	X_1X_3	-9.3064×10^{-3}	-1.983	7.547×10^{-2}
β_{23}	X_2X_3	-3.1858×10^{-1}	-2.262	4.713×10^{-2}
β_{11}	X_1^2	-5.2143×10^{-2}	-11.045	6.343×10^{-7}
β_{22}	X_2^2	-11.3225	-2.489	3.202×10^{-2}
β_{33}	X_3^2	-1.0478×10^{-2}	-4.075	2.232×10^{-3}

Table 4.13. Least squares regression results and significance effects of the regression coefficients for the reduced technological HFPO selectivity model.

Parameter	Term	Coefficient	*t*-value	*p*-value
β_0	intercept	-12001	-9.753	4.688×10^{-7}
β_1	X_1	49.7255	9.698	4.979×10^{-7}
β_2	X_2	66.3316	3.008	1.089×10^{-2}
β_3	X_3	2.7992	3.881	2.185×10^{-3}
β_{23}	X_2X_3	-3.1858×10^{-1}	-1.992	6.952×10^{-2}
β_{11}	X_1^2	-5.2143×10^{-2}	-9.727	4.826×10^{-7}
β_{22}	X_2^2	-11.3225	-2.192	4.881×10^{-2}
β_{33}	X_3^2	-1.0478×10^{-2}	-3.588	3.724×10^{-3}

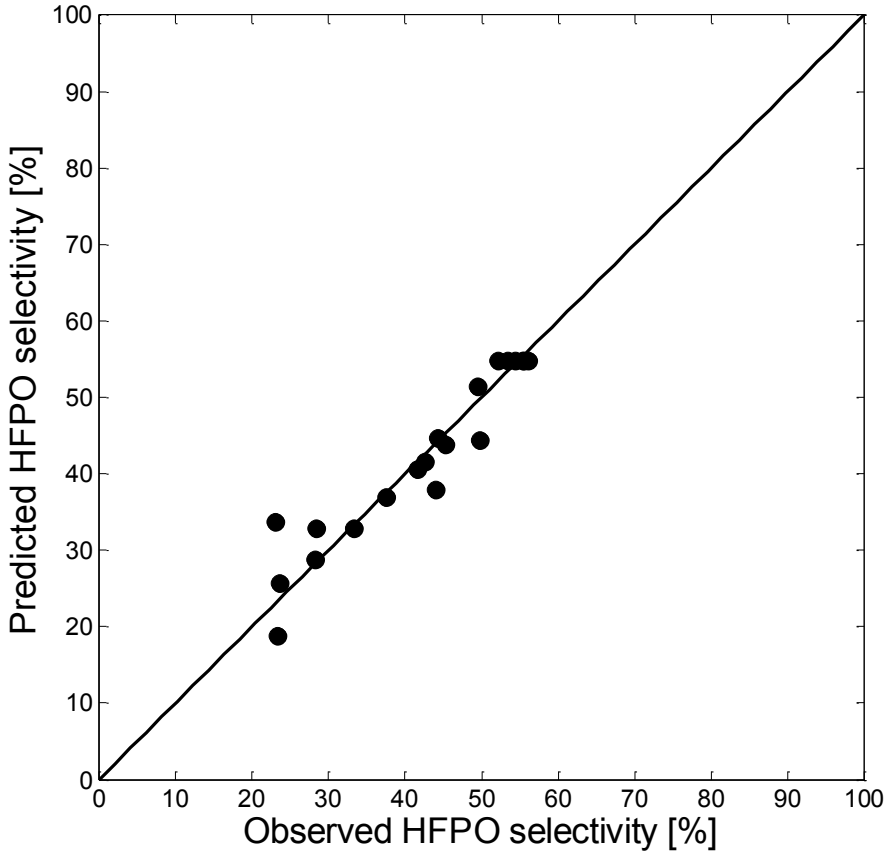

Figure 4.30. Parity plot of the observed and predicted responses for the reduced technological HFPO selectivity model.

Contour and surface plots for each combination of operating variables were generated using the full technological HFPO selectivity model (cf. Figures 4.31-4.33) and were used in assessing the combined effect of any two of the independent variables on the selectivity of HFPO. All combinations appeared to show some interaction between variables, due to the elliptical and inclined shape of the contours. Based on the magnitude of the *p*-value and absolute *t*-value of the individual regression coefficients, the strongest interaction was observed between molar feed ratio and space time. Again, in each of the plots a distinct maximum was observed within the experimental region. An optimum HFPO selectivity of 55.81% was identified at 478.2 K, a HFP/O_2 molar feed ratio of 1.34 mol mol^{-1} and a space time of 113 seconds.

The effect of reaction temperature, HFP/O_2 molar feed ratio and space time on the HFP conversion, HFPO selectivity and yield are presented in Figures 4.34 to 4.36, showing a comparison between experimental data and values predicted by the two full technological models developed in this section. The predicted HFP conversion was calculated from the predicted HFPO selectivity and yield. The experimental and predicted values were generally in good agreement, apart from Figure 4.34 where the predicted conversion of HFP at temperatures greater than 498 K exceeded 100%. These conversion values were calculated using independently developed models for HFPO selectivity and yield, when in-fact the latter are not entirely independent, being related through Equation 4.3. In order to maintain all predicted performance criteria within physical limits, an adjustment to the single response optimization procedure described thus far would have to be made. Essentially, the coefficients of the two quadratic models for HFPO selectivity and yield would have to be determined through a single minimization procedure subject to the following constraint:

$$\frac{Y_{HFPO}}{S_{HFPO}} \leq 1 \tag{4.19}$$

The fit to the experimental data would, however, be worse than the original independent least-squares solution. Since the problem with the predicted conversion did not affect the optimal points obtained in this section, the independent models were retained.

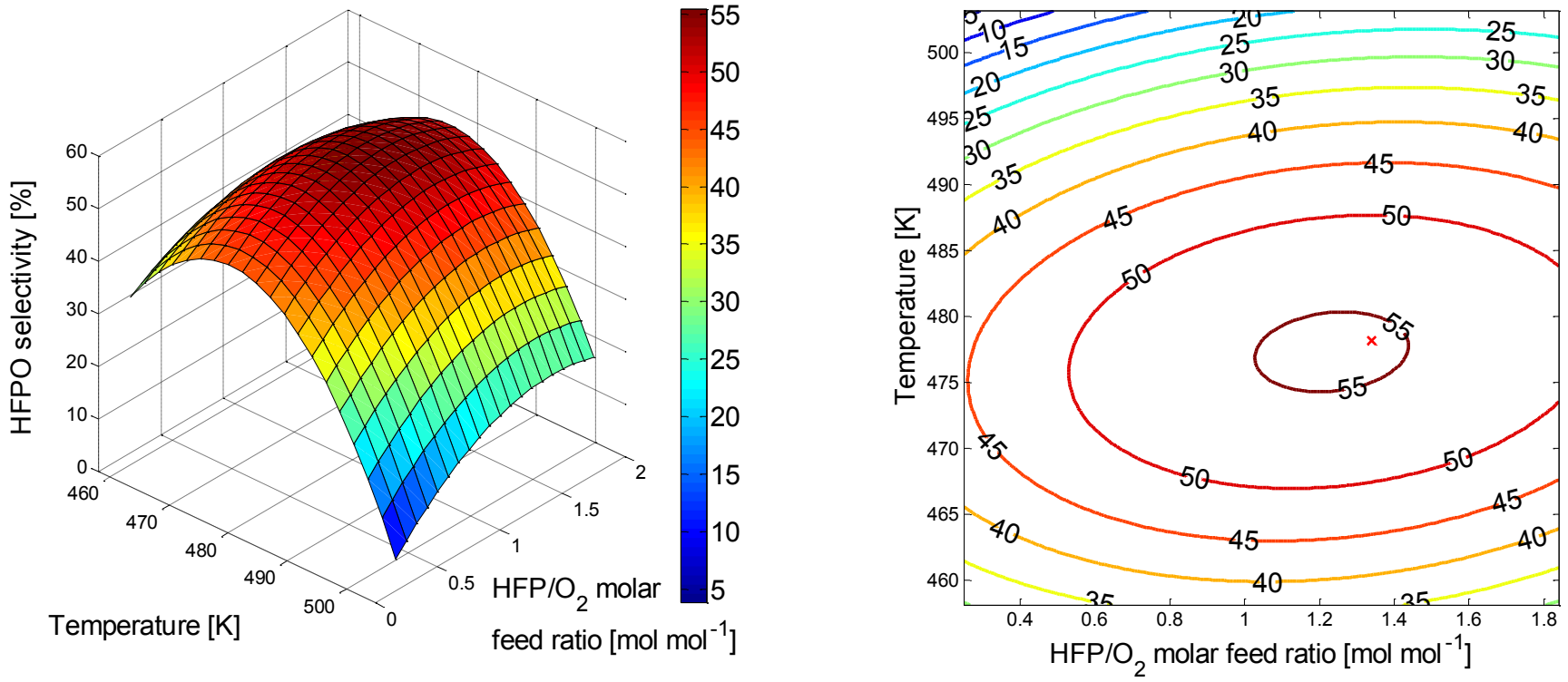

Figure 4.31. Surface and contour plot of HFPO selectivity (%) for reaction temperature and HFP/O_2 molar feed ratio at a fixed space time (120 s).

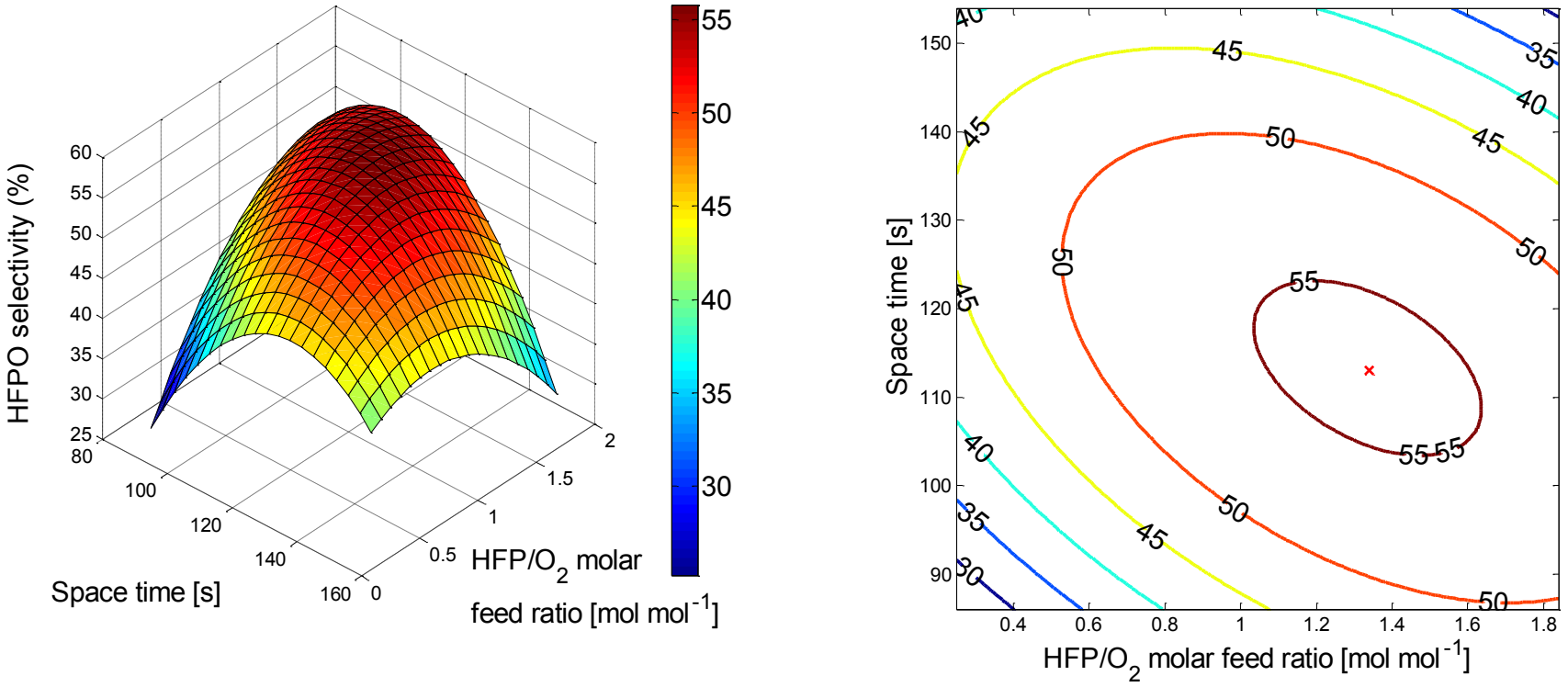

Figure 4.32. Surface and contour plot of HFPO selectivity (%) for space time and HFP/O_2 molar feed ratio at a fixed reaction temperature (478 K).

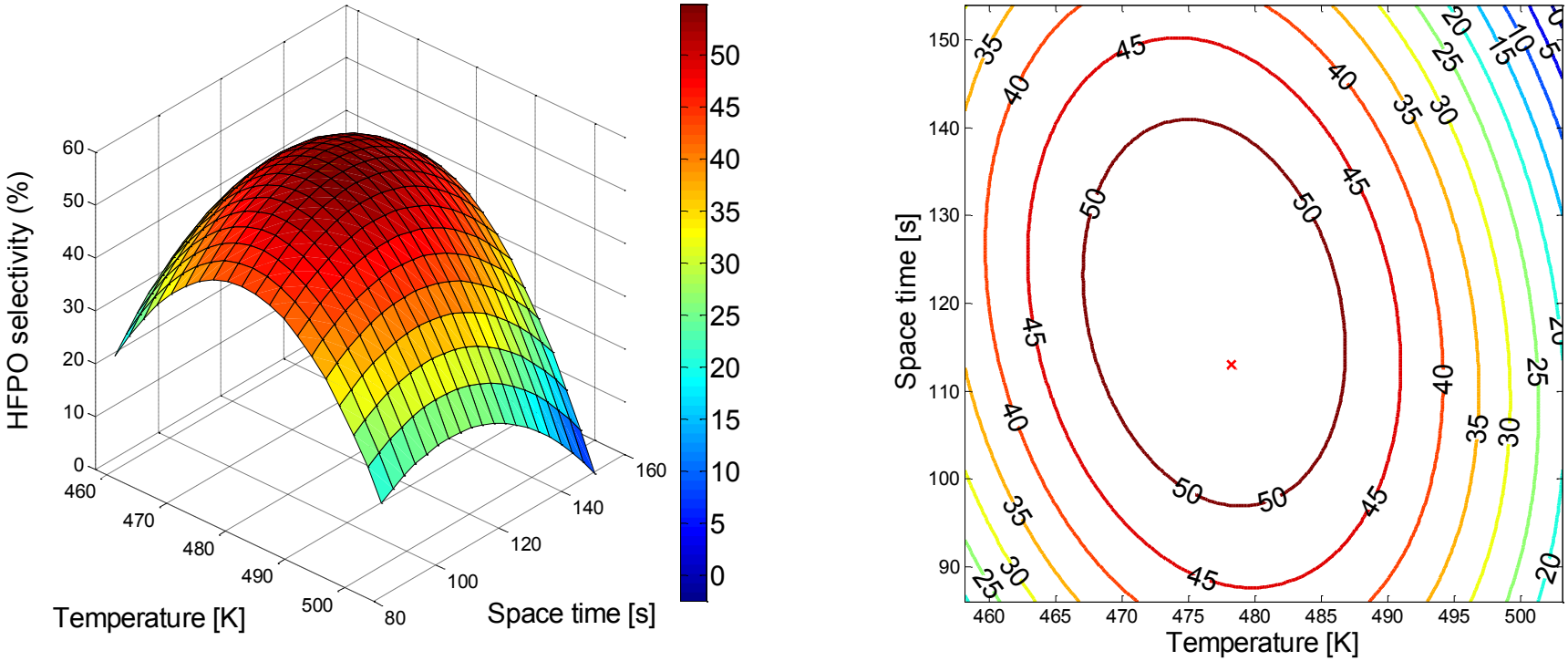

Figure 4.33. Surface and contour plot of HFPO selectivity (%) for space time and reaction temperature at a fixed HFP/O_2 molar feed ratio (1 mol mol^{-1}).

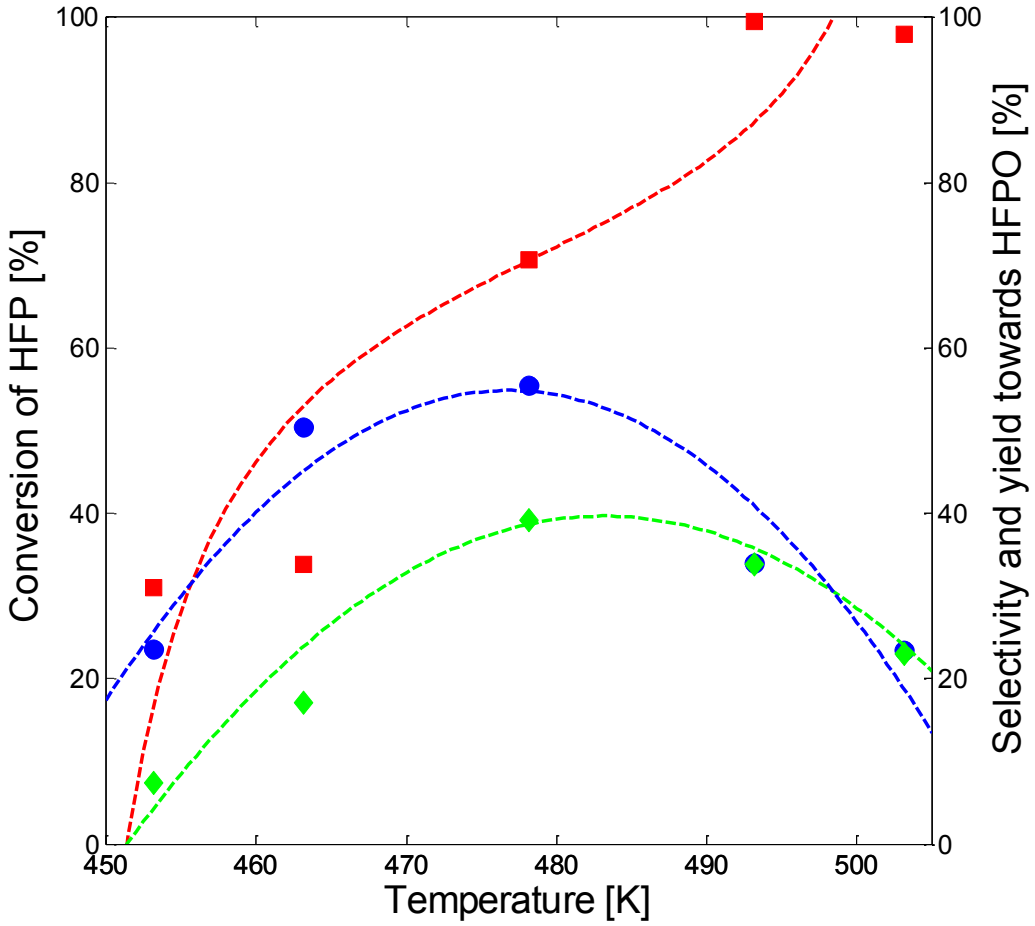

Figure 4.34. The effect of reaction temperature on the conversion of HFP (■, experimental; ---, model), selectivity (●, experimental; ---, model) and yield (◆, experimental; ---, model) towards HFPO at a fixed HFP/O_2 molar feed ratio (1 mol mol^{-1}) and space time (120 s).

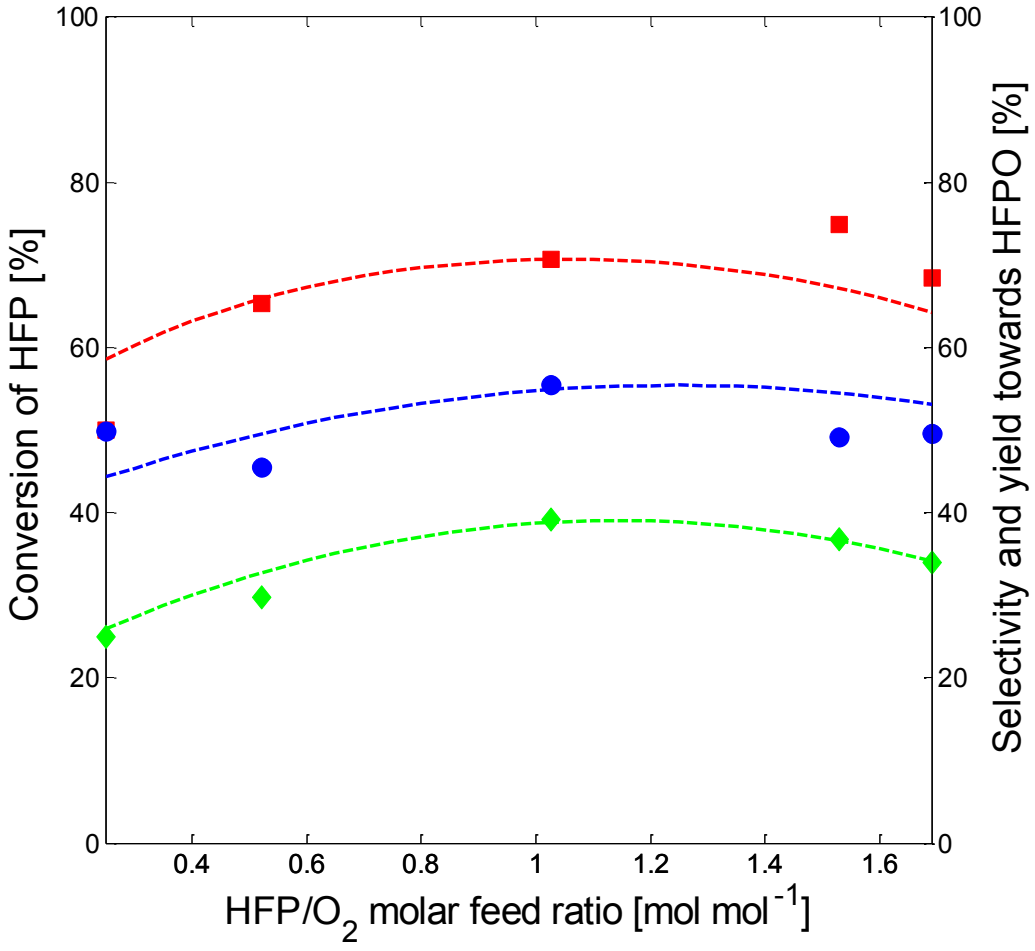

Figure 4.35. The effect of HFP/O_2 molar feed ratio on the conversion of HFP (■, experimental; ---, model), selectivity (●, experimental; ---, model) and yield (◆, experimental; ---, model) towards HFPO at a fixed reaction temperature (478 K) and space time (120 s).

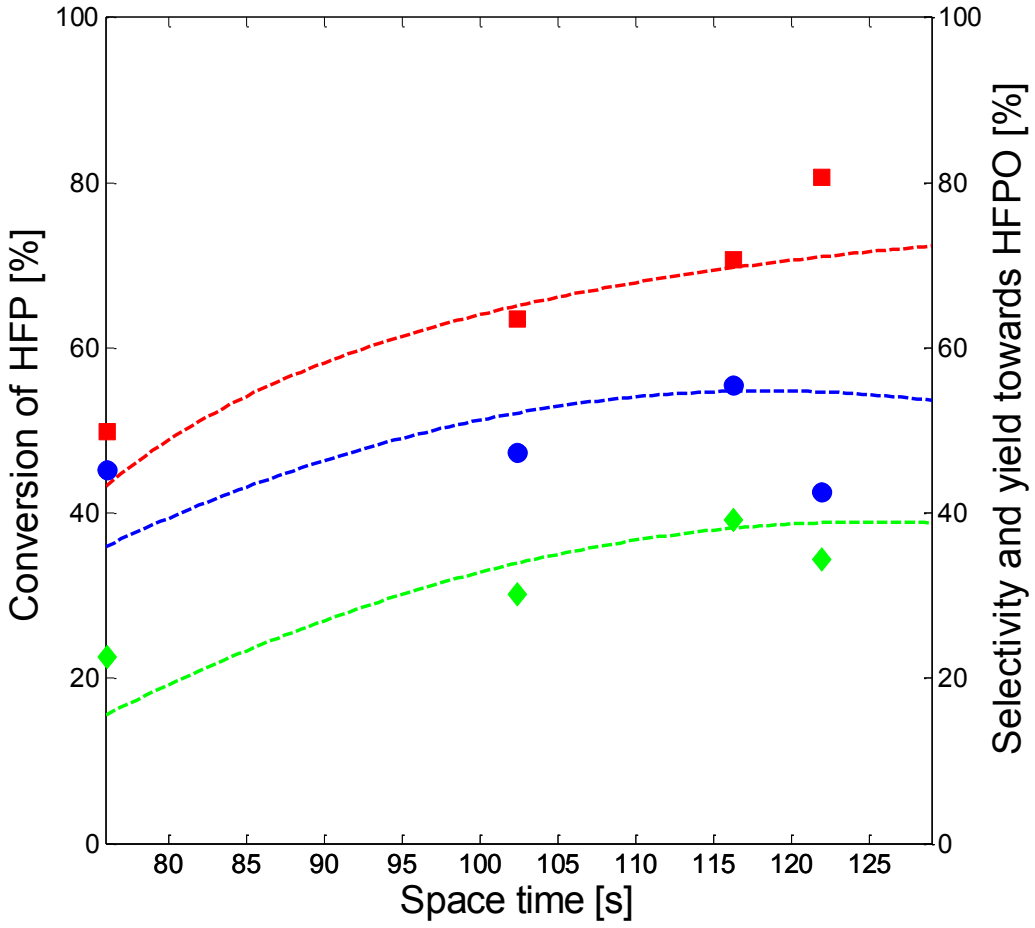

Figure 4.36. The effect of space time on the conversion of HFP (■, experimental; ---, model), selectivity (●, experimental; ---, model) and yield (◆, experimental; ---, model) towards HFPO at a fixed reaction temperature (478 K) and HFP/O_2 molar feed ratio (1 mol mol^{-1}).

4.1.4.2. Multi-response optimization

From a technological point of view, the simultaneous optimization of both yield and selectivity towards HFPO, with respect to operating conditions, was also desired. For nontrivial multi-objective problems of this nature, however, one cannot identify a single solution that simultaneously optimizes each objective. As was observed in the preceding section, the optimization of each individual response function gave dissimilar optimal points. The task in multi-response optimization is to find a set of Pareto optimal or non-inferior solution points and select among its' members a solution that represents the best trade-off between responses (Istadi, 2005). A Pareto set is defined such that when we move from one set of operating conditions to another, at least one individual objective function improves and at least one other worsens.

A single aggregate objective function (AOF) is often used to obtain this set of non-inferior solution points, the former defined as a weighted linear sum of the individual objectives. In this work, the weighted-sum-of-squared-objective-functions (WSSOF) method was used (Istadi, 2005). The single aggregate objective function was constructed by applying a variable weighting factor to the square of each individual response and was optimized at each combination of weighting factors to calculate all non-inferior or Pareto optimal solution points:

$$\text{maximize} \quad f(F_i, W_i) = \sum_{i=1}^{2} W_i \times F_i(\mathbf{X})^2 \tag{4.20}$$

$$\text{subject to} \sum_{i=1}^{2} W_i = 1 \text{ and } 0 \le W_i \le 1$$

where $f(F_i, W_i)$ is the utility function, W_i are the weighting factors, F_i are the individual responses (for HFPO yield and selectivity, obtained through response surface methodology) and $\mathbf{X}$ is the vector of independent operating conditions.

Final optimal operating conditions were selected from all these sets of non-inferior solutions (with corresponding weighting factors) by applying an additional optimality criterion (essentially specifying how much of one objective may be sacrificed in order to improve the other). The additional criterion was obtained by summing normalized responses for each point:

$$\sum \hat{F} = \hat{F}_1 + \hat{F}_2 \tag{4.21}$$

where $\hat{F}_i$ are the normalized responses given by the following expressions:

$$\hat{F}_1 = \frac{F_1 - F_1^L}{F_1^U - F_1^L} \tag{4.22}$$

$$\hat{F}_2 = \frac{F_2 - F_2^L}{F_2^U - F_2^L} \tag{4.23}$$

F_1^U represents the independently optimized value for response 1 (HFPO yield) at which response 2 (HFPO selectivity) is F_2^L, and F_2^U represents the independently optimized value for response 2, at which response 1 is F_1^L. Normalization is required in the general case where the numerical value of the individual responses in the test region may not be of the same order of magnitude, which can lead to bias in the final optimality criterion. The detailed algorithm, according to Istadi (2005) is delineated below:

1. The independent response models ($F_1(\mathbf{X})$ and $F_2(\mathbf{X})$) are developed using response surface methodology (cf. section 4.1.4.1).

2. The models are optimized independently by solving systems of linear equations describing the zero-valued partial differentials of the responses to obtain $F_1^U(\mathbf{X}^*)$ corresponding to $F_2^L(\mathbf{X}^*)$, and $F_2^U(\mathbf{X}^*)$ corresponding to $F_1^L(\mathbf{X}^*)$ where $\mathbf{X}^*$ represents the optimized set of operating conditions for the respective response:

maximize $F_1(\mathbf{X}) = F_1^U(\mathbf{X}^*)$, at this optimum $F_2(\mathbf{X}) = F_2^L(\mathbf{X}^*)$

maximize $F_2(\mathbf{X}) = F_2^U(\mathbf{X}^*)$, at this optimum $F_1(\mathbf{X}) = F_1^L(\mathbf{X}^*)$

3. Apply the single aggregate objective function with appropriate weighting factors for each response model (Equation 4.20), and use the Nelder-Mead simplex technique to optimize (searching from $W_1 = 0$ to $W_1 = 1$)

4. Calculate normalized optimum responses for each model according to Equations 4.22 and 4.23 and sum them to find the optimality criterion $\sum \hat{F}(\mathbf{X}^*)$.

5. Select a maximum value from the sum of normalized optimum responses, with corresponding W_i, $\mathbf{X}^*$, $F_1(\mathbf{X}^*)$ and $F_2(\mathbf{X}^*)$.

Figure 4.37 shows the relationship between the weighting factor W_1 and the sum of the normalized responses. A combined optimum HFPO yield of 40% and selectivity of 55% was obtained at 480 K, with a HFP/O_2 molar feed ratio of 1.21 and a space time of 118 seconds.

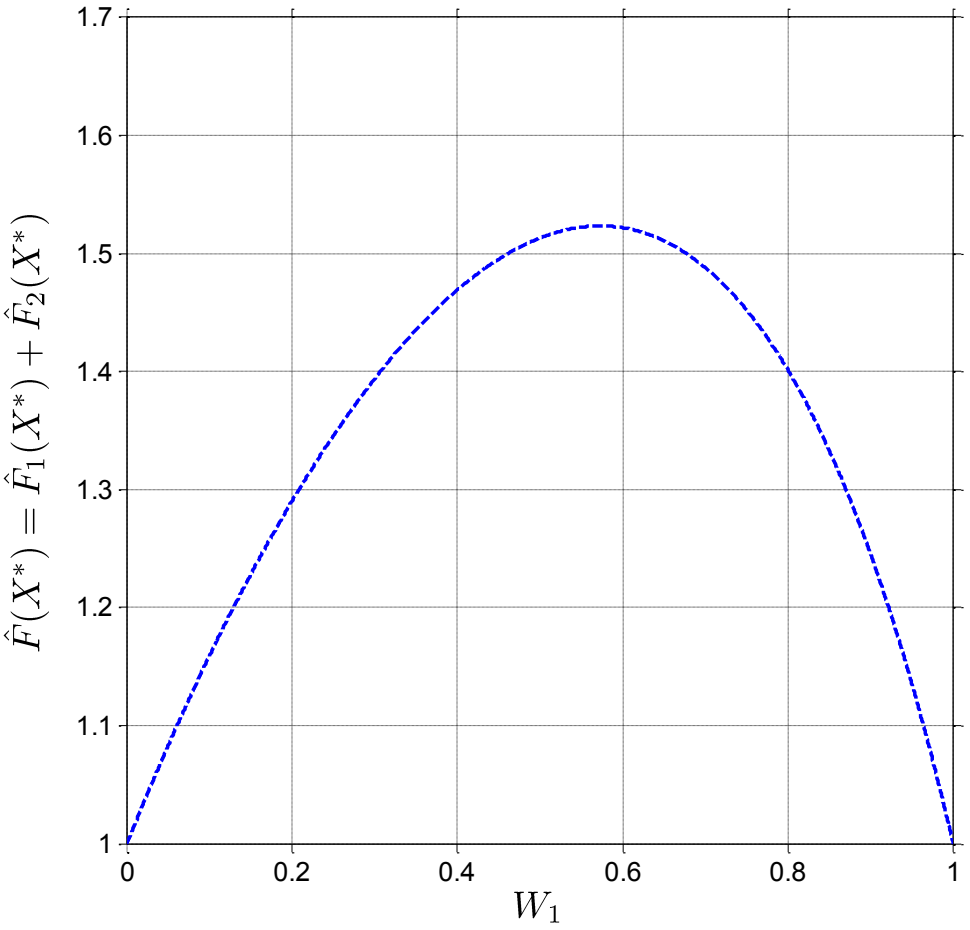

Figure 4.37. Variation in the sum of normalized optimum responses with the weighting factor for response 1 (HFPO yield).

4.1.5. Mathematical modelling of the non-catalytic gas-phase oxidation of HFP

4.1.5.1. Kinetic model development

(a) Reaction mechanism

It is generally accepted that the thermally-initiated, gas-phase oxidation of HFP is a complicated process involving many free-radical reaction steps (Dos Santos Afonso, 2000). It was desired, however, to combine these elementary steps to provide a simple kinetic scheme that could be used to model the oxidation process. Of primary importance, among this sequence of individual steps, was the addition of oxygen to the double bond of the fluoro-olefin to yield the epoxide and acid fluoride by-products. The biradical mechanism of Gilbert et al. (1976) accounted for the formation of the major products that were observed in this work, *viz*. HFPO, trifluoroacetyl fluoride (CF_3COF) and carbonyl fluoride (COF_2). Accordingly, the following two reactions were proposed:

$$C_3F_6 + ½\ O_2 \rightarrow C_3F_6O \qquad (\mathbf{1})$$

$$C_3F_6 + O_2 \rightarrow CF_3COF + COF_2 \qquad (\mathbf{2})$$

At the reaction temperatures considered, however, thermal decomposition of the epoxide and reactions involving the decomposition products also needed to be taken into account. The decomposition of HFPO above 423 K gives, as initial products, difluorocarbene (CF_2) and CF_3COF (Kennedy and Levy, 1976; Cramer and Hillmyer, 1999; Sargeant, 1970):

$$C_3F_6O \rightarrow CF_3COF + CF_2\cdot \qquad (\mathbf{3})$$

The CF_2 produced in reaction 3 has a singlet spin multiplicity (Cramer and Hillmyer, 1999; Lau et al., 2000) and generates C_2F_4 through a bimolecular recombination reaction:

$$CF_2\cdot + CF_2\cdot \rightarrow C_2F_4 \qquad (\mathbf{4})$$

The reaction of C_2F_4 with residual CF_2 gives rise to perfluorocyclopropane (*c*-C_3F_6):

$$C_2F_4 + CF_2\cdot \rightarrow c\text{-}C_3F_6 \qquad (\mathbf{5})$$

The difluorocarbene reaction scheme (reactions 4 and 5) is accepted as a valid route for the elimination of CF_2 in thermal, gas-phase fluorochemistry, having formed the basis for a number of studies in the open literature (Dalby, 1964; Edwards and Small, 1964; Cohen and Heiklen, 1965; Atkinson and McKeagan, 1966; Tyerman, 1968, Keating and Matula, 1977).

The concentrations of HFPO, C_2F_4 and *c*-C_3F_6 in the product gas were found to fall appreciably when the HFP/O_2 molar feed ratio was decreased. This behaviour was observed at all of the temperatures that were investigated (cf. Figures 4.9, 4.12 and 4.13, respectively). For HFPO, these experimental results could be explained in terms of the dependence of the rate of reaction 1 on the concentration of HFP and O_2. If this rate was more strongly dependent on the concentration of HFP, then a lower HFP/O_2 molar feed ratio would result in a lower HFPO exit concentration. For the low temperature, photo-initiated oxidation of HFP the rate of formation of HFPO has in-fact been found to be linearly dependent on the HFP concentration (Shapovalov et al., 1984) and inversely proportional to the oxygen concentration (Shapovalov and Poluéktov, 1992). Non-elementary expressions for the rate of reaction 1, in accordance with the mass-action law, were thus also considered when carrying out kinetic parameter identification.

A lower rate of formation of HFPO would impact directly on the concentration of C_2F_4 and *c*-C_3F_6, since these species evolve from the thermal decomposition of the epoxide. An alternative view was that a secondary route for the consumption of C_2F_4, other than reaction 5, was extant. This route had to be dependent on the concentration of one or both of the reactants. Kennedy and Levy (1976) found that when the gas-phase pyrolysis of HFPO was carried out in the presence of oxygen, the only products obtained were COF_2 and CF_3COF. They concluded that the decomposition of HFPO was rate-determining and oxygen had acted to convert the initial products rapidly to those that were observed. Consequently, the thermal oxidation of C_2F_4 was also considered, with the assumption that this step would be accelerated by a larger concentration of O_2. Regarding the proposed reaction, COF_2 appears to be the predominant product at high temperature (Keating and Matula, 1977; Gilbert et al., 1976). The oxidation most likely proceeds through a radical chain mechanism involving a number of transient species (Heicklen and Knight, 1966; Liu and Davis, 1992). A simple representation of the overall kinetics is obtained from one of the following expressions:

$$C_2F_4 + O_2 \rightarrow 2\ COF_2 \qquad \textbf{(6a)}$$

$$C_2F_4 + \tfrac{1}{2}\ O_2 \rightarrow COF_2 + CF_2^{\bullet} \qquad \textbf{(6b)}$$

Reaction 6a is applicable at very high temperatures (Keating and Matula, 1977; Chowdhury et al., 1987; Liu and Davis, 1992). The simple stoichiometric reaction was not obeyed, however, when the oxidation was carried out at 448 K and reaction 6b was proposed instead (Matula, 1968). Through low-temperature matrix isolation of the C_2F_4 oxidation products, Liu and Davis (1992) confirmed that CF_2 is evolved. Tyerman (1968) as well as Mathias and Miller (1967) have also used reaction 6b to describe the oxidation of C_2F_4. The orbital spin state of CF_2 produced in reaction 6b was suggested in the literature to be singlet (Heicklen and Knight, 1966; Tyerman, 1968; Liu and Davis, 1992). In this work, the singlet difluorocarbene species is expected to be recycled through reactions 4 and 5.

The ratio of CF_3COF/COF_2, as predicted by reactions 1 to 5, should always be greater than 1. This was not observed experimentally. In fact, at all reaction conditions used, there was always a greater amount of COF_2 that CF_3COF present in the product gas (cf. Figure 4.14). Even with the addition of reaction 6b to the sequence, the disparity in the exit concentrations of the two acid fluorides could not be accounted for. A similarly low ratio of CF_3COF/COF_2 was reported by Dawson et al. (2003) and they suggested that at high temperature, CF_3COF may decompose to give COF_2. The decomposition of CF_3COF in the presence of oxygen was not clearly explained by these authors. Presumably there was some form of bond cleavage in the parent molecule followed by oxidation of the radical fragments.

Under the action of a pulsed CO_2 laser and in the absence of oxygen, CF_3COF was suggested by Aslindi et al. (1986) to dissociate via the cleavage of the C-C bond, forming COF and CF_3 radicals. Further reactions gave COF_2, C_2F_6 and C_2F_4 as products. C_2F_6 was conspicuously absent from the product distribution obtained in this work, however.

The photochemistry of CF_3COF in the presence of oxygen was studied by Bierbrauer et al. (1999) and Malanca et al. (2002). The initial step was once again suggested to be C-C bond cleavage. At room temperature the products included COF_2, CO_2, bistrifluoroformyl peroxide (BFFP, $COFO_2COF$), bis(trifluoromethyl)-trioxide (BTFT, $CF_3O_3CF_3$) and CF_3O_2COF. None of the larger molecules were observed in this study. This may have been due to the low thermal stability of BFFP and CF_3O_2COF (Wallington et al., 1994; Bednarek et al., 1996).

If the dissociation of CF_3COF in oxygen at high temperature is believed to proceed via the initial scission of the C-C bond with subsequent reaction of radical fragments, then the overall balanced equation may apply for stable products:

$$2\ CF_3COF + 3\ O_2 \rightarrow CO_2 + CF_3O_3CF_3 + COF_2 \qquad \textbf{(7a)}$$

However, both CO_2 and $CF_3O_3CF_3$ were also not observed experimentally in this work. Thus, a much simpler expression for the oxidation of CF_3COF was used:

$$CF_3COF + \tfrac{1}{2}\ O_2 \rightarrow 2\ COF_2 \qquad \textbf{(7b)}$$

Batey and Trenwith (1961) suggested that the thermal decomposition of CF_3COF gave COF_2 and CF_2 directly, without the interaction of molecular oxygen:

$$CF_3COF \rightarrow COF_2 + CF_2\cdot \qquad \textbf{(7c)}$$

This 1,2-fluorine shift process was also found, computationally, to be the most favoured dissociation channel during photochemical decomposition at room temperature (Fransisco, 1992) but was never verified experimentally at high temperature (Bierbrauer et al., 1999).

The full kinetic model for the thermally-initiated, gas-phase oxidation of HFP with molecular oxygen is given in Table 4.14, together with numerical values for selected kinetic parameters, obtained from the literature. The reaction pathways for the generation of the major products observed in this work are shown in Figure 4.38.

Table 4.14. Reaction model for the thermally-initiated, gas-phase oxidation of HFP with molecular oxygen.[a]

No.	Reaction	Forward reaction			Reverse reaction			Excitation technique	Temperature range [K]	Reference
		$\log_{10}A$	n	E_a	$\log_{10}A$	n	E_a			
1.	$C_3F_6 + ½\ O_2 \rightarrow C_3F_6O$									
2.	$C_3F_6 + O_2 \rightarrow CF_3COF + COF_2$									
3.	$C_3F_6O \rightarrow CF_3COF + CF_2$•	13.20	0	151.80				Thermal	414 – 530	Kennedy and Levy (1976)
		14.19	0	162.01				Thermal	463-503	Krusic et al. (1999)
4.	CF_2• + CF_2• $\rightarrow C_2F_4$	9.57	0.5	5.02				Flash photolysis	298 – 573	Dalby (1964)
		12.94	0	0	16.66	0	294.50	Thermal	803 – 973	Edwards and Small (1964)
		9.39	0.5	1.66				Flash photolysis	298 – 446	Tyerman (1968)
					16.83	0	228.80	Thermal	1500 – 2500	Keating and Matula (1977)
					17.92	0	197.00	Thermal	1500 – 2500	Douglass et al. (1995)
5.	C_2F_4 + CF_2• $\rightarrow$ *c*-C_3F_6	9.09	0.5	35.56	13.25	0	161.50	Flash photolysis	298 – 573	Dalby (1964)
		7.94	0.5	26.61				Flash photolysis	298 – 446	Tyerman (1968)
					13.00	0	182.00	Thermal	1300 – 1600	Hynes et al. (1999)
6.	$C_2F_4 + ½\ O_2 \rightarrow COF_2 + CF_2$•	12.91	0	5.272				Thermal	1500 – 2500	Douglass et al. (1999)
7b.	$CF_3COF + ½\ O_2 \rightarrow 2\ COF_2$									

[a] The temperature dependence of the rate coefficient is given in the form of the modified Arrhenius expression, $k = AT^n\exp(-E_a/RT)$. Units for A, $cm^3\ mol^{-1}\ s^{-1}$ or s^{-1}, as appropriate. Units for E_a, kJ mol^{-1}.

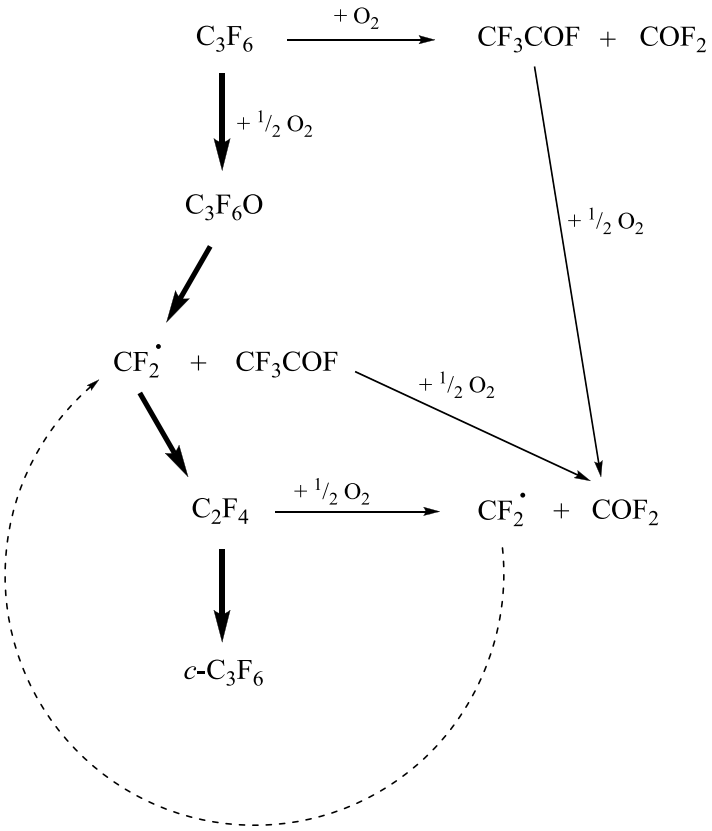

Figure 4.38. Reaction pathways for the thermally-initiated gas-phase oxidation of HFP. The larger arrows indicate the channels with the highest rates.

(b) Thermochemistry

For each of the reactions introduced in the preceding section the rate constants for the forward, k_j, and reverse, k_{-j}, steps are related through the equilibrium constant, K_j. If the rate constants are expressed in units of m^3, moles and seconds whereas the equilibrium constant is referenced to a standard state for gases (1 bar) then the concentration-based equilibrium constant is related to the activity-based equilibrium constant through the following equation (Rodgers, 1978):

$$\frac{k_j}{k_{-j}} = K_{c_j} = K_{a_j} \times \left(\frac{P_\circ}{RT} \right)^{\Sigma \nu_i} \tag{4.24}$$

where $P_\circ$ is the reference pressure and $\sum \nu_i$ is the sum of the stoichiometric coefficients for reaction j.

In this study, calculated values of the equilibrium constant were used to gauge the reversibility of each of the reactions involved. The temperature dependence of the activity-based equilibrium constant is given by:

$$\ln K_a(T) = \frac{-\Delta G^\circ_{rxn}(T)}{RT} \tag{4.25}$$

$-\Delta G^\circ_{rxn}(T) / RT$ is readily calculated at any temperature using the standard heat of reaction and the standard Gibbs energy change of reaction at a reference temperature (298.15 K), and from knowledge of the temperature dependence of the heat capacity of each species involved (Smith et al., 2001):

$$\frac{\Delta G^\circ_{rxn}(T)}{RT} = \frac{\Delta G^\circ_{rxn}(T_0) - \Delta H^\circ_{rxn}(T_0)}{RT_0} + \frac{\Delta H^\circ_{rxn}(T_0)}{RT} + \frac{1}{T}\int_{T_0}^{T} \frac{\Delta C^\circ_P}{R} dT - \int_{T_0}^{T} \frac{\Delta C^\circ_P}{RT} dT \tag{4.26}$$

The standard heat of reaction and standard Gibbs energy change of reaction (at the reference temperature, T_0) may be calculated based on the standard enthalpy of formation and standard entropy of formation of each of the species concerned:

$$\Delta H^{\circ}_{rxn}(T_0) = \sum_i \nu_i \Delta H^{\circ}_{f,i}(T_0) \tag{4.27}$$

$$\Delta S^{\circ}_{rxn}(T_0) = \sum_i \nu_i \Delta S^{\circ}_{f,i}(T_0) \tag{4.28}$$

$$\Delta G^{\circ}_{rxn}(T_0) = \Delta H^{\circ}_{rxn}(T_0) - T_0 \Delta S^{\circ}_{rxn}(T_0) \tag{4.29}$$

Reliable thermochemical property data was therefore required for each of the eight species that were involved in the HFP oxidation process. Data for HFP, COF_2, C_2F_4, CF_2 and O_2 were taken from the Third Millennium Ideal Gas and Condensed Phase Thermochemical Database for Combustion, or IGTD (Burcat and Ruscic, 2005). For HFPO, CF_3COF and *c*-C_3F_6, however, no data was available. Quantum chemical calculations were used to estimate the thermochemical properties of these components. The details of the computational procedures are given in Appendix D. The standard enthalpy of formation of CF_3COF was calculated using the Gaussian-4 composite method (Curtiss et al., 2007). Computations performed for HFPO and *c*-C_3F_6 crashed at some point and could not be completed. For these two compounds the standard enthalpy of formation was predicted using the semi-theoretical T1 recipe of Ohlinger et al. (2009) and the Spartan 10 molecular simulation program. The standard entropies of formation and heat capacities for all three components were computed using the B3LYP density functional theory at the B-3LYP16-31G(2df,p) level, with vibrational frequencies scaled by a factor of 0.9854. All calculations were performed using Gaussian 09 software on a Hewlet Packard machine equipped with a 2.4 GHz Intel Core i5 processor and 4.0 GB RAM.

Thermochemical property data of all eight species used in the equilibrium calculations are presented in Table 4.15, along with comparative data from the NIST-JANAF Tables (Chase, 1998). In order to numerically evaluate the integrals in Equation 4.26, the heat capacity data for O_2, CF_2, COF_2, C_2F_4 and HFP obtained from Burcat and Ruscic (2005), and for HFPO, CF_3COF and *c*-C_3F_6 obtained from the quantum chemical calculations performed in this work, were fitted to the Shomate equation:

$$C^{\circ}_{P_i}(T) = a + bT + cT^2 + dT^3 + eT^{-2} \tag{4.30}$$

Table 4.15. Thermochemical property data at the reference temperature (298.15 K) for species involved in the oxidation of HFP.

Component	$\Delta H°_f$ (298.15 K) [kJ mol^{-1}]				$\Delta S°_f$ (298.15 K) [kJ mol^{-1} K^{-1}]			$C°_p$ (298.15 K) [kJ mol^{-1} K^{-1}]		
	IGTD	**NIST-JANAF**	**G4**	**T1**	**IGTD**	**NIST-JANAF**	**B3LYP**	**IGTD**	**NIST-JANAF**	**B3LYP**
HFP	-1157.25	-	-	-1150.06	-251.92	-	-246.81	121.76	-	120.93
O_2	0	-	0.89		-	0	-0.17	29.38	29.38	29.28
HFPO	-	-	-	-1206.49	-	-	-344.05	-	-	131.24
CF_3COF	-	-	-1022.86	-1019.56	-	-	-183.84	-	-	91.32
CF_2•	-191.25	-182.00	-194.39	-178.24	32.30	32.30	37.99	38.92	38.95	38.80
COF_2	-606.64	-638.90	-607.56	-613.08	-52.11	-52.20	-46.44	47.37	47.25	47.30
C_2F_4	-675.34	-658.56	-672.19	-673.88	-116.94	-117.03	-110.96	80.46	80.46	80.34
c-C_3F_6	-	-	-	-1021.44	-	-	-257.82	-	-	120.79

The regression coefficients for each of the components are listed in Table 4.16.

Table 4.16. Coefficients of the Shomate equation for $C_{P_i}^{\circ}(T)$

Component	*a*	*b*	*c*	*d*	*e*
HFP	8.0475	9.7290×10^{-2}	-9.2801×10^{-5}	3.2551×10^{-8}	-5.0802×10^{4}
O_2	6.1413	1.4353×10^{-3}	3.2653×10^{-6}	-2.6313×10^{-9}	2.0780×10^{4}
HFPO	7.8989	1.0867×10^{-1}	-9.8165×10^{-5}	3.2470×10^{-8}	-9.4721×10^{4}
CF_3COF	7.8525	6.4474×10^{-2}	-5.6185×10^{-5}	1.8148×10^{-8}	-6.5210×10^{4}
CF_2•	3.2219	2.3194×10^{-2}	-1.7970×10^{-5}	4.1590×10^{-9}	5.8343×10^{4}
COF_2	2.5476	3.7077×10^{-2}	-3.1784×10^{-5}	9.8017×10^{-9}	2.5457×10^{4}
C_2F_4	9.0188	4.9273×10^{-2}	-4.5821×10^{-5}	1.6841×10^{-8}	-7.6429×10^{4}
c-C_3F_6	8.6746	9.2002×10^{-2}	-8.2101×10^{-5}	2.6885×10^{-8}	-5.7573×10^{4}

[a] Units of heat capacity, cal mol^{-1} K^{-1}

The activity-based equilibrium constants for reactions 1 to 7b, calculated using Equation 4.26, are given in Table 4.17 at each of the three temperatures that were investigated.

Table 4.17. Logarithm of the activity-based equilibrium constants for the reactions.

No.	Reaction	$\log_{10}K_a$		
		463 K	**478 K**	**493 K**
1.	$C_3F_6 + ½\ O_2 \rightarrow C_3F_6O$	0.7277	0.5522	0.3873
2.	$C_3F_6 + O_2 \rightarrow CF_3COF + COF_2$	54.058	52.3799	50.8034
3.	$C_3F_6O \rightarrow CF_3COF + CF_2$•	10.9009	10.8707	10.8419
4.	CF_2• + CF_2• $\rightarrow C_2F_4$	23.5709	22.5379	21.5682
5.	$C_2F_4 + CF_2$• $\rightarrow$ *c*-C_3F_6	8.4378	7.8930	7.3817
6.	$C_2F_4 + ½\ O_2 \rightarrow COF_2 + CF_2$•	18.8585	18.4191	18.0060
7b.	$CF_3COF + ½\ O_2 \rightarrow 2\ COF_2$	25.5880	24.9069	24.2667

Since these reactions were carried out at a pressure of 4.5 bar, the effect of pressure on the equilibrium constants had to be considered. The pressure dependence of the activity-based equilibrium constant is given by (Ott and Boerio-Goates, 2000):

$$\left(\frac{\partial \ln K_a}{\partial P}\right)_T = -\frac{\Delta V^\circ}{RT} \tag{4.31}$$

where

$$\Delta V^\circ = \sum v_i V_i^\circ \tag{4.32}$$

and V_i° is the molar volume of species i . The evaluation of this partial derivative is complicated by the fact that the molar volumes are also functions of the system pressure. As an approximation, the RHS of Equation 4.31 was evaluated at the experimental conditions (reaction pressure of 4.5 bar and a reaction temperature of either 463, 478 or 493 K) and was used to correct the standard activity-based equilibrium constants, applicable only at the reference pressure of 1 bar, given in Table 4.17. The corrected equilibrium constants are presented in Table 4.18.

Table 4.18. Logarithm of the activity-based equilibrium constants for the reactions, corrected for pressure.

No.	Reaction	$\log_{10} K_a$		
		463 K	**478 K**	**493 K**
1.	$C_3F_6 + ½\ O_2 \rightarrow C_3F_6O$	0.8968	0.7213	0.5564
2.	$C_3F_6 + O_2 \rightarrow CF_3COF + COF_2$	54.0580	52.3799	50.8034
3.	$C_3F_6O \rightarrow CF_3COF + CF_2\bullet$	10.5627	10.5325	10.5037
4.	$CF_2\bullet + CF_2\bullet \rightarrow C_2F_4$	23.9091	22.8761	21.9064
5.	$C_2F_4 + CF_2\bullet \rightarrow c\text{-}C_3F_6$	8.7760	8.2312	7.7199
6.	$C_2F_4 + ½\ O_2 \rightarrow COF_2 + CF_2\bullet$	18.6894	18.2500	17.8369
7b.	$CF_3COF + ½\ O_2 \rightarrow 2\ COF_2$	25.4189	24.7378	24.0976

The activity-based equilibrium constants can be converted to concentration-based equilibrium constants using Equation 4.24. The formal development of this relation, which holds only for an ideal gas, is given in Appendix D. It was essential then to demonstrate that the reaction gas mixture in this work was also ideal. The effect of the compressibility factor on the fugacity coefficient is given by:

$$\ln \phi_i = \int_0^{P_r} (Z_i - 1) \frac{dP_r}{P_r} \tag{4.33}$$

Therefore, for a gas to be considered ideal in the context of chemical reaction equilibria, it would be sufficient to show that the compressibility is close to 1. Pure component compressibility factors of each of the four major constituents of the reaction gas, HFP, O_2, HFPO and COF_2, were estimated using the Pitzer correlation (Smith et al., 2001):

$$Z = Z^0 + \omega Z^1 \tag{4.34}$$

where ω is the accentric factor and the parameters Z^0 and Z^1 were obtained from Lee/Kesler generalized-correlation tables (Smith et al., 2001), based on the calculated reduced properties. The results of these calculations at 463 K, the worst representative case in terms of the departure from ideality, are presented in Table 4.19.

Table 4.19. Thermodynamic parameters of each of the four major constituents of the reaction gas at 463 K.

Component	ω	T_c [K]	P_c [bar]	T_r	P_r	Z^0	Z^1	Z
HFP	0.204	367.15	29	1.261	0.155	0.9750	0.0080	0.9806
O_2	0.022	154.6	50.43	2.996	0.089	1.0003	0.0055	1.0004
HFPO	0.293	359.15	28.96	1.290	0.155	0.9801	0.0081	0.9824
COF_2	0.283	297	57.6	1.559	0.078	0.9910	0.0070	0.9930

[a] Critical data and accentric factors from Yaws (2001)

Of all these components, HFP showed the greatest departure from ideality at this temperature, yet the gas mixture was still regarded as essentially ideal. An extension of the generalized correlation for compressibility to gas mixtures involves evaluating the corresponding-states parameters Z^0 and

Z^l using pseudo-critical properties obtained from simple linear mixing rules (Smith et al., 2001). This method requires some knowledge of the mixture composition, however. Since the values of the pure component compressibilities for all major species were found to be very close to 1, such a rigorous treatment was deemed unnecessary.

The concentration-based equilibrium constants for reactions 1 to 7b are given in Table 4.20 at each of the three temperatures that were investigated. It was predicted that only reaction 1 would practically exhibit reversibility under the experimental conditions considered. Further it was decided to include the rate constant for the reverse step of reaction 1 as a fitting parameter when undertaking identification.

Table 4.20. Logarithm of the concentration-based equilibrium constants for the reactions.

No.	Reaction	$\log_{10}K_c$		
		463 K	**478 K**	**493 K**
1.	$C_3F_6 + ½\ O_2 \rightarrow C_3F_6O$	0.1895	0.0210	-0.1372
2.	$C_3F_6 + O_2 \rightarrow CF_3COF + COF_2$	54.0580	52.3799	50.8034
3.	$C_3F_6O \rightarrow CF_3COF + CF_2\bullet$	11.9772	11.9332	11.8909
4.	$CF_2\bullet + CF_2\bullet \rightarrow C_2F_4$	22.4946	21.4754	20.5192
5.	$C_2F_4 + CF_2\bullet \rightarrow c\text{-}C_3F_6$	7.3615	6.8305	6.3327
6.	$C_2F_4 + ½\ O_2 \rightarrow COF_2 + CF_2\bullet$	19.3967	18.9503	18.5305
7b.	$CF_3COF + ½\ O_2 \rightarrow 2\ COF_2$	26.1262	25.4381	24.7912

4.1.5.2. Reactor modelling

(a) Governing equations

The starting point of any reactive flow problem is the basic statement of the governing equations. According to Bird et al. (2002), the total continuity equation for a muti-component system may be written as:

$$\frac{\partial \rho}{\partial t} + \left(\nabla \cdot \rho \mathbf{v}\right) = 0 \tag{4.35}$$

and species continuity is given by:

$$\frac{d\rho_i}{dt} = -\rho_i \left(\nabla \cdot \mathbf{v}\right) - \left(\nabla \cdot \mathbf{j}_i\right) + R_i \tag{4.36}$$

where $\mathbf{v}$ is the mass average velocity, R_i is the net rate of production of mass of i per unit volume by reaction, and $\mathbf{j}_i$ is the mass flux of species i, which is related to the gradient of the mass fraction, w_i, through the generalized Fick's law:

$$\mathbf{j}_i = -\rho D_{im} \nabla w_i \tag{4.37}$$

Equations 4.35-4.37 can be combined to yield:

$$\frac{\partial \left(\rho w_i\right)}{\partial t} = -\nabla \cdot \left(\rho \mathbf{v} w_i - \rho D_{im} \nabla w_i\right) + R_i \tag{4.38}$$

which may be regarded as a generalized mass balance for species i (Fagley, 1992). Note that ρ_i is equal to ρw_i. The momentum balance is represented by:

$$\frac{\partial \left(\rho \mathbf{v}\right)}{\partial t} + \nabla \cdot \left(\rho \mathbf{v} \mathbf{v}\right) - \nabla \cdot \boldsymbol{\tau} = \sum \rho_i \mathbf{g}_i - \nabla p \tag{4.39}$$

where the components of the stress tensor $\boldsymbol{\tau}$ are assumed to obey the general Newtonian fluid form (Bird et al., 2002).

The equations of change for an isothermal, multi-component system as described, are seldom used in their complete forms to solve reactive flow problems. Often, restricted forms are used for convenience, based on various simplifying assumptions (Bird et al., 2002). The assumption of steady state, for instance, immediately reduces all accumulation terms to zero.

The density of a mixture of ideal gases is given by:

$$\rho = \frac{P\bar{M}}{RT} \tag{4.40}$$

For a non-equimolar reaction occurring in a steady-state flow reactor it can be shown that at any point in the reactor the following relation holds, according to law of conservation of mass:

$$\bar{M} = \frac{F_{tot}^{0}}{F_{tot}} \bar{M}_0 \tag{4.41}$$

where F and $\bar{M}$ are the molar flow-rate and average molar mass, respectively and the index 0 refers to the feed stream. It was understood that the non-equimolar nature of the combined reaction set in this work would therefore manifest as a change in the mass density within the momentum balance and hence the velocity field as well (Jakobsen, 2002, Wan and Ziegler, 1973). Indeed, the average change in the total molar flow-rate between the inlet and outlet points of the reactor, relative to the inlet molar flow-rate, was found to be approximately 14%, across all experiments (cf. Figure 4.39). Rigorous modelling would therefore have required simultaneous solution of the coupled material and momentum balances. To simplify the modelling and to confine the calculations within reasonable limits, a constant density was assumed, with the velocity field dependent only on the flow regime (Hopkins and Golding, 1993).

To determine the regime of flow, the Reynolds number for all experimental points was calculated according to:

$$Re = \frac{d_t v \rho}{\mu} \tag{4.42}$$

where v, ρ and μ were the fluid velocity, density and viscosity evaluated at the inlet and d_t was the reactor tube inner diameter (1.5×10^{-3} m).

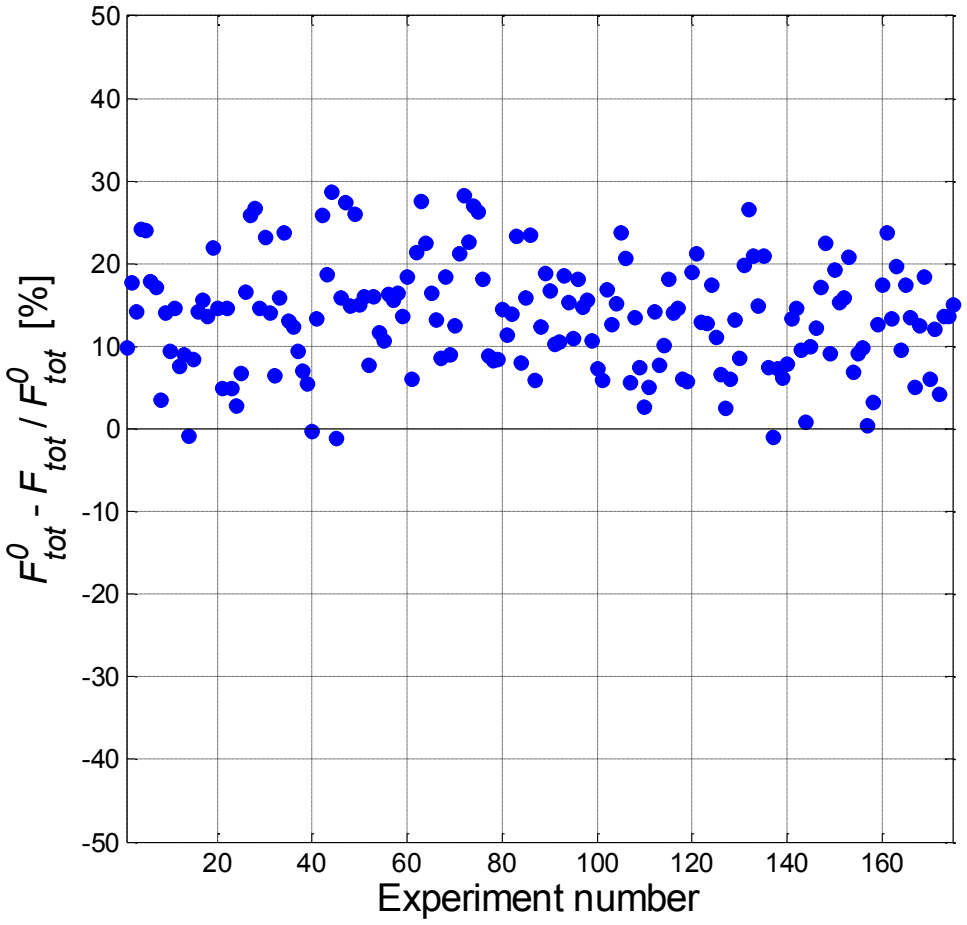

Figure 4.39. Relative change in the total molar flow-rate for all experimental points.

The critical Reynolds number, defined as the highest Reynolds number for which the flow through a coil may still be regarded as viscous or laminar, was given by (Holland and Bragg, 1995):

$$Re_{critical} = 2100\left[1+12\left(\frac{d_t}{d_c}\right)^{0.5}\right] \tag{4.43}$$

where d_c was the coil diameter (0.05 m). All calculated values were found to be below the critical transition value of 6465 for Newtonian flow through coils and the regime of flow could therefore be considered laminar (cf. Figure 4.40). The pure component viscosity of HFP was estimated using the method of Reichenberg (Perry et al., 1997):

$$\mu = \frac{AT_r}{\left[1+0.36T_r\left(T_r-1\right)\right]^{1/6}} \tag{4.44}$$

$$A = \frac{M^{0.5}T_c}{\sum n_i C_i} \tag{4.45}$$

where the viscosity is given in Pa s with the critical temperature in K. The denominator in Equation 4.45 is based on the summation of various atomic group contribution increments given in the literature (Perry et al., 1997). The pure component viscosity of O_2 was estimated using the Chapman-Enskog kinetic theory of gases (Bird et al., 2002):

$$\mu = 2.6693\times10^{-5}\frac{\sqrt{MT}}{\sigma\Omega_u} \tag{4.46}$$

where the viscosity is given in units of g cm^{-1} s^{-1}. The collision diameter, σ for O_2 is 3.433 and the dimensionless quantity Ω_u is a function of the dimensionless temperature $\kappa T/\varepsilon$. The ratio ε/κ for O_2 is 113.

The viscosity of the gas mixture was then calculated using the method of Bromley and Wilke (Perry et al., 1997), based on the pure component viscosities:

$$\mu_m = \sum_{i=1}^{n} \frac{\mu_i}{1 + \sum_{\substack{j=1 \\ j \neq i}}^{n} Q_{ij} \frac{x_j}{x_i}} \tag{4.47}$$

$$Q_{ij} = \frac{1 + \left[\left(\frac{\mu_i}{\mu_j} \right)^{1/2} \left(\frac{M_j}{M_i} \right)^{1/4} \right]^2}{\sqrt{8} \left[1 + \frac{M_i}{M_j} \right]^{1/2}} \tag{4.48}$$

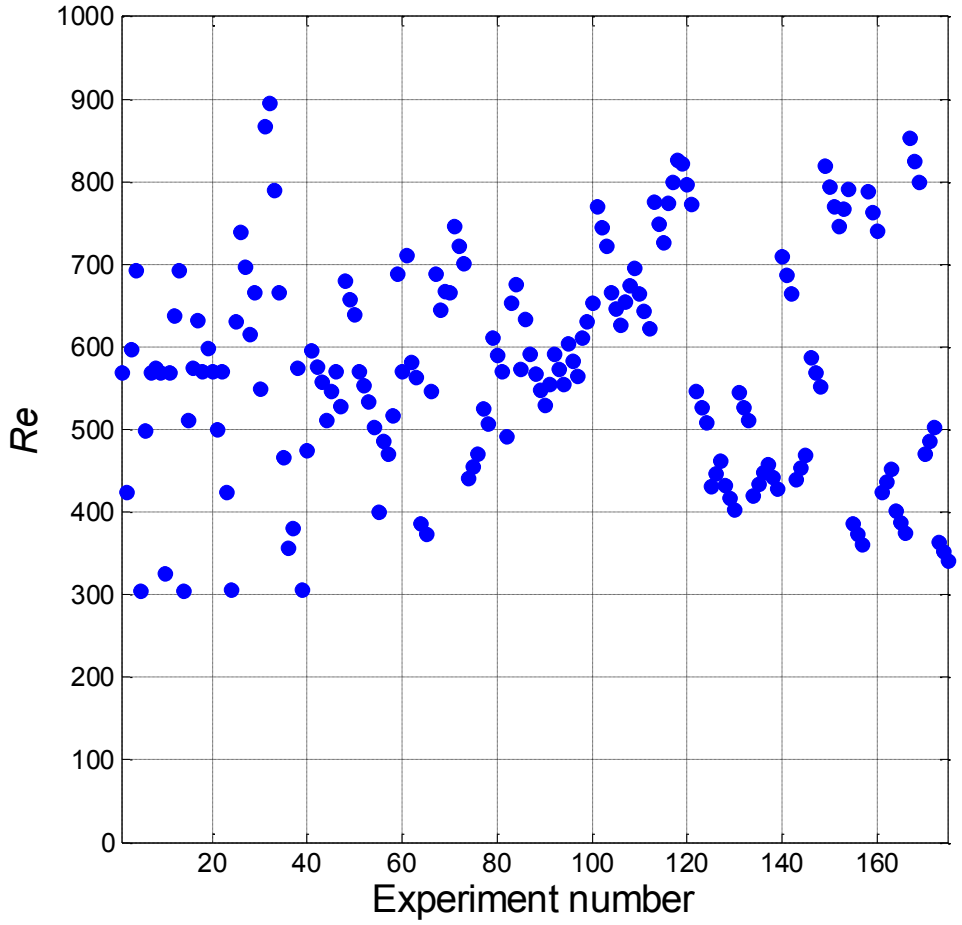

Figure 4.40. Reynolds number for all experimental points, based on reactor inlet conditions.

Assuming axisymmetric flow in a circular tube such that the angular velocity component $v_\theta = 0$, the radial velocity component v_r is negligible compared to the axial component v_z and that v_z is independent of the axial position, the steady-state momemtum balance reduces to (Bird et al., 2002):

$$0 = -\frac{dp}{dz} + \mu \frac{1}{r}\frac{d}{dr}\left(r\frac{dv_z}{dr}\right) \tag{4.49}$$

Equation 4.49 can be solved to give the parabolic velocity profile:

$$v_z(r) = v_{z,\max}\left[1 - \left(\frac{r}{R}\right)^2\right] \tag{4.50}$$

where R is the reactor tube radius and $v_{z,\max}$ is calculated as twice the average velocity, based on the volumetric flow-rate and the cross-sectional area of the tube. An entrance length, given by:

$$l_e = 0.035 d_t Re \tag{4.51}$$

is required for the build-up of the parabolic profile. This value was found to be 0.03 m on average (cf. Figure 4.41). Hence, entrance effects for the 114.3 m long reactor tube were considered negligible.

A simplified steady-state expression of species continuity is given by (Nauman, 2002):

$$v_z \frac{\partial C_i}{\partial z} = \frac{\partial}{\partial z}\left[D_{im}\frac{\partial C_i}{\partial z}\right] + \frac{1}{r}\frac{\partial}{\partial r}\left[D_{im} r \frac{\partial C_i}{\partial r}\right] + R_i \tag{4.52}$$

Substituting the laminar flow parabolic velocity profile yields:

$$v_{z,\max}\left[1 - \left(\frac{r}{R}\right)^2\right]\frac{\partial C_i}{\partial z} = \frac{\partial}{\partial z}\left[D_{im}\frac{\partial C_i}{\partial z}\right] + \frac{1}{r}\frac{\partial}{\partial r}\left[D_{im} r \frac{\partial C_i}{\partial r}\right] + R_i \tag{4.53}$$

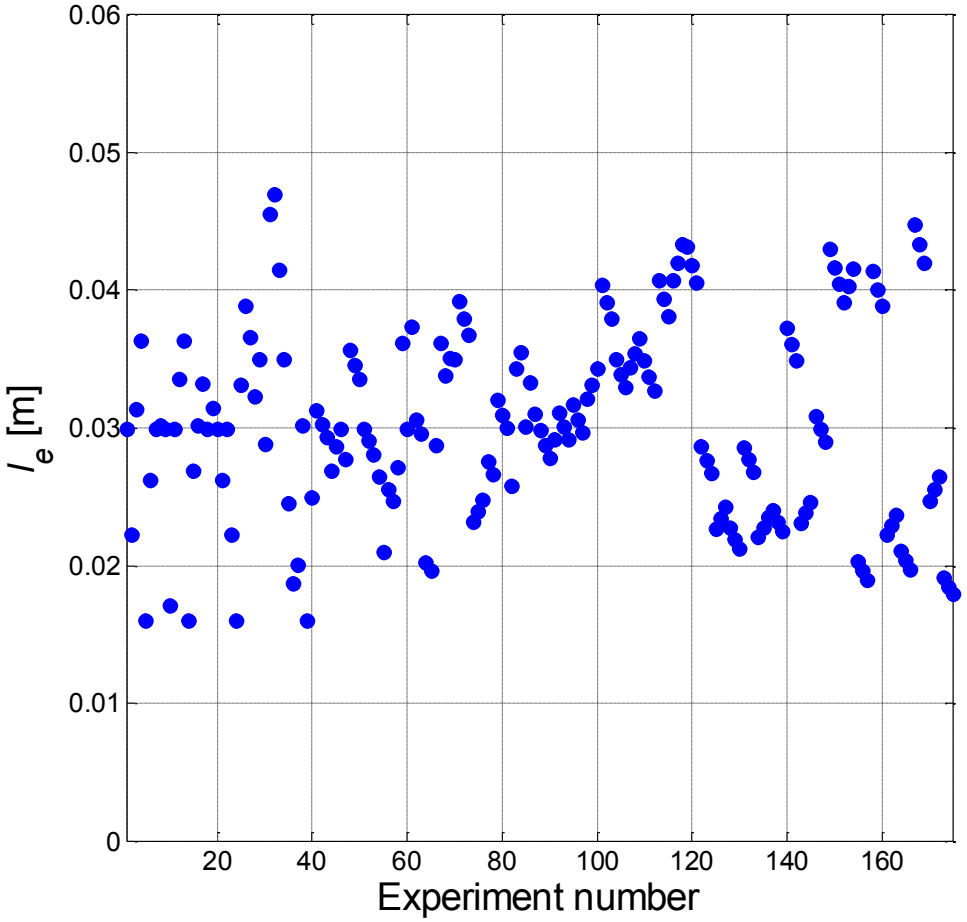

Figure 4.41. Entrance length for all experimental points.

Multicomponent diffusivity is difficult to determine in the general case. Rigorous treatment involves solving the Maxwell-Stefan equations (Bird et al., 2002). In this work, however, the mixture diffusion coefficient of species *i* was estimated using the approximation of Cussler (1976):

$$D_{im} = \frac{(1 - y_i)}{\sum_{\substack{j=1 \\ j \neq i}}^{n} \frac{y_j}{D_{ij}}} \tag{4.54}$$

This approximation was shown by Bird et al. (2002) to be exact when either all D_{ij} are equal or when all species except *i* move at the same velocity (Fagley, 2002). The binary diffusion

coefficients used in Equation 4.54 were estimated using the empirical equation of Fuller, Schettler and Giddings (Seader and Henley, 1998):

$$D_{AB} = \frac{0.00143T^{1.75}}{PM_{AB}^{0.5}\left[\left(\sum v\right)_A^{1/3} + \left(\sum v\right)_B^{1/3}\right]^2} \tag{4.55}$$

where D_{AB} is in $cm^2\ s^{-1}$, P is in atm, T is in K,

$$M_{AB} = \frac{2}{\left(1/M_A\right) + \left(1/M_B\right)} \tag{4.56}$$

and $\sum v$ is the summation of atomic and structural diffusion volumes for each species.

For laminar flow reactors with a high axial aspect ratio (L_t/R_t), axial diffusion can generally be neglected (Nauman, 2002; Nauman and Nigam, 2005). The importance of radial diffusion in a laminar flow reactor is determined by the following dimensionless parameter (Nauman, 2002):

$$\frac{D_A\tau}{R_t^2} \tag{4.57}$$

where τ is the space time. For first order reactions, Merrill and Hamrin (1970) showed that radial diffusion can be ignored if:

$$\frac{D_A\tau}{R_t^2} < 0.003 \tag{4.58}$$

The parameter defined in Equation 4.57 was calculated to be 7.91×10^3 on average, based on the reactor inlet conditions (cf. Figure 4.42), indicating that the radial diffusion term in Equation 4.53 had to be retained.

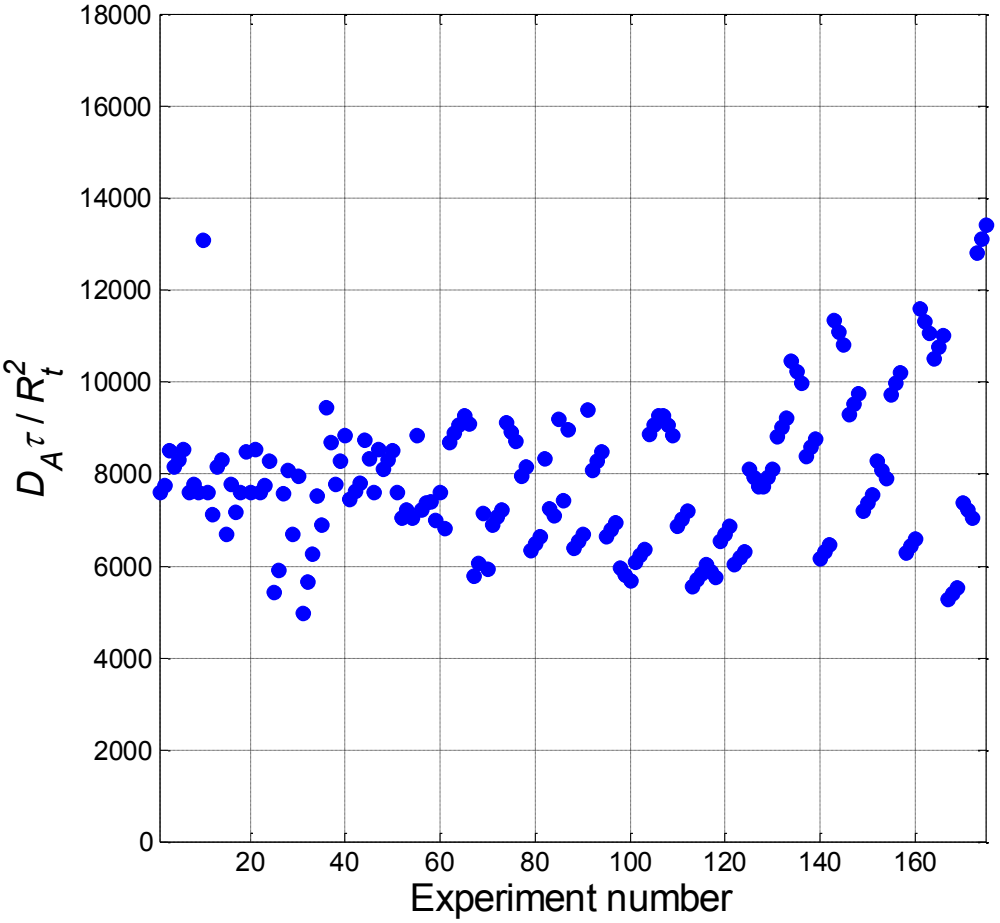

Figure 4.42. Criterion for radial diffusion for all experimental points.

Removing the axial diffusion term from the general balance and assuming that the radial dependence of D_{im} was small gives:

$$v_{z,\max}\left[1-\left(\frac{r}{R}\right)^2\right]\frac{\partial C_i}{\partial z} = D_{im}\frac{\partial^2 C_i}{\partial r^2} + \frac{D_{im}}{r}\frac{\partial C_i}{\partial r} + R_i \tag{4.59}$$

Equation 4.59 is valid for fully developed laminar flow, without axial diffusion, in a straight tube. It was important to consider the hydrodynamics of the flow through the coiled reactor tube used in this study. The action of centrifugal force on fluid elements moving through a coiled tube results in secondary flow in the plane of the tube cross-section (Janssen, 1976). The strong influence of secondary flow on the velocity distribution is well documented in the literature (Trivedi and Vasudeva, 1974; Trivedi and Vasudeva, 1975; Nauman, 1977; Janssen and Hoogendoorn, 1978). It is important to note that the presence of secondary flow in a coiled tube can result in a higher axial pressure gradient, a higher critical Reynolds number for transition to turbulent flow, increased rates of radial heat and mass transfer as well as a substantial decrease in axial dispersion (Janssen and Hoogendoorn, 1978; Agrawal and Nigham, 2001). Trivedi and Vasudeva (1974) showed that secondary flow can also lead to a narrowing of the residence time distribution, closely approximating that of plug flow. The rigorous modelling of reactive flow through a coiled tube requires the solution of the equations of continuity and momentum in toroidal co-ordinates.

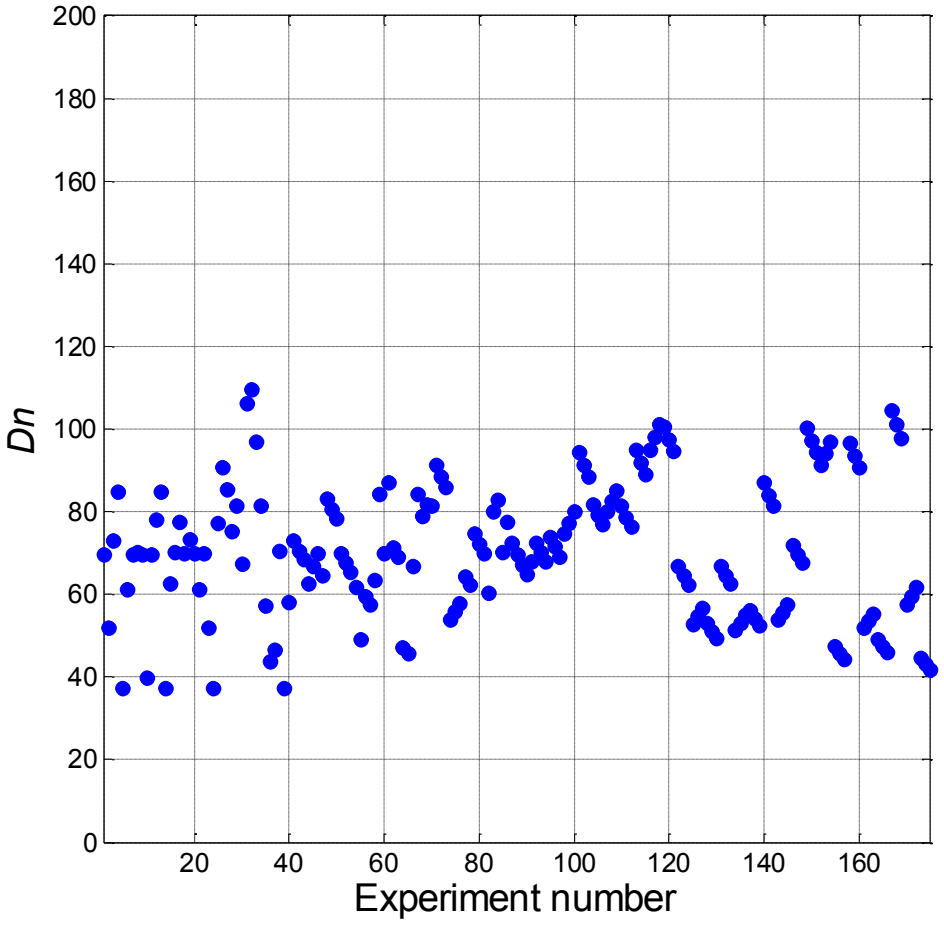

Figure 4.43. Dean number for all experimental points.

The hydrodynamics of the flow through a coiled tube and the importance of inertial forces are characterized by the Dean number $\left(Dn = Re\sqrt{\frac{d_t}{d_c}} \right)$. For low Dean numbers ($Dn$ < 17) secondary flow can be ignored (Janssen and Hoogendoorn, 1978). The strongest effects of secondary flow are obtained at Dn > 100. In this work, the Dean number was found to lie between 37 and 109 (cf. Figure 4.43). In this intermediate range, inertial forces cannot be completely ignored. However, for the sake of simplicity, it was decided to proceed with the straight-tube laminar flow reactor model. Equation 4.59 was therefore used to model the non-catalytic, gas-phase oxidation of HFP.

(b) Numerical solution method

The physical system was a convection-diffusion-reaction system, modelled in cylindrical co-ordinates. The kinetic term in Equation 4.59 was a potential source of nonlinearity in the model. For the reaction scheme given in Table 4.14, involving 8 species, it was necessary to solve 8 simultaneous parabolic partial differential equations (PDE's) having the form of Equation 4.59. The material balances required two boundary conditions in r and one in z:

$$\left.\frac{\partial C_i}{\partial r}\right|_{r=0} = 0 \tag{4.60}$$

$$\left.\frac{\partial C_i}{\partial r}\right|_{r=R_t} = 0 \tag{4.61}$$

$$C_i(r,0) = C_i^0 \tag{4.62}$$

The wall boundary condition applies to a solid tube without transpiration (Nauman, 2002). The centreline boundary condition is consistent with the assumption of an axisymmetric velocity profile without concentration gradients in the angular direction (Nauman, 2002).

The system of parabolic PDE's was solved using the method of lines, which is based on finite difference approximations for the partial derivatives (Shiesser and Griffiths, 2009). It involves the

use of orthogonal collocation in the radial direction coupled with an implicit, linear, multi-step solution algorithm for integration in the axial direction (Hopkins and Golding, 1993). Radial discretization was accomplished through the use of difference formulas to yield the ODE's required for the axial integrator. Figure 4.44 shows the reference grid that was used for the derivation of the difference equations.

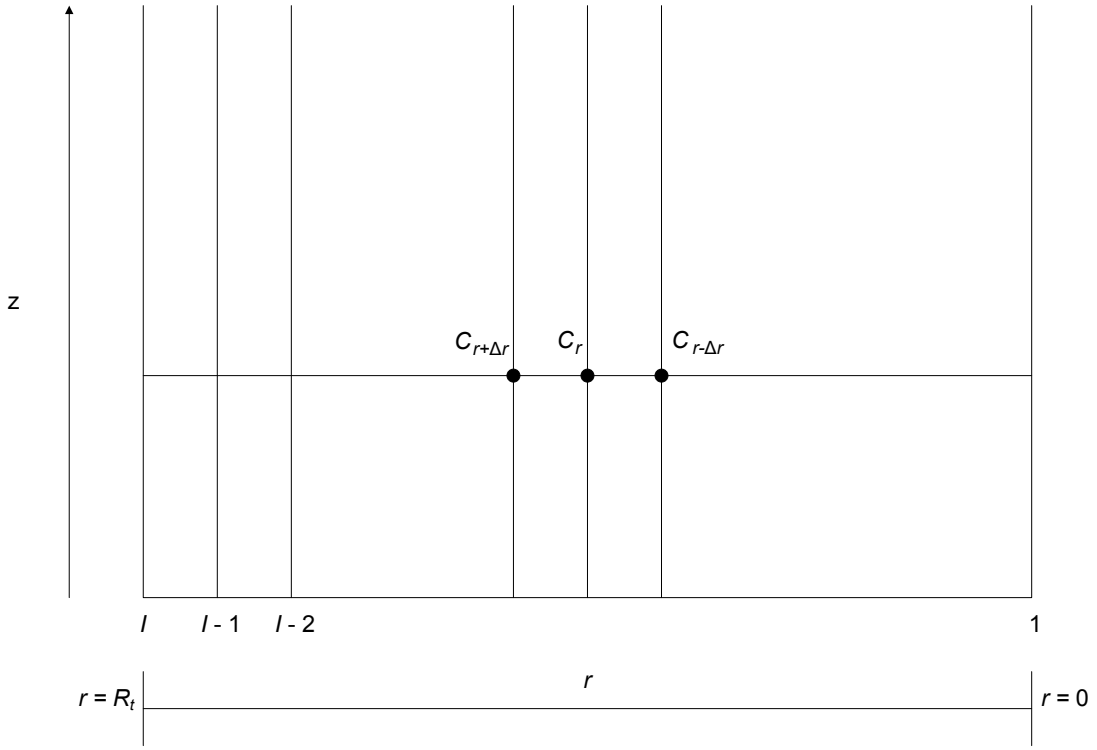

Figure 4.44. Reference grid for the derivation of finite difference equations.

The tube is divided into a number of equally sized increments $\Delta r = R_t$ / I. Programming of the derivatives in z begins with the first derivative radial group in Equation 4.59. For reasons of convergence, a second-order, central difference approximation for the first partial derivative is used (Nauman, 2002):

$$\frac{\partial C_i}{\partial r} \approx \frac{C_i(r+\Delta r, z) - C_i(r-\Delta r, z)}{2\Delta r} \tag{4.63}$$

For the second radial derivatives the following approximation is employed:

$$\frac{\partial^2 C_i}{\partial r^2} \approx \frac{C_i(r+\Delta r,z)-2C_i(r,z)+C_i(r-\Delta r,z)}{\Delta r^2} \tag{4.64}$$

At $r = 0$, the second derivative is approximated as:

$$\begin{aligned}\left.\frac{\partial^2 C_i}{\partial r^2}\right|_{r=0} &\approx \frac{C_i(r+\Delta r,z)-2C_i(r,z)+C_i(r-\Delta r,z)}{\Delta r^2} \\ &\approx 2\frac{C_i(r+\Delta r,z)-C_i(r,z)}{\Delta r^2}\end{aligned} \tag{4.65}$$

where the finite difference approximation of boundary condition 1 (Equation 4.60),

$$\left.\frac{\partial C_i}{\partial r}\right|_{r=0} \approx \frac{C_i(r+\Delta r,z)-C_i(r-\Delta r,z)}{2\Delta r} = 0 \tag{4.66}$$

is used to eliminate the fictitious value $C_i(r\text{-}\Delta r,z)$. The concentration at the wall is found by applying the zero flux boundary condition 2 (Equation 4.61) as well as a second order, forward difference approximation for the first derivative at $r = R_t$:

$$C_i(R_t,z) = \frac{4C_i(I-1,z)-C_i(I-2,z)}{3} \tag{4.67}$$

At $r = 0$, the first derivative radial group in Equation 4.59 is indeterminant,

$$\left.\frac{1}{r}\frac{\partial C_i}{\partial r}\right|_{r=0} = \frac{0}{0} \tag{4.68}$$

as a consequence of boundary condition 1 (Equation 4.60). L'Hospitals rule is applied to regularize this indeterminant form:

$$\lim_{r\to 0}\left(\frac{1}{r}\frac{\partial C_i}{\partial r}\right) = \left(\frac{\partial^2 C}{\partial r^2}\right)_{r=0} \tag{4.69}$$

This second derivative iss given by Equation 4.65. In practice, the concentrations at the interior points $1 \rightarrow I$ - 1 are solved for using the discretized PDE's in z and the concentrations at the wall are given by Equation 4.67. The value of D_{im} in Equation 4.59 is also updated as the solution progresses.

The mixed-cup or average concentration of species i at a particular cross-section of the reactor tube is then calculated according to (Hsu, 1965; Dang and Steinberg, 1977; Nauman, 2002; Shiesser and Griffiths, 2009):

$$\bar{C}_i(r,z) = \frac{\int_0^{R_t} 2\pi r C_i(r,z) v_z dr}{\int_0^{R_t} 2\pi r v_z dr} \tag{4.70}$$

where the radial integration is performed using the trapezoidal rule.

4.1.5.3. Kinetic model identification

The individual rates for the reaction scheme presented in Table 4.14 (cf. section 4.1.5.1) were initially assumed to be given by:

$$r_1^+ = k_1^+ C_{HFP} C_{O_2} \tag{4.71}$$

$$r_1^- = k_1^- C_{HFPO} \tag{4.72}$$

$$r_2 = k_2 C_{HFP} C_{O_2} \tag{4.73}$$

$$r_3 = k_3 C_{HFPO} \tag{4.74}$$

$$r_4 = k_4 C_{CF_2}^2 \tag{4.75}$$

$$r_5 = k_5 C_{C_2F_4} C_{CF_2} \tag{4.76}$$

$$r_6 = k_6 C_{C_2F_4} C_{O_2} \tag{4.77}$$

$$r_{7b} = k_{7b} C_{CF_3COF} C_{O_2} \tag{4.78}$$

Note that only reaction 1 was considered to be practically reversible. The net rate of change due to reaction of the individual species involved in the oxidation of HFP, represented by R_i in the expression developed in section 4.1.5.2 for the species continuity, were constructed based on the same kinetic scheme:

$$R_{HFP} = -k_1^+ C_{HFP} C_{O_2} - k_2 C_{HFP} C_{O_2} + k_1^- C_{HFPO} \tag{4.79}$$

$$R_{O_2} = -0.5k_1^+ C_{HFP} C_{O_2} - k_2 C_{HFP} C_{O_2} - 0.5k_6 C_{C_2F_4} C_{O_2} - 0.5k_{7b} C_{CF_3COF} C_{O_2} + 0.5k_1^- C_{HFPO} \tag{4.80}$$

$$R_{HFPO} = k_1^+ C_{HFP} C_{O_2} - k_3 C_{HFPO} - k_1^- C_{HFPO} \tag{4.81}$$

$$R_{CF_3COF} = k_2 C_{HFP} C_{O_2} + k_3 C_{HFPO} - k_{7b} C_{CF_3COF} C_{O_2} \tag{4.82}$$

$$R_{CF_2} = k_3 C_{HFPO} - 2k_4 C_{CF_2}^2 - k_5 C_{C_2F_4} C_{CF_2} + k_6 C_{C_2F_4} C_{O_2} \tag{4.83}$$

$$R_{COF_2} = k_2 C_{HFP} C_{O_2} + k_6 C_{C_2F_4} C_{O_2} + 2k_{7b} C_{CF_3COF} C_{O_2} \tag{4.84}$$

$$R_{C_2F_4} = k_4 C_{CF_2}^2 - k_5 C_{C_2F_4} C_{CF_2} - k_6 C_{C_2F_4} C_{O_2} \tag{4.85}$$

$$R_{c-C_3F_6} = k_5 C_{C_2F_4} C_{CF_2} \tag{4.86}$$

The temperature dependence of the estimated rate constants was given by the Arrhenius expression:

$$k_j = A_j \exp\left(-\frac{E_{a_j}}{RT}\right) \tag{4.87}$$

where A_j is the pre-exponential factor and E_{a_j} is the activation energy for reaction j. The kinetic parameters appearing in the rate equations for reactions 1, 2, 6 and 7 (cf. Table 4.14) were indentified using the procedures delineated in this section. Kinetic data for reactions 3, 4 and 5 were taken from the literature. For the thermal decomposition of HFPO (reaction 3) the values reported by Krusic et al. (1999) were used. Kinetic data for reactions 4 and 5 were taken from Tyerman (1968) who reviewed and extended the work of Dalby (1964).

Kinetic parameters were obtained through a weighted-least-squares fit of the experimental data to the reaction model. The objective function was defined as:

$$S(\mathbf{b}) = \sum_{i=1}^{n_E}\sum_{k=1}^{n_D}\left[w_{ik}(y_{ik} - g_{ik}(\mathbf{x_i}, \mathbf{b}))\right]^2 \tag{4.88}$$

where w_{ik} is the weighting factor of the k-th dependent variable in the i-th experiment, y_{ik} is the measured value of the k-th dependent variable in the i-th experiment and g_{ik} is the k-th dependent variable in the i-th experiment predicted by the model, based on the vector of independent variables $\mathbf{x_i}$ and the parameter estimates $\mathbf{b}$. There are a total of n_E experiments and n_D dependent variables. In the current context the dependent variables were the exit concentrations of all the species and the independent variables were the reaction temperature, pressure, inlet concentrations and space time.

The identification algorithm is presented as a flow diagram in Figure 4.45. All computational procedures were programmed using MATLAB® (version R2007b, The Mathworks, Inc.) and implemented on a Hewlet Packard machine equipped with a 2.4 GHz Intel Core i5 processor and 4.0 GB RAM. The MATLAB® script files are presented in Appendix H. The calculation was initialized by providing first estimates of the kinetic parameters and reading in the measured independent and dependent variables. Integration of the system of ODE's, developed in section 4.1.5.2 from the original set of PDE's describing the component material balances, was then performed using the MATLAB® function `ode15s`. This ODE solver is a quasi-constant step size

implementation of the numerical differentiation formulas of Klopfenstein (1971) and Reiher (1978), in terms of implicit backward differences. It is particularly useful for stiff problems.

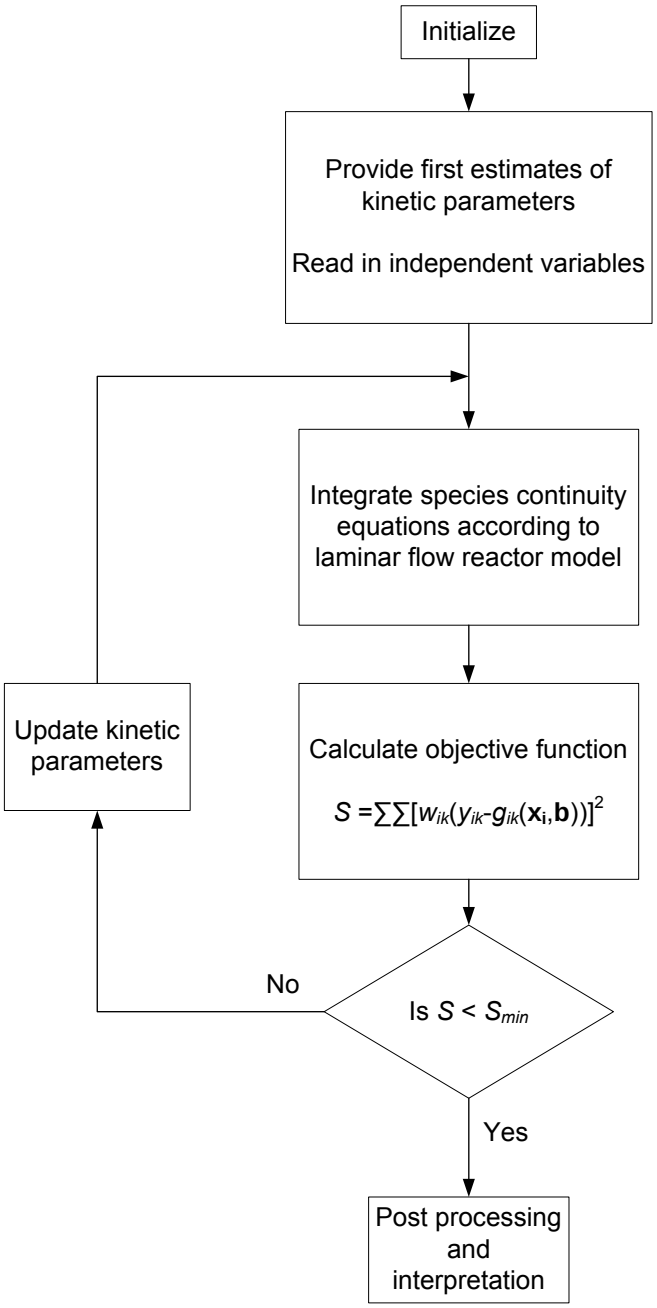

Figure 4.45. A flow diagram of the computational algorithm for kinetic parameter identification.

The objective function was calculated based on the measured and predicted exit concentrations and the appropriate weighting. The optimization was terminated if a predetermined tolerance on the objective function was met, otherwise the kinetic parameters were updated according to the chosen domain-searching-algorithm for the next iteration. The built-in MATLAB® function `lsqnonlin` was selected as the optimization algorithm. It is a subspace trust region method based on the interior-reflective Newton method described by Coleman and Li (1996). It also provides information for the calculation of confidence limits on the estimated parameters.

When computing values for the kinetic parameters by minimizing the sum of squares of residuals between predicted and experimental values, it was essential that the squares of the residuals be normalized by multiplying each by a suitable weighting factor, otherwise the concentrations with the largest numerical values would have a disproportionate weight in the objective function (Ottaway, 1971). If replicate observations were available, the best normalizing factor would have been $1/\sigma_{ik}$ where σ_{ik}^2 is the variance of the *k*-th dependent variable in the *i*-th experiment. However, due to the difficult nature of the experiments, replicate data were not readily available and the use of other normalizing factors had to be explored.

It was initially suggested that an estimated variance of the measured exit concentration data could be obtained from the gas-chromatograph calibration data for each component. The proposed method involved two transformations for each measured data point, shown in Figure 4.46. First the number of moles of component *k* (n_k) calculated using the gas-chromatograph calibration function (cf. Appendix C) and the measured peak area, is plotted against the actual injected number of moles of component *k* ($n_{k,s}$) for multiple determinations. A transformation to concentration is performed for each experimental point *i* using:

$$C_{ik} = \frac{n_k RT_{sample,i}}{P_{sample,i} V_{sample,i}} \times \frac{P_i}{RT_i} \tag{4.89}$$

and

$$C_{ik,s} = \frac{n_{k,s} RT_{sample,i}}{P_{sample,i} V_{sample,i}} \times \frac{P_i}{RT_i} \tag{4.90}$$

where C_{ik} is the calculated concentration of the k-th component in the i-th experiment based on the gas-chromatographic measurements, $C_{ik,s}$ is the actual concentration of the k-th component in the i-th experiment, $P_{sample,i}$, $T_{sample,i}$ and $V_{sample,i}$ are the sample pressure, temperature and volume, respectively, and P_i and T_i are the reactor exit pressure and temperature, respectively.

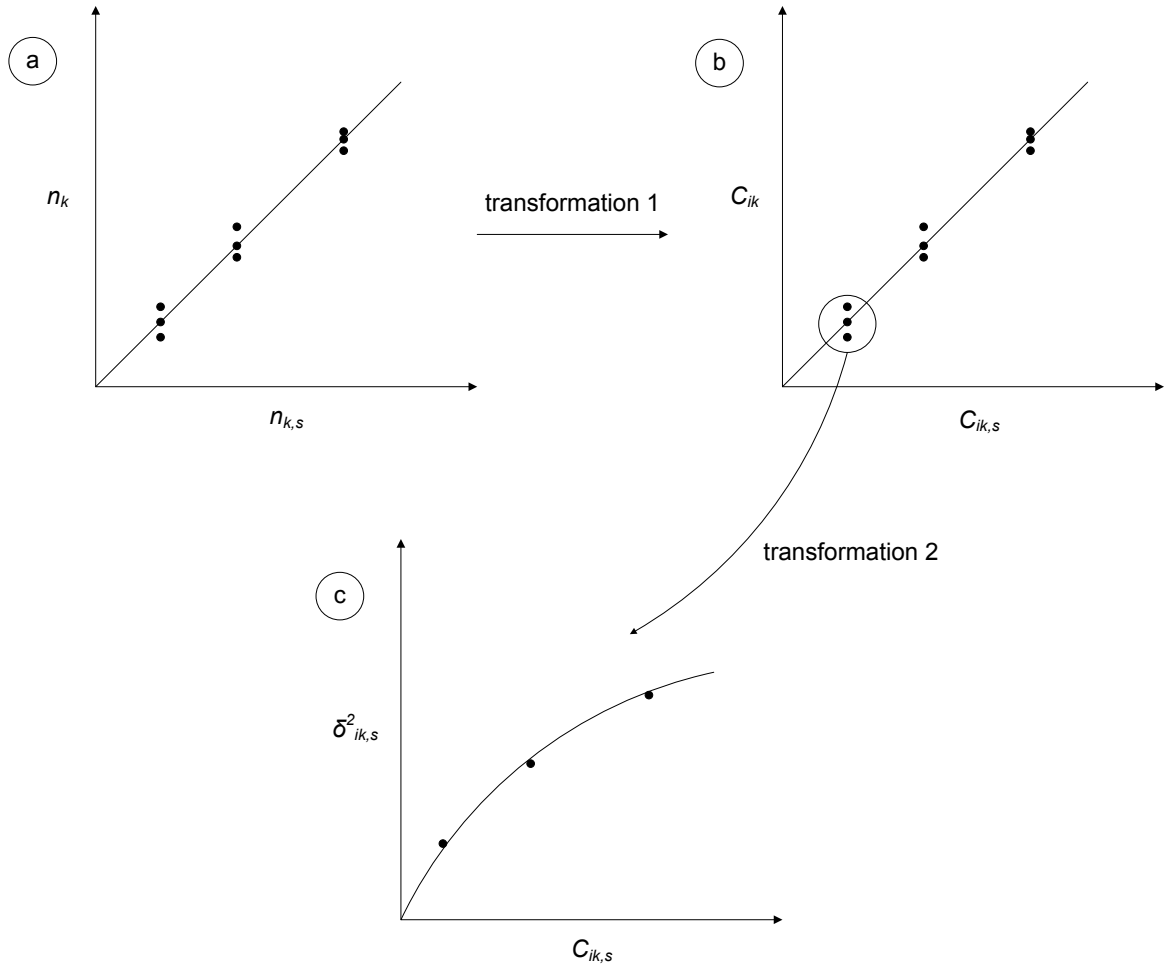

Figure 4.46. Estimation of the local variance of the observed exit concentrations based on gas-chromatograph calibration data.

In the second transformation, a variance is estimated for each group of points corresponding to $C_{ik,s}$ according to:

$$\sigma^2_{ik,s} = \frac{\sum\left(C_{ik} - \bar{C}_{ik}\right)^2}{N-1} \tag{4.91}$$

where N is the number of replicate injections made for one gas-chromatograph calibration data point. This variance is then plotted against $C_{ik,s}$. In practice, the local variance of the observed exit concentrations required for normalization could be obtained from a curve similar to that presented in Figure 4.46 c, where $C_{ik,s}$ then represents the measured concentration of the species.

Figures 4.47 and 4.48 show the estimated variance versus the measured exit concentration plots for HFP and O_2, respectively, for a selected experimental data point, generated using the aforementioned method. No satisfactory correlation between the estimated variance and the measured exit concentration could be found, possibly because of the small number of replicates available (typically between 3 and 5). This method was subsequently abandoned.

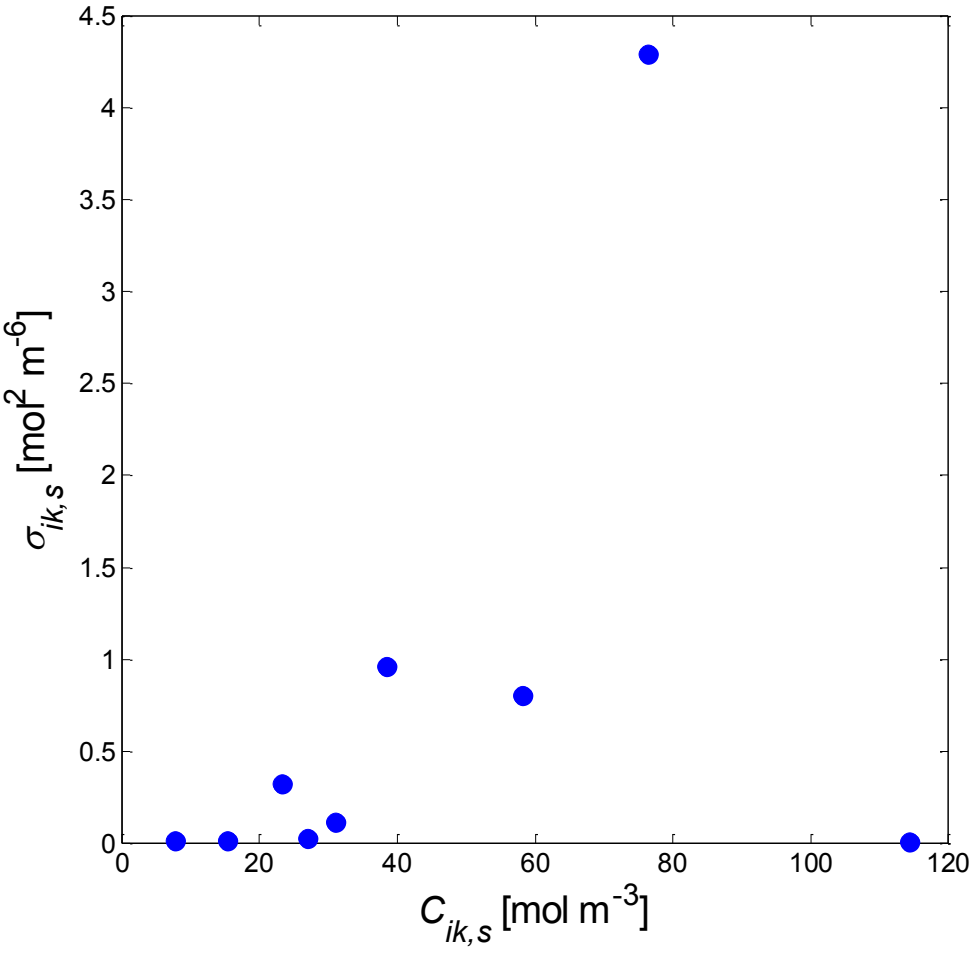

Figure 4.47. Estimated variance versus measured exit concentration plot at one experimental point for HFP.

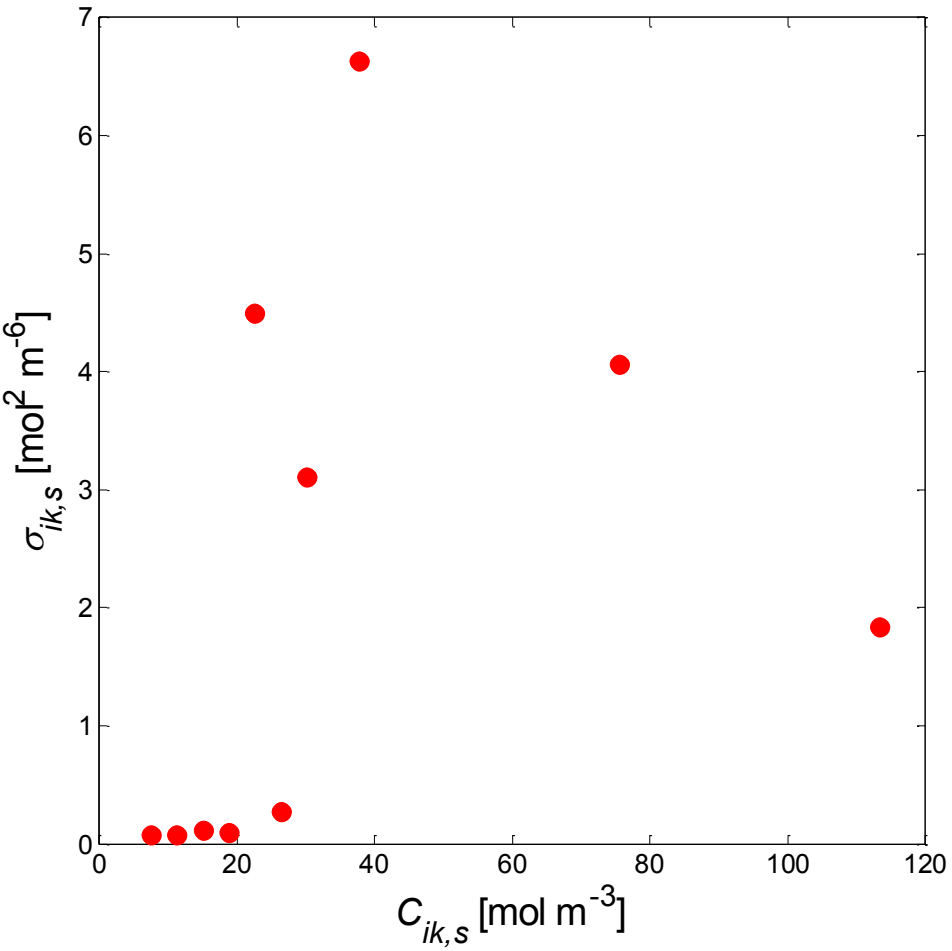

Figure 4.48. Estimated variance versus measured exit concentration plot at one experimental point for O_2

Another proposed method involved substituting the local variance with an estimated measurement error, based on the statistical laws of error propagation (Bevinton and Robinson, 2002). If a function $f(x,y)$ is composed only of multiplication and division operations involving the measured variables x and y, and the errors of the individual measurements are small and independent, then it has been shown that the uncertainty in f is given by (Bevinton and Robinson, 2002):

$$\sigma_f = |f| \times \sqrt{\left(\frac{\sigma_x}{x}\right)^2 + \left(\frac{\sigma_y}{y}\right)^2} \tag{4.92}$$

The reactor exit concentration of each component was given by:

$$C_k = \frac{n_{k,sample}}{n_{tot,sample}} \times C_{tot} \tag{4.93}$$

the total number of moles of the sample injected into the gas-chromatograph by:

$$n_{tot,sample} = \frac{P_{sample} V_{sample}}{RT_{sample}} \tag{4.94}$$

and the total concentration of the reactor product gas by:

$$C_{tot} = \frac{P_{reactor}}{RT_{reactor}} \tag{4.95}$$

P_{sample}, V_{sample} and T_{sample} refer to the analytical sample conditions, $P_{reactor}$ and $T_{reactor}$ refer to the reactor exit conditions and $n_{k,sample}$ is obtained from the peak area for component k on the G.C. chromatogram. Accordingly:

$$\sigma_{n_{tot,sample}} = \left| n_{tot,sample} \right| \times \sqrt{\left(\frac{\sigma_{P_{sample}}}{P_{sample}} \right)^2 + \left(\frac{\sigma_{V_{sample}}}{V_{sample}} \right)^2 + \left(\frac{\sigma_{T_{sample}}}{T_{sample}} \right)^2} \tag{4.96}$$

$$\sigma_{C_{tot}} = \left| C_{tot} \right| \times \sqrt{\left(\frac{\sigma_{P_{reactor}}}{P_{reactor}} \right)^2 + \left(\frac{\sigma_{T_{reactor}}}{T_{reactor}} \right)^2} \tag{4.97}$$

$$\sigma_{C_k} = \left| C_k \right| \times \sqrt{\left(\frac{\sigma_{n_{k,sample}}}{n_{k,sample}} \right)^2 + \left(\frac{\sigma_{n_{Tot,sample}}}{n_{Tot,sample}} \right)^2 + \left(\frac{\sigma_{C_{Tot}}}{C_{Tot}} \right)^2} \tag{4.98}$$

The identification algorithm failed to converge to a satisfactory solution using these artificial weights and this method was also abandoned.

A series of alternative normalizing factors obtained from the literature were tested (Reich et al., 1972; Ottaway, 1973). These are presented in Table 4.21.

Table 4.21. Choice of weighting factors for normalization of the objective function.

	w_{ik}	Principle
1	$\frac{1}{y_{ik}}$	Minimum relative error based on the measured value
2	$\frac{1}{g_{ik}}$	Minimum relative error based on the predicted value
3	$\frac{2}{\left(y_{ik}+g_{ik}\right)}$	Mean of the measured and predicted value

The use of expression 1 in Table 4.21 led to a systematic bias towards small measured values. The opposite was true of expression 2. Only expression 3, the mean of the experimental and calculated values, was found to be an acceptable normalizing factor, providing a satisfactory neutral weighting between large and small measurement values.

The value of A_j is usually much larger than E_{a_j} and these parameters exhibit a very strong, non-linear correlation when fitted to experimental data, i.e. the value of one parameter is strongly dependent on the other (Wojciechowski and Rice, 2003). Poor initial estimates can easily lead to the least-squares solution sinking into a local minimum, which may lie far from the global minimum and the true parameter values. A reliable procedure for finding good starting estimates is to begin by making a series of isothermal fits, estimating the value of k_j at each fixed temperature. Then, for each reaction, the fitted rate constants and the corresponding temperatures are used to form Arrhenius plots of ln$k$ versus $1/T$ (Wojciechowski and Rice, 2003). The gradients and intercepts of these plots yield initial values for the activation energies and pre-exponential factors, respectively, required for a general non-linear least-squares fitting of the total data set.

For the series of isothermal fits, a multi-start technique was employed, providing a random set of initial estimates in each instance and selecting from amongst these the best output solution. It was promptly realized that the reaction orders for the individual species given in Equations 4.71 to 4.78 did not provide the best fit to the experimental data. For reactions 3, 4 and 5 no adjustments could

be made since these were taken directly from the literature. In order to keep the number of fitting parameters to a minimum, it was decided to manually vary the rest of the reaction orders in a systematic manner and observe the effect on the solution. The best fit to the measured data was obtained with the following individual rates for the forward steps of reactions 1 and 7b:

$$r_1^+ = k_1^+ C_{HFP}^2 C_{O_2} \tag{4.99}$$

$$r_{7b} = k_{7b} C_{CF_3COF} C_{O_2}^{0.5} \tag{4.100}$$

Accordingly, the net rate of change due to reaction of the individual species was given by:

$$R_{HFP} = -k_1^+ C_{HFP}^2 C_{O_2} - k_2 C_{HFP} C_{O_2} + k_1^- C_{HFPO} \tag{4.101}$$

$$R_{O_2} = -0.5k_1^+ C_{HFP}^2 C_{O_2} - k_2 C_{HFP} C_{O_2} - 0.5k_6 C_{C_2F_4} C_{O_2} - 0.5k_{7b} C_{CF_3COF} C_{O_2}^{0.5} + 0.5k_1^- C_{HFPO} \tag{4.102}$$

$$R_{HFPO} = k_1^+ C_{HFP}^2 C_{O_2} - k_3 C_{HFPO} - k_1^- C_{HFPO} \tag{4.103}$$

$$R_{CF_3COF} = k_2 C_{HFP} C_{O_2} + k_3 C_{HFPO} - k_{7b} C_{CF_3COF} C_{O_2}^{0.5} \tag{4.104}$$

$$R_{CF_2} = k_3 C_{HFPO} - 2k_4 C_{CF_2}^2 - k_5 C_{C_2F_4} C_{CF_2} + k_6 C_{C_2F_4} C_{O_2} \tag{4.105}$$

$$R_{COF_2} = k_2 C_{HFP} C_{O_2} + k_6 C_{C_2F_4} C_{O_2} + 2k_{7b} C_{CF_3COF} C_{O_2}^{0.5} \tag{4.106}$$

$$R_{C_2F_4} = k_4 C_{CF_2}^2 - k_5 C_{C_2F_4} C_{CF_2} - k_6 C_{C_2F_4} C_{O_2} \tag{4.107}$$

$$R_{c\text{–}C_3F_6} = k_5 C_{C_2F_4} C_{CF_2} \tag{4.108}$$

Table 4.22 gives the estimated rate constants and 95% confidence intervals for reactions 1, 2, 6 and 7b, obtained from the minimization. Figures 4.49 to 4.51 show parity and residual plots for each of the species, based on the estimated rate constants, at each of the three temperatures investigated.

Table 4.22. Estimated rate constants and 95% confidence intervals for the gas-phase oxidation of HFP, obtained using the laminar flow reactor model.

Parameter	Units	Temperature		
		463 K	**478 K**	**493 K**
k_1^+	$\left(\mathrm{m^3/mol}\right)^2 \mathrm{s^{-1}}$	$3.81\times10^{-6} \pm 1.72\times10^{-7}$	$3.51\times10^{-5} \pm 1.42\times10^{-6}$	$9.85\times10^{-4} \pm 2.43\times10^{-5}$
k_1^-	$\mathrm{s^{-1}}$	$3.55\times10^{-2} \pm 5.1\times10^{-3}$	$1.83\times10^{-2} \pm 8.01\times10^{-3}$	$4.66\times10^{-3} \pm 9.12\times10^{-4}$
k_2	$\mathrm{m^3\ mol^{-1}\ s^{-1}}$	$1.17\times10^{-5} \pm 8.04\times10^{-6}$	$1.67\times10^{-4} \pm 7.29\times10^{-5}$	$1.69\times10^{-2} \pm 7.11\times10^{-3}$
k_6	$\mathrm{m^3\ mol^{-1}\ s^{-1}}$	$9.57\times10^{-3} \pm 1.96\times10^{-3}$	$1.64\times10^{-2} \pm 8.05\times10^{-3}$	$2.21\times10^{-2} \pm 8.74\times10^{-3}$
k_{7b}	$\left(\mathrm{m^3/mol}\right)^{1/2} \mathrm{s^{-1}}$	$1.01\times10^{-2} \pm 7.94\times10^{-3}$	$2.21\times10^{-3} \pm 1.20\times10^{-3}$	$1.73\times10^{-3} \pm 8.58\times10^{-4}$

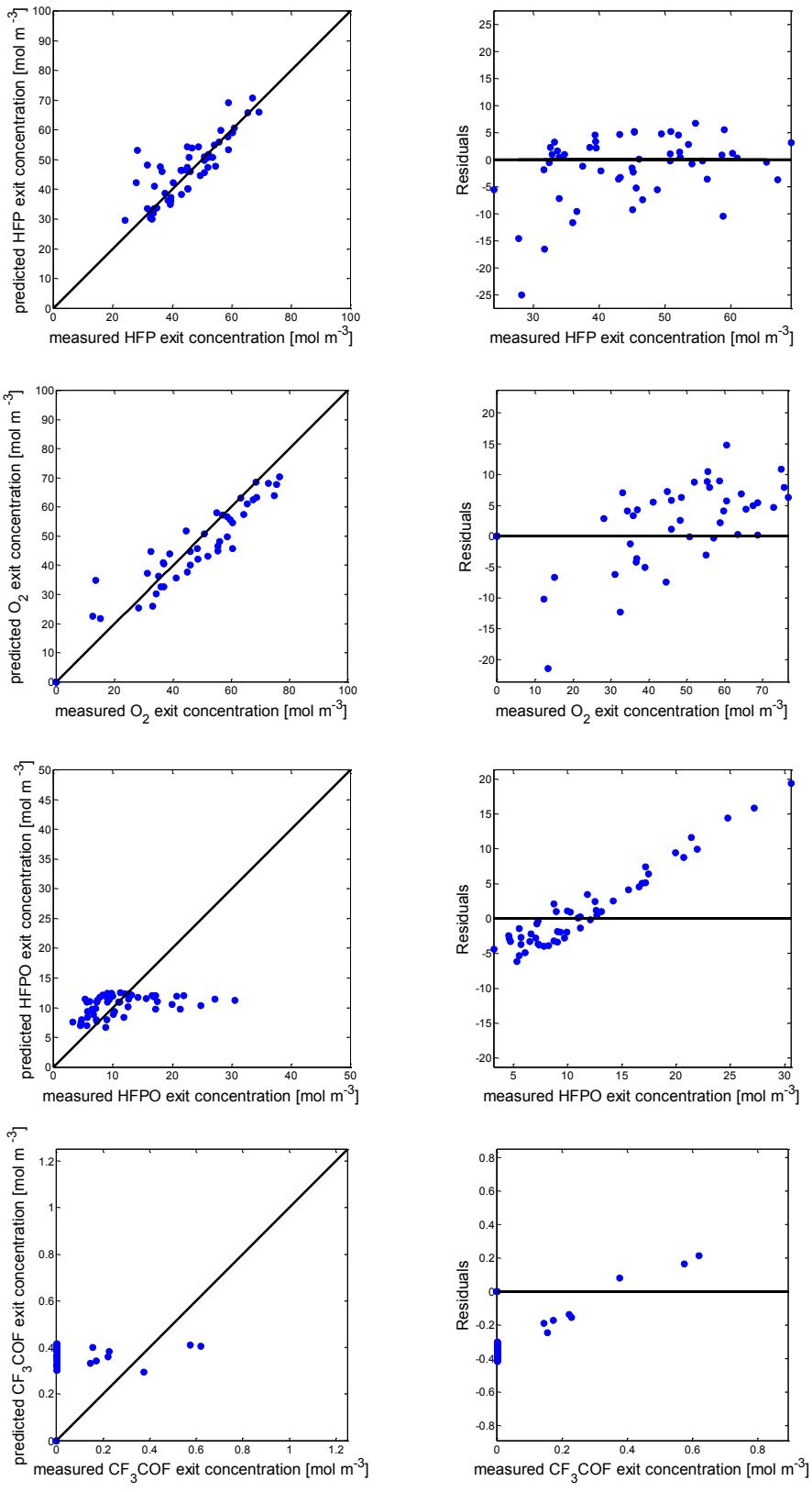

Figure 4.49. Parity and residual plots for individual species at 463 K (Laminar flow reactor model). Residual defined as the difference between measured and predicted values.

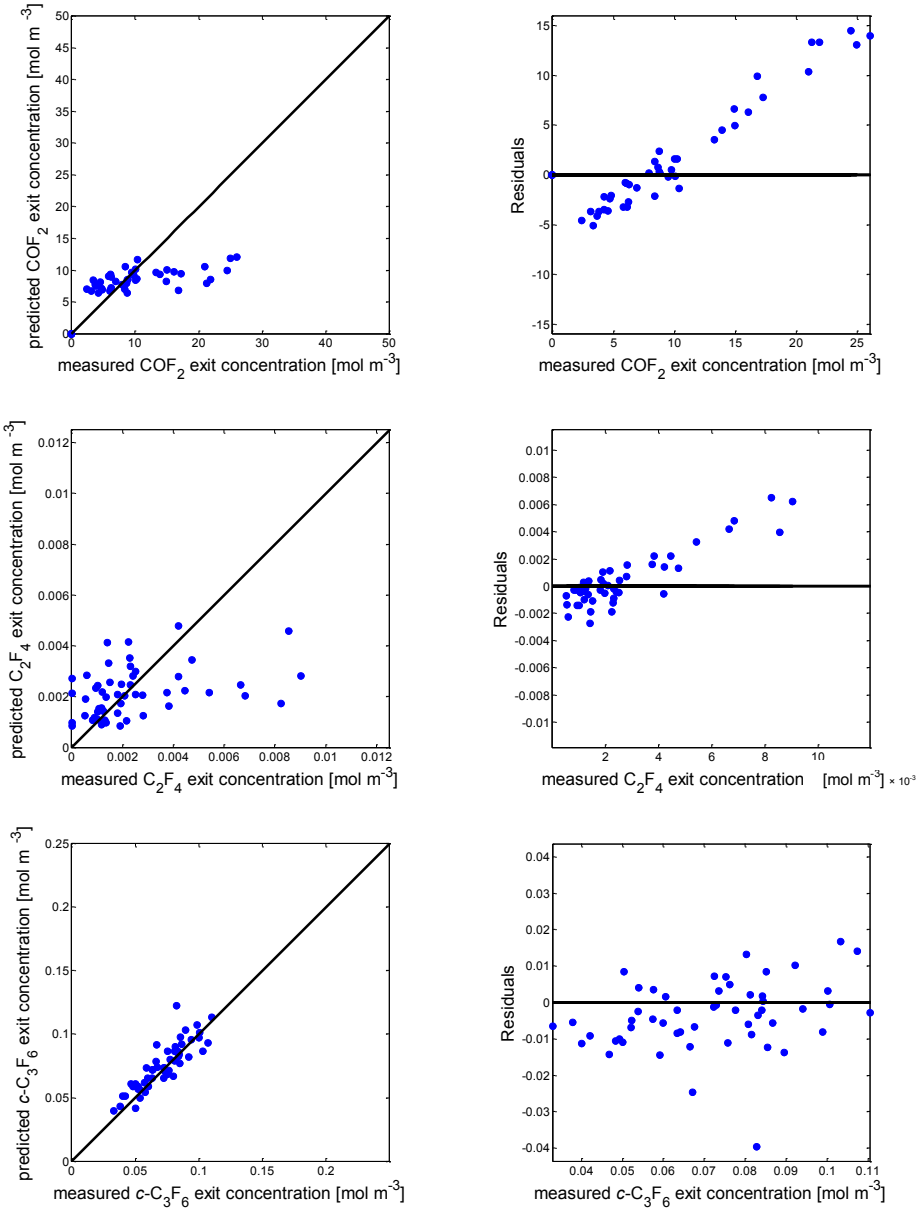

Figure 4.49. (*continued*).

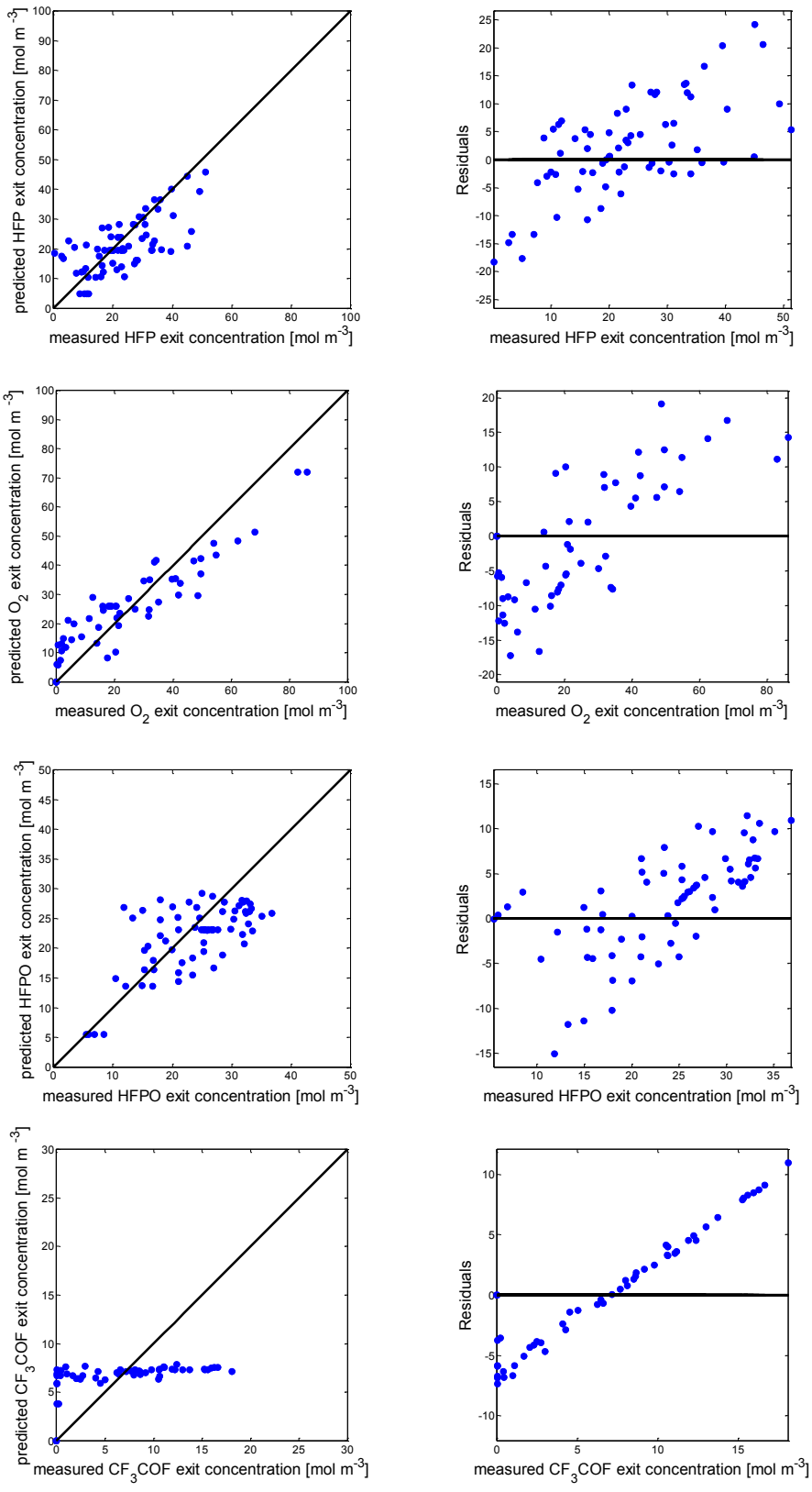

Figure 4.50. Parity and residual plots for individual species at 478 K (Laminar flow reactor model). Residuals defined as the difference between measured and predicted values.

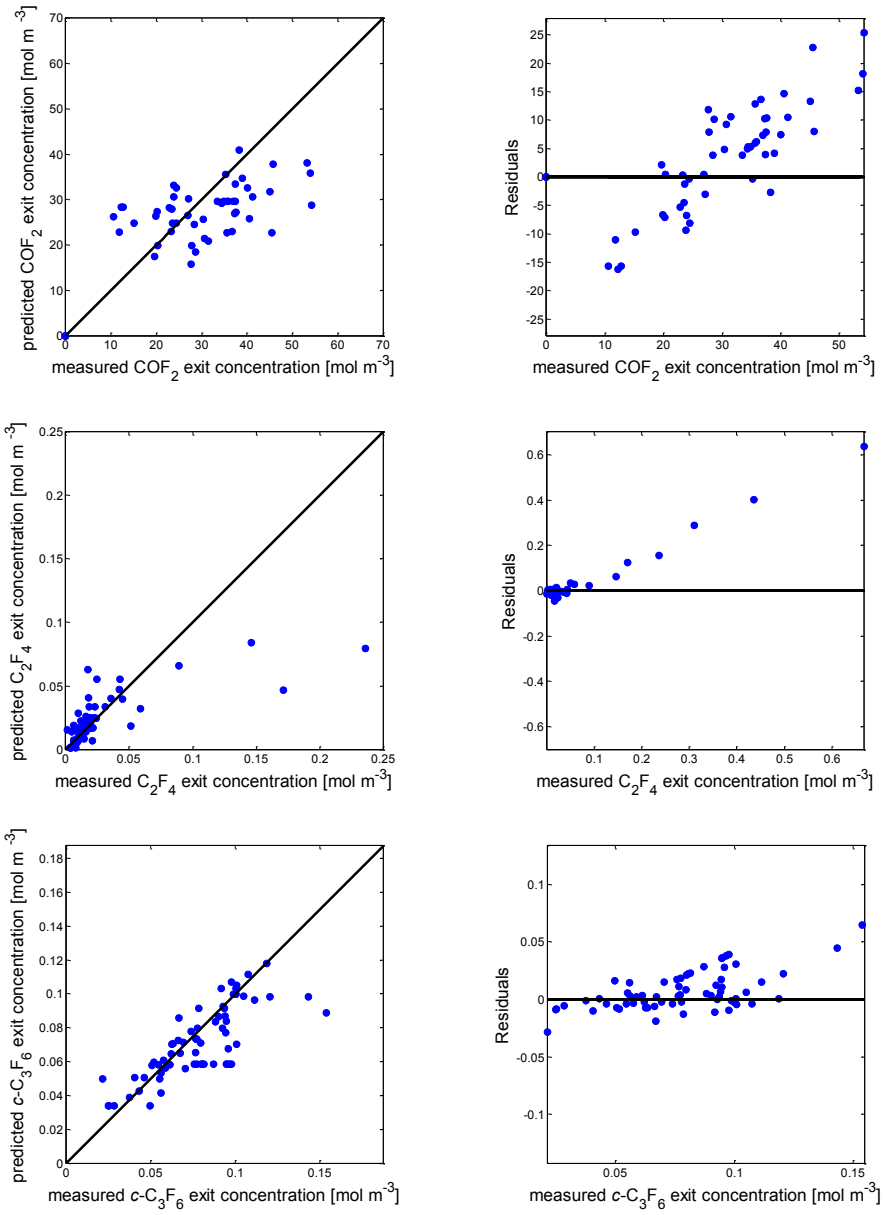

Figure 4.50. (*continued*).

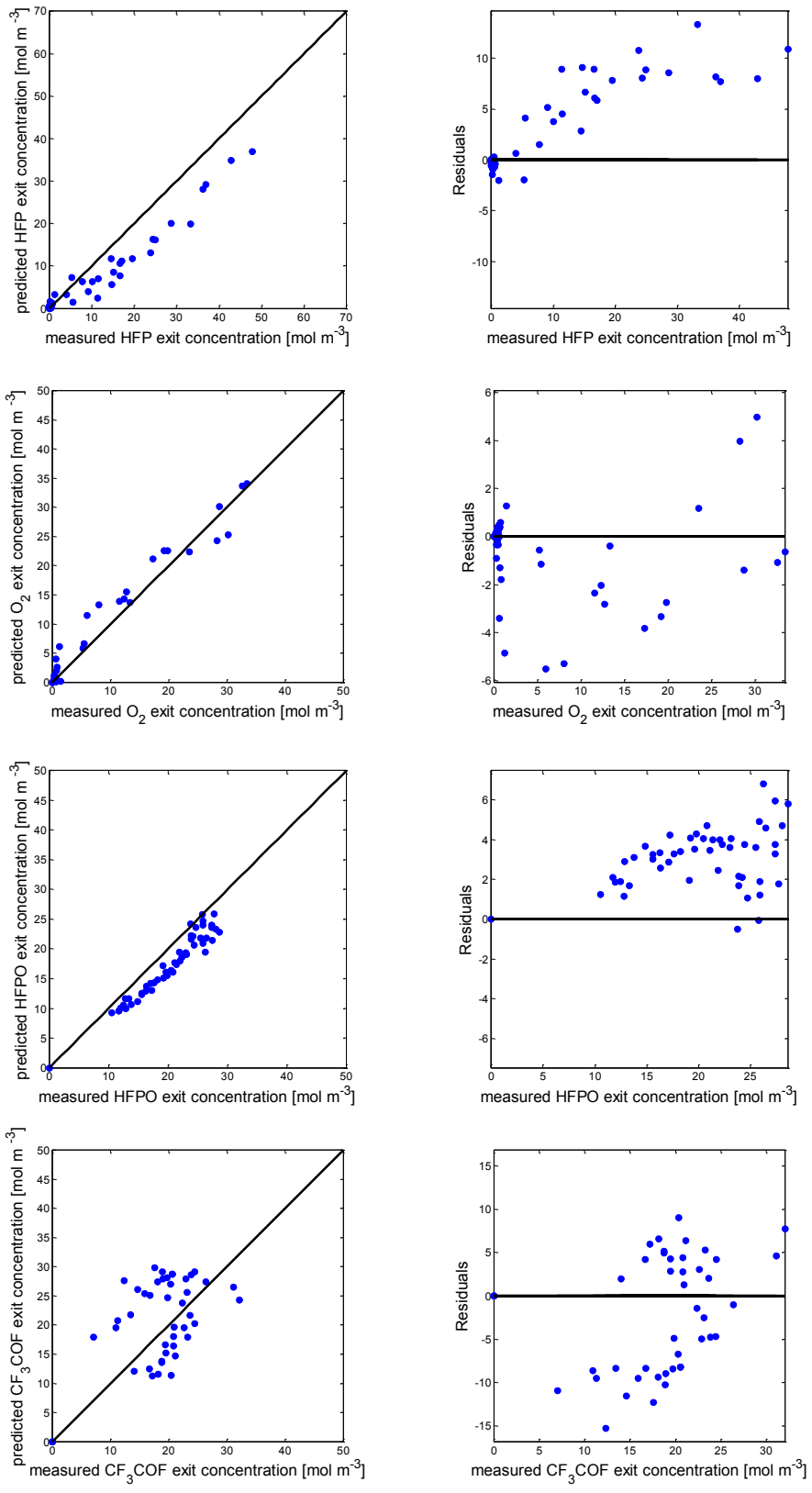

Figure 4.51. Parity and residual plots for individual species at 493 K (Laminar flow reactor model). Residuals defined as the difference between measured and predicted values.

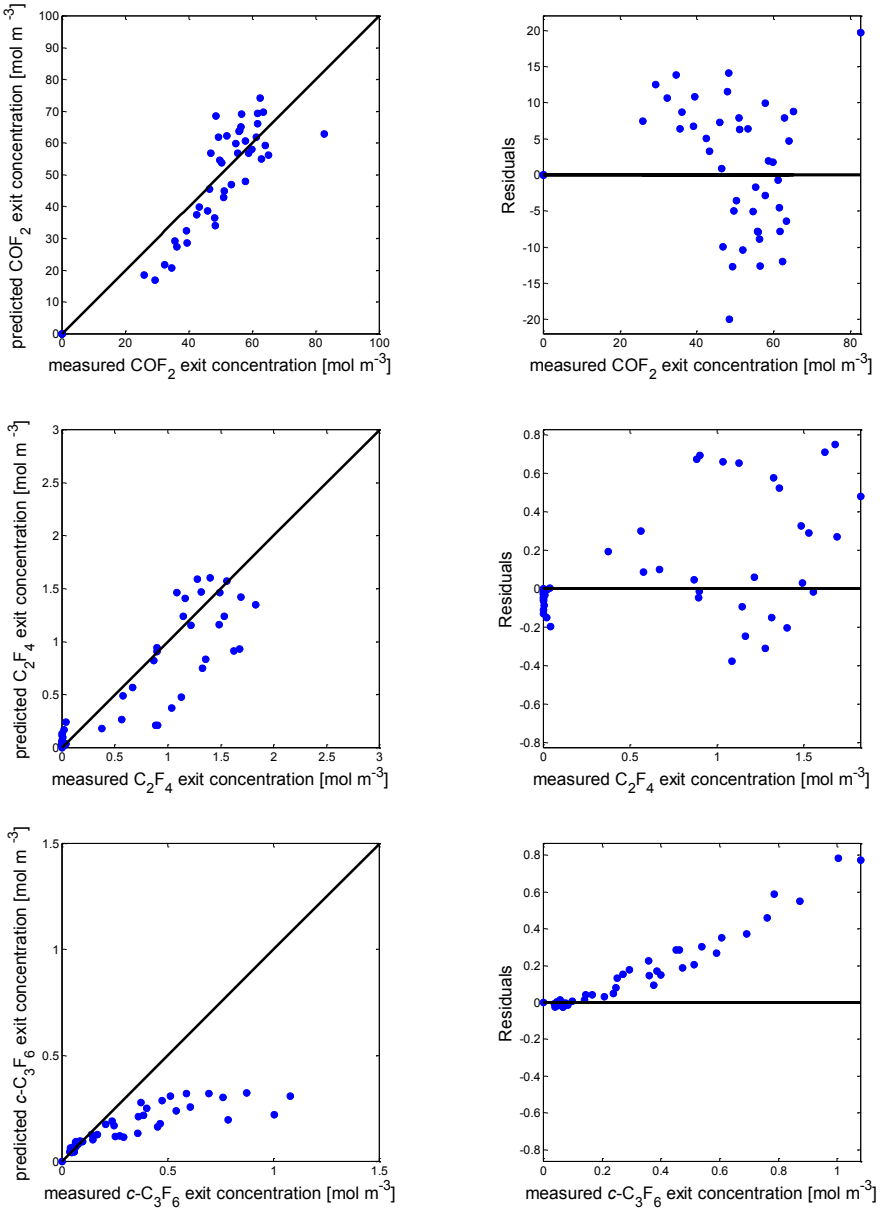

Figure 4.51. (*continued*)

The isothermal data were used to prepare the Arrhenius plots presented in Figures 4.52 to 4.56. The starting estimates for the activation energies and pre-exponential factors obtained from each of the Arrhenius plots, and required for the total data fit, are given in Table 4.23.

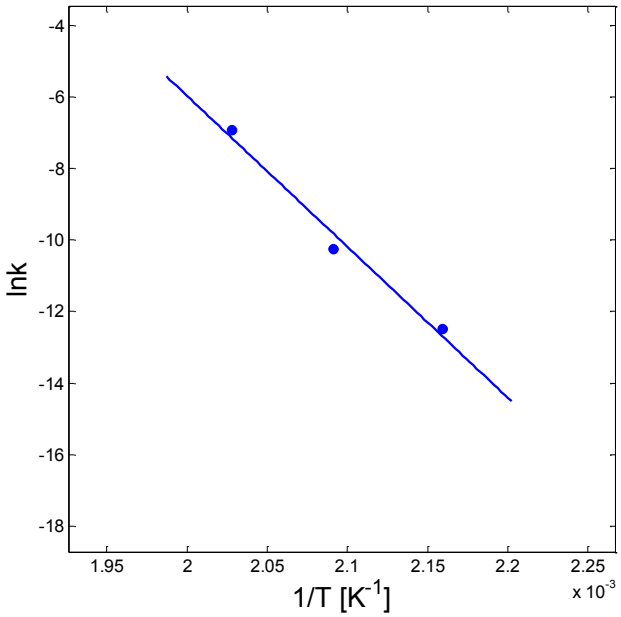

Figure 4.52. Arrhenius plot for reaction 1 (forward), based on isothermal data.

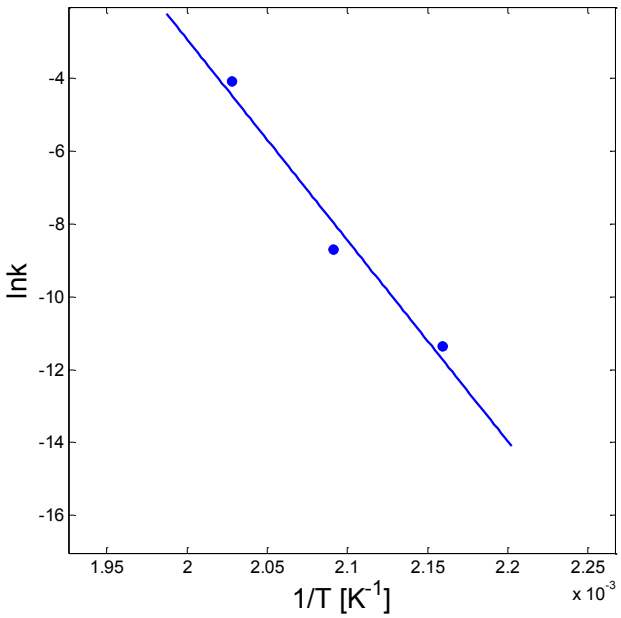

Figure 4.53. Arrhenius plot for reaction 2, based on isothermal data.

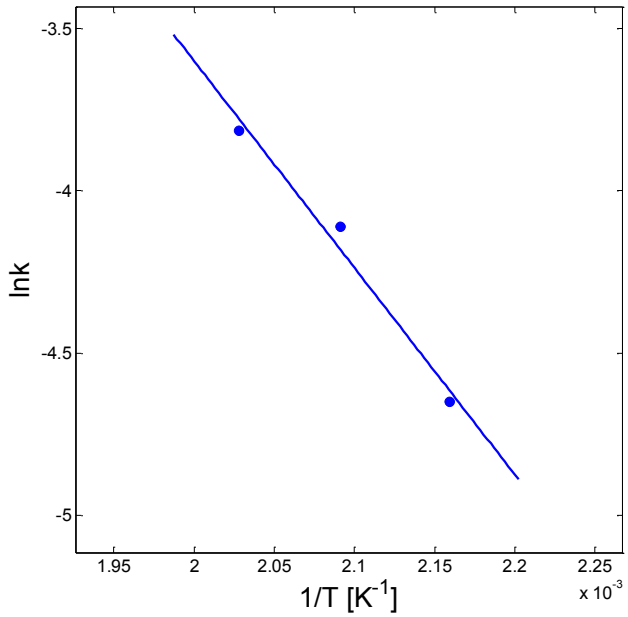

Figure 4.54. Arrhenius plot for reaction 6, based on isothermal data.

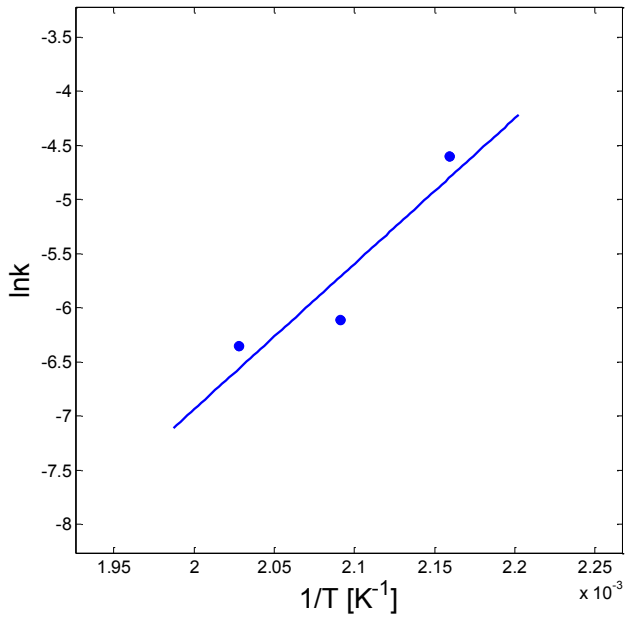

Figure 4.55. Arrhenius plot for reaction 7b, based on isothermal data.

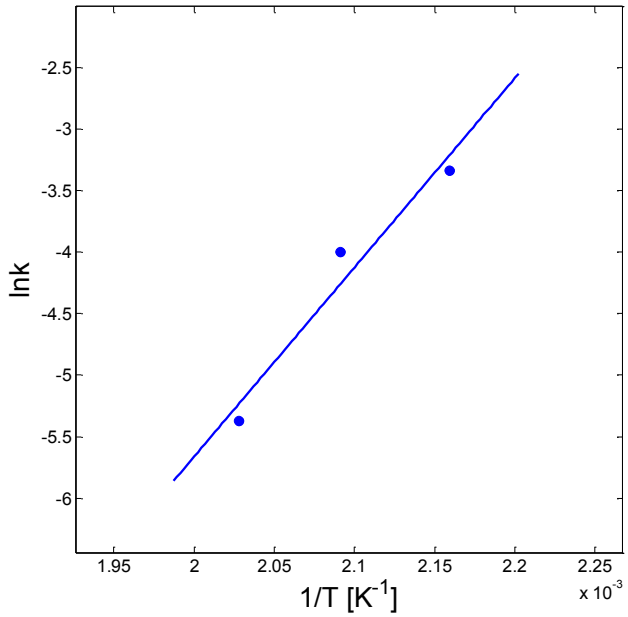

Figure 4.56. Arrhenius plot for reaction 1 (reverse), based on isothermal data.

Table 4.23. Initial kinetic parameter estimates obtained from Arrhenius plots.

Reaction	**Pre-exponential factor[a]**	**Activation energy [kJ mol^{-1}]**
1 (forward)	1.483×10^{34}	350.84
2	5.435×10^{46}	459.47
6	9.305×10^{3}	52.95
7b	2.075×10^{-15}	-111.70
1 (reverse)	1.475×10^{-16}	-127.99

[a] Units for the pre-exponential factors are the same as those given in Table 4.22.

For all temperatures, there was a satisfactory fit of the measured data and distribution of residuals for HFP, O_2, HFPO and COF_2. Less satisfactory fits were obtained for the other oxidation products, particularly CF_3COF and *c*-C_3F_6. An anomalous temperature dependence of the rate constants for reaction 7b and reverse reaction 1 were obtained, i.e. the rate decreased with increasing temperature. It was difficult to offer a theoretical interpretation for a negative activation energy.

The disparity in the numerical values of the activation energy and the pre-exponential factors can still lead to a poor fit even if good starting estimates are available, unless some form of internal scaling of parameters is used. A simple scaling procedure that reduces the correlation and the non-linearity of the correlation between A_j and E_{a_j} involves temperature centring along some temperature T_0 that lies in the middle of the investigated range (Wojciechowski and Rice, 2003). The Arrhenius expression is re-written as:

$$k_j = k_j^0 \exp\left[-\frac{E_{a_j}}{R}\left(\frac{1}{T}-\frac{1}{T_0}\right)\right] \tag{4.109}$$

where

$$k_j^0 = A_j \exp\left(-\frac{E_{a_j}}{RT_0}\right) \tag{4.110}$$

The fitting procedure is used to identify parameters k_j^0 and E_{a_j}, after which A_j is obtained using Equation 4.110. The final parameter estimates obtained using this method are given in Table 4.24. Figure 4.57 shows the parity and residual plots for all species at all data points.

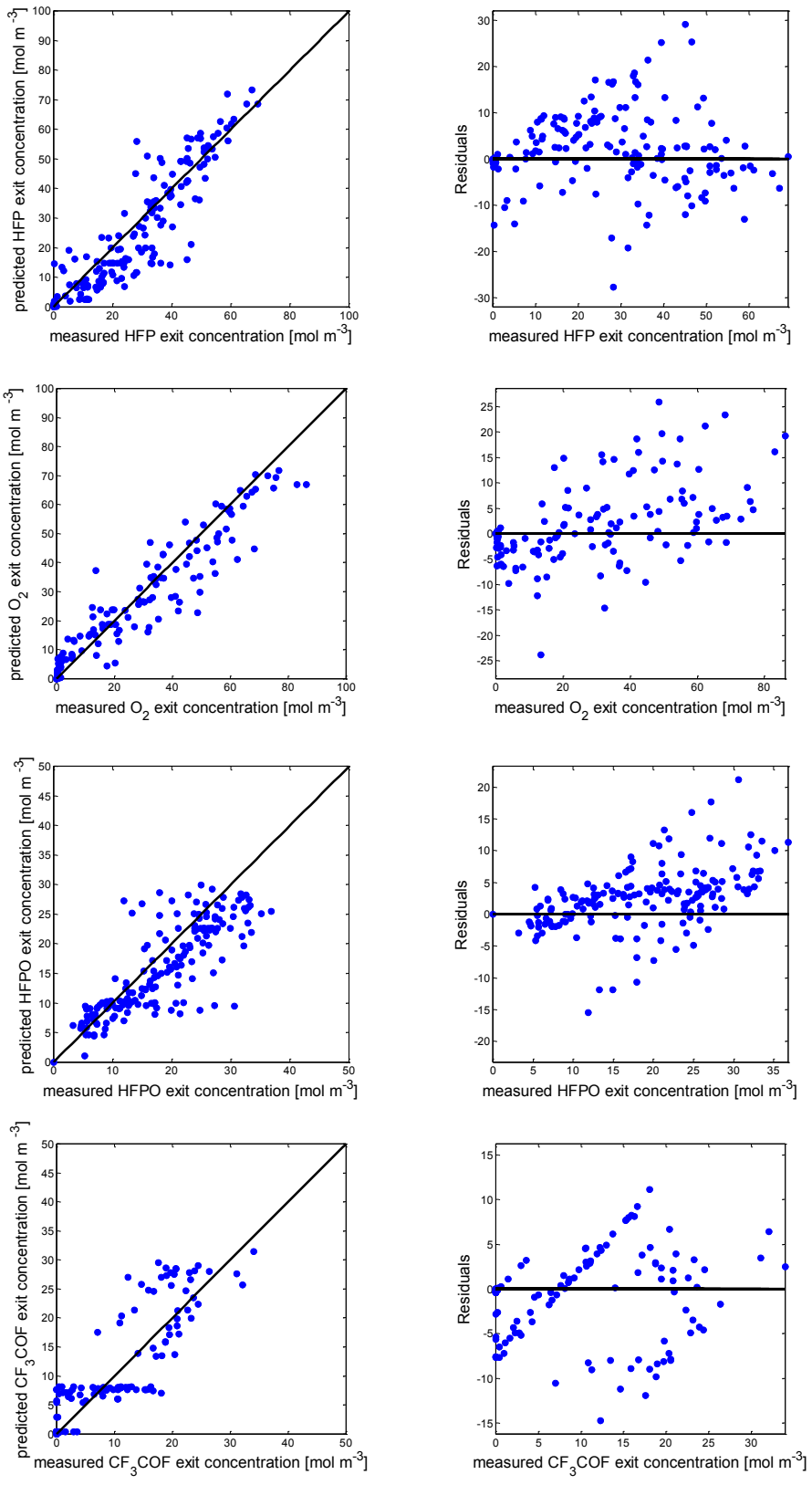

Figure 4.57. Parity and residual plots for all species at all data points (Laminar flow reactor model). Residuals defined as the difference between measured and predicted values.

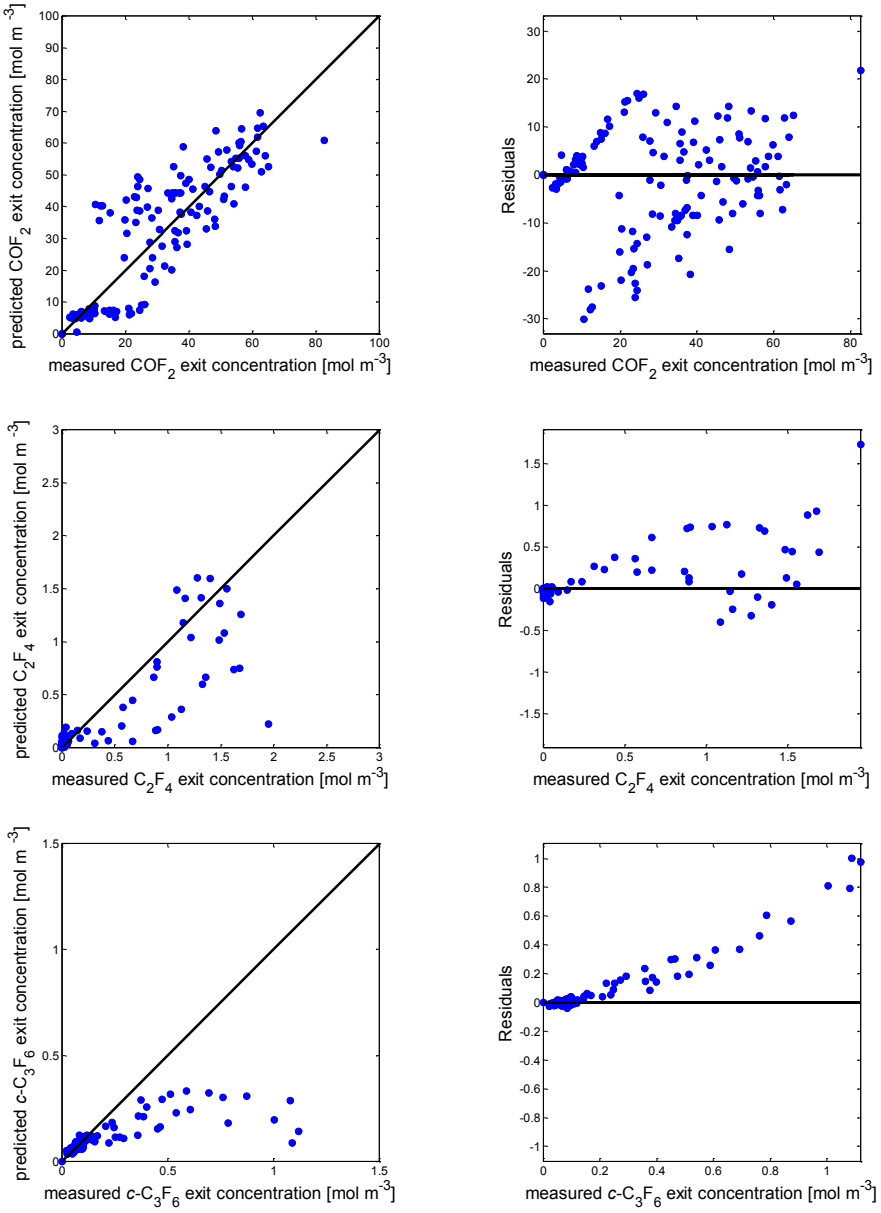

Figure 4.57 (*continued*)

Table 4.24. Final kinetic parameter estimates, obtained using the laminar flow reactor model.

Reaction	Pre-exponential factor[a]	Activation energy [kJ mol^{-1}]
1 (forward)	1.857×10^{31}	325.38
2	4.514×10^{46}	458.78
6	1.098×10^{4}	52.97
7b	2.115×10^{-15}	-111.67
1 (reverse)	1.323×10^{-16}	-127.96

[a] Units for the pre-exponential factors are the same as those given in Table 4.22.

The effect of the HFP/O_2 molar feed ratio on the exit concentration of HFPO, CF_3COF, COF_2, C_2F_4 and *c*-C_3F_6 was simulated at 478 K and a fixed space time of 120 seconds using the kinetic parameters given in Table 4.24. The simulation results are shown in Figures 4.58 and 4.59 together with measured data. Good agreement between experimental and simulated data points was obtained for HFPO, CF_3COF and C_2F_4. The variation in the consumption ratio of HFP/O_2 with the molar feed ratio at the same temperature and space time was also well represented by the model (cf. Figure 4.60). Figures 4.61 to 4.63 show the same plots at 493 K.

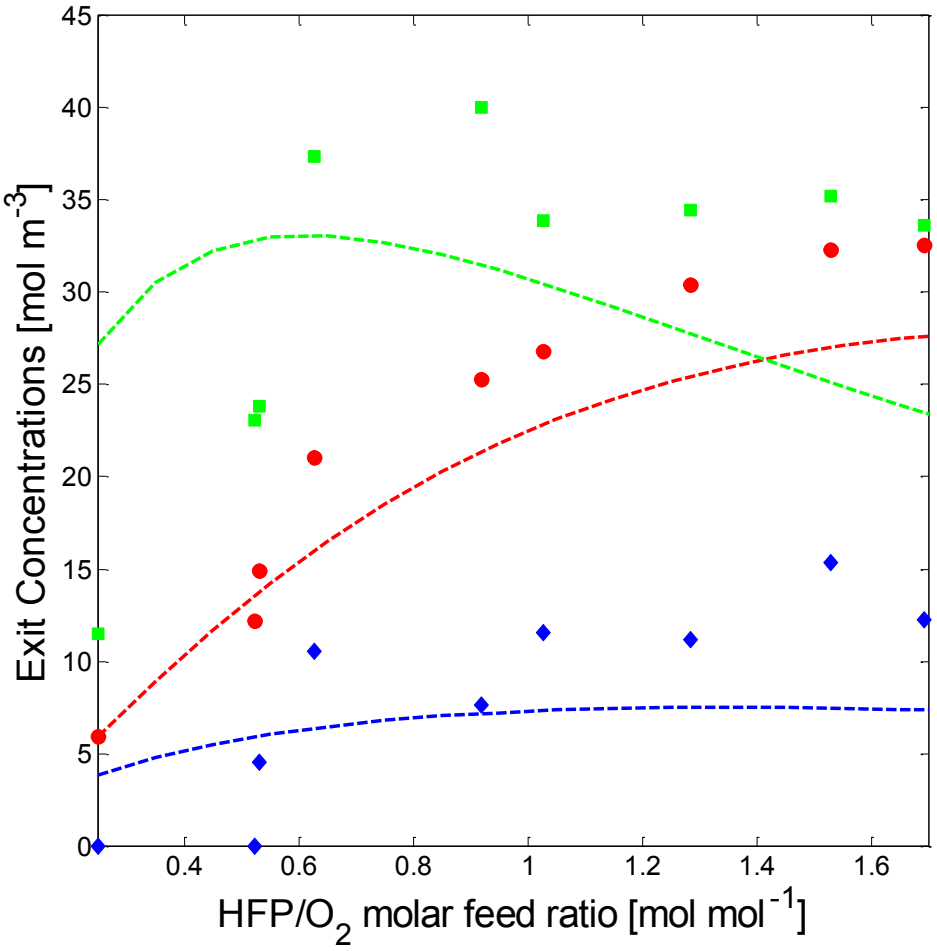

Figure 4.58. Effect of HFP/O_2 molar feed ratio on the exit concentration of HFPO (●, experimental; ---, simulation), CF_3COF (◆, experimental; ---, simulation) and COF_2 (■, experimental; ---, simulation) at 478 K and a fixed space time (120 s).

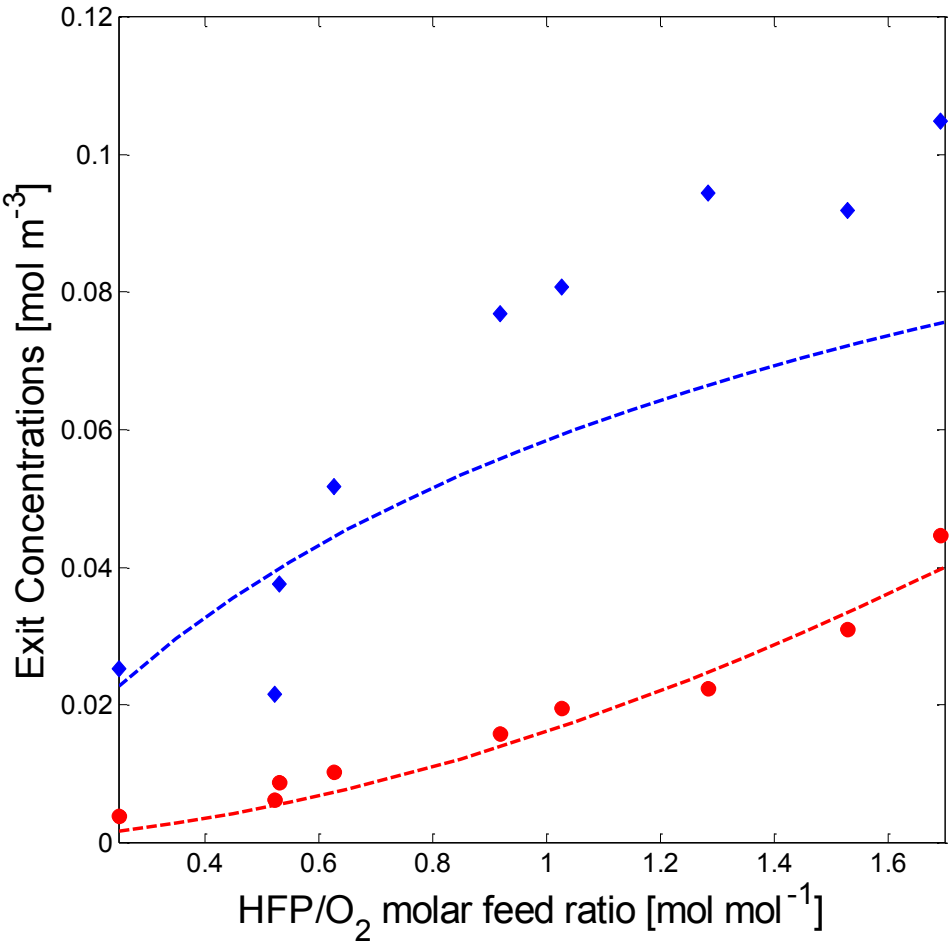

Figure 4.59. Effect of HFP/O_2 molar feed ratio on the exit concentration of C_2F_4 (●, experimental; ---, simulation) and *c*-C_3F_6 (◆, experimental; ---, simulation) at 478 K and a fixed space time (120 s).

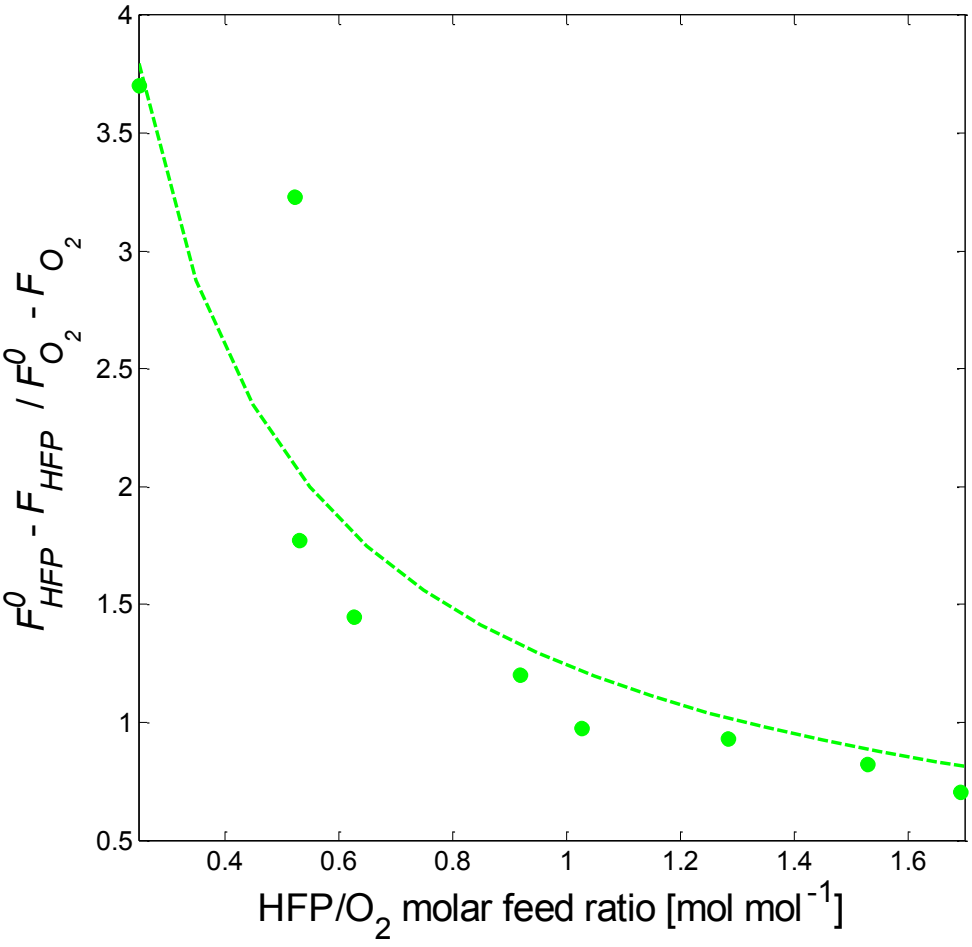

Figure 4.60. Effect of HFP/O_2 molar feed ratio on the HFP/O_2 consumption ratio (●, experimental; ---, simulation) at 478 K and a fixed space time (120 s).

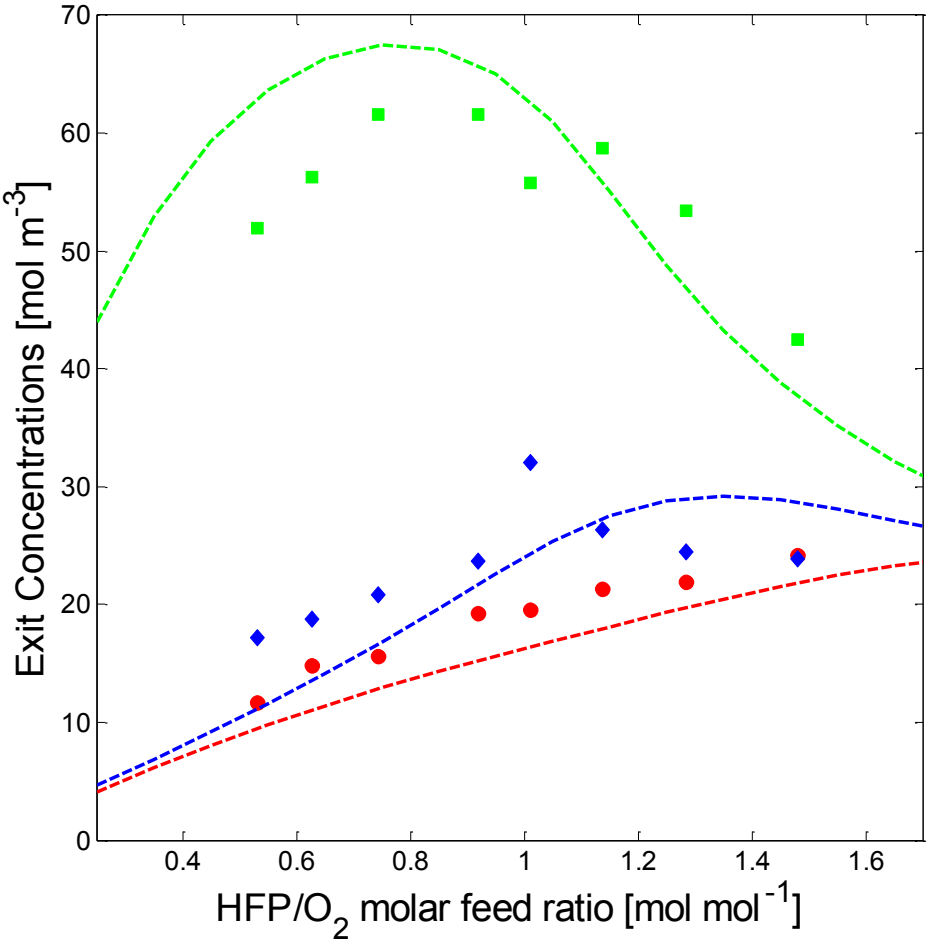

Figure 4.61. Effect of HFP/O_2 molar feed ratio on the exit concentration of HFPO (●, experimental; ---, simulation), CF_3COF (◆, experimental; ---, simulation) and COF_2 (■, experimental; ---, simulation) at 493 K and a fixed space time (120 s).

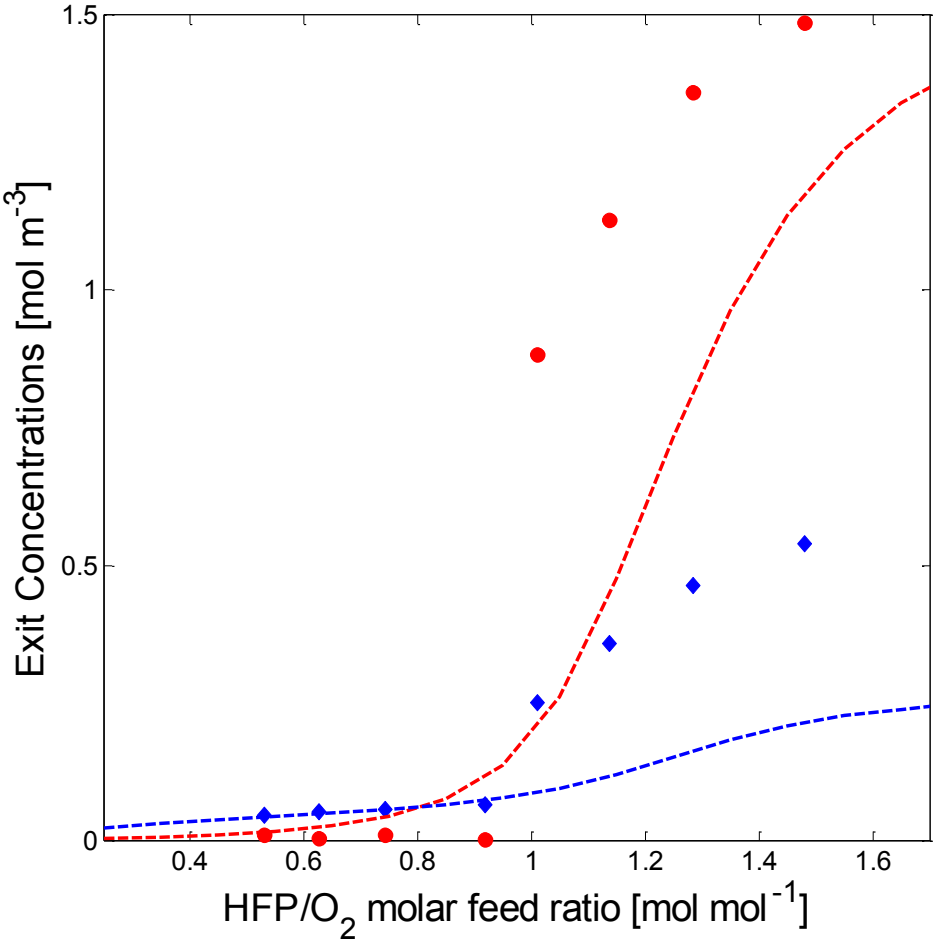

Figure 4.62. Effect of HFP/O_2 molar feed ratio on the exit concentration of C_2F_4 (●, experimental; ---, simulation) and *c*-C_3F_6 (◆, experimental; ---, simulation) at 493 K and a fixed space time (120 s).

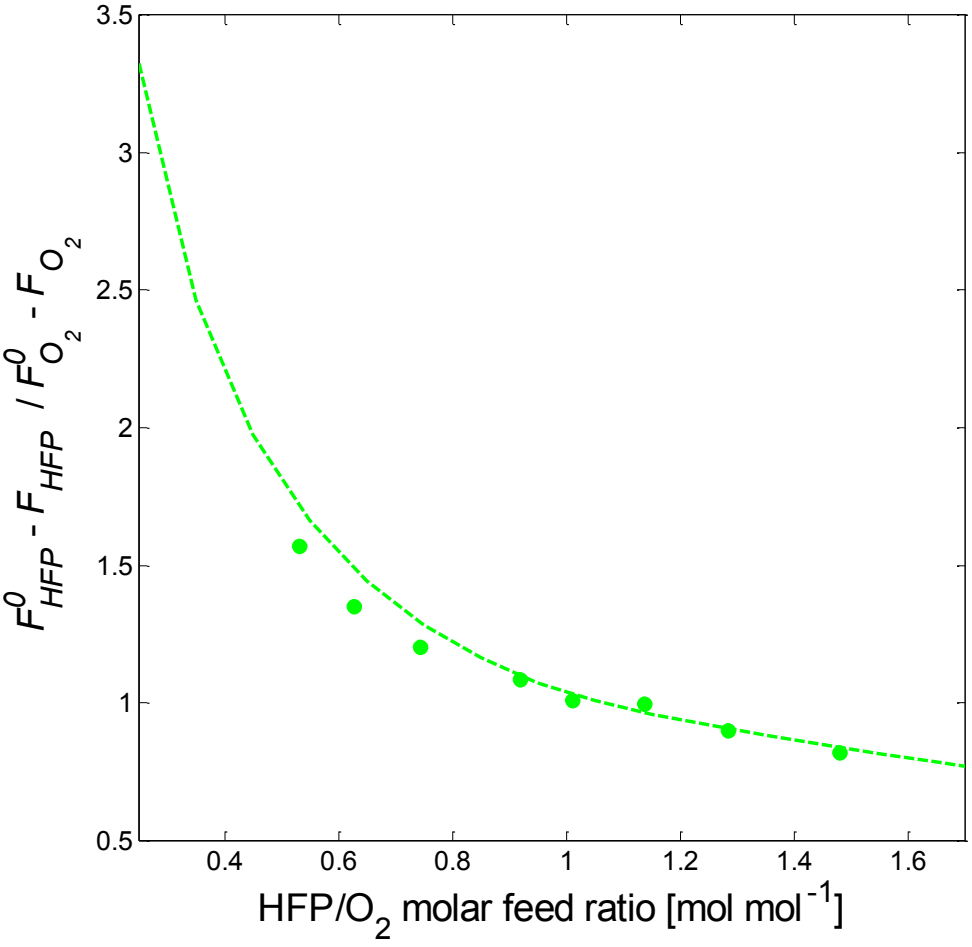

Figure 4.63. Effect of HFP/O_2 molar feed ratio on the HFP/O_2 consumption ratio (●, experimental; ---, simulation) at 493 K and a fixed space time (120 s).

Figures 4.64 and 4.65 show the simulated steady-state, 2-dimensional concentration field for HFP and HFPO, respectively, inside the laminar flow reactor at a single set of reaction conditions (reaction temperature = 480 K, HFP/O_2 molar feed ratio = 1.21 mol mol^{-1} and space time = 118 s). Interestingly, a maximum HFPO concentration in this instance was observed 30 m from the entrance of the reactor tube. Although the simulation was performed using a predefined parabolic velocity profile, the radial concentration profiles were practically flat across the entire length of the tube. This was due to the large amount of radial diffusion. Using the radial diffusion criterion of Merrill and Hamrin (1970) it was estimated that less than 1 tube diameter was required for the equalization of the radial concentration profile.

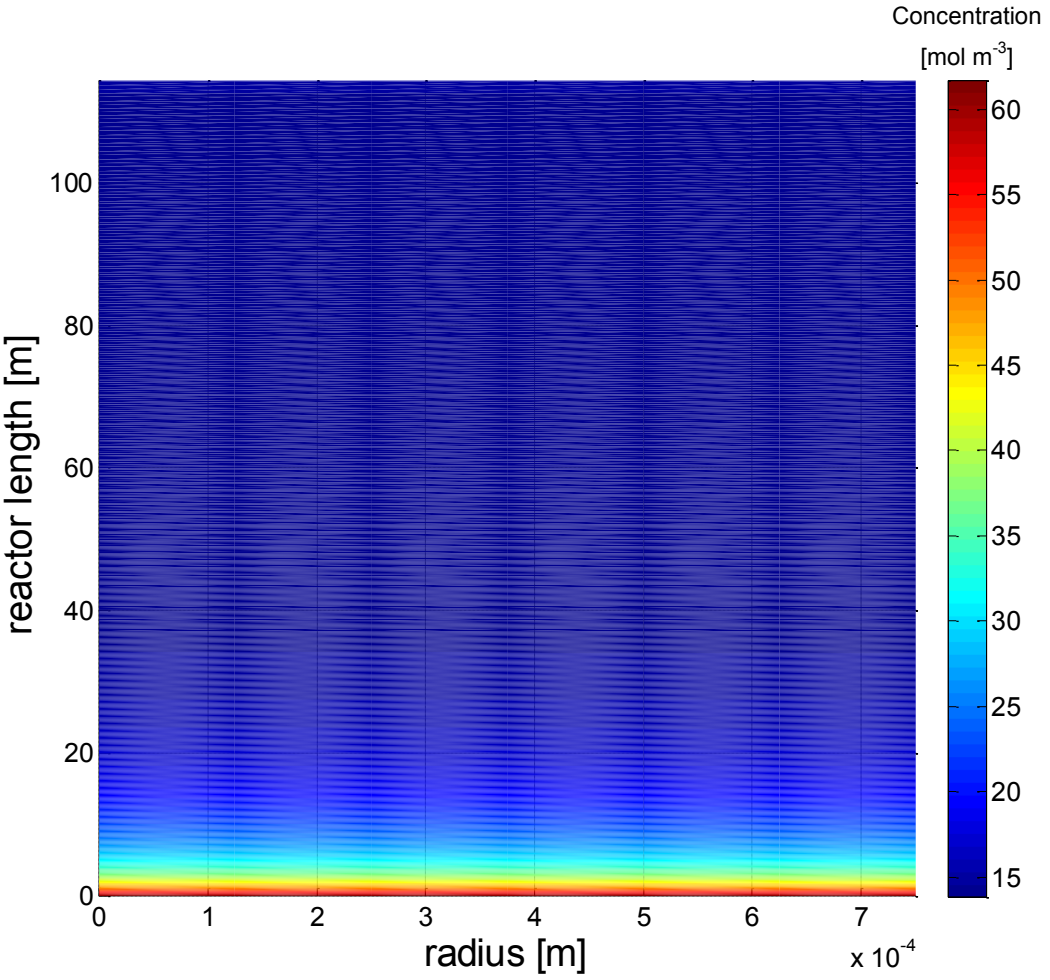

Figure 4.64. Steady-state, 2-dimensional concentration field for HFP inside the laminar flow reactor at 480 K, a HFP/O_2 molar feed ratio of 1.21 mol mol^{-1} and a space time of 118 s.

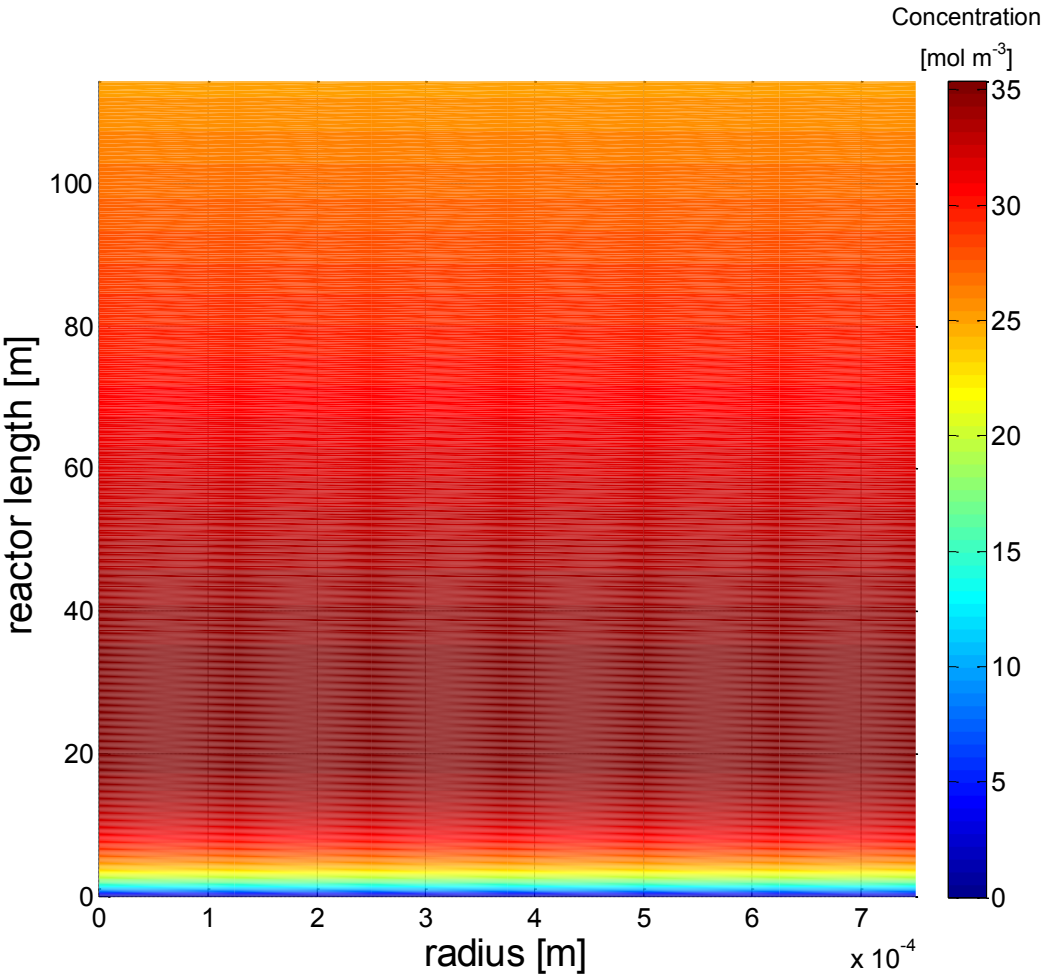

Figure 4.65. Steady-state, 2-dimensional concentration field for HFPO inside the laminar flow reactor at 480 K, a HFP/O_2 molar feed ratio of 1.21 mol mol^{-1} and a space time of 118 s.

For a laminar flow reactor, the average molar flow-rate of species *i* at any particular point of the reactor axial distance is given by:

$$F_i^{LFR}(z) = \int_0^R C_i(r,z)u(r,z)2\pi r dr \tag{4.111}$$

If a uniform radial concentration profile and parabolic velocity profile are assumed, then:

$$\begin{aligned} F_i^{LFR}(z) &= \int_0^R C_i(z)2\bar{u}(z)\left[1-\left(\frac{r}{R}\right)^2\right]2\pi r dr \\ &= 4\pi C_i(z)\bar{u}(z)\int_0^R r\left[1-\left(\frac{r}{R}\right)^2\right]dr \\ &= \pi R^2 C_i(z)\bar{u}(z) \end{aligned} \tag{4.112}$$

This is exactly the same as the molar flow-rate given by a simple plug flow reactor model. The performance of a laminar flow reactor with a fairly uniform radial concentration profile, resulting from a relatively large amount of radial diffusion, closely approaches that of a plug flow reactor (Nauman, 2002; Lee et al., 2000). The assumption of a radially uniform concentration profile in a laminar flow reactor has been shown by Cleland and Wilhelm (1956) to be justified when the length-to-diameter ratio of the reactor is large.

This raised the question as to whether, instead of the complicated laminar-flow reactor (LFR) model, a simple plug-flow reactor (PFR) model would have been adequate for kinetic parameter identification. Importantly, the PFR model would have explicitly accounted for the effect of non-equimolarity on the velocity profile, retaining it flat but with a varying value in the axial direction. For the sake of simplicity, the LFR model developed in this work ignored the effect of non-equimolarity by neglecting the momentum balance. A strong case for the validity of the PFR model was also made when considering the hydrodynamics of flow through the coiled reactor tube. The concept of secondary flow was introduced in section 4.1.5.2. There it was stated that for the sake of simplicity, the influence of inertial forces on fluid elements moving through the reaction zone were neglected when developing the reactor model. Several important effects of secondary flow on reactor performance were also mentioned. Of these, the narrowing of the residence time distribution and the enhancement of radial mass transport through combined diffusion and convection are most

important in the current context. It was therefore likely that the performance of the coiled laminar flow reactor used in this study could be well approximated by the simple PFR model. The identification procedure was repeated using the PFR model, for which the material balance is:

$$\frac{dF_i}{dV} = R_i \tag{4.113}$$

where R_i is the net rate of change of species i due to reaction, dF_i is the differential change in the molar flow-rate of species i and dV is the differential volume. Once again the overall orders for reactions 1, 2, 6 and 7b were varied systematically to determine the most optimum fit.

The orders of the individual rates shown in Equations 4.71 to 4.78 gave the best fit to the experimental data. Note that for forward reaction 1 and 7b, these were different for the LFR and PFR models.

Table 4.25 gives the estimated rate constants and 95% confidence intervals for reactions 1, 2, 6 and 7b, obtained from the data-fitting procedure. Figures 4.66 to 4.68 show parity and residual plots for each of the species, based on the estimated rate constants, at each of the three temperatures investigated.

The isothermal data were used to prepare the Arrhenius plots presented in Figures 4.69 to 4.73. The starting estimates for the activation energies and pre-exponential factors obtained from each of the Arrhenius plots, and required for the total data fit, are given in Table 4.26.

Table 4.25. Estimated rate constants and 95% confidence intervals for the gas-phase oxidation of HFP, obtained using the plug flow reactor model.

Parameter	Units	Temperature		
		463 K	**478 K**	**493 K**
k_1^+	$m^3\ mol^{-1}\ s^{-1}$	$1.01\times10^{-4} \pm 3.86\times10^{-5}$	$9.02\times10^{-4} \pm 1.41\times10^{-5}$	$3.83\times10^{-2} \pm 4.83\times10^{-3}$
k_1^-	s^{-1}	$1.59\times10^{-2} \pm 1.20\times10^{-3}$	$1.62\times10^{-2} \pm 8.69\times10^{-3}$	$1.67\times10^{-2} \pm 9.15\times10^{-3}$
k_2	$m^3\ mol^{-1}\ s^{-1}$	$1.81\times10^{-5} \pm 2.25\times10^{-6}$	$1.71\times10^{-4} \pm 4.41\times10^{-5}$	$1.15\times10^{-2} \pm 1.95\times10^{-3}$
k_6	$m^3\ mol^{-1}\ s^{-1}$	$1.99\times10^{-2} \pm 1.52\times10^{-3}$	$2.10\times10^{-2} \pm 3.96\times10^{-3}$	$2.33\times10^{-2} \pm 9.29\times10^{-3}$
k_{7b}	$m^3\ mol^{-1}\ s^{-1}$	$1.15\times10^{-4} \pm 1.51\times10^{-5}$	$2.01\times10^{-4} \pm 9.41\times10^{-5}$	$2.82\times10^{-4} \pm 7.83\times10^{-5}$

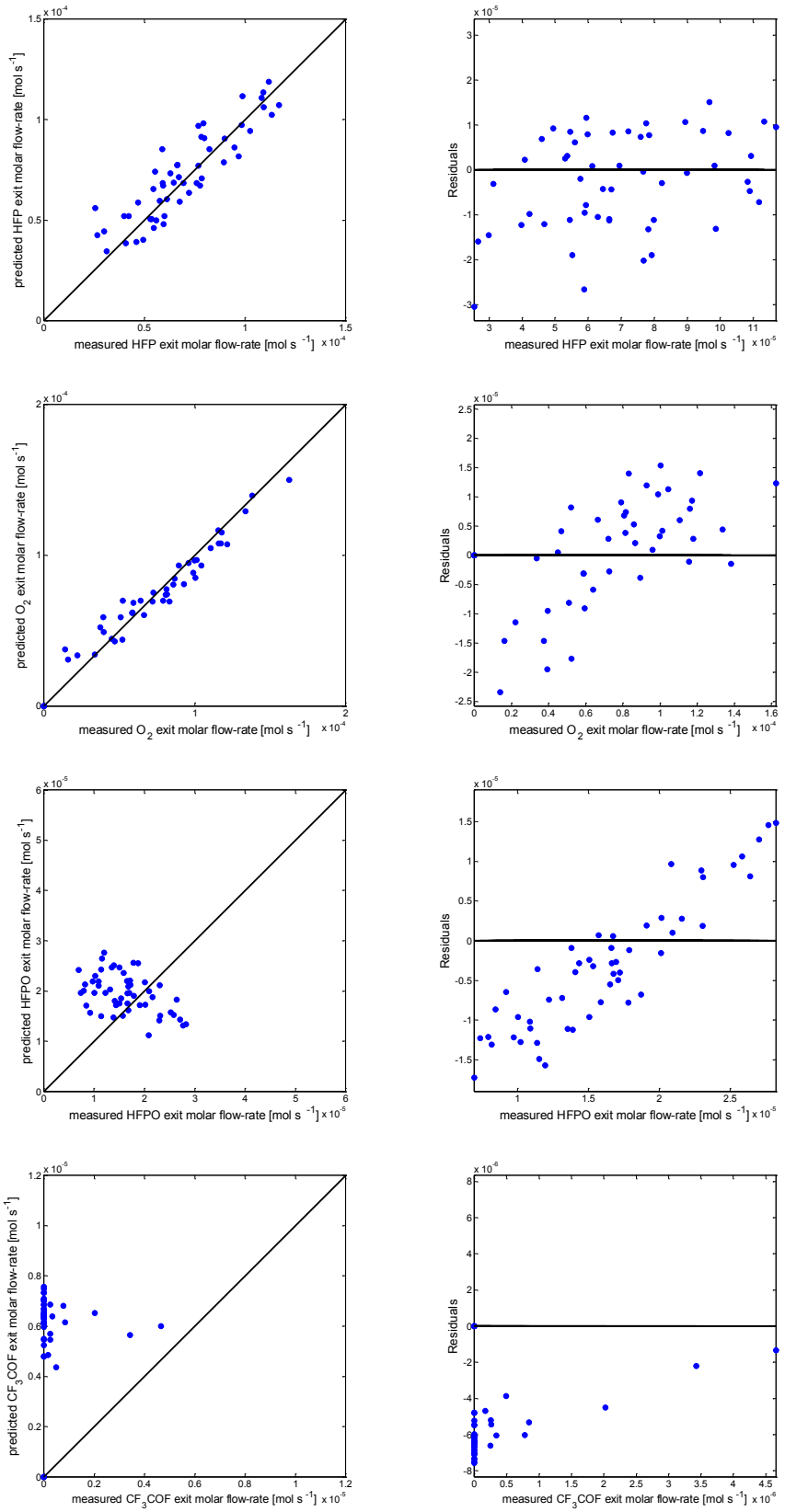

Figure 4.66. Parity and residual plots for individual species at 463 K (Plug flow reactor model). Residuals defined as the difference between measured and predicted values

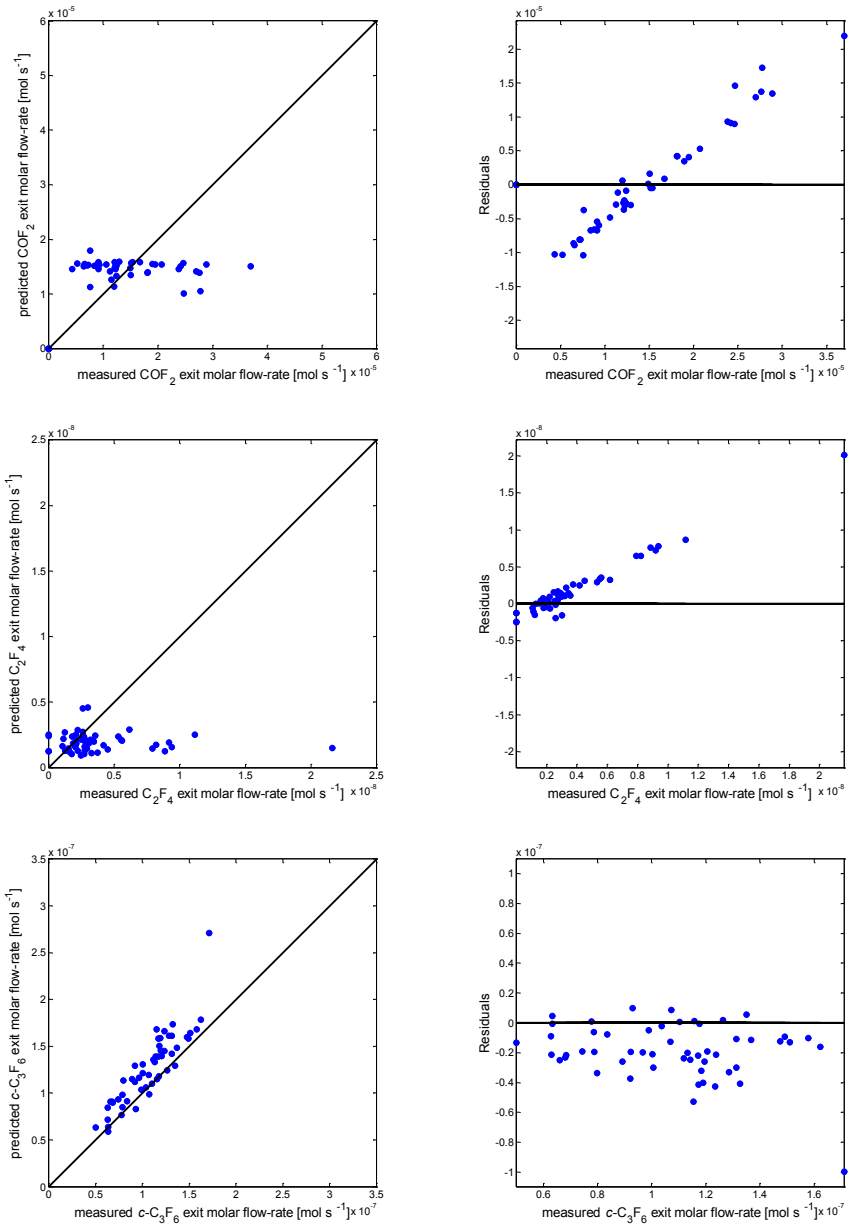

Figure 4.66. (*continued*).

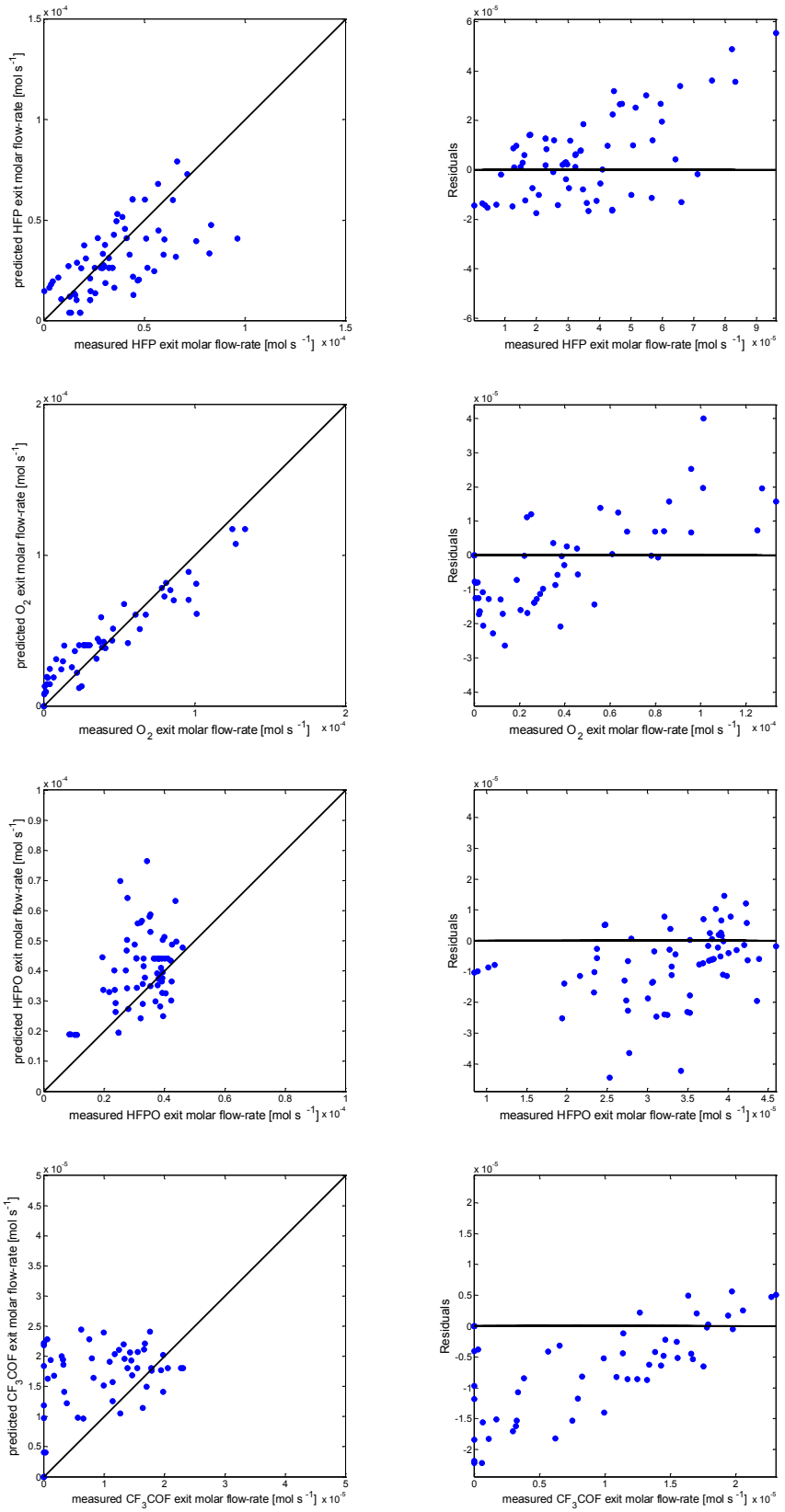

Figure 4.67. Parity and residual plots for individual species at 478 K (Plug flow reactor model). Residuals defined as the difference between measured and predicted values.

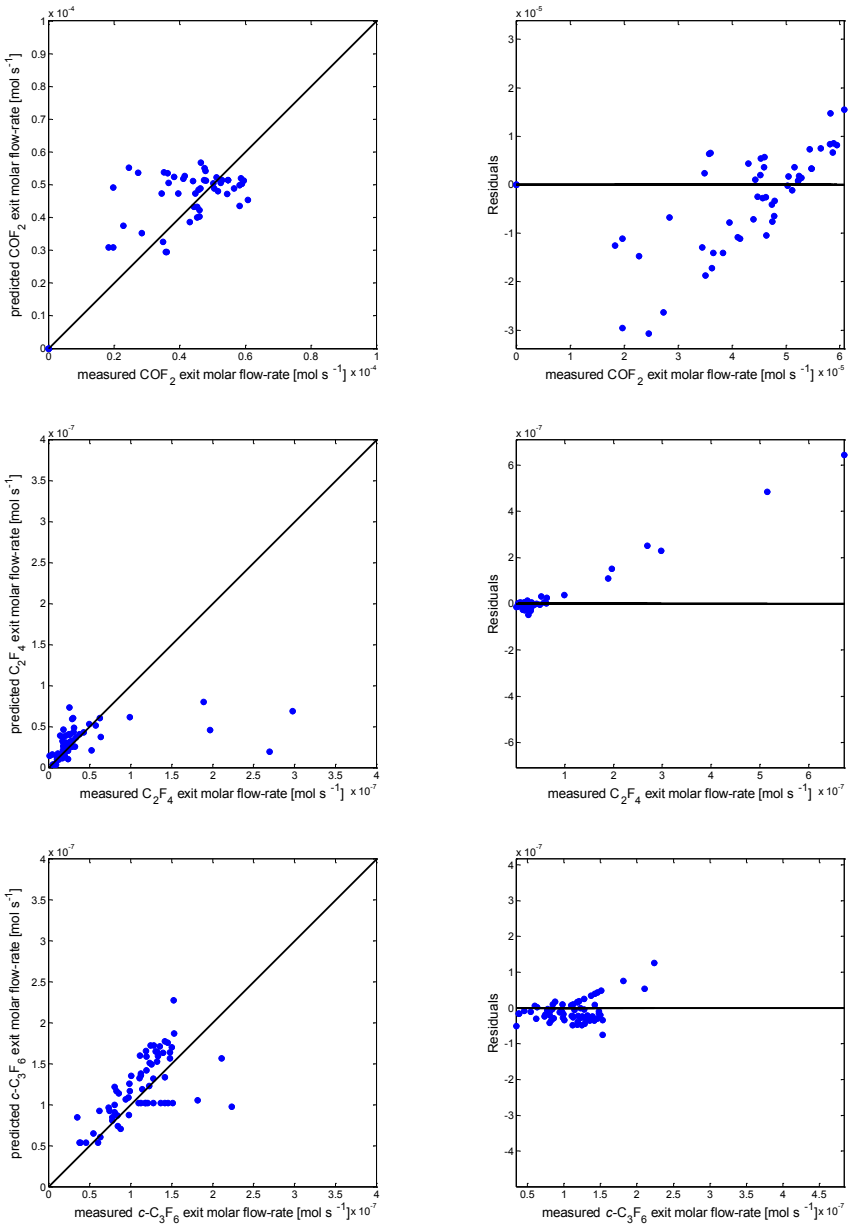

Figure 4.67. (*continued*).

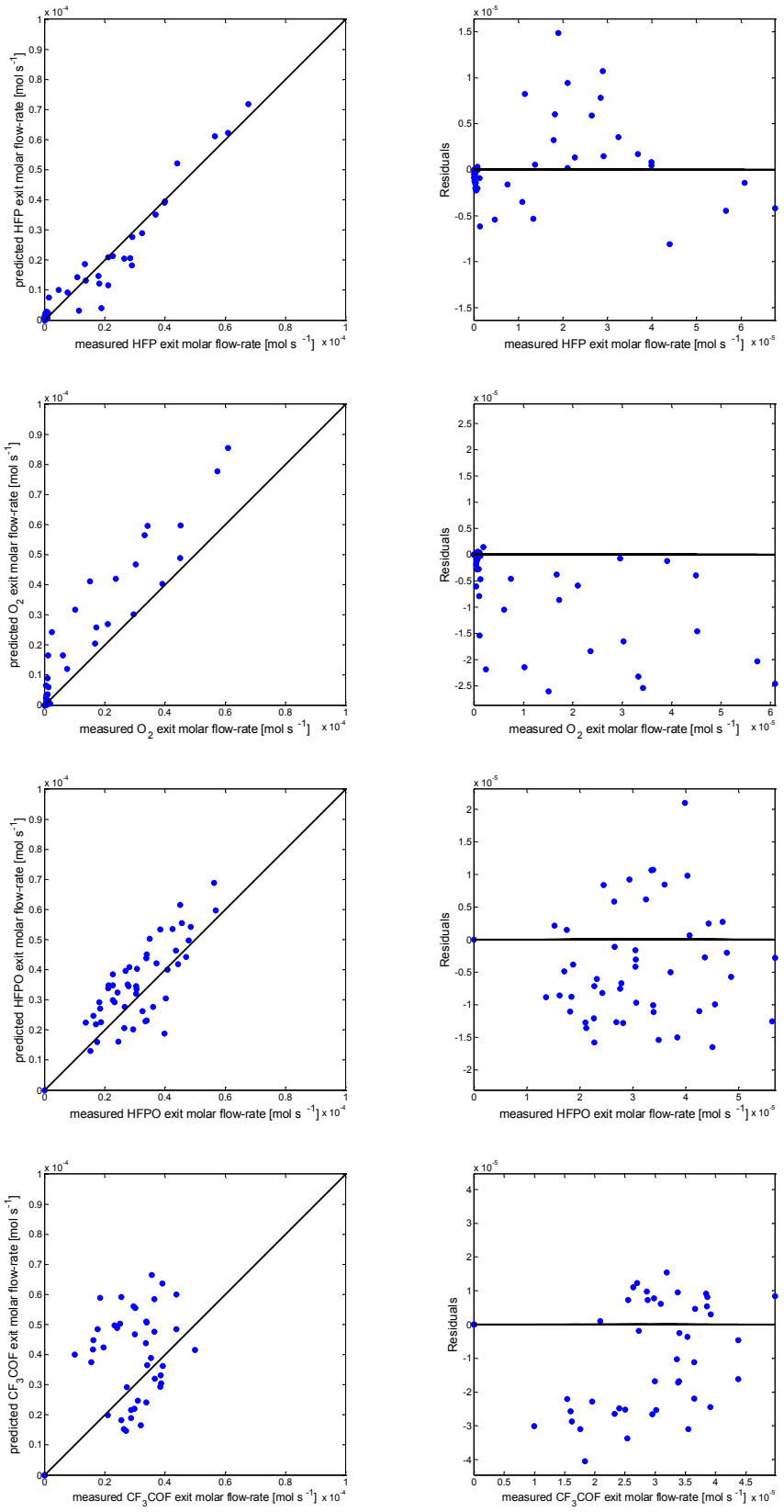

Figure 4.68. Parity and residual plots for individual species at 493 K (Plug flow reactor model). Residuals defined as the difference between the measured and predicted values.

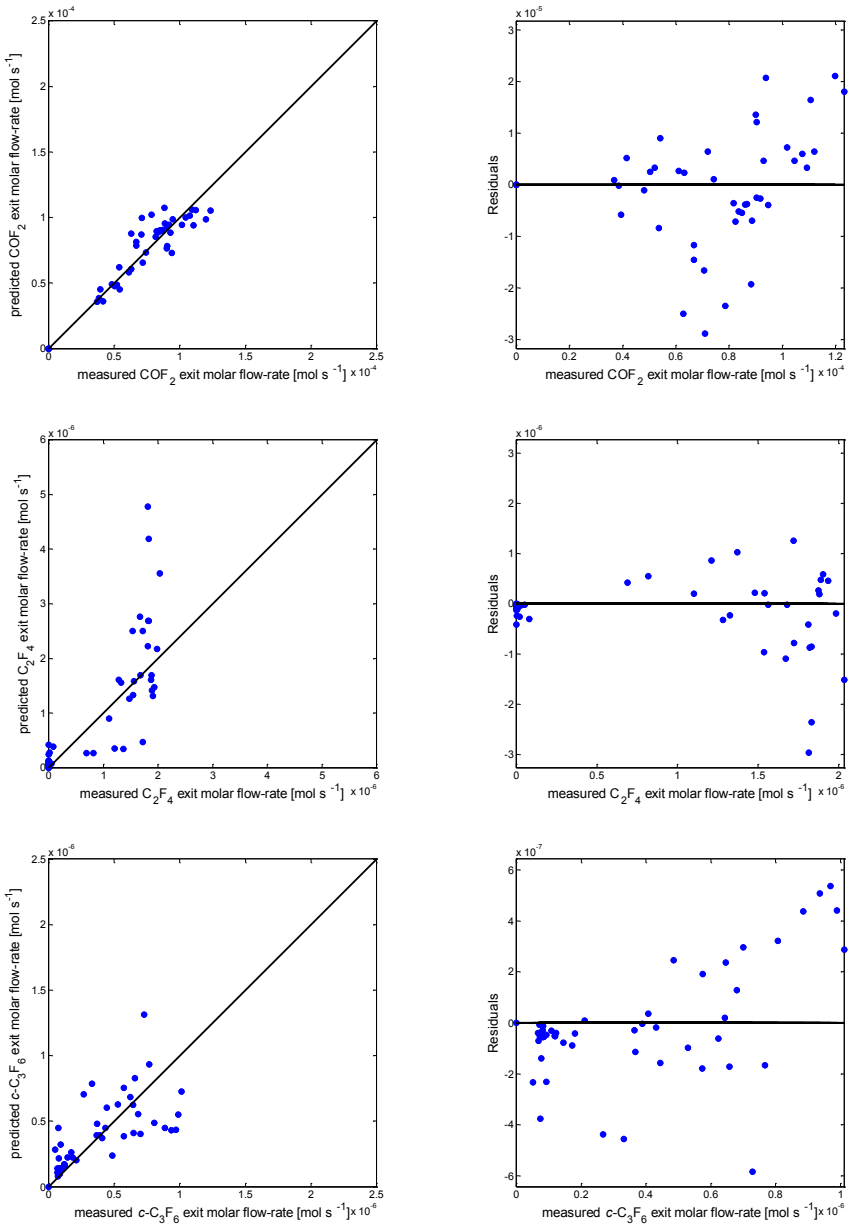

Figure 4.68. (*continued*).

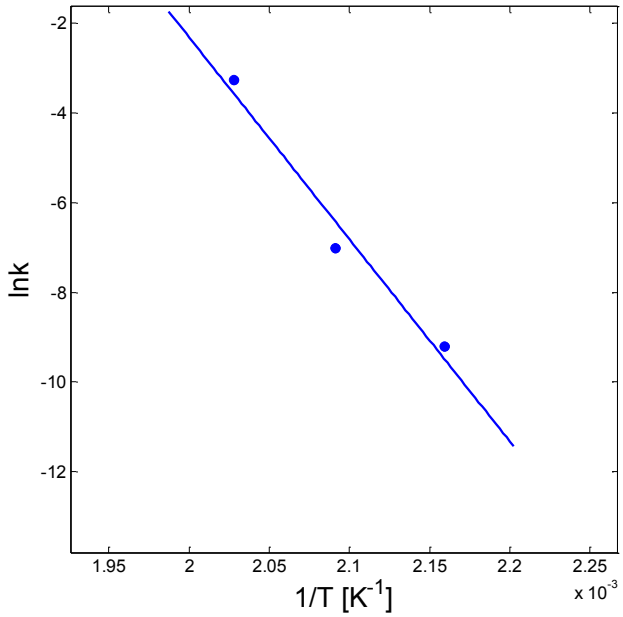

Figure 4.69. Arrhenius plot for reaction 1 (forward), based on isothermal data.

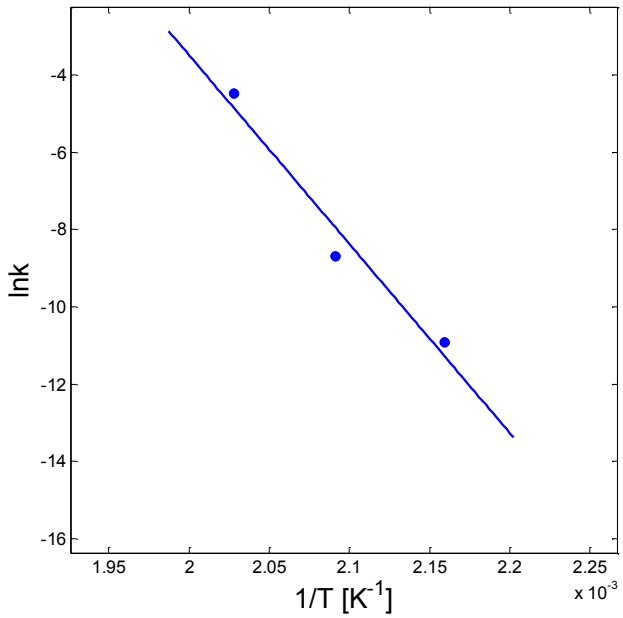

Figure 4.70. Arrhenius plot for reaction 2, based on isothermal data.

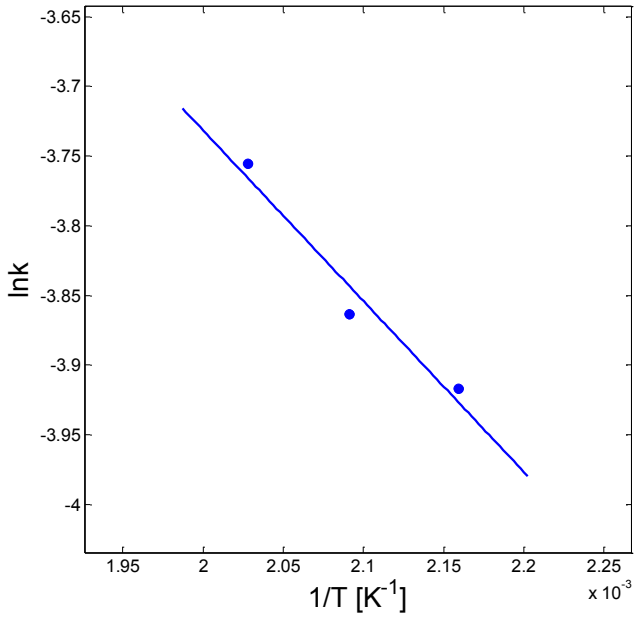

Figure 4.71. Arrhenius plot for reaction 6, based on isothermal data.

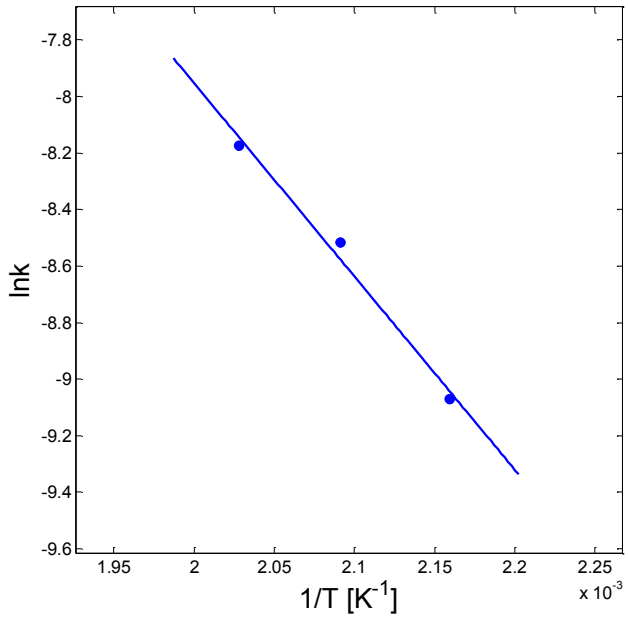

Figure 4.72. Arrhenius plot for reaction 7b, based on isothermal data.

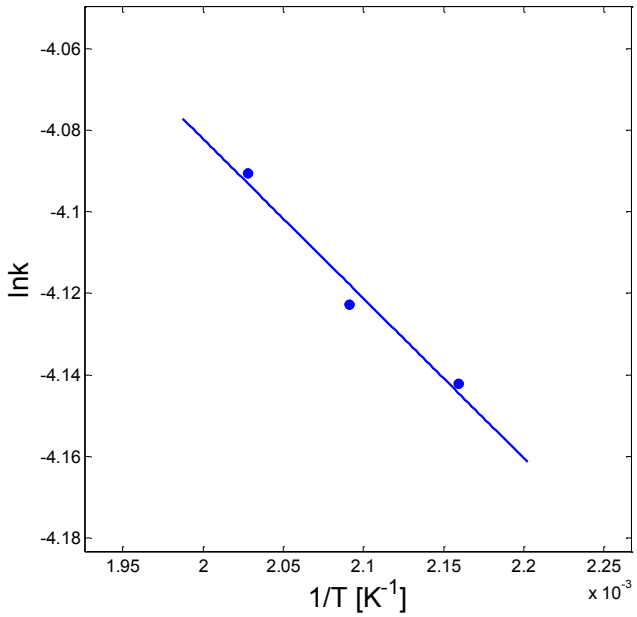

Figure 4.73. Arrhenius plot for reaction 1 (reverse), based on isothermal data.

Table 4.26. Initial kinetic parameter estimates obtained from Arrhenius plots.

Reaction	**Pre-exponential factor[a]**	**Activation energy [kJ mol^{-1}]**
1 (forward)	1.372×10^{38}	374.65
2	1.085×10^{41}	407.23
6	2.781×10^{-1}	10.19
7b	3.082×10^{2}	56.88
1 (reverse)	3.693×10^{-2}	3.256

[a] Units for the pre-exponential factors are the same as those given in Table 4.25.

For all temperatures, the fit to the experimental data and the distribution of residuals for HFP, O_2, HFPO and COF_2 obtained using the PFR model were better than the LFR model. For CF_3COF, C_2F_4 and *c*-C_3F_6 the fit was worse. The confidence intervals for all the estimated kinetic constants obtained using the PFR model were narrower, however. The activation energies for forward reaction 1, reaction 2 and 6, obtained via the Arrhenius plots, were similar to those predicted using the LFR model. The temperature dependence of the all rate constants was phenomenologically correct. Interestingly, the activation energy for reverse reaction 1 was relatively low.

The final parameter estimates obtained using the temperature-scaling method discussed earlier are given in Table 4.27. Figure 4.74 shows the parity and residual plots for all species at all data points.

Table 4.27. Final kinetic parameter estimates and 95% confidence intervals, obtained using the plug flow reactor model.

Reaction	Pre-exponential factor[a]	Activation energy [kJ mol^{-1}]
1 (forward)	$1.263\times10^{38} \pm 6.548\times10^{37}$	373.05 ± 25.15
2	$1.079\times10^{41} \pm 5.307\times10^{40}$	407.24 ± 20.51
6	$2.297\times10^{-1} \pm 3.391\times10^{-2}$	10.21 ± 2.28
7b	$5.452\times10^{2} \pm 1.279\times10^{2}$	56.36 ± 3.87
1 (reverse)	$5.508\times10^{-2} \pm 6.617\times10^{-3}$	3.23 ± 2.17

[a] Units for the pre-exponential factors are the same as those given in Table 4.25.

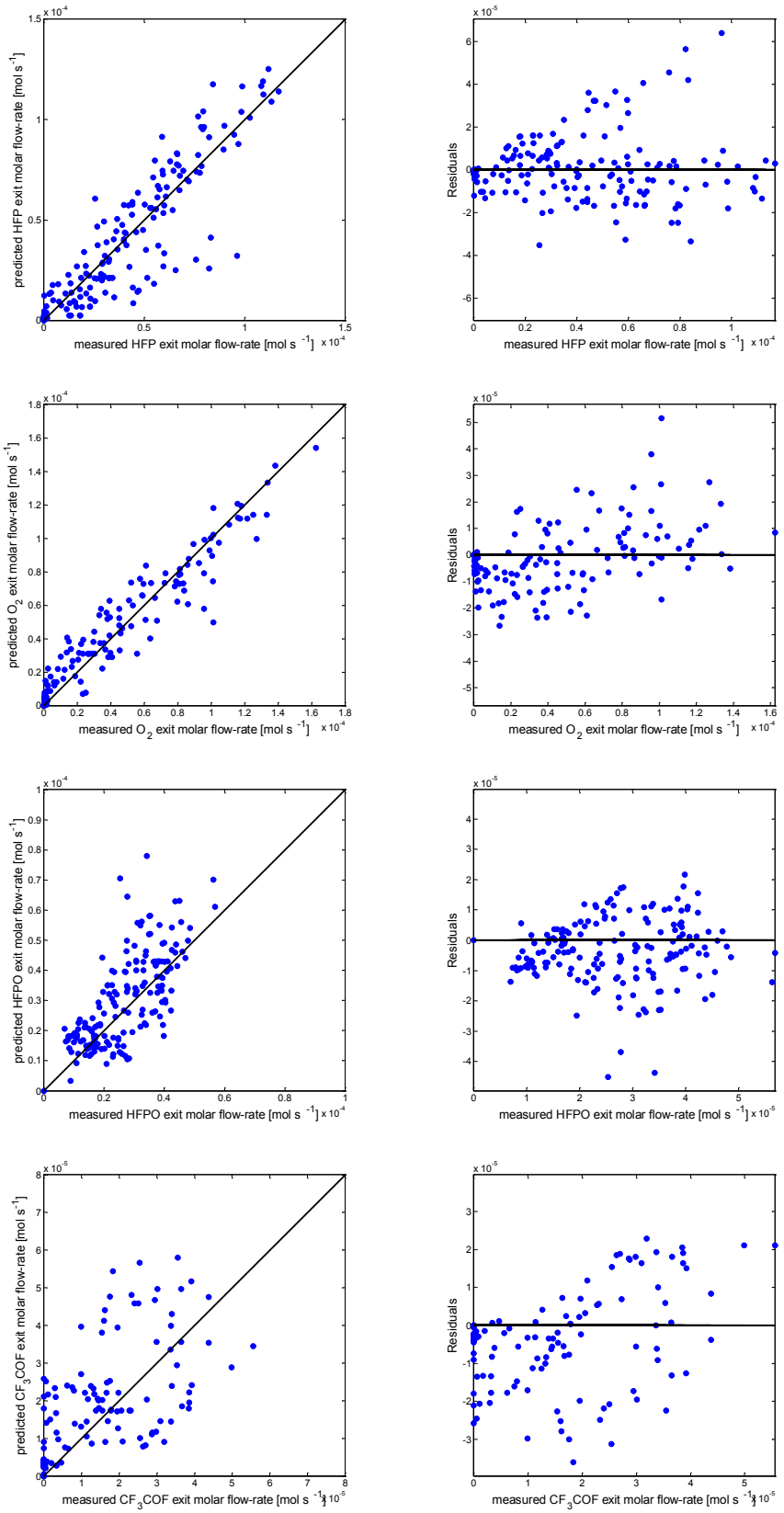

Figure 4.74. Parity and residual plots for all species at all data points (Plug flow reactor model). Residuals defined as the difference between measured and predicted values.

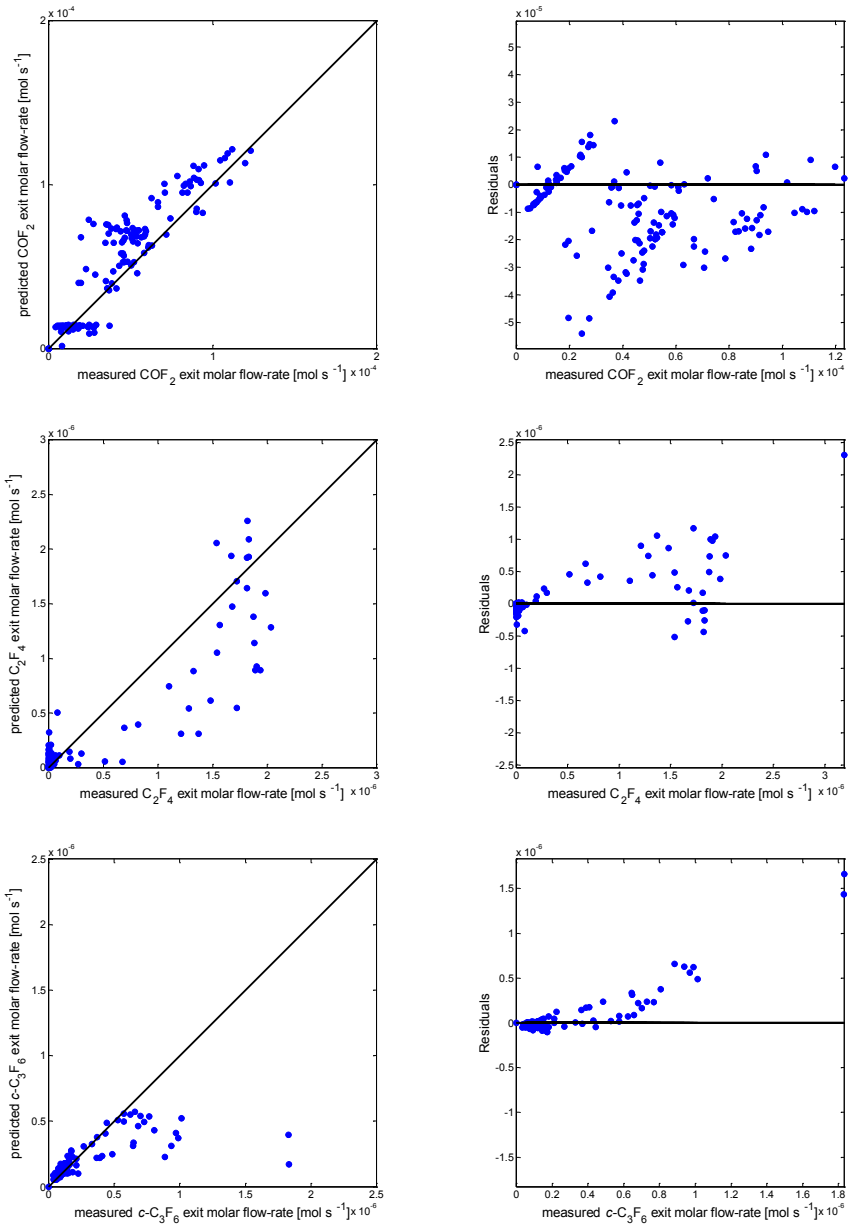

Figure 4.74. (*continued*).

Figures 4.75 and 4.76 show the effect of the HFP/O_2 molar feed ratio on the exit concentration of HFPO, CF_3COF, COF_2, C_2F_4 and *c*-C_3F_6, at 478 K and a fixed space time of 120 seconds. Modelled data, obtained through simulation using the kinetic parameters given in Table 4.27, showed good agreement with the experimental points but deviated for COF_2 at high molar feed ratios. The variation in the consumption ratio of HFP/O_2 with the molar feed ratio was well represented by the model (cf. Figure 4.77). Figures 4.78 to 4.80 show the same plots at 493 K. The simulation results for C_2F_4 and *c*-C_3F_6 in this case were unsatisfactory.

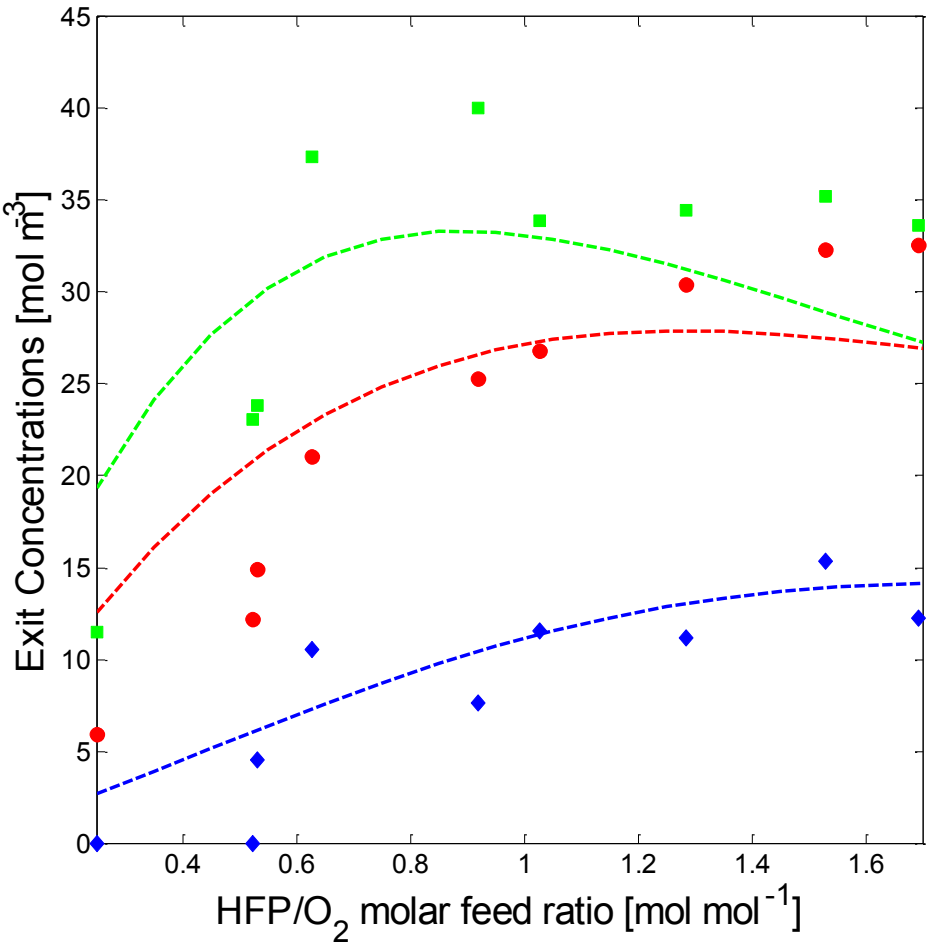

Figure 4.75. Effect of HFP/O_2 molar feed ratio on the exit concentration of HFPO (●, experimental; ---, simulation), CF_3COF (◆, experimental; ---, simulation) and COF_2 (■, experimental; ---, simulation) at 478 K and a fixed space time (120 s).

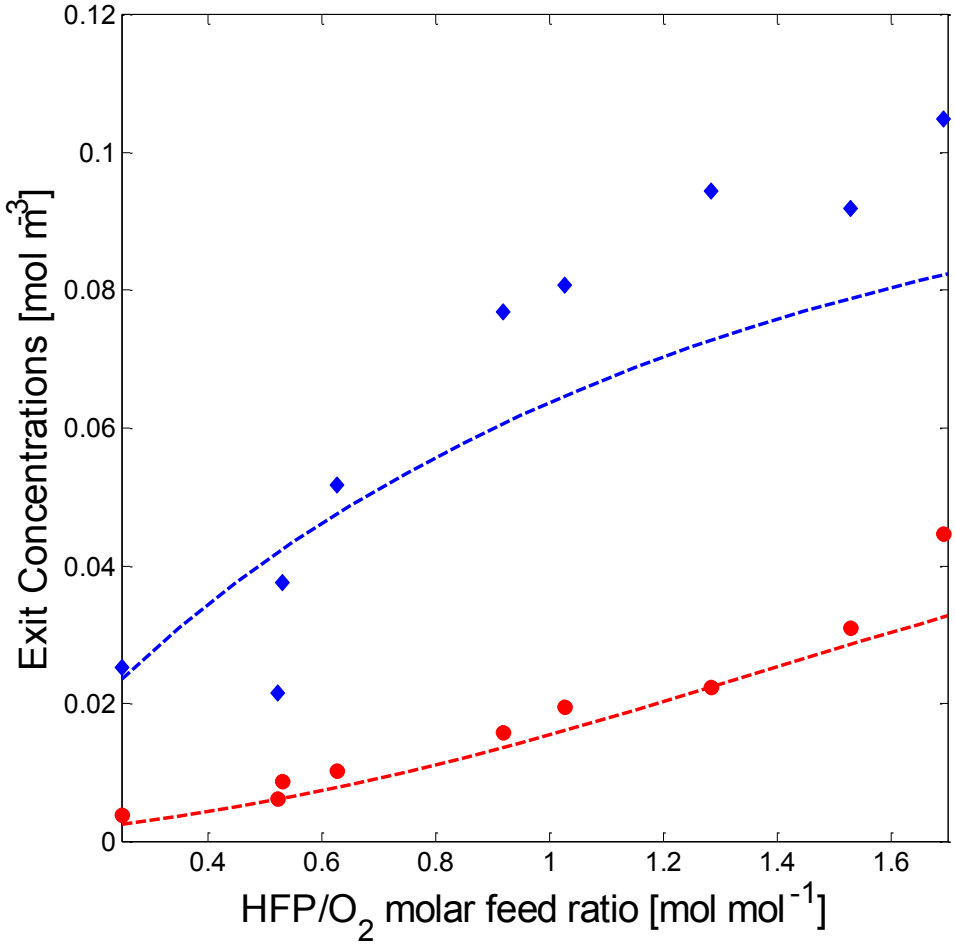

Figure 4.76. Effect of HFP/O_2 molar feed ratio on the exit concentration of C_2F_4 (●, experimental; ---, simulation) and *c*-C_3F_6 (◆, experimental; ---, simulation) at 478 K and a fixed space time (120 s).

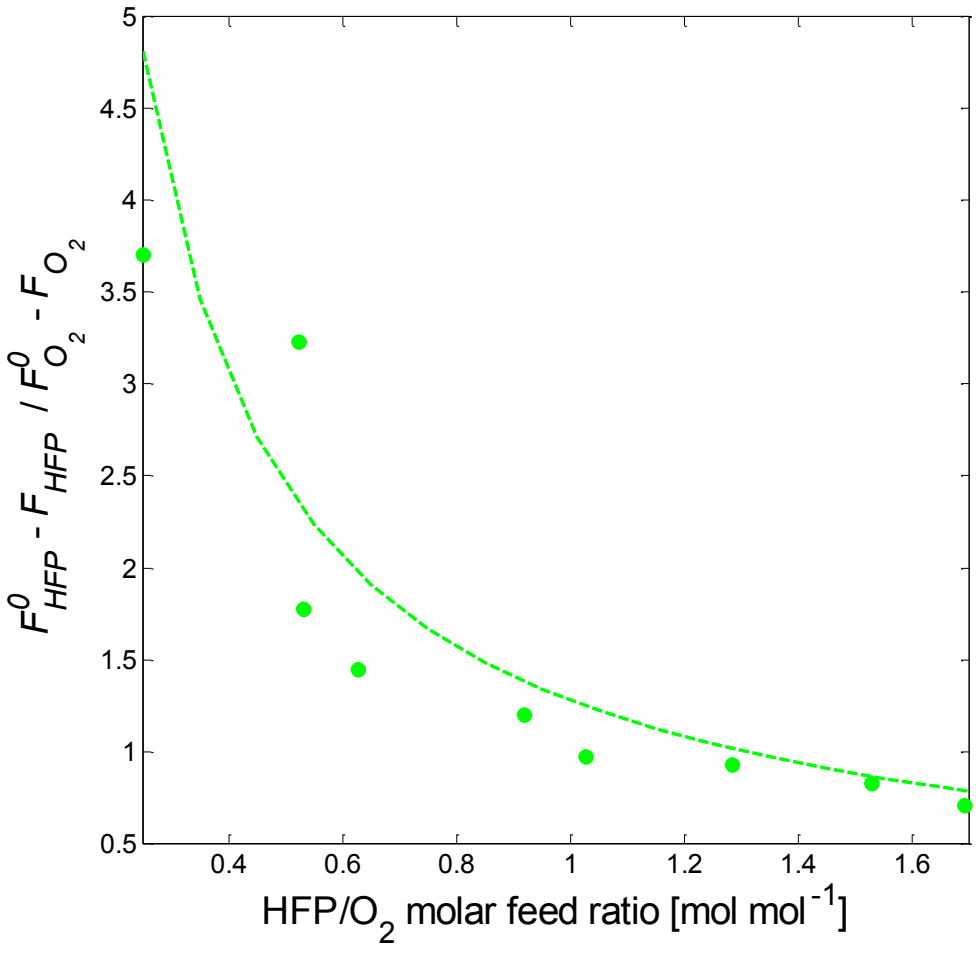

Figure 4.77. Effect of HFP/O_2 molar feed ratio on the HFP/O_2 consumption ratio (●, experimental; ---, simulation) at 478 K and a fixed space time (120 s).

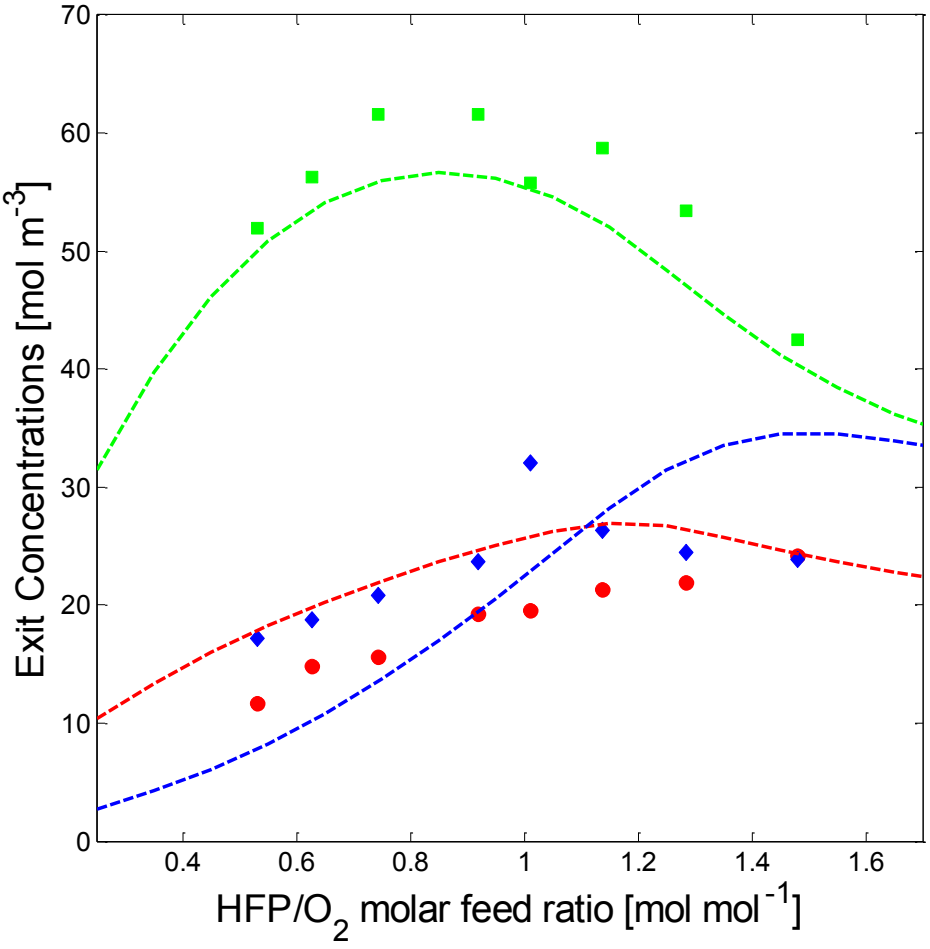

Figure 4.78. Effect of HFP/O_2 molar feed ratio on the exit concentration of HFPO (●, experimental; ---, simulation), CF_3COF (◆, experimental; ---, simulation) and COF_2 (■, experimental; ---, simulation) at 493 K and a fixed space time (120 s).

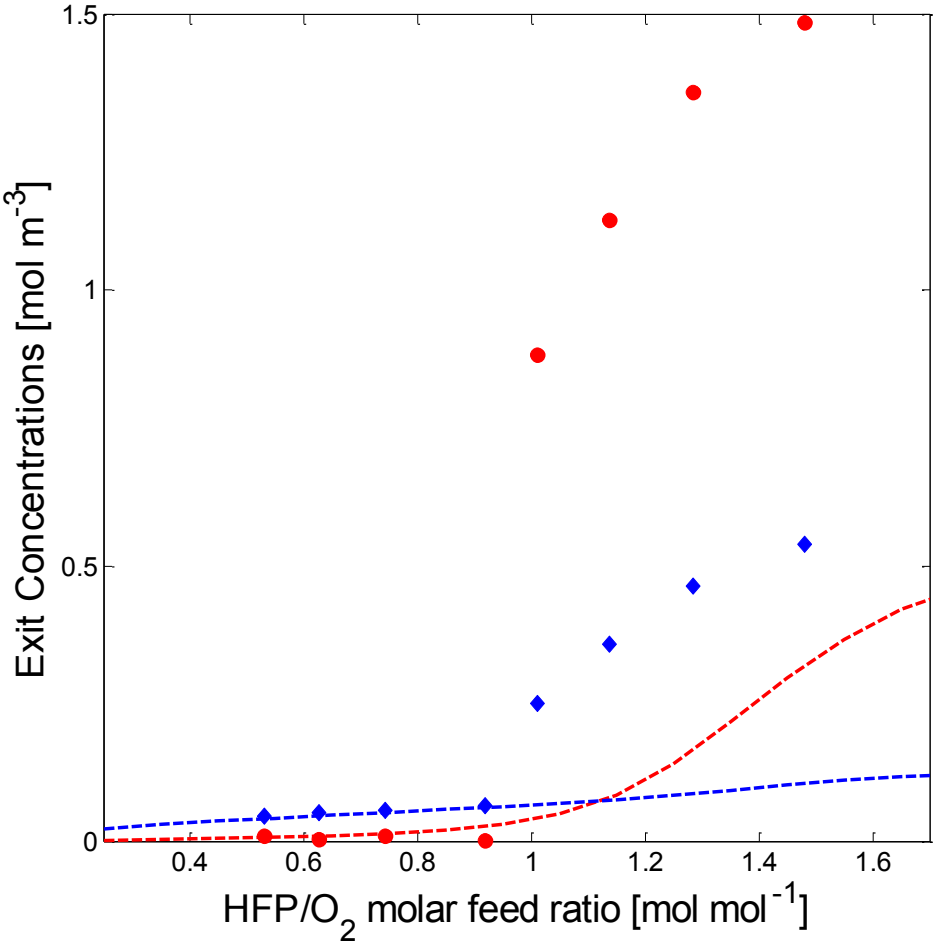

Figure 4.79. Effect of HFP/O_2 molar feed ratio on the exit concentration of C_2F_4 (●, experimental; ---, simulation) and *c*-C_3F_6 (◆, experimental; ---, simulation) at 493 K and a fixed space time (120 s).

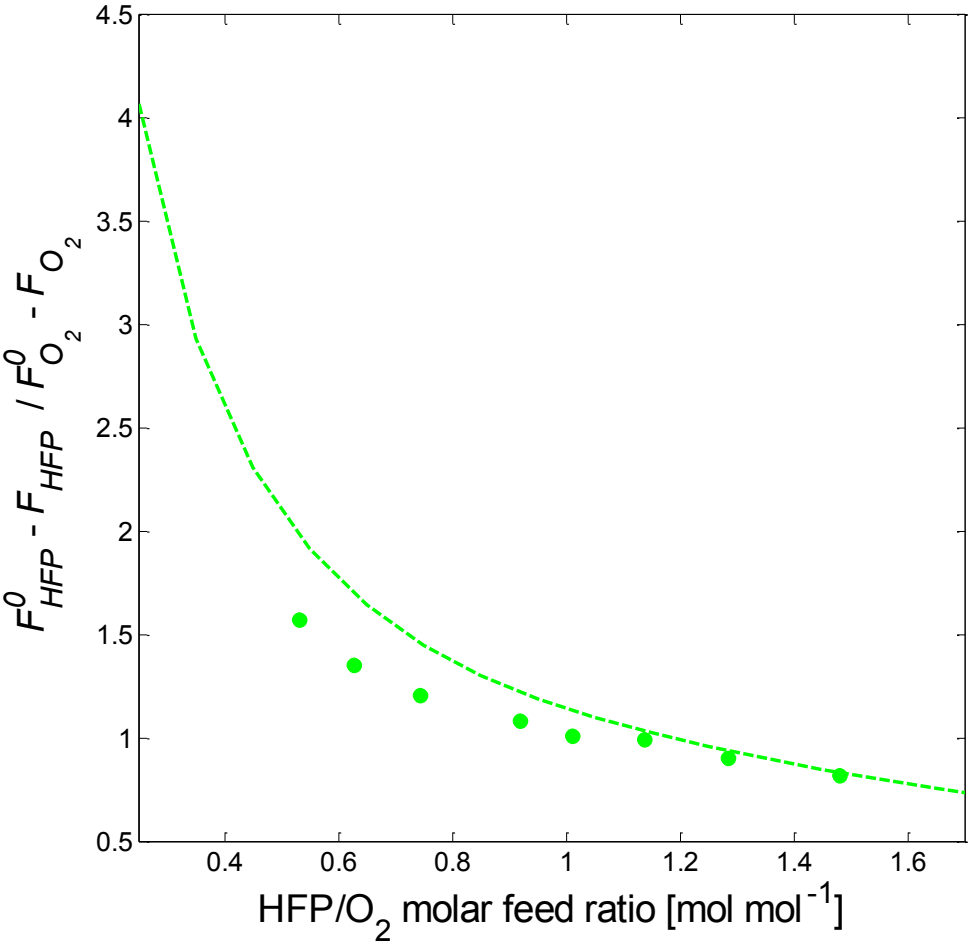

Figure 4.80. Effect of HFP/O_2 molar feed ratio on the HFP/O_2 consumption ratio (●, experimental; ---, simulation) at 493 K and a fixed space time (120 s).

4.2. Catalytic oxidation of HFP

4.2.1. Experimental design

The performances of four catalysts were tested for the epoxidation of HFP. Apart from the CuO/SiO_2 catalysts that were prepared, samples of 1 wt% Au/ZnO and Au/Al_2O_3 were obtained from Mintek South Africa for experimentation. For each of the oxidation catalysts, the influence of reaction temperature, HFP/O_2 molar feed ratio and weight-hourly-space-velocity (WHSV) on the product distribution, were investigated. The WHSV was defined as the total inlet mass flow-rate divided by the mass of the catalyst charge. The experimental design was accomplished by varying only a single factor at a time, whilst maintaining the other two at fixed values.

The Au/Al_2O_3 catalyst was studied under atmospheric pressure within a temperature range of 373-473 K using the 430mm long reactor tube. A HFP/O_2 molar feed ratio of 0.5-1 mol mol^{-1} was used, together with a WHSV between 1.37 h^{-1} and 4.07 h^{-1}. The Au/ ZnO catalyst was tested between 423 and 453 K, at a WHSV of 5.96 and 6.78 h^{-1} and with a HFP/O_2 molar feed ratio of 0.9-2.8 mol mol^{-1}.

Experimental tests on the un-doped CuO/SiO_2 and Cs promoted catalysts were performed between 453 and 493 K, with a HFP/O_2 molar feed ratio of 0.9-4.4 mol mol^{-1} and at a WHSV between 4.72 and 8.63 h^{-1}, using the straight reactor tube. The total operating pressure was maintained at 4.5 bar.

The performance of the $Cs\text{-}CuO/SiO_2$ catalyst was also evaluated using the coiled fixed-bed reactor tube, enabling a study of the reaction at WHSV values between 0.33 and 0.52 h^{-1}, at a reaction temperature of 453 K with HFP/O_2 molar feed ratios between 0.9 and 4.4 mol mol^{-1}. These experiments were also conducted under a total pressure of 4.5 bar.

4.2.2. Main experimental results and observations

The experimental results for 1 wt% Au/Al_2O_3 and Au/ZnO catalysts are presented in Tables 4.28 and 4.29, respectively. Both catalysts exhibited no activity for the epoxidation of HFP, although trace amounts of COF_2 and C_3F_8 were detected in the reactor product gas. Since C_3F_8 was not observed in any of the non-catalytic oxidation experiments carried out at similar reaction conditions, it was assumed that this component was produced through a catalytically induced reaction.

Table 4.28. Results of experiments using 1 wt% Au/Al_2O_3 catalyst for the epoxidation of HFP.

Set 1	Temp [K]	HFP/O_2 [mol mol^{-1}]	WHSV [h^{-1}]	X_{HFP} [%]	S_{HFPO} [%]	S_{COF2} [%]	S_{C3F8} [%]	Mass balance consistency [%]
Exp. 1	373	1.00	2.745	1.19	0.00	0.00	0.00	1.17
Exp. 2	398	1.00	2.745	1.75	0.00	0.00	0.00	1.89
Exp. 3	423	1.00	2.745	1.78	0.00	0.00	0.00	1.91
Exp. 4	423	0.51	2.751	0.39	0.00	0.00	0.00	1.57
Exp.5	423	1.50	2.751	1.71	0.00	0.00	0.00	1.70
Exp. 6	423	1.00	1.373	0.13	0.00	0.00	0.00	3.46
Exp. 7	423	1.00	4.073	1.56	0.00	0.00	0.00	0.13
Exp. 8	473	1.00	2.745	3.75	0.00	21.49	1.05	3.48

Table 4.29. Results of experiments using 1 wt% Au/ZnO catalyst for the epoxidation of HFP.

Set 1	Temp [K]	HFP/O_2 [mol mol^{-1}]	WHSV [h^{-1}]	X_{HFP} [%]	S_{HFPO} [%]	S_{COF2} [%]	S_{C3F8} [%]	Mass balance consistency [%]
Exp. 1	453	2.76	5.963	1.92	0.00	86.37	0.00	0.46
Exp. 2	473	2.76	5.963	2.53	0.00	57.75	5.70	0.46
Exp. 3	483	2.76	5.963	5.42	0.00	37.37	2.87	3.78
Exp. 4	483	0.90	6.789	5.09	0.00	35.37	1.52	2.79
Exp.5	493	0.90	6.789	5.28	0.00	59.15	1.40	1.46

Table 4.30. Results of experiments using 10 wt% CuO/SiO_2 catalyst for the epoxidation of HFP.

Set 1	**Temp [K]**	**HFP/O_2 [mol mol $^{-1}$]**	**WHSV [h^{-1}]**	**X_{HFP} [%]**	**S_{HFPO} [%]**	**S_{COF2} [%]**	**Mass balance consistency [%]**
Exp. 1	453	1.34	8.640	17.21	0.00	1.35	14.96
Exp. 2	473	1.34	8.640	21.73	0.00	2.09	19.31
Exp. 3	493	1.34	8.640	24.53	0.00	3.71	22.09
Exp. 4	493	0.86	5.415	26.35	0.00	2.48	22.57
Exp. 5	493	2.57	5.415	58.57	0.60	79.19	36.11
Exp. 6[a]	453	2.57	5.415	-	-	-	-
Set 2							
Exp. 1	453	2.43	7.024	19.84	0.00	2.41	18.03
Exp. 2	473	2.43	7.024	20.38	0.00	3.43	18.79
Exp. 3	493	2.43	7.024	25.33	0.00	0.18	24.09
Exp. 4	473	2.58	7.340	23.24	0.00	3.27	22.24
Exp. 5	493	2.58	7.340	62.75	0.68	98.95	34.87
Exp. 6[a]	473	2.58	7.340	-	-	-	-

[a] Thermal runaway occurred.

The experimental results for 10 wt% CuO/SiO_2 and Cs-CuO/SiO_2 catalysts are presented in Tables 4.30 and 4.31, respectively. The predominant product was COF_2. Significant thermal events were observed for both catalysts at the end of each set of experiments that were performed. In all cases, the bed temperature was found to rapidly rise to over 750 K immediately after final adjustments of the reaction temperature were made. For the CuO/SiO_2 catalyst this behaviour was twice observed when decreasing the reaction temperature from 493 K. For the Cs-CuO/SiO_2 catalyst, thermal runaway occurred when decreasing the reaction temperature from 483 K and 473 K. In such instances, the feed to the reactor was immediately shut off for safety reasons and the reaction was quenched under a stream of dry nitrogen. After discharging, the colour of the CuO/SiO_2 catalyst had changed from black to deep red-brown and the particles were visually smaller. The reactor exit line was also filled with a green deposit. The Cs-CuO/SiO_2 catalyst on the other hand retained much of its original size and colour and no deposit was found in the reactor exit line.

Table 4.31. Results of experiments using 10 wt% Cs-CuO/SiO_2 catalyst for the epoxidation of HFP.

Set 1	**Temp [K]**	**HFP/O_2 [mol mol $^{-1}$]**	**WHSV [h^{-1}]**	**X_{HFP} [%]**	**S_{HFPO} [%]**	**S_{COF2} [%]**	**Mass balance consistency [%]**
Exp. 1	423	2.76	5.963	10.56	0.00	1.38	9.74
Exp. 2	453	2.76	5.963	10.40	0.00	4.72	9.75
Exp. 3	473	2.76	5.963	12.37	0.00	11.11	11.47
Exp. 4	483	2.76	5.963	12.06	22.88	14.68	8.75
Exp. 5[a]	473	2.76	5.963	-	-	-	-
Set 2							
Exp. 1	453	3.49	6.256	11.41	0.00	2.45	11.41
Exp. 2	463	3.49	6.256	12.45	0.00	6.03	11.78
Exp. 3	473	3.49	6.256	12.62	0.00	3.67	11.80
Exp. 4	473	4.44	4.725	13.71	0.00	3.54	12.94
Exp. 5[a]	463	4.44	4.725	-	-	-	-

[a] Thermal runaway occurred.

Table 4.32 shows the results of experiments conducted using the Cs-CuO/SiO_2 catalyst in the coil-type fixed-bed reactor. Through the use of lower WHSV values, higher conversion of HFP and yield of HFPO was achieved at a reaction temperature of 453 K.

Table 4.32. Results of experiments using 10 wt% Cs-CuO/SiO_2 catalyst in the coil-type fixed-bed reactor for the epoxidation of HFP.

Set 1	**Temp [K]**	**HFP/O_2 [mol mol $^{-1}$]**	**WHSV [h^{-1}]**	**X_{HFP} [%]**	**S_{HFPO} [%]**	**S_{COF2} [%]**	**Mass balance consistency [%]**
Exp. 1	423	2.68	0.524	12.76	0.00	12.66	10.40
Exp. 2	453	2.68	0.524	14.59	16.51	23.78	10.50
Exp. 3	453	0.90	0.485	10.45	33.73	28.33	6.27
Exp. 4	453	4.44	0.337	17.44	27.54	19.12	9.45
Exp. 5	453	0.86	0.387	5.75	85.88	51.87	0.91

The measured BET surface areas of the copper-based catalysts tested for the epoxidation of HFP are shown in Table 4.33.

Table 4.33. BET surface areas of copper-based HFP epoxidation catalysts.

Catalyst	**BET surface area [m^2 g^{-1}]**
10 wt% CuO/SiO_2	285
10 wt% Cs-CuO/SiO_2	283

Chapter 5
Discussion

5.1. Non-catalytic oxidation of HFP

The gas-phase, non-catalytic oxidation of HFP, carried out at a relatively low pressure of 4.5 bar and space time values between 60-180 seconds, required reaction temperatures in excess of 453 K. This was above the decomposition temperature of HFPO. Higher operating pressures may have facilitated the use of lower reaction temperatures, favouring the formation of the epoxide. Industrial experience has shown, however, that the operational risk associated with high-pressure processes is generally greater (Furin, 2006). This may be explained in terms of the reaction mechanism. The oxidation of HFP, although modelled in this work using simplified rate expressions in accordance with the mass-action law, is actually a complex chain process involving initiation, branching and termination steps (Dos Santos Afonso et al., 2000). In a radical chain reaction scheme there exists a competition for radicals or chain carriers between the branching and termination steps. If the propagation steps produce more chain carriers than the termination steps consume, the reaction can become self-accelerating. The population of the chain carriers grows exponentially and a detonation occurs (Helfferich, 2001). For the HFP-O_2 system this sequence of events is more likely to occur at higher pressures. This is the reason why operation at lower pressures is preferred.

The response surface methodology developed and applied in Chapter 4 was found to be adequate for predicting optimal operating conditions with regard to HFPO selectivity and yield. A fortunate result of the single response optimization was that the independently optimized operating conditions for selectivity and yield towards HFPO were very close. This meant that neither response was heavily penalized when the multi-response optimization was carried out.

The optimum operating conditions for the selectivity and yield toward HFPO, as reported in section 4.1.4, are specific to the reactor configuration used in this work. Three strategies are available for scale-up of a tubular reactor of this nature, *viz*. scale-up in parallel (reactor tubes are used in parallel to increase throughput), scale-up in series (the reactor tube is made longer) and scale-up with geometric similarity (the aspect ratio is held constant whilst making the dimensions larger). In all cases, for the same product quality in the small and large reactor, the feed composition, temperature and space time must be kept constant. The number of tubes (N_{tubes}), tube radius (R) and the tube

length (L) may all change upon scale-up. The following scale-up factor is thus defined (Nauman, 2002):

$$S = \frac{(N_{tubes})_2 R_2^2 L_2}{(N_{tubes})_1 R_1^2 L_1} \tag{5.1}$$

The scale-up of an isothermal laminar flow reactor using geometric similarity is not recommended if radial concentration gradients are negligible due to relatively high radial diffusion. For small diameter tubes with a large amount of radial diffusion the performance approaches that of a plug-flow reactor, a condition that is negated when moving to a larger tube. The reactor may also become adiabatic if the scale-up factor is large, since the surface area for heat transfer rises slower than the overall heat transfer coefficient and the heat generation (Nauman, 2002). Series scale-up in this system is also not recommended since the pressure drop across the tube increases by a factor of S^2 (Nauman, 2002). Scale-up in parallel though gives an exact duplication of reaction conditions and may be the best option for this system.

The deficiencies in the gas-phase atomic balances, the observed changes in the conversion of HFP and selectivity towards HFPO, at the same set of operating conditions, after an extended period of time, as well as the presence of the highly viscous, black deposit on the inner walls of the reactor exit piping and the catch-pot, all appear to confirm the formation of some oligomeric oxidation by-products. It would seem that the oligomers produced are retained on the inner surface of the reactor tube. HFP and O_2 entering the reactor continuously add to this film, which would imply that the monomer is being consumed in a competitive reaction, leading to an increase in the conversion of the reactants but a decrease in the selectivity towards HFPO. The following are the types of oligomers that were suggested to be produced at high temperature in the gas-phase (Kartsov et al., 1978):

$CF_3O(CF_2O)_nCF_2OCF_2COF$

$CF_3O(CF_2O)_nCF_2OCOF$

$CF_3O(CF_2O)_mCF_2COF$

$CF_3O(CF_2O)_mOCF_2COF$

$CF_3O(CF_2O)_mCOF$

$CF_3O(CF_2O)_nCOF$

HFP units were not detected in these oligomers by Kartsov et al. (1978), suggesting that the monomer does not add directly to the oligomer chain but has to go through the usual transformation to peroxy and alkoxy radicals as given by the mechanism of Shapovalov (1984) and even by the simple biradical scheme of Gilbert et al. (1978). It is possible that the thermal decomposition of HFPO can also result in the formation of the oligomer film. Sargeant (1970) and Kennedy and Levy (1976) both reported the formation of a small amount of difluorocarbene polymer during the pyrolysis of HFPO, although most of the difluorocarbene decomposition product was consumed in the production of C_2F_4 and *c*-C_3F_6. It is possible that such a polymer could form a film on the reactor inner wall which could also undergo chain extension via radical units evolving from the interaction of HFP and O_2. These events could be implicated in the high-temperature pre-treatment of the reactor walls, as recommended by NECSA researchers (Posma, 2009).

The performance of the coiled laminar-flow reactor used in this investigation was well approximated by a simple plug flow reactor model, as a result of the flattening of the radial concentration profile through extensive radial diffusion. Importantly, the PFR model was able to account for the non-equimolarity of the oxidation process, whereas the original LFR model which neglected the momentum balance did not. It was not possible to make a direct comparison between the identified kinetic parameters obtained from the LFR and PFR models, since different optimum reaction orders were used in each. It was observed, however, that the temperature dependence of all the rate constants obtained using the PFR model adhered to the usual physiochemical constraints, i.e. they increased with increasing temperature. Using the LFR model however, the activation energies of reaction 7b and the reverse step of reaction 1 were found to be negative. It was concluded that the rate parameters obtained using the PFR model gave a better overall representation of the HFP oxidation kinetics.

Very little kinetic data regarding the gas-phase oxidation of HFP are available in the literature. Among the fitted parameters, only the activation energy for the oxidation of C_2F_4 (reaction 6) was given previously by Douglass et al. (1999), based on the work of Umemoto et al. (1985). The estimated value in this work was found to be 10.21 kJ mol^{-1}, compared with a value of 5.27 kJ mol^{-1} reported by Umemoto et al. (1985).

The activation energy for the formation of the acid fluorides (reaction 2, 407.24 kJ mol^{-1}) was found to be 34 kJ mol^{-1} higher than that for the formation of HFPO (reaction 1, 373.05 kJ mol^{-1}) which indicates that a higher reaction temperature favours the direct oxidation of HFP to the by-products.

The difference between the activation energies for the forward and reverse steps of reaction 1 was found to be about 370 kJ mol^{-1}. Theoretically this should have been equal to the standard heat of reaction. Based on the heats of formation for HFP and HFPO given in section 4.3.1.2, the standard heat of reaction 1 was estimated to be 49.24 kJ mol^{-1}. There is a discrepancy of about 321 kJ mol^{-1}. It must be noted, however, that both heats of formation used in the above calculation were obtained from theoretical computations. An early experimental determination of the heat of formation of HFP places the figure at -1080 kJ mol^{-1} (Duss, 1955). The heat of formation of HFPO, calculated from the measured reaction enthalpy for the pyrolysis of the epoxide (Lau et al., 2000), is closer to -1300 kJ mol^{-1}, which would give 220 kJ mol^{-1} as the standard heat of reaction 1. With such conjecture surrounding the actual values for the heats of formation of both HFP and HFPO, it is difficult to completely dismiss the kinetic parameters identified in this work.

None of the 95% confidence intervals, obtained from the fitting algorithm, included a zero value for any of the rate constants that were identified in the preceding section, indicating that all reactions were necessary for the full description of the non-catalytic oxidation process. For a proper model, the distribution of residuals should have been random. Trends observed in the residual analysis usually indicate some incompatibility of the rate expression with the experimental data (Wojciechowski and Rice, 2003). The proposed kinetic model accounted satisfactorily for the consumption of HFP and O_2 as well as the formation of HFPO. Trends in the residual distributions of other species were observed. The amount of COF_2 in the product gas was consistently over-predicted by the model. It is possible that the stoichiometry assumed for reaction 7b does not correctly reflect the kinetics for the dissociation of CF_3COF in the presence of oxygen. Perhaps the radicals that are formed in the first step are not entirely consumed through oxidation to form COF_2, but enter the oligomerization scheme mentioned earlier. This would explain why the simulation gave higher than expected COF_2 exit molar flow-rates. The fitting procedure was also repeated using reaction 7c in place of reaction 7b (cf. section 4.1.5.1), where the former assumes no oxidation step is involved and difluorocarbene is produced. The results were totally unsatisfactory, however, and were not presented in this thesis. The model was able to provide reasonable agreement with the experimental data for C_2F_4 and *c*-C_3F_6 at 463 and 478 K, but deviated at 493 K.

5.2. Catalytic oxidation of HFP

The poor performance of the 1 wt% Au/Al_2O_3 and Au/ZnO catalysts may be due to the low loading of the active component on the catalyst support, which would imply an insufficient number of active sites to induce oxidation of the fluoro-olefin at the reaction conditions considered.

Regarding the experiments performed using the 10 wt% CuO/SiO_2 catalyst, the green deposit found in the reactor exit line was most probably copper (II) fluoride. Hydroxyl groups present on the surface of the support may have interacted with HFP or COF_2 to give HF, which in turn formed the copper fluoride upon reaction with the active component of the catalyst or the inner wall of the copper reactor tube. Copper fluoride was not found in the exit lines when the caesium-promoted catalyst was used, since ion exchange on the catalyst surface during preparation eliminated most of the original hydroxyl groups. The physical loss of solid material from the CuO/SiO_2 catalyst may also be attributed to the interaction of HF with the silica support, giving volatile SiF_4 according to (Ohtani et al., 1990):

$$SiO_2 + 4\ HF \rightarrow SiF_4 + 2\ H_2O \qquad (5.2)$$

The analytical system was not configured to detect this inorganic fluoride, however. Low selectivities towards detectable gas-phase products were obtained, yet appreciable consumption of HFP was reported for the CuO/SiO_2 catalyst. The mass balance consistency, defined as the percent relative error between inlet and outlet total mass flow-rates, was also poor for these sets of experiments. All these facts supported the notion that the fluorine introduced into the system through the perfluorinated olefin was ultimately consumed in the formation of copper fluoride and SiF_4. Practically no HFPO was produced, which was unexpected since a review of the patent literature had revealed that Castellan (1992) had generated the epoxide in 14.6% yield with a HFP conversion of 19.2%, using a CuO/SiO_2 catalyst at similar reaction conditions (cf Table 2.9, section 2.3.1). Notable differences between that study and the current work were that the loading of the copper precursor on the surface of the catalyst used by Castellan (1992) was 6.4 wt% and that the catalyst was pre-treated with a dilute mixture of HF in N_2. No explanation was given by the patent author as to why this activation step was necessary, although it may be suggested now that some form of surface passivation occurred.

Although the HFP conversions obtained with the Cs-CuO/SiO_2 catalyst were lower than those obtained with the CuO/SiO_2 catalyst, the oxidation activity of the former was more pronounced, resulting in higher yields of COF_2 as well as HFPO. If the catalytic oxidation proceeded through a Mars-van-Krevelen redox cycle, this result may have been due to the enhancement of the redox ability of the metal oxide catalyst through caesium promotion (Xue et al., 2009). Alternatively, a reduced loss of surface area through catalyst degradation may have resulted in improved catalytic oxidation activity. Whatever the actual effect of caesium was, its' addition was clearly beneficial.

The thermal runaway observed in the fixed-bed reactor at specific reaction conditions may have been due to a phenomenon called "wrong-way response" (Arnold and Sundaresan, 1989). A sudden decrease in the temperature at the entrance to the bed, brought about in this system by a step change in the jacket temperature coupled with a continuous stream of cold feed-gas, can result in reactant concentration increases in the upstream section of the reactor and the generation of a transient temperature rise in the down-stream portion. This response is caused by the difference in the propagation speed of the concentration and temperature disturbances in the reactor (Luss, 1997). If the reactor attains multiple steady-states, this transient temperature rise may lead to ignition and shift the reactor permanently to a high temperature steady-state (Il'in and Luss, 1993). In doing so, the wrong-way behaviour may initiate undesired, highly exothermic reactions which can lead to thermal runaway (Luss, 1997).

The study of the caesium-promoted catalyst was extended by investigating the oxidation reaction at 453 K but with a lower WHSV to boost the conversion of HFP. Lower feed flow-rates could not be realized in the system due to the physical limitations of the mass-flow controllers, so a longer, coiled reactor tube packed with a larger amount of catalyst was used to manipulate the WHSV. Using a HFP/O_2 molar feed ratio of 0.86 and a WHSV of 0.387, a HFPO selectivity of 85.88% was obtained, which was considerably greater than what was achieved in the non-catalytic system described in Chapter 4. This high selectivity was obtained at a HFP conversion of only 5.75%, but given the recent advances in the separation of HFP/HFPO mixtures (e.g. Ramjugernath, et al., 2010) such a result may be regarded as satisfactory for recycle reactor configurations. The caesium-promoted catalyst shows promise but requires optimization in terms of catalyst loading, calcination temperature and time.

Chapter 6
Conclusions and recommendations

6.1. Non-catalytic oxidation of HFP

The research presented in this thesis addressed the goal of developing a process for the direct gas-phase epoxidation of HFP using molecular oxygen. Both non-catalytic and catalytic routes were considered. The feasible range of operating conditions for the non-catalytic, gas-phase process was identified through a series of preliminary experiments. To avoid detonation, moderate operating pressures had to be used. 4.5 bar was found to be the minimum pressure at which an acceptable level of HFP conversion was achieved. At this pressure, the process could be carried out at a temperature between 453 - 493 K, with a HFP/O_2 molar feed ratio between 0.5 and 2 and space time values of 60 to 180 seconds. The operating conditions were optimized independently for the HFPO selectivity and yield using quadratic response surface methodology. A maximum HFPO selectivity of 55.81% was identified at 478.2 K, a HFP/O_2 molar feed ratio of 1.34 mol mol^{-1} and a space time of 113 seconds. An optimum HFPO yield of 40.10% was identified at 483.2 K, a HFP/O_2 molar feed ratio of 1.16 mol mol^{-1} and a space time of 121 seconds.

In assessing the feasibility of the proposed non-catalytic process it was necessary to compare the optimal HFPO selectivity and yield obtained in this work to that achieved using currently utilized industrial methods. The maximum combined HFPO selectivity and yield, obtained in this work using multi-response optimization techniques, was 56% and 40%, respectively. This was achieved at 480 K, with a HFP/O_2 molar feed ratio of 1.21 and a space time of 118 seconds. It represented the best trade-off between the two performance criteria. In comparison, the epoxidation of HFP with hydrogen peroxide, the most popular commercial method of producing HFPO, gives an epoxide yield of about 55% (Millauer et al., 1985). This process is carried out batch-wise, however, so it lacks the potential throughput of the proposed continuous process, and the high cost of the oxidizer continues to be a disadvantage even after four decades of commercial application. A relatively high HFPO yield of 70% can be obtained using a high-pressure, thermally-initiated, radical-based process (Millauer et al., 1985). The latter is usually carried out in the presence of an organic solvent, however, which may result in large quantities of waste. The oxidation of HFP under elevated operating pressures can also proceed explosively, and it is because of these two disadvantages that this process is usually considered unfavourable (Furin, 2006).

A kinetic model for the non-catalytic, gas-phase oxidation of HFP was developed based on the biradical mechanism of Gilbert et al. (1976). The parameters of the various rate expressions were estimated by nonlinear regression techniques, minimizing the weighted sum of squares of the residuals. The reactor was originally modelled as a laminar flow reactor with radial diffusion. A parabolic velocity profile was also assumed. Since, for the sake of simplicity, the momentum balance was neglected, this model did not account for the non-equimolarity of the oxidation process. The fitting procedure gave an anomalous temperature dependence of the rate constants for the reverse step of reaction 1 and reaction 7b. It was found that the radial concentration profile predicted by the laminar flow reactor model was quite uniform, a consequence of the relatively large amount of radial diffusion and a high length-to-diameter ratio for the reactor. In the real coiled reactor tube this result would have also been brought about by secondary flow induced by inertial forces. The performance of the long and extremely narrow laminar flow reactor closely approached that of a plug flow reactor. Fitting of the experimental data using a plug flow reactor model gave physiochemically consistent results for the kinetic parameters. The key advantage of the plug flow reactor model over the laminar flow reactor model was that the former explicitly accounted for the reaction non-equimolarity. This was important since the measured relative change in the molar flow-rate due to reaction was found to be as much as 30%.

6.2. Catalytic oxidation of HFP

In this work, 10 wt% CuO/SiO_2 was tested as a potential HFP epoxidation catalyst. It was selected based on its proven ability to catalyze the partial oxidation of both hydrocarbons (Gates et al., 1979) as well as perfluorocarbons (Cavanaugh, 1973; Atkins, 1973). In its original form, the catalyst was found to be ineffective, though, undergoing decomposition to copper fluoride and SiF_4 in the presence of HF, which evolved from the interaction of reactive species with surface hydroxyl groups. The addition of a small amount of caesium stabilized the catalyst and resulted in improved selectivity towards HFPO. At a relatively low reaction temperature of 453 K, HFP conversions between 5.75% and 17.44% were obtained. A high HFPO selectivity of 85.88% was obtained at a HFP/O_2 molar feed ratio of 0.86 and a WHSV of 0.337 h^{-1}. It appeared that the best selectivity towards HFPO could be achieved using close to an equimolar mixture of HFP and oxygen. The amount of experimental work carried out using the caesium-doped catalyst was minimal, however, and optimal reaction conditions could not be clearly identified.

6.3. General remarks regarding the gas-phase HFP oxidation process

Copper, as the material of construction for the reactor tube, offered several advantages over stainless steel, including having a higher thermal conductivity for heat transfer and a considerably lower cost. The greater ductility of copper also meant that the tubing was easier to bend and form into the required helical coil shape for the non-catalytic study. Most importantly, the copper surface exhibited no activity for the isomerisation of HFPO to HFA. On the other hand, previous studies have shown that stainless steel strongly catalyzes the decomposition, isomerization and polymerization of HFP and HFPO (Kartsov et al., 1975; Kartsov et al., 1978).

The caustic scrubber used for the treatment of the reactor effluent in this work was not found to be cost effective, since the scrubber solution had to be frequently replaced. For commercial application, alternatives such as low-temperature distillation or membrane separation would have to be considered, since these unit operations require no chemical reagents and produce less waste. Since these processes are also non-destructive, carbonyl fluoride and trifluoroacetyl fluoride, the major by-products of HFP oxidation, can be recovered and marketed for use in SiO_2 etching processes.

An investigation carried out by Shapovalov (2000 b) regarding the effect of reaction temperature on the yield of oligomers obtained from the photo-initiated, low-temperature, liquid-phase oxidation of HFP showed that lower reaction temperatures favoured the formation of the high-molecular weight moieties. It would appear that the oligomerization of HFP cannot be completely suppressed even during high temperature, non-catalytic oxidation. It is not clear at this stage whether the copper reactor surface used in this work catalyzed the oligomerization. Unfortunately, the polymerized products could not be analyzed by conventional means. Special F^{19} NMR measurements, which were unavailable at the time, would have been required to determine the molecular structure. Dismantling of the reactor assembly would have also been required to obtain the necessary samples for analysis.

6.4. Recommendations

As a refinement of the laminar flow reactor model used in this work, the simultaneous solution of the material and momentum balances, to account for the reaction non-equimolarity, could be considered. The use of an adaptive grid, with smaller grid spacing near the wall could also be used, since the stability of the solution is usually weakest where the velocity approaches zero (Nauman, 2002). At the highest level of model hierarchy, laminar flow through a coiled tube with secondary flow can also be considered. Ultimately though, these types of complex models would offer little improvement in the identified kinetic parameters, since the reactor performance is adequately represented by the simple plug flow reactor model. Of greater importance is the generation of replicate experimental data, such that the weighted least squares minimization can be properly defined using the variance of the measurements. The normalization factor used in this work is mathematically inferior.

It is proposed that a future study be dedicated to the analysis of the oligomeric products evolving from the high temperature, non-catalytic oxidation of HFP, since very little is known about the structure and properties of these substances. Consideration should also be given to alternative quantitative techniques for the analysis of the gaseous reactor products, other than gas-chromatography. This investigation highlighted some of the difficulties associated with the sampling of and calibration for several fluorocarbon species involved in the oxidation of HFP. In particular, the aggressive nature of the acyl fluoride by-products necessitated the use of special gas-chromatograph column materials and handling procedures. Infra-red spectrophotometry may provide a suitable alternative to gas-chromatography, especially for the analysis of these compounds (Croce and Castellano, 1988).

An analogy can be drawn between the development of the epoxidation process for HFP and that of propene. Most attempts to produce propylene oxide commercially by direct non-catalytic oxidation of propene have also proven to be unsuccessful (Weissermel and Arpe, 1997). At acceptable levels of conversion, the low selectivity and large number of by-products obtained using these processes make them unattractive. Chlorohydrin and indirect oxidation processes based on hydroperoxides, developed decades ago, dominate to this day. There is nevertheless a great urgency among the research community to develop a direct oxidation process employing molecular oxygen for the production of propylene oxide. The only break-through in recent years has been the development of a process employing a rare earth metal-oxide/SiO_2 catalyst suspended in acetone (Weissermel and

Arpe, 1997). It has been shown in the present work that a catalyst can vastly improve the selectivity of the relatively low-pressure, gas-phase HFP epoxidation reaction as well, from 55% to above 85%, and perhaps the evolution of this process must proceed with the catalyzed route. To this end, a more rigorous development of the caesium-doped CuO/SiO_2 catalyst should be carried out. It is suggested that initially a high-level, statistical experimental design be used to identify the optimal catalyst loading, calcination temperature and period. Experimental techniques similar to those presented in Chapter 4 can then be used to probe for optimal reaction conditions.

References

1. Agrawal, S. and Nigam, K.D.P., "Modelling of a coiled tubular chemical reactor", *Chemical Engineering Journal* **84** (2001) 437-444.
2. Alouche, A., "Preparation and characterization of copper and/or cerium catalysts supported on alumina or ceria", *Jordan Journal of Mechanical and Industrial Engineering* **2** (2008) 111-116.
3. Antony, J., "Design of experiments for engineers and scientists", Elsevier, Amsterdam, 2003.
4. Arce, V., dos Santos Afonso, M., Romano, R.M. and Czarnowski, J., "Thermal gas-phase oxidation of trifluorobromoethene, CF_2CFBr, initiated by NO_2", *Journal of the Argentine Chemical Society* **93** (2005) 123-136.
5. Arito, H. and Soda, R., "Pyrolysis products of polytetrafluoroethylene and polyfluoroethylene with reference to inhalation toxicity", *Annals of Occupational Hygiene* **20** (1977) 247-255.
6. Atkinson, B. and McKeagan, D., "The thermal decomposition of perfluorocyclopropane", *Chemical Communications* **7** (1966) 189-190.
7. Arnold, E.W., III and Sundaresan, S., "Dynamics of packed-bed reactors loaded with oxide catalysts", *AIChE Journal* **5** (1989) 746-754.
8. Aslindi, E.B., Zarubin, V.T. and Turishchev, Y.S., "The investigation of dissociation of trifluoroacetyl fluoride in the field of pulsed CO_2 laser", *Laser Chemistry* **6** (1986) 373-380.
9. Bednarek, G., Argüello, G.A. and Zellner, R., "FTIR-Spectroscopic study of reactions of FCO and FC(O)OO radicals in the presence of O_2 and NO_2", *Berichte der Bunsen-Gesellschaft für Physikalische Chemie* **100** (1996) 445-454.
10. Bevinton, P. and Robinson, D.K., "Data reduction and error analysis for the physical sciences", McGraw-Hill, New York, 2002.
11. Bierbrauer, K.L., Chiappero, M.S., Malanca, F.E. and Argüello, G.A., "Photochemistry of perfluoroacetyl fluoride. Kinetics of the reaction between CF_3 and FCO radicals", *Journal of Photochemistry and Photobiology A: Chemistry* **122** (1999) 73-78.
12. Blades, A.T., "The flame ionization detector", *Journal of Chromatographic Science* **11** (1973) 251-255.
13. Burcat, A. and Ruscic, B., "Third millennium ideal gas and condensed phase thermochemical database for combustion with updates from active thermochemical tables", ANL-05/20 and TAE 960, Technion-IIT, Aerospace Engineering and Argonne National Laboratory, Chemistr Division, September, 2005.

14. Batey, W. and Trenwith, A.B., "The thermal decomposition of hexafluoroacetone", *Journal of the Chemical Society* (1961) 1388-1392.
15. Blades, A.T., "Response of the flame ionization detector to fluoro-alkanes", *Journal of Chromatographic Science* **11** (1973) 267-269.
16. Bird, R.B., Stewart, W.E. and Lightfoot, E.N., "Transport phenomena", 2nd Edition, John Wiley and Sons, Inc., New York, 2002.
17. Box, G.E.P. and Lucas, H.L., "Design of experiments in nonlinear situations", *Biometrica* **46** (1959) 77-90.
18. Bright, R.N. and Matula, R.A., "Gas chromatographic separation of low molecular weight fluorocarbons", *Journal of Chromatography* **35** (1968) 217-222.
19. Brown, H.C., "Thermal reactions of perfluorobutyne-2 and perfluoropropene", *Journal of Organic Chemistry* **22** (1957) 1256-1257.
20. Bulushev, D.A., Kiwi-Minsker, L., Zaikovskii, V.I., Lapina, O.B., Ivanov, A.A., Reshetnikov, S.I. and Renken, A., "Effect of potassium doping on the structural and catalytic properties of V/Ti-oxide in selective toluene oxidation", *Applied Catalysis A: General* **202** (2000) 243-250.
21. Buzzi-Ferraris, G. and Manenti, F., "Kinetic model analysis", *Chemical Engineering Science* **64** (2009) 1061-1074.
22. Carlson, D.P., "Method of preparation of halogenated epoxides", US patent 3,536,733 (1970).
23. Carter, E.A. and Goddard, W.A., III, "Chemisorption of oxygen, chlorine, hydrogen, hydroxide and ethylene on silver clusters: a model for the olefin epoxidation reaction", *Surface Science* **209** (1989) 243-289.
24. Castellan, A., Gregorio, G. and Padovan, M., "Process for oxidizing fluorinated olefins and catalysts useful for the purpose", US patent 5,120,866 (1992).
25. Cavanaugh, R.J., "Epoxidation of hexafluoropropylene", US patent 3,755,438 (1973).
26. Chase, M.W., Jr., "NIST-JANAF Thermochemical tables, 4th Edition", *Journal of Physical Chemisty Reference Data*, Monograph 9 (1998) 1-1951.
27. Choudhary, V.R., Jha, R., Chaudhari, N.K. and Jana, P., "Supported copper oxide as a highly active/selective catalyst for the epoxidation of styrene by TBHP to styrene oxide", *Catalysis Communications* **8** (2007) 1556-1560.
28. Chowdhury, P.K., Pola, J., Rama Rao K.V.S. and Mittal, J.P., "TEA CO_2 laser driven oxidation of tetrafluoroethene and decafluorocyclopentane with molecular oxygen. Evidence for the dioxetane mechanism", *Chemical Physics Letters* **142** (1987) 252-254.

29. Clayton, J.W., "Toxicology of the fluoroalkenes: review and research needs", *Environmental Health Perspectives* **21** (1977) 255-267.
30. Cleland, F.A. and Wilhelm, R.H., "Diffusion and reaction in viscous-flow tubular reactor", *AIChE Journal* **2** (1956) 489-497.
31. Cohen, N. and Heicklen, J., "Mercury-sensitized photolysis of C_2F_4", *The Journal of Chemical Physics* **43** (1965) 871-873.
32. Coleman, T.F. and Li, Y., "An interior, trust region approach for nonlinear minimization subject to bounds", *SIAM Journal of Optimization* **6** (1996) 418-445.
33. Cordischi, D., Lenzi, M., Mele, A., "Kinetics of the oxidation of tetrafluoroethylene by molecular oxygen", *Transactions of the Faraday Society* **60** (1964) 2047-2053.
34. Cramer, C.J. and Hillmyer, M.A., "Perfluorocarbenes produced by thermal cracking. Barriers to generation and rearrangement", *Journal of Organic Chemistry* **64** (1999) 4850-4859.
35. Croce, A.E. and Castellano, E., "Carbonyl fluoride infrared spectrophotometric determination", *Journal of Fluorine Chemistry* **44** (1989) 267-273.
36. Cropley, R.L., Williams, F.J., Vaughan, O.P.H., Urquhart, A.J., Tikhov, M.S. and Lambert, R.M., "Copper is highly effective for the epoxidation of a "difficult" alkene, whereas silver is not", *Surface Science* **578** (2005) L85-L88.
37. Cuadros-Rodríguez, L., Bagur-González, M.G., Sánchez-Viñas, M., González-Casado, A. and Gómez-Sáez, A.M., "Principles of analytical calibration/quantification for the separation sciences", *Journal of Chromatography: A* **1158** (2007) 33-46.
38. Culbertson, J.A., Prins, J.M. and Grimsrud, E.P., "Improvements in the detection and analysis of CF_3-containing compounds in the background atmosphere by gas chromatography- high-resolution mass spectrometry", *Journal of Chromatography A* **903** (2000) 261-265.
39. Curtiss, L.A. and Raghavachari, K., "Gaussian-3 and related methods for accurate thermochemistry", *Theoretical Chemistry Accounts* **108** (2002) 61-70.
40. Curtiss, L.A., Redfern, P.C. and Raghavachari, K., "Gaussian-4 theory", *The Journal of Chemical Physics* **126** (2007) 084108.
41. Cussler, E.L., "Multicomponent Diffusion", Elsevier, Amsterdam, 1976.
42. Dalby, F.W., "Flash photolysis measurement of the kinetics of CF_2 reactions", *The Journal of Chemical Physics* **41** (1964) 2297-2303.
43. Dang, V. and Steinberg, M., "Laminar flow mass transfer with axial diffusion in a tube with chemical reaction", *Chemical Engineering Science* **32** (1977) 326-328.

44. Dawson J.P., Pingitore, M.A. and Ritter, E.R., "Experimental and computational study of gas-phase oxidation of hexafluoropropylene with molecular oxygen", *Proceedings of the technical meeting of the eastern states section of the combustion institute* (2003) 177-180.
45. Doskocil, E.J. and Mueller, G.M., "Role of Cs promotion of Ag/AlOOH catalysts for the epoxidation of 1,3-butadiene: effects on surface acidity and basicity", *Journal of Catalysis* **234** (2005) 143-150.
46. Dos Santos Afonso, M., Romano, R.M., della Védova, C.O. and Czarnowski, J., "Kinetics and mechanism of the thermal gas-phase oxidation of hexafluoropropene in the presence of trifluoromethylhypofluorite, CF_3OF", *Physical Chemistry Chemical Physics* **2** (2000) 1393-1399.
47. Douglass, C.H., Ladouceur, H.D., Shamamian, V.A. and McDonald, J.R., "Combustion chemistry in premixed C_2F_4-O_2 flames", *Combustion and Flame* **100** (1995) 529-542.
48. Duss, H.C., "Thermochemical studies on fluorocarbons" *Industrial and Engineering Chemistry* **47** (1955) 1445-1449.
49. Ebnesajjad, S., "Fluoropolymers", in "Encyclopedia of chemical processing", Taylor and Francis, New York, 2006, pp. 1031-1041.
50. Edwards, J.W. and Small, P.A., "Pyrolysis of chlorodifluoromethane and the heat of formation of chlorodifluoromethane and difluoromethylene", *Nature* **202** (1964) 1329.
51. Eleuterio, H.S., "Fluorocarbon epoxides", US patent 3,358,003 (1967).
52. Fagley, J.C., Jr., "Simulation of transport in laminar, tubular reactors and application to ethane pyrolysis", *Industrial and Engineering Chemistry Research* **31** (1992) 58-69.
53. Fan, J. and Yates, J.T, Jr., "Infrared study of the oxidation of hexafluoropropene on TiO_2", *Journal of Physical Chemistry* **98** (1994) 10621-10627.
54. Farris, M.M., Klinghoffer, A.A., Rossin, J.A. and Tevault, D.E., "Deactivation of a Pt/Al_2O_3 catalysts during the oxidation of hexafluoropropylene", *Catalysis Today* **11** (1992) 501-516.
55. Faucitano, A., Buttafava, A., Comincioli, V., Marchionni, G. and de Pasquale, R.J., "Kinetic modelling of the low-temperature photo-oxidation of hexafluoropropene", *Journal of Physical Organic Chemistry* **4** (1991) 293-300.
56. Fikry, F.A., Gibson, E.K., Jr., Bafus, D.A., "Analysis of low molecular weight perfluoroalkanes by gas chromatography with helium ionization detection", *Analytical Chemistry* **52** (1980) 1377-1379.
57. Francisco, J.S., "Dissociation dynamics of $CF_3C(O)X$ compounds (where X=H, F and Cl)", *Chemical Physics* **163** (1992) 27-36.

58. Froment, G., "Model discrimination and parameter estimation in heterogeneous catalysis", *AIChE Journal* **21** (1975) 1041-1057.
59. Furin, G.G., "Synthesis of 2,3-epoxyperfluoroalkanes by means of oxidation of fluorine-containing olefins", *Chemistry for Sustainable Development* **14** (2006) 97-110.
60. Gates, B.C., Katzer, J.R. and Schuit, G.C.A., "Chemistry of catalytic processes", McGraw-Hill, New York, 1979.
61. Gilbert, J.R., Slagle, I.R., Graham, R.E. and Gutman, D., "Direct identification of reactive routes and measurement of rate constants in the reactions of oxygen atoms with fluoroethylenes", *The Journal of Physical Chemistry* **80** (1976) 14-18.
62. Guiochon, G. and Guillemin, C.L., "Quantitative gas chromatography for laboratory analyses and on-line process control", Elsevier, New York, 1988.
63. Harrison, D.P., Hall, J.W. and Rase, H.S., "An automatic precision microreactor", *Industrial and Engineering Chemistry* **57** (1965) 19-24.
64. Hauptschein, M., Fainberg, A.H. and Braid, M., "The thermal dimerization of perfluoropropene", *Journal of the American Chemical Society* **80** (1957) 842-845.
65. Heicklen, J. and Knight, V., "The mercury-photosensitized oxidation of perfluoropropene", *The Journal of Physical Chemistry* **69** (1965) 3641-3642.
66. Heicklen, J. and Knight, V., "Reaction of oxygen atoms with tetrafluoroethylene in the presence of molecular oxygen", *Journal of Physical Chemistry* **70** (1966) 3893-3901.
67. Helfferich, F.G., "Kinetics of homogenous multistep reactions", Comprehensive chemical kinetics, Vol. 38, Elsevier, Amsterdam, 2001.
68. Holland, F.A. and Bragg, R., "Fluid flow for chemical engineers", 2nd Edition, Edward Arnold, London, 1995.
69. Hopkins, J.S. and Golding, J.A., "The effect of heat transfer rate on the characteristics and operation of a tubular reactor", *The Chemical Engineering Journal* **51** (1993) 7-18.
70. Hsu, C., "A method of solution for mass transfer with chemical reaction under conditions of viscous flow in a tubular reactor", *AIChE Journal* **11** (1965) 938-940.
71. Huang, Z., Zhang, Y., Zhao, C., Qin, J., Li, H., Xue, M. and Liu, Y., "Direct gas-phase epoxidation of hexafluoropropylene with molecular oxygen using Ag catalyst", *Applied Catalysis A: General* **303** (2006) 18-22.
72. Hunter, M.C., Bartle, K.D., Seakins, P.W. and Lewis, A.C., "Direct measurement of atmospheric formaldehyde using gas chromatography-pulse discharge ionisation detection", *Analytical Communications* **36** (1999) 101-104.

73. Hynes, R.C., Mackie, J.C. and Masri, A.R., "Shock tube study of the oxidation of C_3F_6 by N_2O", *Journal of Physical Chemistry A* **103** (1999) 5967-5977.
74. Igumnov, S.M., Lekontseva, G.I., Shipigusev, A.A., Gomzyakova, O.D. and Soshin, V.A., "Synthesis of hexafluoroacetone by catalytic oxidation of hexafluoropropylene", *Russian Journal of Applied Chemistry* **74** No. 1 (2001) 170-171.
75. Ikeda, M., Miura, M. and Aoshima, A., "Process for the production of hexafluoropropylene oxide", US patent 4,902,810 (1990).
76. Il'in, A. and Luss, D., "Wrong-way behaviour of packed-bed reactors: Influence of an undesired consecutive reaction", *Industrial and Engineering Chemistry Research* **32** (1993) 247-252.
77. Istadi, N.A.S.A., "A hybrid numerical approach for multi-reponses optimization of process parameters and catalyst compositions in CO_2 OCM process over CaO-MnO/CeO_2 catalyst", *Chemical Engineering Journal* **106** (2005) 213-227.
78. Jakobsen, H.A., Lindborg, H. and Handeland, V., "A numerical study of the interactions between viscous flow transport and kinetics in fixed bed reactors", *Computers and Chemical Engineering* **26** (2002) 33-357.
79. Jankowiak, J.T. and Barteau, M.A., "Ethylene epoxidation over silver and copper-silver bimetallic catalysts: I. Kinetics and selectivity", *Journal of Catalysis* **236** (2005) 366-378.
80. Janssen, L.A.M., "Axial dispersion in laminar flow through coiled tubes", *Chemical Engineering Science* **31** (1976) 215-218.
81. Janssen, L.A.M. and Hoogendoorn, C.J., "Laminar convective heat transfer in helical coiled tubes", *International Journal of Heat and Mass Transfer* **21** (1978) 1197-1206.
82. Jin, G., Lu, G., Guo, Y., Guo, Y., Wang, J. and Liu, X., "Epoxidation of propylene by molecular oxygen over modified Ag-MoO_3 catalyst", *Catalysis Letters* **87** (2003) 249-252.
83. Jones, J.H., Daubert, T.E. and Fenske, M.R., "Vapor phase noncatalyric oxidation of olefins", *Industrial and Engineering Chemistry Process Design and Development* **8** (1969) 196-205.
84. Kállai, M., Máte, V. and Bala, J., "Effects of experimental conditions on the determination of the effective carbon number", *Chromatographia* **57** (2003) 639-644.
85. Kartsov, S.V., Valov, P.I., Sokolov, L.F., Blyumberg, E.A. and Sokolov, S.V., "Liquid-phase oxidation of hexafluoropropylene", *Russian Chemical Bulletin* **24** (1975) 2114-2118.
86. Kartsov, S.V., Valov, P.I., Sokolov, L.F. and Sokolov, S.V., "The role of the reactor surface in the liquid-phase oxidation of hexafluoropropylene", *Russian Chemical Bulletin* **27** (1978) 2006-2010.

87. Keating, E.L. and Matula R.A., "The high temperature oxidation of tetrafluoroethylene", *Journal of Chemical Physics* **66** (1977) 1237-1244.

88. Kennedy, R.C. and Levy, J.B., "The pyrolysis of hexafluoropropylene oxide", *Journal of Fluorine Chemistry* **7** (1976) 101-114.

89. Kittrell, J.R., Hunter, W.G. and Watson, C.C., "Obtaining precise parameter estimates for nonlinear catalytic rate models", *AIChE Journal* **12** (1966) 5.

90. Klopfenstein, R.W., "Numerical differentiation formulas for stiff systems of ordinary differential equations", *RCA Review* **32** (1971) 447-462.

91. Krusic, P.J., Roe, D.C. and Smart, B.E., "Kinetics of hexafluoropropylene oxide pyrolysis studied by gas-phase NMR kinetic measurements made easy", *Israeli Journal of Chemistry* **39** (1999) 117-123.

92. Kuricheva, O.V., Dunyakhin, V.A., Timofeev, V.V. and Zhitnev, Yu. N., "The reaction of C_3F_6 with dioxygen under IR laser initiation", *Russian Chemical Bulletin* **48** (1999) 45-49.

93. Kurosaki, A. and Okazaki, S., "Preparation of hexafluoroacetone by vapour phase oxidation of hexafluoropropene", *Chemistry Letters* (1988) 17-20.

94. Łągiewczyk, M. and Czech, Z., "Oxidation of hexafluoropropylene to hexafluoropropylene oxide using oxygen", *Polish Journal of Chemical Technology* **12** (2010) 1-3.

95. Lambert, R.M., Williams, F.J., Cropley, R.L. and Palermo, A., "Heterogeneous alkene epoxidation: past, present and future", *Journal of Molecular Catalysis A: Chemical* **228** (2005) 27-33.

96. Lau, K.K.S., Gleason, K.K. and Trout, B.L., "Thermochemistry of gas phase CF_2 reactions: A density functional theory study", *Journal of Chemical Physics* **113** (2000) 4103-4108.

97. Laurens, J.B., de Coning, J.P. and Swinley, J.M., "Gas chromatographic analysis of trace gas impurities in tungsten hexafluoride", *Journal of Chromatography: A* **911** (2001) 107-112.

98. Lawson, J.R., "Three-liquid-phase epoxidation of hexafluoropropylene at low pH", European patent 0 414 569 A2 (1990).

99. Lawson, J.R., "Two-liquid-phase epoxidation of hexafluoropropylene at low pH", European patent 0 473 398 A1 (1991).

100. Lazić, Z.R., "Design of experiments in chemical engineering", Wiley-VCH, Weinheim, 2004.

101. Lebbe, J., "Quantitative analysis", in Tranchant, J. (Ed.), "Practical manual of gas chromatography", Elsevier, New York, 1969.

102. Lee, J.C., Yetter, R.A., Dryer, F.L., Tomboulides, A.G. and Orszag, S.A., "Simulation and analysis of laminar flow reactors", *Combustion Science and Technology* **159** (2000) 199-212.
103. Lee, T.H., Woo, J.Y., Rhee, H.W., Kim, H.S. and Kim, H., "Synthesis of hexafluoropropylene epoxide using active oxygen", *Applied Chemistry* **5** (2001) 120-123.
104. Liu, L. and Davis S.R., "Matrix isolation spectroscopic study of tetrafluoroethylene oxidation", *Journal of Physical Chemistry* **96** (1992) 9719-9724.
105. Lucas, K., "Applied statistical thermodynamics", Springer-Verlag, Berlin, 1991.
106. Luss, D., "Temperature fronts and patterns in catalytic systems", *Industrial and Engineering Chemistry Research* **36** (1997) 2931-2944.
107. Maksimov, B.N., Kornilov, V.V., Melnychenko, B.A. and Kosareva, L.N., "Perfluoropolyethers. Synthesis and applications", *Russian Journal of Applied Chemistry* **82** (2009) 1706-1710.
108. Malanca, F.E., Paci, M.B. and Argüello, G.A., "Photochemistry of perfluoroacyl halides in the presence of O_2 and CO", *Journal of Photochemistry and Photobiology A: Chemistry* **150** (2002) 1-6.
109. Mathias, E. and Miller, G.H., "The decomposition of polytetrafluoroethylene in a glow discharge", *The Journal of Physical Chemistry* **71** (1967) 2671-2675.
110. Matula, R.A., "The thermal decomposition of perfluoropropene", *The Journal of Physical Chemistry* **72** (1968) 3054-3056.
111. Matula, R.A., "Combustion kinetics of tetrafluoroethylene", Final technical report, Air Force Office of Scientific Research, July, 1968.
112. McQuarrie, D.A. and Simon, J.D., "Molecular Thermodynamics", University Science Books, Sausalito, California, 1999.
113. Meissner, E. and Wróblewska, A., "Oxidation of hexafluoropropylene with molecular oxygen", *Polish Journal of Chemical Technology* **9** (2007) 20-22.
114. Merril, L.S., Jr. and Hamrin, C.E., Jr., "Conversion and temperature profiles for complex reactions in laminar and plug flow", *AIChE Journal* **16** (1970) 194-198.
115. Meylan, W.M. and Howard, P.H., "Computer estimation of the atmospheric gas-phase reaction of organic compounds with hydroxyl radicals and ozone", *Chemosphere* **26** (1993) 2293-2299.
116. Millar, G.J. and Rochester, C.H., "A Fourier-transform infrared study of CO_2 and CO_2/H_2 interactions with caesium-doped copper catalysts", *Topics in Catalysis* **3** (1996) 103-114.

117. Millauer, H., Schwertfeger, W. and Siegemund, G., "Hexafluoropropylene oxide - a key compound in organofluorine chemistry", *Angewandte Chemie International Edition English* **24** (1985) 161-179.
118. Monnier, J.R., Stavinoha J.L., Jr. and Minga, R.L., "Stability and distribution of cesium in Cs-promoted silver catalysts used for butadiene epoxidation", *Journal of Catalysis* **226** (2004) 401-409.
119. Montgomery, D.C. and Runger, G.C., "Applied statistics and probability for engineers", 4th Ed., John Wiley and Sons, Inc., New York, 2007.
120. Moore, A.L., "Fluoroelastomers Handbook: the definitive user's guide", William Andrew, New York, 2006.
121. Nauman, E.B., "The residence time distribution for laminar flow in helically coiled tubes", *Chemical Engineering Science* **32** (1977) 287-293.
122. Nauman, E.B. and Nigam, A., "On axial diffusion in laminar-flow reactors", *Industrial and Engineering Chemistry Research* **44** (2005) 5031-5035.
123. Nauman, E.B., "Chemical reactor design, optimization and scaleup", McGraw-Hill, New York, 2002.
124. Oda, Y., Uchida, K. and Morikawa, S., "Preparation of hexafluoropropylene epoxide", Japan patent 52053804 (1977).
125. Oda, Y., Uchida, K. and Morikawa, S., "Preparation of hexafluoropropylene epoxide", Japan patent 52053806 (1977).
126. Ohlinger, W.S., Klunzinger, P.E., Deppmeier, B.J. and Hehre, W.J., "Efficient calculation of heats of formation", *Journal of Physical Chemistry: A* **113** (2009) 2165-2175.
127. Ohsaka, Y. and Tohzuka, T., "Process for preparing hexafluoropropene oxide", US patent 4,288,376 (1981).
128. Ohtani, B., Ueda, Y., Nishimoto, S., Kagiya, T. and Hachisuka, H., "Photocatalytic oxidative decomposition of fluoroalkenes by titanium dioxide", *Journal of the Chemical Society Perkin Transactions* **2** (1990) 1955-1960.
129. O'Mahony, T.K.P., Cox, A.P., Roberts, D.J., "Gas chromatographic separation of perfluorocarbons", *Journal of Chromatography* **637** (1993) 1-11.
130. Ottaway, J.H., "Normalization factors in the fitting of exponential curves to results obtained in isotopic-tracer studies", *Biochemical Journal* **125** (1971) 44P-45P.
131. Ottaway, J.H., "Normalization in the fitting of data by iterative methods. Application to tracer kinetics and enzyme kinetics", *Biochemical Journal* **134** (1973) 729-736.

132. Pandey, S.K. and Kim, K., "The fundamental properties of the direct injection method in the analysis of gaseous reduced sulphur by gas chromatography with a pulse flame photometric detector", *Analytica Chimica Acta* **615** (2008) 165-173.
133. Perego, C. and Villa, P., "Catalyst preparation methods", *Catalysis Today* **34** (1997) 281-305.
134. Perry, R.H., Green, D.W. and Maloney, J.O, "Perry's chemical engineers' handbook", 7th Edition, McGraw-Hill, New York, 1997.
135. Pinna, F., "Supported metal catalysts preparation", *Catalysis Today* **41** (1998) 129-137.
136. Posma, J., personal communication from NECSA, 2009.
137. Raal, J.D. and Mühlbauer, A.L., "Phase equilibria - measurement and computation", Taylor and Francis, Washington, 1998.
138. Ramjugernath, D., Naidoo, P., Subramoney, S.C. and Nelson, W.M., "Recovery of components making up a liquid mixture", US patent 20100105932 A1.
139. Reich, J.G., Wangermann, G., Falck, M and Rohde, K., "A general strategy for parameter estimation for isoteric and allosteric-kinetic data and binding measurements", *European Journal of Biochemistry* **26** (1972) 368-379.
140. Reiher, T. "Statilitätsuntersuchungen bei rückwärtigen differentiationsformeln in abhängigkeit von einem parameter", Technical Report 11, Sektion Mathematik, Humbolt-Universität zu Berlin, 1978.
141. Rodgers A.S. "Thermochemistry of fluorocarbon radicals", in Root, J.W. (Ed.), "Fluorine-containing free radicals, kinetics and dynamics of reactions", ACS Symposium Series, Vol. 66, American Chemical Society, New York, 1978.
142. Romano, R.M., Della Védova, C.O. and Czarnowski, J., "Kinetics and mechanism of the thermal gas-phase oxidation of perfluorobutene-2 in presence of trifluoromethyl hypofluorite", *International Journal of Chemical Kinetics* **35** (2003) 532-541.
143. Romano, R.M. and Czarnowski, J., "Kinetics and mechanism of the thermal gas-phase reaction between NO_2 and perfluoropropene", *Zeitschrift für Physikalische Chemie* **218** (2004) 575-597.
144. Sargeant, P.B., "Fluorocyclopropanes. I. Preparation and nuclear magnetic resonance spectra", *Journal of Organic Chemistry* **35** (1970) 678-682.
145. Saunders, D. and Heicklen, J., "The reaction of oxygen atoms with perfluoropropene", *Journal of the American Chemical Society* **87** (1965) 4062-4068.

146. Saunders, D. and Heicklen, J., "Some reactions of oxygen atoms. I. C_2F_4, C_3F_6, C_2H_2, C_2H_4, C_3H_6, 1-C_4H_8, C_2H_6, *c*-C_3H_6 and C_3H_8", *The Journal of Physical Chemistry* **70** (1966) 1950-1958.

147. Scheel, L.D., Lane, W.C. and Coleman, W.E., "The toxicity of polytetrafluoroethylene pyrolysis products including carbonyl fluoride and a reaction product, silicon tetrafluoride", *American Industrial Hygiene Association Journal* **29** (1968) 41-48.

148. Schiesser, W.E. and Griffiths, G.W., "A compendium of partial differential equation models, method of lines analysis with MATLAB", Cambridge University Press, 2009.

149. Seader, J.D. and Henley, E.J., "Separation process principles", John Wiley and Sons, Inc., New York, 1998.

150. Shapovalov, V.V. and Mezentsev, A.I., "Chromatographic analysis of low-molecular-weight products of oxidation of hexafluoropropylene by molecular oxygen", *Industrial Laboratory* **62** No. 6 (1996) 343-344.

151. Shapovalov, V.V., Poluéktov V.A. and Ryabinin, N.A., "Kinetics and mechanism of the liquid-phase low-temperature oxidation of hexafluoropropene", *Russian Journal of Physical Chemistry* **58** (1984) 364-368.

152. Shapovalov, V.V. and Poluéktov, V.A., "On the formation mechanism of hexafluoropropylene oxide in low-temperature liquid-phase oxidation of hexafluoropropylene by molecular oxygen", *Reaction Kinetics and Catalysis Letters* **48** (1992) 375-378.

153. Shapovalov, V.V. and Poluéktov, V.A., "The mechanism of chain termination in the reaction of low temperature liquid-phase oxidation of hexafluoropropylene at low oxygen pressures", *Kinetics and Catalysis* **34** (1993) 380-382.

154. Shapovalov, V.V. and Poluéktov, V.A., "Mechanism of the formation of trifluoroaetyl fluoride and carbonyl fluoride in the low temperature liquid phase oxidation of hexafluoropropene with molecular oxygen", *Theoretical and Experimental Chemistry* **28** (1993) 173-176.

155. Shapovalov, V.V. and Poluéktov, V.A., "Synthesis of hexafluoropropylene oxide", *Russian Journal of Organic Chemistry* **30** (1994) 329.

156. Shapovalov, V.V and Poluéktov, V.A., "Influence of oxygen pressure on molecular weight of perfluoropolyether polyperoxide-product of low-temperature liquid-phase oxidation of hexafluoropropylene by molecular oxygen", *Russian Journal of Applied Chemistry* **67** (1994) 1650-1652.

157. Shapovalov, V.V. and Poluéktov, V.A., "Possible inhibition, by oxygen, of the low-temperature liquid-phase oxidation of hexafluoropropylene", *Theoretical and Experimental Chemistry* **29** (1994) 13-15.
158. Shapovalov, V.V. and Poluéktov, V.A., "On the mechanism of formation of low-molecular weight fluoroanhydrides during low-temperature liquid-phase oxidation of hexafluoropropylene with molecular oxygen", *Chemical Physics Reports* **13** (1995) 1053-1055.
159. Shapovalov, V.V. and Poluéktov, V.A., "Synthesis of 1,2-epoxyhexafluoropropane by liquid-phase oxidation of hexafluoropropene with oxygen", *Russian Journal of Organic Chemistry* **34** (1998) 1357.
160. Shapovalov, V.V., "Formation of alkyl radicals that are relatively unreactive with each other and with oxygen, in the low-temperature liquid-phase oxidation of hexafluoropropylene by molecular oxygen", *Theoretical and Experimental Chemistry* **34** (1998) 227-228.
161. Shapovalov, V.V., "Low-temperature liquid-phase radiation-induced oxidation of hexafluoropropylene with molecular oxygen: effect of reaction conditions on the structure of perfluoropolyether polyperoxide", *High Energy Chemistry* **34** (2000) 412-413.
162. Shapovalov, V.V., "Molecular weight of perfluoropolyether polyperoxide, the major product of low-temperature liquid-phase oxidation of hexafluoropropylene with molecular oxygen", *Russian Journal of Applied Chemistry* **73** (2000) 1470-1471.
163. Shapovalov, V.V., "The effect of reagent concentrations on the rate of perfluoropolyether polyperoxide formation", *Russian Journal of Physical Chemistry* **76** (2002) 494-495.
164. Shoshin, V.A., Tihonova, L.G. and Lekontseva, G.I., "Initiated oxidation of perfluoroolefins", *Fluorine Notes* **5** (1999) 4-6.
165. Sianesi, D., Pasetti, A. and Corti, C., "Photooxidation of perfluoroolefins; polyperoxides and polyethers of hexafluoropropene", *Die Makromolekulare Chemie* **86** (1965) 308-311.
166. Sianessi, D., Bernardi, G. and Moggi, G., "Polyoxyperfluoromethylene compounds and process of their preparation", US Patent 3,721,696 (1973).
167. Sianessi, D., Guarda, P.A. and Marchionni, G., "A kinetic and mechanistic study of the low-temperature fluorine-initiated copolymerization of tetrafluroethylene with oxygen", *Macromolecules* **32** (1999) 7768-7780.
168. Simandl, G.J., "World fluorspar and resources, market and deposit examples from British Columbia, Canada", British Columbia geological survey, Information circular, 2009.

169. Smith, J.M., Van Ness, H.C. and Abbott, M.M., "Introduction to chemical engineering thermodynamics", 6th Ed., McGraw-Hill, New York, 2001.

170. Spivey, J.J., "Complete catalytic oxidation of volatile organics", *Industrial and Engineering Chemistry Research* **26** (1987) 2165-2180.

171. Sternberg, J.C., Gallaway, W.S., and Jones, D.T.L., "Quantitative analysis", in Brenner, N., Callen, J.E. and Weiss, M.D. (Eds.), "Gas chromatography", Academic Press, New York, 1962.

172. Tranchant, J., "Qualitative analysis", in Tranchant, J. (Ed.), "Practical manual of gas chromatography", Elsevier, New York, 1969.

173. Trivedi, R.N. and Vasudeva, K., "RTD for diffusion free laminar flow in helical coils", *Chemical Engineering Science* **29** (1974) 2291-2295.

174. Trivedi, R.N. and Vasudeva, K., "Axial dispersion in laminar flow in helical coils", *Chemical Engineering Science* **30** (1975) 317-325.

175. Tyerman, W.J.R., "Rate parameters for reactions of ground-state difluorocarbene and determination of the absolute intensity of the A^1B_1-X^1A_1 Absorption bands.

176. Umemoto, H., Sugiyama, K., Tsunashima, S. and Sato, S., "The Arrhenius parameters for the reactions of O atoms with ethane and five fluoroethenes", *Bulletin of the Chemical Society of Japan* **58** (1985) 1228-1233.

177. Vaughan, O.P.H., Kyriakou, G., Macleod, N., Tikhov, M. and Lambert, R.M., "Copper as a selective catalyst for the epoxidation of propene", *Journal of Catalysis* **236** (2005) 401-404.

178. Wallington, T.J., Ellerman, T., Nielsen, O.J. and Sehested, J., "Atmospheric chemistry of FCO_x radicals: UV spectra and self-reaction kinetics of FCO and $FC(O)O_2$ and kinetics of some reactions of FCO_x with O_2, O_3 and NO at 296 K", *Journal of Physical Chemistry* **98** (1994) 2346-2356.

179. Wallington, T.J. and Nielsen, O.L., "Atmospheric chemistry and environmental impact of hydrofluorocarbons (HFCs) and hydrofluoroethers (HFEs)", in Neilson, A.H. (Ed.), "The handbook of environmental chemistry - Organofluorines", Vol. 3, Springer-Verlag, Berlin, 2002.

180. Wan, C.G. and Ziegler, E.N., "Effect of dispersion on tubular reactor yield for variable density cases", *Chemical Engineering Science* **28** (1973) 1641-1652.

181. Wang, Y., Chu, H., Zhu, W. and Zhang, Q., "Copper-based efficient catalysts for propylene epoxidation by molecular oxygen", *Catalysis Today* **131** (2008) 496-504.

182. Wissermel, K. and Arpe, H.J., "Industrial organic chemistry", 3rd Edition, Wiley, New York, 1997.

183. Wojciechowski, B.W. and Rice, N.M., "Experimental methods in kinetic studies", 2nd Edition, Elsevier, Amsterdam, 2003.

184. Wróblewska, A., Milchert, E. and Meissner, E., "Oxidation of hexafluoropropylene with oxygen to hexafluoropropylene oxide", *Organic Process Research and Development* **14** (2010) 272-277.

185. Xue, L., He, H., Liu, C., Zhang, C. and Zhang, B., "Promotion effects and mechanism of alkali metals and alkaline earth metals on cobalt-cerium composite oxide catalysts for N_2O decomposition", *Environmental Science and Technology* **43** (2009) 890-895.

186. Yaws, C.L., "Matheson gas data-book", McGraw-Hill, New York, 2001.

187. Zachariah, M.R., Westmoreland, P.R., Burgess, D.R.F., Jr., Tsang, W. and Melius, C.F., "Theoretical prediction of thermochemical and kinetic properties of fluorocarbons", in Miziolek, A.W. (Ed.), "Halon Replacements", ACS Symposium Series, Vol. 611, American Chemical Society, New York, 1995.

188. Zenkevich, I.G., Ivanova, T.L. and Zigel, A.N., "Gas-chromatographic identification of the products of the thermal degradation of a tetrafluoroethylene and perfluoro(propyl vinyl ether) copolymer", *Journal of Analytical Chemistry* **58** (2003) 251-256.

189. Zhang, Y., Zhang, H., Huang, Z., Wang, H., Qin, J., "Method for preparation of solid catalysts for synthesis of hexafluoropropylene oxide", Chinese patent CN 1954911 (2007).

Appendix A. Instrument calibrations

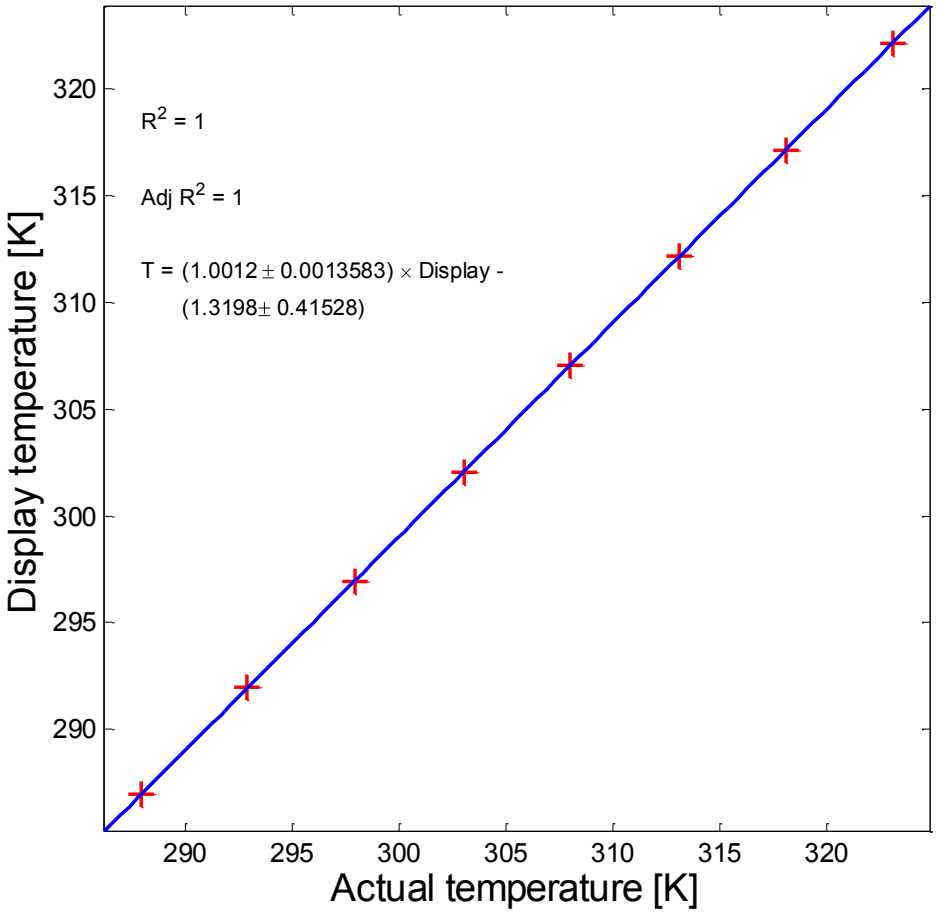

Figure A.1. G.C. sample loop resistance thermometer calibration plot.

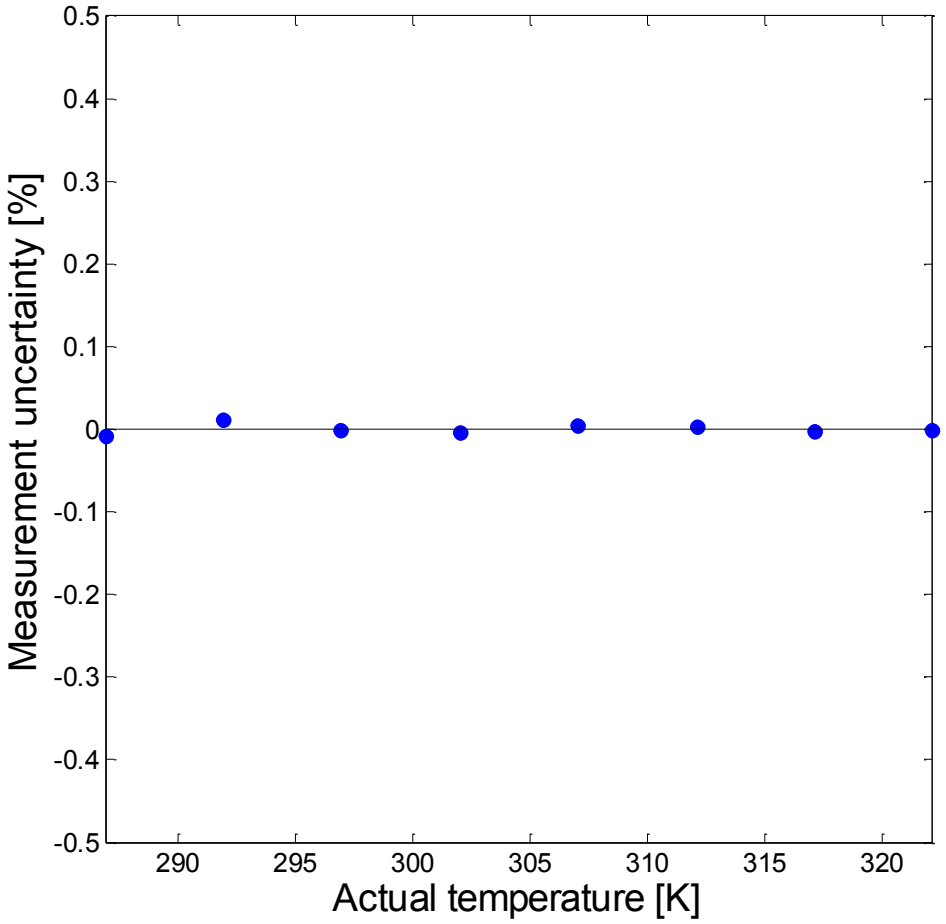

Figure A.2. G.C. sample loop resistance thermometer measurement uncertainty (relative difference between measured and predicted value).

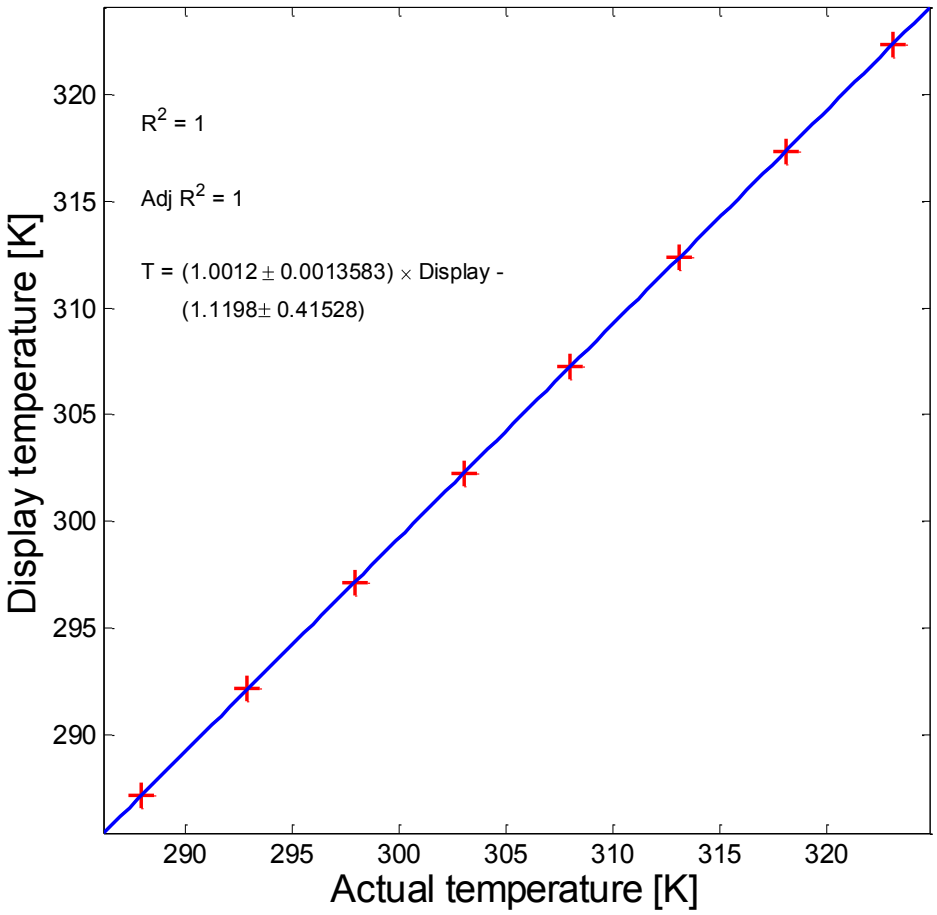

Figure A.3. Wet-test meter resistance thermometer calibration plot.

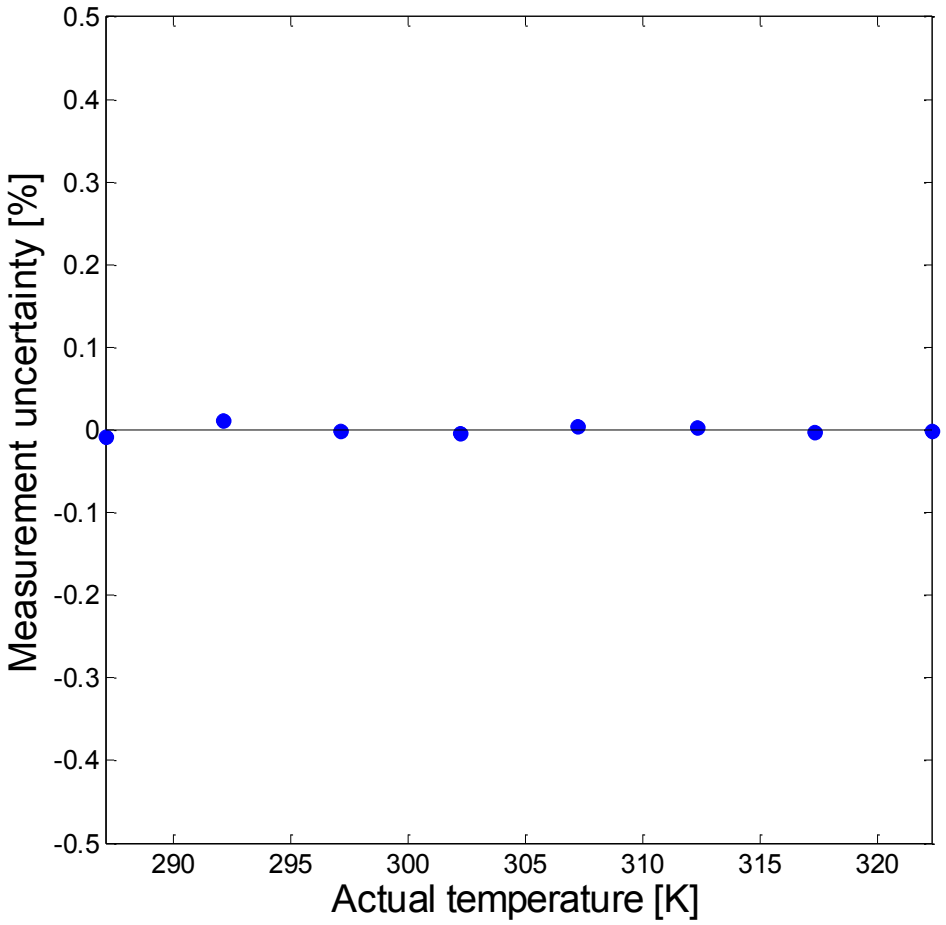

Figure A.4. Wet-test meter resistance thermometer measurement uncertainty (relative difference between measured and predicted value).

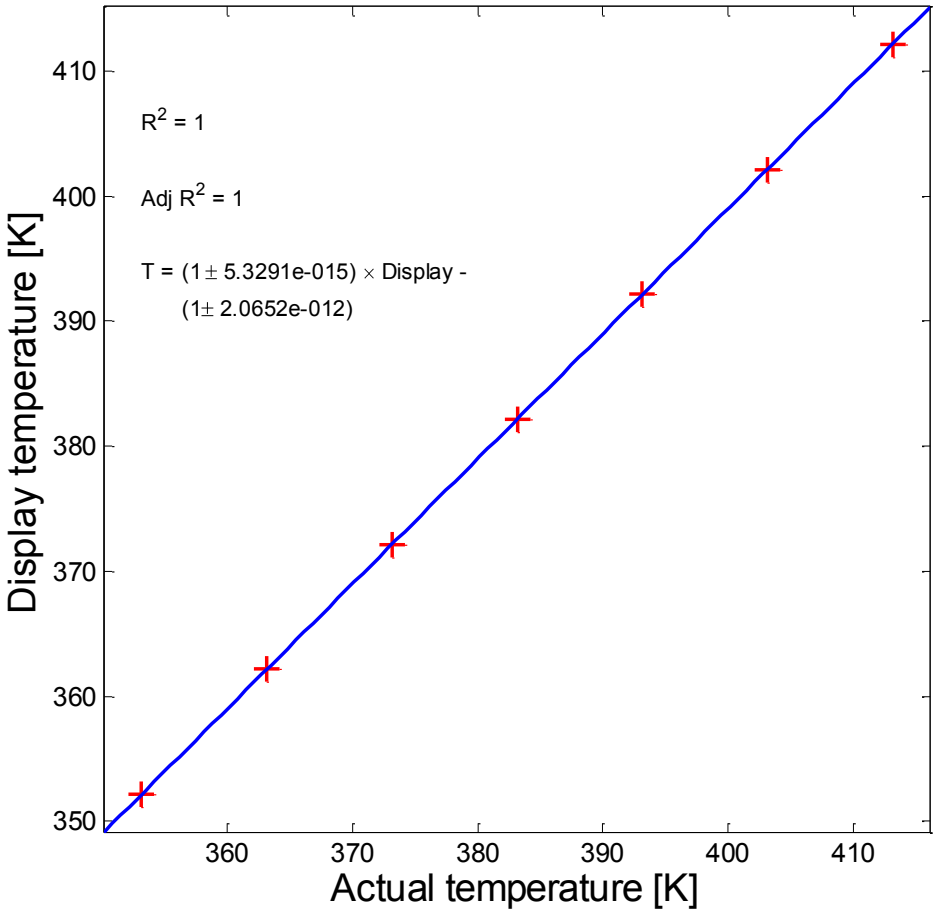

Figure A.5. Laminar -flow reactor primary Type-K thermocouple calibration plot.

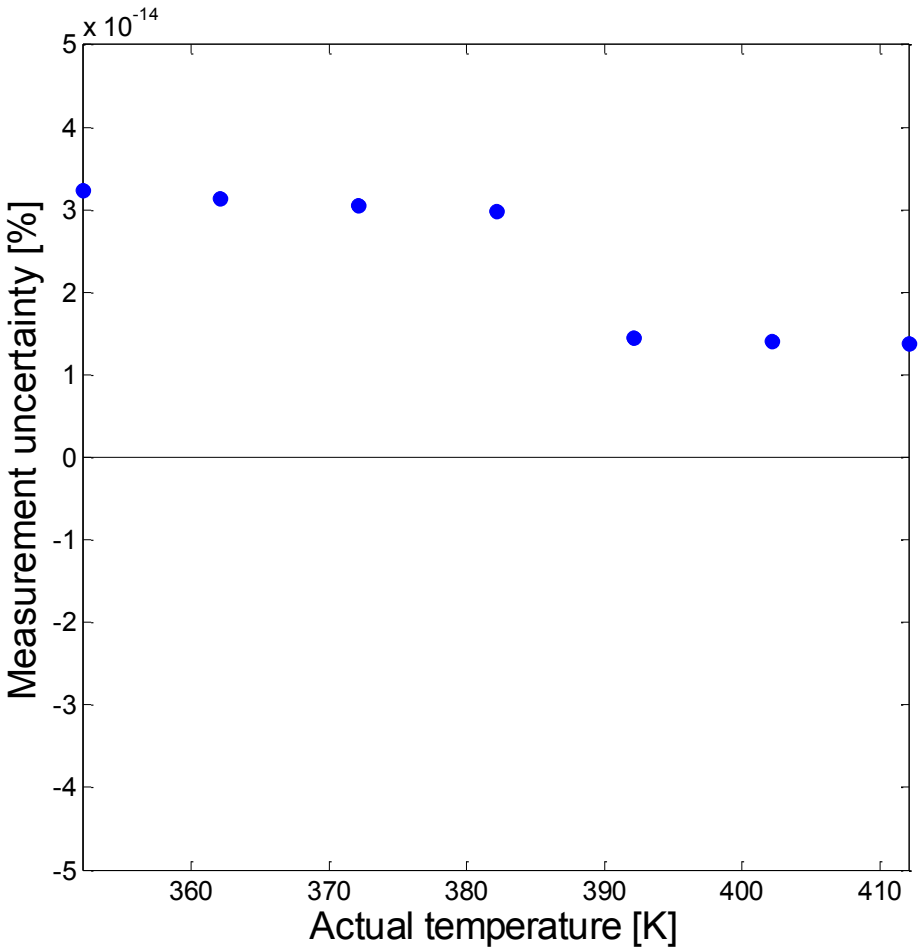

Figure A.6. Laminar-flow reactor primary Type-K thermocouple measurement uncertainty (relative difference between measured and predicted value).

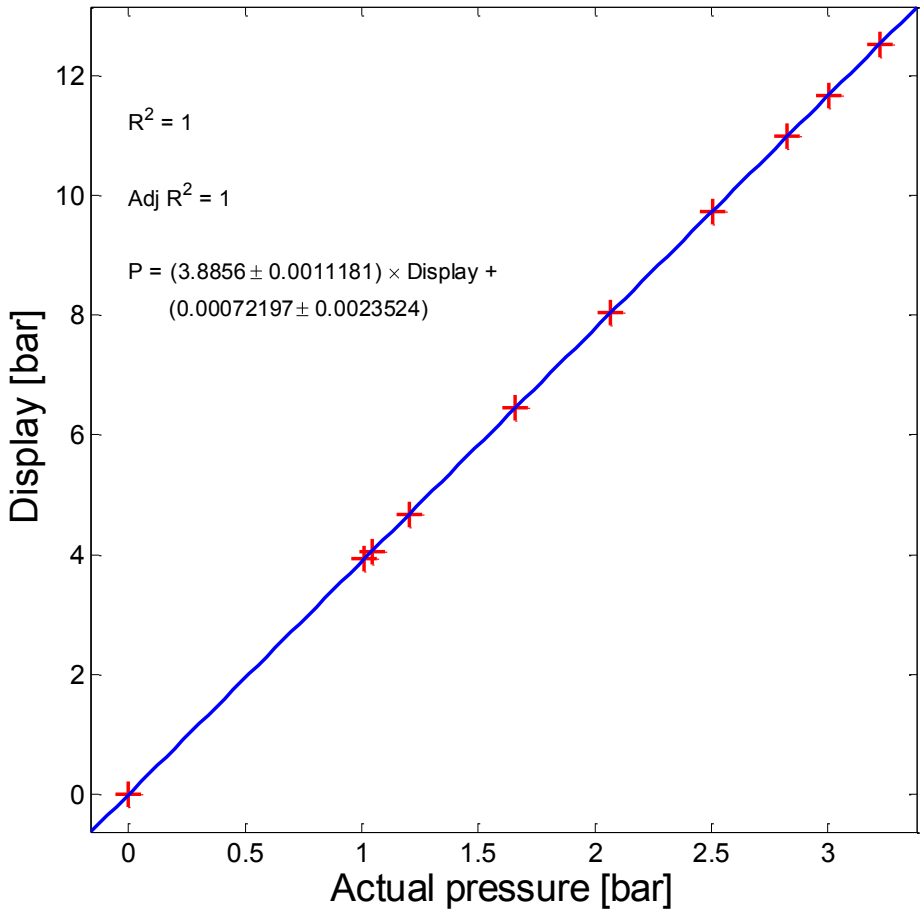

Figure A.7. G.C. sample loop Sensotec TJE 0-100psia pressure transducer calibration plot.

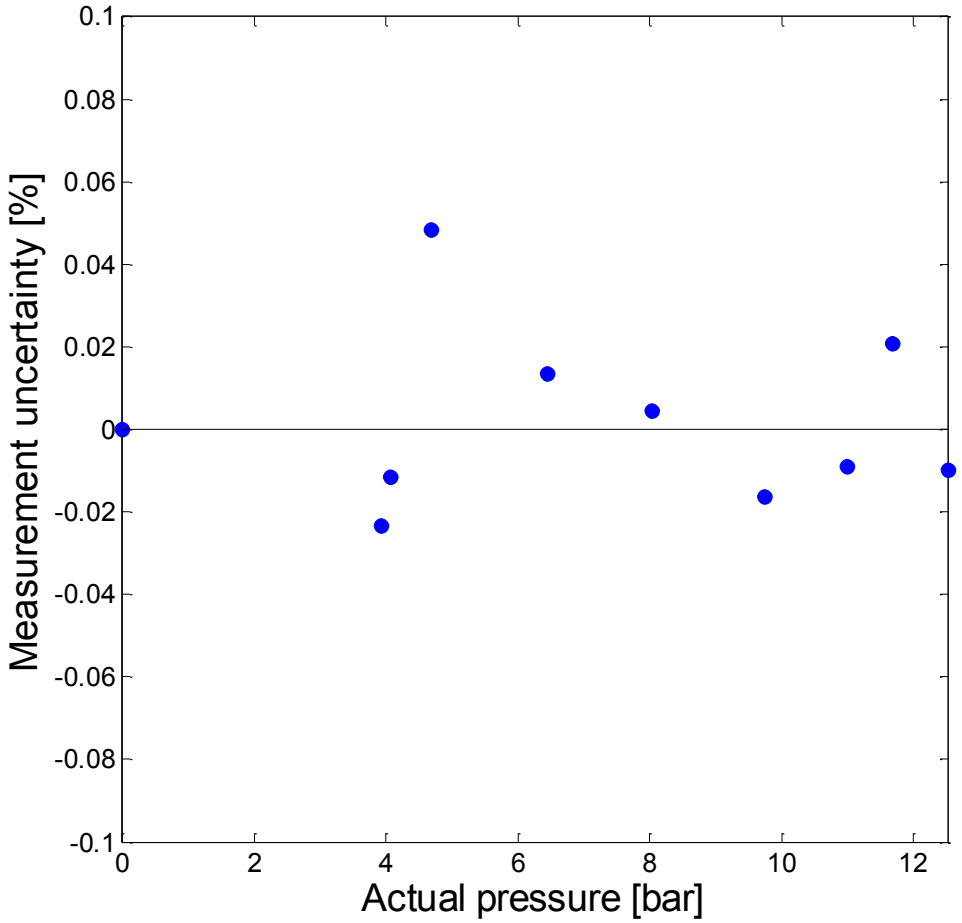

Figure A.8. G.C. sample loop Sensotec TJE 0-100psia pressure transducer measurement uncertainty (relative difference between measured and predicted value).

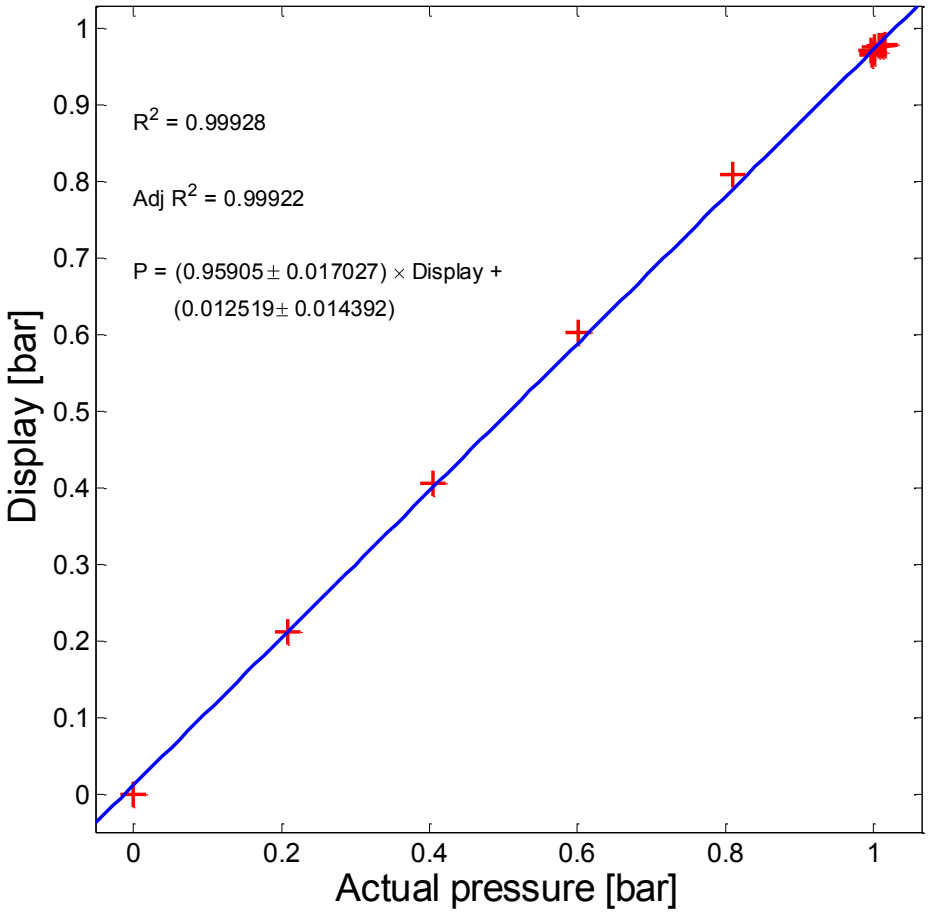

Figure A.9. Wet-test meter Sensotec THE 0-25psia pressure transducer calibration plot.

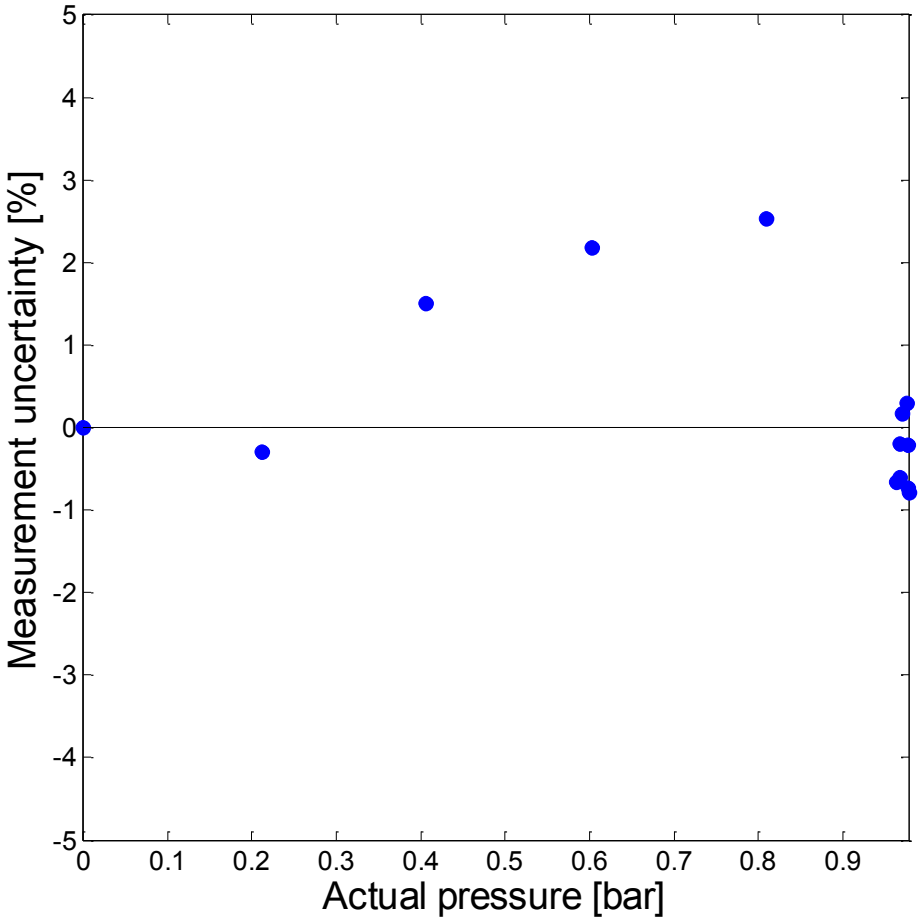

Figure A.10. Wet-test meter Sensotec THE 0-25psia pressure transducer measurement uncertainty (relative difference between measured and predicted value).

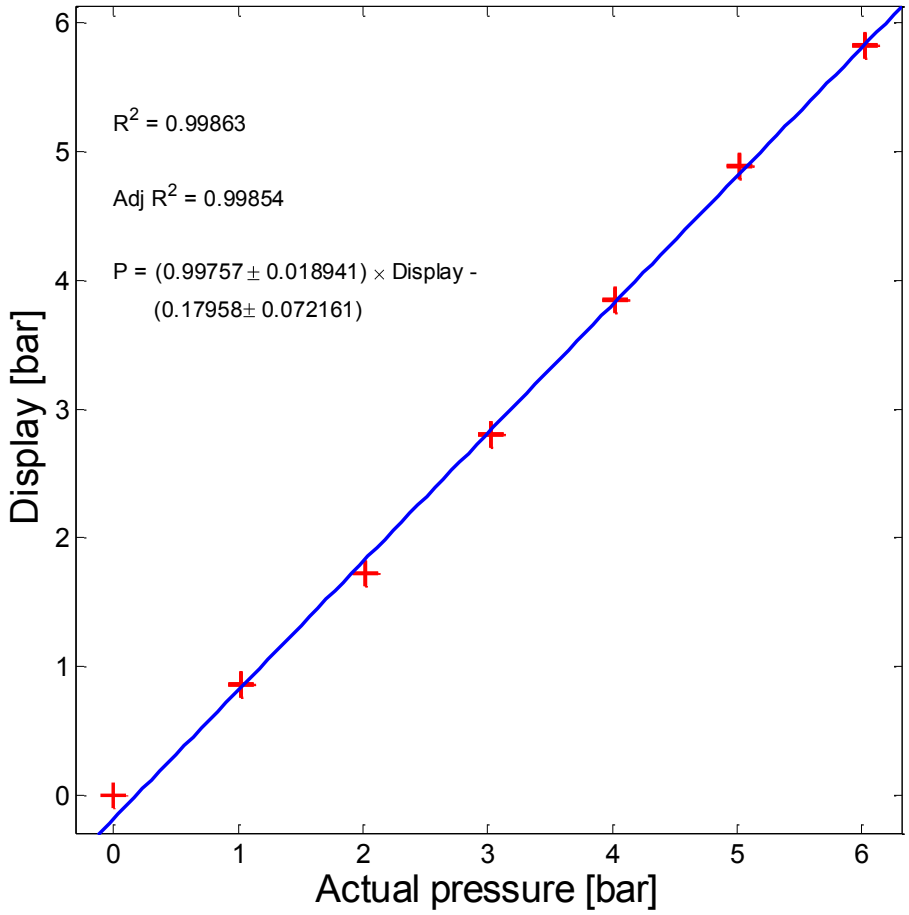

Figure A.11. Reactor inlet Wika S10 0-40 bar pressure transmitter calibration plot.

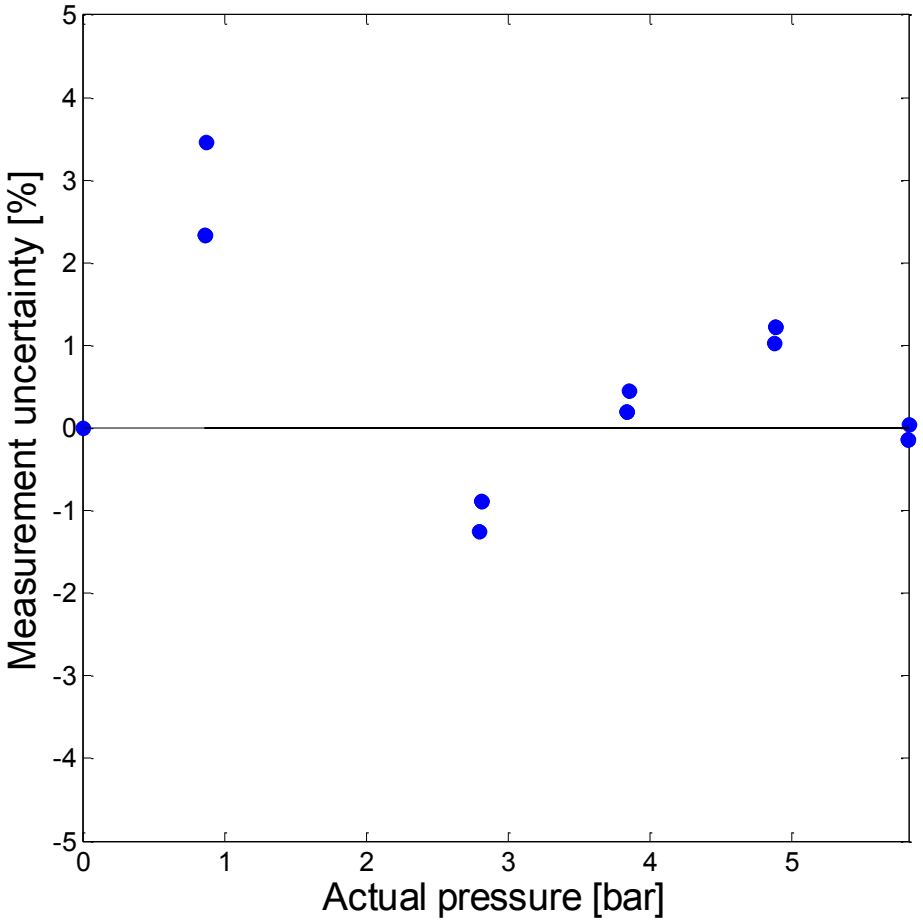

Figure A.12. Reactor inlet Wika S10 0-40 bar pressure transmitter measurement uncertainty (relative difference between measured and predicted value).

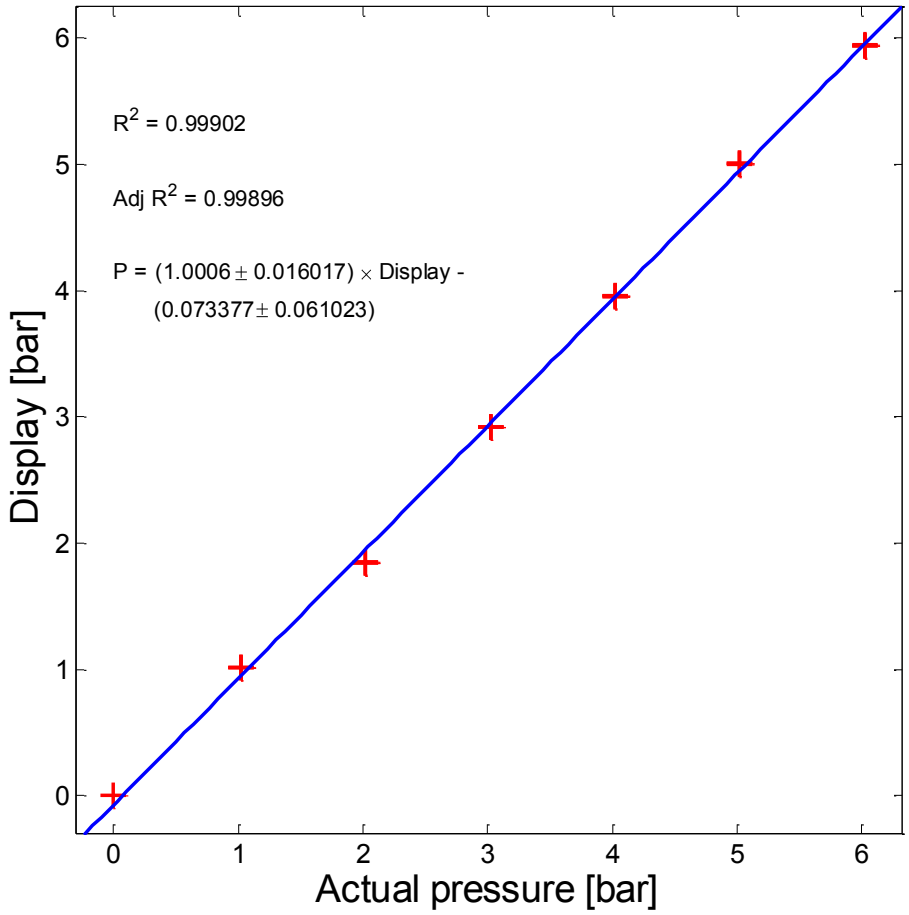

Figure A.13. Reactor outlet Wika S10 0-40 bar pressure transmitter calibration plot.

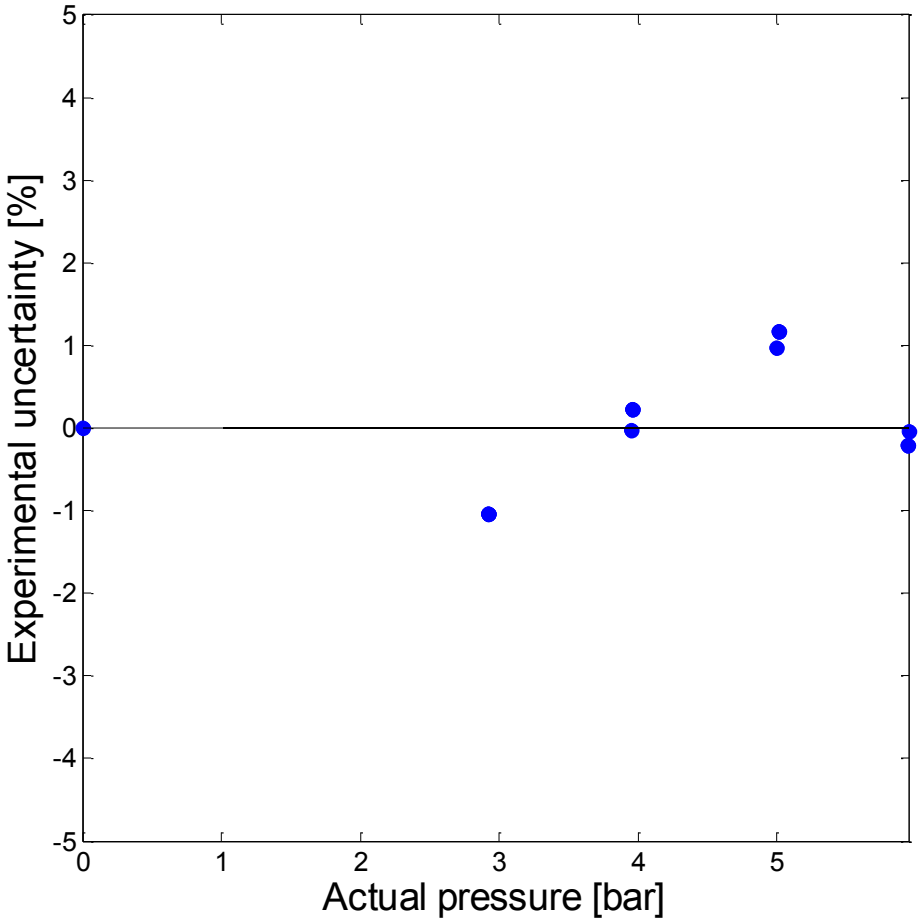

Figure A.14. Reactor outlet Wika S10 0-40 bar pressure transmitter measurement uncertainty (relative difference between measured and predicted value).

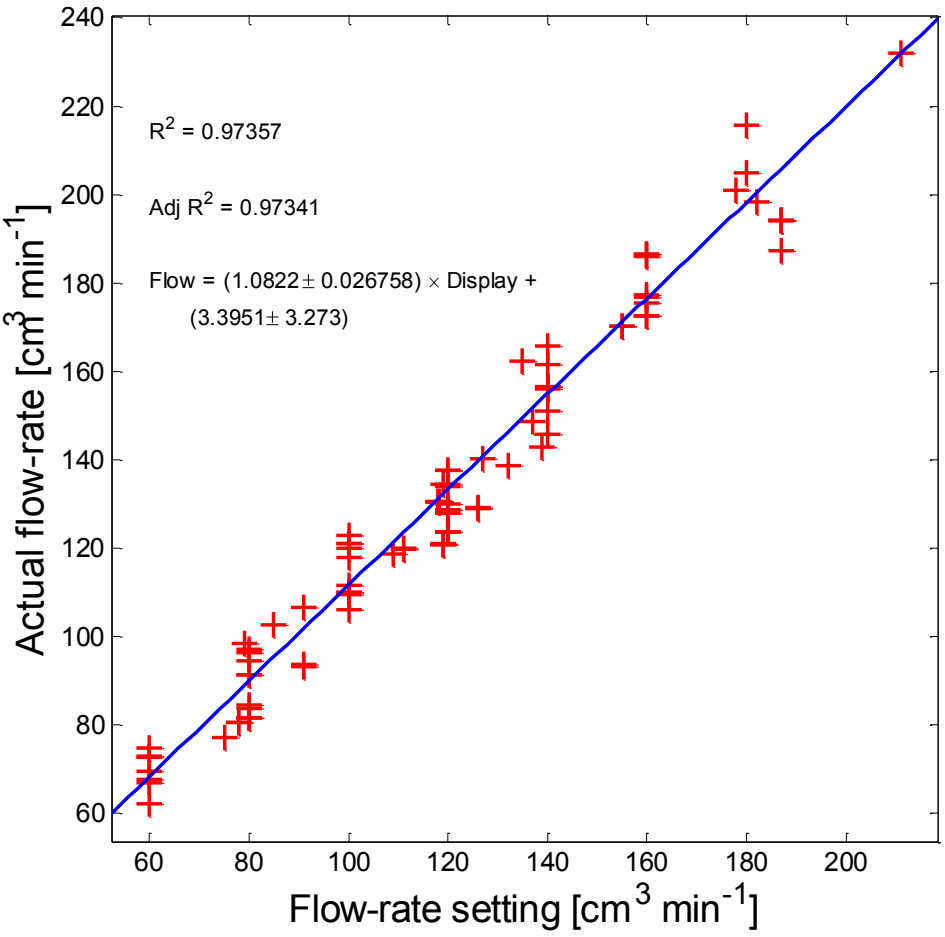

Figure A.15. Bronkhorst El-flow 0-1 l min^{-1} oxygen mass-flow controller calibration plot.

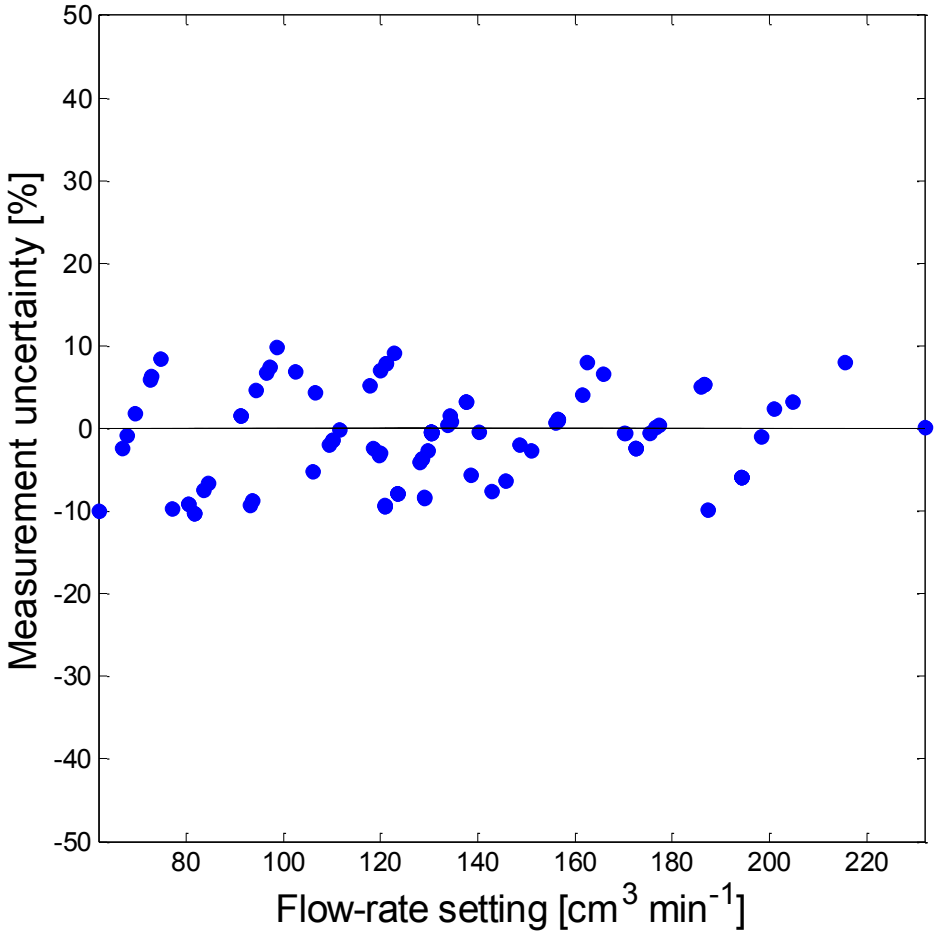

Figure A.16. Bronkhorst El-flow 0-1 l min^{-1} oxygen mass-flow controller measurement uncertainty (relative difference between measured and predicted value).

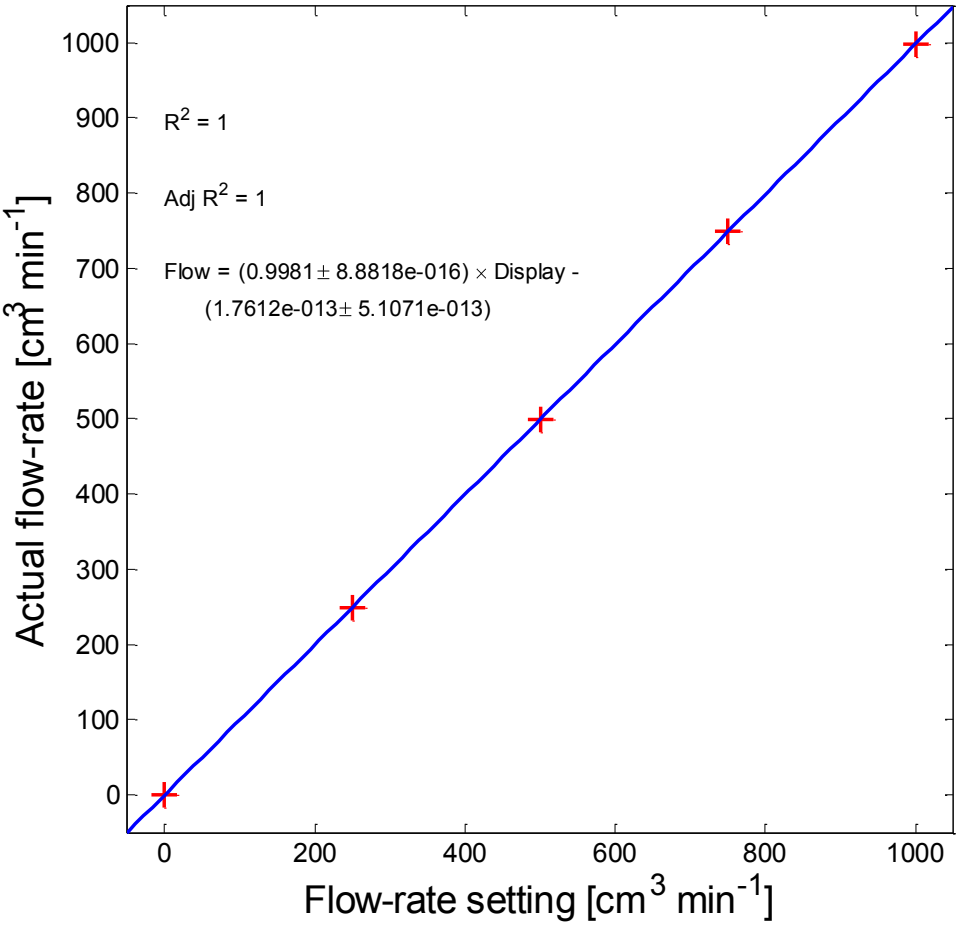

Figure A.17. Bronkhorst El-flow 0-1 l min^{-1} oxygen mass-flow controller manufacturer's calibration plot.

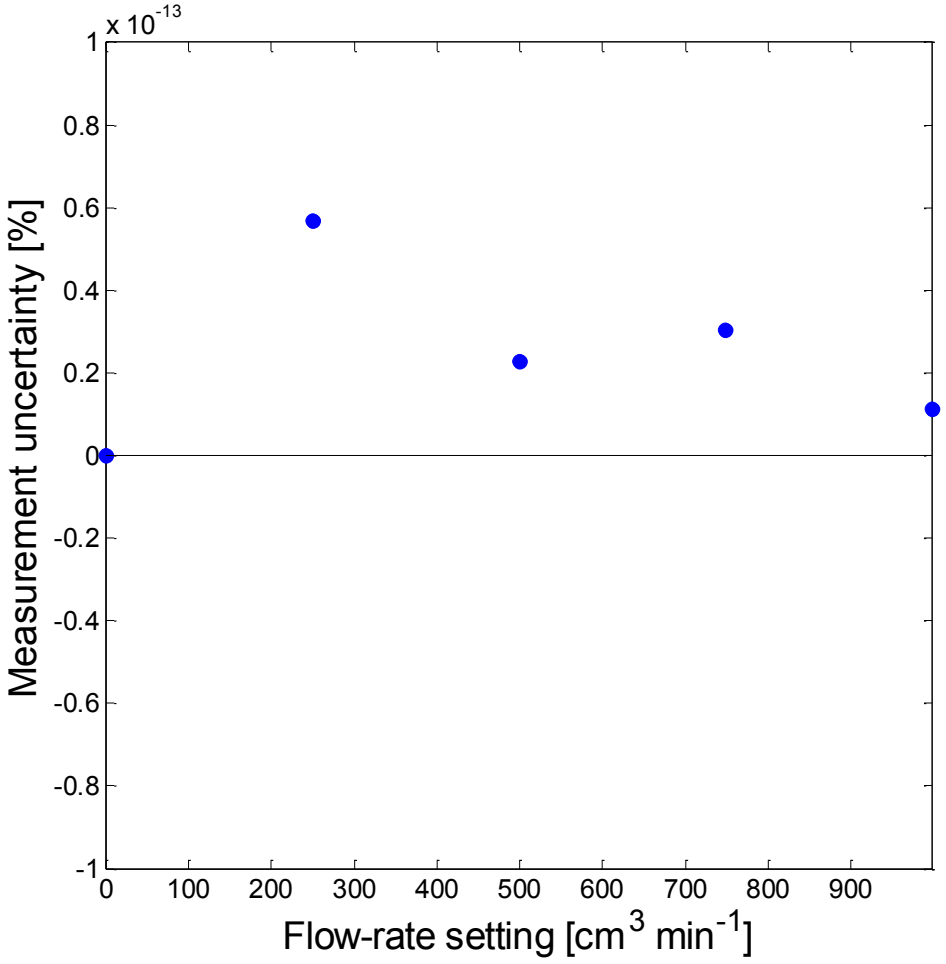

Figure A.18. Bronkhorst El-flow 0-1 l min^{-1} oxygen mass-flow controller manufacturer's measurement uncertainty (relative difference between measured and predicted value).

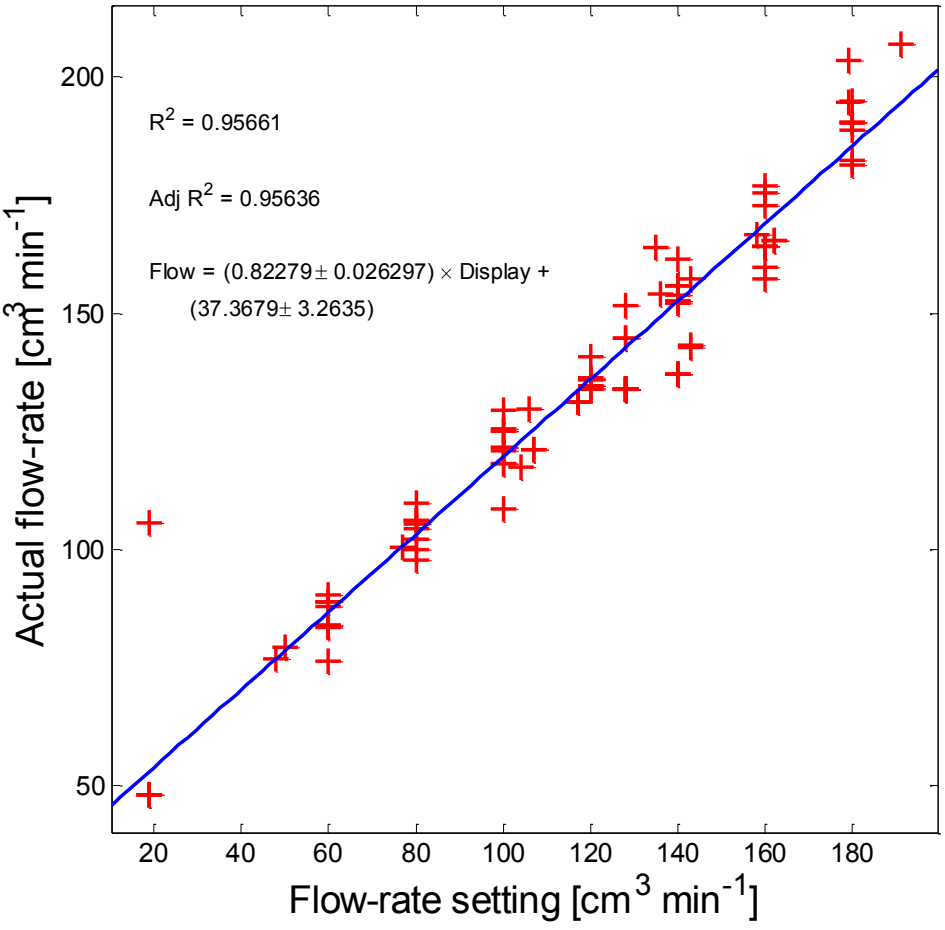

Figure A.19. Celerity 1660 0-1 l min^{-1} HFP mass-flow controller calibration plot.

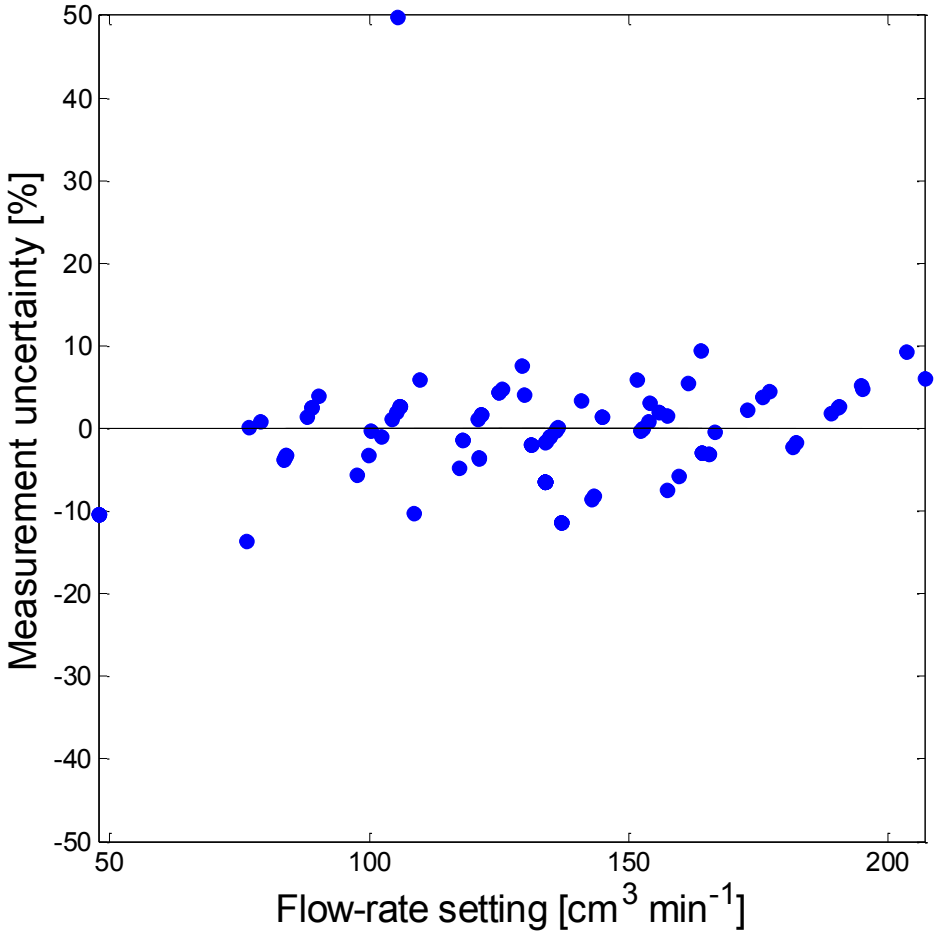

Figure A.20. Celerity 1660 0-1 l min^{-1} HFP mass-flow controller measurement uncertainty (relative difference between measured and predicted value).

Appendix B. Mechanical sketches

Pt. No.	Description	Material	Qty.
1	Nut M30 (pitch 3.5 mm)	Stainless steel	6
2	Flange ASA - 150	Stainless steel	1
3	Reactor tube ($^1/_8$ inch nominal tube)	Copper	4
4	Oil jacket (6 inch Schedule 40)	Stainless steel	1

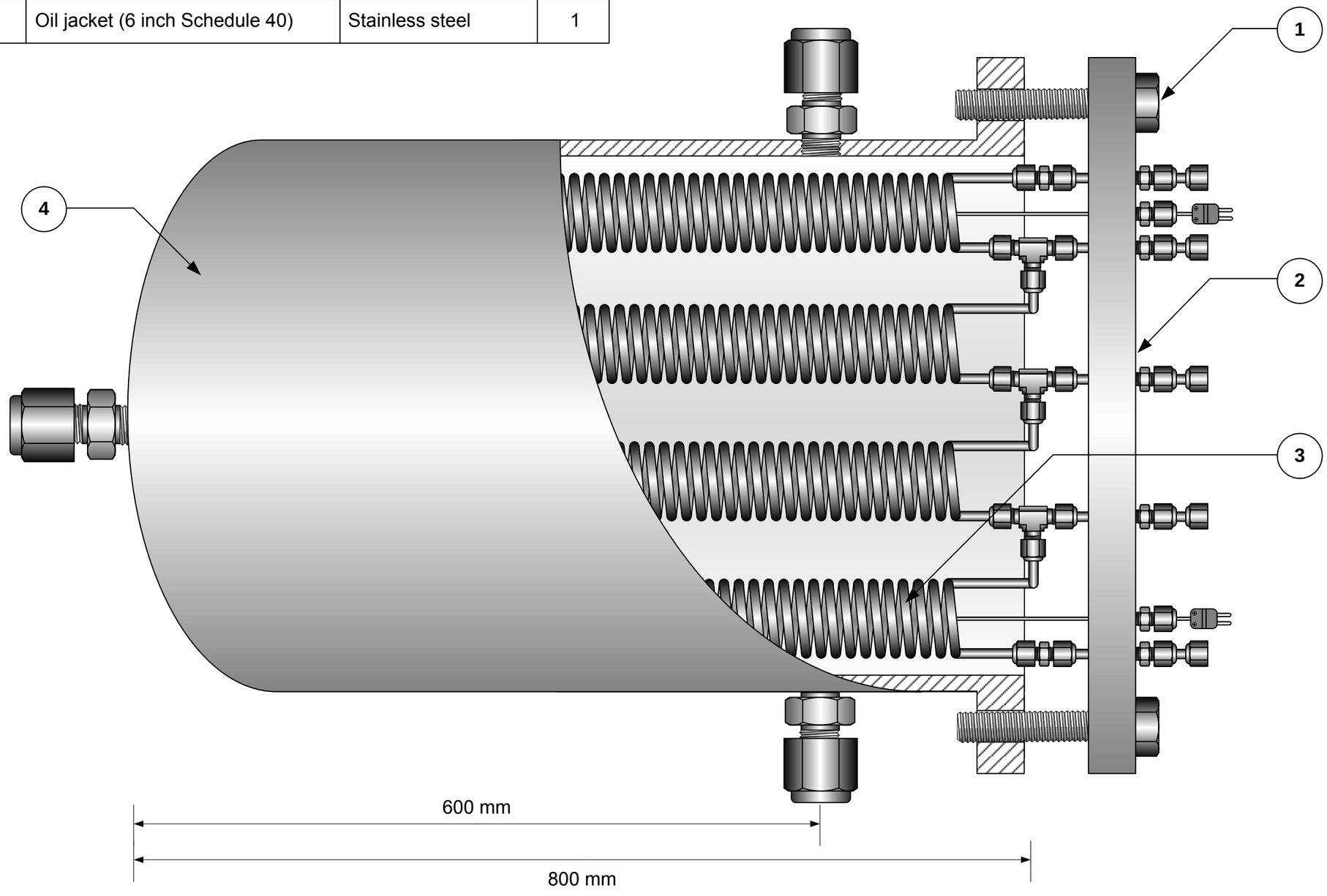

UNIVERSITY OF KWAZULU-NATAL

DRAWING TITLE

COIL TYPE LAMINAR FLOW REACTOR

DRAWN BY DAVID LOKHAT | **SCALE** NONE | **DATED** 28 NOV 2011

DWG NUMBER 0002 | **REV** 1

Pt. No.	Description	Material	Qty.
1	Nut M22 (pitch 2.5 mm)	Carbon steel	12
2	Flange 150(PN20)	Carbon steel	2
3	Reactor tube (½ inch nominal tube)	Copper	1
4	Oil jacket (4 inch nominal pipe)	Carbon steel	1

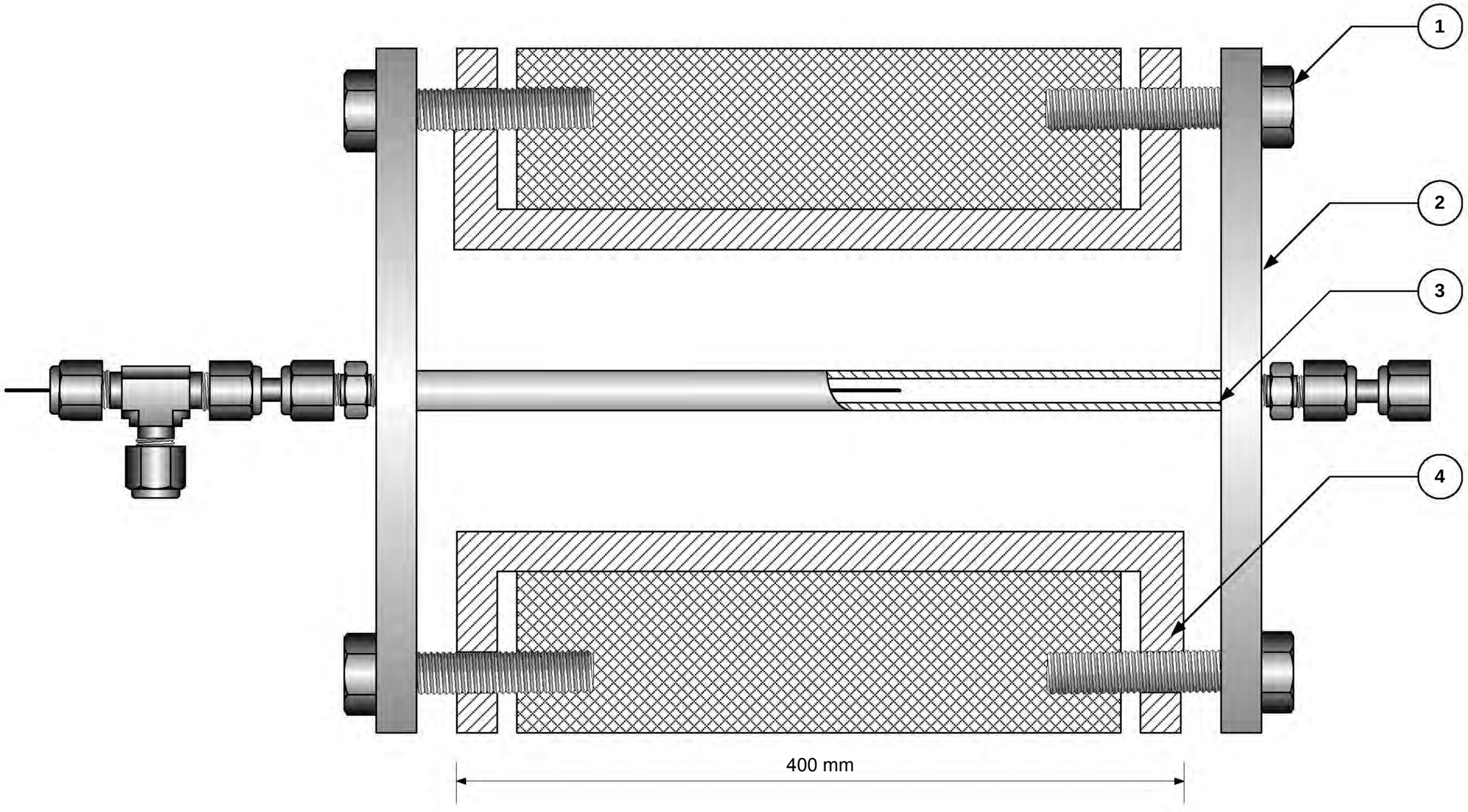

UNIVERSITY OF KWAZULU-NATAL

DRAWING TITLE

FIXED-BED CATALYTIC REACTOR

DRAWN BY DAVID LOKHAT | **SCALE** NONE | **DATED** 28 NOV 2011

DWG NUMBER 0003

REV 0

Appendix C. Gas chromatograph calibration plots

C.1. Shimadzu G.C. 2010 flame ionization detector calibration data.

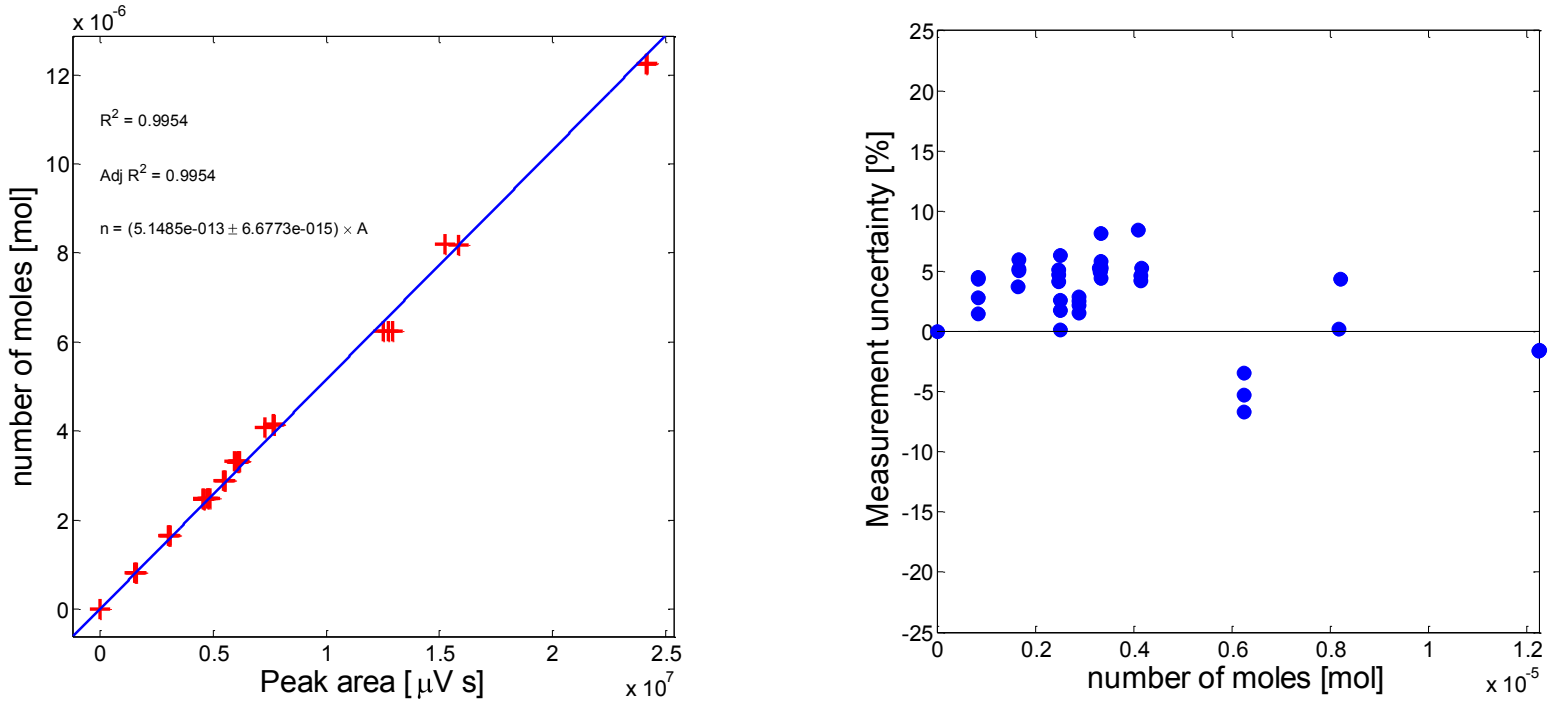

Figure C.1. Shimadzu G.C. 2010 FID calibration plot and calculated measurement uncertainty for HFP. Data fitted to a first-order, zero-intercept function (uncertainty defined as the relative difference between measured and predicted value).

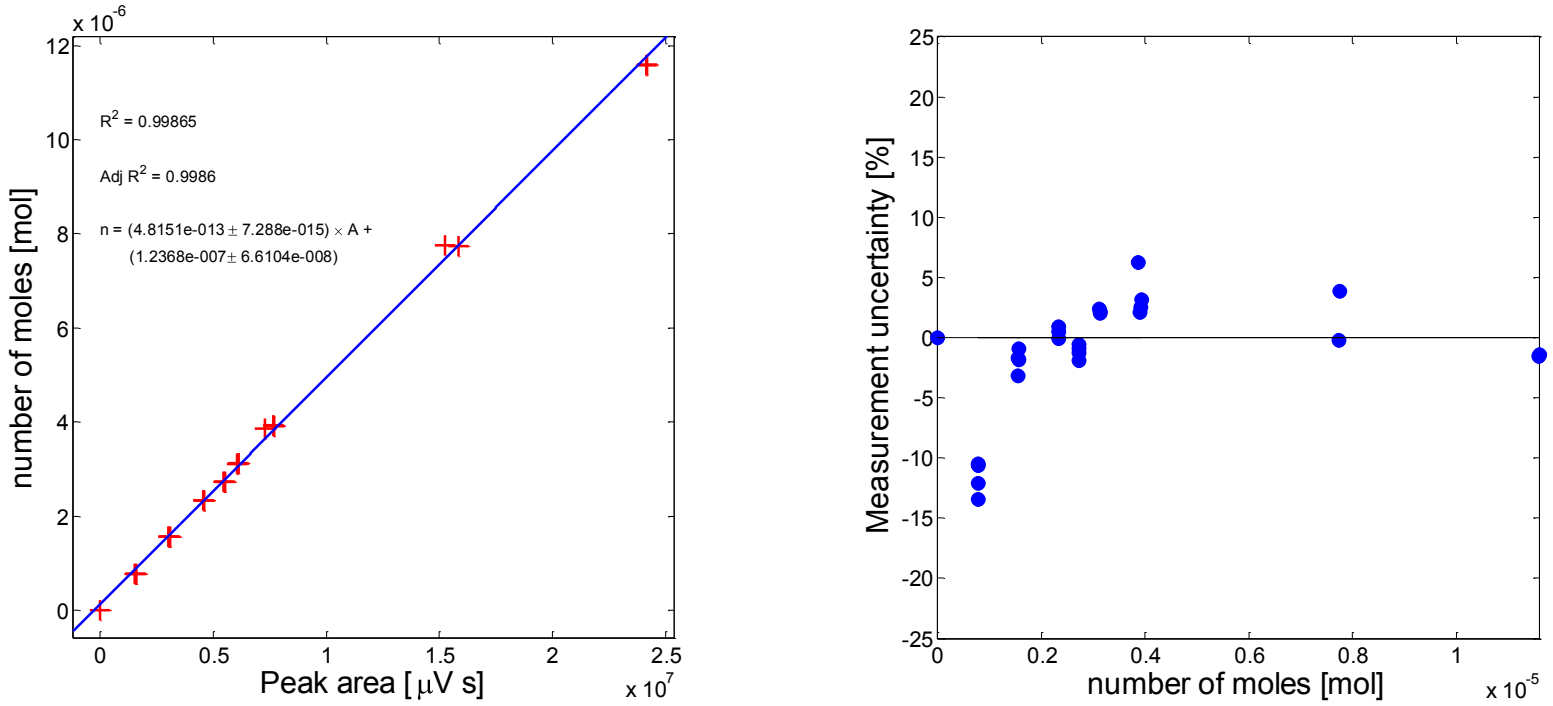

Figure C.2. Shimadzu G.C. 2010 FID calibration plot and calculated measurement uncertainty for HFP. Data fitted to a first-order function (uncertainty defined as the relative difference between measured and predicted value).

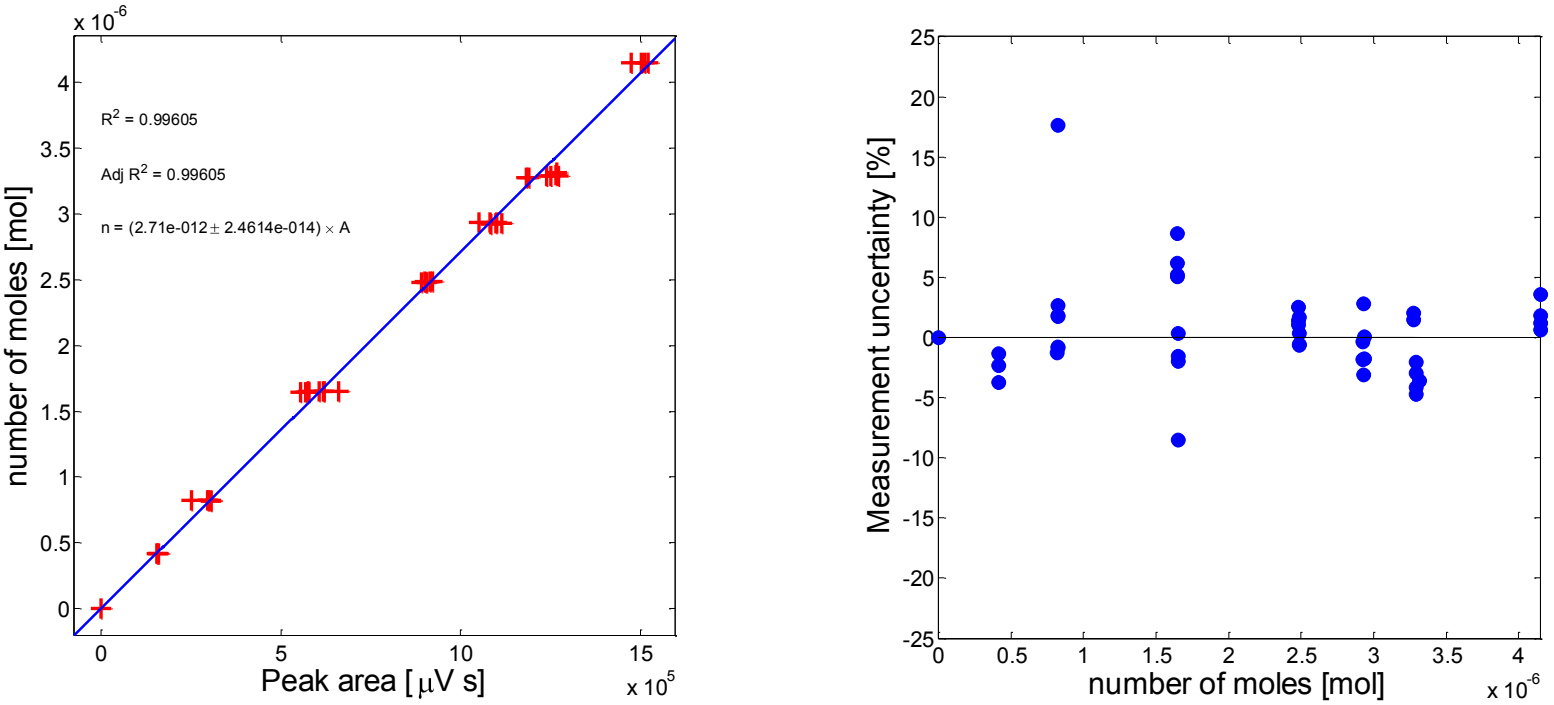

Figure C.3. Shimadzu G.C. 2010 FID calibration plot and calculated measurement uncertainty for HFPO. Data fitted to a first-order, zero-intercept function (uncertainty defined as the relative difference between measured and predicted value).

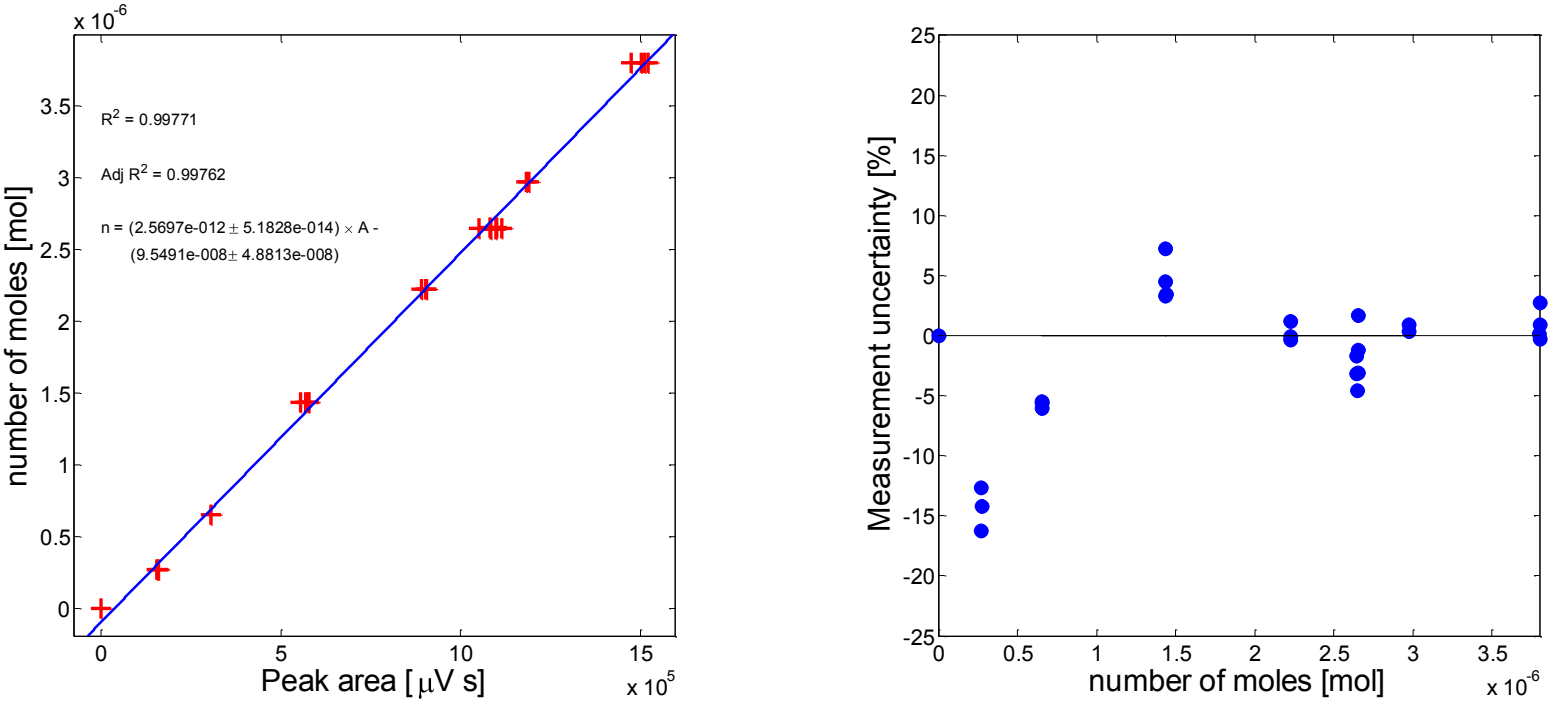

Figure C.4. Shimadzu G.C. 2010 FID calibration plot and calculated measurement uncertainty for HFPO. Data fitted to a first-order function (uncertainty defined as the relative difference between measured and predicted value).

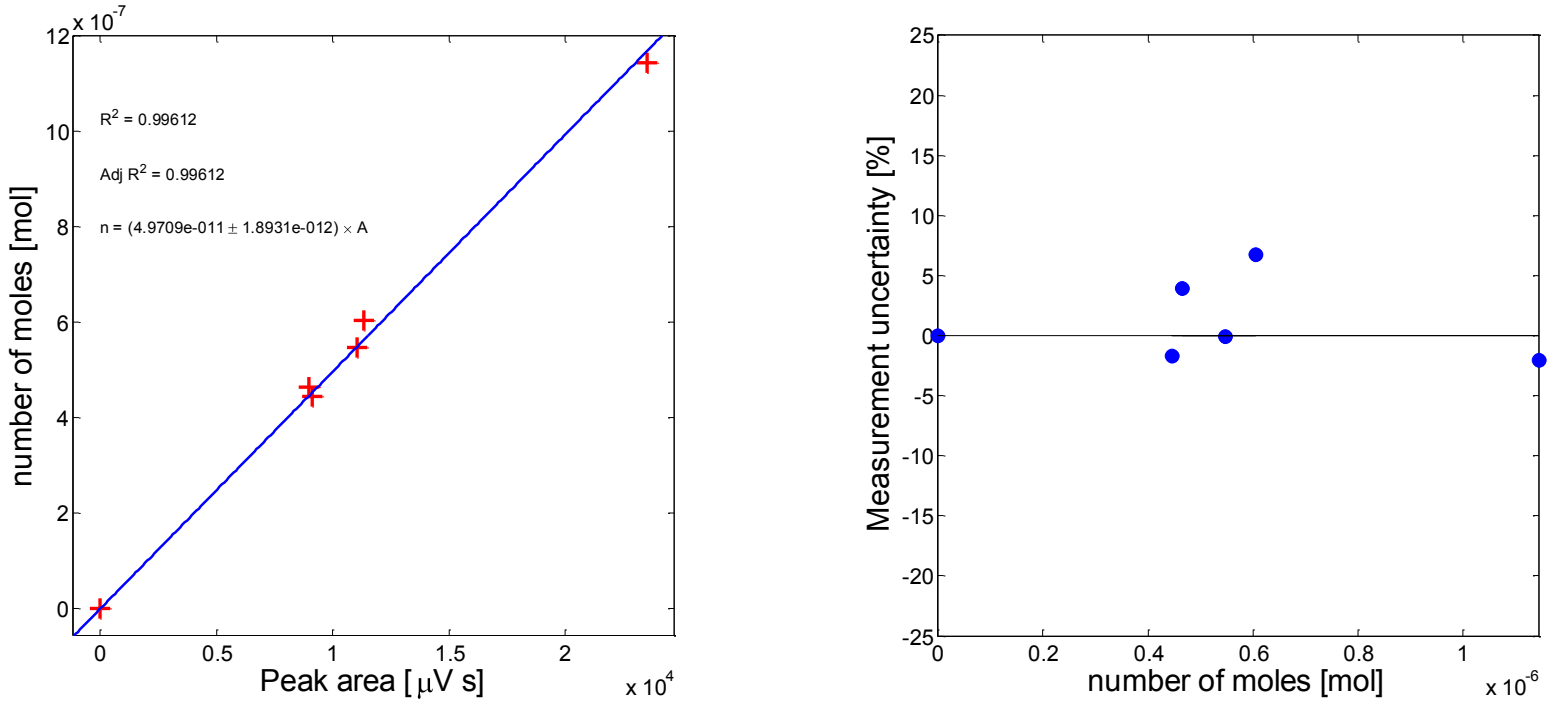

Figure C.5. Shimadzu G.C. 2010 FID calibration plot and calculated measurement uncertainty for CF_3OCF_3. Data fitted to a first-order, zero-intercept function (uncertainty defined as the relative difference between measured and predicted value).

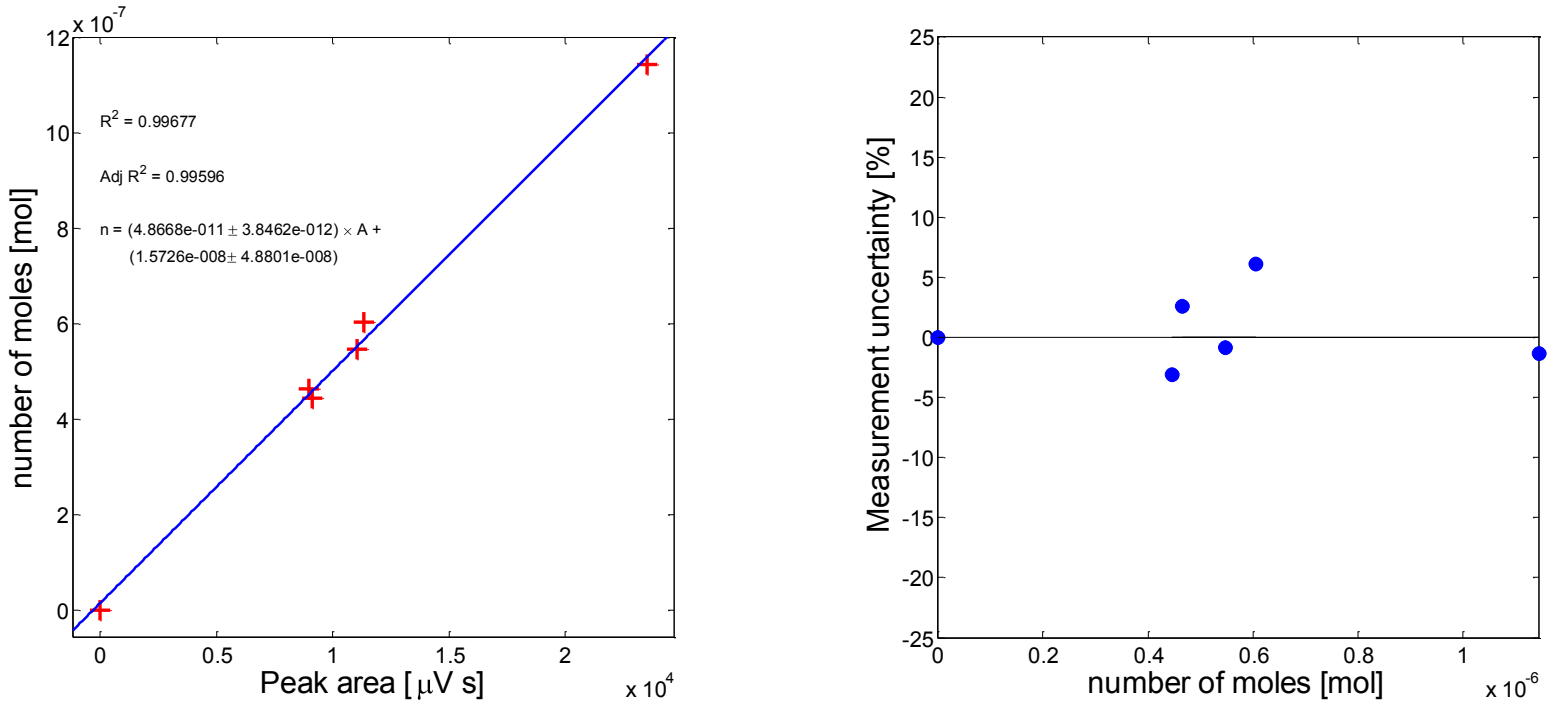

Figure C.6. Shimadzu G.C. 2010 FID calibration plot and calculated measurement uncertainty for CF_3OCF_3. Data fitted to a first-order function (uncertainty defined as the relative difference between measured and predicted value).

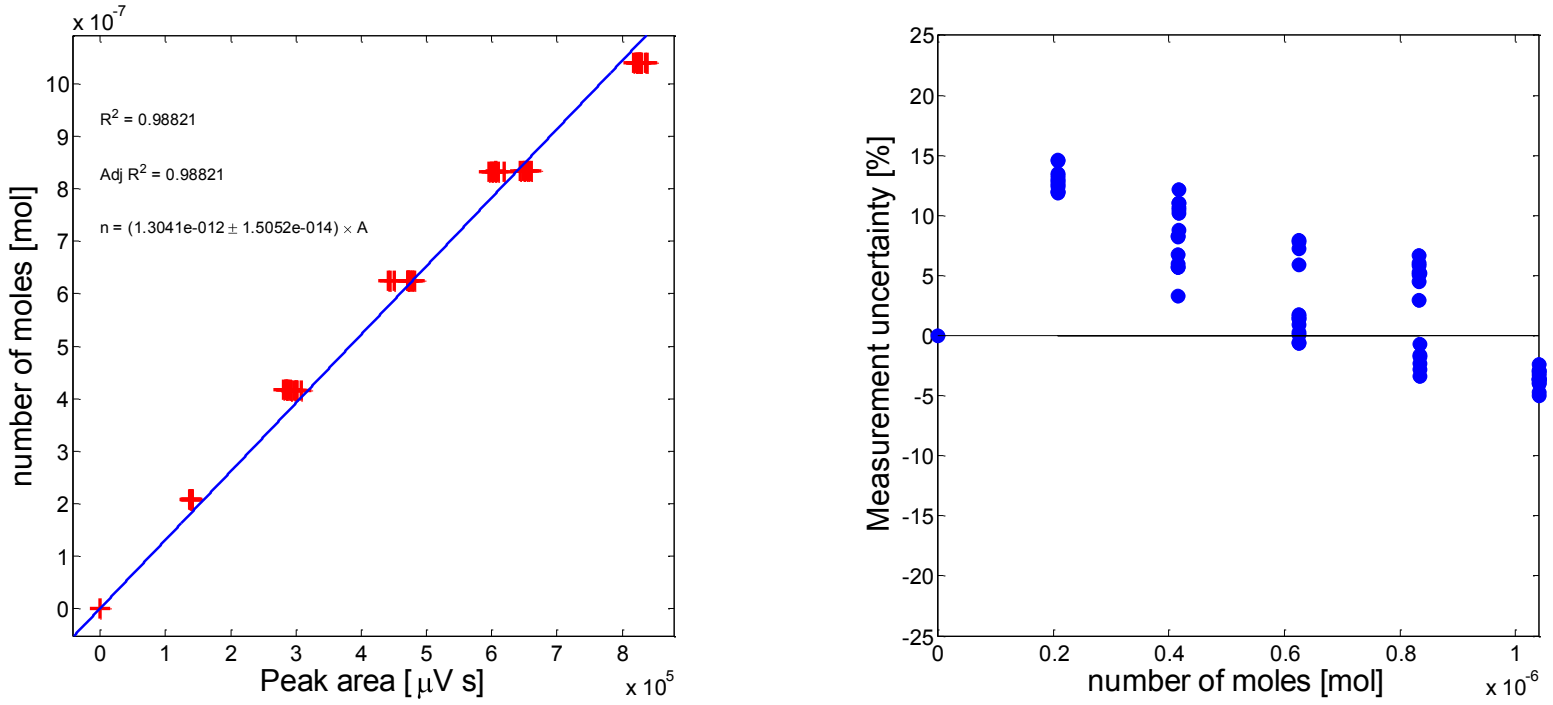

Figure C.7. Shimadzu G.C. 2010 FID calibration plot and calculated measurement uncertainty for C_2F_4. Data fitted to a first-order, zero-intercept function (uncertainty defined as the relative difference between measured and predicted value).

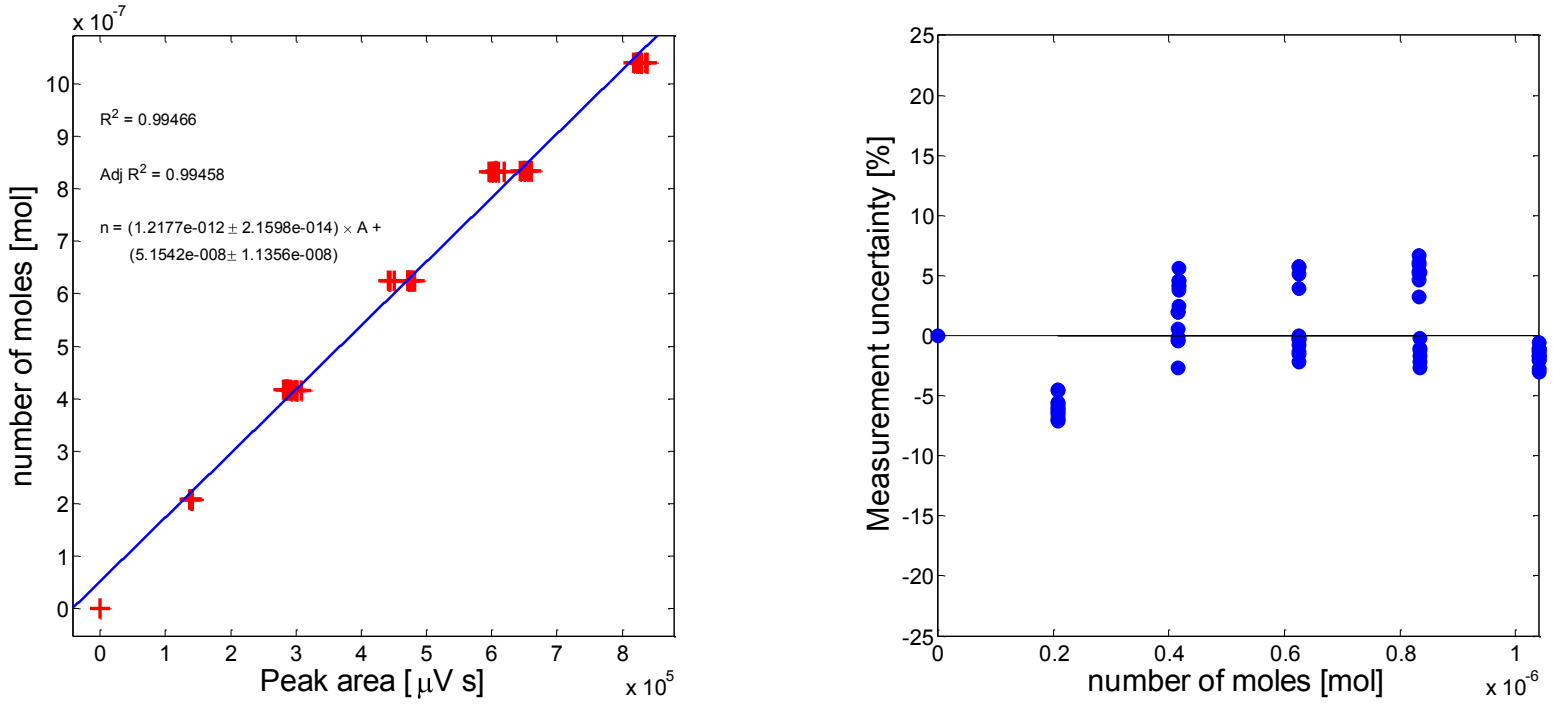

Figure C.8. Shimadzu G.C. 2010 FID calibration plot and calculated measurement uncertainty for C_2F_4. Data fitted to a first-order function (uncertainty defined as the relative difference between measured and predicted value).

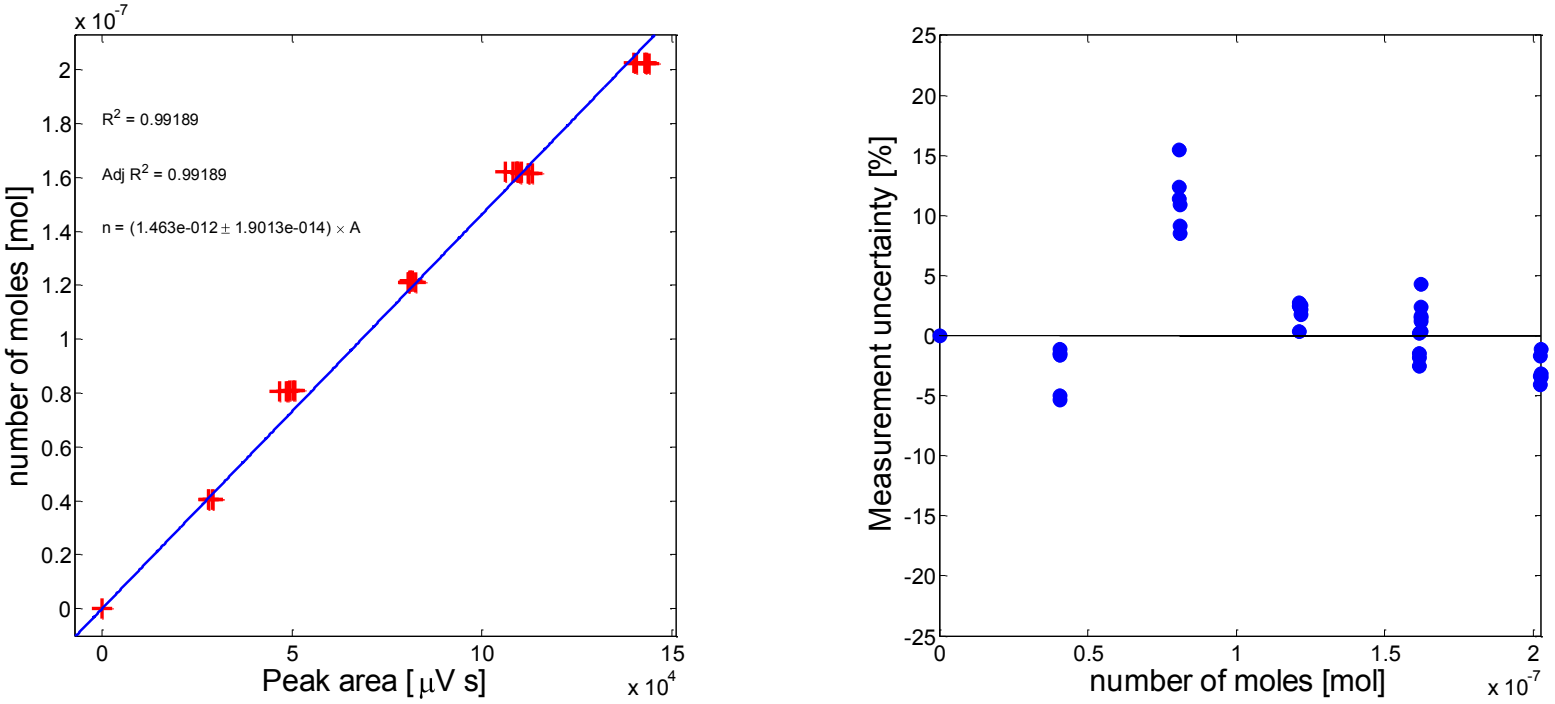

Figure C.9. Shimadzu G.C. 2010 FID calibration plot and calculated measurement uncertainty for *c*-C_3F_6. Data fitted to a first-order, zero-intercept function (uncertainty defined as the relative difference between measured and predicted value).

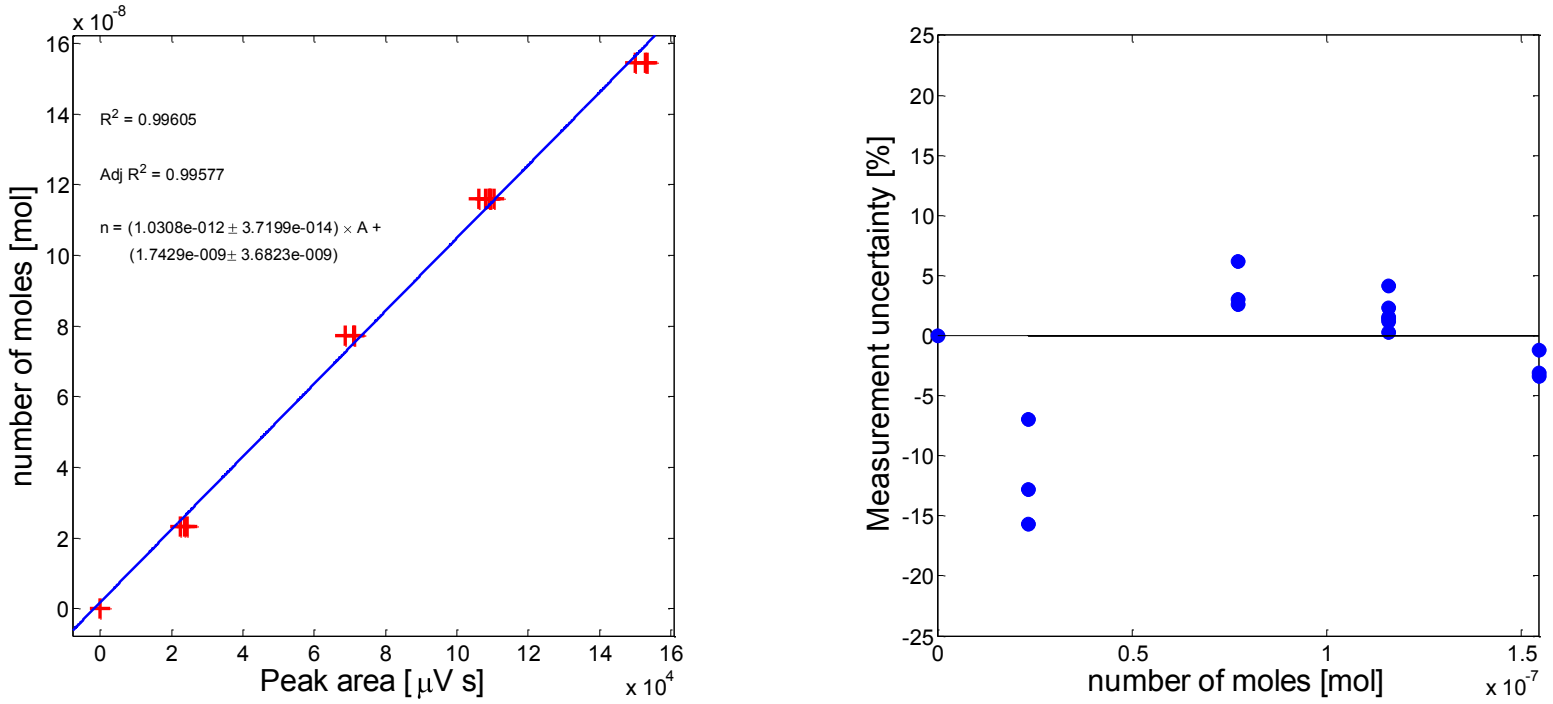

Figure C.10. Shimadzu G.C. 2010 FID calibration plot and calculated measurement uncertainty for *c*-C_3F_6. Data fitted to a first-order function (uncertainty defined as the relative difference between measured and predicted value).

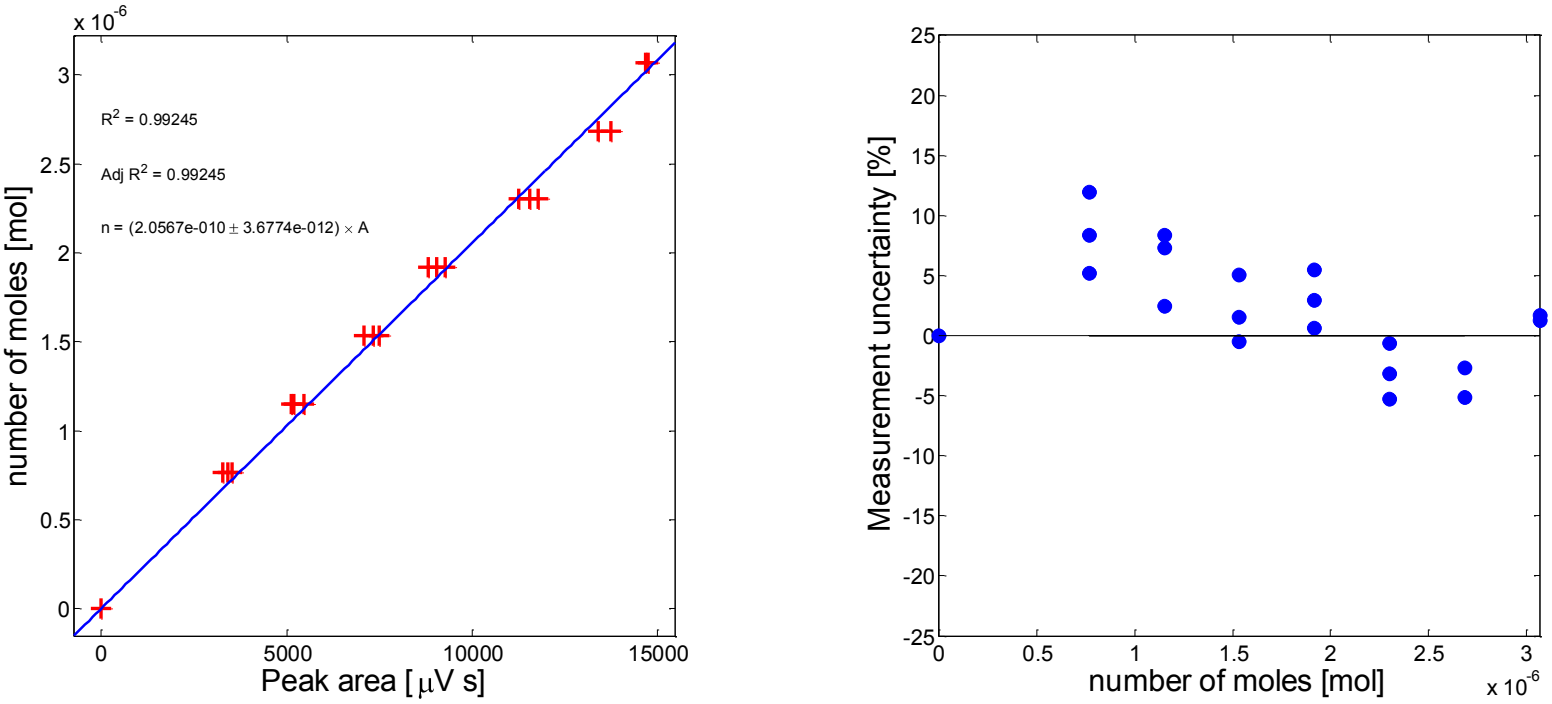

Figure C.11. Shimadzu G.C. 2010 FID calibration plot and calculated measurement uncertainty for C_2F_6. Data fitted to a first-order, zero-intercept function (uncertainty defined as the relative difference between measured and predicted value).

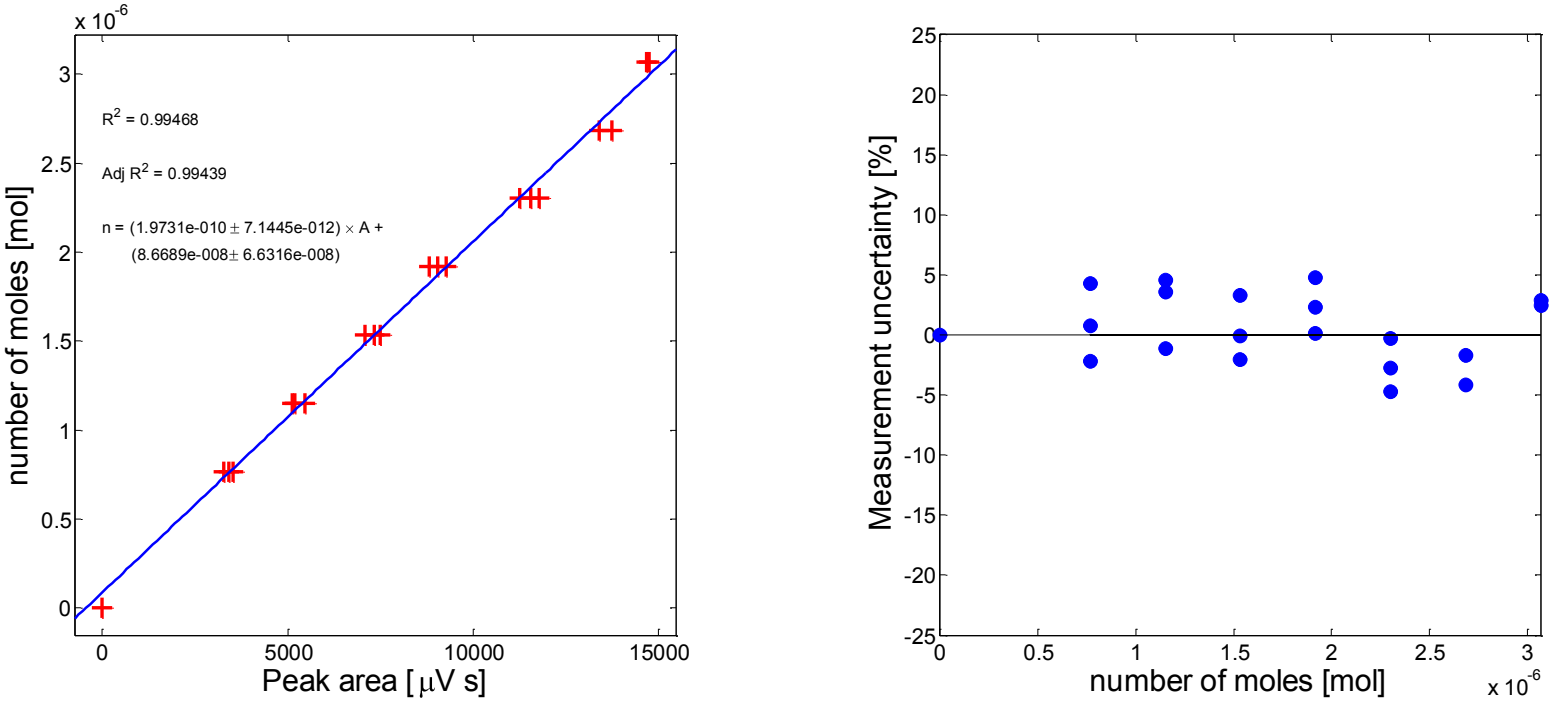

Figure C.12. Shimadzu G.C. 2010 FID calibration plot and calculated measurement uncertainty for C_2F_6. Data fitted to a first-order function (uncertainty defined as the relative difference between measured and predicted value).

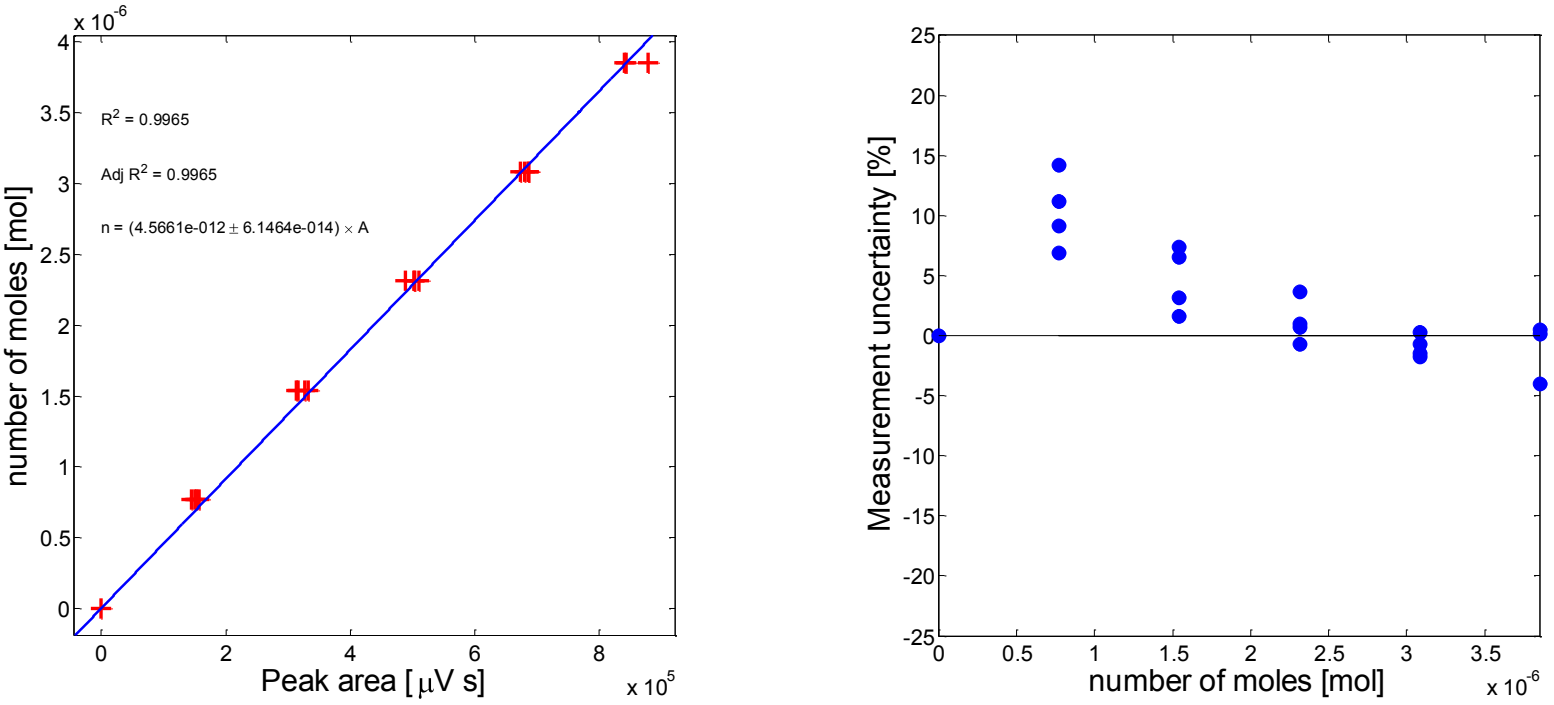

Figure C.13. Shimadzu G.C. 2010 FID calibration plot and calculated measurement uncertainty for C_3F_8. Data fitted to a first-order, zero-intercept function (uncertainty defined as the relative difference between measured and predicted value).

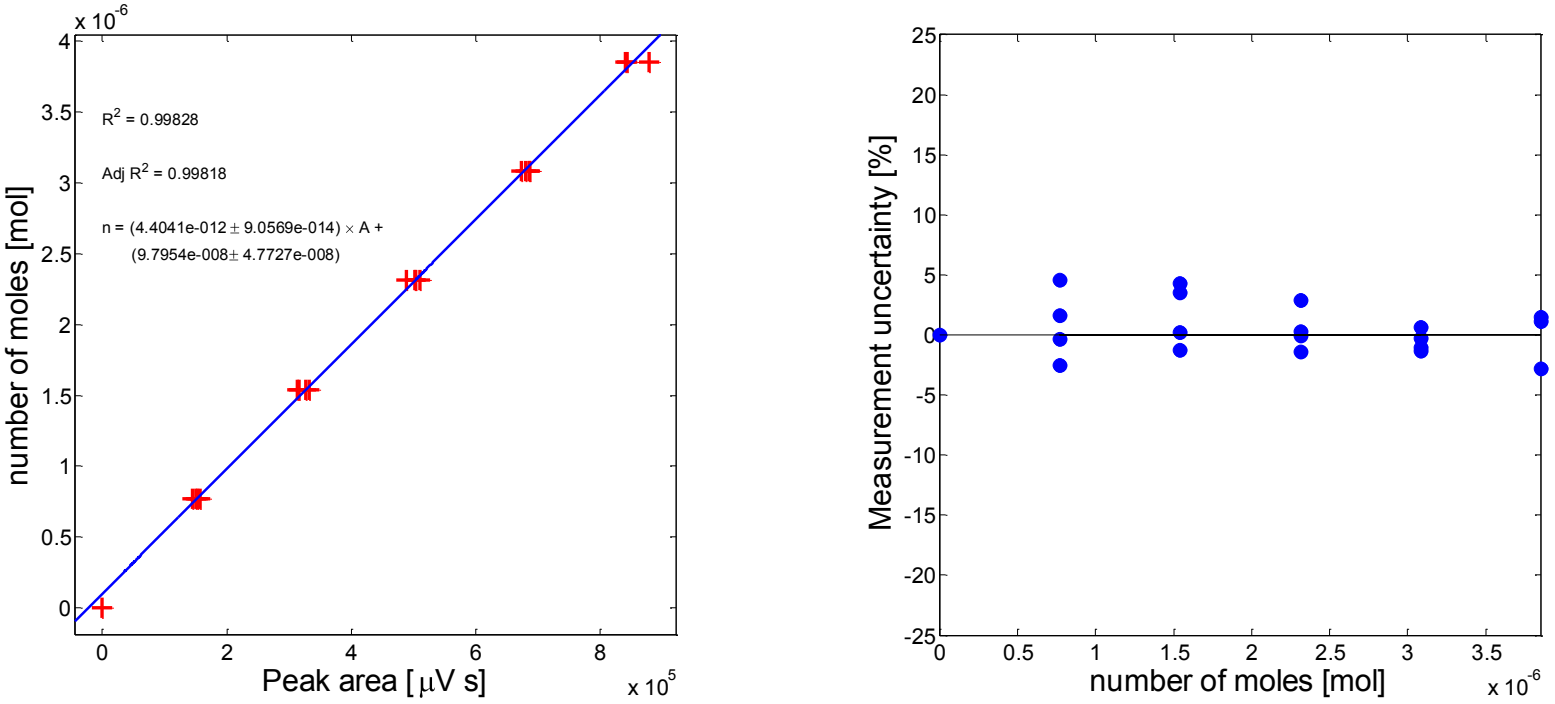

Figure C.14. Shimadzu G.C. 2010 FID calibration plot and calculated measurement uncertainty for C_3F_8. Data fitted to a first-order function (uncertainty defined as the relative difference between measured and predicted value).

C.2. Shimadzu G.C. 2010 thermal conductivity detector calibration data.

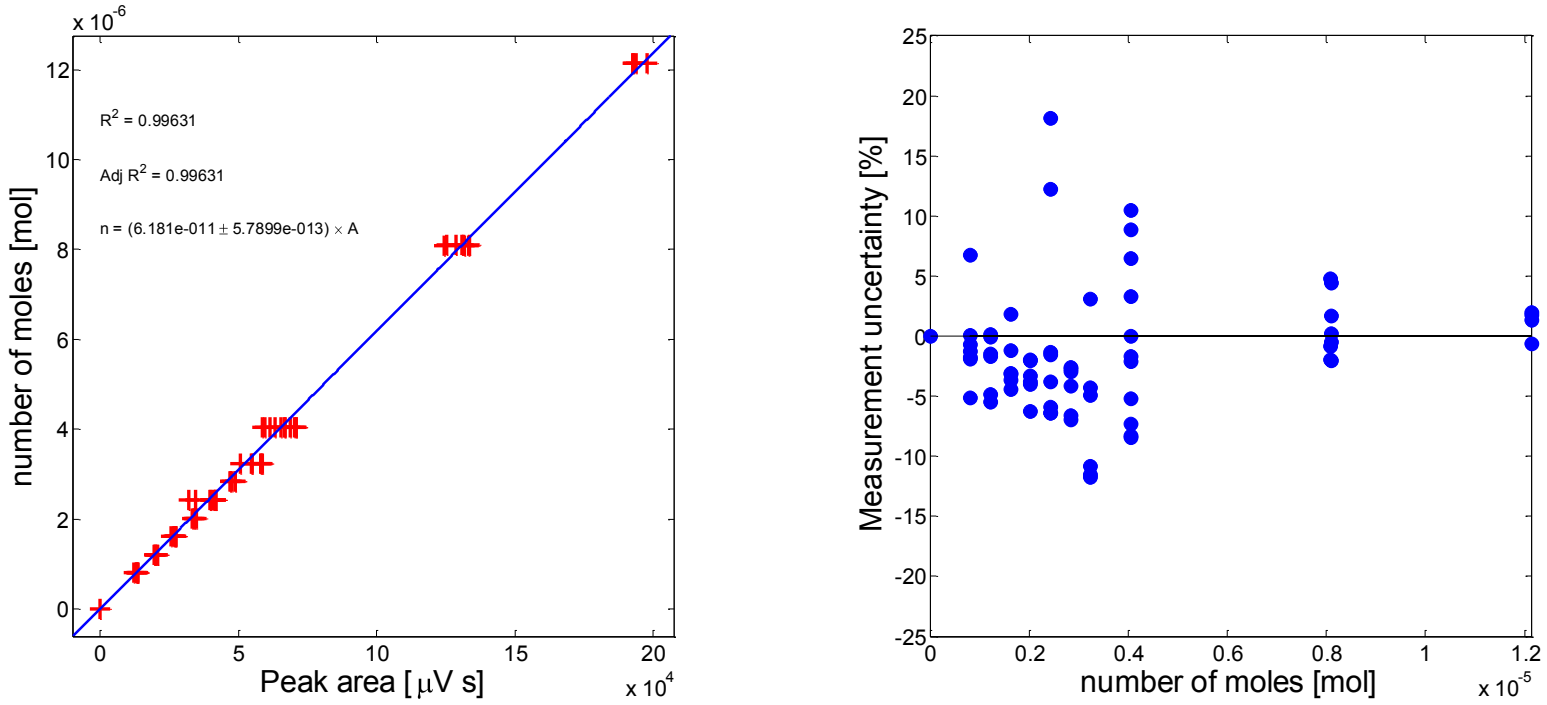

Figure C.15. Shimadzu G.C. 2010 TCD calibration plot and calculated measurement uncertainty for O_2. Data fitted to a first-order, zero-intercept function (uncertainty defined as the relative difference between measured and predicted value).

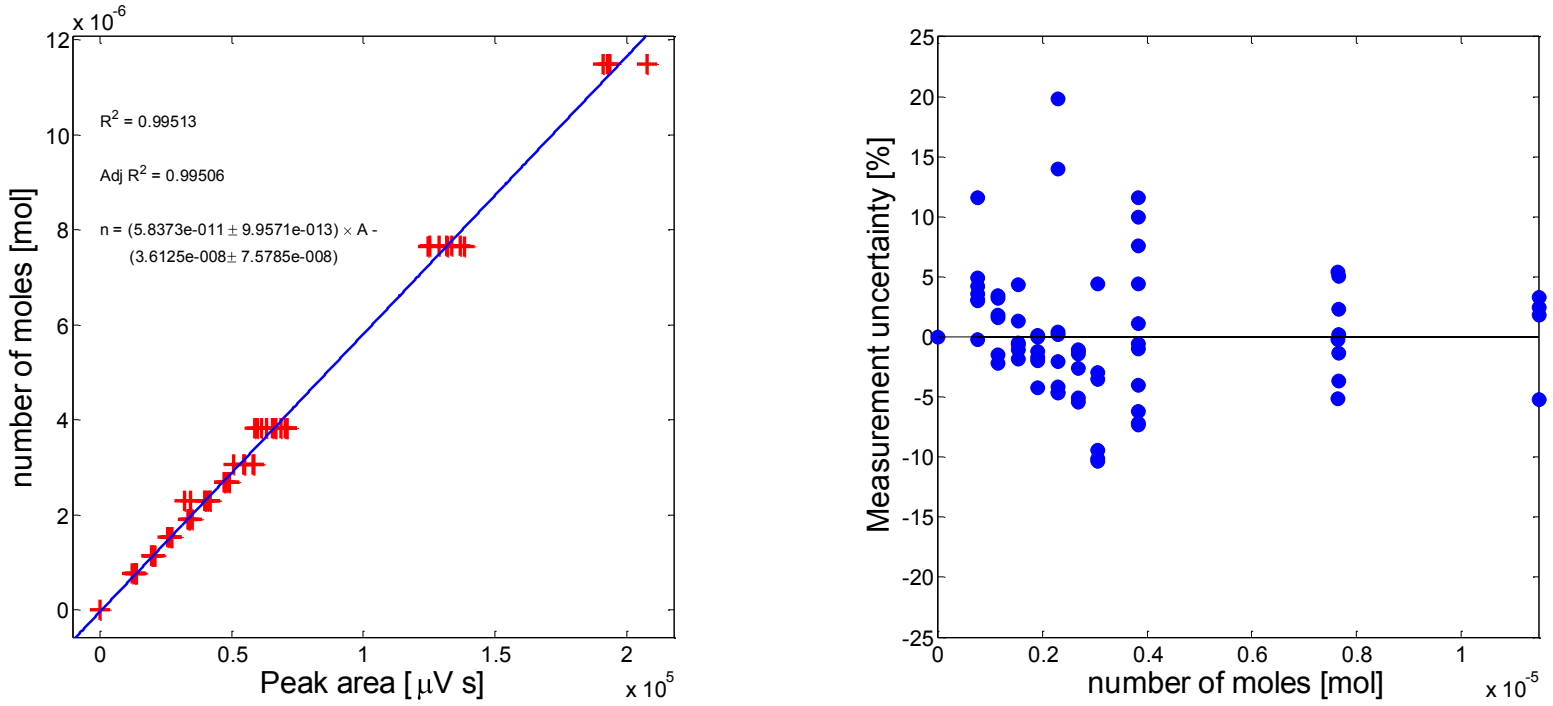

Figure C.16. Shimadzu G.C. 2010 TCD calibration plot and calculated measurement uncertainty for O_2. Data fitted to a first-order function (uncertainty defined as the relative difference between measured and predicted value).

C.3. Shimadzu G.C. 2014 thermal conductivity detector calibration data.

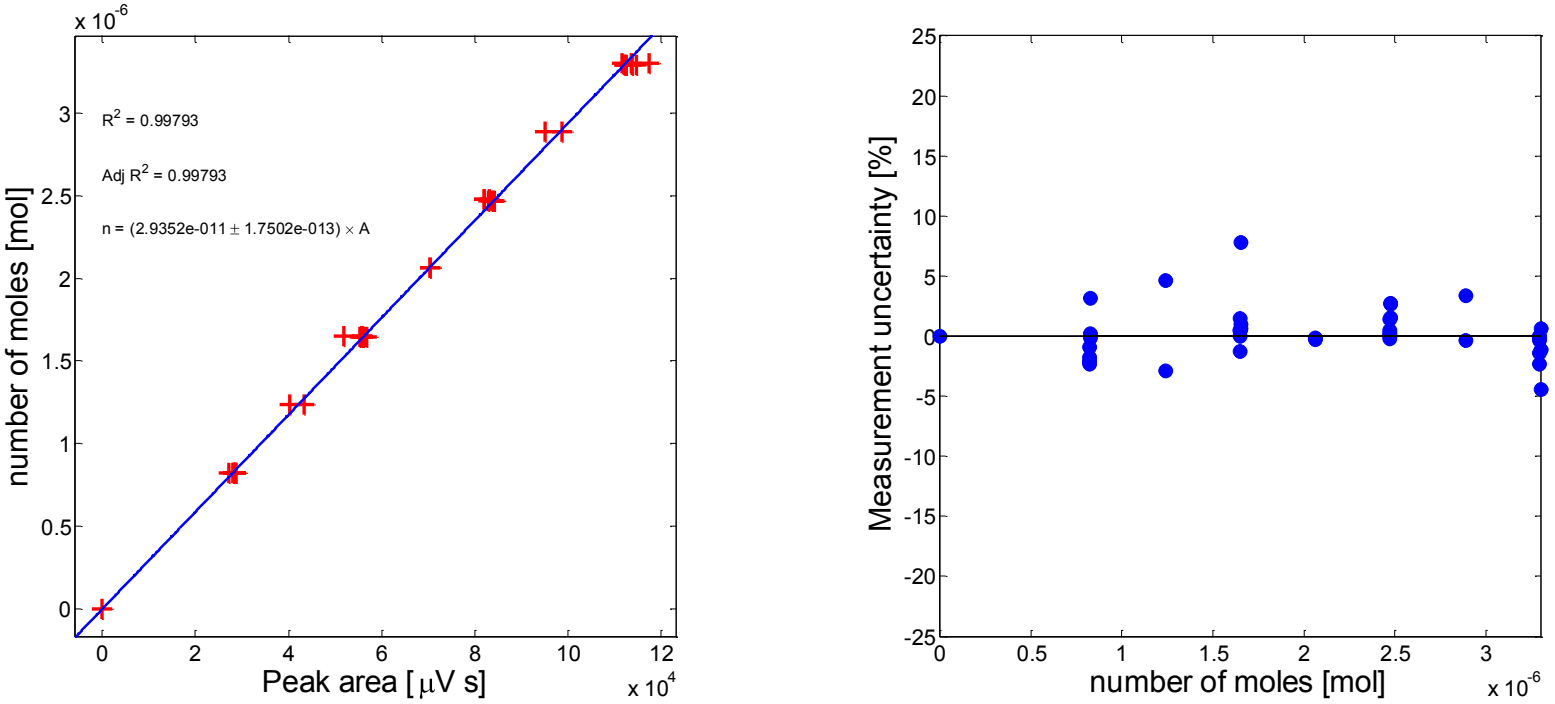

Figure C.17. Shimadzu G.C. 2014 TCD calibration plot and calculated measurement uncertainty for O_2. Data fitted to a first-order, zero-intercept function (uncertainty defined as the relative difference between measured and predicted value).

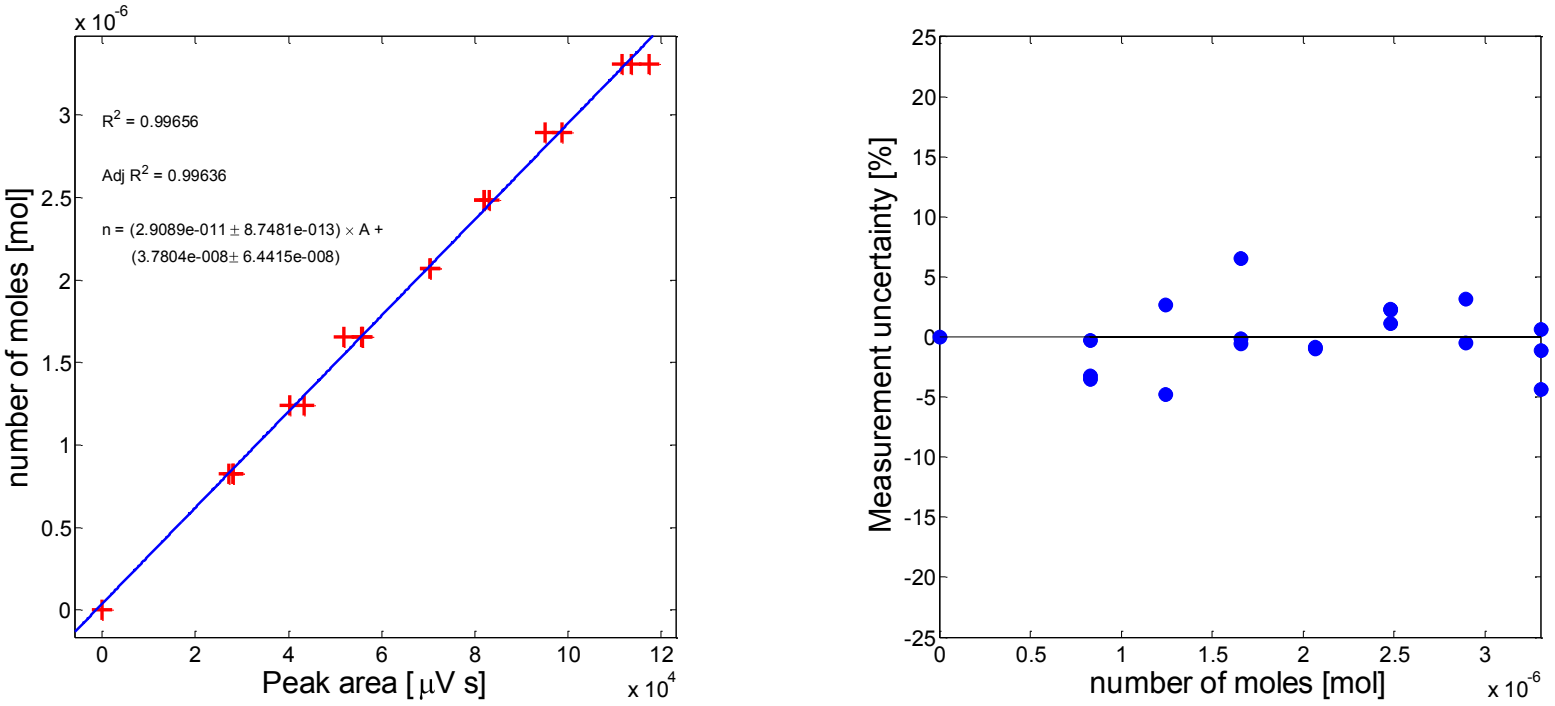

Figure C.18. Shimadzu G.C. 2014 TCD calibration plot and calculated measurement uncertainty for O_2. Data fitted to a first-order function (uncertainty defined as the relative difference between measured and predicted value).

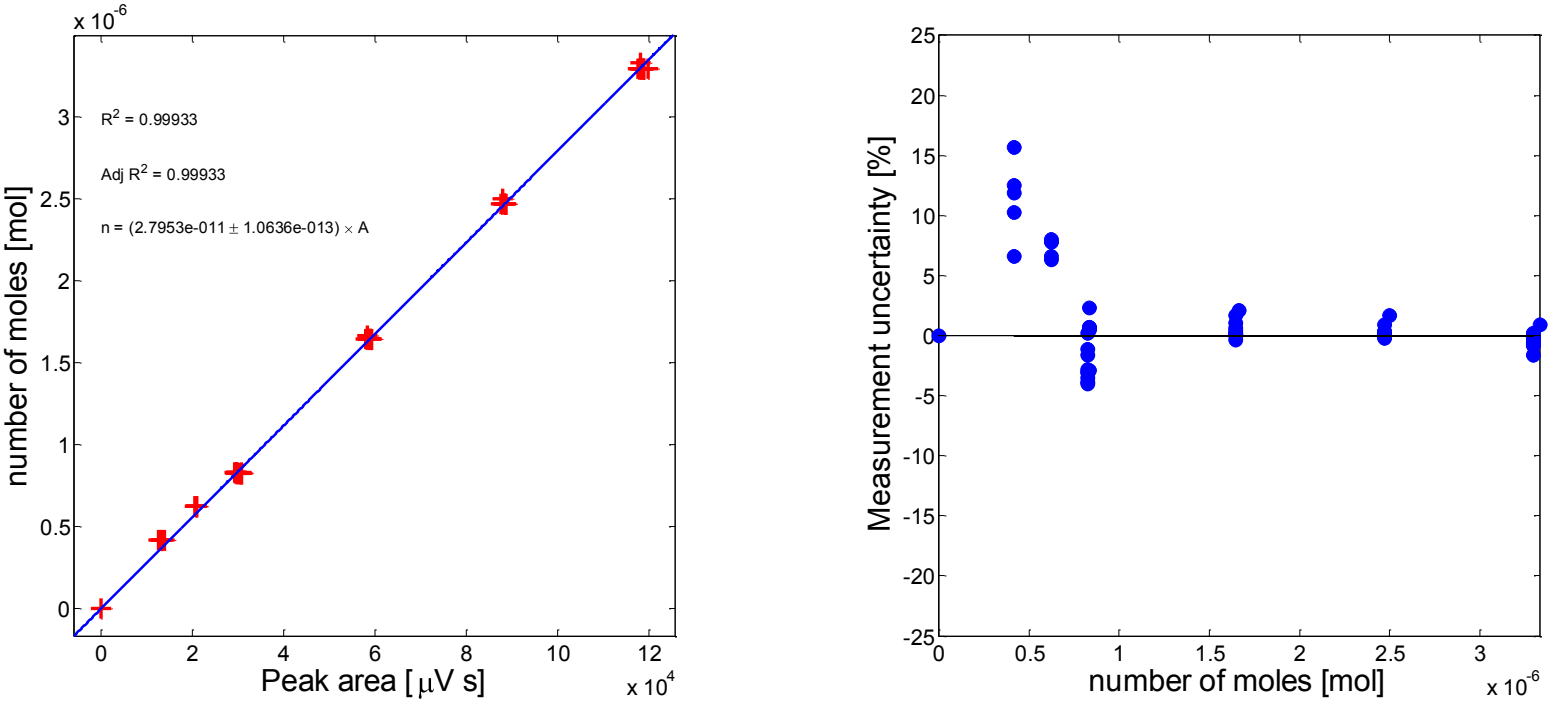

Figure C.19. Shimadzu G.C. 2014 TCD calibration plot and calculated measurement uncertainty for air. Data fitted to a first-order, zero-intercept function (uncertainty defined as the relative difference between measured and predicted value).

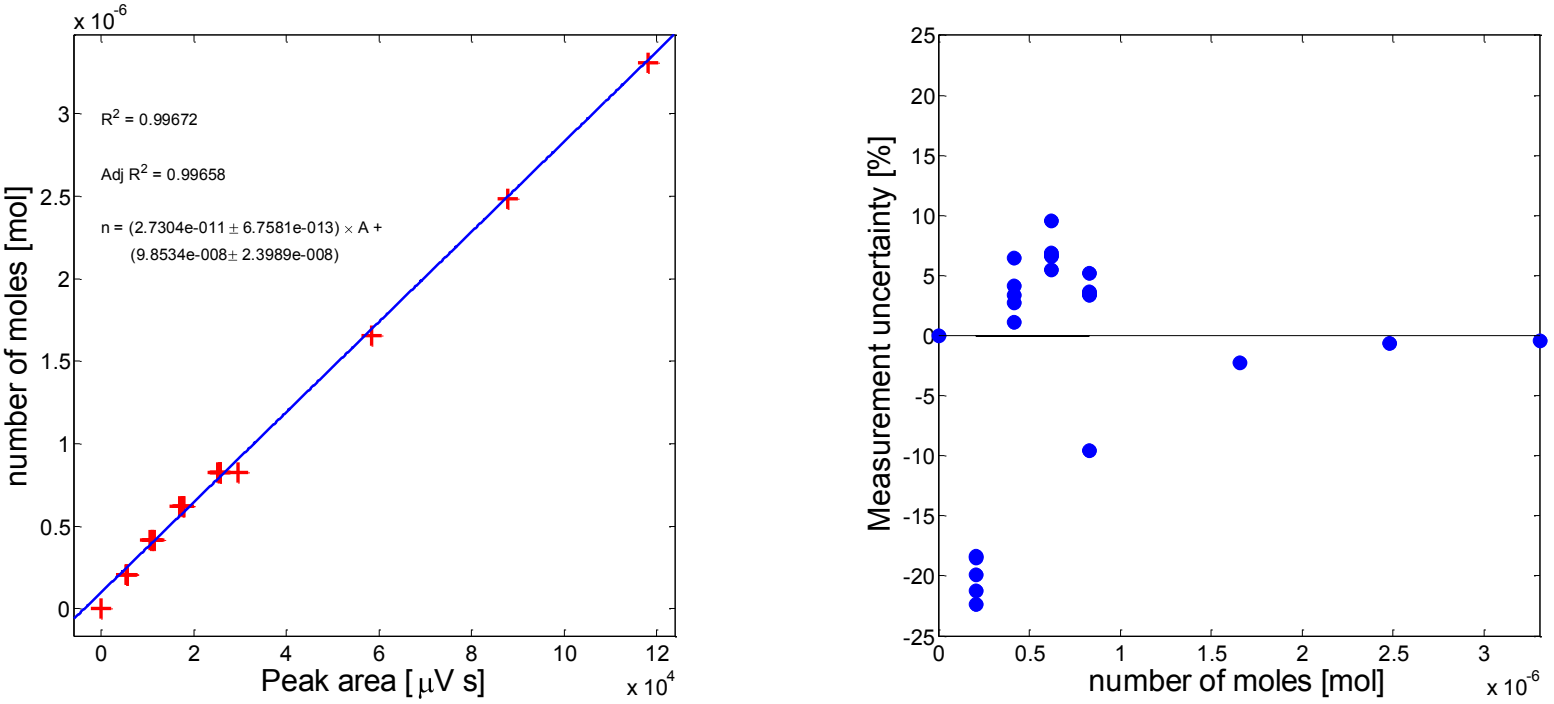

Figure C.20. Shimadzu G.C. 2014 TCD calibration plot and calculated measurement uncertainty for air. Data fitted to a first-order function (uncertainty defined as the relative difference between measured and predicted value).

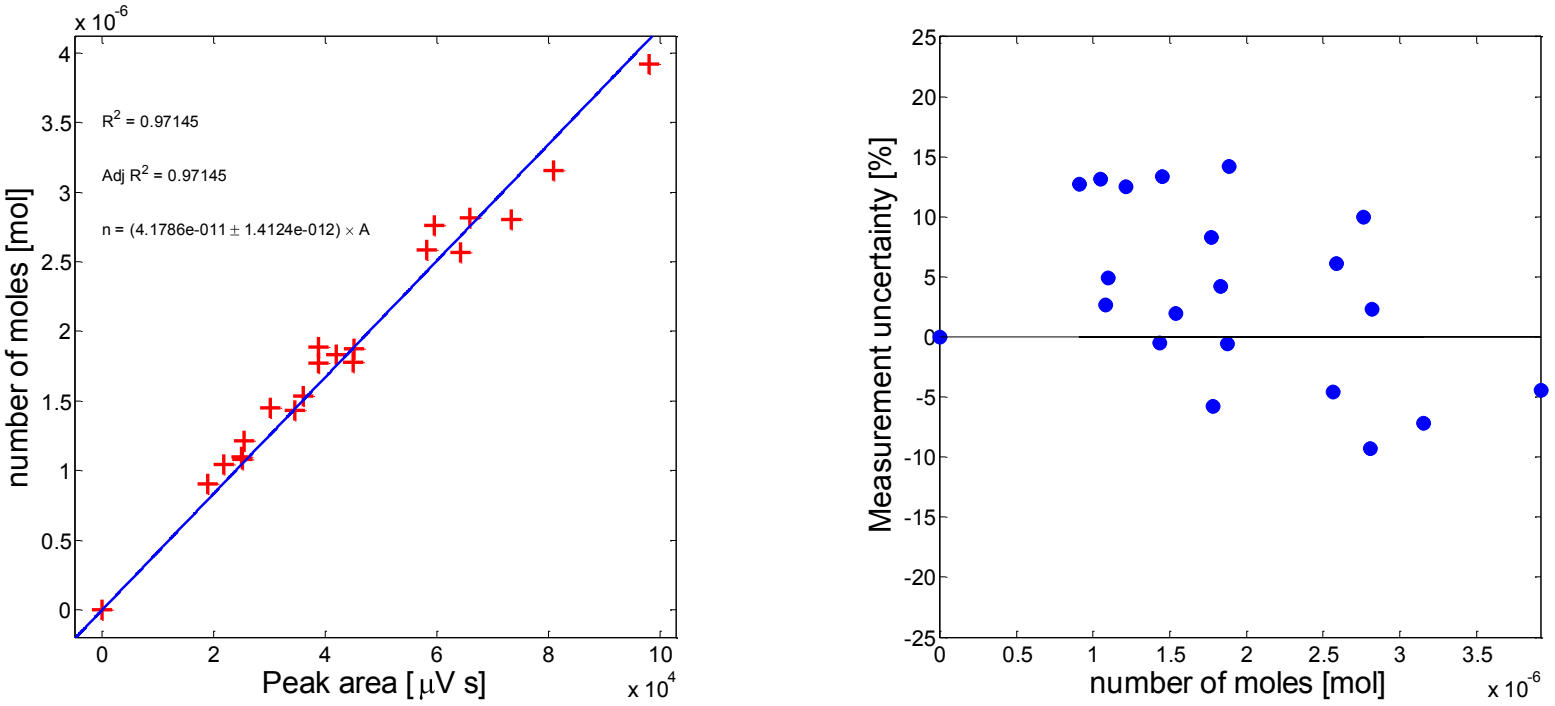

Figure C.21. Shimadzu G.C. 2014 TCD calibration plot and calculated measurement uncertainty for CF_3COF. Data fitted to a first-order, zero-intercept function (uncertainty defined as the relative difference between measured and predicted value).

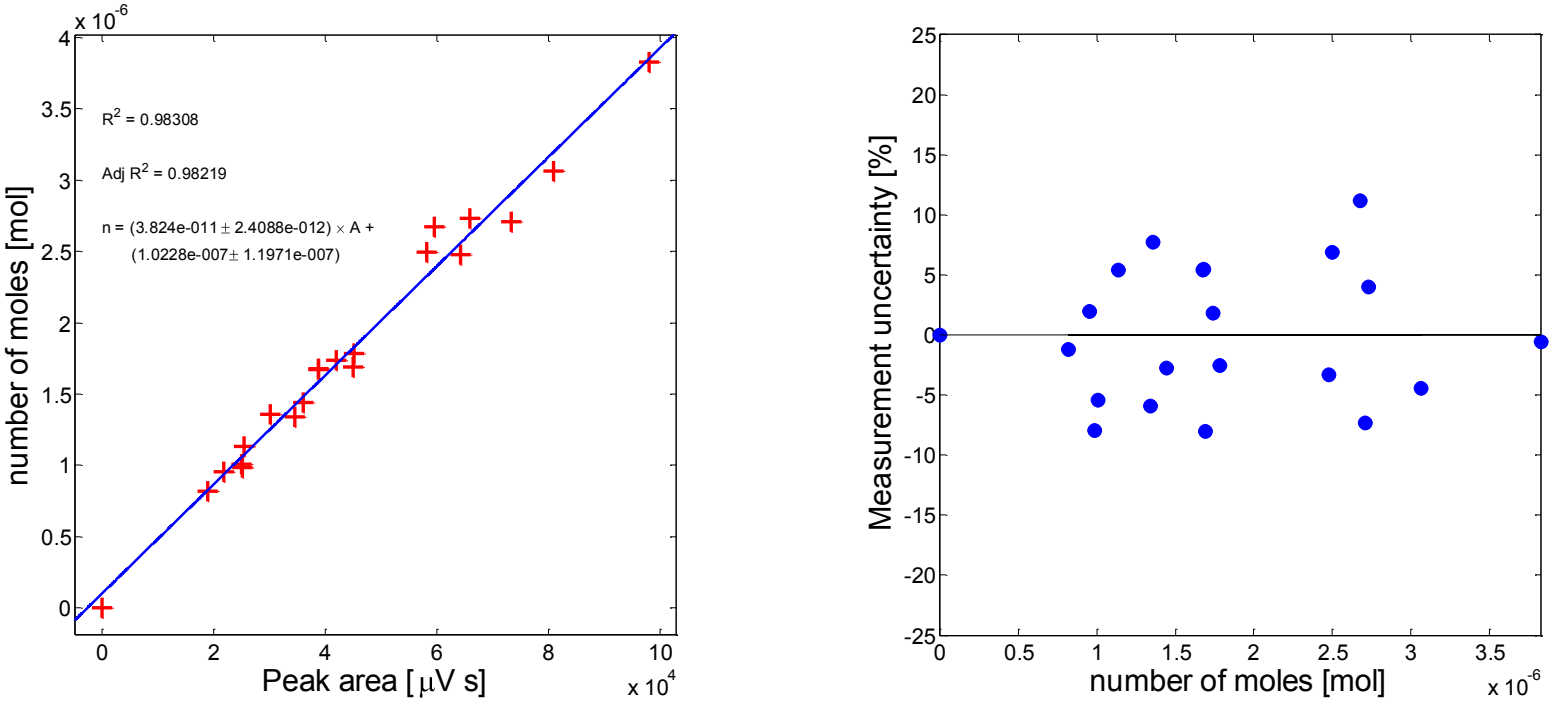

Figure C.22. Shimadzu G.C. 2014 TCD calibration plot and calculated measurement uncertainty for CF_3COF. Data fitted to a first-order function (uncertainty defined as the relative difference between measured and predicted value).

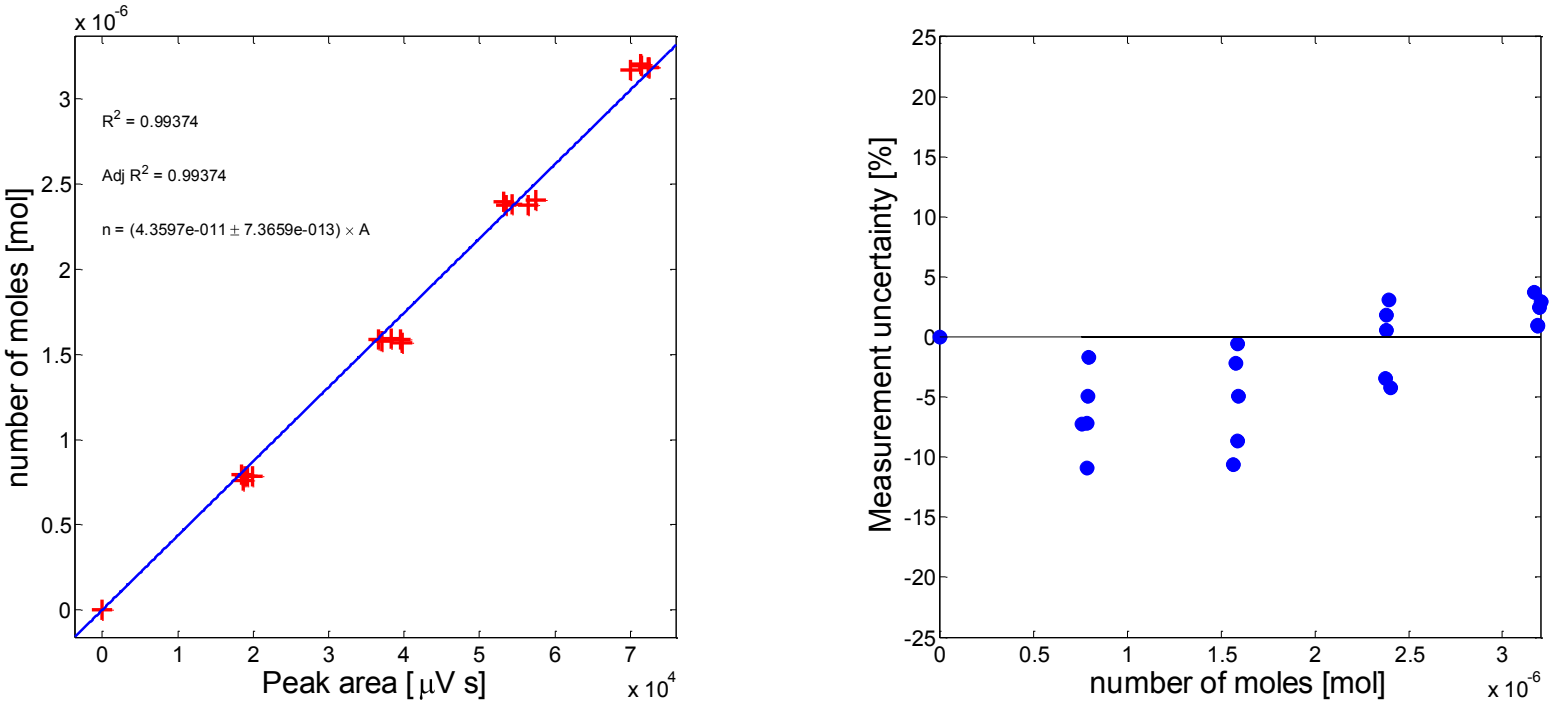

Figure C.23. Shimadzu G.C. 2014 TCD calibration plot and calculated measurement uncertainty for COF_2. Data fitted to a first-order, zero-intercept function (uncertainty defined as the relative difference between measured and predicted value).

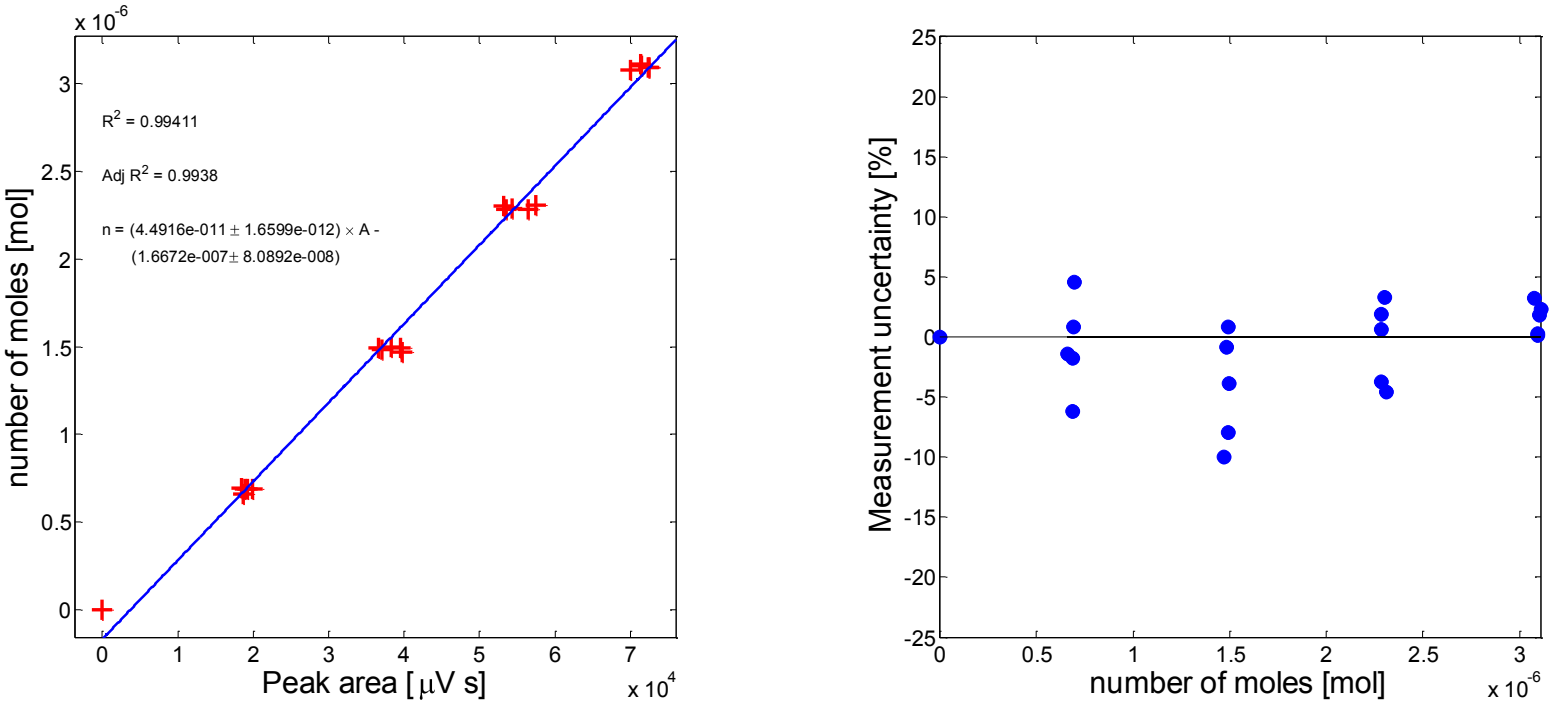

Figure C.24. Shimadzu G.C. 2014 TCD calibration plot and calculated measurement uncertainty for COF_2. Data fitted to a first-order function (uncertainty defined as the relative difference between measured and predicted value).

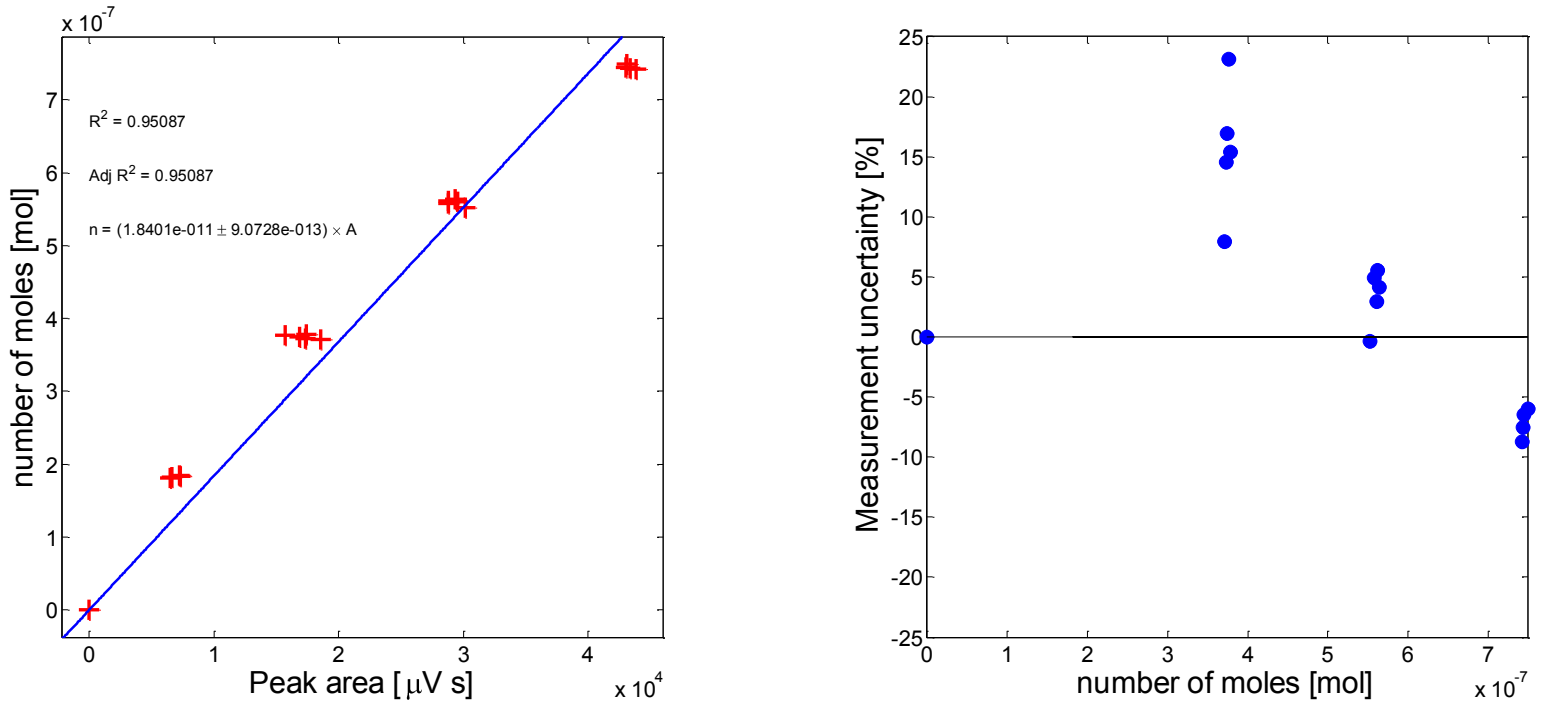

Figure C.25. Shimadzu G.C. 2014 TCD calibration plot and calculated measurement uncertainty for *c*-C_3F_6. Data fitted to a first-order, zero-intercept function (uncertainty defined as the relative difference between measured and predicted value).

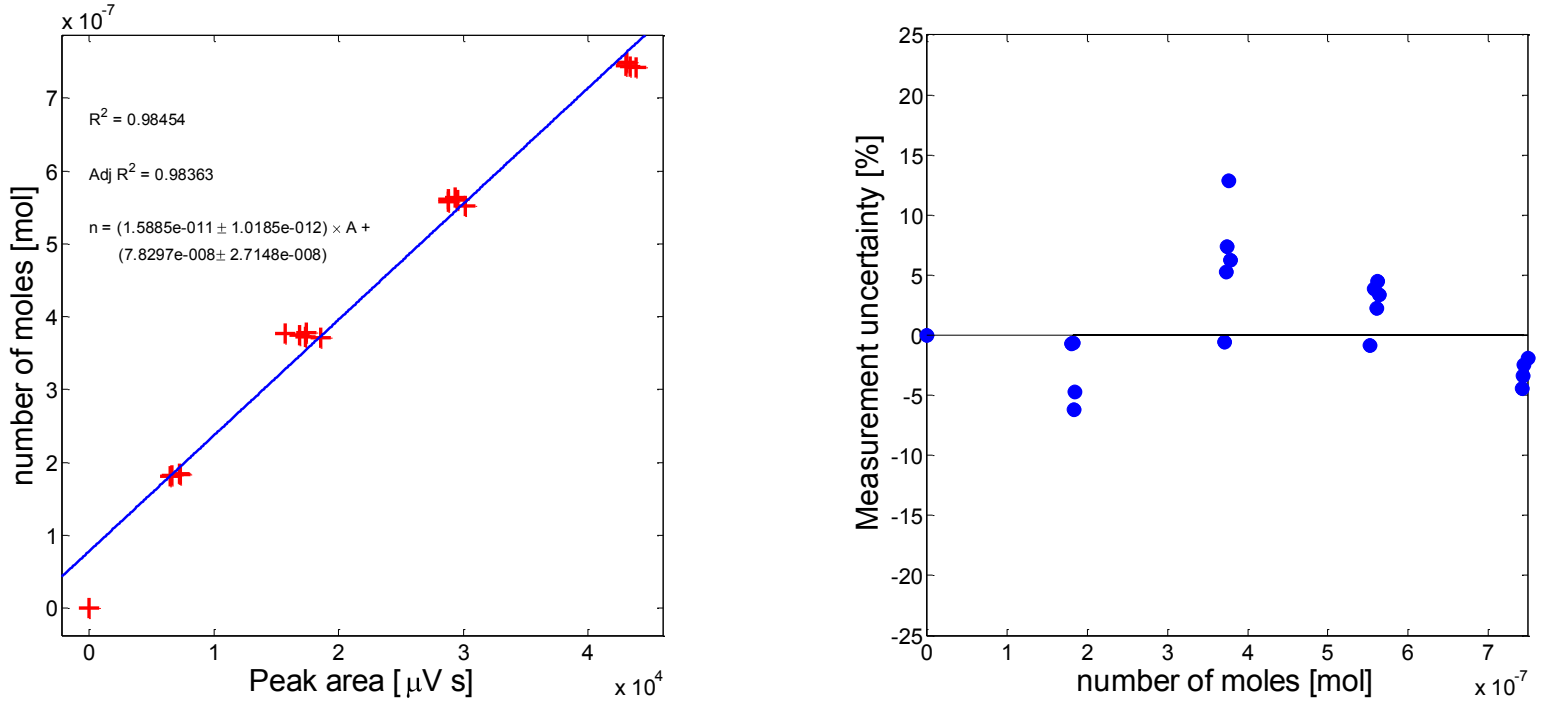

Figure C.26. Shimadzu G.C. 2014 TCD calibration plot and calculated measurement uncertainty for *c*-C_3F_6. Data fitted to a first-order function (uncertainty defined as the relative difference between measured and predicted value).

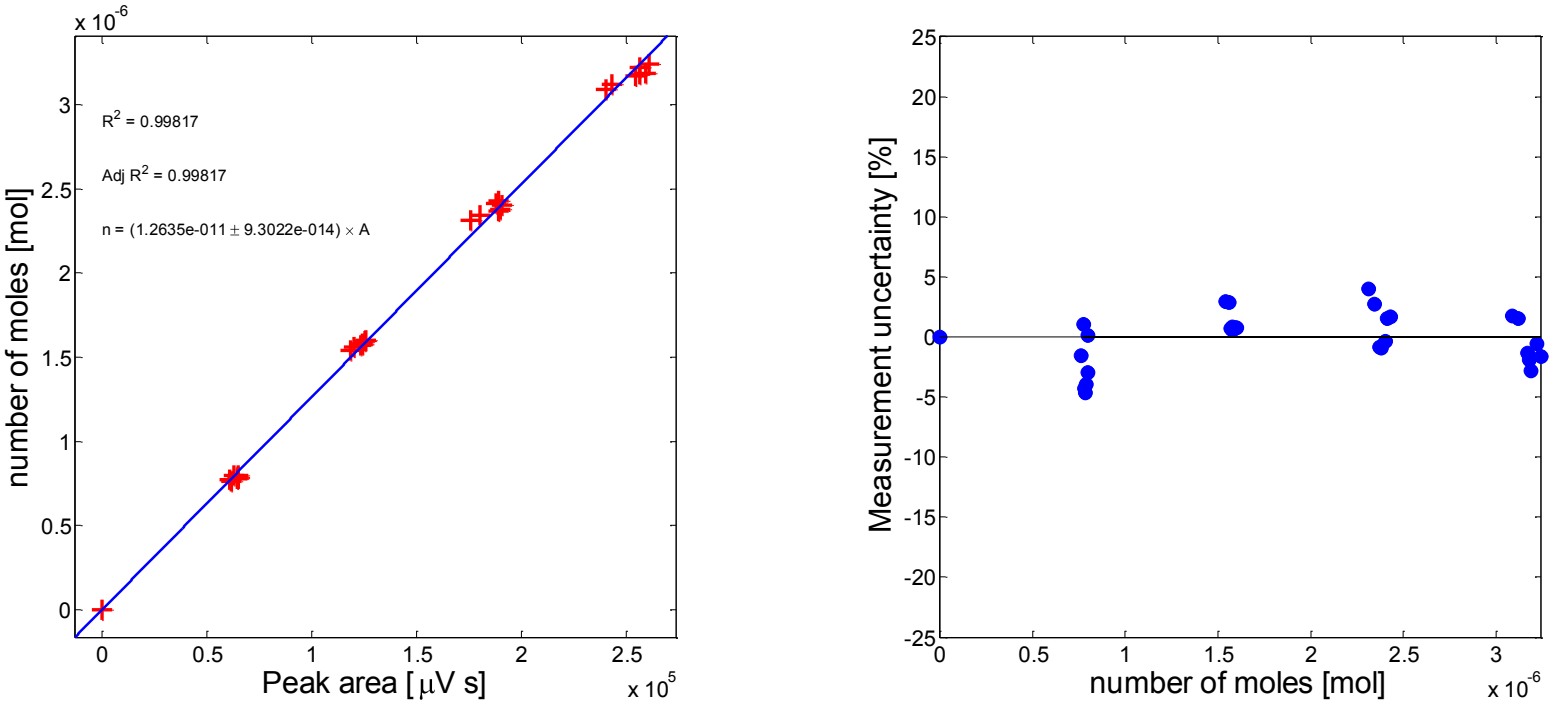

Figure C.27. Shimadzu G.C. 2014 TCD calibration plot and calculated measurement uncertainty for HFP. Data fitted to a first-order, zero-intercept function (uncertainty defined as the relative difference between measured and predicted value).

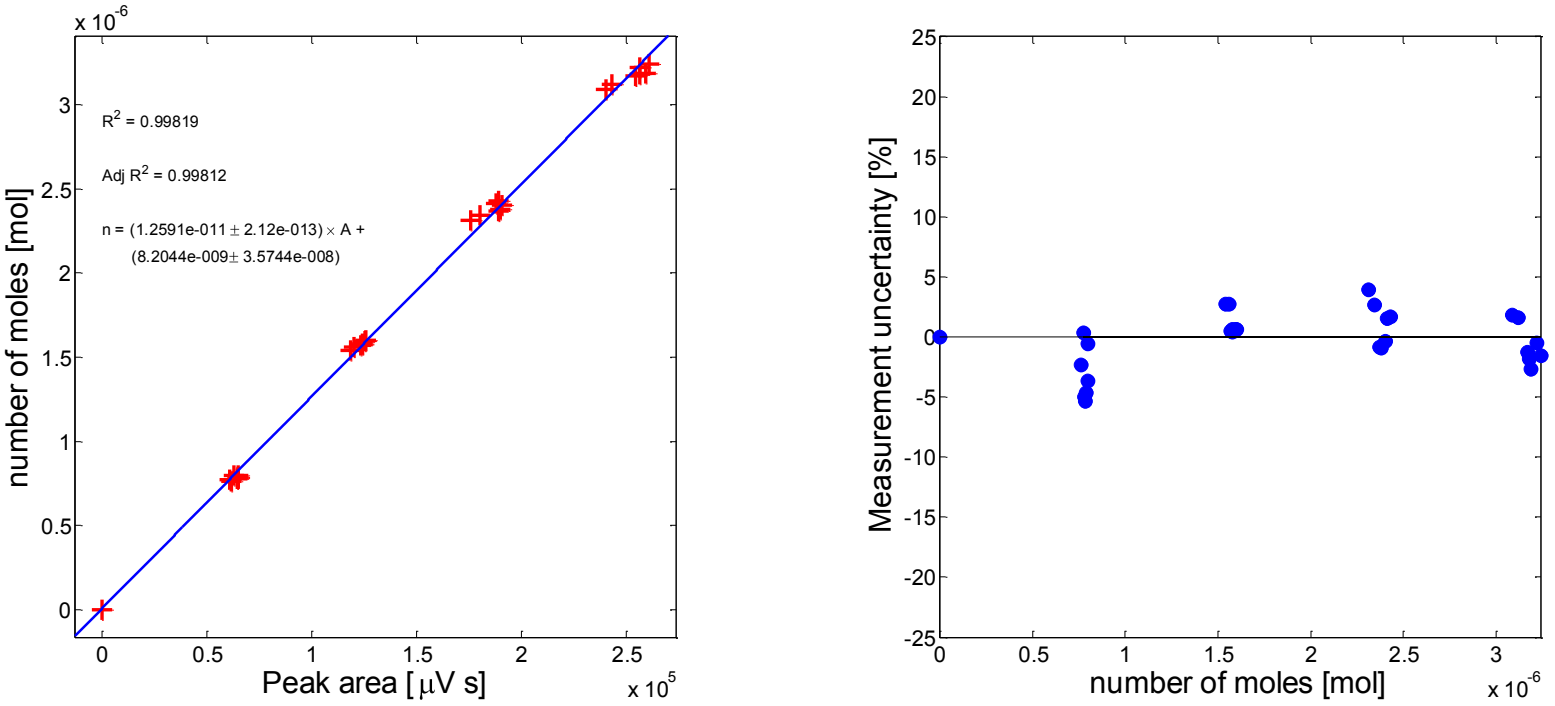

Figure C.28. Shimadzu G.C. 2014 TCD calibration plot and calculated measurement uncertainty for HFP. Data fitted to a first-order function (uncertainty defined as the relative difference between measured and predicted value).

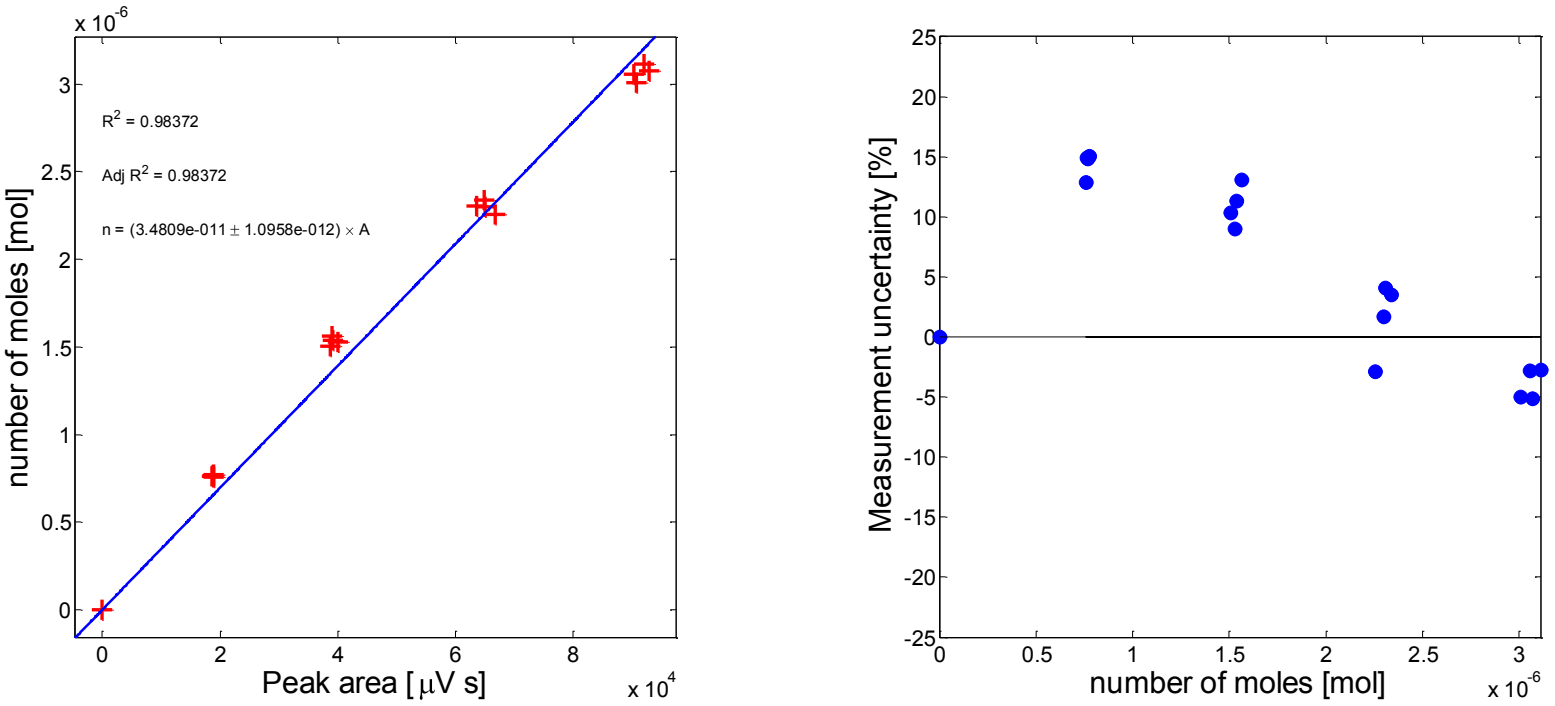

Figure C.29. Shimadzu G.C. 2014 TCD calibration plot and calculated measurement uncertainty for CF_3OCF_3. Data fitted to a first-order, zero-intercept function (uncertainty defined as the relative difference between measured and predicted value).

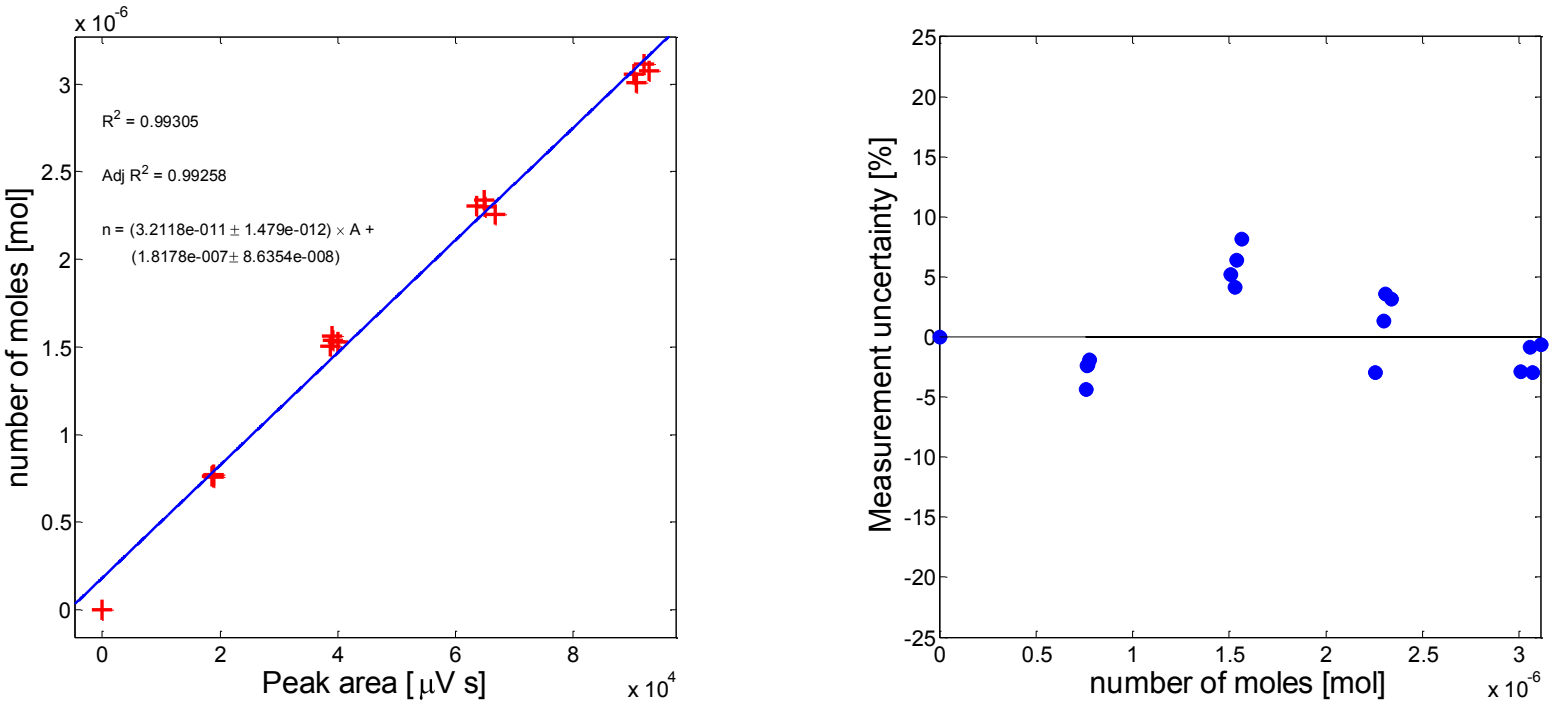

Figure C.30. Shimadzu G.C. 2014 TCD calibration plot and calculated measurement uncertainty for CF_3OCF_3. Data fitted to a first-order function (uncertainty defined as the relative difference between measured and predicted value).

Appendix D. Theoretical basis for thermochemical calculations.

D.1. Canonical partition function of a single particle

Statistical thermodynamics introduces the concept of the canonical partition function and establishes its relationships to other thermodynamic quantities including those which can be measured experimentally. The canonical partition function of a single particle, sometimes known as the molecular partition function, is defined as:

$$q(T) = \sum_{\substack{\text{energy} \\ \text{states } i}} \exp\left(-\frac{\varepsilon_i}{kT}\right) = \sum_{\substack{\text{energy} \\ \text{levels } j}} \omega(\varepsilon_j) \exp\left(-\frac{\varepsilon_j}{kT}\right) \tag{D.1}$$

where $\omega(\varepsilon_j)$ is the degeneracy of the energy level ε_j (the number of states with that energy), k is the Boltzmann constant, and T is the system temperature. Note that the summation goes either over all possible energy states of the particle or over all energy levels while accounting for their degeneracies.

Monoatomic, diatomic and polyatomic molecules are entities which may exhibit various modes of movement in three-dimensional space (translational, rotational and vibrational). They also have a quite complicated electronic and nuclear structure. As a result, there are numerous energy states associated with these internal degrees of freedom. Fortunately, in most of the applications all these energy states can be considered to be independent so that the total energy of a molecule can be written as a sum of completely independent energy modes:

$$\varepsilon = \varepsilon_{tra} + \varepsilon_{rot} + \varepsilon_{vib} + \varepsilon_{ele} + \varepsilon_{nuc} \tag{D.2}$$

Then the canonical partition function of a single molecule can be presented as a product of partition functions defined for individual modes:

$$q = q_{tra}\, q_{rot}\, q_{vib}\, q_{ele}\, q_{nuc} \tag{D.3}$$

Translational partition function

According to quantum mechanics, the translational energy states of a single particle in three-dimensional space are given by:

$$\varepsilon_{xyz} = \frac{h^2}{8mV^{2/3}}(x^2 + y^2 + z^2) \tag{D.4}$$

where m is the particle mass, h is the Planck's constant, and x, y, z are quantum numbers. Then, on summing over all energy states (rather than energy levels), the translational partition function of a particle becomes:

$$q_{tra} = \sum_{x=1}^{\infty}\sum_{y=1}^{\infty}\sum_{z=1}^{\infty} \exp\left[-\frac{h^2}{8mkTV^{2/3}}(x^2 + y^2 + z^2)\right] = \left[\sum_{n=1}^{\infty}\exp\left(-\frac{h^2 n^2}{8mkTV^{2/3}}\right)\right]^3 \tag{D.5}$$

In an excellent approximation, the final sum in Equation D.5 can be replaced with an integral to give:

$$q_{tra} = \left(\frac{2\pi mkT}{h^2}\right)^{3/2} V \tag{D.6}$$

Rotational partition function

In order to describe external rotational energy states, quantum mechanics uses a simple model of point masses rotating around their centre of mass. The model referred to as the rigid rotor (top) assumes fixed distances between the masses involved and is characterized in general by three moments of inertia (I_a, I_b and I_c). There are two degenerate or three non-degenerate rotational energy modes, depending on whether the molecule is linear or nonlinear, respectively. Monoatomic molecules exhibit no rotational modes. Energy levels of a rigid rotor depend on the rotor symmetry. They can be determined analytically for diatomic and linear polyatomic molecules (I_a=0, I_b=I_c=I) as well as nonlinear molecules showing some symmetry such as spherical rotors (I_a=I_b=I_c), prolate symmetrical rotors (I_a<I_b=I_c) and oblate symmetrical rotors (I_a= I_b<I_c). The asymmetric rotor problem (I_a≠I_b≠I_c) is not analytically solvable. Nevertheless, the energy level parameters for asymmetric molecules can be determined numerically using advanced computational methods of quantum mechanics.

It can be shown, based on an approximation similar to that used in Equation D.6, that for a linear molecule the rotational partition function is:

$$q_{rot} = \frac{T}{\sigma \Theta} \tag{D.7}$$

while for a nonlinear molecule:

$$q_{rot} = \frac{\sqrt{\pi}}{\sigma}\left(\frac{T^3}{\Theta_a \Theta_b \Theta_c}\right)^{1/2} \tag{D.8}$$

where σ is the rotational symmetry number, i.e. the number of ways the molecule can be oriented which are indistinguishable from each other. The rotational temperatures Θ_a, Θ_b, Θ_c and Θ are defined in terms of the corresponding moments of inertia, e.g:

$$\Theta_a = \frac{h^2}{8\pi^2 k I_a} \tag{D.9}$$

The approximation used to derive Equations D.7 and D.8 is valid for temperatures well exceeding the rotational temperatures (T>5Θ). However, with only one exception (H_2), this condition is satisfied for all temperatures above 273 K. Table D.1 shows the key parameters of the rotational partition function for the molecules of interest.

In polyatomic nonlinear molecules individual molecular groups may rotate relative to each other. This degree of freedom is referred to as internal rotation. Accounting for this effect is not easy (Lucas, 1991). Here it was neglected.

Vibrational partition function

The quantum-mechanical analog of the classical harmonic oscillator is used to approximate vibrational energy states of a single molecule of an ideal gas. A linear molecule composed of n atoms has s=3n-5 vibrational degrees of freedom and hence, it exhibits the same number of vibrational energy modes. Similarly, a nonlinear molecule exhibits s=3n-6 vibrational modes. For a diatomic molecule, the vibration energy mode is a bond stretching motion while for a polyatomic

molecule there is a collection of bond stretching and bond bending motions. The energy level represented by the *i*-th mode is given by:

$$\varepsilon_{i,j} = (j + \tfrac{1}{2}) h k \Theta_{v,i} \tag{D.10}$$

where $\Theta_{v,i}$ is the vibrational temperature of the *i*-th mode resulting from quantum-mechanical calculations of the molecule, and j = 0,1,2, …, ∞ are quantum numbers. Each of the vibrational energy levels is non-degenerate ($\omega_{i,j}$ = 1). Consequently, the vibrational partition function of a single molecule can be presented as:

$$q_{vib} = \prod_{i=1}^{s} q_{vib,i} = \prod_{i=1}^{s} \sum_{j=0}^{\infty} \omega_{i,j} \exp\left(-\frac{\varepsilon_{i,j}}{kT}\right) = \prod_{i=1}^{s} \sum_{j=0}^{\infty} \exp\left(-(j + \tfrac{1}{2}) \frac{\Theta_{v,i}}{T}\right) \tag{D.11}$$

The final sum in the above equation can be evaluated easily by recognizing it to be a geometric series:

$$q_{vib} = \prod_{i=1}^{s} \frac{\exp\left(-\tfrac{1}{2}\Theta_{v,i} / T\right)}{1 - \exp\left(-\Theta_{v,i} / T\right)} \tag{D.12}$$

Vibrational temperatures calculated by electronic structure theory can be improved by introducing a scaling factor in order to reproduce particular experimental properties (e.g. spectroscopically observed vibrational frequencies or zero-point energies). Such scale factors depend on the level of electronic structure theory and the one-electron basis set, the combination of which is known as an electronic model chemistry. For the B3LYP/6-31G(2df,p) model chemistry used here, a scaling factor of 0.9854 was found to be optimal (Curtiss & Raghavachari, 2002). Table D.2 lists all vibrational temperatures calculated for the molecules of interest.

Electronic partition function

The electronic energy states depend on the electronic structure of the atoms which is specific to each atomic species. In practice, the calculation of the electronic partition function uses energy data obtained from ultraviolet spectroscopic measurements. The partition function is then computed as follows:

$$q_{ele} = \sum_{\substack{\text{electronic} \\ \text{levels } j}} \omega_{ele,j} \exp\left(-\frac{\varepsilon_{ele,j}}{kT}\right) \tag{D.13}$$

The first term of the above sum corresponds to the energy level of the ground electronic state of a particle (atom, molecule). By convention, this energy level is assumed to be zero. The following terms correspond to excited energy levels. The first and higher electronic excitation energies are much greater than kT. Therefore, they are assumed to be inaccessible at any temperature. Consequently, the degeneracy of the ground state alone is an excellent approximation to the electronic partition function:

$$q_{elec} = \omega_{elec,1} \tag{D.14}$$

For all molecules discussed in the thesis, apart from O_2, the ground state degeneracy $\omega_{ele,1}$ is 1. The ground state of the oxygen molecule, the so-called triplet oxygen, has a degeneracy of 3.

Nuclear partition function

The nuclear energy state of atoms remains intact for processes of interest including chemical reactions. Hence, the nuclear partition function will not affect any measurable thermodynamic property and can be ignored ($q_{nuc} = 1$).

D.2. Canonical partition function of an ideal gas

The theoretical determination of the canonical partition function for systems involving interacting particles such those constituting real gases, liquids and solids, is an extremely difficult task. Since the respective calculation requires the knowledge of intermolecular forces, canonical partition functions of real systems are generally not known. Nevertheless, the task can be accomplished with a considerable success if the theory is applied to simpler systems such as ideal gases where by definition no interaction between individual particles exists.

It can be shown that the canonical partition function for a system of N identical (indistinguishable) non-interacting particles contained in volume V at temperature T is:

$$Q(N,V,\beta) = \frac{q^N}{N!} \tag{D.15}$$

It turns out that many important thermodynamic relations involve $\ln Q$ rather than Q. Using then Stirling's approximation for large N, Equation D.15 can be converted to the following form:

$$\ln Q = N \ln q - \ln N! = N(\ln q - \ln N + 1) \tag{D.16}$$

where according to Equation D.3:

$$\ln q = \ln q_{tra} + \ln q_{rot} + \ln q_{vib} + \ln q_{ele} + \ln q_{nuc} \tag{D.17}$$

Equation D.15 was derived under the assumption that the number of particle energy states is much greater than the number of particles, and hence the probability of two particles being in the same energy state is very small. This is always the case for systems being of interest to chemical engineering.

D.3. Thermodynamic properties of an ideal gas

If the canonical partition function is available in the form of a mathematical expression all conventional thermodynamic properties of the system can be derived from it. In particular, it can be shown that (McQuarrie & Simon, 1999):

the internal energy is

$$U = kT^2 \left(\frac{\partial \ln Q}{\partial T} \right)_{V,N} \tag{D.18}$$

the system pressure is

$$P = kT \left(\frac{\partial \ln Q}{\partial V} \right)_{T,N} \tag{D.19}$$

and the entropy is

$$S = k \left[\ln Q + T \left(\frac{\partial \ln Q}{\partial T} \right)_{V,N} \right] \tag{D.20}$$

Other thermodynamic functions of state such as enthalpy H, Helmholtz free energy A, Gibbs free energy as well as heat capacities C_P and C_V can be derived from their classic definitions involving U and S.

Pressure

The system pressure P (in other words, the ideal gas equation of state), can be derived easily as the only volume-dependent term in the partition function is the translation term q_{tra}. From Equation D.6:

$$\ln q_{tra} = \frac{3}{2}\ln\left(\frac{2\pi mkT}{h^2}\right) + \ln V \tag{D.21}$$

and then Equations D.17 and D.19 yield immediately:

$$P = NkT\left(\frac{\partial \ln q_{tra}}{\partial V}\right)_{T,N} = \frac{NkT}{V} \tag{D.22}$$

Internal energy

On using Equations D.3, D.16 and D.17, the thermodynamic functions U and S can be presented in a form which explicitly shows contributions from different energy modes. Thus, for the internal energy we have:

$$U = U_{tra} + U_{rot} + U_{vib} + U_{ele} + U_{nuc} \tag{D.23}$$

where according to Equation D.18, for each energy *mode* (*tra*, *rot*, *vib*, *ele* and *nuc*):

$$U_{mode} = NkT^2\left(\frac{\partial \ln q_{mode}}{\partial T}\right)_{V,N} \tag{D.24}$$

Individual contributions can easily be evaluated by straightforward differentiation. The relations presented below are valid for one mole of an ideal gas ($N = 6.0221415\times10^{23}$ and $R = Nk$):

$$U_{tra} = 3/2\ RT \tag{D.25}$$

$$U_{rot} = \begin{cases} RT & \text{linear molecules} \\ 3/2\ RT & \text{nonlinear molecules} \end{cases} \tag{D.26}$$

$$U_{vib} = R\sum_{i=1}^{s}\Theta_{v,i}\left[\frac{1}{2}+\frac{1}{\exp(\Theta_{v,i}/T)-1}\right] \tag{D.27}$$

$$U_{ele} = U_{nuc} = 0 \tag{D.28}$$

Entropy

Analogously, for the entropy S we have:

$$S = S_{tra} + S_{rot} + S_{vib} + S_{ele} + S_{nuc} \tag{D.29}$$

However, because of the presence of $\ln Q$ in Equation D.20, the translation term needs to be modified slightly:

$$S_{tra} = Nk\left[\ln q_{tra} - \ln N + 1 + T\left(\frac{\partial \ln q_{tra}}{\partial T}\right)_{V,N}\right] \tag{D.30}$$

while the remaining energy modes (*rot*, *vib*, *ele* and *nuc*) can be expressed in the identical form:

$$S_{mode} = Nk\left[\ln q_{mode} + T\left(\frac{\partial \ln q_{mode}}{\partial T}\right)_{V,N}\right] \tag{D.31}$$

Thus, contributions to the molar entropy are as follows:

$$S_{tra} = \frac{5}{2}R + R\ln\left[\left(\frac{2\pi mkT}{h^2}\right)^{3/2}\frac{kT}{P}\right] \tag{D.32}$$

$$S_{rot} = \begin{cases} R + R\ln\dfrac{T}{\sigma\Theta} & \text{linear molecule} \\ \dfrac{3}{2}R + R\ln\left[\dfrac{\sqrt{\pi}}{\sigma}\left(\dfrac{T^3}{\Theta_a\,\Theta_b\,\Theta_c}\right)^{1/2}\right] & \text{nonlinear molecule} \end{cases} \tag{D.33}$$

$$S_{vib} = R\sum_{i=1}^{s}\left\{\frac{\Theta_{v,i}}{T}\frac{1}{\exp(\Theta_{v,i}/T)-1} - \ln\left[1-\exp(-\Theta_{v,i}/T)\right]\right\} \tag{D.34}$$

$$S_{elec} = R\,\ln\omega_{elec,1} \tag{D.35}$$

$$S_{nuc} = 0 \tag{D.36}$$

Heat capacities

The molar heat capacity at constant volume can be obtained by direct differentiation of the internal energy U:

$$C_V = \left(\frac{\partial U}{\partial T}\right)_V \tag{D.37}$$

The contributions from different energy modes are:

$$C_{V,tra} = 3/2\,R \tag{D.38}$$

$$C_{V,rot} = \begin{cases} R & \text{linear molecules} \\ 3/2\,R & \text{nonlinear molecules} \end{cases} \tag{D.39}$$

$$C_{V,vib} = R\sum_{i=1}^{s}\exp(\Theta_{v,i}/T)\left[\frac{\Theta_{v,i}/T}{\exp(\Theta_{v,i}/T)-1}\right]^2 \tag{D.40}$$

$$C_{V,ele} = C_{V,nuc} = 0 \tag{D.41}$$

Then, the molar heat capacity of an ideal gas at constant pressure can be calculated from:

$$C_P = C_V + R \tag{D.42}$$

Other thermodynamic functions

Molar enthalpy: $$H = U + PV = U + RT \tag{D.43}$$

Molar Helmholtz free energy: $$A = U - TS \tag{D.44}$$

Molar Gibbs free energy: $$G = H - TS \tag{D.45}$$

Values of thermodynamic functions calculated with the B3LYP/6-31G(2df,p) model chemistry (scaling factor 0.9854) at 298.15 K are shown in Table D.3.

Standard enthalpy of formation

The standard enthalpy of formation of a chemical compound is defined as a change in enthalpy accompanying the hypothetical reaction of forming the compound from its elements, with each substance in its thermodynamic standard state at the given temperature and pressure conditions. Thermodynamic cycles are useful graphical tools which help establish mutual relations between enthalpies at different thermodynamic states of substances. As an example, Figure D.1 shows a thermodynamic cycle for the enthalpy of formation of hexafluoropropylene oxide from the standard states of carbon, fluorine and oxygen at 298.15 K and 1 bar. The standard state adopted for the elemental carbon is graphite while the standard state used for fluorine and oxygen is the respective diatomic gas.

The enthalpy of formation of a molecule cannot be calculated directly with standard methods of quantum mechanics because enthalpies of the elements in their standard states (e.g. C in graphite) cannot be determined with the same methods of calculation. Instead, the enthalpy of formation is calculated indirectly by combining experimental and theoretical data and making use of thermodynamic cycles. As it can be seen from Figure D.1, the data which are sufficient to determine the standard enthalpy of formation involve:

- $\Delta H_i^e(298.15\,\mathrm{K}) = H_i^e(298.15\,\mathrm{K}) - H_i^e(0\,\mathrm{K})$, the change of enthalpy of the *i*-th element in its standard state during a temperature change from 0 to 298.15 K

- $\Delta H_{f,i}^e(0\ \mathrm{K})$, the enthalpy of formation of isolated atoms from the *i*-th element in its standard state at 0 K

- ΣD_0, the atomization (dissociation) energy of the compound at 0 K

- $H(298.15\ \mathrm{K}) - H(0\ \mathrm{K})$, the change of enthalpy of the compound during a temperature change from 0 to 298.15 K

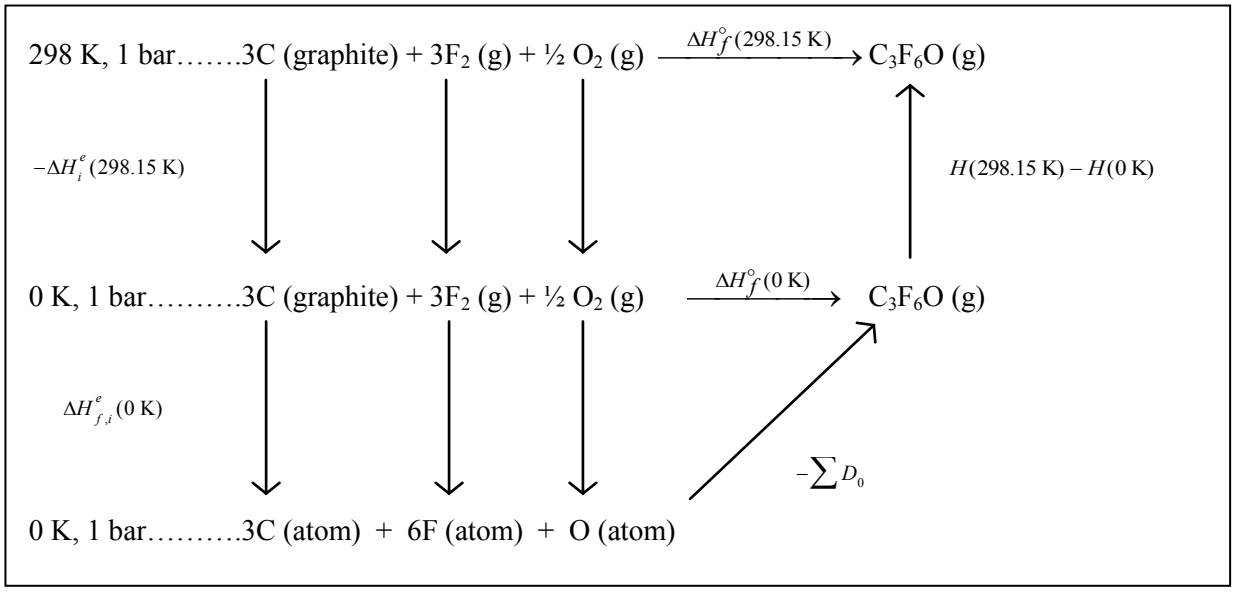

Figure D.1 HFPO (C_3F_6O) thermochemical cycle.

According to the thermodynamic cycle from Figure D.1, with the above data available, the standard enthalpy of formation can be calculated as follows:

$$\Delta H_f^o(298.15\ \mathrm{K}) = \Delta H_f^o(0\ \mathrm{K}) - \sum_i x_i\, \Delta H_i^e(298.15\ \mathrm{K}) + H(298.15\ \mathrm{K}) - H(0\ \mathrm{K}) \qquad \text{(D.46)}$$

where

$$\Delta H_f^o(0\ \mathrm{K}) = \sum_i x_i\, \Delta H_{f,i}^e(0\ \mathrm{K}) - \Sigma D_0 \qquad \text{(D.47)}$$

Experimental data on $\Delta H^e_{f,i}(0\,\mathrm{K})$ and $\Delta H^e_i(298.15\,\mathrm{K})$ can be obtained from the NIST-JANAF Tables (Chase, 1998). Those ΔH^e_i values from the tables which are referred to diatomic gases must be divided by 2. Specific data for carbon, fluorine and oxygen are shown in Table D.4. The calculation method for the enthalpy *H* of a compound as a function of temperature was described earlier. In particular, *H*(0 K) equals to the so-called zero-point vibrational energy:

$$H(0\ \mathrm{K}) \;=\; E_v^{ZPE} \;=\; \frac{1}{2} R \sum_{i=1}^{s} \Theta_{v,i} \tag{D.48}$$

Values of *H*(0 K) and *H*(298.15 K) are given in Table D.3.

The atomization energy of a molecule at 0 K is defined as:

$$\Sigma D_0 \;=\; \sum_i n_i E_{a,i} \;-\; E_m \tag{D.49}$$

where $E_{a,i}$ is the quantum mechanical energy of a single atom of the *i*-th element constituting the molecule, n_i is the number of these atoms in the molecule, and E_m is the quantum mechanical energy of the molecule (including the zero-point vibrational energy E_v^{ZPE}), both energies at 0 K. The quantum mechanical energies of individual atoms have been determined numerically using various model chemistries (HF, B3LYP, MP4, CISD, CCSD, G4, etc. in combination with different basis sets). $E_{a,i}$ values for carbon, oxygen and fluorine obtained with the recently developed Gaussian-4 (G4) composite method (Curtiss et al., 2007) are presented in Table D.5. The quantum mechanical energies of molecular oxygen, difluoromethylene, carbonyl fluoride, tetrafluoroethylene and trifluoroacetyl fluoride were calculated using the G4 method and the Gaussian 09 program. Results of these calculations, including atomization energies, are presented in Table D.6. Computations performed for hexafluorocyclopropane, hexafluoropropylene and hexafluoropropylene oxide crashed at some point and could not be completed. Apparently, these molecules were too large and heavy to be handled by the program considering limited computational power available. Therefore, for these three compounds the entire approach was abandoned and the standard enthalpy of formation was predicted using the slightly less accurate semi-theoretical T1 recipe of Ohlinger et al. (2009) and the Spartan 10 molecular simulation program.

The final calculation results of standard enthalpies of formation obtained with Gaussian 09 as well as those produced by Spartan 10 are presented in Table D.7.

Standard Gibbs free energy of formation

The calculation of the standard Gibbs free energy of formation of a compound is straightforward:

$$\Delta G_f^{\circ}(298.15\,\mathrm{K}) \;=\; \Delta H_f^{\circ}(298.15\,\mathrm{K}) - 298.15\;\Delta S_f^{\circ}(298.15\,\mathrm{K}) \tag{D.50}$$

where

$$\Delta S_f^{\circ}(298.15\,\mathrm{K}) \;=\; S(298.15\,\mathrm{K}) - \sum_i n_i S_i^{e}(298.15\,\mathrm{K}) \tag{D.51}$$

Experimental standard entropies of elements, $S_i^{e}(298.15\,\mathrm{K})$, are available from the NIST-JANAF Tables (Chase, 1998). Those entropy values from the tables which are referred to diatomic gases must be divided by 2. $S_i^{e}(298.15\,\mathrm{K})$ data for carbon, oxygen and fluorine have been included in Table D.4. The calculation method for the entropy *S* of compounds as a function of temperature was described earlier. Values of *S*(298.15 K) are given in Table D.3.

The calculated standard entropies and Gibbs free energies of formation for the investigated compounds are shown in Table D.8.

D.4. Thermodynamics of chemical reaction equilibrium

The reaction equilibrium constant K_a is defined as

$$\ln K_a(T) \;=\; -\frac{\Delta G_{rxn}^{\circ}(T)}{RT} \tag{D.52}$$

where the Gibbs free energy change on reaction ΔG_{rxn}° can be determined from the Gibbs free energies of reactants (ν_i<0) and products (ν_i>0) of the reaction:

$$\Delta G_{rxn}^{\circ} \;=\; \sum_i \nu_i \Delta G_{f,i}^{\circ} \tag{D.53}$$

The equilibrium constant can also be expressed in terms of activities a_i:

$$K_a(T) = \prod_i a_i^{\nu_i} \tag{D.54}$$

Since in turn, activities are defined in terms of fugacities f_i:

$$a_i = \frac{f_i}{P_o} \tag{D.55}$$

where P_o is the standard pressure assumed to be 1 bar, the equilibrium constant can be written as:

$$K_a(T) = P_o^{-\Sigma\nu_i} \prod_i f_i^{\nu_i} \tag{D.56}$$

Eventually, the fugacities can expressed in terms of partial pressures using fugacity coefficients ϕ_i:

$$K_a(T) = P_o^{-\Sigma\nu_i} \prod_i \phi_i^{\nu_i} \prod_i p_i^{\nu_i} \tag{D.57}$$

For ideal gases the above equation can be simplified letting ϕ_i=1:

$$K_a(T) = P_o^{-\Sigma\nu_i} \prod_i p_i^{\nu_i} \tag{D.58}$$

or in terms of molar concentrations C_i:

$$K_a(T) = \left(\frac{P_o}{RT}\right)^{-\Sigma\nu_i} \prod_i C_i^{\nu_i} \tag{D.59}$$

The reaction equilibrium constant K_a is a function of temperature. Although this relationship results directly from Equation D.52, it is practically much more convenient to use the equivalent van't Hoff equation:

$$\left(\frac{\partial \ln K_a}{\partial T}\right)_P = \frac{\Delta H^o_{rxn}(T)}{RT^2} \tag{D.60}$$

According to Kirchoff's law:

$$\Delta H^o_{rxn}(T) = \Delta H^o_{rxn}(T_0) + \int_{T_0}^{T} \sum_i \nu_i C_{Pi}(T)\, dT \tag{D.61}$$

where T_0 was assumed to be 298.15 K. For the sake of convenience, the $C_{Pi}(T)$ data generated in quantum-mechanical calculations were correlated against temperature using the form of the widely used Shomate equation:

$$C_{P_i}(T) = a + bT + cT^2 + dT^3 + eT^{-2} \tag{D.62}$$

The correlation coefficients of the Shomate equation obtained for the compounds of interest are listed in Table D.9.

Combining Equations D.60, D.61 and D.62, and integrating from T_0 to T gives the temperature dependence of the reaction equilibrium constant:

$$\begin{aligned} \ln\frac{K_a(T)}{K_a(T_0)} = {} & \frac{\Delta a}{R}\ln\frac{T}{T_0} + \frac{\Delta b}{2R}(T - T_0) + \frac{\Delta c}{6R}(T^2 - T_0^2) + \frac{\Delta d}{12R}(T^3 - T_0^3) + \frac{\Delta e}{2R}(T^{-2} - T_0^{-2}) \\ & + \frac{1}{R}\left(\Delta H^{\circ}_{rxn}(T_0) + \Delta a\, T_0 + \frac{\Delta b}{2}T_0^2 + \frac{\Delta c}{3}T_0^3 + \frac{\Delta d}{4}T_0^4 - \frac{\Delta e}{T_0}\right)\left(\frac{1}{T} - \frac{1}{T_0}\right) \end{aligned} \tag{D.63}$$

where, for example (similarly for *b*, *c*, d and e):

$$\Delta a = \sum_i \nu_i a_i \tag{D.64}$$

The reaction equilibrium constant K_a at standard conditions can be obtained directly from Equation D.52:

$$K_a(T_0) = \exp\left(-\frac{\Delta G^{\circ}_{rxn}(T_0)}{RT_0}\right) \tag{D.65}$$

The required Gibbs free energy change on reaction $\Delta G^{\circ}_{rxn}(T_0)$ is then:

$$\Delta G^{\circ}_{rxn}(T_0) = \Delta H^{\circ}_{rxn}(T_0) - T_0\ \Delta S^{\circ}_{rxn}(T_0) \tag{D.66}$$

where

$$\Delta H^{\circ}_{rxn}(T_0) = \sum_i \nu_i \Delta H^{\circ}_{f,i}(T_0) \tag{D.67}$$

$$\Delta S^{\circ}_{rxn}(T_0) = \sum_i \nu_i \Delta S^{\circ}_{f,i}(T_0) \tag{D.68}$$

Table D.1. Basic parameters of the rotational partition function of molecules (B3LYP/6-31G(2df,p) model chemistry).

Molecule	Geometry	σ	Θ_a, K	Θ_b, K	Θ_c, K
Molecular oxygen	linear	2	2.08387	-	-
Difluoromethylene	nonlinear	1	4.17987	0.60224	0.52640
Carbonyl fluoride	nonlinear	1	0.56741	0.56320	0.28265
Tetrafluoroethylene	nonlinear	2	0.26447	0.15560	0.09796
Trifluoroacetyl fluoride	nonlinear	1	0.18400	0.11959	0.09881
Hexafluorocyclopropane	nonlinear	1	0.08017	0.08016	0.07435
Hexafluoropropylene	nonlinear	1	0.12260	0.06037	0.04743
Hexafluoropropylene oxide	nonlinear	1	0.10601	0.05300	0.04503

Table D.2. Scaled vibrational temperatures of molecules (B3LYP/6-31G(2df,p) model chemistry and a scaling factor of 0.9854).

Molecule	Vibrational temperatures $\Theta_{v,i}$, K
Molecular oxygen	2360.01
Difluoromethylene	955.59, 1633.25, 1790.79
Carbonyl fluoride	828.84, 878.98, 1124.70, 1403.63, 1818.72, 2822.26
Tetrafluoroethylene	280.47, 286.25, 564.69, 606.31, 743.04, 782.02, 787.43, 1140.59, 1714.32, 1929.78, 1933.35, 2723.46
Trifluoroacetyl fluoride	64.39, 314.85, 329.77, 542.01, 600.27, 730.50, 839.06, 982.21, 1091.25, 1152.68, 1593.65, 1720.28, 1799.39, 1896.78, 2774.58
Hexafluorocyclopropane	179.65, 180.27, 255.86, 355.82, 356.17, 356.35, 504.71, 711.85, 712.26, 774.32, 774.68, 1050.97, 1130.09, 1229.42, 1230.18, 1803.47, 1804.09, 1822.74, 1822.92, 1837.67, 2199.92
Hexafluoropropylene	44.74, 175.65, 254.90, 343.37, 356.17, 514.05, 524.27, 659.58. 728.82, 812.88, 856.27, 935.45, 937.91, 1094.57, 1491.74, 1681.30, 1739.18, 1752.43, 1915.51, 1990.28, 2610.65
Hexafluoropropylene oxide	64.18, 191.56, 227.64, 344.05, 376.03, 436.11, 492.85, 606.52, 719.00, 761.01, 801.46, 823.76, 869.91, 1027.33, 1103.63, 1143.52, 1464.74, 1611.91, 1678.79, 1734.56, 1764.83, 1841.92, 1936.48, 2217.96

Table D.3. Thermodynamic functions calculated with the B3LYP/6-31G(2df,p) model chemistry and a scaling factor of 0.9854. T_0 = 298.15

Molecule	$U(T_0)$ kJ/mol	$H(0)$ kJ/mol	$H(T_0)$ kJ/mol	$S(T_0)$ J/(mol·K)	$G(T_0)$ kJ/mol
Molecular oxygen	16.01	9.81	18.49	204.99	-42.63
Difluoromethylene	26.07	18.20	28.54	246.53	-44.96
Carbonyl fluoride	45.55	36.89	48.03	264.68	-30.89
Tetrafluoroethylene	69.94	56.07	72.42	306.08	-18.84
Trifluoroacetyl fluoride	84.29	68.29	86.77	335.80	-13.35
Hexafluorocyclopropane	108.31	87.66	110.79	367.77	1.14
Hexafluoropropylene	109.94	89.02	112.41	378.78	-0.52
Hexafluoropropylene oxide	122.74	100.74	125.22	384.12	10.70

Table D.4. Thermochemical data for the elemental carbon, oxygen and fluorine (Chase, 1998).

Property	Carbon, C	Oxygen, O	Fluorine, F
$\Delta H^e_{f,i}(0\ \mathrm{K})$, kJ/mol	711.185	246.790	77.284
$H^e_i(0\ \mathrm{K})$, kJ/mol	-1.051	-4.342	-4.413
$H^e_i(298.15\ \mathrm{K})$, kJ/mol	0	0	0
$\Delta H^e_i(298.15\ \mathrm{K})$, kJ/mol	1.051	4.342	4.413
$S^e_i(298.15\ \mathrm{K})$, J/(mol·K)	5.74	102.574	101.395

Table D.5. Quantum mechanical zero-point energies of elemental carbon, oxygen and fluorine obtained with the Gaussian-4 composite method (G4) [Curtiss et al., 2007].

Element	Energy, hartree
Carbon, C	-37.83417
Oxygen, O	-75.04550
Fluorine, F	-99.70498

Table D.6. Quantum mechanical zero-point energies (including E_v^{ZPE}) and atomization energies of individual compounds. 1 hartree = 2625.4996 kJ/mol

Molecule	Zero-point energy, E_m hartree	Atomization energy, ΣD_0	
		hartree	kJ/mol
Molecular oxygen	-150.278656	0.187656	492.691
Difluoromethylene	-237.648088	0.403958	1060.592
Carbonyl fluoride	-312.943600	0.653970	1716.998
Tetrafluoroethylene	-475.402483	0.914223	2400.292
Trifluoroacetyl fluoride	-550.674693	1.140933	2995.519

Table D.7. Standard enthalpies of formation obtained by quantum mechanical calculation.

Molecule	$\Delta H_f^\circ(298.15\,\mathrm{K})$, kJ/mol	
	value	method
Molecular oxygen	0.89	G4
Difluoromethylene	-194.37	G4
Carbonyl fluoride	-607.54	G4
Tetrafluoroethylene	-672.19	G4
Trifluoroacetyl fluoride	-1022.84	G4
Hexafluorocyclopropane	-1021.43	T1
Hexafluoropropylene	-1150.04	T1
Hexafluoropropylene oxide	-1206.49	T1

Table D.8. Standard entropies and Gibbs free energies of formation obtained by quantum mechanical calculation.

Molecule	$\Delta S_f^{\circ}(298.15\,\mathrm{K})$, J/(mol·K)		$\Delta G_f^{\circ}(298.15\,\mathrm{K})$, kJ/mol	
	value	method	value	method
Molecular oxygen	-0.16	G4	0.93	G4
Difluoromethylene	38.00	G4	-205.70	G4
Carbonyl fluoride	-46.43	G4	-593.70	G4
Tetrafluoroethylene	-110.98	G4	-639.10	G4
Trifluoroacetyl fluoride	-183.83	G4	-968.03	G4
Hexafluorocyclopropane	-257.82	G4	-944.56	G4+T1
Hexafluoropropylene	-246.81	G4	-1076.45	G4+T1
Hexafluoropropylene oxide	-344.04	G4	-1103.91	G4+T1

Table D.9. Coefficients of the Shomate equation (correlation of quantum mechanical calculation data). Heat capacity at constant pressure, J/(mol·K), *versus* temperature, K. *T* = 273-1000 K

Molecule	*a*	*b*	*c*	*d*	*e*
Molecular oxygen	22.778043	0.01744203	-4.7259479e-6	-1.2498789e-9	1.5572064e+5
Difluoromethylene	14.322259	0.10031320	-9.0631063e-5	2.9917606e-8	1.6296102e+5
Carbonyl fluoride	17.160356	0.13475432	-1.1333644e-4	3.5810909e-8	-8.1074989e+4
Tetrafluoroethylene	40.325127	0.18717940	-1.5379960e-4	4.7229287e-8	-2.9953593e+5
Trifluoroacetyl fluoride	32.854883	0.26975762	-2.3507704e-4	7.5929373e-8	-2.7283794e+5
Hexafluorocyclopropane	36.294516	0.38493730	-3.4351239e-4	1.1248643e-7	-2.4088498e+5
Hexafluoropropylene	44.074818	0.35626012	-3.1116496e-4	1.0038215e-7	-3.8815083e+5
Hexafluoropropylene oxide	33.049018	0.45469294	-4.1072235e-4	1.3585516e-7	-3.9631205e+5

Table D.10 shows the heats of reaction for each of the reactions concerned, which were calculated based on the enthalpies of formation and heat capacity data presented in this section. Reaction 2 in particular was highly exothermic.

Table D.10. Heats of reaction based on estimated enthalpies of formation and heat capacity data.

No.	Reaction	ΔH_{rxn}		
		463 K	**478 K**	**493 K**
1.	$C_3F_6 + ½\ O_2 \rightarrow C_3F_6O$	-48.63	-49.62	-49.61
2.	$C_3F_6 + O_2 \rightarrow CF_3COF + COF_2$	-474.40	-474.55	-474.66
3.	$C_3F_6O \rightarrow CF_3COF + CF_2\bullet$	-8.47	-8.60	-8.74
4.	$CF_2\bullet + CF_2\bullet \rightarrow C_2F_4$	-292.12	-292.01	-291.90
5.	$C_2F_4 + CF_2\bullet \rightarrow c\text{-}C_3F_6$	-154.10	-153.97	-153.84
6.	$C_2F_4 + ½\ O_2 \rightarrow COF_2 + CF_2\bullet$	-124.17	-124.31	-124.44
7b.	$CF_3COF + ½\ O_2 \rightarrow 2\ COF_2$	-192.48	-192.66	-192.84

Appendix E. Sample calculations

Sample calculations for one experimental run are presented here. The conversion of measurement values using instrument calibration data is not shown.

Feed gas:

$$\text{Total injected moles} = n^0_{loop} = \frac{P^0_{loop} \times V^0_{loop}}{R \times T^0_{loop}} = \frac{(104.85 \times 10^3 \text{ Pa}) \times (0.295 \times 10^{-6} \text{ m}^3)}{(8.314 \text{ J mol}^{-1}\text{K}^{-1}) \times (290.85 \text{ K})} = 1.2554 \times 10^{-5} \text{ mol}$$

$$\text{Total inlet volumetric flow-rate} = \dot{V}^0_{Tot} = \frac{\text{WTM volume}}{\text{WTM time}} = \frac{0.3775 \times 10^{-3} \text{ m}^3}{1.250 \text{ min}} = 0.3020 \times 10^{-3} \text{ m}^3 \text{ min}^{-1}$$

$$\text{Total inlet molar flow-rate} = \frac{P_{WTM} \times V^0_{Tot}}{R \times T_{WTM}} = \frac{(99.5031 \times 10^3 \text{ Pa}) \times (0.3020 \times 10^{-3} \text{ m}^3 \text{ min}^{-1}}{(8.314 \text{ J mol}^{-1}\text{K}^{-1}) \times (292.25 \text{ K})}$$
$$= 1.2350 \times 10^{-2} \text{ mol min}^{-1}$$

$$C_{Tot} = \frac{P_{reactor}}{R \times T_{reactor}} = \frac{4.5 \times 10^5 \text{ Pa}}{(8.314 \text{ J mol}^{-1}\text{K}^{-1}) \times (478.15 \text{ K})} = 113.19 \text{ mol m}^{-3}$$

For each individual component, the mole fraction is given by the ratio of the number of moles of the particular species, obtained from the G.C. peak area and calibration data, to the total number of moles injected, e.g.,

$$x^0_{HFP} = \frac{n^0_{HFP}}{n^0_{loop}} = \frac{7.0622 \times 10^{-6} \text{ mol}}{1.2554 \times 10^{-5} \text{ mol}} = 0.56255$$

The individual molar flow-rates are then calculated by multiplying the mole fraction and the total molar flow-rate, e.g.,

$$\text{HFP inlet molar flow-rate} = F^0_{HFP} = x^0_{HFP} \times F^0_{Tot} = 0.56255 \times 1.2350 \times 10^{-2} \text{ mol min}^{-1}$$
$$= 6.9476 \times 10^{-3} \text{ mol min}^{-1}$$

Product gas:

Shimadzu G.C. 2010

$$\text{Total injected moles} = n_{loop} = \frac{P_{loop} \times V_{loop}}{R \times T_{loop}} = \frac{(104.30 \times 10^3 \text{ Pa}) \times (0.295 \times 10^{-6} \text{ m}^3)}{(8.314 \text{ J mol}^{-1}\text{K}^{-1}) \times (292.85 \text{ K})} = 1.2405 \times 10^{-5} \text{ mol}$$

Shimadzu G.C. 2014

$$\text{Total injected moles} = n_{syringe} = \frac{P_{syringe} \times V_{syringe}}{R \times T_{syringe}} = \frac{(100.045 \times 10^3 \text{ Pa}) \times (0.13 \times 10^{-6} \text{ m}^3)}{(8.314 \text{ J mol}^{-1}\text{K}^{-1}) \times (294.455 \text{ K})}$$
$$= 5.3304 \times 10^{-6} \text{ mol}$$

$$\text{Total outlet volumetric flow-rate} = \dot{V}_{Tot} = \frac{\text{WTM volume}}{\text{WTM time}} = \frac{0.3225 \times 10^{-3} \text{ m}^3}{1.391 \text{ min}} = 0.2318 \times 10^{-3} \text{ m}^3 \text{ min}^{-1}$$

$$\text{Total outlet molar flow-rate} = \frac{P_{WTM} \times V_{Tot}}{R \times T_{WTM}} = \frac{(100.045 \times 10^3 \text{ Pa}) \times (0.2318 \times 10^{-3} \text{ m}^3 \text{ min}^{-1}}{(8.314 \text{ J mol}^{-1}\text{K}^{-1}) \times (294.45 \text{ K})}$$
$$= 9.4689 \times 10^{-3} \text{ mol min}^{-1}$$

For each individual component, the mole fraction is again given by the ratio of the number of moles of the particular species, obtained from the G.C. peak area and calibration data, to the total number of moles injected, e.g.,

$$x_{HFP} = \frac{n_{HFP}}{n_{loop}} = \frac{2.3813 \times 10^{-6} \text{ mol}}{1.2405 \times 10^{-5} \text{ mol}} = 0.1920$$

The individual molar flow-rates are then calculated by multiplying the mole fraction and the total molar flow-rate, e.g.,

$$\text{HFP outlet molar flow-rate} = F_{HFP} = x_{HFP} \times F_{Tot} = 0.1920 \times 9.4689 \times 10^{-3} \text{ mol min}^{-1}$$
$$= 1.8180 \times 10^{-3} \text{ mol min}^{-1}$$

$$X_{HFP} = \frac{F_{HFP}^{0} - F_{HFP}}{F_{HFP}^{0}} \times 100\% = \frac{6.9476 \times 10^{-3} - 1.8180 \times 10^{-3}}{6.9476 \times 10^{-3}} \times 100\% = 73.83\%$$

$$S_{HFPO} = \frac{F_{HFPO}}{F_{HFP}^{0} - F_{HFP}} \times 100\% = \frac{2.7587 \times 10^{-3}}{6.9476 \times 10^{-3} - 1.8180 \times 10^{-3}} \times 100\% = 53.78\%$$

$$Y_{HFPO} = \frac{F_{HFPO}}{F_{HFP}^{0}} \times 100\% = \frac{2.7587 \times 10^{-3}}{6.9476 \times 10^{-3}} \times 100\% = 39.71\%$$

Appendix F. Raw experimental data

Table F.1. Raw experimental data for the non-catalytic oxidation of HFP.[a]

	Conditions			Feed						Product						
No.	Temp [K]	HFP/O_2 [mol mol^{-1}]	Space time [s]	WTM T [K]	WTM P [kPa]	WTM flow [L h^{-1}]	GC loop T [K]	GC loop P [kPa]	WTM T [K]	WTM P [kPa]	WTM flow [L h^{-1}]	GC loop T [K]	GC loop P [kPa]	Syringe V [ml]	Sample T [K]	Sample P [kPa]
3a	373	1.00	60	298.4	100.4	9.68	294.3	99.5	298.4	100.4	9.98	294.3	99.5	0.10	294.3	99.5
4a	423	1.00	60	294.5	100.2	8.53	295.2	99.2	294.5	100.2	8.54	295.2	99.2	0.12	295.2	99.2
4b	473	1.00	120	296.1	99.9	3.82	295.2	99.1	296.1	99.9	3.80	295.2	99.1	0.10	295.2	99.1
4c	473	1.00	120	296.2	99.9	3.82	295.3	98.8	296.2	99.9	3.81	295.3	98.8	0.12	295.3	98.8
7a	473	1.00	120	295.4	102.1	7.63	293.4	101.3	295.4	102.1	7.54	293.4	101.3	0.10	293.4	101.3
8a	473	1.00	120	298.3	100.3	9.54	296.1	99.9	298.3	100.3	9.46	296.1	99.9	0.11	296.1	99.9
8b	473	1.00	120	298.3	101.5	11.45	296.1	101.5	298.3	101.5	11.32	296.1	101.5	0.13	296.1	101.5
8c	473	1.00	120	298.3	100.0	17.17	296.1	102.3	298.3	100.0	16.32	296.1	102.3	0.11	296.1	102.3
20a	478	1.03	116	296.8	103.2	16.93	296.3	105.2	301.2	102.7	15.56	300.4	104.3	0.10	301.2	102.7
20b	478	0.52	119	296.5	103.7	16.50	296.1	104.6	301.8	102.3	14.00	300.7	103.3	0.10	301.8	102.3
21a	478	1.53	130	296.5	103.0	15.15	296.2	105.1	300.4	102.1	13.28	299.5	103.7	0.10	300.4	102.1
21b	478	2.06	125	302.4	102.0	16.24	301.4	105.0	301.1	101.8	12.29	300.1	103.7	0.10	301.1	101.8
21c	478	0.25	127	297.8	103.4	15.52	297.2	103.7	301.1	108.0	11.41	300.4	106.7	0.10	301.1	108.0
22a	493	1.01	124	296.5	103.7	15.34	296.1	104.6	299.5	102.3	12.89	298.4	103.7	0.10	299.5	102.3
22b	478	1.03	116	296.8	103.2	16.93	296.3	105.2	299.7	102.3	14.27	298.7	104.7	0.10	299.7	102.3
22c	463	1.09	126	296.7	103.3	16.12	296.4	102.5	299.5	102.5	15.81	298.8	105.0	0.10	299.5	102.5
22d	478	1.03	116	296.8	103.2	16.93	296.3	105.2	299.2	102.4	14.78	298.4	104.7	0.10	299.2	102.4
23a	478	0.99	200	296.7	103.3	9.82	296.4	102.5	300.2	102.0	9.11	299.2	101.9	0.10	300.2	102.0
23b	478	1.03	116	296.8	103.2	16.93	296.3	105.2	300.8	102.3	14.78	299.8	104.6	0.10	300.8	102.3
23c	459	1.12	117	296.4	103.3	17.49	296.3	105.5	301.1	102.4	16.56	299.7	105.5	0.10	301.1	102.4
24a	478	2.06	125	302.4	102.0	16.24	301.4	105.0	300.5	101.4	14.78	299.5	103.7	0.10	300.5	101.4
24b	478	0.25	127	297.8	103.4	15.52	297.2	103.7	301.1	101.5	16.14	300.4	103.2	0.10	301.1	101.5
24c	463	0.56	108	296.9	103.2	18.76	296.5	105.5	301.1	101.8	17.67	300.2	105.2	0.10	301.1	101.8
25a	463	1.09	126	296.7	103.3	16.12	296.4	102.5	296.4	101.4	14.06	295.2	104.3	0.11	295.1	101.4
25b	463	1.12	116	296.4	103.3	17.49	296.3	105.5	297.2	101.3	15.08	296.1	104.9	0.09	295.9	101.3
25c	478	1.03	116	296.8	103.2	16.93	296.3	105.2	297.4	101.1	14.94	296.4	104.0	0.10	296.2	101.1
25d	478	1.53	130	296.5	103.0	15.19	296.2	105.1	298.0	101.0	12.14	296.9	103.8	0.11	296.7	101.0
25e	478	1.03	116	296.8	103.2	16.93	296.3	105.2	298.0	100.9	14.85	297.2	103.7	0.11	297.1	100.9
25f	493	1.01	124	296.5	103.7	15.35	296.1	104.6	298.3	101.8	14.96	297.3	102.9	0.12	297.2	101.7
25g	478	1.03	116	296.8	103.2	16.93	296.3	105.2	298.2	100.9	14.85	297.3	103.6	0.11	297.2	100.9
26a	478	0.52	119	296.5	103.7	16.50	296.1	104.6	296.6	100.9	16.13	295.7	103.1	0.10	295.5	100.9

Table F.1. (*continued*)

No.	Conditions			Feed						Product						
	Temp [K]	HFP/O_2 [mol mol^{-1}]	Space time [s]	WTM T [K]	WTM P [kPa]	WTM flow [L h^{-1}]	GC loop T [K]	GC loop P [kPa]	WTM T [K]	WTM P [kPa]	WTM flow [L h^{-1}]	GC loop T [K]	GC loop P [kPa]	Syringe V [ml]	Sample T [K]	Sample P [kPa]
26b	478	0.25	127	297.8	103.4	15.52	297.2	103.7	296.9	100.7	15.44	296.0	102.9	0.10	295.8	100.7
26c	463	0.56	88	295.3	111.0	21.43	295.6	113.1	297.4	101.2	22.06	296.4	106.0	0.09	296.2	101.2
26d	453	1.01	99	302.0	110.3	19.89	301.8	111.8	297.5	100.8	17.89	296.7	105.9	0.09	296.5	100.8
26e	478	1.69	116	298.2	102.7	17.14	297.9	104.3	297.5	100.2	12.98	296.6	102.9	0.11	296.4	100.2
26f	493	1.48	117	296.9	111.3	15.09	296.8	111.3	297.5	100.3	12.30	296.6	102.6	0.12	296.4	100.3
26g	478	1.10	102	296.6	103.7	19.11	296.3	106.4	297.6	100.9	16.83	296.6	104.5	0.11	296.4	100.9
27a	478	1.05	122	303.2	110.1	15.46	302.3	109.9	296.6	102.3	12.51	295.7	104.2	0.11	295.5	101.8
27b	478	1.01	76	302.3	110.3	24.65	301.4	114.0	296.9	104.7	21.94	296.1	110.3	0.10	295.9	101.7
27c	463	1.48	91	296.0	111.4	20.55	295.8	114.2	297.3	104.7	20.51	296.2	111.0	0.09	296.0	101.8
28a	493	1.45	91	296.1	111.1	19.53	296.2	113.7	296.5	102.1	17.89	295.2	105.8	0.12	295.1	101.8
28b	463	1.45	122	296.9	111.0	15.51	297.4	111.5	296.7	101.8	12.89	295.2	104.9	0.09	295.1	101.8
28c	493	0.51	100	296.9	103.2	19.14	296.5	104.9	297.1	101.8	16.88	295.9	105.4	0.11	295.7	101.8
28d	493	0.57	137	297.2	103.2	13.96	296.7	103.3	297.1	101.7	12.41	296.1	103.4	0.12	295.9	101.7
28e	463	0.52	141	297.5	103.0	14.50	297.2	103.1	297.2	101.6	13.31	296.0	103.6	0.10	295.8	101.6
28f	463	1.08	126	296.7	103.3	16.12	296.4	102.5	297.4	102.3	15.17	296.2	105.2	0.10	296.0	101.7
28g	478	0.25	127	297.8	103.4	15.52	297.2	103.7	297.3	101.7	14.90	296.2	104.0	0.10	296.0	101.7
28h	503	0.99	124	298.1	102.6	15.25	297.8	103.6	297.6	101.8	15.38	296.5	103.8	0.13	296.3	101.8
29a	463	1.06	120	290.0	99.8	17.05	288.8	105.2	293.9	100.4	14.90	292.7	104.3	0.09	293.9	100.4
29b	478	1.06	117	290.0	99.8	17.05	288.8	105.2	294.6	100.4	12.75	293.4	103.7	0.10	294.6	100.4
29c	493	1.06	113	290.0	99.8	17.05	288.8	105.2	295.2	100.2	14.06	294.0	103.6	0.11	295.2	100.2
29d	493	1.14	127	291.7	99.5	15.35	290.4	103.9	295.5	99.8	11.05	294.3	102.3	0.13	295.5	99.8
29e	463	1.14	135	291.7	99.5	15.35	290.4	103.9	295.7	99.8	15.68	294.5	103.1	0.10	295.7	99.8
29f	478	1.03	116	296.8	103.2	16.93	296.3	105.2	295.7	99.7	14.70	294.6	103.6	0.11	294.5	99.7
29g	478	1.14	131	291.7	99.5	15.35	290.4	103.9	295.8	100.1	11.21	294.5	102.4	0.12	295.8	100.1
30a	463	1.86	131	291.5	101.2	15.50	290.3	106.8	294.0	103.5	13.00	292.8	107.6	0.09	294.0	103.5
30b	478	1.86	127	291.5	101.2	15.50	290.3	106.8	295.4	100.4	11.71	294.2	104.1	0.12	295.4	100.4
30c	493	1.86	123	291.5	101.2	15.50	290.3	106.8	295.8	100.4	13.45	294.6	103.8	0.12	295.8	100.4
30d	478	1.03	116	296.8	103.2	16.93	296.3	105.2	296.1	101.1	14.47	294.9	104.7	0.11	294.8	101.1
30e	463	0.78	114	290.0	100.4	17.88	288.8	105.5	296.1	101.9	16.59	294.7	105.4	0.10	296.1	101.9
30f	478	0.78	111	290.0	100.4	17.88	288.8	105.5	294.1	101.7	15.04	295.0	104.9	0.11	294.1	101.7
31a	463	0.61	114	293.8	101.2	18.00	292.6	106.1	291.9	103.8	15.40	290.6	107.2	0.09	291.9	103.8

Table F.1. (*continued*)

No.	Conditions			Feed						Product						
	Temp [K]	HFP/O_2 [mol mol^{-1}]	Space time [s]	WTM T [K]	WTM P [kPa]	WTM flow [L h^{-1}]	GC loop T [K]	GC loop P [kPa]	WTM T [K]	WTM P [kPa]	WTM flow [L h^{-1}]	GC loop T [K]	GC loop P [kPa]	Syringe V [ml]	Sample T [K]	Sample P [kPa]
32a	463	0.61	143	292.1	101.2	14.25	290.9	105.0	293.4	101.1	12.78	292.2	103.6	0.10	293.4	101.1
32b	478	0.61	110	293.8	101.2	18.00	292.6	106.1	293.9	101.3	15.04	292.6	104.4	0.10	293.9	101.3
32c	493	0.61	107	293.8	101.2	18.00	292.6	106.1	294.5	101.1	15.23	293.3	104.0	0.11	294.5	101.1
32d	493	0.78	107	290.0	100.4	17.88	288.8	105.5	294.8	100.9	15.11	293.6	104.2	0.12	294.8	100.9
32e	478	1.33	107	289.5	100.2	18.50	288.4	106.8	295.0	100.9	16.17	293.8	104.9	0.11	295.0	100.9
32f	478	1.03	116	296.8	103.2	16.93	296.3	105.2	295.2	100.9	14.06	294.0	105.5	0.12	293.9	100.9
32g	463	1.33	110	289.5	100.2	18.50	288.4	106.8	295.6	101.7	17.50	294.5	106.2	0.09	295.6	101.7
33a	463	1.48	140	291.9	99.4	14.77	290.6	103.8	293.4	101.8	11.40	292.4	104.9	0.09	293.4	101.8
33b	478	1.48	136	291.9	99.4	14.77	290.6	103.8	294.1	101.7	10.53	293.0	104.5	0.10	294.1	101.7
33c	478	0.61	139	292.1	101.2	14.25	290.9	105.0	294.4	101.7	11.06	293.3	104.5	0.11	294.4	101.7
33d	493	0.61	134	292.1	101.2	14.25	290.9	105.0	294.9	101.0	12.03	293.8	103.5	0.12	294.9	101.0
33e	493	1.48	132	291.9	99.4	14.77	290.6	103.8	295.1	101.1	12.75	293.9	105.4	0.13	295.1	101.1
33f	463	0.82	94	289.9	100.6	21.74	288.9	107.3	295.4	101.7	20.07	294.2	107.7	0.10	295.4	101.7
33g	493	0.82	88	289.9	100.6	21.74	288.9	107.3	295.6	101.1	18.00	294.4	107.3	0.12	295.6	101.1
33h	493	1.33	104	289.5	100.2	18.50	288.4	106.8	295.9	101.1	17.06	294.7	105.5	0.13	295.9	101.1
33i	478	0.82	91	289.9	100.6	21.74	288.9	107.3	296.2	101.3	19.30	295.1	106.7	0.10	296.2	101.3
34a	463	1.55	112	292.8	99.5	18.61	291.5	105.5	292.0	100.1	14.53	290.1	105.2	0.09	292.0	100.1
34b	478	1.55	108	292.8	99.5	18.61	291.5	105.5	292.0	99.9	13.25	290.9	104.4	0.09	292.0	99.9
34c	493	1.55	105	292.8	99.5	18.61	291.5	105.5	292.8	99.8	14.36	291.6	104.4	0.11	292.8	99.8
34d	493	0.88	132	292.9	101.7	14.45	291.6	104.9	293.4	99.5	10.80	292.3	102.8	0.12	293.4	99.5
34e	478	0.88	136	292.9	101.7	14.45	291.6	104.9	293.6	99.5	10.91	292.6	102.5	0.12	293.6	99.5
34f	463	0.88	141	292.9	101.7	14.45	291.6	104.9	293.8	99.5	12.12	292.8	103.4	0.10	293.8	99.5
34g	463	0.92	129	290.3	99.8	15.96	289.2	104.6	294.1	100.0	14.71	293.2	104.4	0.10	294.1	100.0
34h	478	0.92	125	290.3	99.8	15.96	289.2	104.6	294.5	99.6	14.89	293.5	103.6	0.11	294.5	99.6
35a	463	0.76	103	289.9	100.5	19.85	288.7	106.6	292.8	101.2	18.22	291.6	106.8	0.09	292.8	101.2
35b	478	0.76	99	289.9	100.5	19.85	288.7	106.6	293.3	101.0	17.10	292.2	105.8	0.10	293.3	101.0
35c	493	0.76	96	289.9	100.5	19.85	288.7	106.6	293.7	100.2	17.89	292.5	105.2	0.12	293.7	100.2
35d	493	0.92	121	290.3	99.8	15.96	289.2	104.6	294.1	99.9	13.90	292.9	103.7	0.13	294.1	99.9
35e	478	1.29	111	292.7	99.5	18.12	291.3	104.9	294.5	100.0	13.90	293.4	104.3	0.13	294.5	100.0
35f	463	1.29	115	292.7	99.5	18.12	291.3	104.9	294.7	100.1	16.68	293.7	104.9	0.10	294.7	100.1
35g	478	1.68	141	293.4	101.0	14.13	292.4	106.0	295.0	99.7	12.11	293.9	104.2	0.13	295.0	99.7

Table F.1. (*continued*)

No.	Conditions			Feed						Product						
	Temp [K]	HFP/O_2 [mol mol^{-1}]	Space time [s]	WTM T [K]	WTM P [kPa]	WTM flow [L h^{-1}]	GC loop T [K]	GC loop P [kPa]	WTM T [K]	WTM P [kPa]	WTM flow [L h^{-1}]	GC loop T [K]	GC loop P [kPa]	Syringe V [ml]	Sample T [K]	Sample P [kPa]
35h	493	1.29	108	292.7	99.5	18.12	291.3	104.9	295.1	99.9	13.92	294.0	103.8	0.13	295.1	99.9
36a	463	1.68	145	293.4	101.0	14.13	292.4	106.0	291.5	100.5	13.28	290.3	104.9	0.10	291.5	100.5
36b	463	0.65	103	290.0	100.6	19.70	288.8	106.0	292.1	100.8	17.36	290.9	105.8	0.10	292.1	100.8
36c	478	0.65	100	290.0	100.6	19.70	288.8	106.0	292.7	100.6	16.12	291.5	105.2	0.10	292.7	100.6
36d	493	0.65	97	290.0	100.6	19.70	288.8	106.0	293.0	100.4	16.59	291.9	105.1	0.12	293.0	100.4
36e	493	1.68	136	293.4	101.0	14.13	292.4	106.0	293.2	100.5	12.73	292.0	104.2	0.13	293.2	100.5
36f	463	1.28	131	292.1	99.5	15.85	290.9	104.3	293.7	100.8	14.07	292.5	105.0	0.10	293.7	100.8
36g	478	1.28	127	292.1	99.5	15.85	290.9	104.3	293.7	100.3	12.87	292.6	104.2	0.12	293.7	100.3
36h	493	1.28	123	292.1	99.5	15.85	290.9	104.3	294.1	100.2	13.41	293.2	104.0	0.13	294.1	100.2
37a	463	0.83	107	289.5	100.4	18.98	288.3	106.0	290.5	102.0	16.67	289.4	107.4	0.09	290.5	102.0
37b	478	0.83	104	289.5	100.4	18.98	288.3	106.0	290.8	102.2	15.33	289.6	106.9	0.10	290.8	102.2
37c	493	0.83	101	289.5	100.4	18.98	288.3	106.0	291.2	101.5	16.10	290.1	106.1	0.13	291.2	101.5
37d	493	0.69	86	290.0	100.6	22.18	288.7	107.1	291.3	101.8	18.59	290.2	107.2	0.13	291.3	101.8
37e	478	0.69	89	290.0	100.6	22.18	288.7	107.1	291.5	101.7	19.70	290.4	107.6	0.10	291.5	101.7
37f	463	0.69	92	290.0	100.6	22.18	288.7	107.1	291.7	102.2	20.34	290.7	108.0	0.10	291.7	102.2
37g	463	1.21	98	289.5	100.5	20.69	288.3	107.4	292.1	102.2	19.33	291.1	108.4	0.09	292.1	102.2
37h	478	1.21	95	289.5	100.5	20.69	288.3	107.4	292.4	101.4	17.21	291.2	107.0	0.11	292.4	101.4
37i	493	1.21	92	289.5	100.5	20.69	288.3	107.4	292.4	101.3	18.11	291.2	107.3	0.13	292.4	101.3
38a	463	2.27	143	293.5	100.9	14.35	292.3	105.5	291.8	101.1	12.07	290.7	105.1	0.09	291.8	101.1
38b	478	2.27	139	293.5	100.9	14.35	292.3	105.5	292.3	100.9	10.88	291.0	104.7	0.12	292.3	100.9
38c	493	2.27	135	293.5	100.9	14.35	292.3	105.5	292.7	101.0	11.34	291.5	105.5	0.13	292.7	101.0
38d	493	2.57	134	292.9	101.1	14.30	291.6	106.2	293.0	101.0	13.51	291.9	105.1	0.15	293.0	101.0
38e	478	2.57	139	292.9	101.1	14.30	291.6	106.2	293.3	100.9	12.41	292.2	105.2	0.13	293.3	100.9
38f	463	2.57	143	292.9	101.1	14.30	291.6	106.2	293.5	101.2	13.24	292.4	105.7	0.11	293.5	101.2
38g	463	1.14	111	292.4	99.6	18.69	291.0	105.4	293.8	101.7	17.89	292.8	107.4	0.10	293.8	101.7
38h	478	1.14	107	292.4	99.6	18.69	291.0	105.4	293.9	101.4	17.51	292.9	106.9	0.11	293.9	101.4
38i	493	1.14	104	292.4	99.6	18.69	291.0	105.4	294.1	101.2	15.87	293.0	105.8	0.13	294.1	101.2
39a	463	0.99	90	289.8	100.7	22.61	288.6	108.0	292.5	102.3	20.71	291.4	109.2	0.09	292.5	102.3
39b	478	0.99	87	289.8	100.7	22.61	288.6	108.0	292.7	102.3	20.19	291.6	108.7	0.09	292.7	102.3
39c	493	0.99	84	289.8	100.7	22.61	288.6	108.0	293.1	102.7	18.37	292.1	107.4	0.13	293.1	102.5
39d	493	1.26	87	290.0	100.7	21.87	288.8	108.1	293.4	101.6	18.85	292.4	107.6	0.14	293.4	101.6

Table F.1. (*continued*)

No.	Conditions			Feed						Product						
	Temp [K]	HFP/O_2 [mol mol^{-1}]	Space time [s]	WTM T [K]	WTM P [kPa]	WTM flow [L h^{-1}]	GC loop T [K]	GC loop P [kPa]	WTM T [K]	WTM P [kPa]	WTM flow [L h^{-1}]	GC loop T [K]	GC loop P [kPa]	Syringe V [ml]	Sample T [K]	Sample P [kPa]
39e	478	1.26	90	290.0	100.7	21.87	288.8	108.1	293.7	102.0	18.67	292.6	107.7	0.11	293.7	102.0
39f	463	1.26	93	290.0	100.7	21.87	288.8	108.1	294.0	101.9	20.57	293.0	108.6	0.09	294.0	101.9
39g	463	1.74	106	291.9	101.5	19.21	290.7	108.1	294.0	101.5	18.22	293.0	107.8	0.09	294.0	101.5
39h	478	1.74	103	291.9	101.5	19.21	290.7	108.1	294.2	101.3	15.69	293.2	106.5	0.11	294.2	101.3
39i	493	1.74	99	291.9	101.5	19.21	290.7	108.1	294.4	101.3	15.28	293.3	106.8	0.14	294.4	101.3
40a	463	0.51	98	294.2	101.2	21.04	293.0	106.4	291.2	101.5	18.09	290.1	106.5	0.09	291.2	101.5
40b	478	0.51	95	294.2	101.2	21.04	293.0	106.4	291.8	101.4	18.15	290.7	106.3	0.09	291.8	101.4
40c	493	0.51	92	294.2	101.2	21.04	293.0	106.4	292.3	101.5	17.22	291.1	106.1	0.11	292.3	101.5
40d	493	0.63	118	290.7	101.2	16.23	289.4	105.8	292.7	101.1	14.53	291.5	105.0	0.12	292.7	101.1
40e	478	0.63	121	290.7	101.2	16.23	289.4	105.8	292.9	101.1	15.27	291.8	105.1	0.11	292.9	101.1
40f	463	0.63	125	290.7	101.2	16.23	289.4	105.8	292.9	101.1	15.94	291.9	105.6	0.10	292.9	101.1
40g	463	0.53	125	291.0	101.1	16.25	289.8	105.2	293.0	101.3	15.36	291.9	105.0	0.09	293.0	101.3
40h	478	0.53	121	291.0	101.1	16.25	289.8	105.2	293.2	101.3	14.19	292.1	104.7	0.10	293.2	101.3
40i	493	0.53	117	291.0	101.1	16.25	289.8	105.2	293.3	101.0	14.99	292.3	104.6	0.12	293.3	101.0
41a	463	1.29	142	293.9	101.0	14.43	292.8	106.5	291.6	100.5	11.53	290.6	104.2	0.10	291.6	100.5
41b	478	1.29	138	293.9	101.0	14.43	292.8	106.5	292.1	100.6	10.56	291.1	104.2	0.10	292.1	100.6
41c	493	1.29	134	293.9	101.0	14.43	292.8	106.5	292.8	100.9	11.37	291.8	104.3	0.10	292.8	100.9
41d	493	1.08	152	294.1	100.9	12.76	292.9	104.3	293.1	100.2	10.90	292.0	102.8	0.10	293.1	100.2
41e	478	1.08	156	294.1	100.9	12.76	292.9	104.3	293.4	100.1	10.14	292.4	103.1	0.14	293.4	100.1
41f	463	1.08	161	294.1	100.9	12.76	292.9	104.3	293.6	100.4	11.84	292.6	103.7	0.11	293.6	100.4
41g	463	0.74	135	291.7	101.2	15.04	290.5	105.4	293.8	100.4	15.42	292.7	104.3	0.10	293.8	100.4
41h	478	0.74	131	291.7	101.2	15.04	290.5	105.4	293.9	100.4	14.16	292.9	104.0	0.12	293.9	100.4
41i	493	0.74	127	291.7	101.2	15.04	290.5	105.4	294.1	100.4	14.32	293.1	104.1	0.13	294.1	100.4
42a	463	1.03	100	289.4	100.3	20.42	288.3	106.7	292.8	100.5	19.00	291.6	106.5	0.09	292.8	100.5
42b	478	1.03	97	289.4	100.3	20.42	288.3	106.7	293.0	100.4	17.88	292.0	106.0	0.11	293.0	100.4
42c	493	1.03	94	289.4	100.3	20.42	288.3	106.7	293.3	100.5	17.65	292.2	106.9	0.13	293.3	100.5
42d	493	1.49	165	291.5	99.3	11.84	290.3	102.9	293.5	99.8	10.73	292.6	102.5	0.13	293.5	99.8
42e	478	1.49	170	291.5	99.3	11.84	290.3	102.9	293.9	100.3	11.72	292.8	103.1	0.14	293.9	100.3
42f	463	1.49	175	291.5	99.3	11.84	290.3	102.9	294.0	100.3	10.65	293.0	103.6	0.12	294.0	100.3
42g	463	1.82	151	294.4	100.9	13.70	293.3	104.9	294.2	100.4	12.07	293.2	103.7	0.10	294.2	100.4
42h	478	1.82	146	294.4	100.9	13.70	293.3	104.9	294.2	102.4	11.18	293.2	103.8	0.09	294.2	102.4

Table F.1. (*continued*)

No.	Conditions			Feed						Product						
	Temp [K]	HFP/O_2 [mol mol^{-1}]	Space time [s]	WTM T [K]	WTM P [kPa]	WTM flow [L h^{-1}]	GC loop T [K]	GC loop P [kPa]	WTM T [K]	WTM P [kPa]	WTM flow [L h^{-1}]	GC loop T [K]	GC loop P [kPa]	Syringe V [ml]	Sample T [K]	Sample P [kPa]
42i	493	1.82	141	294.4	100.9	13.70	293.3	104.9	294.2	102.5	10.45	293.1	103.6	0.12	294.2	102.5
43a	463	2.26	116	291.1	101.2	17.44	289.8	107.4	292.6	101.1	15.96	291.3	106.9	0.09	292.6	101.1
43b	478	2.26	113	291.1	101.2	17.44	289.8	107.4	293.2	101.2	14.19	292.1	106.0	0.13	293.2	101.2
43c	493	2.26	109	291.1	101.2	17.44	289.8	107.4	293.5	101.0	14.92	292.5	105.9	0.12	293.5	101.0
43d	493	2.72	120	292.5	101.2	15.97	291.2	106.8	293.8	101.1	13.50	292.8	105.5	0.12	293.8	101.1
43e	478	2.72	124	292.5	101.2	15.97	291.2	106.8	294.1	100.9	12.75	292.9	105.2	0.13	294.1	100.9
43f	463	2.72	128	292.5	101.2	15.97	291.2	106.8	294.3	100.4	15.07	293.2	105.9	0.09	294.3	100.4
43g	463	0.71	157	293.3	100.9	13.03	292.2	104.3	294.4	100.3	11.97	293.5	103.4	0.10	294.4	100.3
43h	478	0.71	153	293.3	100.9	13.03	292.2	104.3	294.6	100.1	11.91	293.5	103.6	0.11	294.6	100.1
43i	493	0.71	148	293.3	100.9	13.03	292.2	104.3	294.7	100.2	13.13	293.6	103.1	0.13	294.7	100.2
44a	463	1.40	102	290.1	100.6	20.04	288.9	107.6	289.9	100.9	19.30	288.8	107.7	0.10	289.9	100.9
44b	478	1.40	99	290.1	100.6	20.04	288.9	107.6	289.9	100.8	17.45	288.8	107.2	0.10	289.9	100.8
44c	493	1.40	96	290.1	100.6	20.04	288.9	107.6	290.0	100.6	16.52	288.8	106.5	0.10	290.0	100.6
44d	493	1.43	168	294.1	100.7	11.52	292.9	103.9	289.8	100.1	8.71	288.6	103.8	0.10	289.8	100.1
44e	478	1.43	173	294.1	100.7	11.52	292.9	103.9	289.8	100.1	9.89	288.5	103.3	0.10	289.8	100.1
44f	463	1.43	179	294.1	100.7	11.52	292.9	103.9	289.7	100.5	9.13	288.5	103.3	0.10	289.7	100.5
44g	463	0.94	170	284.0	100.8	11.72	293.0	103.9	289.7	100.5	10.84	288.4	103.6	0.10	289.7	100.5
44h	478	0.94	165	284.0	100.8	11.72	293.0	103.9	289.6	100.8	9.87	288.4	103.6	0.10	289.6	100.8
44i	493	0.94	160	284.0	100.8	11.72	293.0	103.9	289.7	100.6	10.36	288.4	104.3	0.10	289.7	100.6
45a	463	1.10	85	290.0	100.8	23.78	288.8	108.7	289.3	101.9	22.30	288.1	109.4	0.10	289.3	101.9
45b	478	1.10	83	290.0	100.8	23.78	288.8	108.7	289.5	102.1	20.52	288.2	109.6	0.10	289.5	102.1
45c	493	1.10	80	290.0	100.8	23.78	288.8	108.7	289.5	101.5	19.25	288.3	107.7	0.10	289.5	101.5
45d	493	0.61	107	293.8	101.2	18.00	292.6	106.1	289.8	101.0	16.71	288.6	105.9	0.10	289.8	101.0
45e	478	0.61	110	293.8	101.2	18.00	292.6	106.1	289.9	100.7	15.67	288.7	105.6	0.10	289.9	100.7
45f	463	0.61	114	293.8	101.2	18.00	292.6	106.1	290.1	101.3	17.00	288.9	105.9	0.10	290.1	101.3
45g	463	1.20	207	291.2	99.3	10.00	289.9	102.1	290.4	100.2	8.53	289.2	102.9	0.10	290.4	100.2
45h	478	1.20	201	291.2	99.3	10.00	289.9	102.1	290.6	100.4	8.53	289.4	103.2	0.10	290.6	100.4
45i	493	1.20	195	291.2	99.3	10.00	289.9	102.1	290.7	100.3	8.39	289.5	102.4	0.10	290.7	100.3

[a] WTM refers to wet-test meter.

Table F.2. Raw experimental data for the catalytic oxidation of HFP over Au/Al_2O_3.

No.	Conditions			Feed						Product						
	Temp [K]	HFP/O_2 [mol mol^{-1}]	WHSV [h^{-1}]	WTM T [K]	WTM P [kPa]	WTM flow [L h^{-1}]	GC loop T [K]	GC loop P [kPa]	WTM T [K]	WTM P [kPa]	WTM flow [L h^{-1}]	GC loop T [K]	GC loop P [kPa]	Syringe V [ml]	Sample T [K]	Sample P [kPa]
1	373	1.00	2.75	284.0	100.7	8.00	293.0	103.9	292.8	100.0	7.96	291.8	102.4	0.11	292.8	100.0
2	398	1.00	2.75	284.0	100.7	8.00	293.0	103.9	293.4	100.0	7.90	292.4	102.4	0.10	293.4	100.0
3	423	1.00	2.75	284.0	100.7	8.00	288.8	108.7	294.0	100.0	7.92	293.1	102.3	0.10	294.0	100.0
4	423	0.51	2.75	290.0	100.8	10.00	288.8	108.7	294.2	100.1	10.00	293.1	102.9	0.10	294.2	100.1
5	423	1.50	2.75	290.0	100.8	7.00	288.8	108.7	294.5	99.8	7.08	293.5	101.9	0.10	294.5	99.8
6	423	1.00	1.37	290.0	100.8	3.80	292.6	106.1	294.7	99.6	3.68	293.7	101.1	0.10	294.7	99.6
7	423	1.00	4.07	293.8	100.8	12.20	292.6	106.1	294.9	100.0	12.34	293.8	103.2	0.10	294.9	100.0
8	473	1.00	2.75	293.8	100.8	7.80	292.6	106.1	295.0	99.8	7.85	294.1	102.1	0.10	295.0	99.8

Table F.3. Raw experimental data for the catalytic oxidation of HFP over Au/ZnO.

No.	Conditions			Feed						Product						
	Temp [K]	HFP/O_2 [mol mol^{-1}]	WHSV [h^{-1}]	WTM T [K]	WTM P [kPa]	WTM flow [L h^{-1}]	GC loop T [K]	GC loop P [kPa]	WTM T [K]	WTM P [kPa]	WTM flow [L h^{-1}]	GC loop T [K]	GC loop P [kPa]	Syringe V [ml]	Sample T [K]	Sample P [kPa]
1	453	2.76	5.96	295.0	99.1	6.22	294.2	101.4	295.7	99.8	6.34	294.8	101.9	0.17	295.7	99.8
2	473	2.76	5.96	295.0	99.1	6.22	294.2	101.4	296.2	99.6	6.43	295.2	101.6	0.17	296.2	99.6
3	483	2.76	5.96	295.0	99.1	6.22	294.2	101.4	296.4	99.6	6.13	295.6	101.9	0.16	296.4	99.6
4	483	0.90	6.79	296.5	99.3	9.59	295.7	102.1	296.7	99.8	9.55	295.8	102.4	0.17	296.7	99.8
5	493	0.90	6.79	296.5	99.3	9.59	295.7	102.1	296.9	99.7	9.89	296.0	102.8	0.17	296.9	99.7

Table F.4. Raw experimental data for the catalytic oxidation of HFP over CuO/SiO_2.

No.	Conditions			Feed					Product							
	Temp [K]	HFP/O_2 [mol mol^{-1}]	WHSV [h^{-1}]	WTM T [K]	WTM P [kPa]	WTM flow [L h^{-1}]	GC loop T [K]	GC loop P [kPa]	WTM T [K]	WTM P [kPa]	WTM flow [L h^{-1}]	GC loop T [K]	GC loop P [kPa]	Syringe V [ml]	Sample T [K]	Sample P [kPa]
1	453	1.34	8.64	297.5	99.3	10.81	296.5	102.4	292.0	101.0	9.36	291.0	104.0	0.16	292.0	101.0
2	473	1.34	8.64	297.5	99.3	10.81	296.5	102.4	291.9	100.9	8.93	290.9	103.8	0.16	291.9	100.9
3	493	1.34	8.64	297.5	99.3	10.81	296.5	102.4	292.1	100.9	8.63	291.1	103.7	0.16	292.1	100.9
4	493	0.86	5.42	297.2	99.1	7.80	296.4	101.6	293.3	100.6	6.34	292.2	102.4	0.17	293.3	100.6
5	493	2.57	5.14	296.8	99.0	5.48	296.1	101.0	293.6	100.4	4.44	292.6	102.0	0.18	293.6	100.4
6	453	2.43	7.02	296.2	99.2	7.54	295.5	101.8	296.3	98.9	6.54	295.6	101.4	0.17	296.3	98.9
7	473	2.43	7.02	296.2	99.2	7.54	295.5	101.8	296.9	98.9	6.44	296.1	101.4	0.17	296.9	98.9
8	493	2.43	7.02	296.2	99.2	7.54	295.5	101.8	297.7	98.8	6.03	296.8	100.9	0.12	297.7	98.8
9	473	2.58	7.34	297.1	99.1	7.82	296.3	101.6	298.0	98.8	6.28	296.9	101.1	0.17	298.0	98.8
10	493	2.58	7.34	297.1	99.1	7.82	296.3	101.6	299.0	99.0	6.76	297.0	102.3	0.18	298.1	99.0

Table F.5. Raw experimental data for the catalytic oxidation of HFP over $Cs\text{-}CuO/SiO_2$.

No.	Conditions			Feed					Product							
	Temp [K]	HFP/O_2 [mol mol^{-1}]	WHSV [h^{-1}]	WTM T [K]	WTM P [kPa]	WTM flow [L h^{-1}]	GC loop T [K]	GC loop P [kPa]	WTM T [K]	WTM P [kPa]	WTM flow [L h^{-1}]	GC loop T [K]	GC loop P [kPa]	Syringe V [ml]	Sample T [K]	Sample P [kPa]
1	423	2.76	5.96	295.0	99.1	6.22	294.2	101.4	296.4	98.8	5.80	295.6	101.0	0.17	296.4	98.8
2	453	2.76	5.96	295.0	99.1	6.22	294.2	101.4	296.8	98.8	5.76	296.0	100.9	0.17	296.8	98.8
3	473	2.76	5.96	295.0	99.1	6.22	294.2	101.4	297.2	98.6	5.66	296.1	100.7	0.19	297.2	98.6
4	483	2.76	5.96	295.0	99.1	6.22	294.2	101.4	297.5	98.9	5.69	296.4	100.6	0.20	297.5	98.9
5	453	3.49	6.26	295.5	99.2	6.27	294.6	101.6	297.1	99.3	5.56	296.1	101.6	0.16	297.1	99.3
6	463	3.49	6.26	295.5	99.2	6.27	294.6	101.6	297.7	99.3	5.65	296.8	101.6	0.16	297.7	99.3
7	473	3.49	6.26	295.5	99.2	6.27	294.6	101.6	298.2	99.3	5.70	297.3	101.5	0.28	298.2	99.3
8	473	4.44	4.73	297.1	99.1	4.59	295.3	101.0	298.5	99.2	4.10	297.5	101.1	0.28	298.5	99.2
9	423	2.58	0.52	297.1	99.1	7.82	296.3	101.6	295.7	99.4	7.35	294.7	102.5	0.17	295.7	99.4
10	453	2.58	0.52	297.1	99.1	7.82	296.3	101.6	296.0	99.4	7.03	294.9	102.5	0.18	295.8	99.4
11	453	0.90	0.48	296.5	99.3	9.59	295.7	102.1	296.2	99.5	8.84	295.1	102.9	0.18	296.2	99.5
12	453	4.44	0.34	297.1	99.1	4.59	295.3	101.0	296.4	99.2	4.36	295.3	101.9	0.21	296.4	99.2
13	453	0.86	0.39	297.2	99.1	7.80	296.4	101.6	296.6	99.4	7.48	295.7	102.5	0.18	296.6	99.4

Appendix G. Chemical data table

Table G.1. Data table of chemicals used in this work.

IUPAC name	CAS number	Supplier	Supplier specified purity [%]	Determined purity [%]
1,1,2,3,3,3-hexafluoro-1-propene	116-15-4	NECSA	-	99.8 (G.C.)
2,2,3-trifluoro-3-(trifluoromethyl)-oxirane	428-59-1	NECSA	-	99.5 (G.C.)
1,1,1,3,3,3-hexafluoro-2-propanone	684-16-2	ABCR GmbH and Co. KG	98	-
Carbonyl fluoride	353-50-4	ABCR GmbH and Co. KG	97	-
Trifluoroacetyl fluoride	353-34-7	ABCR GmbH and Co. KG	99.5	-
1,12,2-tetrafluoro-ethene	116-14-3	ABCR GmbH and Co. KG	99	-
1,1,2,2,3,3-hexafluoro-propane	931-91-9	ABCR GmbH and Co. KG	97	-
Oxygen	7782-44-7	Afrox	99.5	-
Tetrafluoromethane	75-73-0	NECSA	-	99.9 (G.C.)
1,1,1,2,2,3,3,3-octafluoro-propane	76-19-7	Air Products	98	-
1,1,1,2,2,2-hexafluoro-ethane	76-16-4	Fedgas	99.9	-

Appendix H. MATLAB® script files

H.1. Kinetic parameter identification, laminar flow reactor model (Isothermal fit).

H.1.1. Main program file.

```
close all
clear all
clc

global Ftot0 Cin Cout W AW T P Ac nr nrr r dr drs r0 MM SV R Dm vr c2

% Constants

Ac= 1.76715E-06;          % m^2    cross sectional area of reactor
r0= (0.75/1000);          % m      reactor radius
MM=[150.02 31.988 166 116.015 50.0075 66.007 100.0150 150.02];  % molar masses
SV=[135.9 16.3 142.01 96.71 45.3 51.41 90.6 135.9];  % diffusion volumes, Fuller correlation for diffusivity

R=8.314;                  %Universal gas constant J/mol K

% Observed experimental data

Ftot0=xlsread('kineticdata.xls','493data','C4:AZ4'); % total inlet flow-rate for all data points
T=xlsread('kineticdata.xls','493data','C2:AZ2');     % temperatures for all data points
Cin=xlsread('kineticdata.xls','493data','C9:AZ16');  % inlet concentrations for all data points
Cout=xlsread('kineticdata.xls','493data','C19:AZ26');  % outlet concentrations for all data points
W=xlsread('kineticdata.xls','493data','C29:AZ36');   % weighting for all data points
P=xlsread('kineticdata.xls','493data','C3:AZ3');     % Pressure for all data points

%Grid in radial direction

nr=7;               % number of radial points, including wall
nrr=nr-1;           % number of radial points, excluding wall

dr=r0/(nr-1);       % radial increment
for j=1:nr;
    r(j)=(j-1)*dr;
end
drs=dr^2;           % square of radial increment
```

```
% number of data points c2

c1=size(Ftot0);
c2=c1(2);

lb=[0 0 0 0 0];                                % lower bounds for parameter estimates
ub=[inf inf inf inf inf];                      % upper bounds for parameter estimates
k0=[0.00098541 0.0169364 0.0220494 0.0017348 0.00466081]; % initial values for parameter estimates

options=optimset('Display','iter','MaxIter',10,'MaxFunEvals',1000,'TolFun',1e-20,'TolX',1e-20,'LargeScale','on');

[k,resnorm,residual,exitflag,output,lambda,jacobian]=lsqnonlin(@myfun2,k0,lb,ub,options);

ci=nlparci(k,residual,jacobian);               % confidence limits for parameter estimates

% Regression evaluation

CHFP_pred=zeros(1,c2);
CO2_pred=zeros(1,c2);
CHFPO_pred=zeros(1,c2);
CCF3COF_pred=zeros(1,c2);
CCOF2_pred=zeros(1,c2);
CC2F4_pred=zeros(1,c2);
CcC3F6_pred=zeros(1,c2);

for c3=1:c2;                    % cycle through data points

    Ftot0_p=Ftot0(c3);          % total inlet flow-rate for one data point     (mol/s)
    Cinp=Cin(:,c3);             % inlet concentrations for one data point      (mol/m^3)
    Coutp=Cout(:,c3);           % outlet concentrations for one data point     (mol/m^3)
    Wp=W(:,c3);                 % weighting for one data point
    Tp=T(c3);                   % reaction temperature for one data point      (Kelvin)
    Pp=P(c3);                   % reaction pressure for one data point         (Pascals)

    Ctot_p=Pp/(8.314*Tp);       %mol/m^3       total concentration for one data point

    Ca0_p=Cinp(1);                   %mol/m^3   individual inlet concentrations for one data point
    Cb0_p=Cinp(2);                   %mol/m^3
    Cc0_p=Cinp(3);                   %mol/m^3
    Cd0_p=Cinp(4);                   %mol/m^3
    Ce0_p=Cinp(5);                   %mol/m^3
    Cf0_p=Cinp(6);                   %mol/m^3
```

```
Cg0_p=Cinp(7);                    %mol/m^3
Ch0_p=Cinp(8);                    %mol/m^3

qtot0_p=(Ftot0_p*8.314*Tp)/Pp;        %m^3/s    total inlet volumetric flowrate for one data point

v0_p=qtot0_p/Ac;                      %m/s      inlet mean velocity for one data point

% Initial conditions

for j=1:nrr;
    Ca(j)=Ca0_p;
    Cb(j)=Cb0_p;
    Cc(j)=Cc0_p;
    Cd(j)=Cd0_p;
    Ce(j)=Ce0_p;
    Cf(j)=Cf0_p;
    Cg(j)=Cg0_p;
    Ch(j)=Ch0_p;
end

y0=[Ca Cb Cc Cd Ce Cf Cg Ch];

reltol=1e-11;
abstol=1e-11;

counters1=8*nrr;

for counters2=1:counters1;
    NN(counters2)=counters2;
end

options=odeset('RelTol',reltol,'AbsTol',abstol,'NonNegative',NN);
[z,y]=ode15s(@(z,y) rates3(z,y,k,Tp,Pp,v0_p,Ctot_p),[0 114.3],y0,options);

c4=size(y);
c5=c4(1);

CaW=(1/3)*(4*y(:,nrr)-y(:,nrr-1));
CbW=(1/3)*(4*y(:,2*nrr)-y(:,2*nrr-1));
CcW=(1/3)*(4*y(:,3*nrr)-y(:,3*nrr-1));
CdW=(1/3)*(4*y(:,4*nrr)-y(:,4*nrr-1));
CeW=(1/3)*(4*y(:,5*nrr)-y(:,5*nrr-1));
CfW=(1/3)*(4*y(:,6*nrr)-y(:,6*nrr-1));
```

```
CgW=(1/3)*(4*y(:,7*nrr)-y(:,7*nrr-1));
ChW=(1/3)*(4*y(:,8*nrr)-y(:,8*nrr-1));

y=[y(:,1:nrr) CaW y(:,nrr+1:2*nrr) CbW y(:,2*nrr+1:3*nrr) CcW y(:,3*nrr+1:4*nrr)...
    CdW y(:,4*nrr+1:5*nrr) CeW y(:,5*nrr+1:6*nrr) CfW y(:,6*nrr+1:7*nrr) CgW y(:,7*nrr+1:8*nrr) ChW];

% Numerical integration at the reactor outlet for average
% concentrations

for j=1:nr;
    ya_pred(j)=y(c5,j);          % Concentration of each species at the exit over all radial points
    yb_pred(j)=y(c5,nr+j);
    yc_pred(j)=y(c5,2*nr+j);
    yd_pred(j)=y(c5,3*nr+j);
    ye_pred(j)=y(c5,4*nr+j);
    yf_pred(j)=y(c5,5*nr+j);
    yg_pred(j)=y(c5,6*nr+j);
    yh_pred(j)=y(c5,7*nr+j);
end

for j=1:nr;

    ya_pred_int(j)=(ya_pred(j))*r(j)*(1-((r(j))^(2))/(r0^2));  %Integration over radial dimension
    yb_pred_int(j)=(yb_pred(j))*r(j)*(1-((r(j))^(2))/(r0^2));
    yc_pred_int(j)=(yc_pred(j))*r(j)*(1-((r(j))^(2))/(r0^2));
    yd_pred_int(j)=(yd_pred(j))*r(j)*(1-((r(j))^(2))/(r0^2));
    ye_pred_int(j)=(ye_pred(j))*r(j)*(1-((r(j))^(2))/(r0^2));
    yf_pred_int(j)=(yf_pred(j))*r(j)*(1-((r(j))^(2))/(r0^2));
    yg_pred_int(j)=(yg_pred(j))*r(j)*(1-((r(j))^(2))/(r0^2));
    yh_pred_int(j)=(yh_pred(j))*r(j)*(1-((r(j))^(2))/(r0^2));
    yden(j)=r(j)*(1-(r(j)^2)/(r0^2));
end

den=trapz(r,yden);

Ca_pred=trapz(r,ya_pred_int);     % Predicted outlet concentration of each species
Ca_pred=Ca_pred/den;

Cb_pred=trapz(r,yb_pred_int);
Cb_pred=Cb_pred/den;

Cc_pred=trapz(r,yc_pred_int);
Cc_pred=Cc_pred/den;
```

```
    Cd_pred=trapz(r,yd_pred_int);
    Cd_pred=Cd_pred/den;

    Ce_pred=trapz(r,ye_pred_int);
    Ce_pred=Ce_pred/den;

    Cf_pred=trapz(r,yf_pred_int);
    Cf_pred=Cf_pred/den;

    Cg_pred=trapz(r,yg_pred_int);
    Cg_pred=Cg_pred/den;

    Ch_pred=trapz(r,yh_pred_int);
    Ch_pred=Ch_pred/den;

    CHFP_pred(c3)=Ca_pred;
    CO2_pred(c3)=Cb_pred;
    CHFPO_pred(c3)=Cc_pred;
    CCF3COF_pred(c3)=Cd_pred;
    CCOF2_pred(c3)=Cf_pred;
    CC2F4_pred(c3)=Cg_pred;
    CcC3F6_pred(c3)=Ch_pred;
end

CHFP=Cout(1,:);
CO2=Cout(2,:);
CHFPO=Cout(3,:);
CCF3COF=Cout(4,:);
CCOF2=Cout(6,:);
CC2F4=Cout(7,:);
CcC3F6=Cout(8,:);

WHFP=W(1,:);
WO2=W(2,:);
WHFPO=W(3,:);
WCF3COF=W(4,:);
WCOF2=W(6,:);
WC2F4=W(7,:);
WcC3F6=W(8,:);


CHFP_pred=WHFP.*CHFP_pred;
```

```
CO2_pred=WO2.*CO2_pred;
CHFPO_pred=WHFPO.*CHFPO_pred;
CCF3COF_pred=WCF3COF.*CCF3COF_pred;
CCOF2_pred=WCOF2.*CCOF2_pred;
CC2F4_pred=WC2F4.*CC2F4_pred;
CcC3F6_pred=WcC3F6.*CcC3F6_pred;

CHFP=WHFP.*CHFP;
CO2=WO2.*CO2;
CHFPO=WHFPO.*CHFPO;
CCF3COF=WCF3COF.*CCF3COF;
CCOF2=WCOF2.*CCOF2;
CC2F4=WC2F4.*CC2F4;
CcC3F6=WcC3F6.*CcC3F6;

Zline=zeros(1,c2);
%-----------------------------------
figure(1)

plot(CHFP,CHFP_pred,'bo','MarkerFaceColor','blue','MarkerSize',8)

FFDx1=linspace(0,100,100);
FFDy1=linspace(0,100,100);

hold on

plot(FFDx1,FFDy1,'k-','LineWidth',3)

axis square
xlim([0 70])
ylim([0 70])

xlabel('measured HFP exit concentration [mol m^{-3}]','FontName','Arial','FontSize',20,'FontWeight','normal')
ylabel('predicted HFP exit concentration [mol m^{-3}]','FontName','Arial','FontSize',20,'FontWeight','normal')

set(gca,'FontName','Arial','FontSize',14)

hold off
%-----------------------------------
figure(2)

RHFP=CHFP-CHFP_pred;
counter1=max([max(RHFP) abs(min(RHFP))]);
```

```
plot(CHFP,RHFP,'bo','MarkerFaceColor','blue','MarkerSize',8)
hold on
plot(CHFP,Zline,'k-','LineWidth',3)
axis tight
ylim([-1*(counter1+0.1*counter1) (counter1+0.1*counter1)])
axis square

xlabel('measured HFP exit concentration [mol m^{-3}]','FontName','Arial','FontSize',20,'FontWeight','normal')
ylabel('Residuals','FontName','Arial','FontSize',20,'FontWeight','normal')

set(gca,'FontName','Arial','FontSize',14)
hold off
%-------------------------------------
figure(3)

plot(CO2,CO2_pred,'bo','MarkerFaceColor','blue','MarkerSize',8)

FFDx2=linspace(0,100,100);
FFDy2=linspace(0,100,100);

hold on

plot(FFDx2,FFDy2,'k-','LineWidth',3)

axis square
xlim([0 50])
ylim([0 50])

xlabel('measured O_{2} exit concentration [mol m^{-3}]','FontName','Arial','FontSize',20,'FontWeight','normal')
ylabel('predicted O_{2} exit concentration [mol m^{-3}]','FontName','Arial','FontSize',20,'FontWeight','normal')

set(gca,'FontName','Arial','FontSize',14)
hold off
%-------------------------------------
figure(4)

RO2=CO2-CO2_pred;
counter2=max([max(RO2) abs(min(RO2))]);
plot(CO2,RO2,'bo','MarkerFaceColor','blue','MarkerSize',8)
hold on
plot(CO2,Zline,'k-','LineWidth',3)
axis tight
ylim([-1*(counter2+0.1*counter2) (counter2+0.1*counter2)])
```

```
axis square

xlabel('measured O_{2} exit concentration [mol m^{-3}]','FontName','Arial','FontSize',20,'FontWeight','normal')
ylabel('Residuals','FontName','Arial','FontSize',20,'FontWeight','normal')

set(gca,'FontName','Arial','FontSize',14)
hold off
%-----------------------------------
figure(5)

plot(CHFPO,CHFPO_pred,'bo','MarkerFaceColor','blue','MarkerSize',8)

FFDx3=linspace(0,100,100);
FFDy3=linspace(0,100,100);

hold on

plot(FFDx3,FFDy3,'k-','LineWidth',3)

axis square
xlim([0 50])
ylim([0 50])

xlabel('measured HFPO exit concentration [mol m^{-3}]','FontName','Arial','FontSize',20,'FontWeight','normal')
ylabel('predicted HFPO exit concentration [mol m^{-3}]','FontName','Arial','FontSize',20,'FontWeight','normal')
set(gca,'FontName','Arial','FontSize',14)

hold off
%-----------------------------------
figure(6)

RHFPO=CHFPO-CHFPO_pred;
counter3=max([max(RHFPO) abs(min(RHFPO))]);
plot(CHFPO,RHFPO,'bo','MarkerFaceColor','blue','MarkerSize',8)
hold on
plot(CHFPO,Zline,'k-','LineWidth',3)
axis tight
ylim([-1*(counter3+0.1*counter3) (counter3+0.1*counter3)])
axis square

xlabel('measured HFPO exit concentration [mol m^{-3}]','FontName','Arial','FontSize',20,'FontWeight','normal')
ylabel('Residuals','FontName','Arial','FontSize',20,'FontWeight','normal')
```

```
set(gca,'FontName','Arial','FontSize',14)
hold off
%-----------------------------------
figure(7)

plot(CCF3COF,CCF3COF_pred,'bo','MarkerFaceColor','blue','MarkerSize',8)

FFDx4=linspace(0,100,100);
FFDy4=linspace(0,100,100);

hold on

plot(FFDx4,FFDy4,'k-','LineWidth',3)

axis square
xlim([0 50])
ylim([0 50])

xlabel('measured CF_{3}COF exit concentration [mol m^{-3}]','FontName','Arial','FontSize',20,'FontWeight','normal')
ylabel('predicted CF_{3}COF exit concentration [mol m^{-3}]','FontName','Arial','FontSize',20,'FontWeight','normal')
set(gca,'FontName','Arial','FontSize',14)
hold off
%-----------------------------------
figure(8)

RCF3COF=CCF3COF-CCF3COF_pred;
counter4=max([max(RCF3COF) abs(min(RCF3COF))]);
plot(CCF3COF,RCF3COF,'bo','MarkerFaceColor','blue','MarkerSize',8)
hold on
plot(CCF3COF,Zline,'k-','LineWidth',3)
axis tight
ylim([-1*(counter4+0.1*counter4) (counter4+0.1*counter4)])
axis square

xlabel('measured CF_{3}COF exit concentration [mol m^{-3}]','FontName','Arial','FontSize',20,'FontWeight','normal')
ylabel('Residuals','FontName','Arial','FontSize',20,'FontWeight','normal')

set(gca,'FontName','Arial','FontSize',14)
hold off
%-----------------------------------
figure(9)
```

```
plot(CCOF2,CCOF2_pred,'bo','MarkerFaceColor','blue','MarkerSize',8)

FFDx5=linspace(0,100,100);
FFDy5=linspace(0,100,100);

hold on

plot(FFDx5,FFDy5,'k-','LineWidth',3)

axis square
xlim([0 100])
ylim([0 100])

xlabel('measured COF_{2} exit concentration [mol m^{-3}]','FontName','Arial','FontSize',20,'FontWeight','normal')
ylabel('predicted COF_{2} exit concentration [mol m^{-3}]','FontName','Arial','FontSize',20,'FontWeight','normal')
set(gca,'FontName','Arial','FontSize',14)
hold off
%-----------------------------------
figure(10)

RCOF2=CCOF2-CCOF2_pred;
counter5=max([max(RCOF2) abs(min(RCOF2))]);
plot(CCOF2,RCOF2,'bo','MarkerFaceColor','blue','MarkerSize',8)
hold on

plot(CCOF2,Zline,'k-','LineWidth',3)
axis tight
ylim([-1*(counter5+0.1*counter5) (counter5+0.1*counter5)])
axis square

xlabel('measured COF_{2} exit concentration [mol m^{-3}]','FontName','Arial','FontSize',20,'FontWeight','normal')
ylabel('Residuals','FontName','Arial','FontSize',20,'FontWeight','normal')

set(gca,'FontName','Arial','FontSize',14)
hold off
%-----------------------------------
figure(11)

plot(CC2F4,CC2F4_pred,'bo','MarkerFaceColor','blue','MarkerSize',8)

FFDx6=linspace(0,100,100);
FFDy6=linspace(0,100,100);
```

```
hold on

plot(FFDx6,FFDy6,'k-','LineWidth',3)

axis square
xlim([0 3])
ylim([0 3])

xlabel('measured C_{2}F_{4} exit concentration [mol m^{-3}]','FontName','Arial','FontSize',20,'FontWeight','normal')
ylabel('predicted C_{2}F_{4} exit concentration [mol m^{-3}]','FontName','Arial','FontSize',20,'FontWeight','normal')
set(gca,'FontName','Arial','FontSize',14)
hold off
%----------------------------------
figure(12)

RC2F4=CC2F4-CC2F4_pred;
counter6=max([max(RC2F4) abs(min(RC2F4))]);
plot(CC2F4,RC2F4,'bo','MarkerFaceColor','blue','MarkerSize',8)
hold on
plot(CC2F4,Zline,'k-','LineWidth',3)
axis tight
ylim([-1*(counter6+0.1*counter6) (counter6+0.1*counter6)])
axis square

xlabel('measured C_{2}F_{4} exit concentration [mol m^{-3}]','FontName','Arial','FontSize',20,'FontWeight','normal')
ylabel('Residuals','FontName','Arial','FontSize',20,'FontWeight','normal')

set(gca,'FontName','Arial','FontSize',14)

hold off
%----------------------------------
figure(13)

plot(CcC3F6,CcC3F6_pred,'bo','MarkerFaceColor','blue','MarkerSize',8)

FFDx7=linspace(0,100,100);
FFDy7=linspace(0,100,100);

hold on

plot(FFDx7,FFDy7,'k-','LineWidth',3)
```

```
axis square
xlim([0 1.5])
ylim([0 1.5])

xlabel('measured \itc\rm-C_{3}F_{6} exit concentration [mol m^{-
3}]','FontName','Arial','FontSize',20,'FontWeight','normal')
ylabel('predicted \itc\rm-C_{3}F_{6} exit concentration [mol m^{-
3}]','FontName','Arial','FontSize',20,'FontWeight','normal')
set(gca,'FontName','Arial','FontSize',14)
hold off
%-----------------------------------
figure(14)

RcC3F6=CcC3F6-CcC3F6_pred;
counter7=max([max(RcC3F6) abs(min(RcC3F6))]);

plot(CcC3F6,RcC3F6,'bo','MarkerFaceColor','blue','MarkerSize',8)
hold on
plot(CcC3F6,Zline,'k-','LineWidth',3)

axis tight
ylim([-1*(counter7+0.1*counter7) (counter7+0.1*counter7)])
axis square

xlabel('measured \itc\rm-C_{3}F_{6} exit concentration [mol m^{-
3}]','FontName','Arial','FontSize',20,'FontWeight','normal')
ylabel('Residuals','FontName','Arial','FontSize',20,'FontWeight','normal')

set(gca,'FontName','Arial','FontSize',14)

hold off
```

H.1.2. Objective function file

```
function Fob=myfun2(k)

global Ftot0 Cin Cout W AW T P Ac nr nrr r dr drs r0 MM SV R Dm vr c2

Fob=zeros(8,c2);

for c3=1:c2;                    % cycle through data points

    Ftot0_p=Ftot0(c3);          % total inlet flow-rate for one data point     (mol/s)
    Cinp=Cin(:,c3);             % inlet concentrations for one data point      (mol/m^3)
    Coutp=Cout(:,c3);           % outlet concentrations for one data point     (mol/m^3)
    Wp=W(:,c3);                 % weighting for one data point
    Tp=T(c3);                   % reaction temperature for one data point      (Kelvin)
    Pp=P(c3);                   % reaction pressure for one data point         (Pascals)

    Ctot_p=Pp/(8.314*Tp);       %mol/m^3       total concentration for one data point

    Ca0_p=Cinp(1);                  %mol/m^3       individual inlet concentrations for one data point
    Cb0_p=Cinp(2);                  %mol/m^3
    Cc0_p=Cinp(3);                  %mol/m^3
    Cd0_p=Cinp(4);                  %mol/m^3
    Ce0_p=Cinp(5);                  %mol/m^3
    Cf0_p=Cinp(6);                  %mol/m^3
    Cg0_p=Cinp(7);                  %mol/m^3
    Ch0_p=Cinp(8);                  %mol/m^3

    qtot0_p=(Ftot0_p*8.314*Tp)/Pp;      %m^3/s   total inlet volumetric flowrate for one data point

    v0_p=qtot0_p/Ac;                    %m/s     inlet mean velocity for one data point

    % Initial conditions

    for j=1:nrr;
        Ca(j)=Ca0_p;
        Cb(j)=Cb0_p;
        Cc(j)=Cc0_p;
        Cd(j)=Cd0_p;
        Ce(j)=Ce0_p;
        Cf(j)=Cf0_p;
        Cg(j)=Cg0_p;
```

```
    Ch(j)=Ch0_p;
end

y0=[Ca Cb Cc Cd Ce Cf Cg Ch];

reltol=1e-11;
abstol=1e-11;

counters1=8*nrr;

for counters2=1:counters1;
    NN(counters2)=counters2;
end

options=odeset('RelTol',reltol,'AbsTol',abstol,'NonNegative',NN);
[z,y]=ode15s(@(z,y) rates3(z,y,k,Tp,Pp,v0_p,Ctot_p),[0 114.3],y0,options);

c4=size(y);
c5=c4(1);

CaW=(1/3)*(4*y(:,nrr)-y(:,nrr-1));
CbW=(1/3)*(4*y(:,2*nrr)-y(:,2*nrr-1));
CcW=(1/3)*(4*y(:,3*nrr)-y(:,3*nrr-1));
CdW=(1/3)*(4*y(:,4*nrr)-y(:,4*nrr-1));
CeW=(1/3)*(4*y(:,5*nrr)-y(:,5*nrr-1));
CfW=(1/3)*(4*y(:,6*nrr)-y(:,6*nrr-1));
CgW=(1/3)*(4*y(:,7*nrr)-y(:,7*nrr-1));
ChW=(1/3)*(4*y(:,8*nrr)-y(:,8*nrr-1));

y=[y(:,1:nrr) CaW y(:,nrr+1:2*nrr) CbW y(:,2*nrr+1:3*nrr) CcW y(:,3*nrr+1:4*nrr)...
CdW y(:,4*nrr+1:5*nrr) CeW y(:,5*nrr+1:6*nrr) CfW y(:,6*nrr+1:7*nrr) CgW y(:,7*nrr+1:8*nrr) ChW];

% Numerical integration at the reactor outlet for average
% concentrations

for j=1:nr;
    ya_pred(j)=y(c5,j);           % Concentration of each species at the exit over all radial points
    yb_pred(j)=y(c5,nr+j);
    yc_pred(j)=y(c5,2*nr+j);
    yd_pred(j)=y(c5,3*nr+j);
    ye_pred(j)=y(c5,4*nr+j);
    yf_pred(j)=y(c5,5*nr+j);
    yg_pred(j)=y(c5,6*nr+j);
```

```
        yh_pred(j)=y(c5,7*nr+j);
    end

    for j=1:nr;

        ya_pred_int(j)=(ya_pred(j))*r(j)*(1-((r(j))^(2))/(r0^2));   %Evaluation of integral
        yb_pred_int(j)=(yb_pred(j))*r(j)*(1-((r(j))^(2))/(r0^2));
        yc_pred_int(j)=(yc_pred(j))*r(j)*(1-((r(j))^(2))/(r0^2));
        yd_pred_int(j)=(yd_pred(j))*r(j)*(1-((r(j))^(2))/(r0^2));
        ye_pred_int(j)=(ye_pred(j))*r(j)*(1-((r(j))^(2))/(r0^2));
        yf_pred_int(j)=(yf_pred(j))*r(j)*(1-((r(j))^(2))/(r0^2));
        yg_pred_int(j)=(yg_pred(j))*r(j)*(1-((r(j))^(2))/(r0^2));
        yh_pred_int(j)=(yh_pred(j))*r(j)*(1-((r(j))^(2))/(r0^2));
        yden(j)=r(j)*(1-(r(j)^2)/(r0^2));
    end

    den=trapz(r,yden);

    Ca_pred=trapz(r,ya_pred_int);     % Predicted outlet concentration of each species
    Ca_pred=Ca_pred/den;

    Cb_pred=trapz(r,yb_pred_int);
    Cb_pred=Cb_pred/den;

    Cc_pred=trapz(r,yc_pred_int);
    Cc_pred=Cc_pred/den;

    Cd_pred=trapz(r,yd_pred_int);
    Cd_pred=Cd_pred/den;

    Ce_pred=trapz(r,ye_pred_int);
    Ce_pred=Ce_pred/den;

    Cf_pred=trapz(r,yf_pred_int);
    Cf_pred=Cf_pred/den;

    Cg_pred=trapz(r,yg_pred_int);
    Cg_pred=Cg_pred/den;

    Ch_pred=trapz(r,yh_pred_int);
    Ch_pred=Ch_pred/den;

% elements of the objective function
```

```
    Fob(1,c3)=(Wp(1))*((2*(Coutp(1)-Ca_pred)/(Coutp(1)+Ca_pred))^(2))^(1*0.5);
    Fob(2,c3)=(Wp(2))*((2*(Coutp(2)-Cb_pred)/(Coutp(2)+Cb_pred))^(2))^(1*0.5);
    Fob(3,c3)=(Wp(3))*((2*(Coutp(3)-Cc_pred)/(Coutp(3)+Cc_pred))^(2))^(1*0.5);
    Fob(4,c3)=(Wp(4))*((2*(Coutp(4)-Cd_pred)/(Coutp(4)+Cd_pred))^(2))^(1*0.5);
    Fob(5,c3)=(Wp(5))*((2*(Coutp(5)-Ce_pred)/(Coutp(5)+Ce_pred))^(2))^(1*0.5);
    Fob(6,c3)=(Wp(6))*((2*(Coutp(6)-Cf_pred)/(Coutp(6)+Cf_pred))^(2))^(1*0.5);
    Fob(7,c3)=(Wp(7))*((2*(Coutp(7)-Cg_pred)/(Coutp(7)+Cg_pred))^(2))^(1*0.5);
    Fob(8,c3)=(Wp(8))*((2*(Coutp(8)-Ch_pred)/(Coutp(8)+Ch_pred))^(2))^(1*0.5);

end

Fob=reshape(Fob,1,[]);
Fob=Fob';
```

H.1.3. Function handle for the ODE integrator

```
function yz=rates3(z,y,k,Tp,Pp,v0_p,Ctot_p)

global Ftot0 Cin Cout W T P Ac nr nrr r dr drs r0 MM SV R Dm vr c2

k1=k(1);                                                  % HFP + 1/2O2 -> HFPO
k2=k(2);                                                  % HFP + O2 -> CF3COF + COF2
k3=(10^14.19)*exp(-162000/(8.314*Tp));                    % HFPO -> CF3COF + CF2 (From Krusic 1999)
k4=(10^9.39)*(1e-06)*((Tp)^0.5)*exp(-1660/(8.314*Tp));    % CF2 + CF2 -> C2F4 (From Tyerman 1968)
k5=(10^7.94)*(1e-06)*((Tp)^0.5)*exp(-26610/(8.314*Tp));   % CF2 + C2F4 -> c-C3F6 (From Tyerman 1968)
k6=k(3);                                                  % C2F4 + 1/2O2 -> COF2 + CF2
k7=k(4);                                                  % CF3COF + 1/2 O2 -> 2COF2
k11=k(5);                                                 % HFPO -> HFP + 1/2O2

% Convert 1D input vector into individual concentration vectors

for j=1:nrr;
    Ca(j)=y(j);
    Cb(j)=y(nrr+j);
    Cc(j)=y(2*nrr+j);
    Cd(j)=y(3*nrr+j);
    Ce(j)=y(4*nrr+j);
    Cf(j)=y(5*nrr+j);
    Cg(j)=y(6*nrr+j);
    Ch(j)=y(7*nrr+j);
```

```
end

% Concentrations at the wall computed from the two preceding radial points

Ca(nr)=(4*Ca(nr-1) - Ca(nr-2))/(3);
Cb(nr)=(4*Cb(nr-1) - Cb(nr-2))/(3);
Cc(nr)=(4*Cc(nr-1) - Cc(nr-2))/(3);
Cd(nr)=(4*Cd(nr-1) - Cd(nr-2))/(3);
Ce(nr)=(4*Ce(nr-1) - Ce(nr-2))/(3);
Cf(nr)=(4*Cf(nr-1) - Cf(nr-2))/(3);
Cg(nr)=(4*Cg(nr-1) - Cg(nr-2))/(3);
Ch(nr)=(4*Ch(nr-1) - Ch(nr-2))/(3);

% Step through the grid points for r

for j=1:nrr;

% First derivatives of concentration 1/r*Cir   Note already has been
% divided by 1/r

    if(j==1);
        Car(j)=2.0*(Ca(j+1)-Ca(j))/drs;
        Cbr(j)=2.0*(Cb(j+1)-Cb(j))/drs;
        Ccr(j)=2.0*(Cc(j+1)-Cc(j))/drs;
        Cdr(j)=2.0*(Cd(j+1)-Cd(j))/drs;
        Cer(j)=2.0*(Ce(j+1)-Ce(j))/drs;
        Cfr(j)=2.0*(Cf(j+1)-Cf(j))/drs;
        Cgr(j)=2.0*(Cg(j+1)-Cg(j))/drs;
        Chr(j)=2.0*(Ch(j+1)-Ch(j))/drs;

    else
        Car(j)=(1.0/r(j))*(Ca(j+1)-Ca(j-1))/(2.0*dr);
        Cbr(j)=(1.0/r(j))*(Cb(j+1)-Cb(j-1))/(2.0*dr);
        Ccr(j)=(1.0/r(j))*(Cc(j+1)-Cc(j-1))/(2.0*dr);
        Cdr(j)=(1.0/r(j))*(Cd(j+1)-Cd(j-1))/(2.0*dr);
        Cer(j)=(1.0/r(j))*(Ce(j+1)-Ce(j-1))/(2.0*dr);
        Cfr(j)=(1.0/r(j))*(Cf(j+1)-Cf(j-1))/(2.0*dr);
        Cgr(j)=(1.0/r(j))*(Cg(j+1)-Cg(j-1))/(2.0*dr);
        Chr(j)=(1.0/r(j))*(Ch(j+1)-Ch(j-1))/(2.0*dr);
    end

% Second derivatives of concentration
```

```
    if(j==1);
        Carr(j)=2.0*(Ca(j+1)-Ca(j))/drs;
        Cbrr(j)=2.0*(Cb(j+1)-Cb(j))/drs;
        Ccrr(j)=2.0*(Cc(j+1)-Cc(j))/drs;
        Cdrr(j)=2.0*(Cd(j+1)-Cd(j))/drs;
        Cerr(j)=2.0*(Ce(j+1)-Ce(j))/drs;
        Cfrr(j)=2.0*(Cf(j+1)-Cf(j))/drs;
        Cgrr(j)=2.0*(Cg(j+1)-Cg(j))/drs;
        Chrr(j)=2.0*(Ch(j+1)-Ch(j))/drs;

    else
        Carr(j)=(Ca(j+1)-2.0*Ca(j)+Ca(j-1))/drs;
        Cbrr(j)=(Cb(j+1)-2.0*Cb(j)+Cb(j-1))/drs;
        Ccrr(j)=(Cc(j+1)-2.0*Cc(j)+Cc(j-1))/drs;
        Cdrr(j)=(Cd(j+1)-2.0*Cd(j)+Cd(j-1))/drs;
        Cerr(j)=(Ce(j+1)-2.0*Ce(j)+Ce(j-1))/drs;
        Cfrr(j)=(Cf(j+1)-2.0*Cf(j)+Cf(j-1))/drs;
        Cgrr(j)=(Cg(j+1)-2.0*Cg(j)+Cg(j-1))/drs;
        Chrr(j)=(Ch(j+1)-2.0*Ch(j)+Ch(j-1))/drs;
    end

% Multicomponent diffusion coefficients

    Xa=Ca(j)/Ctot_p;                        %mole fractions at radial point
    Xb=Cb(j)/Ctot_p;
    Xc=Cc(j)/Ctot_p;
    Xd=Cd(j)/Ctot_p;
    Xe=Ce(j)/Ctot_p;
    Xf=Cf(j)/Ctot_p;
    Xg=Cg(j)/Ctot_p;
    Xh=Ch(j)/Ctot_p;

    X=[Xa Xb Xc Xd Xe Xf Xg Xh]; % vector of mole fractions at radial point

    Dm=multdiff1(Tp,Pp,X,MM,SV); % m^2/s vector of diffusion coefficients at radial point

% Rate equations, forward as well as reverse for reaction 1

    R1=k1*((Ca(j))^(1))*((Cb(j))^(0.5));
    RR1=k11*Cc(j);
    R2=k2*((Ca(j))^(1))*((Cb(j))^(1));
    R3=k3*((Cc(j))^(1));
    R4=k4*Ce(j)*Ce(j);
```

```
    R5=k5*Ce(j)*Cg(j);
    R6=k6*((Cg(j))^(1))*((Cb(j))^(1));
    R7=k7*((Cd(j))^(1))*((Cb(j))^(0.5));

    Ra=-R1-R2+RR1;
    Rb=-0.5*R1+0.5*RR1-R2-0.5*R6-0.5*R7;
    Rc=R1-R3-RR1;
    Rd=R2+R3-R7;
    Re=R3-2*R4-R5+R6;
    Rf=R2+2*R7+R6;
    Rg=R4-R5-R6;
    Rh=R5;

% Partial differential equations

    vr=2*v0_p*(1-(r(j)^2)/(r0^2));          % velocity

        Caz(j)=(Dm(1)/vr)*(Car(j)+Carr(j)) + (Ra/vr);
        Cbz(j)=(Dm(2)/vr)*(Cbr(j)+Cbrr(j)) + (Rb/vr);
        Ccz(j)=(Dm(3)/vr)*(Ccr(j)+Ccrr(j)) + (Rc/vr);
        Cdz(j)=(Dm(4)/vr)*(Cdr(j)+Cdrr(j)) + (Rd/vr);
        Cez(j)=(Dm(5)/vr)*(Cer(j)+Cerr(j)) + (Re/vr);
        Cfz(j)=(Dm(6)/vr)*(Cfr(j)+Cfrr(j)) + (Rf/vr);
        Cgz(j)=(Dm(7)/vr)*(Cgr(j)+Cgrr(j)) + (Rg/vr);
        Chz(j)=(Dm(8)/vr)*(Chr(j)+Chrr(j)) + (Rh/vr);

end

% 2D to 1D matrices

syz=8*nrr;
yz=zeros(1,syz);

for j=1:nrr;

    yz(j)=Caz(j);
    yz(nrr+j)=Cbz(j);
    yz(2*nrr+j)=Ccz(j);
    yz(3*nrr+j)=Cdz(j);
    yz(4*nrr+j)=Cez(j);
    yz(5*nrr+j)=Cfz(j);
    yz(6*nrr+j)=Cgz(j);
    yz(7*nrr+j)=Chz(j);
```

```
end

yz=yz';
```

H.1.4. Auxiliary file for the calculation of multicomponent diffusion coefficients.

```
function diffu=multdiff1(Tp,Pp,X,MM,SV)

Mav=zeros(8,8);
Dij=zeros(8,8);

Ppp=Pp*9.869233e-006;

for counter1=1:8;

    for counter2=1:8;

        Mav(counter1,counter2)= (2)/(1/MM(counter1)+1/MM(counter2));

        if counter1==counter2;
            Dij(counter1,counter2)=0;

        else
            Dij(counter1,counter2)= (0.00143*Tp^1.75)/(Ppp*((Mav(counter1,counter2))^0.5)...
                *((SV(counter1))^(1/3) + (SV(counter2))^(1/3))^2);
        end


    end
end

D1m=(1-X(1))*(X(2)/(Dij(1,2)) + X(3)/(Dij(1,3)) + X(4)/(Dij(1,4)) + X(5)/(Dij(1,5)))...
    + X(6)/(Dij(1,6)) + X(7)/(Dij(1,7)) + X(8)/(Dij(1,8)))^(-1);

D2m=(1-X(2))*(X(1)/(Dij(2,1)) + X(3)/(Dij(2,3)) + X(4)/(Dij(2,4)) + X(5)/(Dij(2,5)))...
    + X(6)/(Dij(2,6)) + X(7)/(Dij(2,7)) + X(8)/(Dij(2,8)))^(-1);

D3m=(1-X(3))*(X(1)/(Dij(3,1)) + X(2)/(Dij(3,2)) + X(4)/(Dij(3,4)) + X(5)/(Dij(3,5)))...
    + X(6)/(Dij(3,6)) + X(7)/(Dij(3,7)) + X(8)/(Dij(3,8)))^(-1);
```

```
D4m=(1-X(4))*(X(1)/(Dij(4,1)) + X(2)/(Dij(4,2)) + X(3)/(Dij(4,3)) + X(5)/(Dij(4,5))...
    + X(6)/(Dij(4,6)) + X(7)/(Dij(4,7)) + X(8)/(Dij(4,8)))^(-1);

D5m=(1-X(5))*(X(1)/(Dij(5,1)) + X(2)/(Dij(5,2)) + X(3)/(Dij(5,3)) + X(4)/(Dij(5,4))...
    + X(6)/(Dij(5,6)) + X(7)/(Dij(5,7)) + X(8)/(Dij(5,8)))^(-1);

D6m=(1-X(6))*(X(1)/(Dij(6,1)) + X(2)/(Dij(6,2)) + X(3)/(Dij(6,3)) + X(4)/(Dij(6,4))...
    + X(5)/(Dij(6,5)) + X(7)/(Dij(6,7)) + X(8)/(Dij(6,8)))^(-1);

D7m=(1-X(7))*(X(1)/(Dij(7,1)) + X(2)/(Dij(7,2)) + X(3)/(Dij(7,3)) + X(4)/(Dij(7,4))...
    + X(5)/(Dij(7,5)) + X(6)/(Dij(7,6)) + X(8)/(Dij(7,8)))^(-1);

D8m=(1-X(8))*(X(1)/(Dij(8,1)) + X(2)/(Dij(8,2)) + X(3)/(Dij(8,3)) + X(4)/(Dij(8,4))...
    + X(5)/(Dij(8,5)) + X(6)/(Dij(8,6)) + X(7)/(Dij(8,7)))^(-1);


Dim = (1/10000)*[D1m D2m D3m D4m D5m D6m D7m D8m];

diffu=Dim;
```

H.2. Kinetic parameter identification, laminar flow reactor model (Total data fit).

H.2.1. Main program file.

```
close all
clear all
clc

global Ftot0 Cin Cout W AW T P Ac nr nrr r dr drs r0 MM SV R Dm vr c2 Tcent

% Constants

Ac= 1.76715E-06;                          % m^2    cross sectional area of reactor
r0= (0.75/1000);                          % m      reactor radius
MM=[150.02 31.988 166 116.015 50.0075 66.007 100.0150 150.02]; % molar masses
SV=[135.9 16.3 142.01 96.71 45.3 51.41 90.6 135.9];     % diffusion volumes, Fuller correlation for diffusivity

R=8.314;                            %Universal gas constant J/mol K

% Observed experimental data
```

```
Ftot0=xlsread('kineticdata.xls','totaldata','C4:FU4');      % total inlet flow-rate for all data points
T=xlsread('kineticdata.xls','totaldata','C2:FU2');          % temperatures for all data points
Cin=xlsread('kineticdata.xls','totaldata','C9:FU16');       % inlet concentrations for all data points
Cout=xlsread('kineticdata.xls','totaldata','C19:FU26');     % outlet concentrations for all data points
W=xlsread('kineticdata.xls','totaldata','C29:FU36');        % weighting for all data points
P=xlsread('kineticdata.xls','totaldata','C3:FU3');           % Pressure for all data points

%Grid in radial direction

nr=7;               % number of radial points, including wall
nrr=nr-1;           % number of radial points, excluding wall

dr=r0/(nr-1);       % radial increment
for j=1:nr;
    r(j)=(j-1)*dr;
end
drs=dr^2;           % square of radial increment

% number of data points c2

c1=size(Ftot0);
c2=c1(2);

lb=[0 0 0 0 0 0 0 0 -inf 0];                    % lower bounds for parameter estimates
ub=[inf inf inf inf inf inf inf inf inf inf];    % upper bounds for parameter estimates
A0=[1.2408e+32 1.0504e+40 5.6453e+04 4.7147e-15 9.51139e+76]; % Pre-exponential factor
Ea=[317.8007 399.4845 60.0885 -107.9877 748.9974];  % Activation energy [kJ/mol]
Ea=1000*Ea;

Tcent=478.15;

A_prime=A0.*exp(-Ea./(8.314*Tcent));

k0=[A_prime Ea];

options=optimset('Display','iter','MaxIter',10,'MaxFunEvals',1000,'TolFun',1e-20,'TolX',1e-20,'LargeScale','on');

[k,resnorm,residual,exitflag,output,lambda,jacobian]=lsqnonlin(@myfun2,k0,lb,ub,options);

ci=nlparci(k,residual,jacobian);       % confidence limits for parameter estimates

% Regression evaluation
```

```
CHFP_pred=zeros(1,c2);
CO2_pred=zeros(1,c2);
CHFPO_pred=zeros(1,c2);
CCF3COF_pred=zeros(1,c2);
CCOF2_pred=zeros(1,c2);
CC2F4_pred=zeros(1,c2);
CcC3F6_pred=zeros(1,c2);

for c3=1:c2;                          % cycle through data points

    Ftot0_p=Ftot0(c3);          % total inlet flow-rate for one data point     (mol/s)
    Cinp=Cin(:,c3);             % inlet concentrations for one data point      (mol/m^3)
    Coutp=Cout(:,c3);           % outlet concentrations for one data point     (mol/m^3)
    Wp=W(:,c3);                 % weighting for one data point
    Tp=T(c3);                   % reaction temperature for one data point      (Kelvin)
    Pp=P(c3);                   % reaction pressure for one data point         (Pascals)

    Ctot_p=Pp/(8.314*Tp);       %mol/m^3       total concentration for one data point

    Ca0_p=Cinp(1);                   %mol/m^3   individual inlet concentrations for one data point
    Cb0_p=Cinp(2);                   %mol/m^3
    Cc0_p=Cinp(3);                   %mol/m^3
    Cd0_p=Cinp(4);                   %mol/m^3
    Ce0_p=Cinp(5);                   %mol/m^3
    Cf0_p=Cinp(6);                   %mol/m^3
    Cg0_p=Cinp(7);                   %mol/m^3
    Ch0_p=Cinp(8);                   %mol/m^3

    qtot0_p=(Ftot0_p*8.314*Tp)/Pp;       %m^3/s  total inlet volumetric flowrate for one data point

    v0_p=qtot0_p/Ac;                     %m/s    inlet mean velocity for one data point

    % Initial conditions

    for j=1:nrr;
        Ca(j)=Ca0_p;
        Cb(j)=Cb0_p;
        Cc(j)=Cc0_p;
        Cd(j)=Cd0_p;
        Ce(j)=Ce0_p;
        Cf(j)=Cf0_p;
        Cg(j)=Cg0_p;
```

```
    Ch(j)=Ch0_p;
end

y0=[Ca Cb Cc Cd Ce Cf Cg Ch];

reltol=1e-11;
abstol=1e-11;

counters1=8*nrr;

for counters2=1:counters1;
    NN(counters2)=counters2;
end

options=odeset('RelTol',reltol,'AbsTol',abstol,'NonNegative',NN);
[z,y]=ode15s(@(z,y) rates3(z,y,k,Tp,Pp,v0_p,Ctot_p),[0 114.3],y0,options);

c4=size(y);
c5=c4(1);

CaW=(1/3)*(4*y(:,nrr)-y(:,nrr-1));
CbW=(1/3)*(4*y(:,2*nrr)-y(:,2*nrr-1));
CcW=(1/3)*(4*y(:,3*nrr)-y(:,3*nrr-1));
CdW=(1/3)*(4*y(:,4*nrr)-y(:,4*nrr-1));
CeW=(1/3)*(4*y(:,5*nrr)-y(:,5*nrr-1));
CfW=(1/3)*(4*y(:,6*nrr)-y(:,6*nrr-1));
CgW=(1/3)*(4*y(:,7*nrr)-y(:,7*nrr-1));
ChW=(1/3)*(4*y(:,8*nrr)-y(:,8*nrr-1));

y=[y(:,1:nrr) CaW y(:,nrr+1:2*nrr) CbW y(:,2*nrr+1:3*nrr) CcW y(:,3*nrr+1:4*nrr)...
    CdW y(:,4*nrr+1:5*nrr) CeW y(:,5*nrr+1:6*nrr) CfW y(:,6*nrr+1:7*nrr) CgW y(:,7*nrr+1:8*nrr) ChW];

% Numerical integration at the reactor outlet for average
% concentrations

for j=1:nr;
    ya_pred(j)=y(c5,j);       % Concentration of each species at the exit over all radial points
    yb_pred(j)=y(c5,nr+j);
    yc_pred(j)=y(c5,2*nr+j);
    yd_pred(j)=y(c5,3*nr+j);
    ye_pred(j)=y(c5,4*nr+j);
    yf_pred(j)=y(c5,5*nr+j);
    yg_pred(j)=y(c5,6*nr+j);
```

```
    yh_pred(j)=y(c5,7*nr+j);
end

for j=1:nr;

    ya_pred_int(j)=(ya_pred(j))*r(j)*(1-((r(j))^(2))/(r0^2));  %Evaluation of integral
    yb_pred_int(j)=(yb_pred(j))*r(j)*(1-((r(j))^(2))/(r0^2));
    yc_pred_int(j)=(yc_pred(j))*r(j)*(1-((r(j))^(2))/(r0^2));
    yd_pred_int(j)=(yd_pred(j))*r(j)*(1-((r(j))^(2))/(r0^2));
    ye_pred_int(j)=(ye_pred(j))*r(j)*(1-((r(j))^(2))/(r0^2));
    yf_pred_int(j)=(yf_pred(j))*r(j)*(1-((r(j))^(2))/(r0^2));
    yg_pred_int(j)=(yg_pred(j))*r(j)*(1-((r(j))^(2))/(r0^2));
    yh_pred_int(j)=(yh_pred(j))*r(j)*(1-((r(j))^(2))/(r0^2));
    yden(j)=r(j)*(1-(r(j)^2)/(r0^2));
end

den=trapz(r,yden);

Ca_pred=trapz(r,ya_pred_int);           % Predicted outlet concentration of each species
Ca_pred=Ca_pred/den;

Cb_pred=trapz(r,yb_pred_int);
Cb_pred=Cb_pred/den;

Cc_pred=trapz(r,yc_pred_int);
Cc_pred=Cc_pred/den;

Cd_pred=trapz(r,yd_pred_int);
Cd_pred=Cd_pred/den;

Ce_pred=trapz(r,ye_pred_int);
Ce_pred=Ce_pred/den;

Cf_pred=trapz(r,yf_pred_int);
Cf_pred=Cf_pred/den;

Cg_pred=trapz(r,yg_pred_int);
Cg_pred=Cg_pred/den;

Ch_pred=trapz(r,yh_pred_int);
Ch_pred=Ch_pred/den;

CHFP_pred(c3)=Ca_pred;
```

```
    CO2_pred(c3)=Cb_pred;
    CHFPO_pred(c3)=Cc_pred;
    CCF3COF_pred(c3)=Cd_pred;
    CCOF2_pred(c3)=Cf_pred;
    CC2F4_pred(c3)=Cg_pred;
    CcC3F6_pred(c3)=Ch_pred;
end


CHFP=Cout(1,:);
CO2=Cout(2,:);
CHFPO=Cout(3,:);
CCF3COF=Cout(4,:);
CCOF2=Cout(6,:);
CC2F4=Cout(7,:);
CcC3F6=Cout(8,:);

WHFP=W(1,:);
WO2=W(2,:);
WHFPO=W(3,:);
WCF3COF=W(4,:);
WCOF2=W(6,:);
WC2F4=W(7,:);
WcC3F6=W(8,:);


CHFP_pred=WHFP.*CHFP_pred;
CO2_pred=WO2.*CO2_pred;
CHFPO_pred=WHFPO.*CHFPO_pred;
CCF3COF_pred=WCF3COF.*CCF3COF_pred;
CCOF2_pred=WCOF2.*CCOF2_pred;
CC2F4_pred=WC2F4.*CC2F4_pred;
CcC3F6_pred=WcC3F6.*CcC3F6_pred;

CHFP=WHFP.*CHFP;
CO2=WO2.*CO2;
CHFPO=WHFPO.*CHFPO;
CCF3COF=WCF3COF.*CCF3COF;
CCOF2=WCOF2.*CCOF2;
CC2F4=WC2F4.*CC2F4;
CcC3F6=WcC3F6.*CcC3F6;

Zline=zeros(1,c2);
```

```
%-----------------------------------
figure(1)

plot(CHFP,CHFP_pred,'bo','MarkerFaceColor','blue','MarkerSize',8)

FFDx1=linspace(0,100,100);
FFDy1=linspace(0,100,100);

hold on

plot(FFDx1,FFDy1,'k-','LineWidth',3)

axis square
xlim([0 100])
ylim([0 100])

xlabel('measured HFP exit concentration [mol m^{-3}]','FontName','Arial','FontSize',20,'FontWeight','normal')
ylabel('predicted HFP exit concentration [mol m^{-3}]','FontName','Arial','FontSize',20,'FontWeight','normal')

set(gca,'FontName','Arial','FontSize',14)

hold off
%-----------------------------------
figure(2)

RHFP=CHFP-CHFP_pred;
counter1=max([max(RHFP) abs(min(RHFP))]);
plot(CHFP,RHFP,'bo','MarkerFaceColor','blue','MarkerSize',8)
hold on
plot(CHFP,Zline,'k-','LineWidth',3)
axis tight
ylim([-1*(counter1+0.1*counter1) (counter1+0.1*counter1)])
axis square

xlabel('measured HFP exit concentration [mol m^{-3}]','FontName','Arial','FontSize',20,'FontWeight','normal')
ylabel('Residuals','FontName','Arial','FontSize',20,'FontWeight','normal')


set(gca,'FontName','Arial','FontSize',14)
hold off
%-----------------------------------
figure(3)
```

```
plot(CO2,CO2_pred,'bo','MarkerFaceColor','blue','MarkerSize',8)

FFDx2=linspace(0,100,100);
FFDy2=linspace(0,100,100);

hold on

plot(FFDx2,FFDy2,'k-','LineWidth',3)

axis square
xlim([0 100])
ylim([0 100])

xlabel('measured O_{2} exit concentration [mol m^{-3}]','FontName','Arial','FontSize',20,'FontWeight','normal')
ylabel('predicted O_{2} exit concentration [mol m^{-3}]','FontName','Arial','FontSize',20,'FontWeight','normal')

set(gca,'FontName','Arial','FontSize',14)
hold off
%-----------------------------------
figure(4)

RO2=CO2-CO2_pred;
counter2=max([max(RO2) abs(min(RO2))]);
plot(CO2,RO2,'bo','MarkerFaceColor','blue','MarkerSize',8)
hold on
plot(CO2,Zline,'k-','LineWidth',3)
axis tight
ylim([-1*(counter2+0.1*counter2) (counter2+0.1*counter2)])

axis square

xlabel('measured O_{2} exit concentration [mol m^{-3}]','FontName','Arial','FontSize',20,'FontWeight','normal')
ylabel('Residuals','FontName','Arial','FontSize',20,'FontWeight','normal')


set(gca,'FontName','Arial','FontSize',14)
hold off
%-----------------------------------
figure(5)

plot(CHFPO,CHFPO_pred,'bo','MarkerFaceColor','blue','MarkerSize',8)

FFDx3=linspace(0,100,100);
```

```
FFDy3=linspace(0,100,100);

hold on

plot(FFDx3,FFDy3,'k-','LineWidth',3)

axis square
xlim([0 50])
ylim([0 50])

xlabel('measured HFPO exit concentration [mol m^{-3}]','FontName','Arial','FontSize',20,'FontWeight','normal')
ylabel('predicted HFPO exit concentration [mol m^{-3}]','FontName','Arial','FontSize',20,'FontWeight','normal')
set(gca,'FontName','Arial','FontSize',14)

hold off
%-----------------------------------
figure(6)

RHFPO=CHFPO-CHFPO_pred;
counter3=max([max(RHFPO) abs(min(RHFPO))]);
plot(CHFPO,RHFPO,'bo','MarkerFaceColor','blue','MarkerSize',8)
hold on
plot(CHFPO,Zline,'k-','LineWidth',3)
axis tight
ylim([-1*(counter3+0.1*counter3) (counter3+0.1*counter3)])
axis square

xlabel('measured HFPO exit concentration [mol m^{-3}]','FontName','Arial','FontSize',20,'FontWeight','normal')
ylabel('Residuals','FontName','Arial','FontSize',20,'FontWeight','normal')


set(gca,'FontName','Arial','FontSize',14)
hold off
%-----------------------------------
figure(7)

plot(CCF3COF,CCF3COF_pred,'bo','MarkerFaceColor','blue','MarkerSize',8)

FFDx4=linspace(0,100,100);
FFDy4=linspace(0,100,100);

hold on
```

```
plot(FFDx4,FFDy4,'k-','LineWidth',3)

axis square
xlim([0 50])
ylim([0 50])

xlabel('measured CF_{3}COF exit concentration [mol m^{-3}]','FontName','Arial','FontSize',20,'FontWeight','normal')
ylabel('predicted CF_{3}COF exit concentration [mol m^{-3}]','FontName','Arial','FontSize',20,'FontWeight','normal')
set(gca,'FontName','Arial','FontSize',14)
hold off
%-----------------------------------
figure(8)

RCF3COF=CCF3COF-CCF3COF_pred;
counter4=max([max(RCF3COF) abs(min(RCF3COF))]);
plot(CCF3COF,RCF3COF,'bo','MarkerFaceColor','blue','MarkerSize',8)
hold on
plot(CCF3COF,Zline,'k-','LineWidth',3)
axis tight
ylim([-1*(counter4+0.1*counter4) (counter4+0.1*counter4)])
axis square

xlabel('measured CF_{3}COF exit concentration [mol m^{-3}]','FontName','Arial','FontSize',20,'FontWeight','normal')
ylabel('Residuals','FontName','Arial','FontSize',20,'FontWeight','normal')


set(gca,'FontName','Arial','FontSize',14)
hold off
%-------------------------------------
figure(9)

plot(CCOF2,CCOF2_pred,'bo','MarkerFaceColor','blue','MarkerSize',8)

FFDx5=linspace(0,100,100);
FFDy5=linspace(0,100,100);

hold on

plot(FFDx5,FFDy5,'k-','LineWidth',3)

axis square
xlim([0 100])
ylim([0 100])
```

```
xlabel('measured COF_{2} exit concentration [mol m^{-3}]','FontName','Arial','FontSize',20,'FontWeight','normal')
ylabel('predicted COF_{2} exit concentration [mol m^{-3}]','FontName','Arial','FontSize',20,'FontWeight','normal')
set(gca,'FontName','Arial','FontSize',14)
hold off
%----------------------------------
figure(10)

RCOF2=CCOF2-CCOF2_pred;
counter5=max([max(RCOF2) abs(min(RCOF2))]);
plot(CCOF2,RCOF2,'bo','MarkerFaceColor','blue','MarkerSize',8)
hold on

plot(CCOF2,Zline,'k-','LineWidth',3)
axis tight
ylim([-1*(counter5+0.1*counter5) (counter5+0.1*counter5)])
axis square

xlabel('measured COF_{2} exit concentration [mol m^{-3}]','FontName','Arial','FontSize',20,'FontWeight','normal')
ylabel('Residuals','FontName','Arial','FontSize',20,'FontWeight','normal')


set(gca,'FontName','Arial','FontSize',14)
hold off
%----------------------------------
figure(11)

plot(CC2F4,CC2F4_pred,'bo','MarkerFaceColor','blue','MarkerSize',8)

FFDx6=linspace(0,100,100);
FFDy6=linspace(0,100,100);

hold on

plot(FFDx6,FFDy6,'k-','LineWidth',3)

axis square
xlim([0 3])
ylim([0 3])

xlabel('measured C_{2}F_{4} exit concentration [mol m^{-3}]','FontName','Arial','FontSize',20,'FontWeight','normal')
ylabel('predicted C_{2}F_{4} exit concentration [mol m^{-3}]','FontName','Arial','FontSize',20,'FontWeight','normal')
set(gca,'FontName','Arial','FontSize',14)
```

```
hold off
%----------------------------------
figure(12)

RC2F4=CC2F4-CC2F4_pred;
counter6=max([max(RC2F4) abs(min(RC2F4))]);
plot(CC2F4,RC2F4,'bo','MarkerFaceColor','blue','MarkerSize',8)
hold on
plot(CC2F4,Zline,'k-','LineWidth',3)
axis tight
ylim([-1*(counter6+0.1*counter6) (counter6+0.1*counter6)])
axis square

xlabel('measured C_{2}F_{4} exit concentration [mol m^{-3}]','FontName','Arial','FontSize',20,'FontWeight','normal')
ylabel('Residuals','FontName','Arial','FontSize',20,'FontWeight','normal')

set(gca,'FontName','Arial','FontSize',14)

hold off
%----------------------------------
figure(13)

plot(CcC3F6,CcC3F6_pred,'bo','MarkerFaceColor','blue','MarkerSize',8)

FFDx7=linspace(0,100,100);
FFDy7=linspace(0,100,100);

hold on

plot(FFDx7,FFDy7,'k-','LineWidth',3)

axis square
xlim([0 1.5])
ylim([0 1.5])

xlabel('measured \itc\rm-C_{3}F_{6} exit concentration [mol m^{-
3}]','FontName','Arial','FontSize',20,'FontWeight','normal')
ylabel('predicted \itc\rm-C_{3}F_{6} exit concentration [mol m^{-
3}]','FontName','Arial','FontSize',20,'FontWeight','normal')
set(gca,'FontName','Arial','FontSize',14)
hold off
%----------------------------------
figure(14)
```

```
RcC3F6=CcC3F6-CcC3F6_pred;
counter7=max([max(RcC3F6) abs(min(RcC3F6))]);

plot(CcC3F6,RcC3F6,'bo','MarkerFaceColor','blue','MarkerSize',8)
hold on
plot(CcC3F6,Zline,'k-','LineWidth',3)

axis tight
ylim([-1*(counter7+0.1*counter7) (counter7+0.1*counter7)])
axis square

xlabel('measured \itc\rm-C_{3}F_{6} exit concentration [mol m^{-
3}]','FontName','Arial','FontSize',20,'FontWeight','normal')
ylabel('Residuals','FontName','Arial','FontSize',20,'FontWeight','normal')

set(gca,'FontName','Arial','FontSize',14)

hold off

Activation_Energy=k(6:10)

Preexponential=(k(1:5))./(exp(-1*Activation_Energy./(8.314*Tcent)))
```

H.2.2. Function handle for the ODE integrator.

```
function yz=rates3(z,y,k,Tp,Pp,v0_p,Ctot_p)

global Ftot0 Cin Cout W T P Ac nr nrr r dr drs r0 MM SV R Dm vr c2 Tcent

k1=(k(1))*exp(-1*(k(6)/8.314)*(1/Tp - 1/Tcent));          % HFP + 1/2O2 -> HFPO
k2=(k(2))*exp(-1*(k(7)/8.314)*(1/Tp - 1/Tcent));          % HFP + O2 -> CF3COF + COF2
k3=(10^14.19)*exp(-162000/(8.314*Tp));                    % HFPO -> CF3COF + CF2 (From Krusic 1999)
k4=(10^9.39)*(1e-06)*((Tp)^0.5)*exp(-1660/(8.314*Tp));    % CF2 + CF2 -> C2F4 (From Tyerman 1968)
k5=(10^7.94)*(1e-06)*((Tp)^0.5)*exp(-26610/(8.314*Tp));   % CF2 + C2F4 -> c-C3F6 (From Tyerman 1968)
k6=(k(3))*exp(-1*(k(8)/8.314)*(1/Tp - 1/Tcent));          % C2F4 + 1/2O2 -> COF2 + CF2
k7=(k(4))*exp(-1*(k(9)/8.314)*(1/Tp - 1/Tcent));          % CF3COF + 1/2 O2 -> 2COF2
k11=(k(5))*exp(-1*(k(10)/8.314)*(1/Tp - 1/Tcent));        % HFPO -> HFP + 1/2O2

% Convert 1D input vector into individual concentration vectors
```

```
for j=1:nrr;
    Ca(j)=y(j);
    Cb(j)=y(nrr+j);
    Cc(j)=y(2*nrr+j);
    Cd(j)=y(3*nrr+j);
    Ce(j)=y(4*nrr+j);
    Cf(j)=y(5*nrr+j);
    Cg(j)=y(6*nrr+j);
    Ch(j)=y(7*nrr+j);
end

% Concentrations at the wall computed from the two preceding radial points

Ca(nr)=(4*Ca(nr-1) - Ca(nr-2))/(3);
Cb(nr)=(4*Cb(nr-1) - Cb(nr-2))/(3);
Cc(nr)=(4*Cc(nr-1) - Cc(nr-2))/(3);
Cd(nr)=(4*Cd(nr-1) - Cd(nr-2))/(3);
Ce(nr)=(4*Ce(nr-1) - Ce(nr-2))/(3);
Cf(nr)=(4*Cf(nr-1) - Cf(nr-2))/(3);
Cg(nr)=(4*Cg(nr-1) - Cg(nr-2))/(3);
Ch(nr)=(4*Ch(nr-1) - Ch(nr-2))/(3);

% Step through the grid points for r

for j=1:nrr;

% First derivatives of concentration 1/r*Cir   Note already has been
% divided by 1/r

    if(j==1);
        Car(j)=2.0*(Ca(j+1)-Ca(j))/drs;
        Cbr(j)=2.0*(Cb(j+1)-Cb(j))/drs;
        Ccr(j)=2.0*(Cc(j+1)-Cc(j))/drs;
        Cdr(j)=2.0*(Cd(j+1)-Cd(j))/drs;
        Cer(j)=2.0*(Ce(j+1)-Ce(j))/drs;
        Cfr(j)=2.0*(Cf(j+1)-Cf(j))/drs;
        Cgr(j)=2.0*(Cg(j+1)-Cg(j))/drs;
        Chr(j)=2.0*(Ch(j+1)-Ch(j))/drs;

    else
        Car(j)=(1.0/r(j))*(Ca(j+1)-Ca(j-1))/(2.0*dr);
        Cbr(j)=(1.0/r(j))*(Cb(j+1)-Cb(j-1))/(2.0*dr);
        Ccr(j)=(1.0/r(j))*(Cc(j+1)-Cc(j-1))/(2.0*dr);
```

```
        Cdr(j)=(1.0/r(j))*(Cd(j+1)-Cd(j-1))/(2.0*dr);
        Cer(j)=(1.0/r(j))*(Ce(j+1)-Ce(j-1))/(2.0*dr);
        Cfr(j)=(1.0/r(j))*(Cf(j+1)-Cf(j-1))/(2.0*dr);
        Cgr(j)=(1.0/r(j))*(Cg(j+1)-Cg(j-1))/(2.0*dr);
        Chr(j)=(1.0/r(j))*(Ch(j+1)-Ch(j-1))/(2.0*dr);
    end

% Second derivatives of concentration

    if(j==1);
        Carr(j)=2.0*(Ca(j+1)-Ca(j))/drs;
        Cbrr(j)=2.0*(Cb(j+1)-Cb(j))/drs;
        Ccrr(j)=2.0*(Cc(j+1)-Cc(j))/drs;
        Cdrr(j)=2.0*(Cd(j+1)-Cd(j))/drs;
        Cerr(j)=2.0*(Ce(j+1)-Ce(j))/drs;
        Cfrr(j)=2.0*(Cf(j+1)-Cf(j))/drs;
        Cgrr(j)=2.0*(Cg(j+1)-Cg(j))/drs;
        Chrr(j)=2.0*(Ch(j+1)-Ch(j))/drs;

    else
        Carr(j)=(Ca(j+1)-2.0*Ca(j)+Ca(j-1))/drs;
        Cbrr(j)=(Cb(j+1)-2.0*Cb(j)+Cb(j-1))/drs;
        Ccrr(j)=(Cc(j+1)-2.0*Cc(j)+Cc(j-1))/drs;
        Cdrr(j)=(Cd(j+1)-2.0*Cd(j)+Cd(j-1))/drs;
        Cerr(j)=(Ce(j+1)-2.0*Ce(j)+Ce(j-1))/drs;
        Cfrr(j)=(Cf(j+1)-2.0*Cf(j)+Cf(j-1))/drs;
        Cgrr(j)=(Cg(j+1)-2.0*Cg(j)+Cg(j-1))/drs;
        Chrr(j)=(Ch(j+1)-2.0*Ch(j)+Ch(j-1))/drs;
    end

% Multicomponent diffusion coefficients

    Xa=Ca(j)/Ctot_p;        %mole fractions at radial point
    Xb=Cb(j)/Ctot_p;
    Xc=Cc(j)/Ctot_p;
    Xd=Cd(j)/Ctot_p;
    Xe=Ce(j)/Ctot_p;
    Xf=Cf(j)/Ctot_p;
    Xg=Cg(j)/Ctot_p;
    Xh=Ch(j)/Ctot_p;

    X=[Xa Xb Xc Xd Xe Xf Xg Xh];   % vector of mole fractions at radial point
```

```
    Dm=multdiff1(Tp,Pp,X,MM,SV);   % m^2/s vector of diffusion coefficients at radial point

% Rate equations, forward as well as reverse for reaction 1

    R1=k1*((Ca(j))^(1))*((Cb(j))^(0.5));
    RR1=k11*Cc(j);
    R2=k2*((Ca(j))^(1))*((Cb(j))^(1));
    R3=k3*((Cc(j))^(1));
    R4=k4*Ce(j)*Ce(j);
    R5=k5*Ce(j)*Cg(j);
    R6=k6*((Cg(j))^(1))*((Cb(j))^(1));
    R7=k7*((Cd(j))^(1))*((Cb(j))^(0.5));


    Ra=-R1-R2+RR1;
    Rb=-0.5*R1+0.5*RR1-R2-0.5*R6-0.5*R7;
    Rc=R1-R3-RR1;
    Rd=R2+R3-R7;
    Re=R3-2*R4-R5+R6;
    Rf=R2+2*R7+R6;
    Rg=R4-R5-R6;
    Rh=R5;

% Partial differential equations

    vr=2*v0_p*(1-(r(j)^2)/(r0^2));          % velocity

        Caz(j)=(Dm(1)/vr)*(Car(j)+Carr(j)) + (Ra/vr);
        Cbz(j)=(Dm(2)/vr)*(Cbr(j)+Cbrr(j)) + (Rb/vr);
        Ccz(j)=(Dm(3)/vr)*(Ccr(j)+Ccrr(j)) + (Rc/vr);
        Cdz(j)=(Dm(4)/vr)*(Cdr(j)+Cdrr(j)) + (Rd/vr);
        Cez(j)=(Dm(5)/vr)*(Cer(j)+Cerr(j)) + (Re/vr);
        Cfz(j)=(Dm(6)/vr)*(Cfr(j)+Cfrr(j)) + (Rf/vr);
        Cgz(j)=(Dm(7)/vr)*(Cgr(j)+Cgrr(j)) + (Rg/vr);
        Chz(j)=(Dm(8)/vr)*(Chr(j)+Chrr(j)) + (Rh/vr);

end

% 2D to 1D matrices

syz=8*nrr;
yz=zeros(1,syz);
```

```
for j=1:nrr;

    yz(j)=Caz(j);
    yz(nrr+j)=Cbz(j);
    yz(2*nrr+j)=Ccz(j);
    yz(3*nrr+j)=Cdz(j);
    yz(4*nrr+j)=Cez(j);
    yz(5*nrr+j)=Cfz(j);
    yz(6*nrr+j)=Cgz(j);
    yz(7*nrr+j)=Chz(j);

end

yz=yz';
```

H.3. Kinetic parameter identification, plug flow reactor model (Isothermal fit).

H.3.1 Main program file.

```
close all
clear all
clc

% Global variables
global Ftot_out Fin T Fout W Ac c2

% Constants
Ac = 1.76715E-06;

% Observed experimental data

Fin=xlsread('ratedata.xls','493data','C9:AZ16');  % inlet flow-rates for all data points
T=xlsread('ratedata.xls','493data','C2:AZ2');     % temperatures for all data points
Fout=xlsread('ratedata.xls','493data','C20:AZ27');% outlet flow-rates for all data points
Ftot_out=xlsread('ratedata.xls','493data','C5:AZ5'); % total outlet flow-rate for all data points
W=xlsread('ratedata.xls','493data','C31:AZ39');   % weighting for all data points

for counters1=1:8;

    NN(counters1)=counters1;
end
```

```
lb=[0 0 0 0 0];
ub=[inf inf inf inf inf];
k0=[0.03831 0.01152322 0.02386487 0.0007007 0.02579631];    % initial parameter estimates

c1=size(Fout);
c2=c1(2);

options=optimset('Display','iter','MaxIter',5,'MaxFunEvals',1000,'TolFun',1e-20,'TolX',1e-20,'LargeScale','on');

[k,resnorm,residual,exitflag,output,lambda,jacobian]=lsqnonlin(@myfun,k0,lb,ub,options);

ci=nlparci(k,residual,jacobian);

% regression evaluation

FHFP_pred=zeros(1,c2);
FO2_pred=zeros(1,c2);
FHFPO_pred=zeros(1,c2);
FCF3COF_pred=zeros(1,c2);
FCOF2_pred=zeros(1,c2);
FC2F4_pred=zeros(1,c2);
FcC3F6_pred=zeros(1,c2);

for c3=1:c2;                    % cycle through data points

    Finp=Fin(:,c3);             % inlet flow-rates for one data point
    Tp=T(c3);                   % reaction temperature for one data point

    options=odeset('BDF','off','NonNegative',NN,'AbsTol',1e-12);
    [z,F]=ode15s(@(z,F) rates1(z,F,k,Tp),[0 114.3],Finp,options);

    c4=size(F);
    c5=c4(1);

    Fout_pred=F(c5,:);              % outlet flow-rates predicted by model

    Ftot_out_pred=sum(F(c5,:));

    FHFP_pred(1,c3)=Fout_pred(1);
    FO2_pred(1,c3)=Fout_pred(2);
    FHFPO_pred(1,c3)=Fout_pred(3);
    FCF3COF_pred(1,c3)=Fout_pred(4);
```

```
    FCOF2_pred(1,c3)=Fout_pred(6);
    FC2F4_pred(1,c3)=Fout_pred(7);
    FcC3F6_pred(1,c3)=Fout_pred(8);

end

FHFP=Fout(1,:);           % measured outlet flow-rates
FO2=Fout(2,:);
FHFPO=Fout(3,:);
FCF3COF=Fout(4,:);
FCOF2=Fout(6,:);
FC2F4=Fout(7,:);
FcC3F6=Fout(8,:);

WHFP=W(1,:);              % weighting factors
WO2=W(2,:);
WHFPO=W(3,:);
WCF3COF=W(4,:);
WCOF2=W(6,:);
WC2F4=W(7,:);
WcC3F6=W(8,:);

FHFP_pred=WHFP.*FHFP_pred;
FO2_pred=WO2.*FO2_pred;
FHFPO_pred=WHFPO.*FHFPO_pred;
FCF3COF_pred=WCF3COF.*FCF3COF_pred;
FCOF2_pred=WCOF2.*FCOF2_pred;
FC2F4_pred=WC2F4.*FC2F4_pred;
FcC3F6_pred=WcC3F6.*FcC3F6_pred;

FHFP=WHFP.*FHFP;
FO2=WO2.*FO2;
FHFPO=WHFPO.*FHFPO;
FCF3COF=WCF3COF.*FCF3COF;
FCOF2=WCOF2.*FCOF2;
FC2F4=WC2F4.*FC2F4;
FcC3F6=WcC3F6.*FcC3F6;

Zline=zeros(1,c2);

%-----------------------------------
figure(1)
```

```
plot(FHFP,FHFP_pred,'bo','MarkerFaceColor','blue','MarkerSize',8)

FFDx1=linspace(0,100,100);
FFDy1=linspace(0,100,100);

hold on

plot(FFDx1,FFDy1,'k-','LineWidth',3)

axis square
xlim([0 1e-04])
ylim([0 1e-04])

xlabel('measured HFP exit molar flow-rate [mol s^{-1}]','FontName','Arial','FontSize',18,'FontWeight','normal')
ylabel('predicted HFP exit molar flow-rate [mol s^{-1}]','FontName','Arial','FontSize',18,'FontWeight','normal')

set(gca,'FontName','Arial','FontSize',14)

hold off

%-------------------------------------
figure(2)

RHFP=FHFP-FHFP_pred;
counter1=max([max(RHFP) abs(min(RHFP))]);
plot(FHFP,RHFP,'bo','MarkerFaceColor','blue','MarkerSize',8)
hold on
plot(FHFP,Zline,'k-','LineWidth',3)
axis tight
ylim([-1*(counter1+0.1*counter1) (counter1+0.1*counter1)])
axis square

xlabel('measured HFP exit molar flow-rate [mol s^{-1}]','FontName','Arial','FontSize',18,'FontWeight','normal')
ylabel('Residuals','FontName','Arial','FontSize',18,'FontWeight','normal')

set(gca,'FontName','Arial','FontSize',14)
hold off
%-------------------------------------
figure(3)

plot(FO2,FO2_pred,'bo','MarkerFaceColor','blue','MarkerSize',8)

FFDx2=linspace(0,100,100);
```

```
FFDy2=linspace(0,100,100);

hold on

plot(FFDx2,FFDy2,'k-','LineWidth',3)

axis square
xlim([0 1e-04])
ylim([0 1e-04])

xlabel('measured O_{2} exit molar flow-rate [mol s^{-1}]','FontName','Arial','FontSize',18,'FontWeight','normal')
ylabel('predicted O_{2} exit molar flow-rate [mol s^{-1}]','FontName','Arial','FontSize',18,'FontWeight','normal')

set(gca,'FontName','Arial','FontSize',14)
hold off

%-----------------------------------
figure(4)

RO2=FO2-FO2_pred;
counter2=max([max(RO2) abs(min(RO2))]);
plot(FO2,RO2,'bo','MarkerFaceColor','blue','MarkerSize',8)
hold on
plot(FO2,Zline,'k-','LineWidth',3)
axis tight
ylim([-1*(counter2+0.1*counter2) (counter2+0.1*counter2)])

axis square

xlabel('measured O_{2} exit molar flow-rate [mol s^{-1}]','FontName','Arial','FontSize',18,'FontWeight','normal')
ylabel('Residuals','FontName','Arial','FontSize',18,'FontWeight','normal')

set(gca,'FontName','Arial','FontSize',14)
hold off
%-----------------------------------
figure(5)

plot(FHFPO,FHFPO_pred,'bo','MarkerFaceColor','blue','MarkerSize',8)

FFDx3=linspace(0,100,100);
FFDy3=linspace(0,100,100);

hold on
```

```
plot(FFDx3,FFDy3,'k-','LineWidth',3)

axis square
xlim([0 1e-04])
ylim([0 1e-04])

xlabel('measured HFPO exit molar flow-rate [mol s^{-1}]','FontName','Arial','FontSize',18,'FontWeight','normal')
ylabel('predicted HFPO exit molar flow-rate [mol s^{-1}]','FontName','Arial','FontSize',18,'FontWeight','normal')
set(gca,'FontName','Arial','FontSize',14)

hold off
%-----------------------------------
figure(6)

RHFPO=FHFPO-FHFPO_pred;
counter3=max([max(RHFPO) abs(min(RHFPO))]);
plot(FHFPO,RHFPO,'bo','MarkerFaceColor','blue','MarkerSize',8)
hold on
plot(FHFPO,Zline,'k-','LineWidth',3)
axis tight
ylim([-1*(counter3+0.1*counter3) (counter3+0.1*counter3)])
axis square

xlabel('measured HFPO exit molar flow-rate [mol s^{-1}]','FontName','Arial','FontSize',18,'FontWeight','normal')
ylabel('Residuals','FontName','Arial','FontSize',18,'FontWeight','normal')

set(gca,'FontName','Arial','FontSize',14)
hold off
%-----------------------------------
figure(7)

plot(FCF3COF,FCF3COF_pred,'bo','MarkerFaceColor','blue','MarkerSize',8)

FFDx4=linspace(0,100,100);
FFDy4=linspace(0,100,100);

hold on

plot(FFDx4,FFDy4,'k-','LineWidth',3)

axis square
xlim([0 1e-04])
```

```
ylim([0 1e-04])

xlabel('measured CF_{3}COF exit molar flow-rate [mol s^{-1}]','FontName','Arial','FontSize',18,'FontWeight','normal')
ylabel('predicted CF_{3}COF exit molar flow-rate [mol s^{-1}]','FontName','Arial','FontSize',18,'FontWeight','normal')
set(gca,'FontName','Arial','FontSize',14)
hold off
%-----------------------------------
figure(8)

RCF3COF=FCF3COF-FCF3COF_pred;
counter4=max([max(RCF3COF) abs(min(RCF3COF))]);
plot(FCF3COF,RCF3COF,'bo','MarkerFaceColor','blue','MarkerSize',8)
hold on
plot(FCF3COF,Zline,'k-','LineWidth',3)
axis tight
ylim([-1*(counter4+0.1*counter4) (counter4+0.1*counter4)])
axis square

xlabel('measured CF_{3}COF exit molar flow-rate [mol s^{-1}]','FontName','Arial','FontSize',18,'FontWeight','normal')
ylabel('Residuals','FontName','Arial','FontSize',18,'FontWeight','normal')

set(gca,'FontName','Arial','FontSize',14)
hold off
%-------------------------------------
figure(9)

plot(FCOF2,FCOF2_pred,'bo','MarkerFaceColor','blue','MarkerSize',8)

FFDx5=linspace(0,100,100);
FFDy5=linspace(0,100,100);

hold on

plot(FFDx5,FFDy5,'k-','LineWidth',3)

axis square
xlim([0 2.5e-04])
ylim([0 2.5e-04])

xlabel('measured COF_{2} exit molar flow-rate [mol s^{-1}]','FontName','Arial','FontSize',18,'FontWeight','normal')
ylabel('predicted COF_{2} exit molar flow-rate [mol s^{-1}]','FontName','Arial','FontSize',18,'FontWeight','normal')
set(gca,'FontName','Arial','FontSize',14)
hold off
```

```
%----------------------------------
figure(10)

RCOF2=FCOF2-FCOF2_pred;
counter5=max([max(RCOF2) abs(min(RCOF2))]);
plot(FCOF2,RCOF2,'bo','MarkerFaceColor','blue','MarkerSize',8)
hold on

plot(FCOF2,Zline,'k-','LineWidth',3)
axis tight
ylim([-1*(counter5+0.1*counter5) (counter5+0.1*counter5)])
axis square

xlabel('measured COF_{2} exit molar flow-rate [mol s^{-1}]','FontName','Arial','FontSize',18,'FontWeight','normal')
ylabel('Residuals','FontName','Arial','FontSize',18,'FontWeight','normal')

set(gca,'FontName','Arial','FontSize',14)
hold off
%----------------------------------
figure(11)

plot(FC2F4,FC2F4_pred,'bo','MarkerFaceColor','blue','MarkerSize',8)

FFDx6=linspace(0,100,100);
FFDy6=linspace(0,100,100);

hold on

plot(FFDx6,FFDy6,'k-','LineWidth',3)

axis square
xlim([0 6e-06])
ylim([0 6e-06])

xlabel('measured C_{2}F_{4} exit molar flow-rate [mol s^{-1}]','FontName','Arial','FontSize',18,'FontWeight','normal')
ylabel('predicted C_{2}F_{4} exit molar flow-rate [mol s^{-1}]','FontName','Arial','FontSize',18,'FontWeight','normal')
set(gca,'FontName','Arial','FontSize',14)
hold off
%----------------------------------
figure(12)

RC2F4=FC2F4-FC2F4_pred;
counter6=max([max(RC2F4) abs(min(RC2F4))]);
```

```
plot(FC2F4,RC2F4,'bo','MarkerFaceColor','blue','MarkerSize',8)
hold on
plot(FC2F4,Zline,'k-','LineWidth',3)
axis tight
ylim([-1*(counter6+0.1*counter6) (counter6+0.1*counter6)])
axis square

xlabel('measured C_{2}F_{4} exit molar flow-rate [mol s^{-1}]','FontName','Arial','FontSize',18,'FontWeight','normal')
ylabel('Residuals','FontName','Arial','FontSize',18,'FontWeight','normal')

set(gca,'FontName','Arial','FontSize',14)

hold off
%----------------------------------
figure(13)

plot(FcC3F6,FcC3F6_pred,'bo','MarkerFaceColor','blue','MarkerSize',8)

FFDx7=linspace(0,100,100);
FFDy7=linspace(0,100,100);

hold on

plot(FFDx7,FFDy7,'k-','LineWidth',3)

axis square
xlim([0 2.5e-06])
ylim([0 2.5e-06])

xlabel('measured \itc\rm-C_{3}F_{6} exit molar flow-rate [mol s^{-
1}]','FontName','Arial','FontSize',18,'FontWeight','normal')
ylabel('predicted \itc\rm-C_{3}F_{6} exit molar flow-rate [mol s^{-
1}]','FontName','Arial','FontSize',18,'FontWeight','normal')
set(gca,'FontName','Arial','FontSize',14)
hold off
%----------------------------------
figure(14)

RcC3F6=FcC3F6-FcC3F6_pred;
counter7=max([max(RcC3F6) abs(min(RcC3F6))]);

plot(FcC3F6,RcC3F6,'bo','MarkerFaceColor','blue','MarkerSize',8)
hold on
```

```
plot(FcC3F6,Zline,'k-','LineWidth',3)

axis tight
ylim([-1*(counter7+0.1*counter7) (counter7+0.1*counter7)])
axis square

xlabel('measured \itc\rm-C_{3}F_{6} exit molar flow-rate [mol s^{-
1}]','FontName','Arial','FontSize',18,'FontWeight','normal')
ylabel('Residuals','FontName','Arial','FontSize',18,'FontWeight','normal')

set(gca,'FontName','Arial','FontSize',14)

hold off
```

H.3.2. Objective function file.

```
function Fob=myfun(k)

% Global variables
global Ftot_out Fin T Fout W Ac c2

Fob=zeros(9,c2);

for c3=1:c2;                    % cycle through data points

    Finp=Fin(:,c3);             % inlet flow-rates for one data point
    Foutp=Fout(:,c3);           % outlet flow-rates for one data point
    Wp=W(:,c3);                 % weighting for one data point
    Tp=T(c3);                   % reaction temperature for one data point
    Ftot_outp=Ftot_out(c3);     % total outlet flow-rate for one data point

    options=odeset('BDF','off','NonNegative',[1 2 3 4 5 6 7 8],'AbsTol',1e-12);
    [z,F]=ode15s(@(z,F) rates1(z,F,k,Tp),[0 114.3],Finp,options);

    c4=size(F);
    c5=c4(1);

    Fout_pred=F(c5,:);              % outlet flow-rates predicted by model
    Ftot_out_pred=sum(F(c5,:));     % total outlet flow-rate predicted by model
```

```
    for c6=1:8;

        Fob(c6,c3)=(Wp(c6))*((2*(Fout_pred(c6)-Foutp(c6))/(Fout_pred(c6)+Foutp(c6)))^(2))^(2*0.5);

    end

   Fob(9,c3)=(Wp(9))*((2*(Ftot_out_pred-Ftot_outp)/(Ftot_out_pred+Ftot_outp))^(2))^(2*0.5);

end

Fob=reshape(Fob,1,[]);
Fob=Fob';
```

H.3.3. Function handle for the ODE integrator.

```
function dF = rates1(z,F,k,Tp)
% Global variables
global Fin T Fout Ac c2

P=4.5e+05;                                          %Pascals
dF=zeros(8,1);
C=zeros(8,1);

k1=k(1);
k2=k(2);
k3=(10^14.19)*exp(-162000/(8.314*Tp));                  % HFPO -> CF3COF + CF2 (From Krusic 1999)
k4=(10^9.39)*(1e-06)*((Tp)^0.5)*exp(-1660/(8.314*Tp)); % CF2 + CF2 -> C2F4 (From Tyerman 1968)
k5=(10^7.94)*(1e-06)*((Tp)^0.5)*exp(-26610/(8.314*Tp));% CF2 + C2F4 -> c-C3F6 (From Tyerman 1968)
k6=k(3);
k7=k(4);
k11=k(5);

Ftot = F(1)+F(2)+F(3)+F(4)+F(5)+F(6)+F(7)+F(8);  %mol/s

q=(Ftot*8.314*Tp)/(P);                              % m3/s

C(1)=F(1)/q;                                        % mol/m3
C(2)=F(2)/q;
C(3)=F(3)/q;
```

```
C(4)=F(4)/q;
C(5)=F(5)/q;
C(6)=F(6)/q;
C(7)=F(7)/q;
C(8)=F(8)/q;

r1=k1*(C(1)^1)*(C(2)^1);
r2=k2*(C(1)^1)*(C(2)^1);
r3=k3*C(3);
r4=k4*C(5)*C(5);
r5=k5*C(5)*C(7);
r6=k6*(C(7)^1)*(C(2)^1);
r7=k7*(C(4)^1)*(C(2)^1);
r11=k11*(C(3));

dF(1)=(-r1-r2+r11)*Ac;
dF(2)=(-0.5*r1-r2-0.5*r6-0.5*r7+0.5*r11)*Ac;
dF(3)=(r1-r3-r11)*Ac;
dF(4)=(r2+r3-r7)*Ac;
dF(5)=(r3-2*r4-r5+r6)*Ac;
dF(6)=(r2+r6+2*r7)*Ac;
dF(7)=(r4-r5-r6)*Ac;
dF(8)=(r5)*Ac;
```

H.4. Kinetic parameter identification, plug flow reactor model (Total data fit).

H.4.1. Main program file.

```
close all
clear all
clc

% Global variables
global Ftot_out Fin T Fout W Ac c2 Tcent

% Constants

Ac = 1.76715E-06;
```

```
% Observed experimental data

Fin=xlsread('ratedata.xls','totaldata','C9:FU16');     % inlet flow-rates for all data points
T=xlsread('ratedata.xls','totaldata','C2:FU2');        % temperatures for all data points
Fout=xlsread('ratedata.xls','totaldata','C20:FU27');   % outlet flow-rates for all data points
Ftot_out=xlsread('ratedata.xls','totaldata','C5:FU5');% total outlet flow-rate for all data points
W=xlsread('ratedata.xls','totaldata','C31:FU39');      % weighting for all data points

for counters1=1:8;

    NN(counters1)=counters1;
end

lb=[0 0 0 0 0 0 0 0 0 0];                        % lower bounds for parameter estimates
ub=[inf inf inf inf inf inf inf inf inf inf];      % upper bounds for parameter estimates
A0=[1.0093127e+19 7.080636026e+24 6.078848693e+4 2.780708677e+02 0.036905];% Pre-exponential factor
Ea=[202.6386 262.5843 66.7299 52.74886 1.489677]; % Activation energy [kJ/mol]
Ea=1000*Ea;

Tcent=478.15;

A_prime=A0.*exp(-Ea./(8.314*Tcent));

k0=[A_prime Ea];

% number of data points c2

c1=size(Fout);
c2=c1(2);

options=optimset('Display','iter','MaxIter',0,'MaxFunEvals',1000,'TolFun',1e-20,'TolX',1e-20,'LargeScale','on');

[k,resnorm,residual,exitflag,output,lambda,jacobian]=lsqnonlin(@myfun,k0,lb,ub,options);

ci=nlparci(k,residual,jacobian);

% regression evaluation

FHFP_pred=zeros(1,c2);
FO2_pred=zeros(1,c2);
FHFPO_pred=zeros(1,c2);
FCF3COF_pred=zeros(1,c2);
FCOF2_pred=zeros(1,c2);
```

```
FC2F4_pred=zeros(1,c2);
FcC3F6_pred=zeros(1,c2);

for c3=1:c2;                    % cycle through data points

    Finp=Fin(:,c3);             % inlet flow-rates for one data point
    Tp=T(c3);                   % reaction temperature for one data point


    options=odeset('BDF','off','NonNegative',NN,'AbsTol',1e-12);
    [z,F]=ode15s(@(z,F) rates1(z,F,k,Tp),[0 114.3],Finp,options);

    c4=size(F);
    c5=c4(1);

    Fout_pred=F(c5,:);           % outlet flow-rates predicted by model

    Ftot_out_pred=sum(F(c5,:));

    FHFP_pred(1,c3)=Fout_pred(1);
    FO2_pred(1,c3)=Fout_pred(2);
    FHFPO_pred(1,c3)=Fout_pred(3);
    FCF3COF_pred(1,c3)=Fout_pred(4);
    FCOF2_pred(1,c3)=Fout_pred(6);
    FC2F4_pred(1,c3)=Fout_pred(7);
    FcC3F6_pred(1,c3)=Fout_pred(8);

end

FHFP=Fout(1,:);                 % measured outlet flow-rates
FO2=Fout(2,:);
FHFPO=Fout(3,:);
FCF3COF=Fout(4,:);
FCOF2=Fout(6,:);
FC2F4=Fout(7,:);
FcC3F6=Fout(8,:);

WHFP=W(1,:);                    % weighting factors
WO2=W(2,:);
WHFPO=W(3,:);
WCF3COF=W(4,:);
WCOF2=W(6,:);
WC2F4=W(7,:);
```

```
WcC3F6=W(8,:);

FHFP_pred=WHFP.*FHFP_pred;
FO2_pred=WO2.*FO2_pred;
FHFPO_pred=WHFPO.*FHFPO_pred;
FCF3COF_pred=WCF3COF.*FCF3COF_pred;
FCOF2_pred=WCOF2.*FCOF2_pred;
FC2F4_pred=WC2F4.*FC2F4_pred;
FcC3F6_pred=WcC3F6.*FcC3F6_pred;

FHFP=WHFP.*FHFP;
FO2=WO2.*FO2;
FHFPO=WHFPO.*FHFPO;
FCF3COF=WCF3COF.*FCF3COF;
FCOF2=WCOF2.*FCOF2;
FC2F4=WC2F4.*FC2F4;
FcC3F6=WcC3F6.*FcC3F6;

Zline=zeros(1,c2);
%-----------------------------------
figure(1)

plot(FHFP,FHFP_pred,'bo','MarkerFaceColor','blue','MarkerSize',8)

FFDx1=linspace(0,100,100);
FFDy1=linspace(0,100,100);

hold on

plot(FFDx1,FFDy1,'k-','LineWidth',3)

axis square
xlim([0 1.5e-04])
ylim([0 1.5e-04])

xlabel('measured HFP exit molar flow-rate [mol s^{-1}]','FontName','Arial','FontSize',18,'FontWeight','normal')
ylabel('predicted HFP exit molar flow-rate [mol s^{-1}]','FontName','Arial','FontSize',18,'FontWeight','normal')

set(gca,'FontName','Arial','FontSize',14)

hold off
%-----------------------------------
figure(2)
```

```
RHFP=FHFP-FHFP_pred;
counter1=max([max(RHFP) abs(min(RHFP))]);
plot(FHFP,RHFP,'bo','MarkerFaceColor','blue','MarkerSize',8)
hold on
plot(FHFP,Zline,'k-','LineWidth',3)
axis tight
ylim([-1*(counter1+0.1*counter1) (counter1+0.1*counter1)])
axis square

xlabel('measured HFP exit molar flow-rate [mol s^{-1}]','FontName','Arial','FontSize',18,'FontWeight','normal')
ylabel('Residuals','FontName','Arial','FontSize',18,'FontWeight','normal')


set(gca,'FontName','Arial','FontSize',14)
hold off
%-------------------------------------

figure(3)

plot(FO2,FO2_pred,'bo','MarkerFaceColor','blue','MarkerSize',8)

FFDx2=linspace(0,100,100);
FFDy2=linspace(0,100,100);

hold on

plot(FFDx2,FFDy2,'k-','LineWidth',3)

axis square
xlim([0 1.8e-04])
ylim([0 1.8e-04])

xlabel('measured O_{2} exit molar flow-rate [mol s^{-1}]','FontName','Arial','FontSize',18,'FontWeight','normal')
ylabel('predicted O_{2} exit molar flow-rate [mol s^{-1}]','FontName','Arial','FontSize',18,'FontWeight','normal')

set(gca,'FontName','Arial','FontSize',14)
hold off
%-----------------------------------
figure(4)

RO2=FO2-FO2_pred;
counter2=max([max(RO2) abs(min(RO2))]);
```

```
plot(FO2,RO2,'bo','MarkerFaceColor','blue','MarkerSize',8)
hold on
plot(FO2,Zline,'k-','LineWidth',3)
axis tight
ylim([-1*(counter2+0.1*counter2) (counter2+0.1*counter2)])

axis square

xlabel('measured O_{2} exit molar flow-rate [mol s^{-1}]','FontName','Arial','FontSize',18,'FontWeight','normal')
ylabel('Residuals','FontName','Arial','FontSize',18,'FontWeight','normal')


set(gca,'FontName','Arial','FontSize',14)
hold off
%-----------------------------------
figure(5)

plot(FHFPO,FHFPO_pred,'bo','MarkerFaceColor','blue','MarkerSize',8)

FFDx3=linspace(0,100,100);
FFDy3=linspace(0,100,100);

hold on

plot(FFDx3,FFDy3,'k-','LineWidth',3)

axis square
xlim([0 1e-04])
ylim([0 1e-04])

xlabel('measured HFPO exit molar flow-rate [mol s^{-1}]','FontName','Arial','FontSize',18,'FontWeight','normal')
ylabel('predicted HFPO exit molar flow-rate [mol s^{-1}]','FontName','Arial','FontSize',18,'FontWeight','normal')
set(gca,'FontName','Arial','FontSize',14)

hold off
%-----------------------------------
figure(6)

RHFPO=FHFPO-FHFPO_pred;
counter3=max([max(RHFPO) abs(min(RHFPO))]);
plot(FHFPO,RHFPO,'bo','MarkerFaceColor','blue','MarkerSize',8)
hold on
plot(FHFPO,Zline,'k-','LineWidth',3)
```

```
axis tight
ylim([-1*(counter3+0.1*counter3) (counter3+0.1*counter3)])
axis square

xlabel('measured HFPO exit molar flow-rate [mol s^{-1}]','FontName','Arial','FontSize',18,'FontWeight','normal')
ylabel('Residuals','FontName','Arial','FontSize',18,'FontWeight','normal')


set(gca,'FontName','Arial','FontSize',14)
hold off
%-------------------------------------
figure(7)

plot(FCF3COF,FCF3COF_pred,'bo','MarkerFaceColor','blue','MarkerSize',8)

FFDx4=linspace(0,100,100);
FFDy4=linspace(0,100,100);

hold on

plot(FFDx4,FFDy4,'k-','LineWidth',3)

axis square
xlim([0 8e-05])
ylim([0 8e-05])

xlabel('measured CF_{3}COF exit molar flow-rate [mol s^{-1}]','FontName','Arial','FontSize',18,'FontWeight','normal')
ylabel('predicted CF_{3}COF exit molar flow-rate [mol s^{-1}]','FontName','Arial','FontSize',18,'FontWeight','normal')
set(gca,'FontName','Arial','FontSize',14)
hold off
%-------------------------------------
figure(8)

RCF3COF=FCF3COF-FCF3COF_pred;
counter4=max([max(RCF3COF) abs(min(RCF3COF))]);
plot(FCF3COF,RCF3COF,'bo','MarkerFaceColor','blue','MarkerSize',8)
hold on
plot(FCF3COF,Zline,'k-','LineWidth',3)
axis tight
ylim([-1*(counter4+0.1*counter4) (counter4+0.1*counter4)])
axis square

xlabel('measured CF_{3}COF exit molar flow-rate [mol s^{-1}]','FontName','Arial','FontSize',18,'FontWeight','normal')
```

```
ylabel('Residuals','FontName','Arial','FontSize',18,'FontWeight','normal')

set(gca,'FontName','Arial','FontSize',14)
hold off
%-------------------------------------
figure(9)

plot(FCOF2,FCOF2_pred,'bo','MarkerFaceColor','blue','MarkerSize',8)

FFDx5=linspace(0,100,100);
FFDy5=linspace(0,100,100);

hold on

plot(FFDx5,FFDy5,'k-','LineWidth',3)

axis square
xlim([0 2e-04])
ylim([0 2e-04])

xlabel('measured COF_{2} exit molar flow-rate [mol s^{-1}]','FontName','Arial','FontSize',18,'FontWeight','normal')
ylabel('predicted COF_{2} exit molar flow-rate [mol s^{-1}]','FontName','Arial','FontSize',18,'FontWeight','normal')
set(gca,'FontName','Arial','FontSize',14)
hold off
%-----------------------------------
figure(10)

RCOF2=FCOF2-FCOF2_pred;
counter5=max([max(RCOF2) abs(min(RCOF2))]);
plot(FCOF2,RCOF2,'bo','MarkerFaceColor','blue','MarkerSize',8)
hold on

plot(FCOF2,Zline,'k-','LineWidth',3)
axis tight
ylim([-1*(counter5+0.1*counter5) (counter5+0.1*counter5)])
axis square

xlabel('measured COF_{2} exit molar flow-rate [mol s^{-1}]','FontName','Arial','FontSize',18,'FontWeight','normal')
ylabel('Residuals','FontName','Arial','FontSize',18,'FontWeight','normal')

set(gca,'FontName','Arial','FontSize',14)
hold off
%-----------------------------------
```

```
figure(11)

plot(FC2F4,FC2F4_pred,'bo','MarkerFaceColor','blue','MarkerSize',8)

FFDx6=linspace(0,100,100);
FFDy6=linspace(0,100,100);

hold on

plot(FFDx6,FFDy6,'k-','LineWidth',3)

axis square
xlim([0 3e-06])
ylim([0 3e-06])

xlabel('measured C_{2}F_{4} exit molar flow-rate [mol s^{-1}]','FontName','Arial','FontSize',18,'FontWeight','normal')
ylabel('predicted C_{2}F_{4} exit molar flow-rate [mol s^{-1}]','FontName','Arial','FontSize',18,'FontWeight','normal')
set(gca,'FontName','Arial','FontSize',14)
hold off
%-----------------------------------
figure(12)

RC2F4=FC2F4-FC2F4_pred;
counter6=max([max(RC2F4) abs(min(RC2F4))]);
plot(FC2F4,RC2F4,'bo','MarkerFaceColor','blue','MarkerSize',8)
hold on
plot(FC2F4,Zline,'k-','LineWidth',3)
axis tight
ylim([-1*(counter6+0.1*counter6) (counter6+0.1*counter6)])
axis square

xlabel('measured C_{2}F_{4} exit molar flow-rate [mol s^{-1}]','FontName','Arial','FontSize',18,'FontWeight','normal')
ylabel('Residuals','FontName','Arial','FontSize',18,'FontWeight','normal')

set(gca,'FontName','Arial','FontSize',14)

hold off
%-----------------------------------
figure(13)

plot(FcC3F6,FcC3F6_pred,'bo','MarkerFaceColor','blue','MarkerSize',8)

FFDx7=linspace(0,100,100);
```

```
FFDy7=linspace(0,100,100);

hold on

plot(FFDx7,FFDy7,'k-','LineWidth',3)

axis square
xlim([0 2.5e-06])
ylim([0 2.5e-06])

xlabel('measured \itc\rm-C_{3}F_{6} exit molar flow-rate [mol s^{-
1}]','FontName','Arial','FontSize',18,'FontWeight','normal')
ylabel('predicted \itc\rm-C_{3}F_{6} exit molar flow-rate [mol s^{-
1}]','FontName','Arial','FontSize',18,'FontWeight','normal')
set(gca,'FontName','Arial','FontSize',14)
hold off
%-----------------------------------
figure(14)

RcC3F6=FcC3F6-FcC3F6_pred;
counter7=max([max(RcC3F6) abs(min(RcC3F6))]);

plot(FcC3F6,RcC3F6,'bo','MarkerFaceColor','blue','MarkerSize',8)
hold on
plot(FcC3F6,Zline,'k-','LineWidth',3)

axis tight
ylim([-1*(counter7+0.1*counter7) (counter7+0.1*counter7)])
axis square

xlabel('measured \itc\rm-C_{3}F_{6} exit molar flow-rate [mol s^{-
1}]','FontName','Arial','FontSize',18,'FontWeight','normal')
ylabel('Residuals','FontName','Arial','FontSize',18,'FontWeight','normal')

set(gca,'FontName','Arial','FontSize',14)

hold off

Activation_Energy=k(6:10)

Preexponential=(k(1:5))./(exp(-1*Activation_Energy./(8.314*Tcent)))

err1=ci(6:10,1)-Activation_Energy'
```

```
errP=k(1:5)-ci(1:5,1)'

err2=errP./(exp(-1*Activation_Energy./(8.314*Tcent)))
```

H.4.2. Function handle for the ODE integrator.

```
function dF = rates1(z,F,k,Tp)
% Global variables
global Fin T Fout Ac c2 Tcent

P=4.5e+05;                                          %Pascals
dF=zeros(8,1);
C=zeros(8,1);

k1=(k(1))*exp(-1*(k(6)/8.314)*(1/Tp - 1/Tcent));  % HFP + 1/2O2 -> HFPO
k2=(k(2))*exp(-1*(k(7)/8.314)*(1/Tp - 1/Tcent));  % HFP + O2 -> CF3COF + COF2
k3=(10^14.19)*exp(-162000/(8.314*Tp));    % HFPO -> CF3COF + CF2 (From Krusic 1999)
k4=(10^9.39)*(1e-06)*((Tp)^0.5)*exp(-1660/(8.314*Tp)); % CF2 + CF2 -> C2F4 (From Tyerman 1968)
k5=(10^7.94)*(1e-06)*((Tp)^0.5)*exp(-26610/(8.314*Tp));% CF2 + C2F4 -> c-C3F6 (From Tyerman 1968)
k6=(k(3))*exp(-1*(k(8)/8.314)*(1/Tp - 1/Tcent));       % C2F4 + 1/2O2 -> COF2 + CF2
k7=(k(4))*exp(-1*(k(9)/8.314)*(1/Tp - 1/Tcent));       % CF3COF + 1/2 O2 -> 2COF2
k11=(k(5))*exp(-1*(k(10)/8.314)*(1/Tp - 1/Tcent));     % HFPO -> HFP + 1/2O2

Ftot = F(1)+F(2)+F(3)+F(4)+F(5)+F(6)+F(7)+F(8);  %mol/s

q=(Ftot*8.314*Tp)/(P);                             % m3/s

C(1)=F(1)/q;                                       % mol/m3
C(2)=F(2)/q;
C(3)=F(3)/q;
C(4)=F(4)/q;
C(5)=F(5)/q;
C(6)=F(6)/q;
C(7)=F(7)/q;
C(8)=F(8)/q;

r1=k1*(C(1)^1)*(C(2)^1);
r2=k2*(C(1)^1)*(C(2)^1);
r3=k3*C(3);
r4=k4*C(5)*C(5);
```

```
r5=k5*C(5)*C(7);
r6=k6*(C(7)^1)*(C(2)^1);
r7=k7*(C(4)^1)*(C(2)^1);
r11=k11*(C(3));

dF(1)=(-r1-r2+r11)*Ac;
dF(2)=(-0.5*r1-r2-0.5*r6-0.5*r7+0.5*r11)*Ac;
dF(3)=(r1-r3-r11)*Ac;
dF(4)=(r2+r3-r7)*Ac;
dF(5)=(r3-2*r4-r5+r6)*Ac;
dF(6)=(r2+r6+2*r7)*Ac;
dF(7)=(r4-r5-r6)*Ac;
dF(8)=(r5)*Ac;
```

Appendix I. Gas chromatograms

Table I.1. Shimadzu G.C. 2010 calibration for HFP, chromatogram 1.

Peak no.	Area	Volume [µl]
1 (HFP)	7652508.5	100

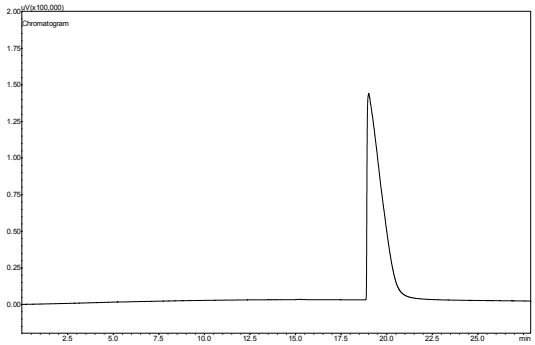

Figure I.1. Shimadzu G.C. 2010 calibration for HFP, chromatogram 1.

Table I.2. Shimadzu G.C. 2010 calibration for HFP, chromatogram 2.

Peak no.	Area	Volume [µl]
1 (HFP)	7669011.2	100

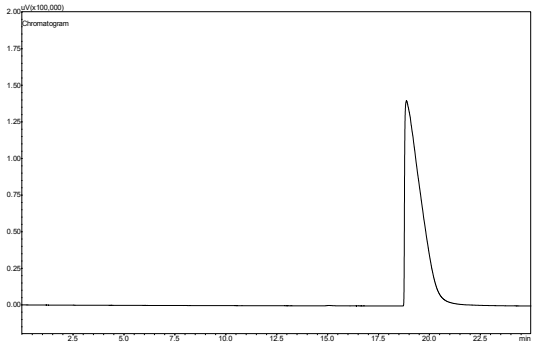

Figure I.2. Shimadzu G.C. 2010 calibration for HFP, chromatogram 2.

Table I.3. Shimadzu G.C. 2010 calibration for HFP, chromatogram 3.

Peak no.	Area	Volume [µl]
1 (HFP)	7686404.3	100

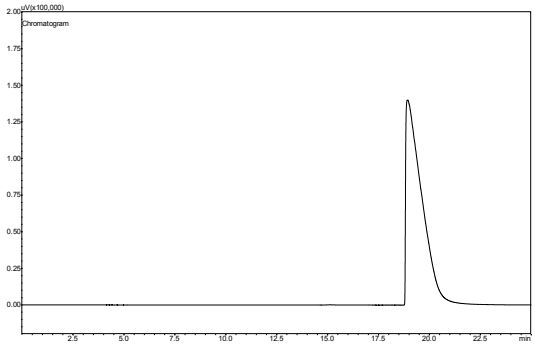

Figure I.3. Shimadzu G.C. 2010 calibration for HFP, chromatogram 3.

Table I.4. Shimadzu G.C. 2010 calibration for HFP, chromatogram 4.

Peak no.	Area	Volume [µl]
1 (HFP)	6097471.4	80

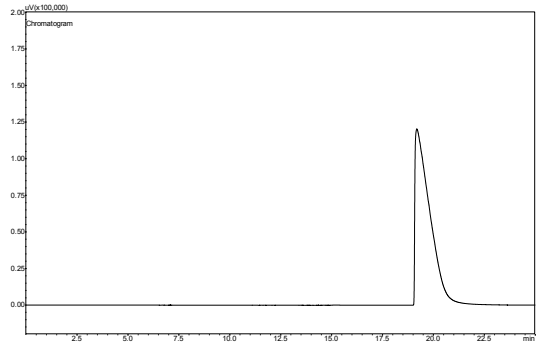

Figure I.4. Shimadzu G.C. 2010 calibration for HFP, chromatogram 4.

Table I.5. Shimadzu G.C. 2010 calibration for HFP, chromatogram 5.

Peak no.	Area	Volume [µl]
1 (HFP)	6104607.2	80

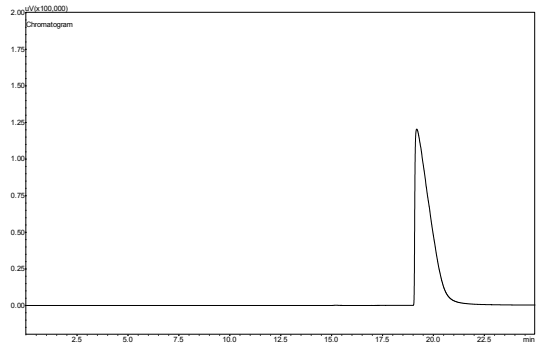

Figure I.5. Shimadzu G.C. 2010 calibration for HFP, chromatogram 5.

Table I.6. Shimadzu G.C. 2010 calibration for HFP, chromatogram 6.

Peak no.	Area	Volume [µl]
1 (HFP)	6064323.1	80

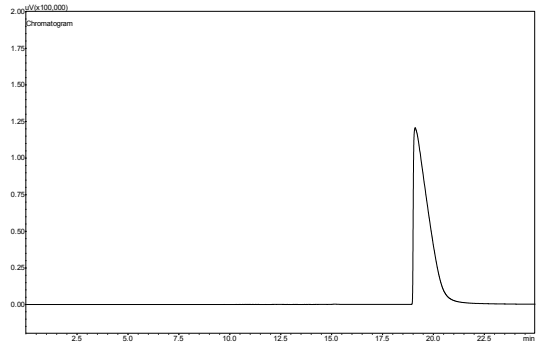

Figure I.6. Shimadzu G.C. 2010 calibration for HFP, chromatogram 6.

Table I.7. Shimadzu G.C. 2010 calibration for HFP, chromatogram 7.

Peak no.	Area	Volume [µl]
1 (HFP)	4572548.9	60
2 (HFP)	4554212.4	60
3 (HFP)	4601977.0	60

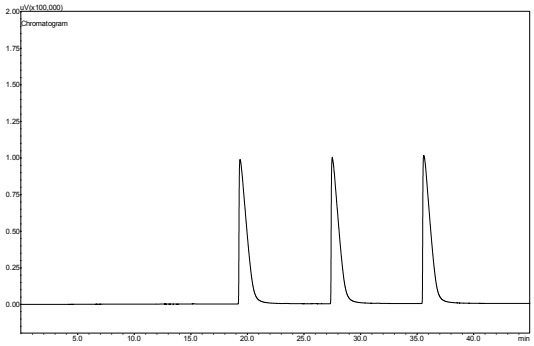

Figure I.7. Shimadzu G.C. 2010 calibration for HFP, chromatogram 7.

Table I.8. Shimadzu G.C. 2010 calibration for HFP, chromatogram 8.

Peak no.	Area	Volume [µl]
1 (HFP)	3033471.3	40
2 (HFP)	3056897.1	40
3 (HFP)	3025357.2	40
4 (HFP)	3075812.5	40

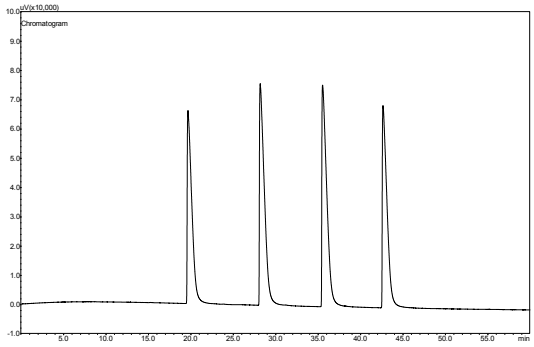

Figure I.8. Shimadzu G.C. 2010 calibration for HFP, chromatogram 8.

Table I.9. Shimadzu G.C. 2010 calibration for HFP, chromatogram 9.

Peak no.	Area	Volume [µl]
1 (HFP)	1530224.7	20
2 (HFP)	1532501.9	20
3 (HFP)	1578334.9	20
4 (HFP)	1556168.7	20

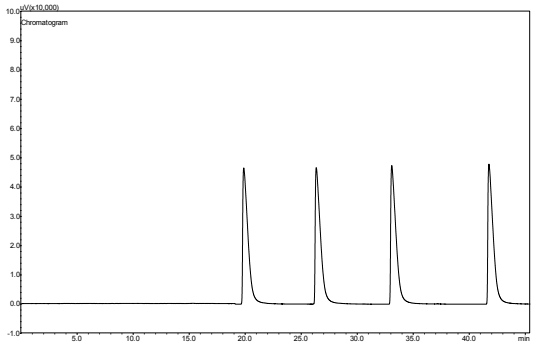

Figure I.9. Shimadzu G.C. 2010 calibration for HFP, chromatogram 9.

Table I.10. Shimadzu G.C. 2010 calibration for HFP, chromatogram 10.

Peak no.	Area	Volume [µl]
1 (HFP)	4572548.9	70
2 (HFP)	4554212.4	70

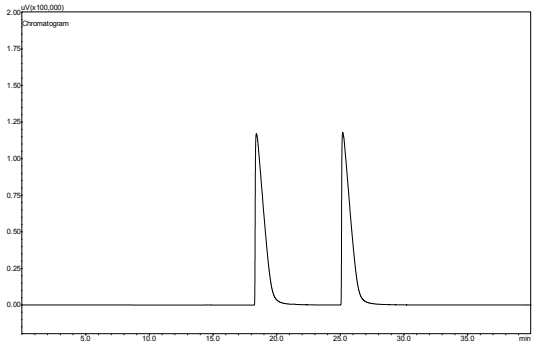

Figure I.10. Shimadzu G.C. 2010 calibration for HFP, chromatogram 10.

Table I.11. Shimadzu G.C. 2010 calibration for HFP, chromatogram 11.

Peak no.	Area	Volume [µl]
1 (HFP)	15840224.2	200
2 (HFP)	24177496	300
3 (HFP)	24166960.2	300
4 (HFP)	7263645.5	100

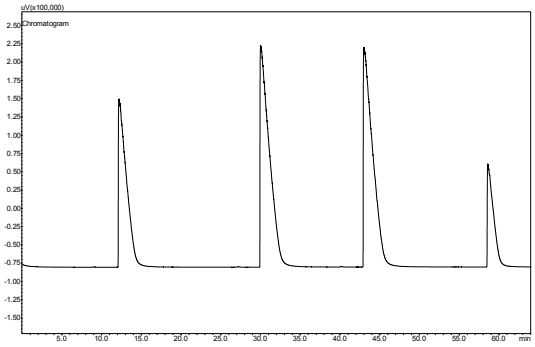

Figure I.8. Shimadzu G.C. 2010 calibration for HFP, chromatogram 11.

Table I.12. Shimadzu G.C. 2010 calibration for HFPO, chromatogram 1.

Peak no.	Area	Volume [µl]
2 (HFPO)	1513279.8	100
4 (HFPO)	1521440.2	100
6 (HFPO)	1503657.1	100
8 (HFPO)	1475375.8	100

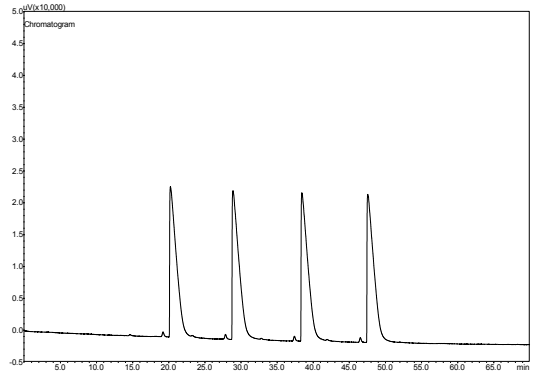

Figure I.12. Shimadzu G.C. 2010 calibration for HFPO, chromatogram 1.

Table I.13. Shimadzu G.C. 2010 calibration for HFPO, chromatogram 2.

Peak no.	Area	Volume [µl]
2 (HFPO)	903141.8	60
4 (HFPO)	905647.1	60
6 (HFPO)	892204.7	60

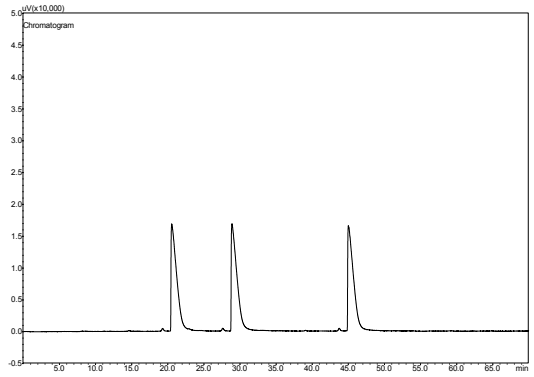

Figure I.13. Shimadzu G.C. 2010 calibration for HFPO, chromatogram 2.

Table I.14. Shimadzu G.C. 2010 calibration for HFPO, chromatogram 3.

Peak no.	Area	Volume [µl]
2 (HFPO)	570058.6	40
4 (HFPO)	555304.3	40
6 (HFPO)	577312.4	40
8 (HFPO)	576803.2	40

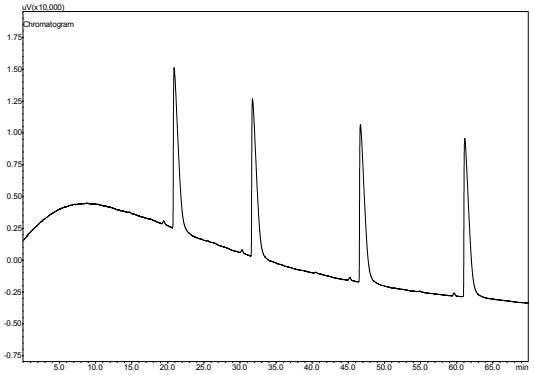

Figure I.14. Shimadzu G.C. 2010 calibration for HFPO, chromatogram 3.

Table I.15. Shimadzu G.C. 2010 calibration for HFPO, chromatogram 4.

Peak no.	Area	Volume [µl]
2 (HFP)	305429.3	20
4 (HFP)	305431.5	20
6 (HFP)	306165.3	20

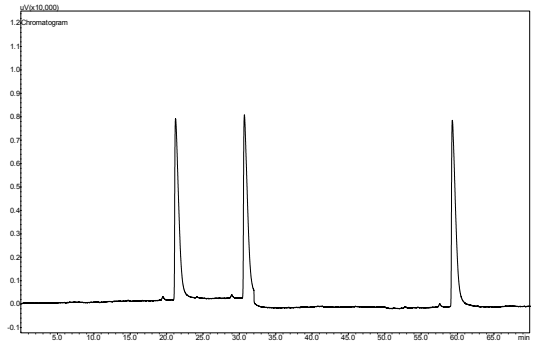

Figure I.15. Shimadzu G.C. 2010 calibration for HFPO, chromatogram 4.

Table I.16. Shimadzu G.C. 2010 calibration for HFPO, chromatogram 5.

Peak no.	Area	Volume [µl]
2 (HFPO)	1190926.7	80
4 (HFPO)	1184060.1	80

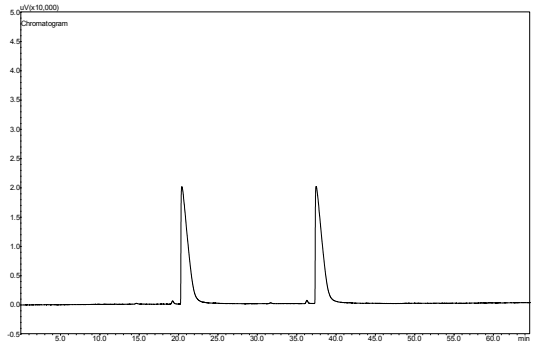

Figure I.16. Shimadzu G.C. 2010 calibration for HFPO, chromatogram 5.

Table I.17. Shimadzu G.C. 2010 calibration for HFPO, chromatogram 6.

Peak no.	Area	Volume [µl]
2 (HFPO)	1114256.6	70
4 (HFPO)	1083598.7	70
6 (HFPO)	1099112.9	70

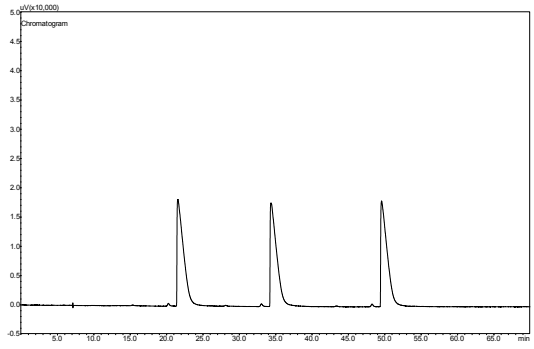

Figure I.17. Shimadzu G.C. 2010 calibration for HFPO, chromatogram 6.

Table I.18. Shimadzu G.C. 2010 calibration for HFPO, chromatogram 7.

Peak no.	Area	Volume [µl]
2 (HFP)	157244.1	10
4 (HFP)	159315.5	10
6 (HFP)	155430.9	10

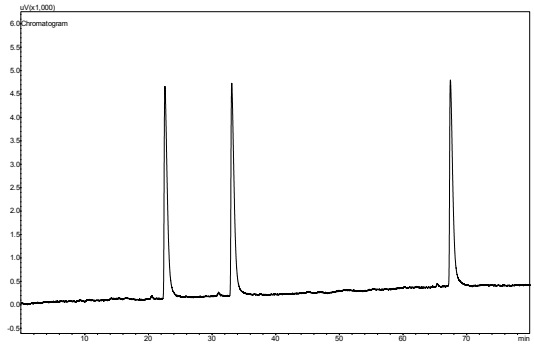

Figure I.18. Shimadzu G.C. 2010 calibration for HFPO, chromatogram 7.

Table I.19. Shimadzu G.C. 2010 calibration for C_2F_4, chromatogram 1.

Peak no.	Area	Volume [µl]
1 (C_2F_4)	619761.5	20
2 (C_2F_4)	605306.7	20
3 (C_2F_4)	601342.8	20
4 (C_2F_4)	609998.6	20
5 (C_2F_4)	596334.3	20
6 (C_2F_4)	600071	20
7 (C_2F_4)	606340.5	20
8 (C_2F_4)	441704.6	15
9 (C_2F_4)	441179.1	15
10 (C_2F_4)	474660.2	15
11 (C_2F_4)	478674.2	15
12 (C_2F_4)	444445.4	15
13 (C_2F_4)	450700	15
14 (C_2F_4)	284379.5	10
15 (C_2F_4)	280660.1	10
16 (C_2F_4)	286878.4	10
17 (C_2F_4)	291518.9	10
18 (C_2F_4)	285448.4	10
19 (C_2F_4)	285991.2	10
20 (C_2F_4)	284189.2	10
21 (C_2F_4)	136570.7	5
22 (C_2F_4)	136449.6	5
23 (C_2F_4)	138445.4	5
24 (C_2F_4)	139766	5
25 (C_2F_4)	139780.5	5
26 (C_2F_4)	138800.6	5
27 (C_2F_4)	139180.1	5

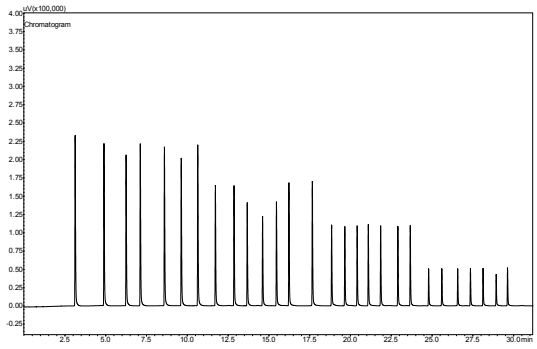

Figure I.19. Shimadzu G.C. 2010 calibration for C_2F_4, chromatogram 1.

Table I.20. Shimadzu G.C. 2010 calibration for C_2F_4, chromatogram 2.

Peak no.	Area	Volume [µl]
1 (C_2F_4)	660792.1	20
2 (C_2F_4)	657274.2	20
3 (C_2F_4)	654091.1	20
4 (C_2F_4)	643680.3	20
5 (C_2F_4)	606200.8	20
6 (C_2F_4)	649556.8	20
7 (C_2F_4)	650496.8	20
8 (C_2F_4)	471399.1	15
9 (C_2F_4)	472324.2	15
10 (C_2F_4)	482097.7	15
11 (C_2F_4)	481999.2	15
12 (C_2F_4)	472594.5	15
13 (C_2F_4)	470804.9	15
14 (C_2F_4)	477687.1	15
15 (C_2F_4)	308499.4	10
16 (C_2F_4)	300046.3	10
17 (C_2F_4)	297612.6	10
18 (C_2F_4)	292789.3	10
19 (C_2F_4)	300973.2	10
20 (C_2F_4)	292683.5	10
21 (C_2F_4)	300868.3	10
22 (C_2F_4)	140517.8	5
23 (C_2F_4)	138007.4	5
24 (C_2F_4)	139837.4	5
25 (C_2F_4)	139314.5	5
26 (C_2F_4)	138933.3	5
27 (C_2F_4)	140619.3	5
28 (C_2F_4)	140302.3	5
29 (C_2F_4)	829634.1	25
30 (C_2F_4)	823857.2	25
31 (C_2F_4)	827275.4	25
32 (C_2F_4)	827054.9	25
33 (C_2F_4)	829391.2	25
34 (C_2F_4)	826110.9	25
35 (C_2F_4)	837791	25
36 (C_2F_4)	835427.6	25
37 (C_2F_4)	822506.4	25
38 (C_2F_4)	820870.9	25
39 (C_2F_4)	826121.6	25
40 (C_2F_4)	826664.1	25
41 (C_2F_4)	821511.9	25
42 (C_2F_4)	816896.7	25

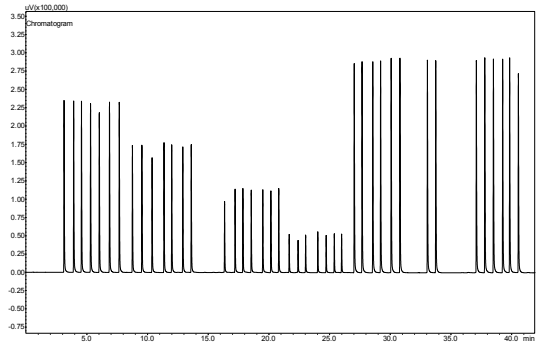

Figure I.19. Shimadzu G.C. 2010 calibration for C_2F_4, chromatogram 2.

Table I.21. Shimadzu G.C. 2010 calibration for C_2F_4, chromatogram 3.

Peak no.	Area	Volume [µl]
1 (C_2F_4)	48672.3	2.5
2 (C_2F_4)	48490.8	2.5
3 (C_2F_4)	47191.8	2.5
4 (C_2F_4)	48176.3	2.5
5 (C_2F_4)	48231.1	2.5
6 (C_2F_4)	48795.7	2.5
7 (C_2F_4)	47614.8	2.5
8 (C_2F_4)	47652.8	2.5
9 (C_2F_4)	48194.5	2.5
10 (C_2F_4)	48951.3	2.5
11 (C_2F_4)	48027.6	2.5
12 (C_2F_4)	48873.9	2.5
13 (C_2F_4)	47812	2.5
14 (C_2F_4)	47427.5	2.5

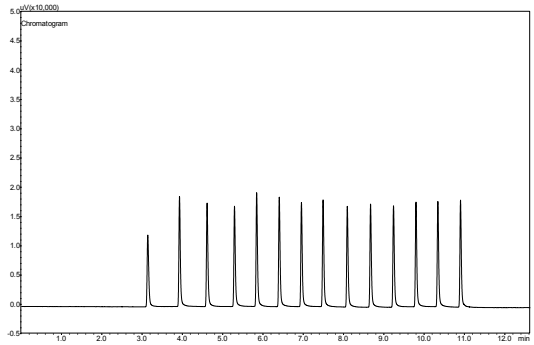

Figure I.21. Shimadzu G.C. 2010 calibration for C_2F_4, chromatogram 3.

Table I.22. Shimadzu G.C. 2010 calibration for *c*-C_3F_6, chromatogram 1.

Peak no.	Area	Volume [µl]
1 (*c*-C_3F_6)	143307.1	5
2 (*c*-C_3F_6)	109017.3	4
3 (*c*-C_3F_6)	81630	3
4 (*c*-C_3F_6)	49356.9	2
5 (*c*-C_3F_6)	108115.5	4

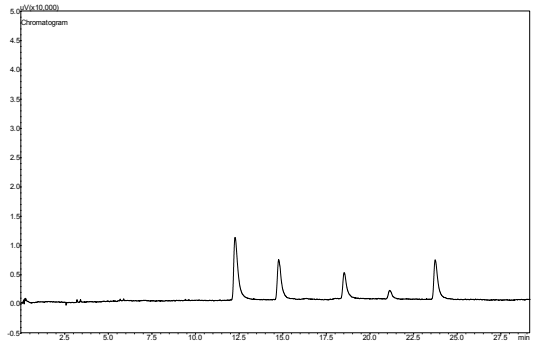

Figure I.22. Shimadzu G.C. 2010 calibration for *c*-C_3F_6, chromatogram 1.

Table I.23. Shimadzu G.C. 2010 calibration for *c*-C_3F_6, chromatogram 2.

Peak no.	Area	Volume [µl]
1 (*c*-C_3F_6)	142847.1	5
2 (*c*-C_3F_6)	109443.3	4
3 (*c*-C_3F_6)	81002	3
4 (*c*-C_3F_6)	50670.7	2
5 (*c*-C_3F_6)	109175.9	4

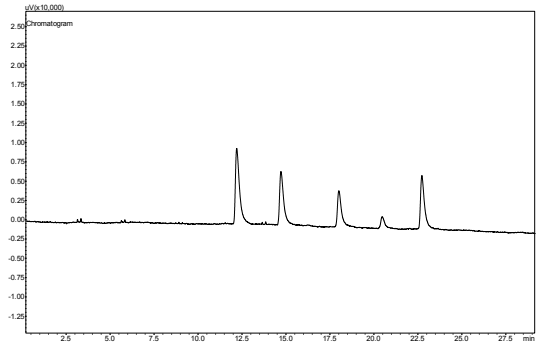

Figure I.23. Shimadzu G.C. 2010 calibration for *c*-C_3F_6, chromatogram 2.

Table I.24. Shimadzu G.C. 2010 calibration for *c*-C_3F_6, chromatogram 3.

Peak no.	Area	Volume [µl]
1 (*c*-C_3F_6)	140038.5	5
2 (*c*-C_3F_6)	106082.6	4
3 (*c*-C_3F_6)	81298.7	3
4 (*c*-C_3F_6)	50331.3	2
5 (*c*-C_3F_6)	110422.6	4

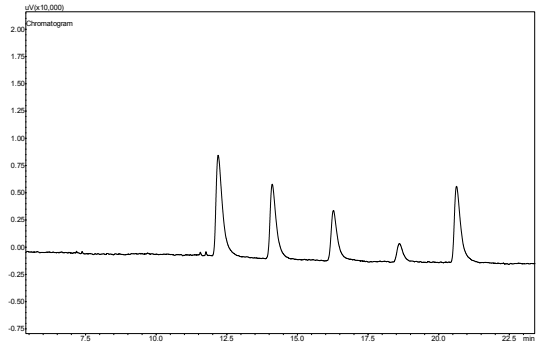

Figure I.24. Shimadzu G.C. 2010 calibration for *c*-C_3F_6, chromatogram 3.

Table I.25. Shimadzu G.C. 2010 calibration for O_2, chromatogram 1.

Peak no.	Area	Volume [µl]
1 (O_2)	73857.8	100
1 (O_2)	74309.6	100
1 (O_2)	74309.6	100

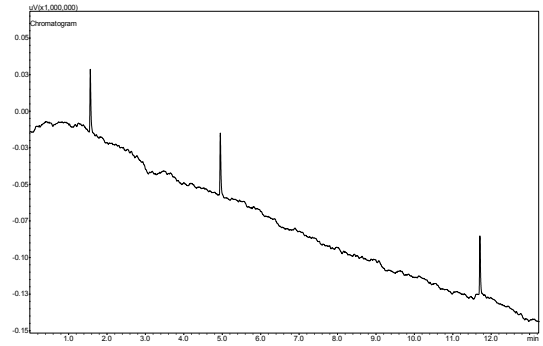

Figure I.25. Shimadzu G.C. 2010 calibration for O_2, chromatogram 1.

Table I.26. Shimadzu G.C. 2010 calibration for O_2, chromatogram 2.

Peak no.	Area	Volume [µl]
1 (O_2)	42094.5	60
2 (O_2)	42094.5	60
3 (O_2)	42375.8	60
4 (O_2)	43417.1	60
5 (O_2)	68938.6	100
6 (O_2)	28408	40
7 (O_2)	47162.7	70
8 (O_2)	48202.4	70

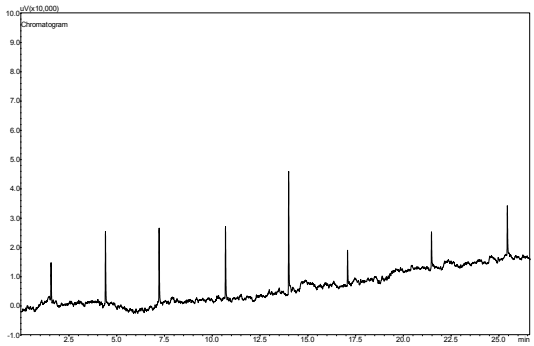

Figure I.26. Shimadzu G.C. 2010 calibration for O_2, chromatogram 2.

Table I.27. Shimadzu G.C. 2010 calibration for O_2, chromatogram 3.

Peak no.	Area	Volume [µl]
1 (O_2)	52071.9	80
1 (O_2)	51747.9	80
1 (O_2)	51938.9	80

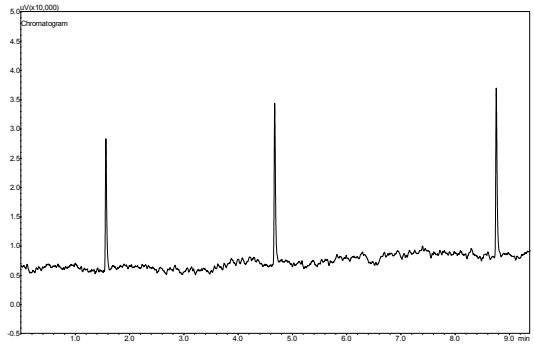

Figure I.27. Shimadzu G.C. 2010 calibration for O_2, chromatogram 3.

Table I.28. Shimadzu G.C. 2010 calibration for O_2, chromatogram 4.

Peak no.	Area	Volume [µl]
1 (O_2)	193007	300
2 (O_2)	193808.5	300
3 (O_2)	133637.3	200
4 (O_2)	131603.7	200
5 (O_2)	128785.9	200
6 (O_2)	125186.5	200
7 (O_2)	130690.4	200
8 (O_2)	192640.2	300
9 (O_2)	197741.7	300
10 (O_2)	65515.6	100
11 (O_2)	58620.3	100
12 (O_2)	61243.2	100
13 (O_2)	63347.8	100
14 (O_2)	59694.4	100
15 (O_2)	58006	80
16 (O_2)	50738.5	80
17 (O_2)	54612.2	80
18 (O_2)	58493.5	80

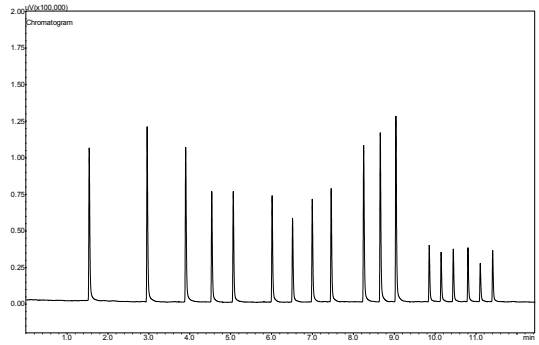

Figure I.28. Shimadzu G.C. 2010 calibration for O_2, chromatogram 4.

Table I.29. Shimadzu G.C. 2010 calibration for O_2, chromatogram 5.

Peak no.	Area	Volume [µl]
1 (O_2)	58375.2	80
2 (O_2)	54925.2	80
3 (O_2)	39777.5	60
4 (O_2)	40763	60
5 (O_2)	41771.9	60
6 (O_2)	41595	60
7 (O_2)	34446.6	60
8 (O_2)	32140.9	60
9 (O_2)	26976.8	40
10 (O_2)	27125.4	40
11 (O_2)	27326.2	40
12 (O_2)	25706.1	40
13 (O_2)	26490.4	40
14 (O_2)	27007.2	40
15 (O_2)	13179.2	20
16 (O_2)	13759.7	20
17 (O_2)	13332.8	20
18 (O_2)	13257.5	20
19 (O_2)	12206	20
20 (O_2)	13081.8	20
21 (O_2)	13321	20
22 (O_2)	47158.1	70
23 (O_2)	48980.9	70
24 (O_2)	47064.7	70
25 (O_2)	46986.6	70
26 (O_2)	48832.3	70
27 (O_2)	47696.1	70
28 (O_2)	34774.5	50
29 (O_2)	34039.8	50
30 (O_2)	33962.1	50
31 (O_2)	33795	50
32 (O_2)	33392.7	50
33 (O_2)	33362.6	50
34 (O_2)	20713.8	30
35 (O_2)	19649.2	30
36 (O_2)	20583.4	30
37 (O_2)	19922.5	30
38 (O_2)	19605.5	30
39 (O_2)	19962.6	30
40 (O_2)	39864.5	60
41 (O_2)	41787.7	60
42 (O_2)	68827.2	100
43 (O_2)	70888.1	100
44 (O_2)	70242.5	100
45 (O_2)	66826.5	100
46 (O_2)	66525.8	100
47 (O_2)	70977.8	100
48 (O_2)	124532.2	200
49 (O_2)	133305.5	200
50 (O_2)	131884.4	200

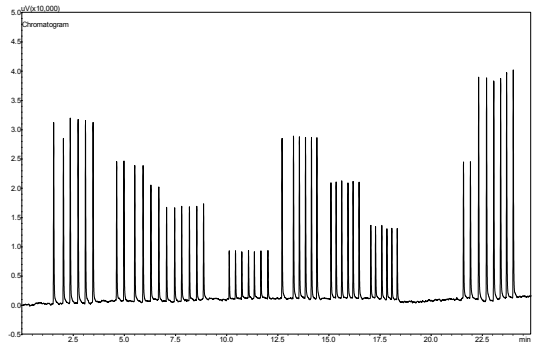

Figure I.29. Shimadzu G.C. 2010 calibration for O_2, chromatogram 5.

Table I.30. Shimadzu G.C. 2014 calibration for COF_2, chromatogram 1.

Peak no.	Area	Volume [µl]
1 (COF_2)	54285.3	60
2 (COF_2)	36651.1	40
3 (COF_2)	19279.7	20
4 (COF_2)	70004.1	80
5 (COF_2)	56433.7	60
6 (COF_2)	39730.9	40
7 (COF_2)	19971.7	20
8 (COF_2)	72352.6	80
9 (COF_2)	53235.6	60
10 (COF_2)	37022.6	40
11 (COF_2)	18643.3	20
12 (COF_2)	72456.5	80
13 (COF_2)	53576.8	60
14 (COF_2)	38295.7	40
15 (COF_2)	18933.3	20
16 (COF_2)	71519.7	80
17 (COF_2)	57471.2	60
18 (COF_2)	39559.8	40
19 (COF_2)	18504.3	20
20 (COF_2)	71356.2	80

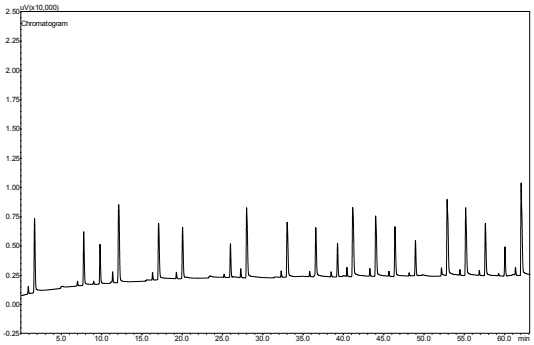

Figure I.30. Shimadzu G.C. 2014 calibration for COF_2, chromatogram 1.

Table I.31. Shimadzu G.C. 2014 calibration for CF_3COF, chromatogram 1.

Peak no.	Area	Volume [µl]
1 (O_2)	35705	24
2 (CF_3COF)	38721.2	46

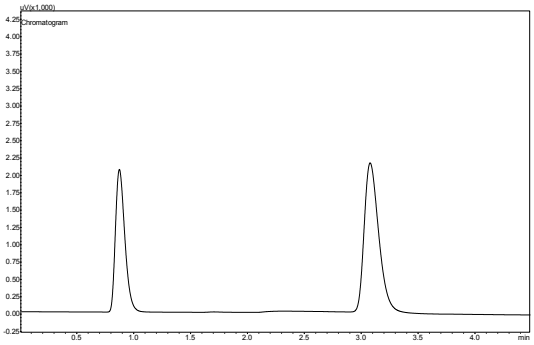

Figure I.31. Shimadzu G.C. 2014 calibration for CF_3COF, chromatogram 1.

Table I.32. Shimadzu G.C. 2014 calibration for CF_3COF, chromatogram 2.

Peak no.	Area	Volume [µl]
1 (O_2)	30358.5	21
2 (CF_3COF)	25374.7	29

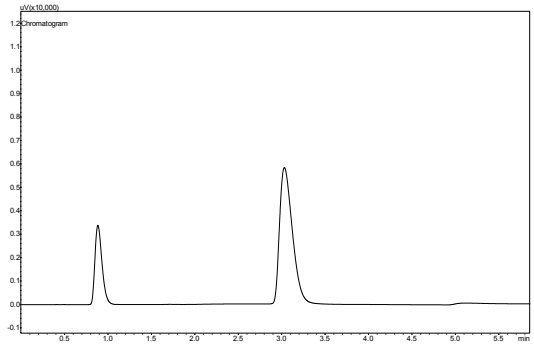

Figure I.32. Shimadzu G.C. 2014 calibration for CF_3COF, chromatogram 2.

Table I.33. Shimadzu G.C. 2014 calibration for CF_3COF, chromatogram 3.

Peak no.	Area	Volume [µl]
1 (O_2)	11750.1	8
2 (CF_3COF)	18956.7	22

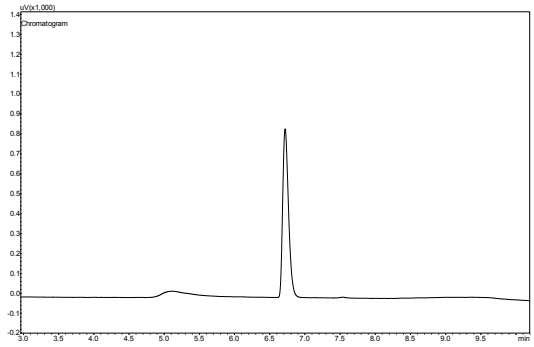

Figure I.33. Shimadzu G.C. 2014 calibration for CF_3COF, chromatogram 3.

Table I.34. Shimadzu G.C. 2014 calibration for CF_3COF, chromatogram 4.

Peak no.	Area	Volume [µl]
1 (O_2)	19206.7	13
2 (CF_3COF)	59455	67

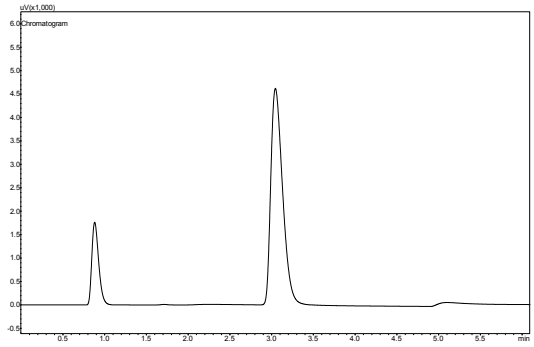

Figure I.34. Shimadzu G.C. 2014 calibration for CF_3COF, chromatogram 4.

Table I.35. Shimadzu G.C. 2014 calibration for CF_3COF, chromatogram 5.

Peak no.	Area	Volume [µl]
1 (O_2)	10033.8	7
2 (CF_3COF)	45044.5	43

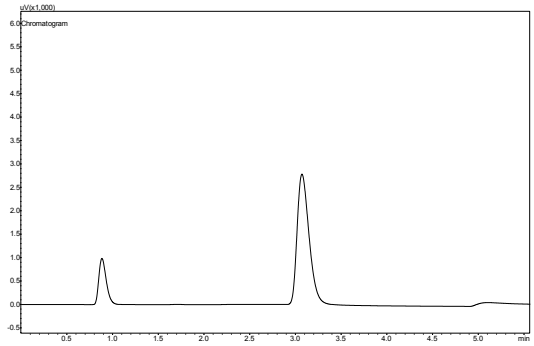

Figure I.35. Shimadzu G.C. 2014 calibration for CF_3COF, chromatogram 5.

Table I.36. Shimadzu G.C. 2014 calibration for CF_3COF, chromatogram 6.

Peak no.	Area	Volume [µl]
1 (O_2)	5565.8	4
2 (CF_3COF)	25174.5	26

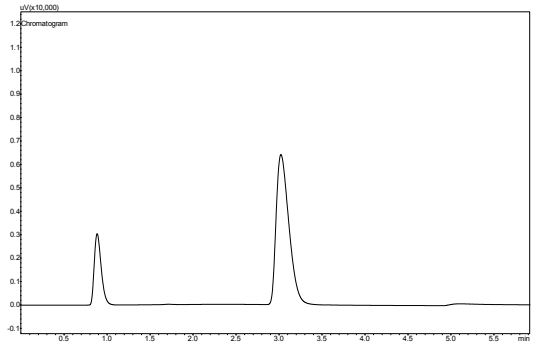

Figure I.36. Shimadzu G.C. 2014 calibration for CF_3COF, chromatogram 6.

Table I.37. Shimadzu G.C. 2014 calibration for CF_3COF, chromatogram 7.

Peak no.	Area	Volume [µl]
1 (O_2)	17148.6	12
2 (CF_3COF)	65880.1	68

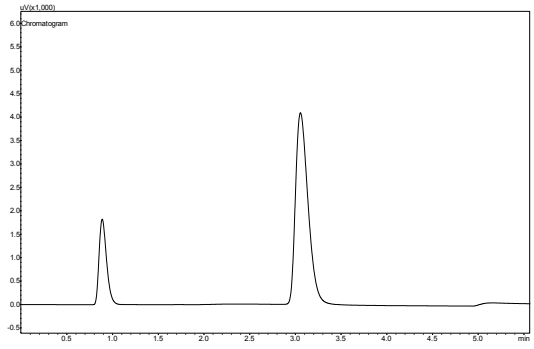

Figure I.37. Shimadzu G.C. 2014 calibration for CF_3COF, chromatogram 7.

Table I.38. Shimadzu G.C. 2014 calibration for CF_3COF, chromatogram 8.

Peak no.	Area	Volume [µl]
1 (O_2)	10401.5	7
2 (CF_3COF)	38823.2	43

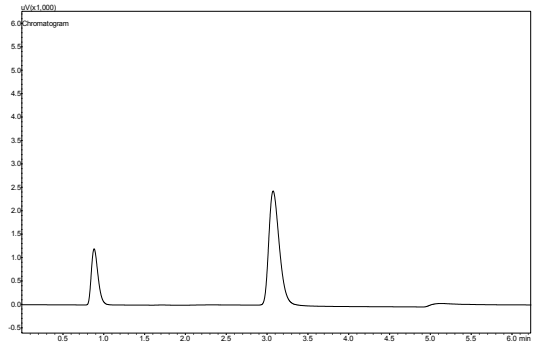

Figure I.38. Shimadzu G.C. 2014 calibration for CF_3COF, chromatogram 8.

Table I.39. Shimadzu G.C. 2014 calibration for CF_3COF, chromatogram 9.

Peak no.	Area	Volume [µl]
1 (O_2)	6823.2	5
2 (CF_3COF)	21724.6	25

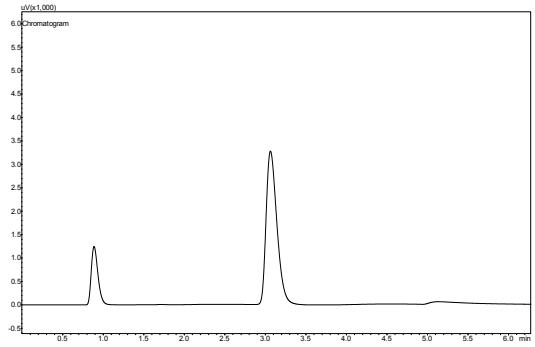

Figure I.39. Shimadzu G.C. 2014 calibration for CF_3COF, chromatogram 9.

Table I.40. Shimadzu G.C. 2014 calibration for CF_3COF, chromatogram 10.

Peak no.	Area	Volume [µl]
1 (O_2)	7090	5
2 (CF_3COF)	30076.9	35

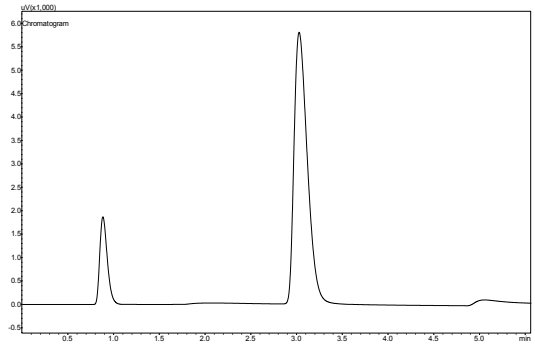

Figure I.40. Shimadzu G.C. 2014 calibration for CF_3COF, chromatogram 10.

Table I.41. Shimadzu G.C. 2014 calibration for CF_3COF, chromatogram 11.

Peak no.	Area	Volume [µl]
1 (O_2)	10672.2	7
2 (CF_3COF)	58113.2	63

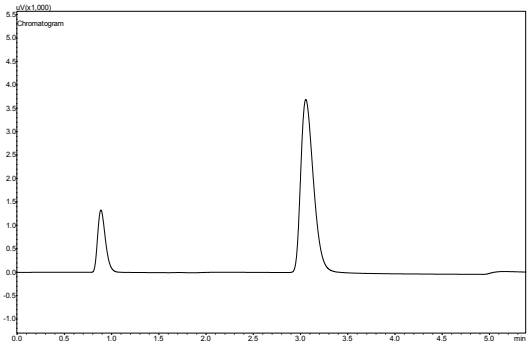

Figure I.41. Shimadzu G.C. 2014 calibration for CF_3COF, chromatogram 11.

Table I.42. Shimadzu G.C. 2014 calibration for CF_3COF, chromatogram 12.

Peak no.	Area	Volume [µl]
1 (O_2)	7642.2	5
2 (CF_3COF)	34494.9	35

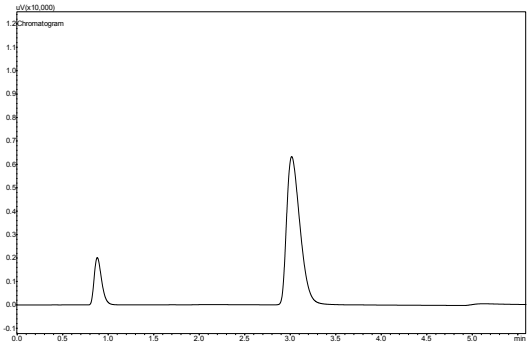

Figure I.42. Shimadzu G.C. 2014 calibration for CF_3COF, chromatogram 12.

Table I.43. Shimadzu G.C. 2014 calibration for CF_3COF, chromatogram 13.

Peak no.	Area	Volume [µl]
1 (O_2)	11450.8	8
2 (CF_3COF)	64164.4	62

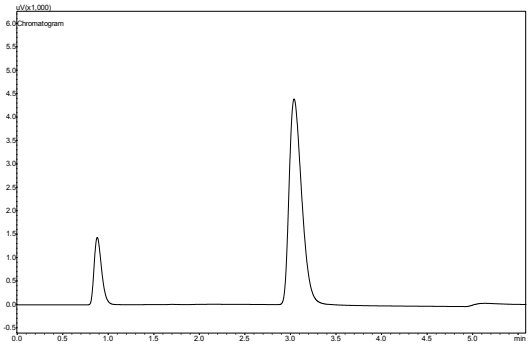

Figure I.43. Shimadzu G.C. 2014 calibration for CF_3COF, chromatogram 13.

Table I.44. Shimadzu G.C. 2014 calibration for CF_3COF, chromatogram 14.

Peak no.	Area	Volume [µl]
1 (O_2)	8190.9	6
2 (CF_3COF)	41969.2	44

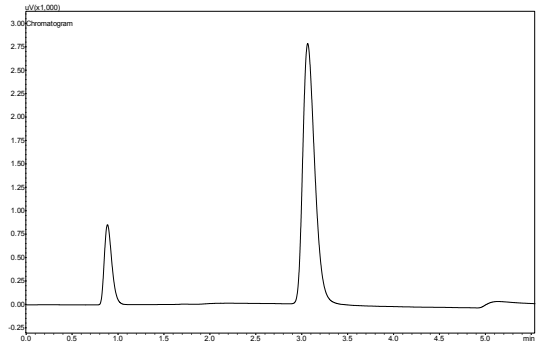

Figure I.44. Shimadzu G.C. 2014 calibration for CF_3COF, chromatogram 14.

Table I.45. Shimadzu G.C. 2014 calibration for CF_3COF, chromatogram 15.

Peak no.	Area	Volume [µl]
1 (O_2)	2874.4	2
2 (CF_3COF)	73352.8	68

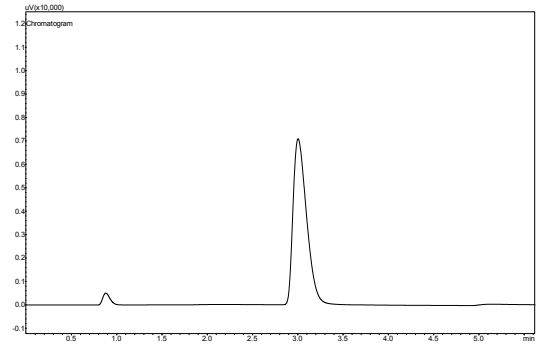

Figure I.45. Shimadzu G.C. 2014 calibration for CF_3COF, chromatogram 15.

Table I.46. Shimadzu G.C. 2014 calibration for CF_3COF, chromatogram 16.

Peak no.	Area	Volume [µl]
1 (O_2)	4879	3
2 (CF_3COF)	25024.5	27

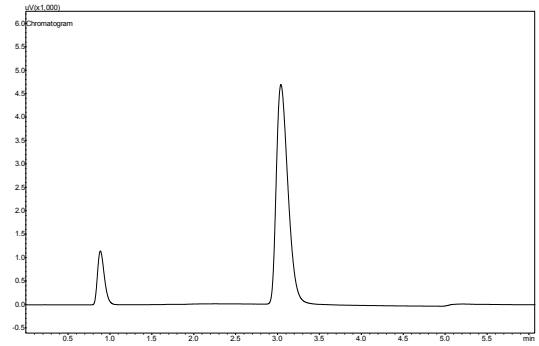

Figure I.46. Shimadzu G.C. 2014 calibration for CF_3COF, chromatogram 16.

Table I.47. Shimadzu G.C. 2014 calibration for CF_3COF, chromatogram 17.

Peak no.	Area	Volume [µl]
1 (O_2)	6545	4
2 (CF_3COF)	45176.2	46

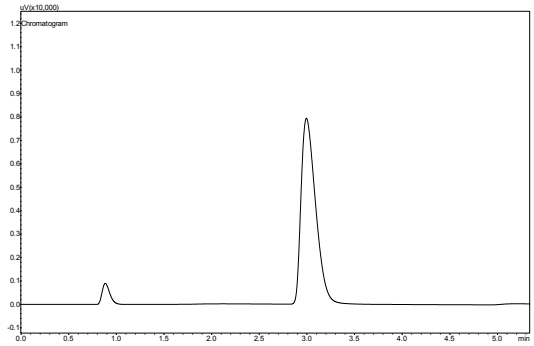

Figure I.47. Shimadzu G.C. 2014 calibration for CF_3COF, chromatogram 17.

Table I.48. Shimadzu G.C. 2014 calibration for CF_3COF, chromatogram 18.

Peak no.	Area	Volume [µl]
1 (O_2)	5061.5	3
2 (CF_3COF)	80912.4	77

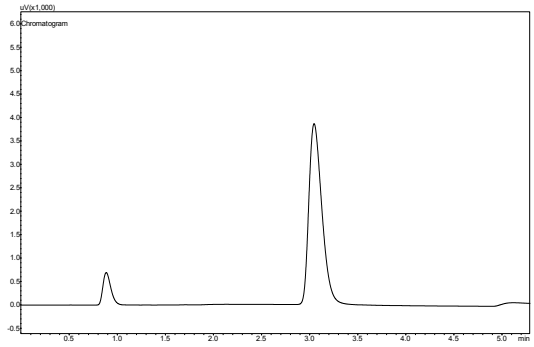

Figure I.48. Shimadzu G.C. 2014 calibration for CF_3COF, chromatogram 18.

Table I.49. Shimadzu G.C. 2014 calibration for CF_3COF, chromatogram 19.

Peak no.	Area	Volume [µl]
1 (O_2)	3967.5	3
2 (CF_3COF)	36075.5	37

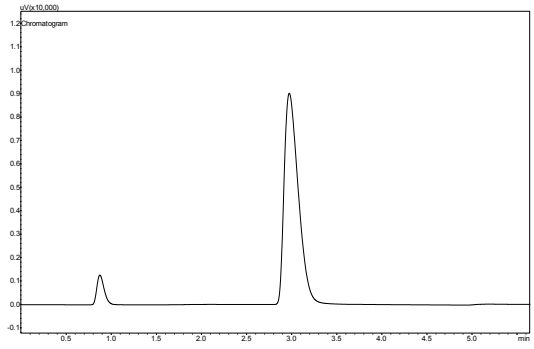

Figure I.49. Shimadzu G.C. 2014 calibration for CF_3COF, chromatogram 19.

Table I.50. Shimadzu G.C. 2014 calibration for O_2, chromatogram 1.

Peak no.	Area	Volume [µl]
1 (O_2)	111719.7	80
2 (O_2)	82032.5	60
3 (O_2)	51849.9	40
4 (O_2)	28149.2	20
5 (O_2)	98728.1	70
6 (O_2)	70483.8	50
7 (O_2)	43403.7	30
8 (O_2)	113710	80
9 (O_2)	82115.3	60
10 (O_2)	55888.8	40
11 (O_2)	27229.7	20

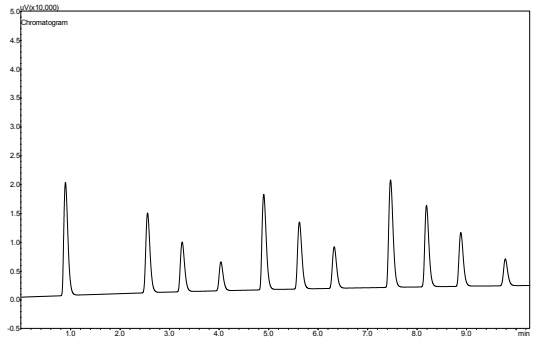

Figure I.50. Shimadzu G.C. 2014 calibration for O_2, chromatogram 1.

Table I.51. Shimadzu G.C. 2014 calibration for O_2, chromatogram 2.

Peak no.	Area	Volume [µl]
1 (O_2)	117419.5	80
2 (O_2)	83072.6	60
3 (O_2)	55662.6	40
4 (O_2)	28053.6	20
5 (O_2)	95066.7	70
6 (O_2)	70408.4	50
7 (O_2)	40213.7	30

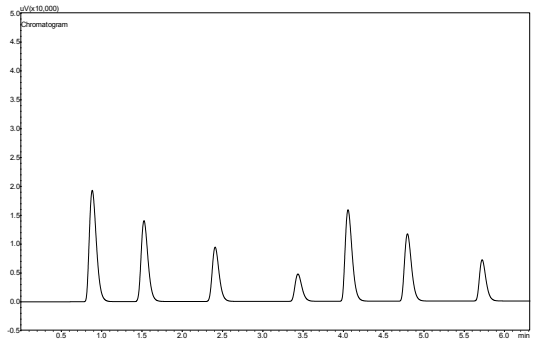

Figure I.51. Shimadzu G.C. 2014 calibration for O_2, chromatogram 2.

Table I.52. Shimadzu G.C. 2014 calibration for O_2, chromatogram 3.

Peak no.	Area	Volume [µl]
1 (O_2)	114743.2	80
2 (O_2)	84286.4	60
3 (O_2)	56805.3	40
4 (O_2)	28644.4	20
5 (O_2)	112182.3	80
6 (O_2)	82918.5	60
7 (O_2)	55809.1	40
8 (O_2)	28293.3	20
9 (O_2)	112306.2	80
10 (O_2)	84137	60
11 (O_2)	55269.3	40
12 (O_2)	28702.4	20

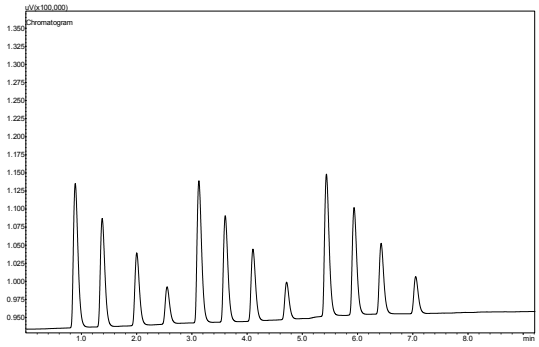

Figure I.52. Shimadzu G.C. 2014 calibration for O_2, chromatogram 3.

Table I.53. Shimadzu G.C. 2014 calibration for O_2, chromatogram 4.

Peak no.	Area	Volume [µl]
1 (O_2)	113755.3	80
2 (O_2)	83892.6	60
3 (O_2)	56090.5	40
4 (O_2)	28637.1	20
5 (O_2)	112538.2	80
6 (O_2)	83998.5	60
7 (O_2)	55792.4	40
8 (O_2)	28640.2	20
9 (O_2)	112254.3	80
10 (O_2)	83732.8	60
11 (O_2)	55845.3	40
12 (O_2)	28531.6	20

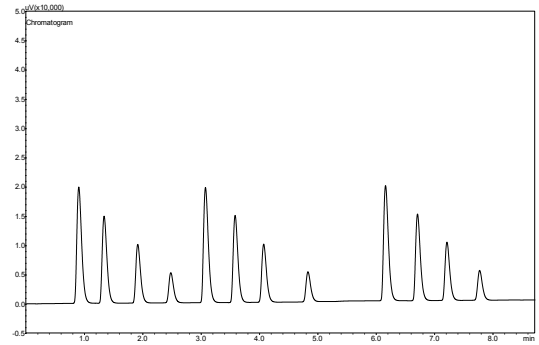

Figure I.53. Shimadzu G.C. 2014 calibration for O_2, chromatogram 4.

Table I.54. Shimadzu G.C. 2010 FID chromatogram, experiment 3a.

Component	Peak area
O_2	-
COF_2	-
CF_3COF	-
C_2F_4	-
c-C_3F_6	-
HFP	9035601.5
HFPO	500640.9

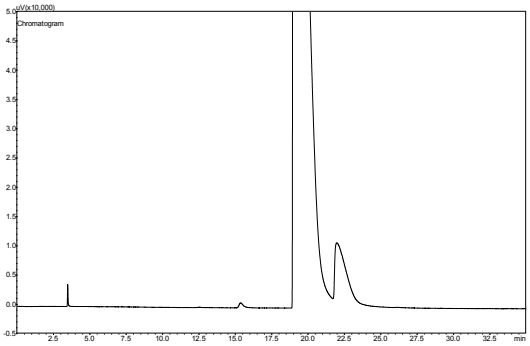

Figure I.54. Shimadzu G.C. 2010 FID chromatogram, experiment 3a.

Table I.55. Shimadzu G.C. 2010 FID chromatogram, experiment 4a.

Component	Peak area
O_2	-
COF_2	-
CF_3COF	-
C_2F_4	-
c-C_3F_6	-
HFP	8841468.6
HFPO	394122.7

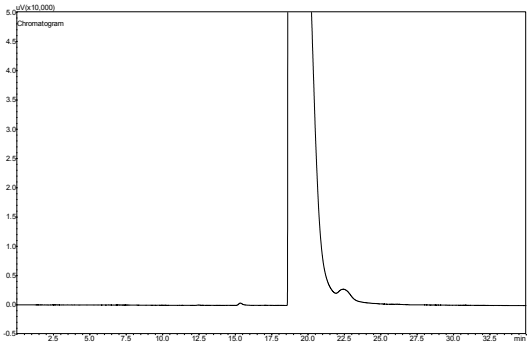

Figure I.55. Shimadzu G.C. 2010 FID chromatogram, experiment 4a.

Table I.56. Shimadzu G.C. 2010 FID chromatogram, experiment 4c.

Component	Peak area
O_2	-
COF_2	-
CF_3COF	-
C_2F_4	-
c-C_3F_6	-
HFP	14746964
HFPO	0

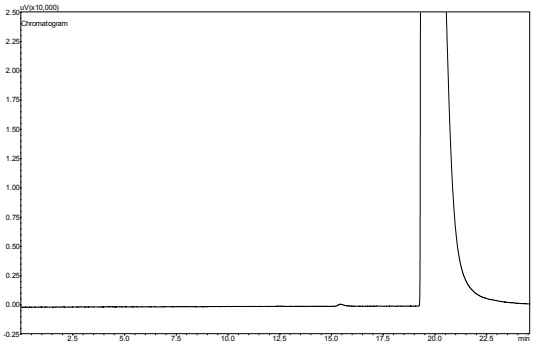

Figure I.56. Shimadzu G.C. 2010 FID chromatogram, experiment 4c.

Table I.57. Shimadzu G.C. 2010 FID chromatogram, experiment 7a.

Component	Peak area
O_2	-
COF_2	-
CF_3COF	-
C_2F_4	76525
c-C_3F_6	20576.3
HFP	3209036
HFPO	1162601

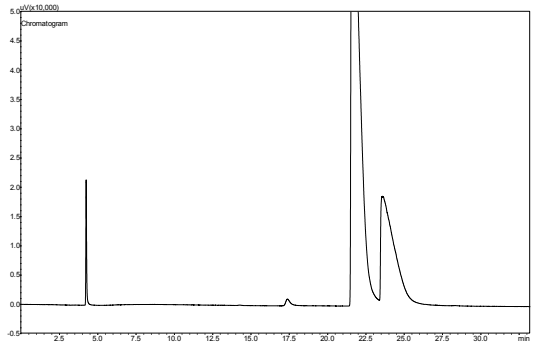

Figure I.57. Shimadzu G.C. 2010 FID chromatogram, experiment 7a.

Table I.58. Shimadzu G.C. 2010 FID chromatogram, experiment 8a.

Component	Peak area
O_2	-
COF_2	-
CF_3COF	-
C_2F_4	159740
c-C_3F_6	61326.8
HFP	361598.6
HFPO	720833.9

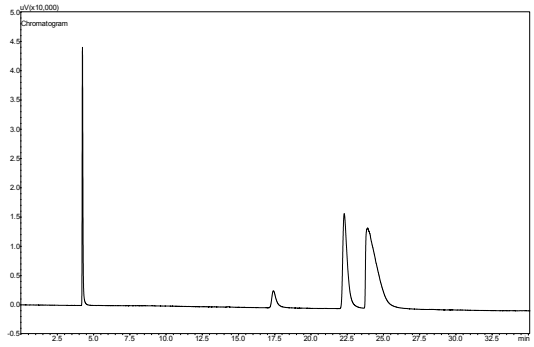

Figure I.58. Shimadzu G.C. 2010 FID chromatogram, experiment 8a.

Table I.59. Shimadzu G.C. 2010 FID chromatogram, experiment 9b.

Component	Peak area
O_2	-
COF_2	-
CF_3COF	-
C_2F_4	862.6
c-C_3F_6	10946.3
HFP	3191092
HFPO	272877.2

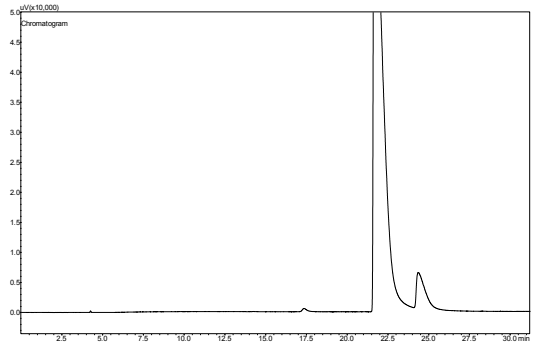

Figure I.59. Shimadzu G.C. 2010 FID chromatogram, experiment 9b.

Table I.60. Shimadzu G.C. 2010 FID chromatogram, experiment 9c.

Component	Peak area
O_2	-
COF_2	-
CF_3COF	-
C_2F_4	347.1
c-C_3F_6	4545.2
HFP	6677721
HFPO	194078.6

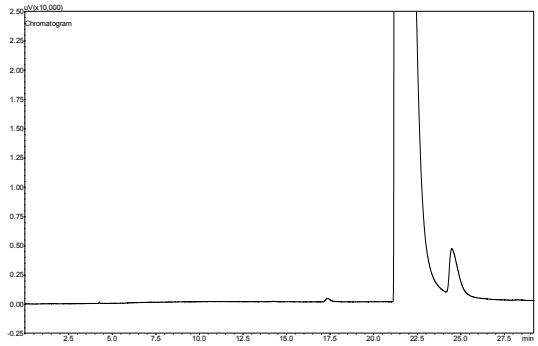

Figure I.60. Shimadzu G.C. 2010 FID chromatogram, experiment 9c.

Table I.61. Shimadzu G.C. 2010 FID chromatogram, experiment 20a.

Component	Peak area
O_2	-
COF_2	-
CF_3COF	-
C_2F_4	939.8
c-C_3F_6	7064.8
HFP	6838197.3
HFPO	832634.5

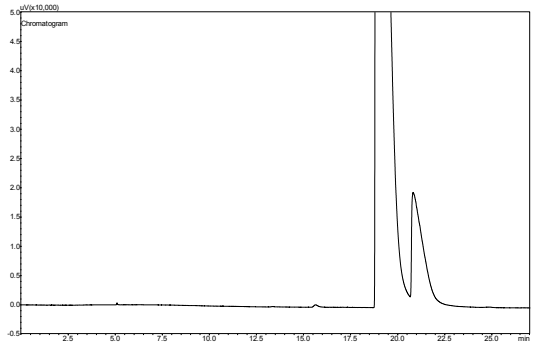

Figure I.61. Shimadzu G.C. 2010 FID chromatogram, experiment 20a.

Table I.62. Shimadzu G.C. 2010 FID chromatogram, experiment 20b.

Component	Peak area
O_2	-
COF_2	-
CF_3COF	-
C_2F_4	632.1
c-C_3F_6	3997.2
HFP	2379468
HFPO	653524.3

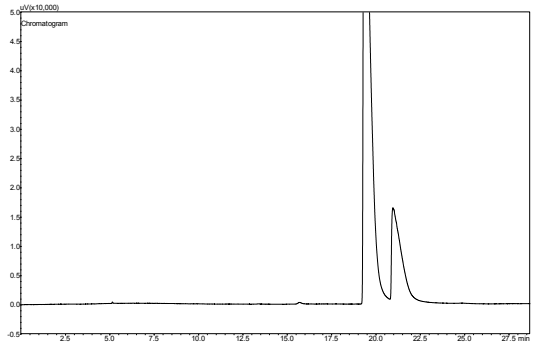

Figure I.62. Shimadzu G.C. 2010 FID chromatogram, experiment 20b.

Table I.63. Shimadzu G.C. 2010 FID chromatogram, experiment 21a.

Component	Peak area
O_2	-
COF_2	-
CF_3COF	-
C_2F_4	1507.8
c-C_3F_6	7310.3
HFP	6384666
HFPO	1122630

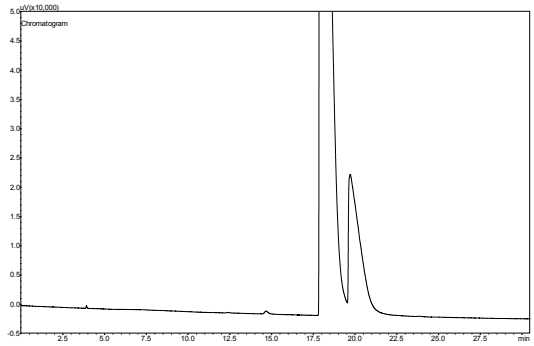

Figure I.63. Shimadzu G.C. 2010 FID chromatogram, experiment 21a.

Table I.64. Shimadzu G.C. 2010 FID chromatogram, experiment 21b.

Component	Peak area
O_2	-
COF_2	-
CF_3COF	-
C_2F_4	1997.5
c-C_3F_6	8775.2
HFP	7440764.2
HFPO	1254234.8

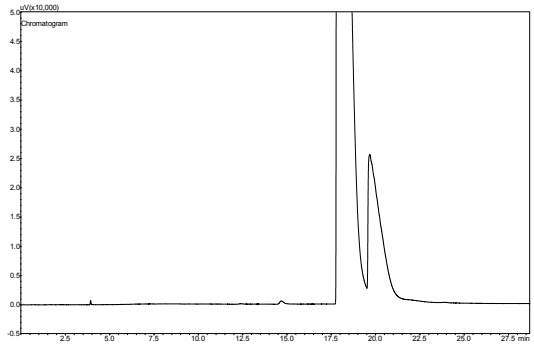

Figure I.64. Shimadzu G.C. 2010 FID chromatogram, experiment 21b.

Table I.65. Shimadzu G.C. 2010 FID chromatogram, experiment 21c.

Component	Peak area
O_2	-
COF_2	-
CF_3COF	-
C_2F_4	639
c-C_3F_6	3727
HFP	2216207.8
HFPO	342040.8

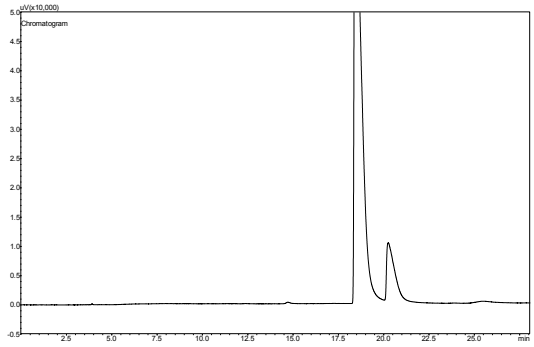

Figure I.65. Shimadzu G.C. 2010 FID chromatogram, experiment 21c.

Table I.66. Shimadzu G.C. 2010 FID chromatogram, experiment 22a.

Component	Peak area
O_2	-
COF_2	-
CF_3COF	-
C_2F_4	76452.2
c-C_3F_6	20496.7
HFP	126397.2
HFPO	845937.3

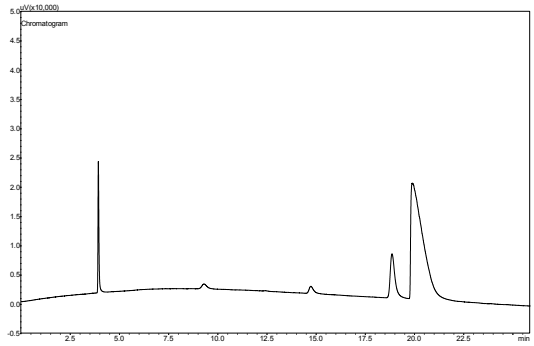

Figure I.66. Shimadzu G.C. 2010 FID chromatogram, experiment 22a.

Table I.67. Shimadzu G.C. 2010 FID chromatogram, experiment 22b.

Component	Peak area
O_2	-
COF_2	-
CF_3COF	-
C_2F_4	1374.4
c-C_3F_6	7021.4
HFP	4980848.5
HFPO	1008912.5

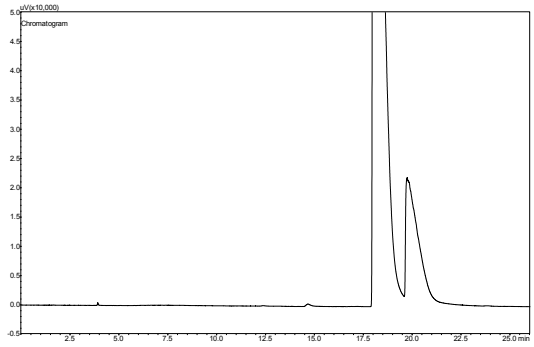

Figure I.67. Shimadzu G.C. 2010 FID chromatogram, experiment 22b.

Table I.68. Shimadzu G.C. 2010 FID chromatogram, experiment 22c.

Component	Peak area
O_2	-
COF_2	-
CF_3COF	-
C_2F_4	145
c-C_3F_6	5426.6
HFP	9151723.8
HFPO	424370.5

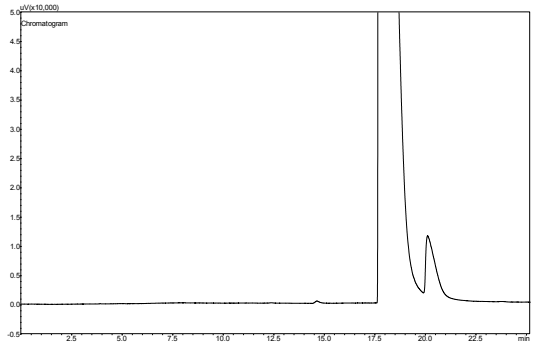

Figure I.68. Shimadzu G.C. 2010 FID chromatogram, experiment 22c.

Table I.69. Shimadzu G.C. 2010 FID chromatogram, experiment 22d.

Component	Peak area
O_2	-
COF_2	-
CF_3COF	-
C_2F_4	1458.7
c-C_3F_6	7224.6
HFP	4543178.1
HFPO	1070854.7

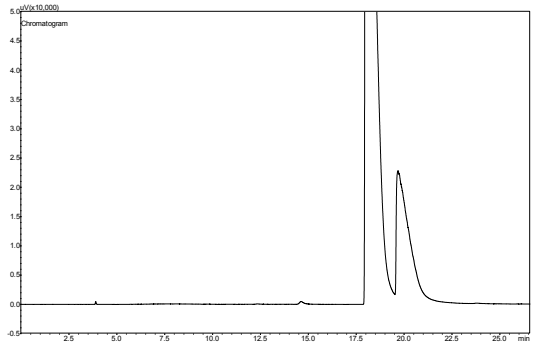

Figure I.69. Shimadzu G.C. 2010 FID chromatogram, experiment 22d.

Table I.70. Shimadzu G.C. 2010 FID chromatogram, experiment 23a.

Component	Peak area
O_2	-
COF_2	-
CF_3COF	-
C_2F_4	84.8
c-C_3F_6	6464.7
HFP	50676.6
HFPO	1046760.6

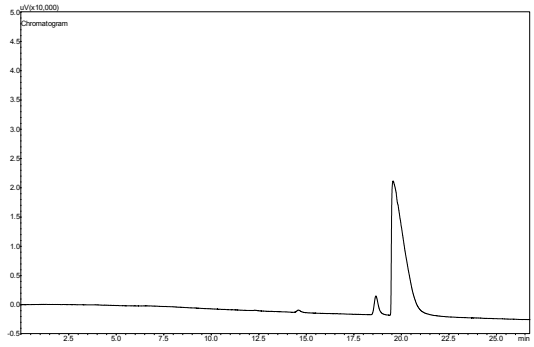

Figure I.70. Shimadzu G.C. 2010 FID chromatogram, experiment 23a.

Table I.71. Shimadzu G.C. 2010 FID chromatogram, experiment 23b.

Component	Peak area
O_2	-
COF_2	-
CF_3COF	-
C_2F_4	1088.9
c-C_3F_6	5877.2
HFP	4781799
HFPO	1014438.9

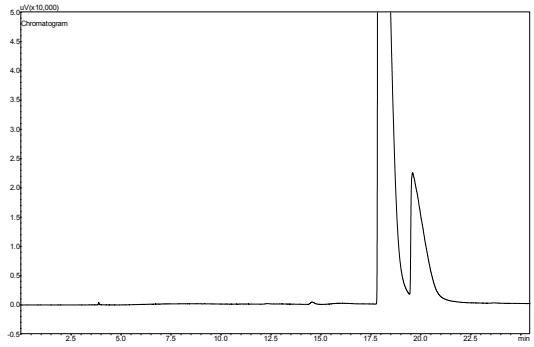

Figure I.71. Shimadzu G.C. 2010 FID chromatogram, experiment 23b.

Table I.72. Shimadzu G.C. 2010 FID chromatogram, experiment 23c.

Component	Peak area
O_2	-
COF_2	-
CF_3COF	-
C_2F_4	-
c-C_3F_6	5791.2
HFP	10040592
HFPO	262558.9

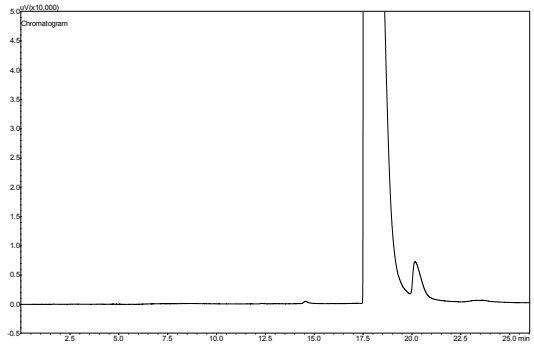

Figure I.72. Shimadzu G.C. 2010 FID chromatogram, experiment 23c.

Table I.73. Shimadzu G.C. 2010 FID chromatogram, experiment 24a.

Component	Peak area
O_2	-
COF_2	-
CF_3COF	-
C_2F_4	3478.5
c-C_3F_6	10444.1
HFP	7056463
HFPO	1132029

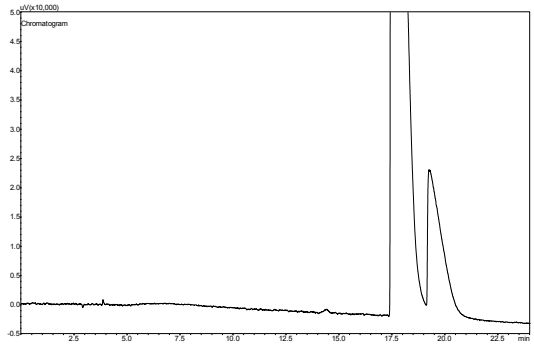

Figure I.73. Shimadzu G.C. 2010 FID chromatogram, experiment 24a.

Table I.74. Shimadzu G.C. 2010 FID chromatogram, experiment 24b.

Component	Peak area
O_2	-
COF_2	-
CF_3COF	-
C_2F_4	358.1
c-C_3F_6	2060.4
HFP	2314330
HFPO	268101.3

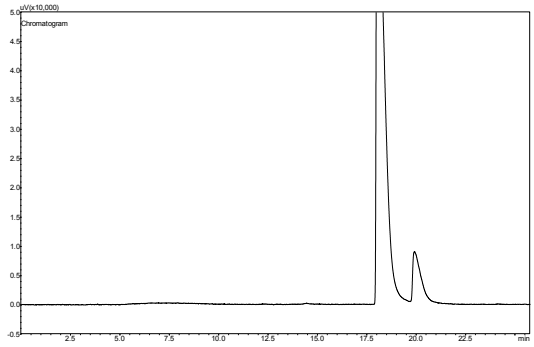

Figure I.74. Shimadzu G.C. 2010 FID chromatogram, experiment 24b.

Table I.75. Shimadzu G.C. 2010 FID chromatogram, experiment 24c.

Component	Peak area
O_2	-
COF_2	-
CF_3COF	-
C_2F_4	-
c-C_3F_6	3340.8
HFP	6665664
HFPO	179050.9

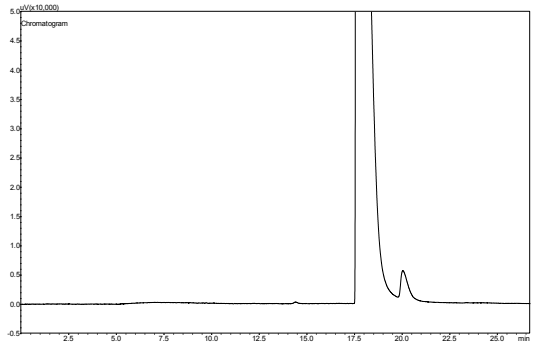

Figure I.75. Shimadzu G.C. 2010 FID chromatogram, experiment 24c.

Table I.76. Shimadzu G.C. 2010 FID chromatogram, experiment 25a.

Component	Peak area
O_2	-
COF_2	-
CF_3COF	-
C_2F_4	202.9
c-C_3F_6	5989.8
HFP	8780437
HFPO	283687.3

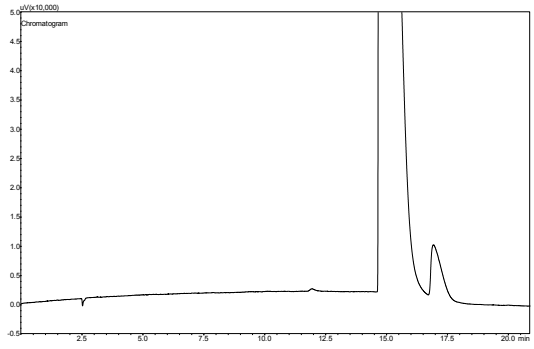

Figure I.76. Shimadzu G.C. 2010 FID chromatogram, experiment 25a.

Table I.77. Shimadzu G.C. 2014 TCD chromatogram, experiment 25a.

Component	Peak area
O_2	77524.1
COF_2	5261.6
CF_3COF	-
C_2F_4	-
c-C_3F_6	-
HFP	-
HFPO	-

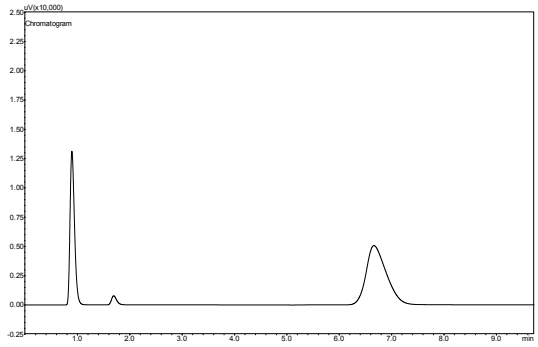

Figure I.77. Shimadzu G.C. 2014 TCD chromatogram, experiment 25a.

Table I.78. Shimadzu G.C. 2010 FID chromatogram, experiment 25b.

Component	Peak area
O_2	-
COF_2	-
CF_3COF	-
C_2F_4	303.7
c-C_3F_6	6080.6
HFP	9265832.9
HFPO	288381

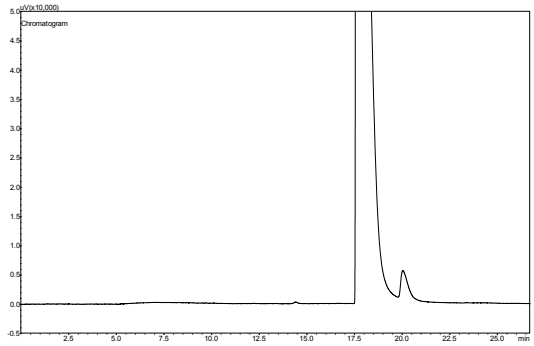

Figure I.78. Shimadzu G.C. 2010 FID chromatogram, experiment 25b.

Table I.79. Shimadzu G.C. 2014 TCD chromatogram, experiment 25b.

Component	Peak area
O_2	59212.3
COF_2	6317.1
CF_3COF	-
C_2F_4	-
c-C_3F_6	-
HFP	-
HFPO	-

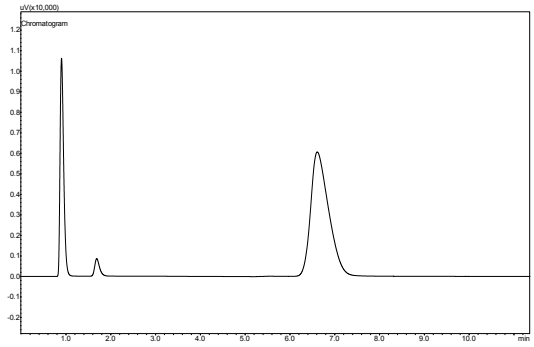

Figure I.79. Shimadzu G.C. 2014 TCD chromatogram, experiment 25b.

Table I.80. Shimadzu G.C. 2010 FID chromatogram, experiment 25c.

Component	Peak area
O_2	-
COF_2	-
CF_3COF	-
C_2F_4	1324.1
c-C_3F_6	6988.1
HFP	3953857.3
HFPO	1013540.5

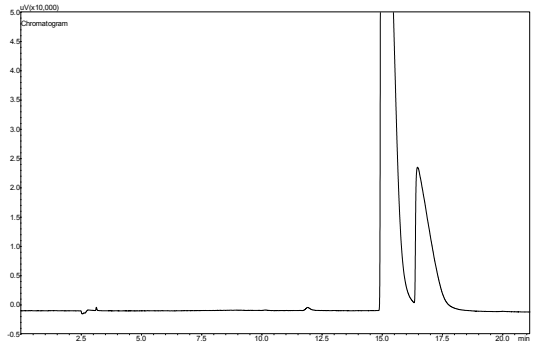

Figure I.80. Shimadzu G.C. 2010 FID chromatogram, experiment 25c.

Table I.81. Shimadzu G.C. 2014 TCD chromatogram, experiment 25c.

Component	Peak area
O_2	24531.9
COF_2	28383.2
CF_3COF	11653.1
C_2F_4	-
c-C_3F_6	-
HFP	-
HFPO	-

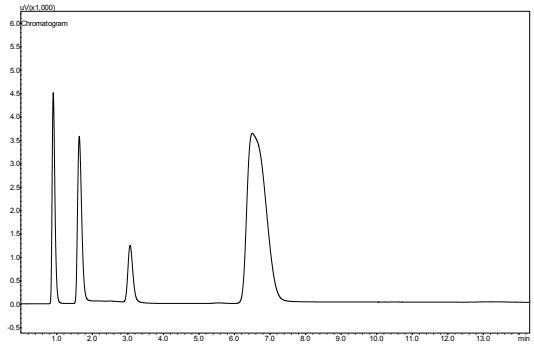

Figure I.81. Shimadzu G.C. 2014 TCD chromatogram, experiment 25c.

Table I.82. Shimadzu G.C. 2010 FID chromatogram, experiment 25d.

Component	Peak area
O_2	-
COF_2	-
CF_3COF	-
C_2F_4	2565.5
c-C_3F_6	6764.8
HFP	4609651.1
HFPO	1284412

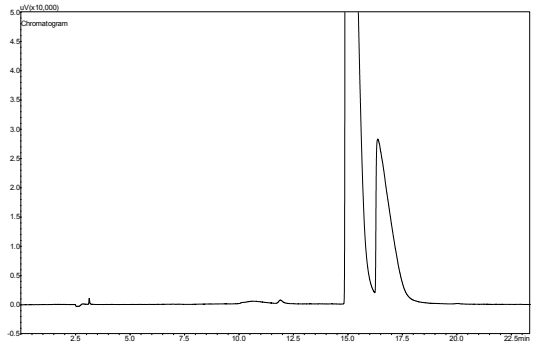

Figure I.82. Shimadzu G.C. 2010 FID chromatogram, experiment 25d.

Table I.83. Shimadzu G.C. 2014 TCD chromatogram, experiment 25d.

Component	Peak area
O_2	6967.7
COF_2	33533.3
CF_3COF	15279.3
C_2F_4	-
c-C_3F_6	-
HFP	-
HFPO	-

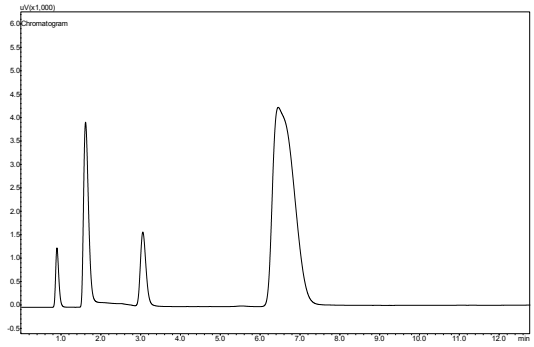

Figure I.83. Shimadzu G.C. 2014 TCD chromatogram, experiment 25d.

Table I.84. Shimadzu G.C. 2010 FID chromatogram, experiment 25e.

Component	Peak area
O_2	-
COF_2	-
CF_3COF	-
C_2F_4	1382.7
c-C_3F_6	5565.3
HFP	4072366.4
HFPO	986676.2

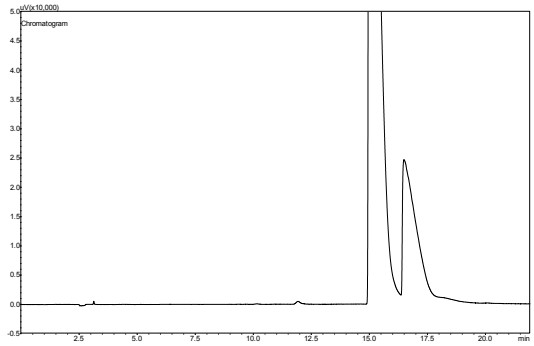

Figure I.84. Shimadzu G.C. 2010 FID chromatogram, experiment 25e.

Table I.85. Shimadzu G.C. 2014 TCD chromatogram, experiment 25e.

Component	Peak area
O_2	23807.6
COF_2	32092.9
CF_3COF	14410.7
C_2F_4	-
c-C_3F_6	-
HFP	-
HFPO	-

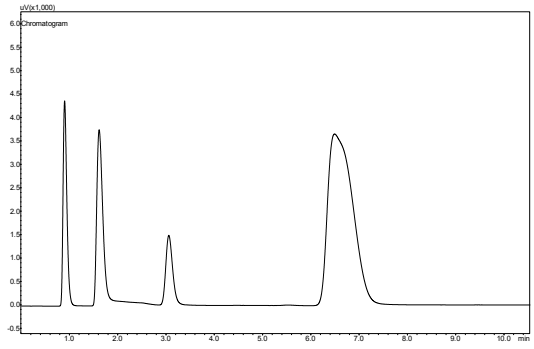

Figure I.85. Shimadzu G.C. 2014 TCD chromatogram, experiment 25e.

Table I.86. Shimadzu G.C. 2010 FID chromatogram, experiment 25f.

Component	Peak area
O_2	-
COF_2	-
CF_3COF	-
C_2F_4	74391.7
c-C_3F_6	18824.2
HFP	69120.1
HFPO	795017

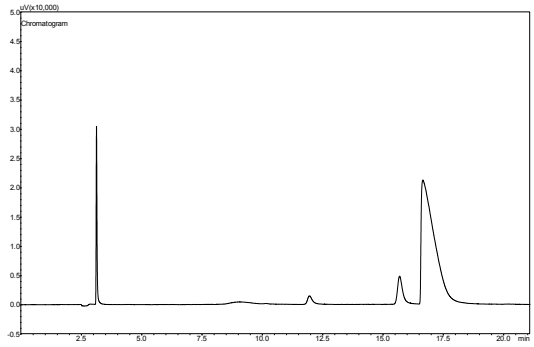

Figure I.86. Shimadzu G.C. 2010 FID chromatogram, experiment 25f.

Table I.87. Shimadzu G.C. 2014 TCD chromatogram, experiment 25f.

Component	Peak area
O_2	1253
COF_2	57332.4
CF_3COF	34400.1
C_2F_4	-
c-C_3F_6	-
HFP	-
HFPO	-

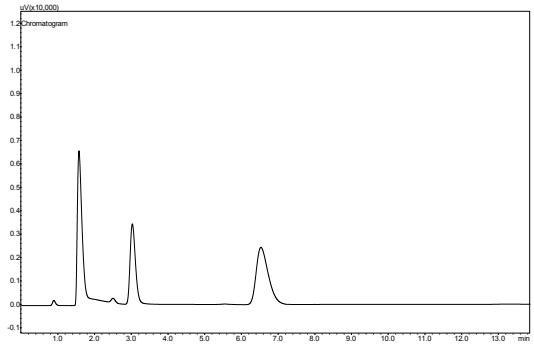

Figure I.87. Shimadzu G.C. 2014 TCD chromatogram, experiment 25f.

Table I.88. Shimadzu G.C. 2010 FID chromatogram, experiment 25g.

Component	Peak area
O_2	-
COF_2	-
CF_3COF	-
C_2F_4	1770
c-C_3F_6	5977.6
HFP	3568544.2
HFPO	1097908.1

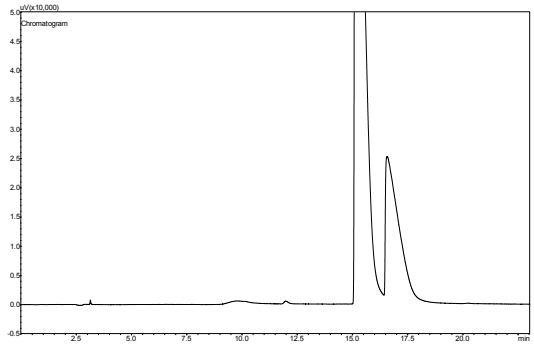

Figure I.88. Shimadzu G.C. 2010 FID chromatogram, experiment 25g.

Table I.89. Shimadzu G.C. 2014 TCD chromatogram, experiment 25g.

Component	Peak area
O_2	22194.8
COF_2	35000.3
CF_3COF	15407.8
C_2F_4	-
c-C_3F_6	-
HFP	-
HFPO	-

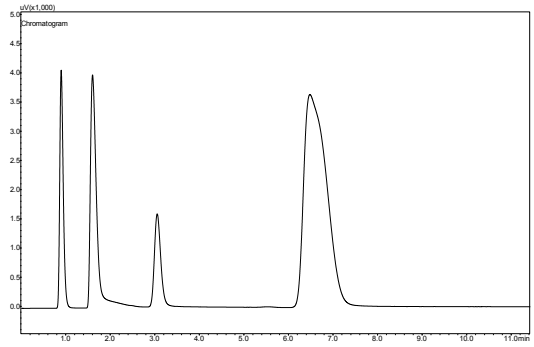

Figure I.89. Shimadzu G.C. 2014 TCD chromatogram, experiment 25g.

Table I.90. Shimadzu G.C. 2010 FID chromatogram, experiment 26a.

Component	Peak area
O_2	-
COF_2	-
CF_3COF	-
C_2F_4	506.3
c-C_3F_6	1574.9
HFP	2957674.7
HFPO	482085

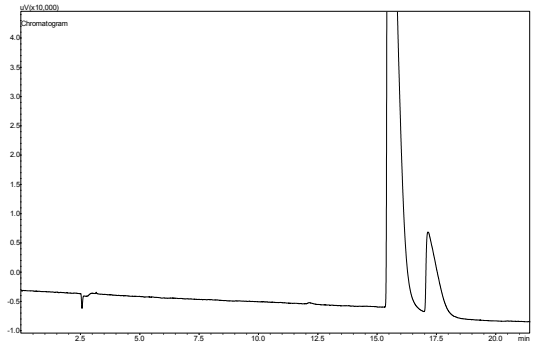

Figure I.90. Shimadzu G.C. 2010 FID chromatogram, experiment 26a.

Table I.91. Shimadzu G.C. 2014 TCD chromatogram, experiment 26a.

Component	Peak area
O_2	74063.6
COF_2	19520.2
CF_3COF	-
C_2F_4	-
c-C_3F_6	-
HFP	-
HFPO	-

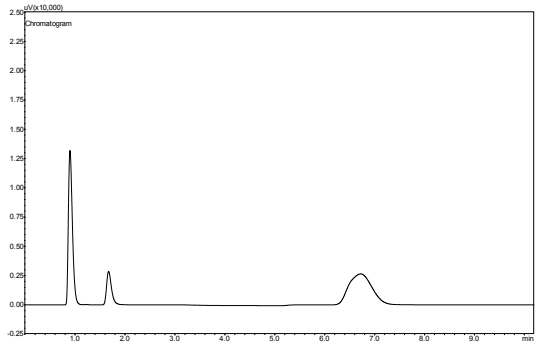

Figure I.91. Shimadzu G.C. 2014 TCD chromatogram, experiment 26a.

Table I.92. Shimadzu G.C. 2010 FID chromatogram, experiment 26b.

Component	Peak area
O_2	-
COF_2	-
CF_3COF	-
C_2F_4	254.1
c-C_3F_6	1832.3
HFP	1823520.3
HFPO	216921.6

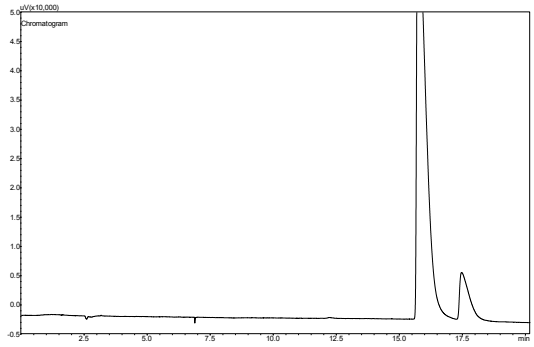

Figure I.92. Shimadzu G.C. 2010 FID chromatogram, experiment 26b.

Table I.93. Shimadzu G.C. 2014 TCD chromatogram, experiment 26b.

Component	Peak area
O_2	110136.3
COF_2	10946.9
CF_3COF	-
C_2F_4	-
c-C_3F_6	-
HFP	-
HFPO	-

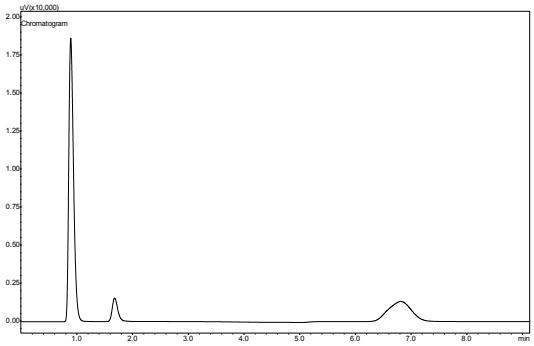

Figure I.93. Shimadzu G.C. 2014 TCD chromatogram, experiment 26b.

Table I.94. Shimadzu G.C. 2010 FID chromatogram, experiment 26c.

Component	Peak area
O_2	-
COF_2	-
CF_3COF	-
C_2F_4	111.3
c-C_3F_6	3940.1
HFP	6971138.7
HFPO	127520.1

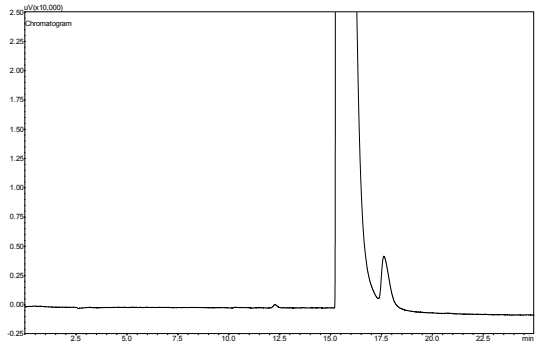

Figure I.94. Shimadzu G.C. 2010 FID chromatogram, experiment 26c.

Table I.95. Shimadzu G.C. 2014 TCD chromatogram, experiment 26c.

Component	Peak area
O_2	85377.8
COF_2	3214.3
CF_3COF	-
C_2F_4	-
c-C_3F_6	-
HFP	-
HFPO	-

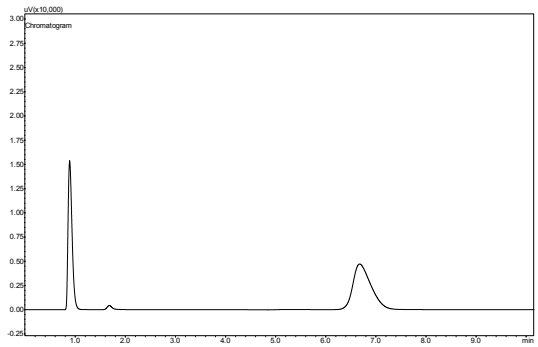

Figure I.95. Shimadzu G.C. 2014 TCD chromatogram, experiment 26c.

Table I.96. Shimadzu G.C. 2010 FID chromatogram, experiment 26d.

Component	Peak area
O_2	-
COF_2	-
CF_3COF	-
C_2F_4	-
c-C_3F_6	5087.6
HFP	10043062.1
HFPO	202377.9

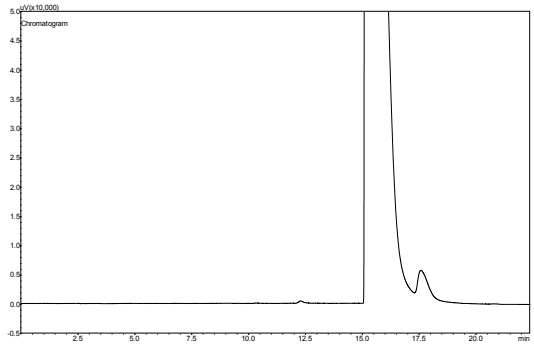

Figure I.96. Shimadzu G.C. 2010 FID chromatogram, experiment 26d.

Table I.97. Shimadzu G.C. 2014 TCD chromatogram, experiment 26d.

Component	Peak area
O_2	63794.1
COF_2	3408.1
CF_3COF	-
C_2F_4	-
c-C_3F_6	-
HFP	-
HFPO	-

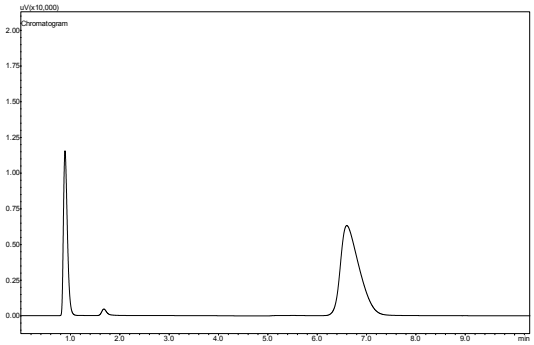

Figure I.97. Shimadzu G.C. 2014 TCD chromatogram, experiment 26d.

Table I.98. Shimadzu G.C. 2010 FID chromatogram, experiment 26e.

Component	Peak area
O_2	-
COF_2	-
CF_3COF	-
C_2F_4	3657.2
c-C_3F_6	7669.8
HFP	6287919.9
HFPO	1284894.9

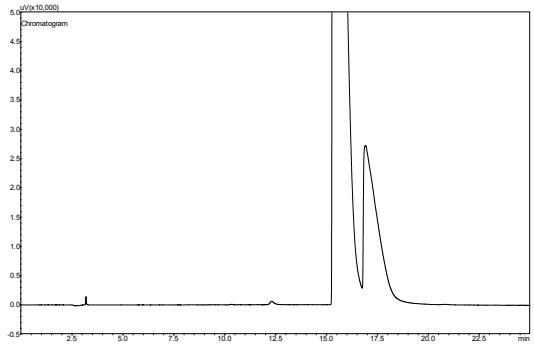

Figure I.98. Shimadzu G.C. 2010 FID chromatogram, experiment 26e.

Table I.99. Shimadzu G.C. 2014 TCD chromatogram, experiment 26e.

Component	Peak area
O_2	2231.3
COF_2	32856.5
CF_3COF	12494.1
C_2F_4	-
c-C_3F_6	-
HFP	-
HFPO	-

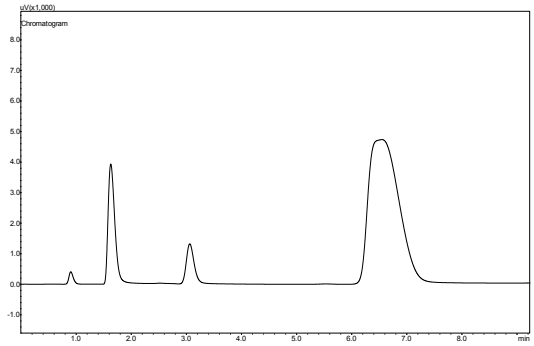

Figure I.99. Shimadzu G.C. 2014 TCD chromatogram, experiment 26e.

Table I.100. Shimadzu G.C. 2010 FID chromatogram, experiment 26f.

Component	Peak area
O_2	-
COF_2	-
CF_3COF	-
C_2F_4	125319.3
c-C_3F_6	40550.6
HFP	3565563.3
HFPO	982179.9

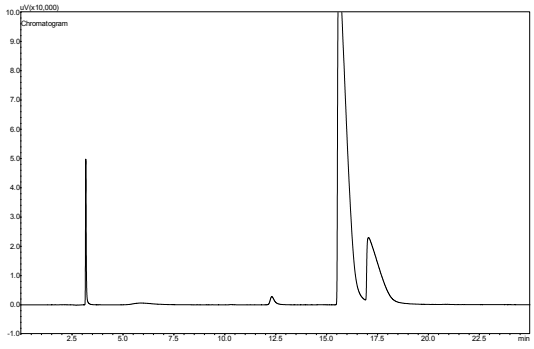

Figure I.100. Shimadzu G.C. 2010 FID chromatogram, experiment 26f.

Table I.101. Shimadzu G.C. 2014 TCD chromatogram, experiment 26f.

Component	Peak area
O_2	690.3
COF_2	44553
CF_3COF	26100.5
C_2F_4	-
c-C_3F_6	-
HFP	-
HFPO	-

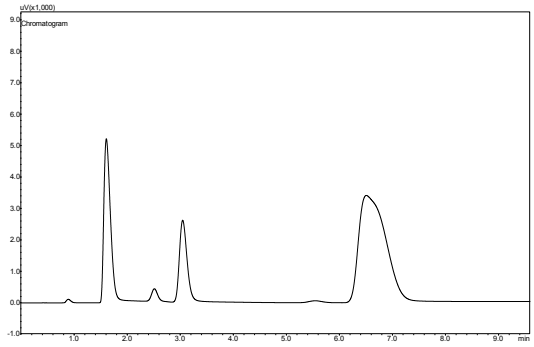

Figure I.101. Shimadzu G.C. 2014 TCD chromatogram, experiment 26f.

Table I.102. Shimadzu G.C. 2010 FID chromatogram, experiment 26g.

Component	Peak area
O_2	-
COF_2	-
CF_3COF	-
C_2F_4	1319.6
c-C_3F_6	80728.9
HFP	5338157.1
HFPO	838505.9

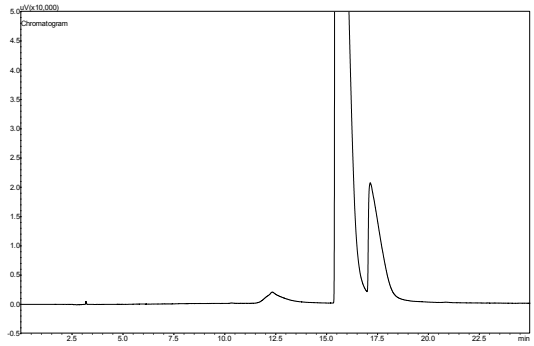

Figure I.102. Shimadzu G.C. 2010 FID chromatogram, experiment 26g.

Table I.103. Shimadzu G.C. 2014 TCD chromatogram, experiment 26g.

Component	Peak area
O_2	37134.5
COF_2	28197.9
CF_3COF	8219.6
C_2F_4	-
c-C_3F_6	-
HFP	-
HFPO	-

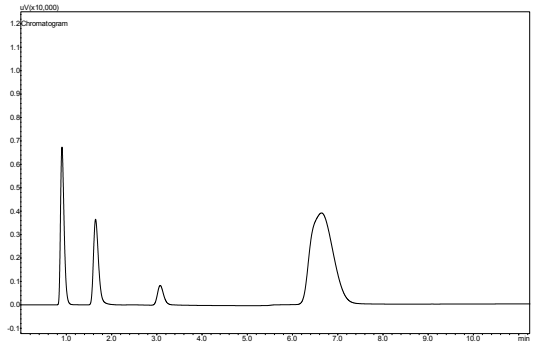

Figure I.103. Shimadzu G.C. 2014 TCD chromatogram, experiment 26g.

Table I.104. Shimadzu G.C. 2010 FID chromatogram, experiment 27a.

Component	Peak area
O_2	-
COF_2	-
CF_3COF	-
C_2F_4	1234.8
c-C_3F_6	6561
HFP	3091301.1
HFPO	1039586.4

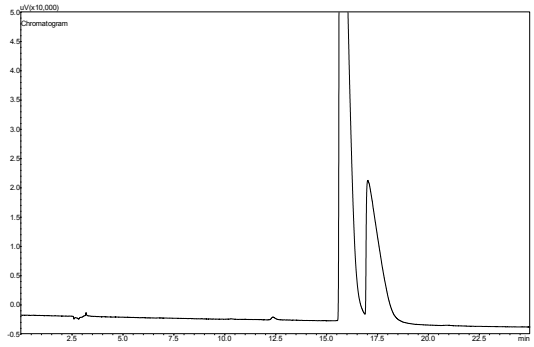

Figure I.104. Shimadzu G.C. 2010 FID chromatogram, experiment 27a.

Table I.105. Shimadzu G.C. 2014 TCD chromatogram, experiment 27a.

Component	Peak area
O_2	22038.9
COF_2	38062.7
CF_3COF	14719.4
C_2F_4	-
c-C_3F_6	-
HFP	-
HFPO	-

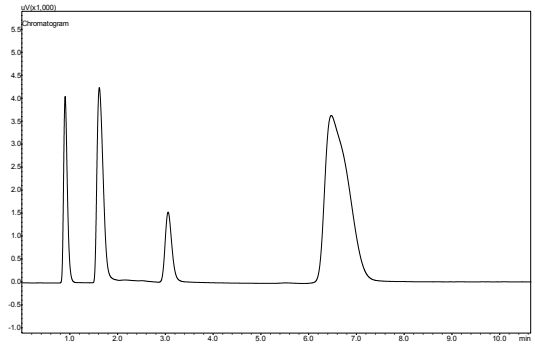

Figure I.105. Shimadzu G.C. 2014 TCD chromatogram, experiment 27a.

Table I.106. Shimadzu G.C. 2010 FID chromatogram, experiment 27b.

Component	Peak area
O_2	-
COF_2	-
CF_3COF	-
C_2F_4	665.8
c-C_3F_6	5243.3
HFP	7398654.9
HFPO	633509.6

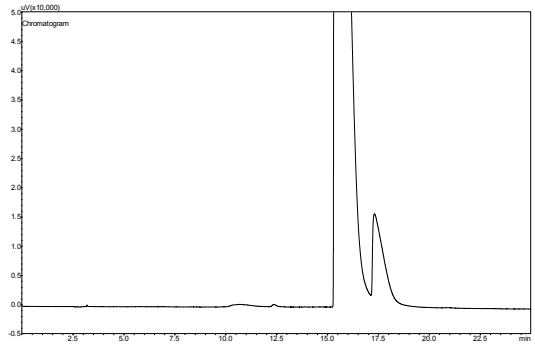

Figure I.106. Shimadzu G.C. 2010 FID chromatogram, experiment 27b.

Table I.107. Shimadzu G.C. 2014 TCD chromatogram, experiment 27b.

Component	Peak area
O_2	50101.2
COF_2	16329.3
CF_3COF	2281.1
C_2F_4	-
c-C_3F_6	-
HFP	-
HFPO	-

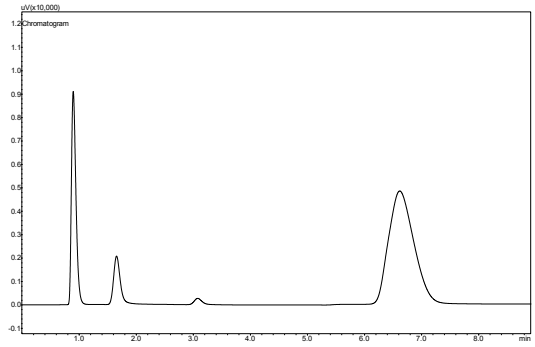

Figure I.107. Shimadzu G.C. 2014 TCD chromatogram, experiment 27b.

Table I.108. Shimadzu G.C. 2010 FID chromatogram, experiment 27c.

Component	Peak area
O_2	-
COF_2	-
CF_3COF	-
C_2F_4	50.5
c-C_3F_6	6334.1
HFP	11755696.7
HFPO	373976.7

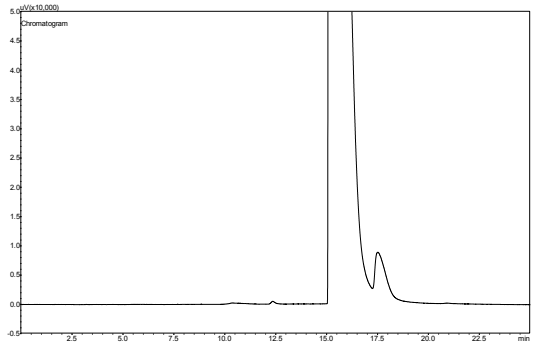

Figure I.108. Shimadzu G.C. 2010 FID chromatogram, experiment 27c.

Table I.109. Shimadzu G.C. 2014 TCD chromatogram, experiment 27c.

Component	Peak area
O_2	47891.8
COF_2	6292.7
CF_3COF	-
C_2F_4	-
c-C_3F_6	-
HFP	-
HFPO	-

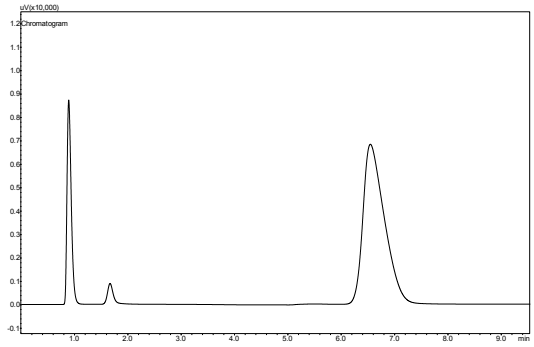

Figure I.109. Shimadzu G.C. 2014 TCD chromatogram, experiment 27c.

Table I.110. Shimadzu G.C. 2010 FID chromatogram, experiment 28a.

Component	Peak area
O_2	-
COF_2	-
CF_3COF	-
C_2F_4	78211.9
c-C_3F_6	18434.8
HFP	3355419
HFPO	1087170

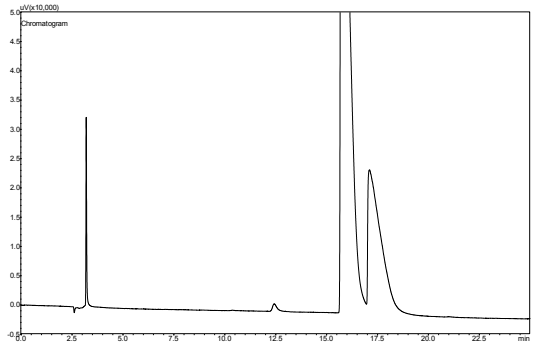

Figure I.110. Shimadzu G.C. 2010 FID chromatogram, experiment 28a.

Table I.111. Shimadzu G.C. 2014 TCD chromatogram, experiment 28a.

Component	Peak area
O_2	905.5
COF_2	48279.4
CF_3COF	19869.2
C_2F_4	-
c-C_3F_6	-
HFP	-
HFPO	-

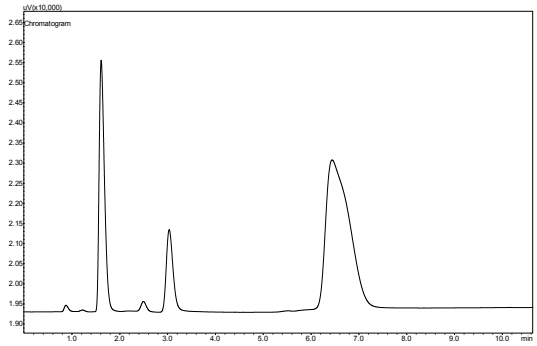

Figure I.111. Shimadzu G.C. 2014 TCD chromatogram, experiment 28a.

Table I.112. Shimadzu G.C. 2010 FID chromatogram, experiment 28b.

Component	Peak area
O_2	-
COF_2	-
CF_3COF	-
C_2F_4	341.9
c-C_3F_6	6819.6
HFP	9591877
HFPO	648270.5

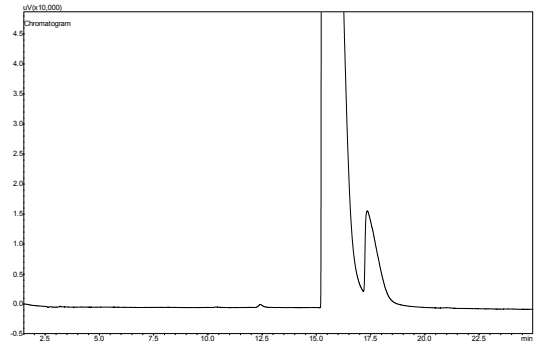

Figure I.112. Shimadzu G.C. 2010 FID chromatogram, experiment 28b.

Table I.113. Shimadzu G.C. 2014 TCD chromatogram, experiment 28b.

Component	Peak area
O_2	35719
COF_2	16902.8
CF_3COF	499.5
C_2F_4	-
c-C_3F_6	-
HFP	-
HFPO	-

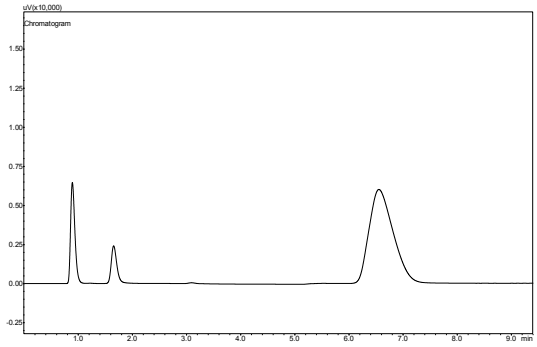

Figure I.113. Shimadzu G.C. 2014 TCD chromatogram, experiment 28b.

Table I.114. Shimadzu G.C. 2010 FID chromatogram, experiment 28c.

Component	Peak area
O_2	-
COF_2	-
CF_3COF	-
C_2F_4	-
c-C_3F_6	3542.4
HFP	45351.7
HFPO	499087.3

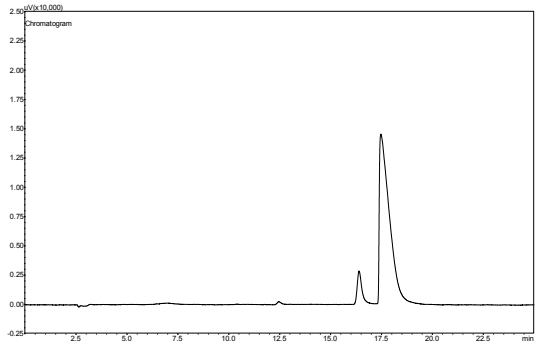

Figure I.114. Shimadzu G.C. 2010 FID chromatogram, experiment 28c.

Table I.115. Shimadzu G.C. 2014 TCD chromatogram, experiment 28c.

Component	Peak area
O_2	48118.7
COF_2	46520.9
CF_3COF	18805.6
C_2F_4	-
c-C_3F_6	-
HFP	-
HFPO	-

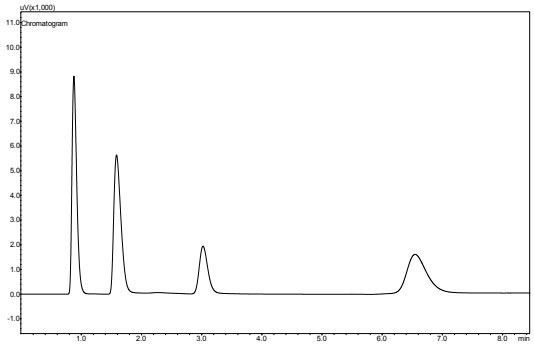

Figure I.115. Shimadzu G.C. 2014 TCD chromatogram, experiment 28c.

Table I.116. Shimadzu G.C. 2010 FID chromatogram, experiment 28d.

Component	Peak area
O_2	-
COF_2	-
CF_3COF	-
C_2F_4	-
c-C_3F_6	2988.1
HFP	9869.3
HFPO	431068.7

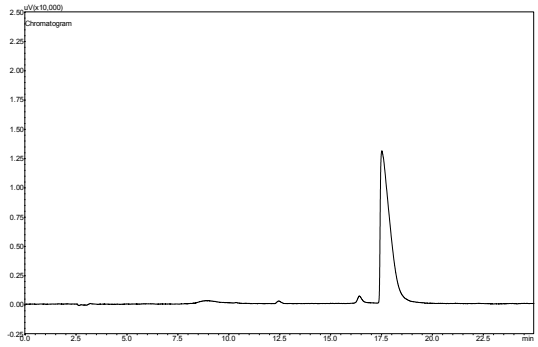

Figure I.116. Shimadzu G.C. 2010 FID chromatogram, experiment 28d.

Table I.117. Shimadzu G.C. 2014 TCD chromatogram, experiment 28d.

Component	Peak area
O_2	45285.3
COF_2	48933
CF_3COF	21425.9
C_2F_4	-
c-C_3F_6	-
HFP	-
HFPO	-

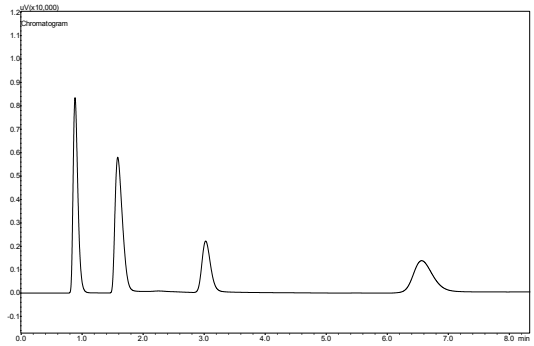

Figure I.117. Shimadzu G.C. 2014 TCD chromatogram, experiment 28d.

Table I.118. Shimadzu G.C. 2010 FID chromatogram, experiment 28e.

Component	Peak area
O_2	-
COF_2	-
CF_3COF	-
C_2F_4	152.5
c-C_3F_6	3452
HFP	4876386.5
HFPO	337627.3

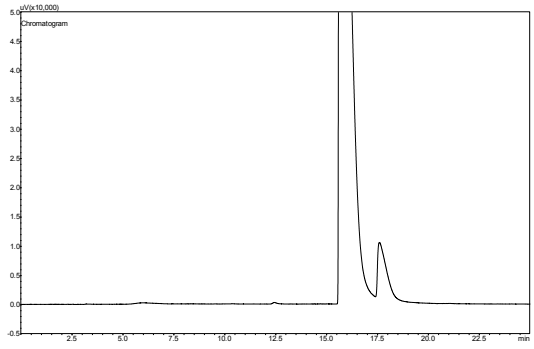

Figure I.118. Shimadzu G.C. 2010 FID chromatogram, experiment 28e.

Table I.119. Shimadzu G.C. 2014 TCD chromatogram, experiment 28e.

Component	Peak area
O_2	81320.1
COF_2	11941.1
CF_3COF	312.5
C_2F_4	-
c-C_3F_6	-
HFP	-
HFPO	-

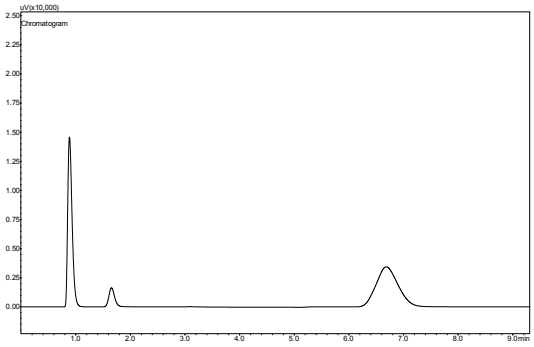

Figure I.119. Shimadzu G.C. 2014 TCD chromatogram, experiment 28e.

Table I.120. Shimadzu G.C. 2010 FID chromatogram, experiment 28f.

Component	Peak area
O_2	-
COF_2	-
CF_3COF	-
C_2F_4	227.5
c-C_3F_6	5857.4
HFP	8896283.1
HFPO	436963.1

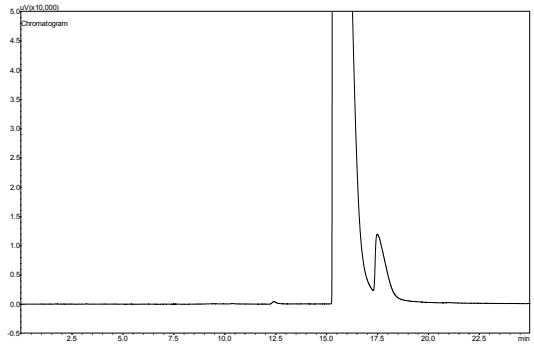

Figure I.120. Shimadzu G.C. 2010 FID chromatogram, experiment 28f.

Table I.121. Shimadzu G.C. 2014 TCD chromatogram, experiment 28f.

Component	Peak area
O_2	55569.2
COF_2	10744.7
CF_3COF	183.6
C_2F_4	-
c-C_3F_6	-
HFP	-
HFPO	-

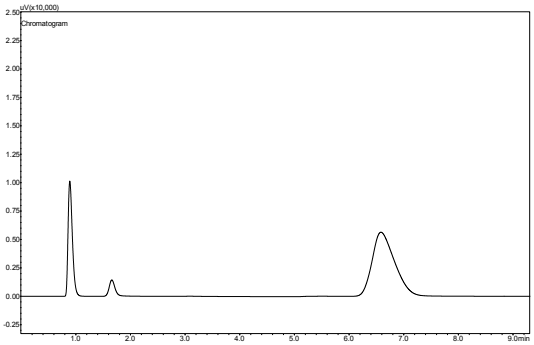

Figure I.121. Shimadzu G.C. 2014 TCD chromatogram, experiment 28f.

Table I.122. Shimadzu G.C. 2010 FID chromatogram, experiment 28g.

Component	Peak area
O_2	-
COF_2	-
CF_3COF	-
C_2F_4	313.2
c-C_3F_6	1863.9
HFP	2490059.7
HFPO	235801.8

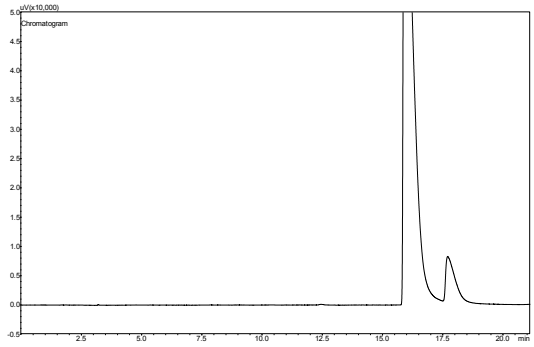

Figure I.121. Shimadzu G.C. 2010 FID chromatogram, experiment 28g.

Table I.123. Shimadzu G.C. 2014 TCD chromatogram, experiment 28g.

Component	Peak area
O_2	101068.9
COF_2	9984.1
CF_3COF	170.1
C_2F_4	-
c-C_3F_6	-
HFP	-
HFPO	-

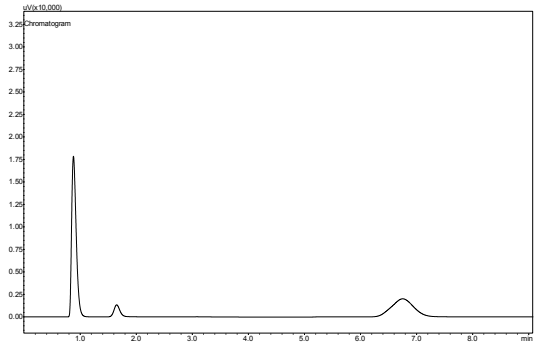

Figure I.123. Shimadzu G.C. 2014 TCD chromatogram, experiment 28g.

Table I.124. Shimadzu G.C. 2010 FID chromatogram, experiment 28h.

Component	Peak area
O_2	-
COF_2	-
CF_3COF	-
C_2F_4	169909.6
c-C_3F_6	86847.2
HFP	237445.7
HFPO	512628.6

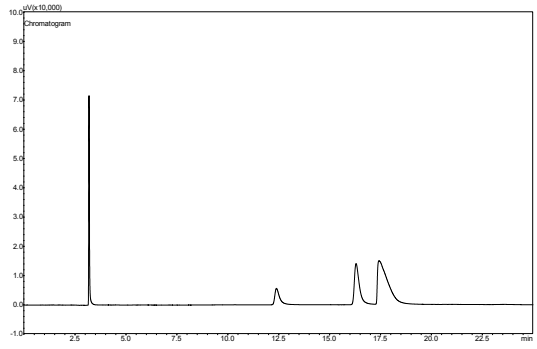

Figure I.124. Shimadzu G.C. 2010 FID chromatogram, experiment 28h.

Table I.125. Shimadzu G.C. 2014 TCD chromatogram, experiment 28h.

Component	Peak area
O_2	2228.5
COF_2	62432.8
CF_3COF	39661.2
C_2F_4	-
c-C_3F_6	-
HFP	-
HFPO	-

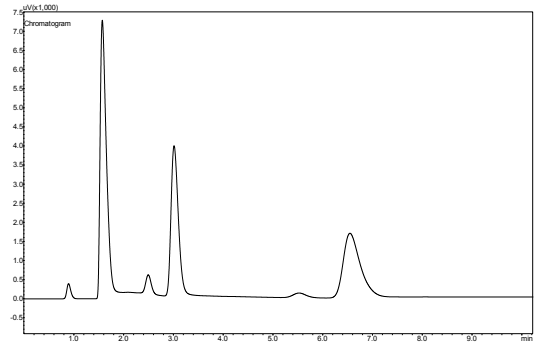

Figure I.125. Shimadzu G.C. 2014 TCD chromatogram, experiment 28h.

Table I.126. Shimadzu G.C. 2010 FID chromatogram, experiment 29a.

Component	Peak area
O_2	-
COF_2	-
CF_3COF	-
C_2F_4	170.7
c-C_3F_6	5345.1
HFP	9523608.4
HFPO	354733

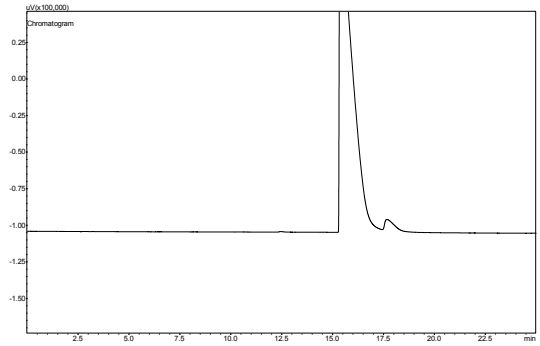

Figure I.126. Shimadzu G.C. 2010 FID chromatogram, experiment 29a.

Table I.127. Shimadzu G.C. 2014 TCD chromatogram, experiment 29a.

Component	Peak area
O_2	61329.4
COF_2	4656.7
CF_3COF	-
C_2F_4	-
c-C_3F_6	-
HFP	-
HFPO	-

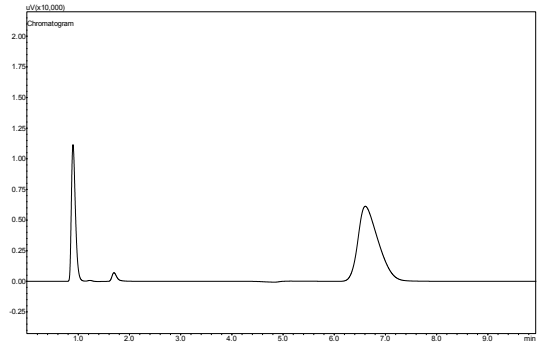

Figure I.127. Shimadzu G.C. 2014 TCD chromatogram, experiment 29a.

Table I.128. Shimadzu G.C. 2010 FID chromatogram, experiment 29b.

Component	Peak area
O_2	-
COF_2	-
CF_3COF	-
C_2F_4	1177.7
c-C_3F_6	4663.8
HFP	4902752.1
HFPO	957938.9

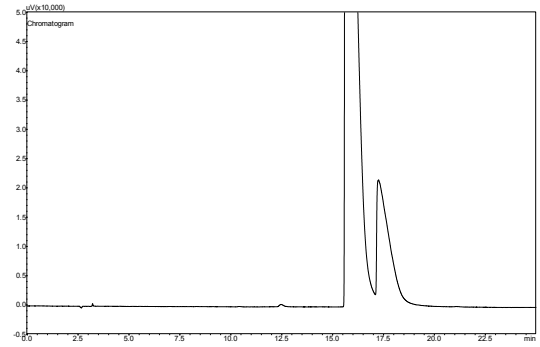

Figure I.128. Shimadzu G.C. 2010 FID chromatogram, experiment 29b.

Table I.129. Shimadzu G.C. 2014 TCD chromatogram, experiment 29b.

Component	Peak area
O_2	37456.5
COF_2	27130.8
CF_3COF	-
C_2F_4	-
c-C_3F_6	-
HFP	-
HFPO	-

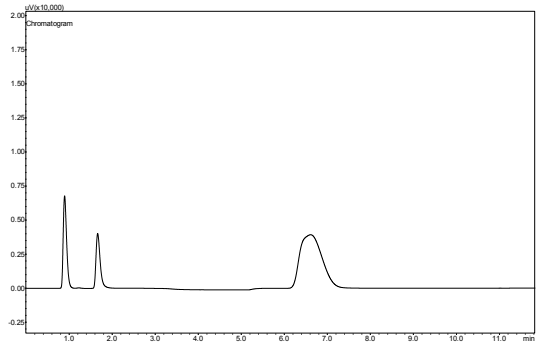

Figure I.129. Shimadzu G.C. 2014 TCD chromatogram, experiment 29b.

Table I.130. Shimadzu G.C. 2010 FID chromatogram, experiment 29c.

Component	Peak area
O_2	-
COF_2	-
CF_3COF	-
C_2F_4	48414
c-C_3F_6	11088
HFP	37882.3
HFPO	871474.2

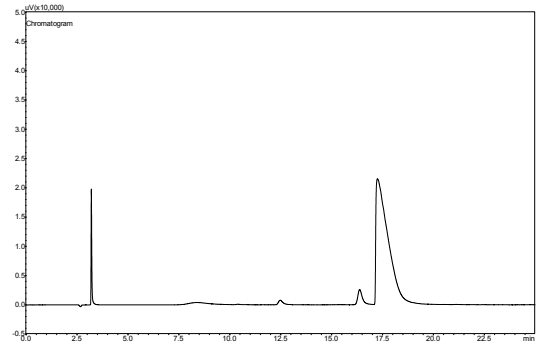

Figure I.130. Shimadzu G.C. 2010 FID chromatogram, experiment 29c.

Table I.131. Shimadzu G.C. 2014 TCD chromatogram, experiment 29c.

Component	Peak area
O_2	997.4
COF_2	60971.5
CF_3COF	22988.9
C_2F_4	-
c-C_3F_6	-
HFP	-
HFPO	-

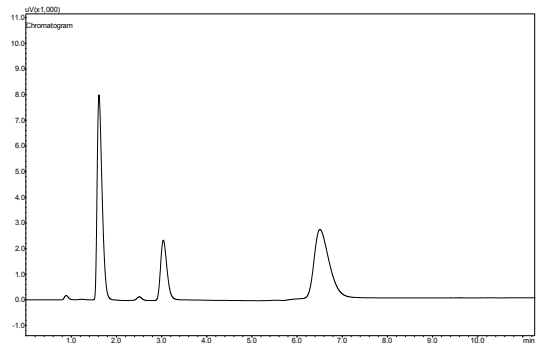

Figure I.131. Shimadzu G.C. 2014 TCD chromatogram, experiment 29c.

Table I.132. Shimadzu G.C. 2010 FID chromatogram, experiment 29d.

Component	Peak area
O_2	-
COF_2	-
CF_3COF	-
C_2F_4	95498.7
c-C_3F_6	27029.3
HFP	256686
HFPO	869977.6

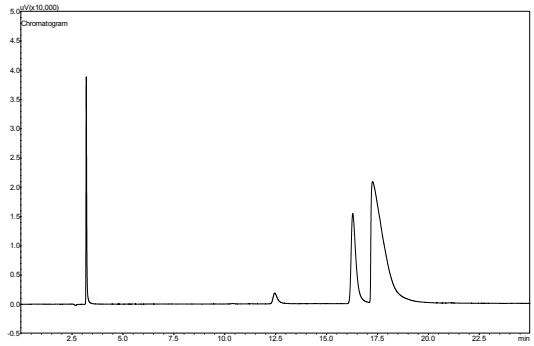

Figure I.132. Shimadzu G.C. 2010 FID chromatogram, experiment 29d.

Table I.133. Shimadzu G.C. 2014 TCD chromatogram, experiment 29d.

Component	Peak area
O_2	977
COF_2	62606.2
CF_3COF	29321.7
C_2F_4	-
c-C_3F_6	-
HFP	-
HFPO	-

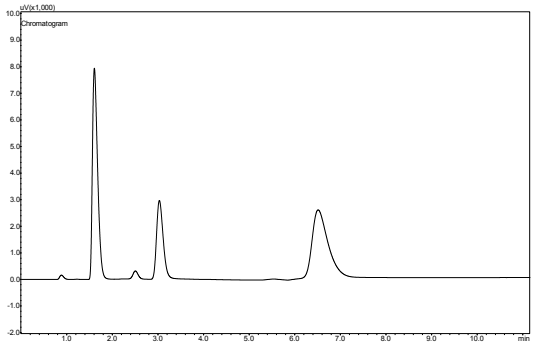

Figure I.133. Shimadzu G.C. 2014 TCD chromatogram, experiment 29d.

Table I.134. Shimadzu G.C. 2010 FID chromatogram, experiment 29e.

Component	Peak area
O_2	-
COF_2	-
CF_3COF	-
C_2F_4	434.5
c-C_3F_6	5206.5
HFP	7291302.5
HFPO	672485.8

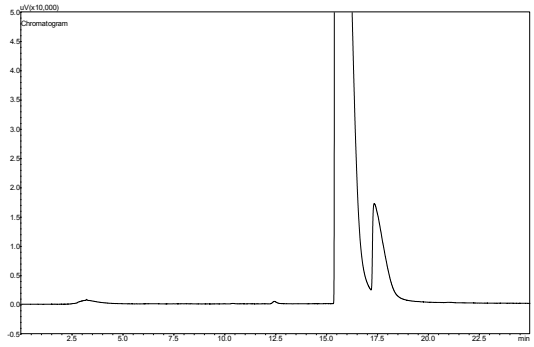

Figure I.134. Shimadzu G.C. 2010 FID chromatogram, experiment 29e.

Table I.135. Shimadzu G.C. 2014 TCD chromatogram, experiment 29e.

Component	Peak area
O_2	46255
COF_2	19559.1
CF_3COF	-
C_2F_4	-
c-C_3F_6	-
HFP	-
HFPO	-

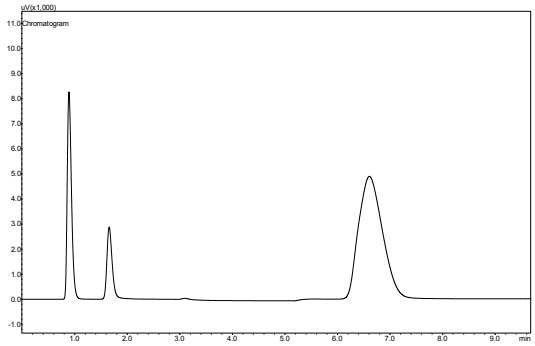

Figure I.135. Shimadzu G.C. 2014 TCD chromatogram, experiment 29e.

Table I.136. Shimadzu G.C. 2010 FID chromatogram, experiment 29f.

Component	Peak area
O_2	-
COF_2	-
CF_3COF	-
C_2F_4	1487.4
c-C_3F_6	6452.7
HFP	4230273.6
HFPO	1044094.3

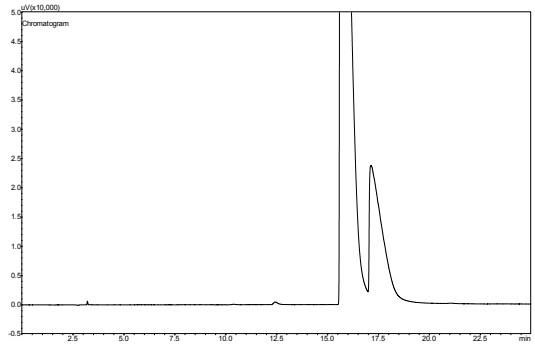

Figure I.136. Shimadzu G.C. 2010 FID chromatogram, experiment 29f.

Table I.137. Shimadzu G.C. 2014 TCD chromatogram, experiment 29f.

Component	Peak area
O_2	26413.1
COF_2	35365.4
CF_3COF	10433.8
C_2F_4	-
c-C_3F_6	-
HFP	-
HFPO	-

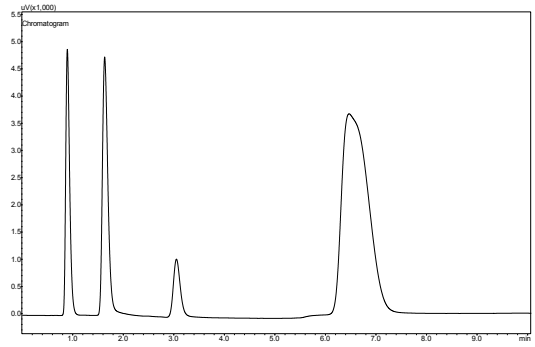

Figure I.137. Shimadzu G.C. 2014 TCD chromatogram, experiment 29f.

Table I.138. Shimadzu G.C. 2010 FID chromatogram, experiment 29g.

Component	Peak area
O_2	-
COF_2	-
CF_3COF	-
C_2F_4	1609.1
c-C_3F_6	5600.8
HFP	2291661
HFPO	1180738

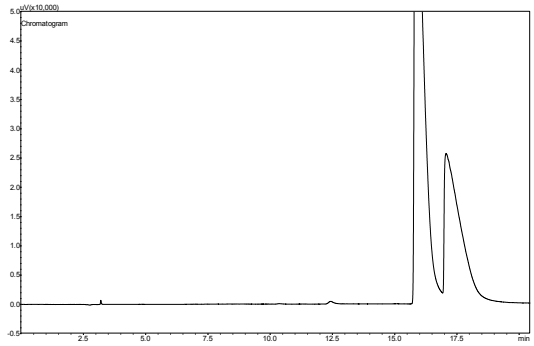

Figure I.138. Shimadzu G.C. 2010 FID chromatogram, experiment 29g.

Table I.139. Shimadzu G.C. 2014 TCD chromatogram, experiment 29g.

Component	Peak area
O_2	16675.5
COF_2	45275.3
CF_3COF	16734.6
C_2F_4	-
c-C_3F_6	-
HFP	-
HFPO	-

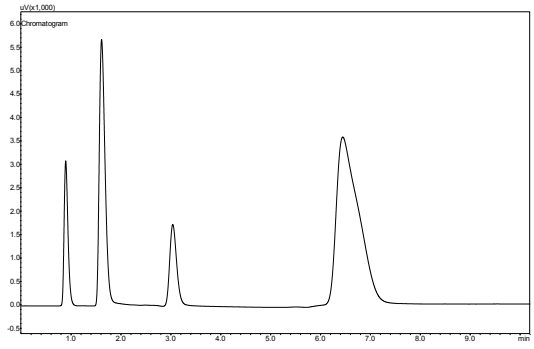

Figure I.139. Shimadzu G.C. 2014 TCD chromatogram, experiment 29g.

Table I.140. Shimadzu G.C. 2010 FID chromatogram, experiment 30a.

Component	Peak area
O_2	-
COF_2	-
CF_3COF	-
C_2F_4	192.6
c-C_3F_6	6711.5
HFP	12989011
HFPO	513627.7

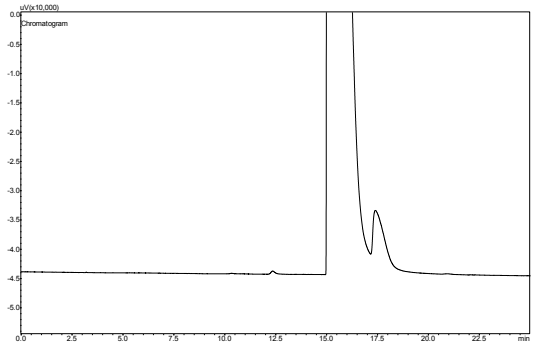

Figure I.140. Shimadzu G.C. 2010 FID chromatogram, experiment 30a.

Table I.141. Shimadzu G.C. 2014 TCD chromatogram, experiment 30a.

Component	Peak area
O_2	37942.9
COF_2	6505.5
CF_3COF	-
C_2F_4	-
c-C_3F_6	-
HFP	-
HFPO	-

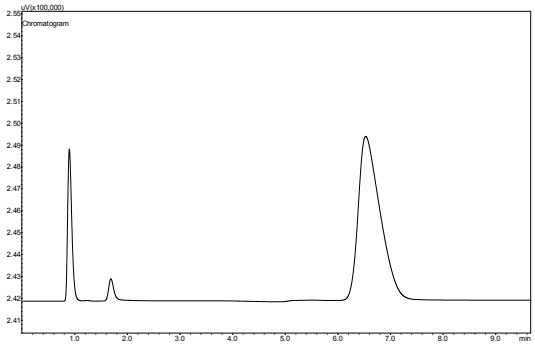

Figure I.141. Shimadzu G.C. 2014 TCD chromatogram, experiment 30a.

Table I.142. Shimadzu G.C. 2010 FID chromatogram, experiment 30b.

Component	Peak area
O_2	-
COF_2	-
CF_3COF	-
C_2F_4	3508.8
c-C_3F_6	7512.4
HFP	6579025.8
HFPO	1330921.3

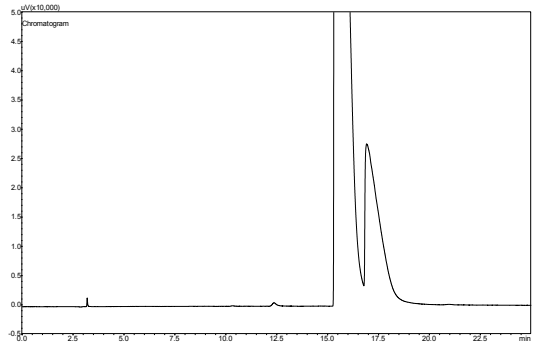

Figure I.142. Shimadzu G.C. 2010 FID chromatogram, experiment 30b.

Table I.143. Shimadzu G.C. 2014 TCD chromatogram, experiment 30b.

Component	Peak area
O_2	2366.1
COF_2	35389.6
CF_3COF	10697.4
C_2F_4	-
c-C_3F_6	-
HFP	-
HFPO	-

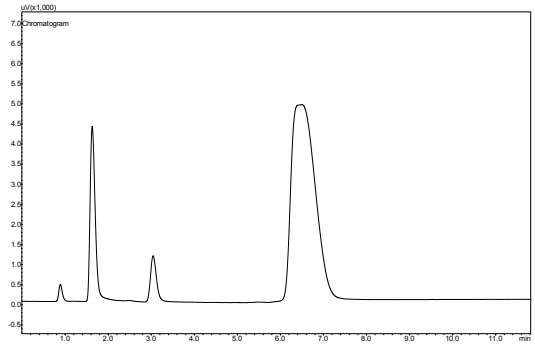

Figure I.143. Shimadzu G.C. 2014 TCD chromatogram, experiment 30b.

Table I.144. Shimadzu G.C. 2010 FID chromatogram, experiment 30c.

Component	Peak area
O_2	-
COF_2	-
CF_3COF	-
C_2F_4	113108.4
c-C_3F_6	36233.6
HFP	6234400.8
HFPO	1069765.2

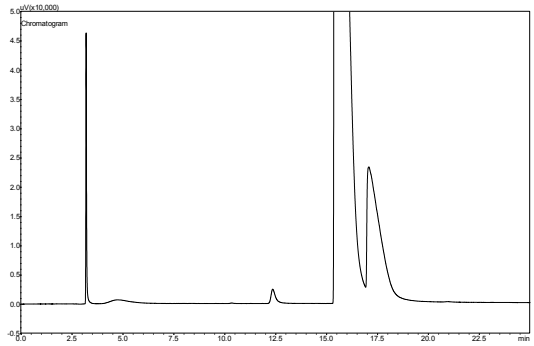

Figure I.144. Shimadzu G.C. 2010 FID chromatogram, experiment 30c.

Table I.145. Shimadzu G.C. 2014 TCD chromatogram, experiment 30c.

Component	Peak area
O_2	854.8
COF_2	37126.6
CF_3COF	17943
C_2F_4	-
c-C_3F_6	-
HFP	-
HFPO	-

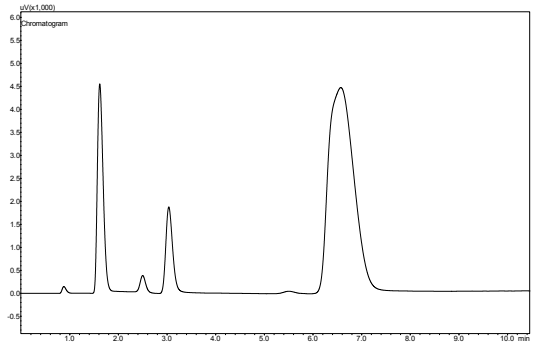

Figure I.145. Shimadzu G.C. 2014 TCD chromatogram, experiment 30c.

Table I.146. Shimadzu G.C. 2010 FID chromatogram, experiment 30d.

Component	Peak area
O_2	-
COF_2	-
CF_3COF	-
C_2F_4	1636.1
c-C_3F_6	6045.3
HFP	4257996.9
HFPO	1081720.9

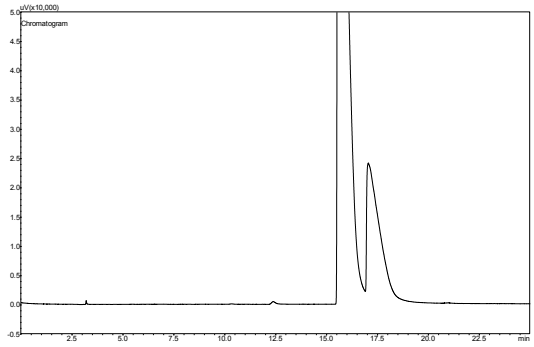

Figure I.146. Shimadzu G.C. 2010 FID chromatogram, experiment 30d.

Table I.147. Shimadzu G.C. 2014 TCD chromatogram, experiment 30d.

Component	Peak area
O_2	25720.3
COF_2	34091.4
CF_3COF	12118.4
C_2F_4	-
c-C_3F_6	-
HFP	-
HFPO	-

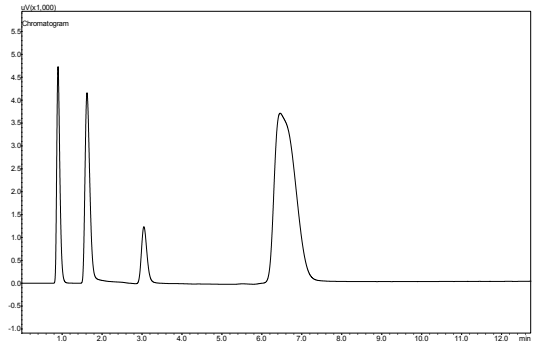

Figure I.147. Shimadzu G.C. 2014 TCD chromatogram, experiment 30d.

Table I.148. Shimadzu G.C. 2010 FID chromatogram, experiment 30e.

Component	Peak area
O_2	-
COF_2	-
CF_3COF	-
C_2F_4	101.9
c-C_3F_6	4416.3
HFP	7770441.6
HFPO	404618.8

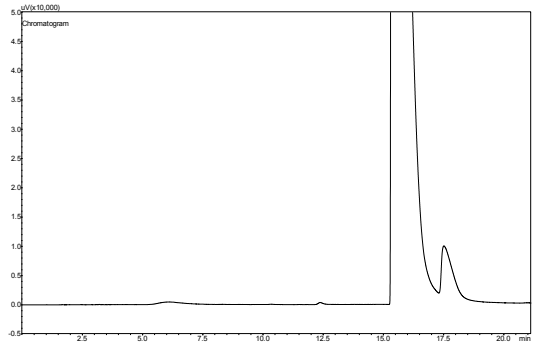

Figure I.148. Shimadzu G.C. 2010 FID chromatogram, experiment 30e.

Table I.150. Shimadzu G.C. 2014 TCD chromatogram, experiment 30e.

Component	Peak area
O_2	68982.7
COF_2	8095.3
CF_3COF	-
C_2F_4	-
c-C_3F_6	-
HFP	-
HFPO	-

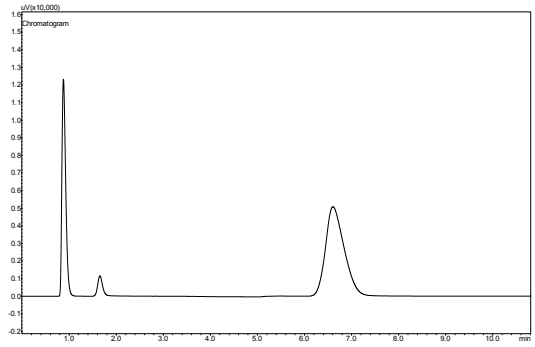

Figure I.150. Shimadzu G.C. 2014 TCD chromatogram, experiment 30e.

Table I.151. Shimadzu G.C. 2010 FID chromatogram, experiment 30f.

Component	Peak area
O_2	-
COF_2	-
CF_3COF	-
C_2F_4	1023.3
c-C_3F_6	4589.3
HFP	4249990.2
HFPO	808081.6

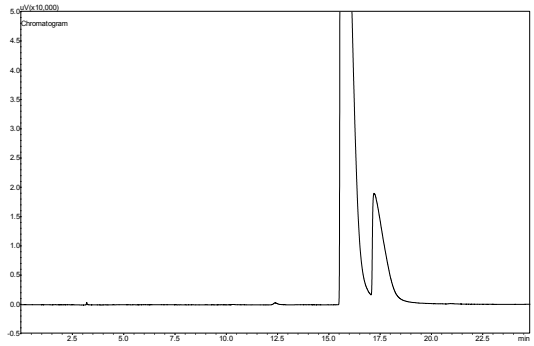

Figure I.151. Shimadzu G.C. 2010 FID chromatogram, experiment 30f.

Table I.152. Shimadzu G.C. 2014 TCD chromatogram, experiment 30f.

Component	Peak area
O_2	52418.3
COF_2	24074.5
CF_3COF	5987.8
C_2F_4	-
c-C_3F_6	-
HFP	-
HFPO	-

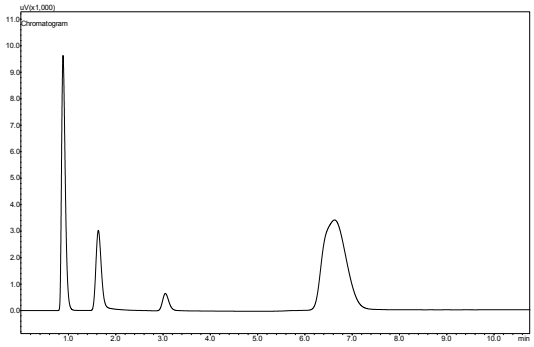

Figure I.152. Shimadzu G.C. 2014 TCD chromatogram, experiment 30f.

Table I.153. Shimadzu G.C. 2010 FID chromatogram, experiment 31a.

Component	Peak area
O_2	-
COF_2	-
CF_3COF	-
C_2F_4	69
c-C_3F_6	3173.7
HFP	7244105.8
HFPO	191220.8

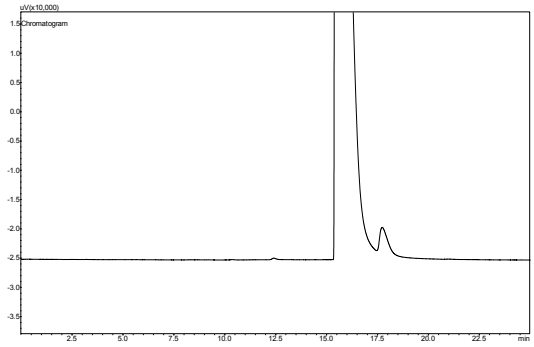

Figure I.153. Shimadzu G.C. 2010 FID chromatogram, experiment 31a.

Table I.154. Shimadzu G.C. 2014 TCD chromatogram, experiment 31a.

Component	Peak area
O_2	86458.1
COF_2	2590.2
CF_3COF	-
C_2F_4	-
c-C_3F_6	-
HFP	-
HFPO	-

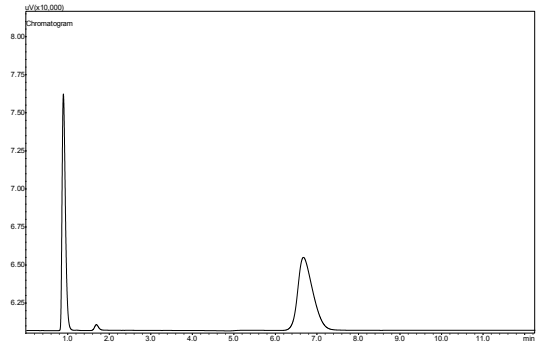

Figure I.154. Shimadzu G.C. 2014 TCD chromatogram, experiment 30d.

Table I.155. Shimadzu G.C. 2010 FID chromatogram, experiment 32a.

Component	Peak area
O_2	-
COF_2	-
CF_3COF	-
C_2F_4	175.5
c-C_3F_6	3638.2
HFP	6656219.3
HFPO	284746.5

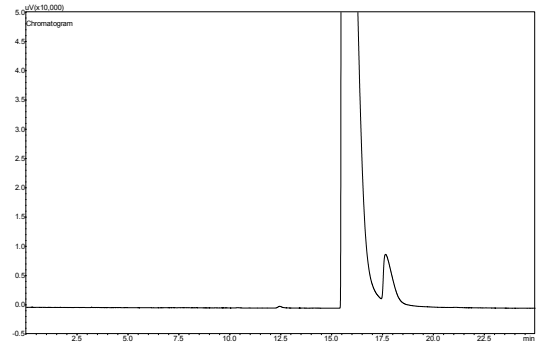

Figure I.155. Shimadzu G.C. 2010 FID chromatogram, experiment 32a.

Table I.156. Shimadzu G.C. 2014 TCD chromatogram, experiment 32a.

Component	Peak area
O_2	79886.8
COF_2	6572.5
CF_3COF	-
C_2F_4	-
c-C_3F_6	-
HFP	-
HFPO	-

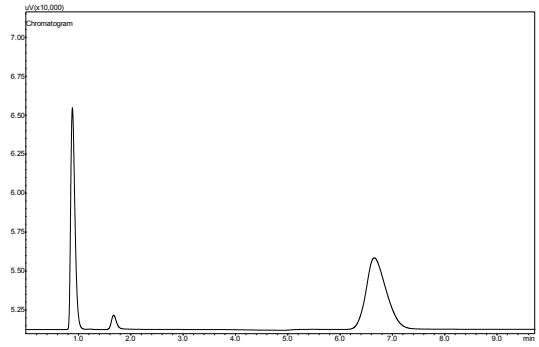

Figure I.156. Shimadzu G.C. 2014 TCD chromatogram, experiment 32a.

Table I.157. Shimadzu G.C. 2010 FID chromatogram, experiment 32b.

Component	Peak area
O_2	-
COF_2	-
CF_3COF	-
C_2F_4	674.8
c-C_3F_6	3043.5
HFP	3575764.4
HFPO	619047.9

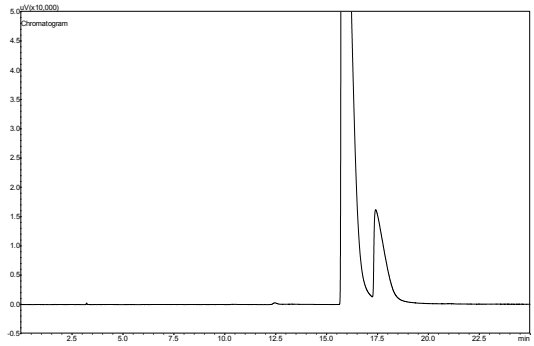

Figure I.157. Shimadzu G.C. 2010 FID chromatogram, experiment 32b.

Table I.158. Shimadzu G.C. 2014 TCD chromatogram, experiment 32b.

Component	Peak area
O_2	68548.1
COF_2	20095.1
CF_3COF	2178.9
C_2F_4	-
c-C_3F_6	-
HFP	-
HFPO	-

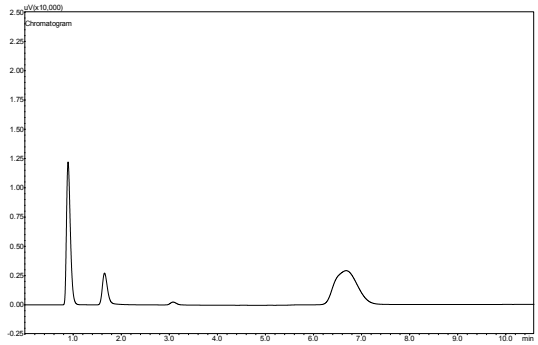

Figure I.158. Shimadzu G.C. 2014 TCD chromatogram, experiment 32b.

Table I.159. Shimadzu G.C. 2010 FID chromatogram, experiment 32c.

Component	Peak area
O_2	-
COF_2	-
CF_3COF	-
C_2F_4	-
c-C_3F_6	3307.2
HFP	10324.3
HFPO	553938.7

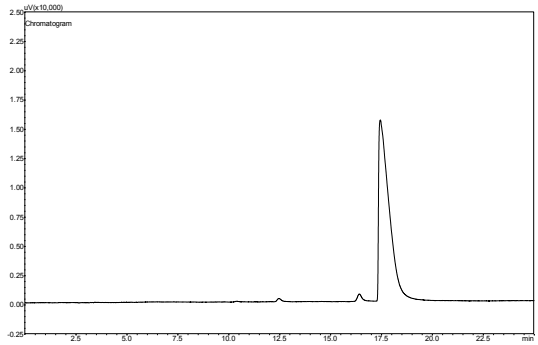

Figure I.159. Shimadzu G.C. 2010 FID chromatogram, experiment 32c.

Table I.160. Shimadzu G.C. 2014 TCD chromatogram, experiment 32c.

Component	Peak area
O_2	40472.6
COF_2	47605.8
CF_3COF	18871.3
C_2F_4	-
c-C_3F_6	-
HFP	-
HFPO	-

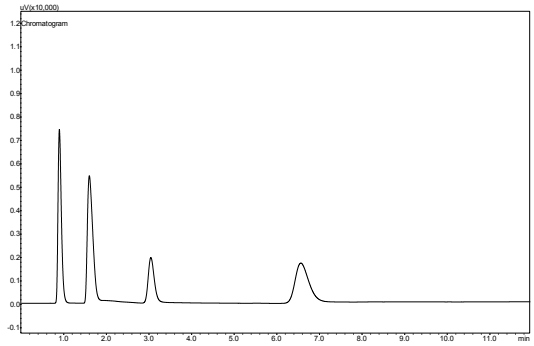

Figure I.160. Shimadzu G.C. 2014 TCD chromatogram, experiment 32c.

Table I.161. Shimadzu G.C. 2010 FID chromatogram, experiment 32d.

Component	Peak area
O_2	-
COF_2	-
CF_3COF	-
C_2F_4	0
c-C_3F_6	3780.5
HFP	3670.8
HFPO	710875.9

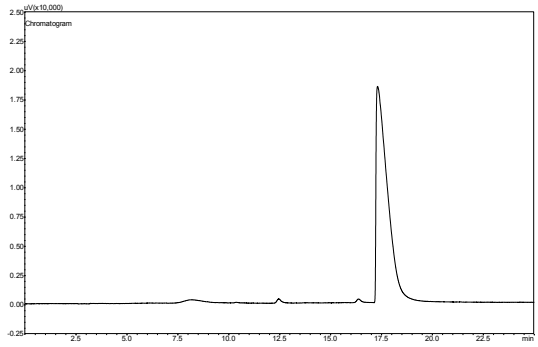

Figure I.161. Shimadzu G.C. 2010 FID chromatogram, experiment 32d.

Table I.162. Shimadzu G.C. 2014 TCD chromatogram, experiment 32d.

Component	Peak area
O_2	20463.3
COF_2	57918.4
CF_3COF	25095.6
C_2F_4	-
c-C_3F_6	-
HFP	-
HFPO	-

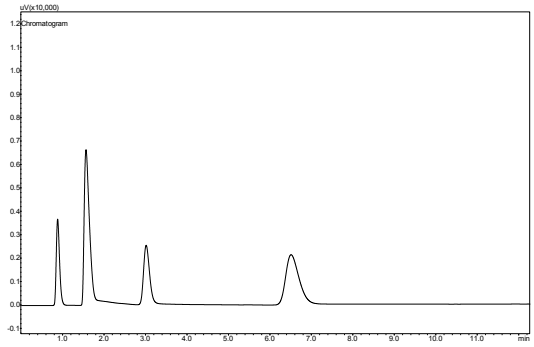

Figure I.162. Shimadzu G.C. 2014 TCD chromatogram, experiment 32d.

Table I.163. Shimadzu G.C. 2010 FID chromatogram, experiment 32e.

Component	Peak area
O_2	-
COF_2	-
CF_3COF	-
C_2F_4	1324.2
c-C_3F_6	5899.3
HFP	6646373.7
HFPO	979111.9

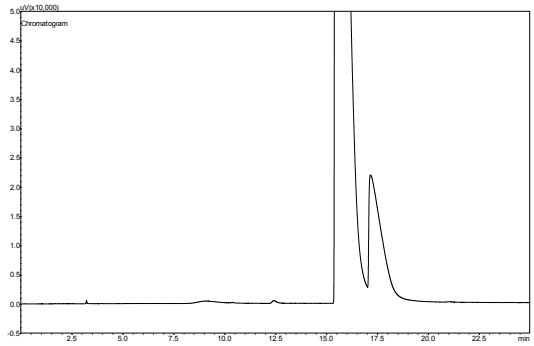

Figure I.163. Shimadzu G.C. 2010 FID chromatogram, experiment 32e.

Table I.164. Shimadzu G.C. 2014 TCD chromatogram, experiment 32e.

Component	Peak area
O_2	29434.8
COF_2	26298.9
CF_3COF	7828.2
C_2F_4	-
c-C_3F_6	-
HFP	-
HFPO	-

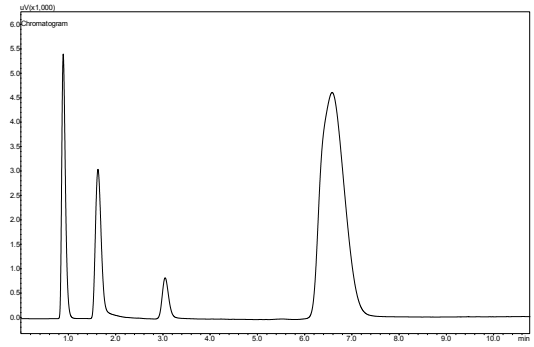

Figure I.164. Shimadzu G.C. 2014 TCD chromatogram, experiment 32e.

Table I.165. Shimadzu G.C. 2010 FID chromatogram, experiment 32f.

Component	Peak area
O_2	-
COF_2	-
CF_3COF	-
C_2F_4	1639.5
c-C_3F_6	5845.3
HFP	4928595.8
HFPO	1083085.9

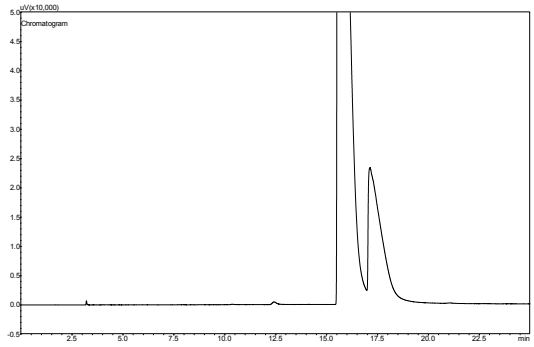

Figure I.165. Shimadzu G.C. 2010 FID chromatogram, experiment 32f.

Table I.166. Shimadzu G.C. 2014 TCD chromatogram, experiment 32f.

Component	Peak area
O_2	124.2
COF_2	4936
CF_3COF	10930321.9
C_2F_4	-
c-C_3F_6	-
HFP	-
HFPO	-

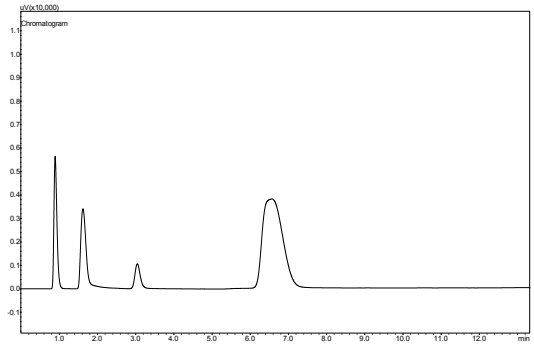

Figure I.166. Shimadzu G.C. 2014 TCD chromatogram, experiment 32f.

Table I.167. Shimadzu G.C. 2010 FID chromatogram, experiment 32g.

Component	Peak area
O_2	-
COF_2	-
CF_3COF	-
C_2F_4	124.2
c-C_3F_6	4936
HFP	10930321.9
HFPO	394810.7

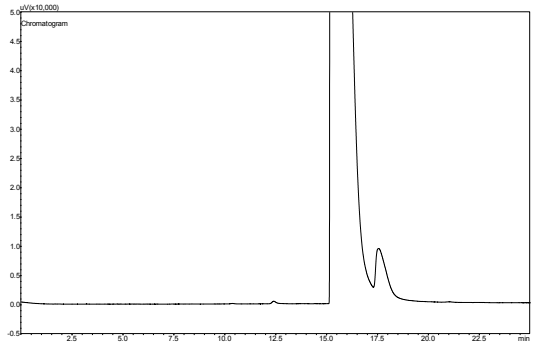

Figure I.167. Shimadzu G.C. 2010 FID chromatogram, experiment 32g.

Table I.168. Shimadzu G.C. 2014 TCD chromatogram, experiment 32g.

Component	Peak area
O_2	51992
COF_2	6603
CF_3COF	-
C_2F_4	-
c-C_3F_6	-
HFP	-
HFPO	-

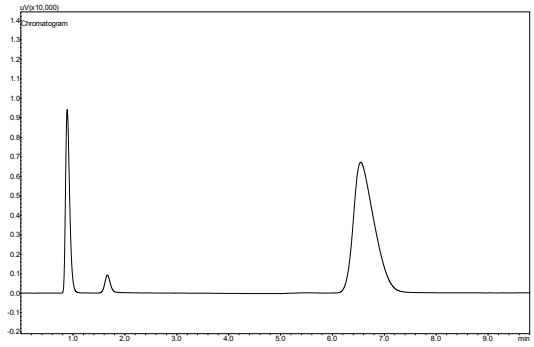

Figure I.168. Shimadzu G.C. 2014 TCD chromatogram, experiment 32g.

Table I.169. Shimadzu G.C. 2010 FID chromatogram, experiment 33a.

Component	Peak area
O_2	-
COF_2	-
CF_3COF	-
C_2F_4	197.5
c-C_3F_6	5965.9
HFP	10154231
HFPO	667454.1

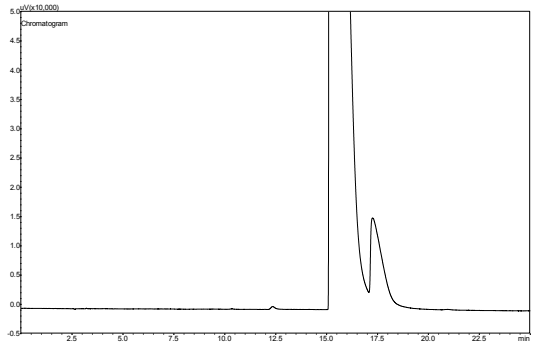

Figure I.169. Shimadzu G.C. 2010 FID chromatogram, experiment 32a.

Table I.170. Shimadzu G.C. 2014 TCD chromatogram, experiment 33a.

Component	Peak area
O_2	39366.9
COF_2	12160.4
CF_3COF	-
C_2F_4	-
c-C_3F_6	-
HFP	-
HFPO	-

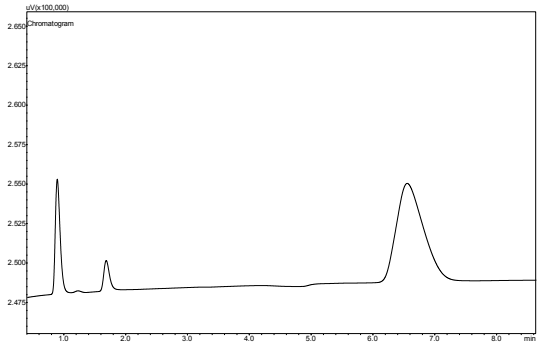

Figure I.170. Shimadzu G.C. 2014 TCD chromatogram, experiment 33a.

Table I.171. Shimadzu G.C. 2010 FID chromatogram, experiment 33b.

Component	Peak area
O_2	-
COF_2	-
CF_3COF	-
C_2F_4	4963.2
c-C_3F_6	7030.8
HFP	3961613.9
HFPO	1423064.1

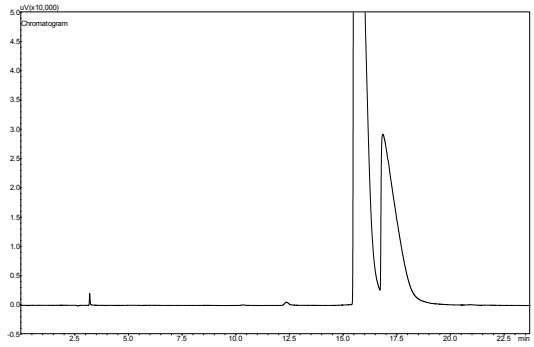

Figure I.171. Shimadzu G.C. 2010 FID chromatogram, experiment 33b.

Table I.172. Shimadzu G.C. 2014 TCD chromatogram, experiment 33b.

Component	Peak area
O_2	2788.7
COF_2	45285.8
CF_3COF	2586.5
C_2F_4	-
c-C_3F_6	-
HFP	-
HFPO	-

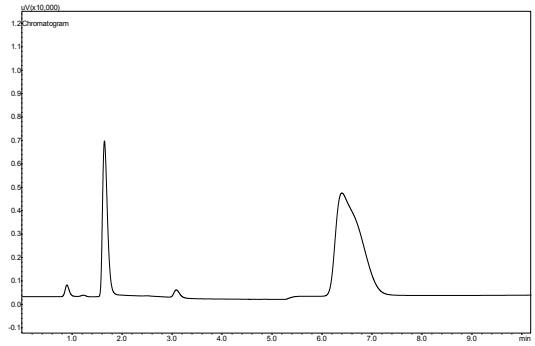

Figure I.172. Shimadzu G.C. 2014 TCD chromatogram, experiment 33b.

Table I.173. Shimadzu G.C. 2010 FID chromatogram, experiment 33c.

Component	Peak area
O_2	-
COF_2	-
CF_3COF	-
C_2F_4	1755.9
c-C_3F_6	4192.3
HFP	1638360.6
HFPO	851870.4

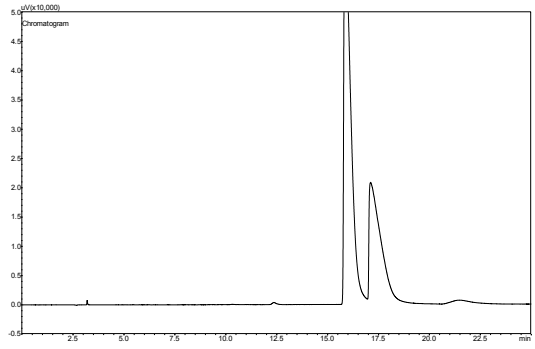

Figure I.173. Shimadzu G.C. 2010 FID chromatogram, experiment 33c.

Table I.174. Shimadzu G.C. 2014 TCD chromatogram, experiment 33c.

Component	Peak area
O_2	45559.1
COF_2	41675
CF_3COF	4760.6
C_2F_4	-
c-C_3F_6	-
HFP	-
HFPO	-

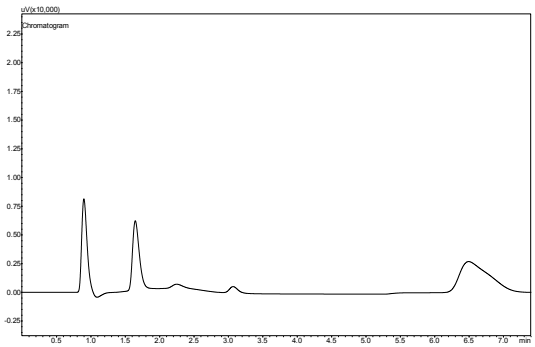

Figure I.174. Shimadzu G.C. 2014 TCD chromatogram, experiment 33c.

Table I.175. Shimadzu G.C. 2010 FID chromatogram, experiment 33d.

Component	Peak area
O_2	-
COF_2	-
CF_3COF	-
C_2F_4	184.1
c-C_3F_6	4421.7
HFP	16011.5
HFPO	531967.4

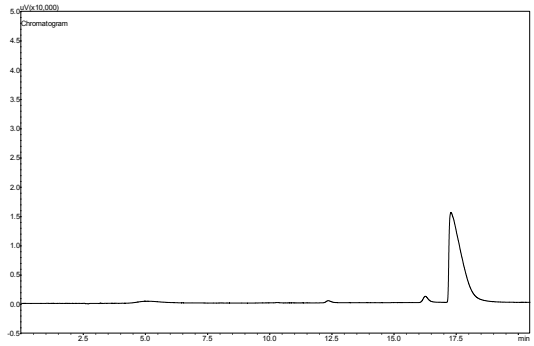

Figure I.175. Shimadzu G.C. 2010 FID chromatogram, experiment 33d.

Table I.176. Shimadzu G.C. 2014 TCD chromatogram, experiment 33d.

Component	Peak area
O_2	34798.3
COF_2	56210.8
CF_3COF	17308.3
C_2F_4	-
c-C_3F_6	-
HFP	-
HFPO	-

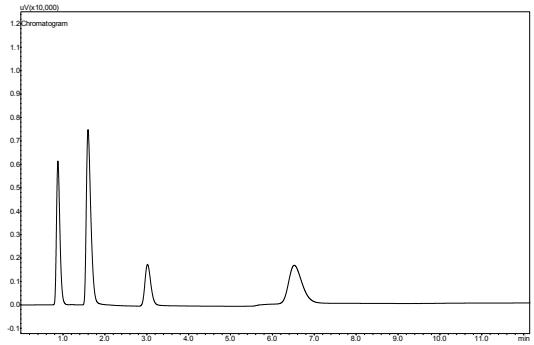

Figure I.176. Shimadzu G.C. 2014 TCD chromatogram, experiment 33d.

Table I.177. Shimadzu G.C. 2010 FID chromatogram, experiment 33e.

Component	Peak area
O_2	-
COF_2	-
CF_3COF	-
C_2F_4	133784.7
c-C_3F_6	47265.8
HFP	3769861.3
HFPO	1025846.2

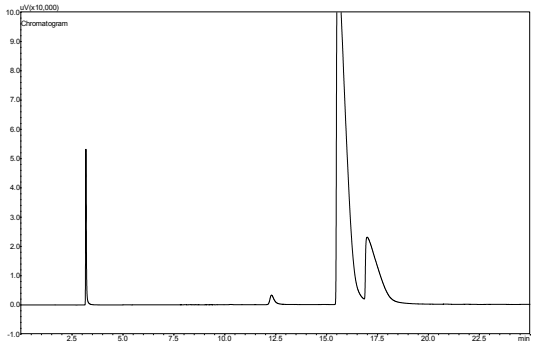

Figure I.177. Shimadzu G.C. 2010 FID chromatogram, experiment 33e.

Table I.178. Shimadzu G.C. 2014 TCD chromatogram, experiment 33e.

Component	Peak area
O_2	2276.2
COF_2	49507.9
CF_3COF	21198
C_2F_4	-
c-C_3F_6	-
HFP	-
HFPO	-

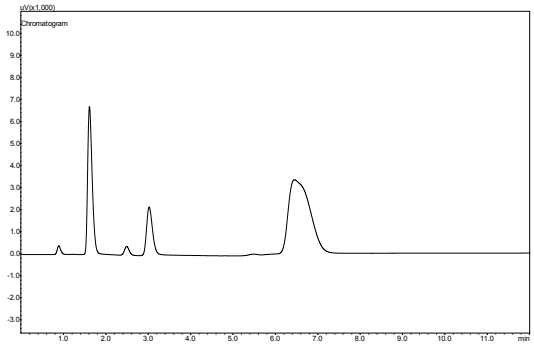

Figure I.178. Shimadzu G.C. 2014 TCD chromatogram, experiment 33e.

Table I.179. Shimadzu G.C. 2010 FID chromatogram, experiment 33f.

Component	Peak area
O_2	-
COF_2	-
CF_3COF	-
C_2F_4	88.9
c-C_3F_6	4283.7
HFP	9616252.6
HFPO	283622.9

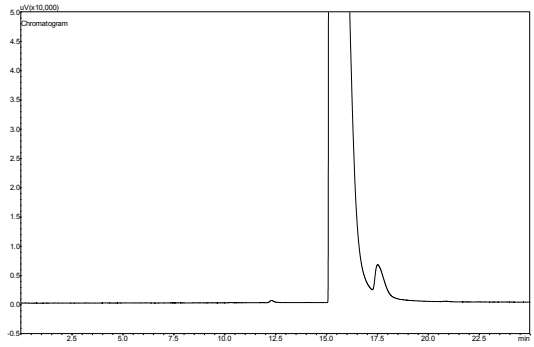

Figure I.179. Shimadzu G.C. 2010 FID chromatogram, experiment 33f.

Table I.180. Shimadzu G.C. 2014 TCD chromatogram, experiment 33f.

Component	Peak area
O_2	68934.2
COF_2	3665.4
CF_3COF	-
C_2F_4	-
c-C_3F_6	-
HFP	-
HFPO	-

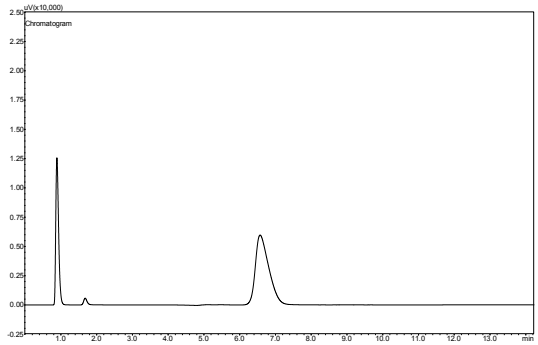

Figure I.180. Shimadzu G.C. 2014 TCD chromatogram, experiment 33f.

Table I.181. Shimadzu G.C. 2010 FID chromatogram, experiment 33g.

Component	Peak area
O_2	-
COF_2	-
CF_3COF	-
C_2F_4	117.5
c-C_3F_6	5010.4
HFP	107725.9
HFPO	874734.9

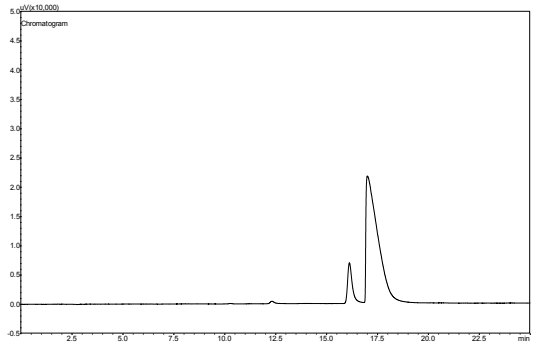

Figure I.181. Shimadzu G.C. 2010 FID chromatogram, experiment 33g.

Table I.182. Shimadzu G.C. 2014 TCD chromatogram, experiment 33g.

Component	Peak area
O_2	12387.5
COF_2	62110.1
CF_3COF	22686
C_2F_4	-
c-C_3F_6	-
HFP	-
HFPO	-

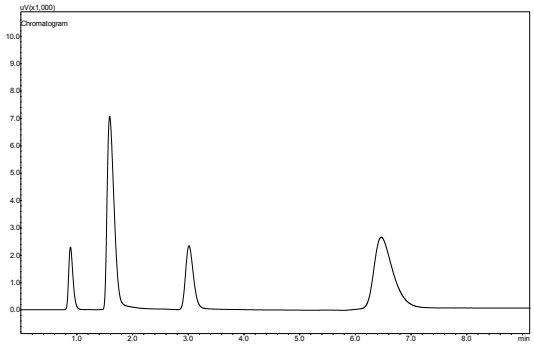

Figure I.182. Shimadzu G.C. 2014 TCD chromatogram, experiment 33g.

Table I.183. Shimadzu G.C. 2010 FID chromatogram, experiment 33h.

Component	Peak area
O_2	-
COF_2	-
CF_3COF	-
C_2F_4	75705.7
c-C_3F_6	16099.8
HFP	2223917
HFPO	1110310.7

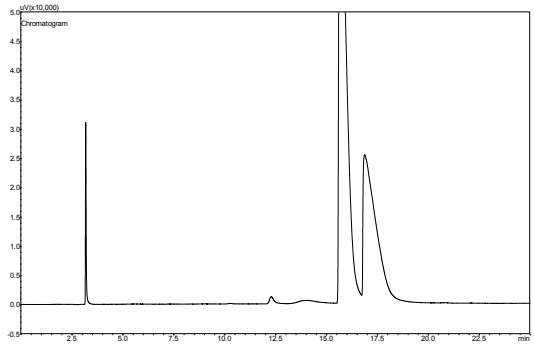

Figure I.183. Shimadzu G.C. 2010 FID chromatogram, experiment 33h.

Table I.184. Shimadzu G.C. 2014 TCD chromatogram, experiment 33h.

Component	Peak area
O_2	1141.6
COF_2	55308.5
CF_3COF	23307.6
C_2F_4	-
c-C_3F_6	-
HFP	-
HFPO	-

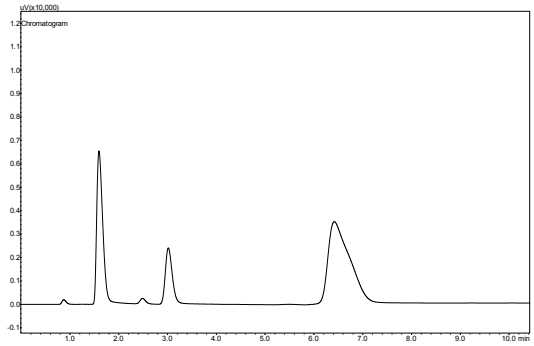

Figure I.184. Shimadzu G.C. 2014 TCD chromatogram, experiment 33h.

Table I.185. Shimadzu G.C. 2010 FID chromatogram, experiment 33i.

Component	Peak area
O_2	-
COF_2	-
CF_3COF	-
C_2F_4	919.4
c-C_3F_6	4389.3
HFP	6095670.4
HFPO	737380.3

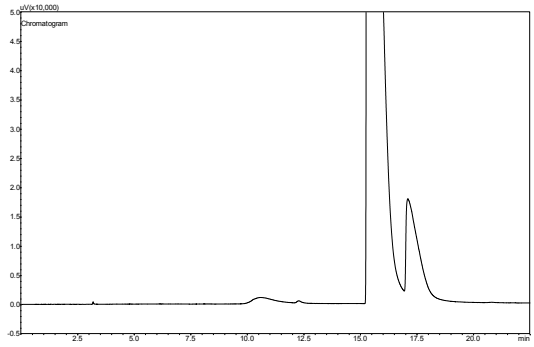

Figure I.185. Shimadzu G.C. 2010 FID chromatogram, experiment 33i.

Table I.186. Shimadzu G.C. 2014 TCD chromatogram, experiment 33i.

Component	Peak area
O_2	51578
COF_2	20676.4
CF_3COF	1470.4
C_2F_4	-
c-C_3F_6	-
HFP	-
HFPO	-

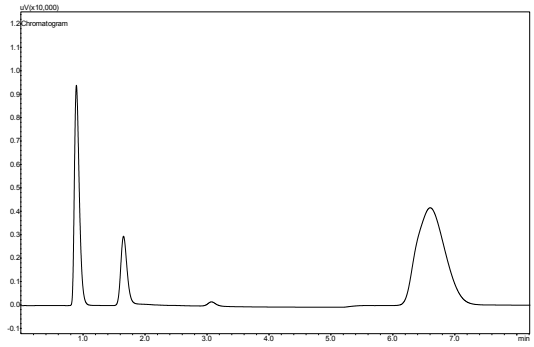

Figure I.186. Shimadzu G.C. 2014 TCD chromatogram, experiment 33i.

Table I.187. Shimadzu G.C. 2010 FID chromatogram, experiment 34a.

Component	Peak area
O_2	-
COF_2	-
CF_3COF	-
C_2F_4	207.6
c-C_3F_6	6414.5
HFP	11706544.4
HFPO	482577.5

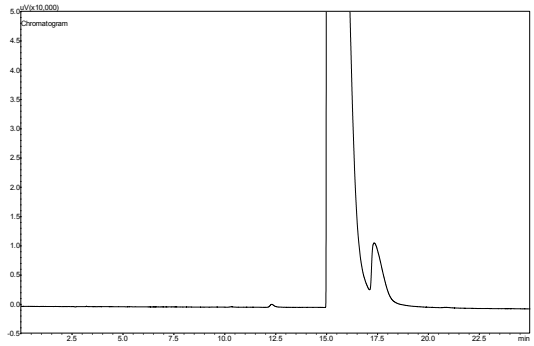

Figure I.187. Shimadzu G.C. 2010 FID chromatogram, experiment 34a.

Table I.188. Shimadzu G.C. 2014 TCD chromatogram, experiment 34a.

Component	Peak area
O_2	43946.5
COF_2	5672.5
CF_3COF	-
C_2F_4	-
c-C_3F_6	-
HFP	-
HFPO	-

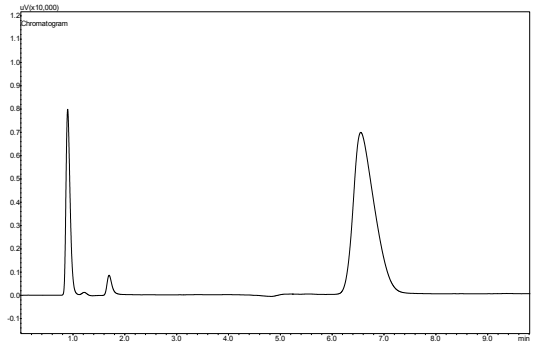

Figure I.188. Shimadzu G.C. 2014 TCD chromatogram, experiment 34a.

Table I.189. Shimadzu G.C. 2010 FID chromatogram, experiment 34b.

Component	Peak area
O_2	-
COF_2	-
CF_3COF	-
C_2F_4	1958.4
c-C_3F_6	7024
HFP	5770314.5
HFPO	1293203.1

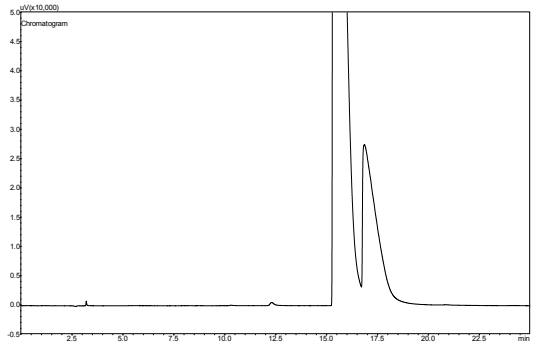

Figure I.189. Shimadzu G.C. 2010 FID chromatogram, experiment 34b.

Table I.190. Shimadzu G.C. 2014 TCD chromatogram, experiment 34b.

Component	Peak area
O_2	9655.2
COF_2	34229.5
CF_3COF	344.1
C_2F_4	-
c-C_3F_6	-
HFP	-
HFPO	-

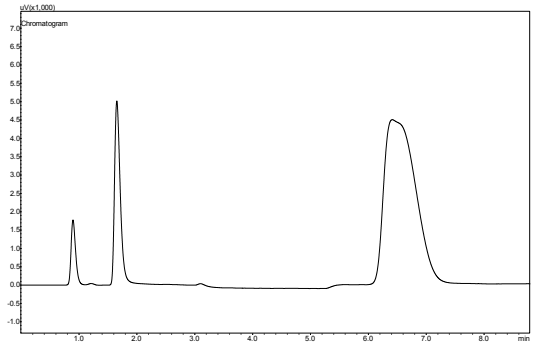

Figure I.190. Shimadzu G.C. 2014 TCD chromatogram, experiment 34b.

Table I.191. Shimadzu G.C. 2010 FID chromatogram, experiment 34c.

Component	Peak area
O_2	-
COF_2	-
CF_3COF	-
C_2F_4	106090.9
c-C_3F_6	29961.2
HFP	4313872.3
HFPO	1147239.4

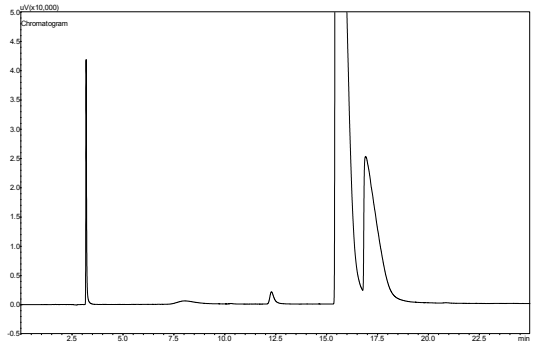

Figure I.191. Shimadzu G.C. 2010 FID chromatogram, experiment 34c.

Table I.192. Shimadzu G.C. 2014 TCD chromatogram, experiment 34c.

Component	Peak area
O_2	1036.6
COF_2	44746.4
CF_3COF	11924.8
C_2F_4	-
c-C_3F_6	-
HFP	-
HFPO	-

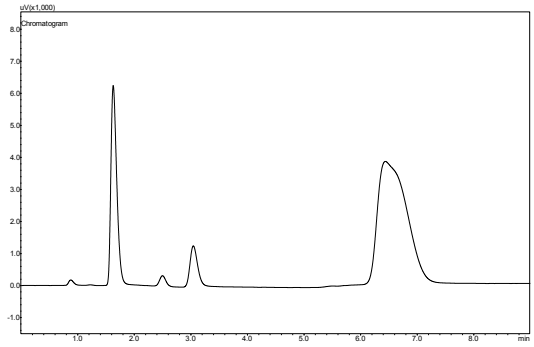

Figure I.192. Shimadzu G.C. 2014 TCD chromatogram, experiment 34c.

Table I.193. Shimadzu G.C. 2010 FID chromatogram, experiment 34d.

Component	Peak area
O_2	-
COF_2	-
CF_3COF	-
C_2F_4	387.8
c-C_3F_6	5816.9
HFP	21146.5
HFPO	672973.3

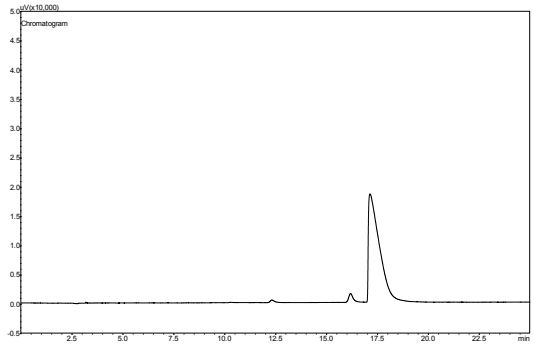

Figure I.193. Shimadzu G.C. 2010 FID chromatogram, experiment 34d.

Table I.194. Shimadzu G.C. 2014 TCD chromatogram, experiment 34d.

Component	Peak area
O_2	8039.4
COF_2	63079.8
CF_3COF	25448.6
C_2F_4	-
c-C_3F_6	-
HFP	-
HFPO	-

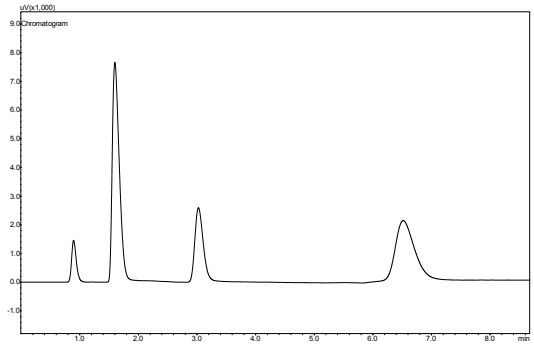

Figure I.194. Shimadzu G.C. 2014 TCD chromatogram, experiment 34d.

Table I.195. Shimadzu G.C. 2010 FID chromatogram, experiment 34e.

Component	Peak area
O_2	-
COF_2	-
CF_3COF	-
C_2F_4	862.5
c-C_3F_6	4964.7
HFP	696315.9
HFPO	1007709.1

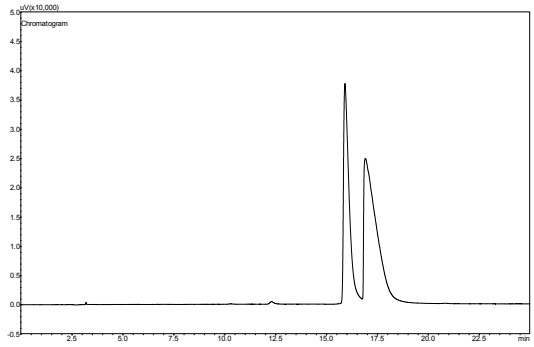

Figure I.195. Shimadzu G.C. 2010 FID chromatogram, experiment 34e.

Table I.196. Shimadzu G.C. 2014 TCD chromatogram, experiment 34e.

Component	Peak area
O_2	18483.1
COF_2	54006.9
CF_3COF	18880.8
C_2F_4	-
c-C_3F_6	-
HFP	-
HFPO	-

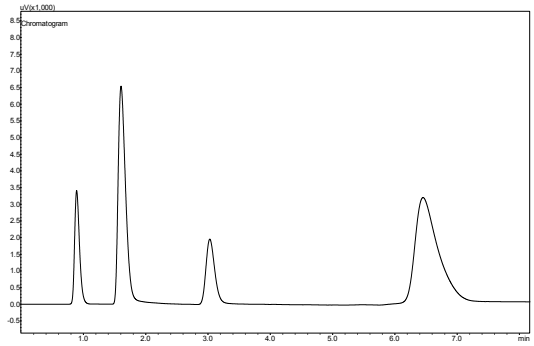

Figure I.196. Shimadzu G.C. 2014 TCD chromatogram, experiment 34e.

Table I.197. Shimadzu G.C. 2010 FID chromatogram, experiment 34f.

Component	Peak area
O_2	-
COF_2	-
CF_3COF	-
C_2F_4	309.5
c-C_3F_6	4562.8
HFP	6948699.8
HFPO	667944.1

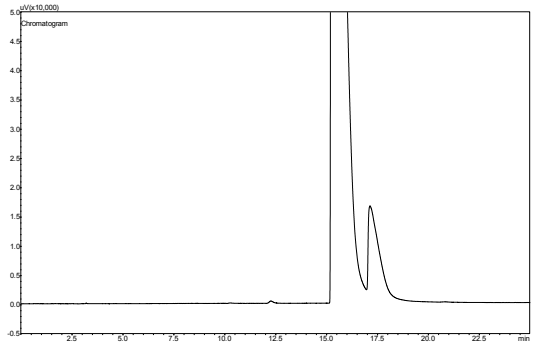

Figure I.197. Shimadzu G.C. 2010 FID chromatogram, experiment 34f.

Table I.198. Shimadzu G.C. 2014 TCD chromatogram, experiment 34f.

Component	Peak area
O_2	53678.2
COF_2	17043.5
CF_3COF	187.2
C_2F_4	-
c-C_3F_6	-
HFP	-
HFPO	-

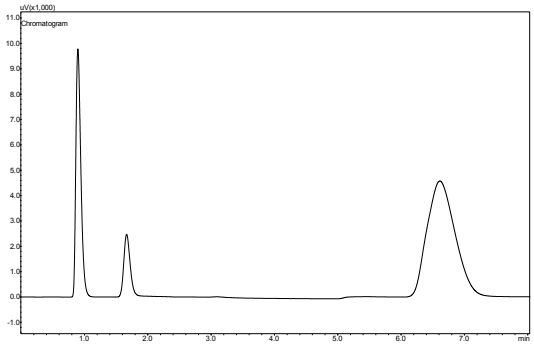

Figure I.198. Shimadzu G.C. 2014 TCD chromatogram, experiment 34f.

Table I.199. Shimadzu G.C. 2010 FID chromatogram, experiment 34g.

Component	Peak area
O_2	-
COF_2	-
CF_3COF	-
C_2F_4	157.1
c-C_3F_6	4909.2
HFP	8318595.2
HFPO	490935.1

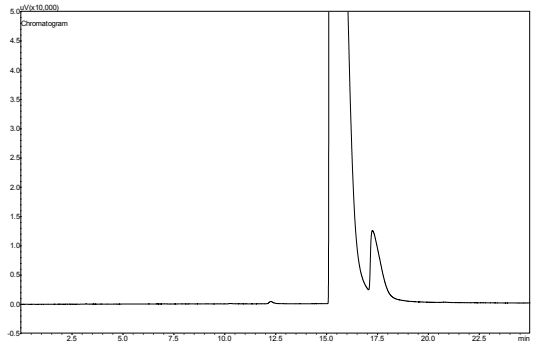

Figure I.199. Shimadzu G.C. 2010 FID chromatogram, experiment 34g.

Table I.200. Shimadzu G.C. 2014 TCD chromatogram, experiment 34g.

Component	Peak area
O_2	60894.9
COF_2	10703.2
CF_3COF	-
C_2F_4	-
c-C_3F_6	-
HFP	-
HFPO	-

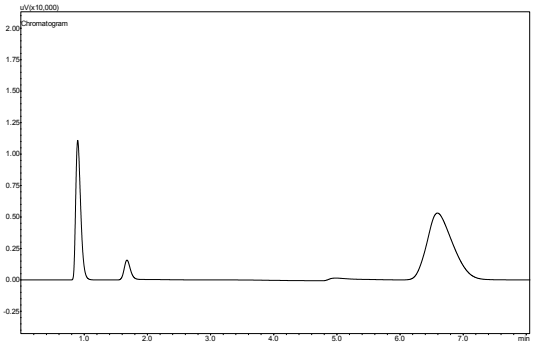

Figure I.200. Shimadzu G.C. 2014 TCD chromatogram, experiment 34g.

Table I.201. Shimadzu G.C. 2010 FID chromatogram, experiment 34h.

Component	Peak area
O_2	-
COF_2	-
CF_3COF	-
C_2F_4	1321.5
c-C_3F_6	5709.1
HFP	3257365
HFPO	1013884.9

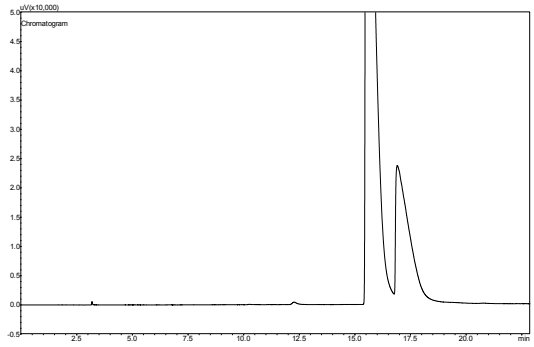

Figure I.201. Shimadzu G.C. 2010 FID chromatogram, experiment 34h.

Table I.202. Shimadzu G.C. 2014 TCD chromatogram, experiment 34h.

Component	Peak area
O_2	34722.1
COF_2	37847
CF_3COF	7544.7
C_2F_4	-
c-C_3F_6	-
HFP	-
HFPO	-

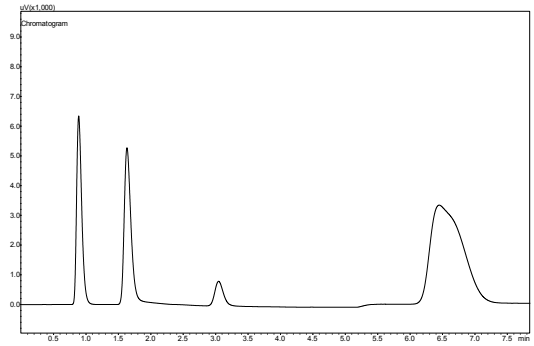

Figure I.202. Shimadzu G.C. 2014 TCD chromatogram, experiment 34h.

Table I.203. Shimadzu G.C. 2010 FID chromatogram, experiment 35a.

Component	Peak area
O_2	-
COF_2	-
CF_3COF	-
C_2F_4	86.5
c-C_3F_6	4302.5
HFP	9145318.7
HFPO	228894.2

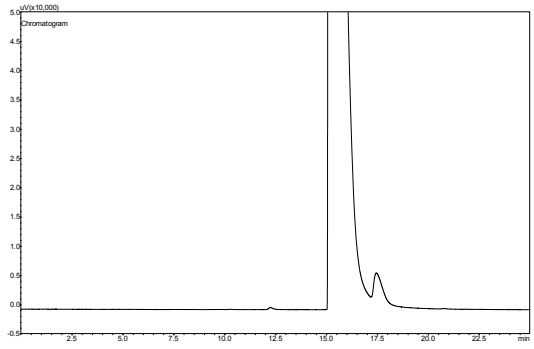

Figure I.203. Shimadzu G.C. 2010 FID chromatogram, experiment 35a.

Table I.204. Shimadzu G.C. 2014 TCD chromatogram, experiment 35a.

Component	Peak area
O_2	74083.9
COF_2	2827
CF_3COF	-
C_2F_4	-
c-C_3F_6	-
HFP	-
HFPO	-

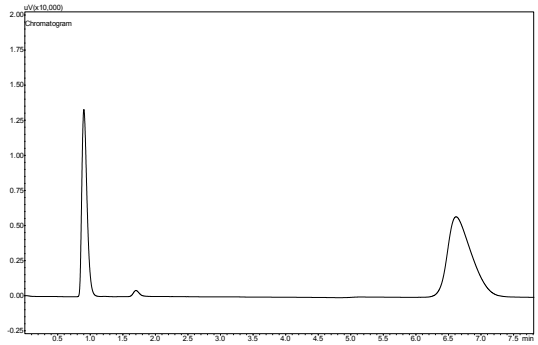

Figure I.204. Shimadzu G.C. 2014 TCD chromatogram, experiment 35a.

Table I.205. Shimadzu G.C. 2010 FID chromatogram, experiment 35b.

Component	Peak area
O_2	-
COF_2	-
CF_3COF	-
C_2F_4	880.2
c-C_3F_6	4277.5
HFP	5882130.3
HFPO	653279.3

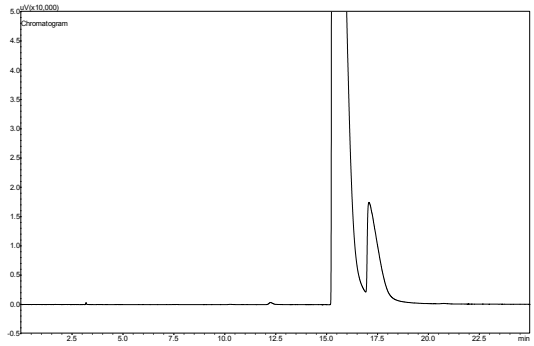

Figure I.205. Shimadzu G.C. 2010 FID chromatogram, experiment 35b.

Table I.206. Shimadzu G.C. 2014 TCD chromatogram, experiment 35b.

Component	Peak area
O_2	59680.5
COF_2	16388.6
CF_3COF	-
C_2F_4	-
c-C_3F_6	-
HFP	-
HFPO	-

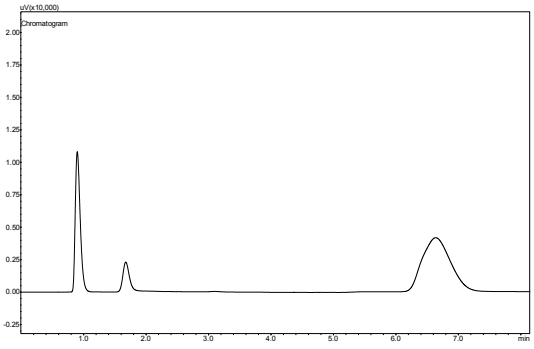

Figure I.206. Shimadzu G.C. 2014 TCD chromatogram, experiment 35b.

Table I.207. Shimadzu G.C. 2010 FID chromatogram, experiment 35c.

Component	Peak area
O_2	-
COF_2	-
CF_3COF	-
C_2F_4	89.8
c-C_3F_6	4540.8
HFP	34273.3
HFPO	769706.5

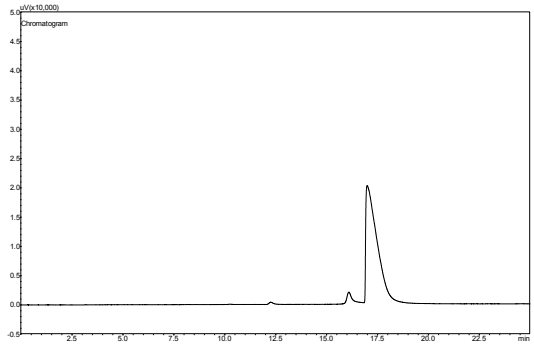

Figure I.207. Shimadzu G.C. 2010 FID chromatogram, experiment 35c.

Table I.208. Shimadzu G.C. 2014 TCD chromatogram, experiment 35c.

Component	Peak area
O_2	18981.3
COF_2	58246.7
CF_3COF	21843.2
C_2F_4	-
c-C_3F_6	-
HFP	-
HFPO	-

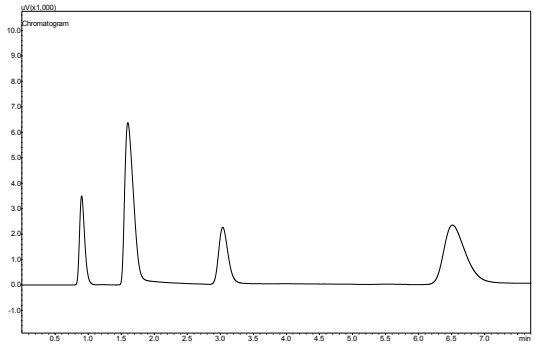

Figure I.208. Shimadzu G.C. 2014 TCD chromatogram, experiment 35c.

Table I.209. Shimadzu G.C. 2010 FID chromatogram, experiment 35d.

Component	Peak area
O_2	-
COF_2	-
CF_3COF	-
C_2F_4	59.5
c-C_3F_6	4951
HFP	9796.1
HFPO	797575.6

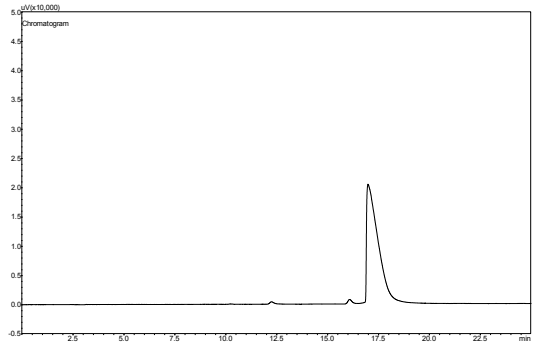

Figure I.209. Shimadzu G.C. 2010 FID chromatogram, experiment 35d.

Table I.210. Shimadzu G.C. 2014 TCD chromatogram, experiment 35d.

Component	Peak area
O_2	8482.3
COF_2	67497.7
CF_3COF	27052.1
C_2F_4	-
c-C_3F_6	-
HFP	-
HFPO	-

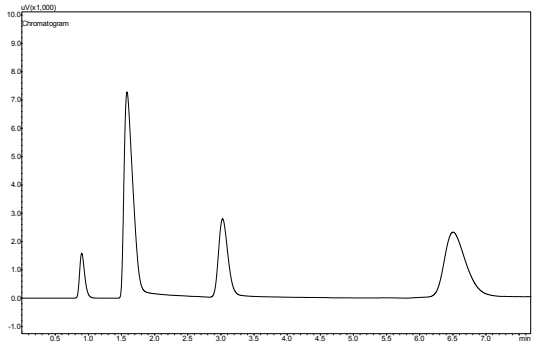

Figure I.210. Shimadzu G.C. 2014 TCD chromatogram, experiment 35d.

Table I.211. Shimadzu G.C. 2010 FID chromatogram, experiment 35e.

Component	Peak area
O_2	-
COF_2	-
CF_3COF	-
C_2F_4	1997.5
c-C_3F_6	7090.4
HFP	4625157.6
HFPO	1333562.8

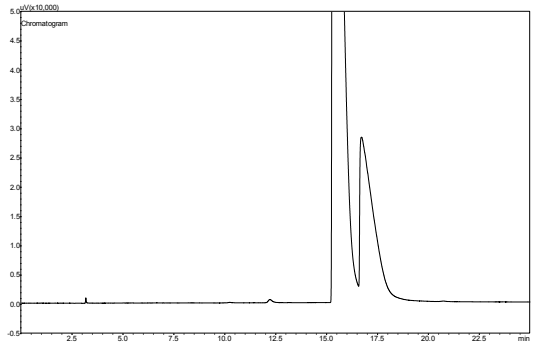

Figure I.211. Shimadzu G.C. 2010 FID chromatogram, experiment 35e.

Table I.212. Shimadzu G.C. 2014 TCD chromatogram, experiment 35e.

Component	Peak area
O_2	9532.6
COF_2	43765
CF_3COF	13419.3
C_2F_4	-
c-C_3F_6	-
HFP	-
HFPO	-

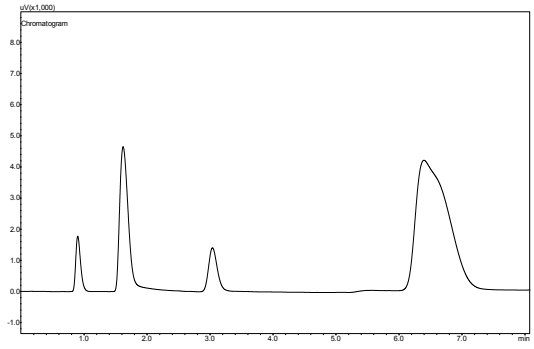

Figure I.212. Shimadzu G.C. 2014 TCD chromatogram, experiment 35e.

Table I.213. Shimadzu G.C. 2010 FID chromatogram, experiment 35f.

Component	Peak area
O_2	-
COF_2	-
CF_3COF	-
C_2F_4	160.6
c-C_3F_6	6147.4
HFP	10515117.6
HFPO	559537.5

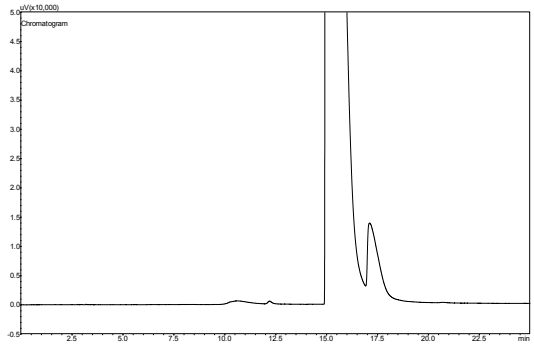

Figure I.213. Shimadzu G.C. 2010 FID chromatogram, experiment 35f.

Table I.214. Shimadzu G.C. 2014 TCD chromatogram, experiment 35f.

Component	Peak area
O_2	43035.2
COF_2	11785
CF_3COF	127.1
C_2F_4	-
c-C_3F_6	-
HFP	-
HFPO	-

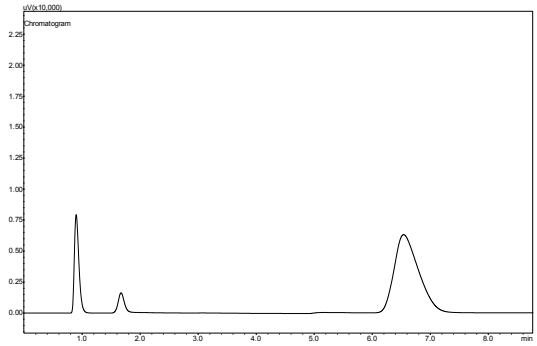

Figure I.214. Shimadzu G.C. 2014 TCD chromatogram, experiment 35f.

Table I.215. Shimadzu G.C. 2010 FID chromatogram, experiment 35g.

Component	Peak area
O_2	-
COF_2	-
CF_3COF	-
C_2F_4	2970.5
c-C_3F_6	7377.8
HFP	6119910.7
HFPO	1307264.6

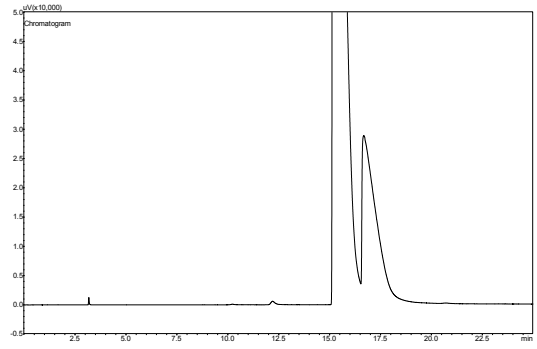

Figure I.215. Shimadzu G.C. 2010 FID chromatogram, experiment 35g.

Table I.216. Shimadzu G.C. 2014 TCD chromatogram, experiment 35g.

Component	Peak area
O_2	4861.5
COF_2	38836.7
CF_3COF	11947.9
C_2F_4	-
c-C_3F_6	-
HFP	-
HFPO	-

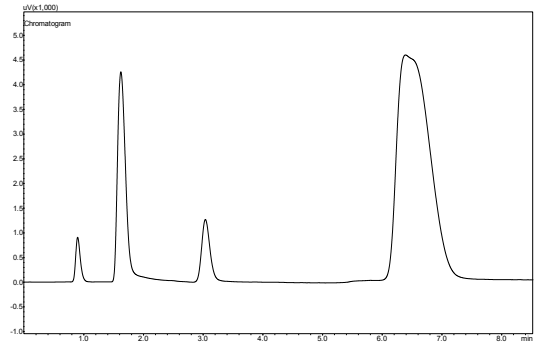

Figure I.216. Shimadzu G.C. 2014 TCD chromatogram, experiment 35g.

Table I.217. Shimadzu G.C. 2010 FID chromatogram, experiment 35h.

Component	Peak area
O_2	-
COF_2	-
CF_3COF	-
C_2F_4	114239.5
c-C_3F_6	34583
HFP	3199387.7
HFPO	1070289

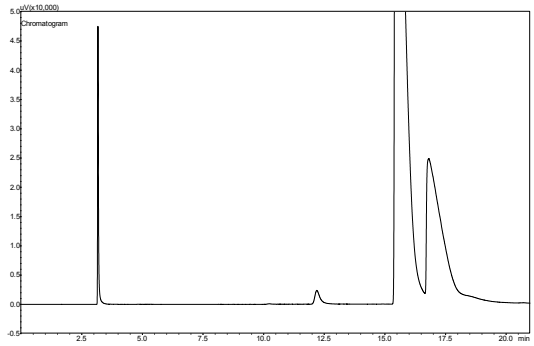

Figure I.217. Shimadzu G.C. 2010 FID chromatogram, experiment 35h.

Table I.218. Shimadzu G.C. 2014 TCD chromatogram, experiment 35h.

Component	Peak area
O_2	590
COF_2	51534.4
CF_3COF	23760.2
C_2F_4	-
c-C_3F_6	-
HFP	-
HFPO	-

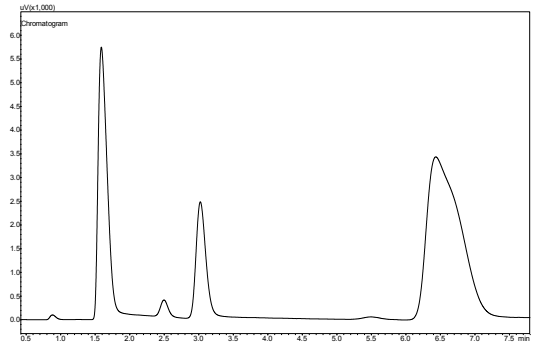

Figure I.218. Shimadzu G.C. 2014 TCD chromatogram, experiment 35h.

Table I.219. Shimadzu G.C. 2010 FID chromatogram, experiment 36a.

Component	Peak area
O_2	-
COF_2	-
CF_3COF	-
C_2F_4	190.9
c-C_3F_6	6300
HFP	12274121.1
HFPO	509233

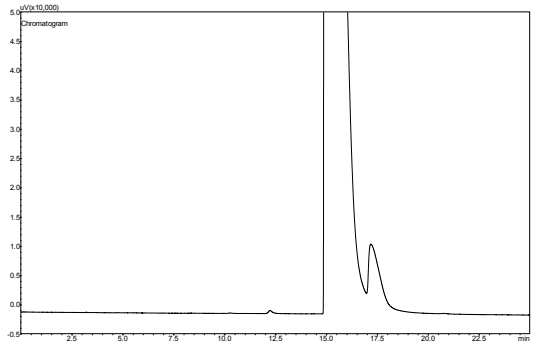

Figure I.219. Shimadzu G.C. 2010 FID chromatogram, experiment 36a.

Table I.220. Shimadzu G.C. 2014 TCD chromatogram, experiment 36a.

Component	Peak area
O_2	41725.8
COF_2	7424.9
CF_3COF	-
C_2F_4	-
c-C_3F_6	-
HFP	-
HFPO	-

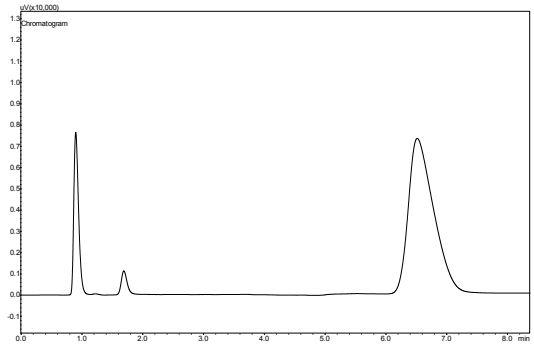

Figure I.220. Shimadzu G.C. 2014 TCD chromatogram, experiment 36a.

Table I.221. Shimadzu G.C. 2010 FID chromatogram, experiment 36b.

Component	Peak area
O_2	-
COF_2	-
CF_3COF	-
C_2F_4	73.6
c-C_3F_6	3858.7
HFP	8299754.8
HFPO	227234.1

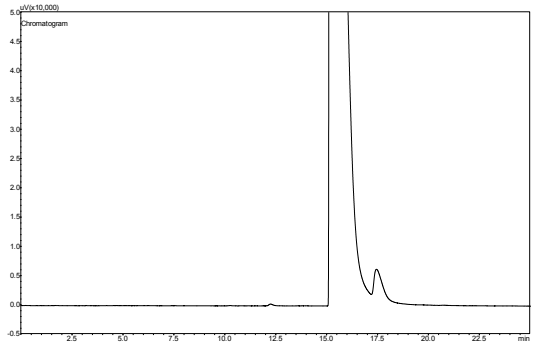

Figure I.221. Shimadzu G.C. 2010 FID chromatogram, experiment 36b.

Table I.222. Shimadzu G.C. 2014 TCD chromatogram, experiment 36b.

Component	Peak area
O_2	78762.4
COF_2	3317
CF_3COF	-
C_2F_4	-
c-C_3F_6	-
HFP	-
HFPO	-

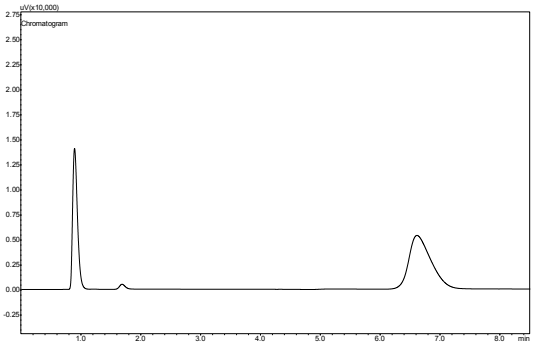

Figure I.222. Shimadzu G.C. 2014 TCD chromatogram, experiment 36b.

Table I.223. Shimadzu G.C. 2010 FID chromatogram, experiment 36c.

Component	Peak area
O_2	-
COF_2	-
CF_3COF	-
C_2F_4	784.2
c-C_3F_6	3850.7
HFP	4618360.9
HFPO	686873.6

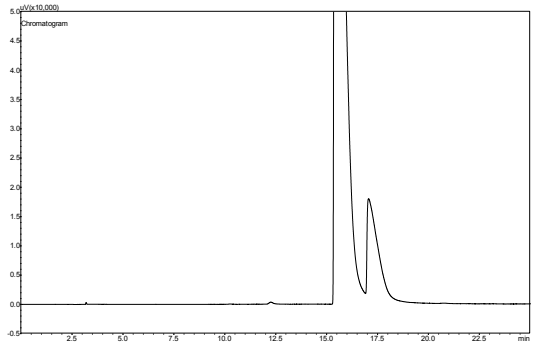

Figure I.223. Shimadzu G.C. 2010 FID chromatogram, experiment 36c.

Table I.224. Shimadzu G.C. 2014 TCD chromatogram, experiment 36c.

Component	Peak area
O_2	62477.1
COF_2	19877.8
CF_3COF	1811.4
C_2F_4	-
c-C_3F_6	-
HFP	-
HFPO	-

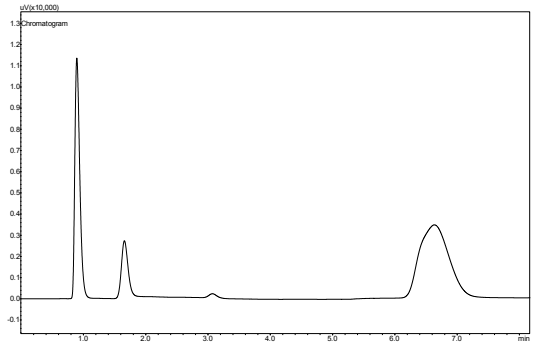

Figure I.224. Shimadzu G.C. 2014 TCD chromatogram, experiment 36c.

Table I.225. Shimadzu G.C. 2010 FID chromatogram, experiment 36d.

Component	Peak area
O_2	-
COF_2	-
CF_3COF	-
C_2F_4	56.7
c-C_3F_6	3746.2
HFP	15907.4
HFPO	685986.4

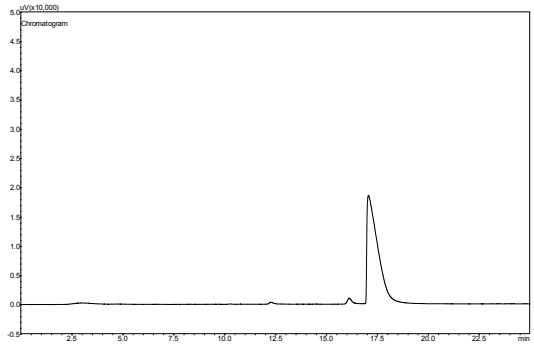

Figure I.225. Shimadzu G.C. 2010 FID chromatogram, experiment 36d.

Table I.226. Shimadzu G.C. 2014 TCD chromatogram, experiment 36d.

Component	Peak area
O_2	29306.7
COF_2	56178.7
CF_3COF	20861.9
C_2F_4	-
c-C_3F_6	-
HFP	-
HFPO	-

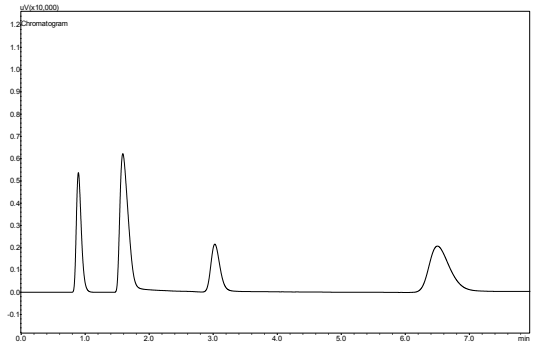

Figure I.226. Shimadzu G.C. 2014 TCD chromatogram, experiment 36d.

Table I.227. Shimadzu G.C. 2010 FID chromatogram, experiment 36e.

Component	Peak area
O_2	-
COF_2	-
CF_3COF	-
C_2F_4	129910.5
c-C_3F_6	59054.3
HFP	5374776.3
HFPO	1066154.1

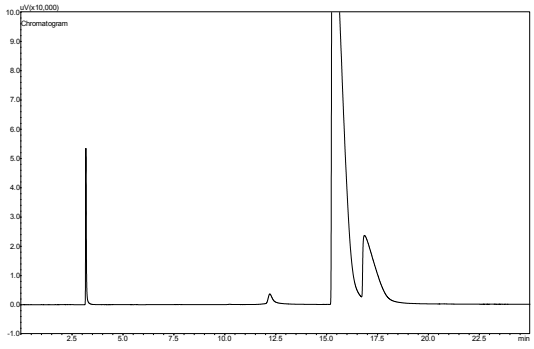

Figure I.227. Shimadzu G.C. 2010 FID chromatogram, experiment 36e.

Table I.228. Shimadzu G.C. 2014 TCD chromatogram, experiment 36e.

Component	Peak area
O_2	706.2
COF_2	42937.3
CF_3COF	20714.6
C_2F_4	-
c-C_3F_6	-
HFP	-
HFPO	-

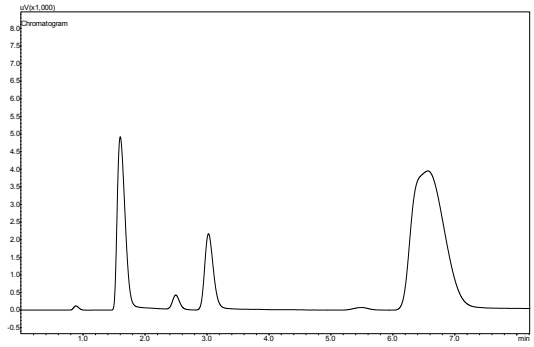

Figure I.228. Shimadzu G.C. 2014 TCD chromatogram, experiment 36e.

Table I.229. Shimadzu G.C. 2010 FID chromatogram, experiment 36f.

Component	Peak area
O_2	-
COF_2	-
CF_3COF	-
C_2F_4	546.3
c-C_3F_6	6237.2
HFP	9482370.6
HFPO	618361.3

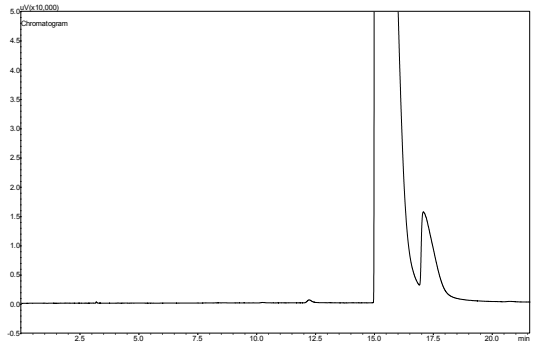

Figure I.229. Shimadzu G.C. 2010 FID chromatogram, experiment 36f.

Table I.230. Shimadzu G.C. 2014 TCD chromatogram, experiment 36f.

Component	Peak area
O_2	44011.2
COF_2	13891.9
CF_3COF	1229.9
C_2F_4	-
c-C_3F_6	-
HFP	-
HFPO	-

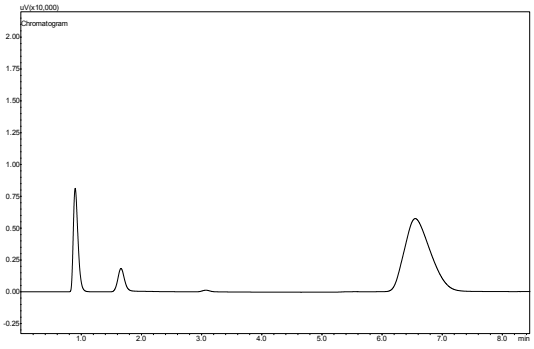

Figure I.230. Shimadzu G.C. 2014 TCD chromatogram, experiment 36f.

Table I.231. Shimadzu G.C. 2010 FID chromatogram, experiment 36g.

Component	Peak area
O_2	-
COF_2	-
CF_3COF	-
C_2F_4	1885.5
c-C_3F_6	7081.5
HFP	4830770
HFPO	1231001.4

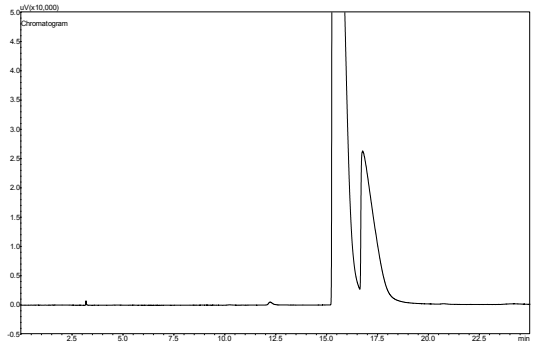

Figure I.231. Shimadzu G.C. 2010 FID chromatogram, experiment 36g.

Table I.232. Shimadzu G.C. 2014 TCD chromatogram, experiment 36g.

Component	Peak area
O_2	21573.8
COF_2	34759.7
CF_3COF	11732.1
C_2F_4	-
c-C_3F_6	-
HFP	-
HFPO	-

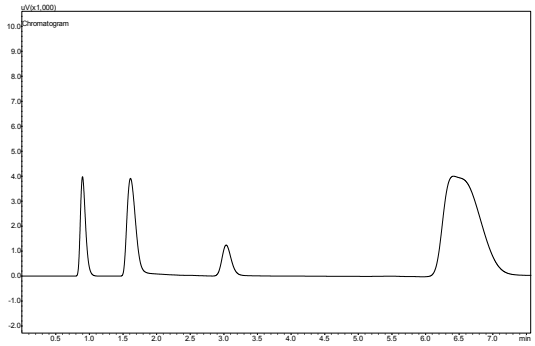

Figure I.232. Shimadzu G.C. 2014 TCD chromatogram, experiment 36g.

Table I.233. Shimadzu G.C. 2010 FID chromatogram, experiment 36h.

Component	Peak area
O_2	-
COF_2	-
CF_3COF	-
C_2F_4	117474
c-C_3F_6	35648.1
HFP	1707369.9
HFPO	909781.8

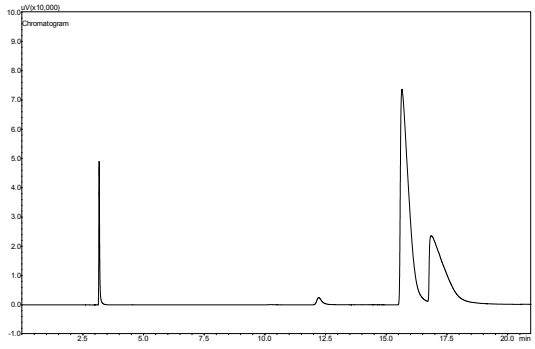

Figure I.233. Shimadzu G.C. 2010 FID chromatogram, experiment 36h.

Table I.234. Shimadzu G.C. 2014 TCD chromatogram, experiment 36h.

Component	Peak area
O_2	730.8
COF_2	58104.7
CF_3COF	27730
C_2F_4	-
c-C_3F_6	-
HFP	-
HFPO	-

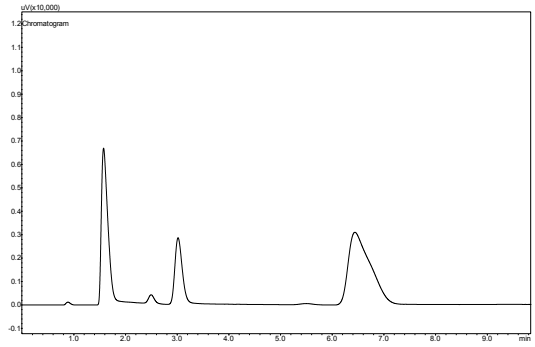

Figure I.234. Shimadzu G.C. 2014 TCD chromatogram, experiment 36h.

Table I.235. Shimadzu G.C. 2010 FID chromatogram, experiment 37a.

Component	Peak area
O_2	-
COF_2	-
CF_3COF	-
C_2F_4	99.9
c-C_3F_6	4535.2
HFP	9755048.8
HFPO	266266.5

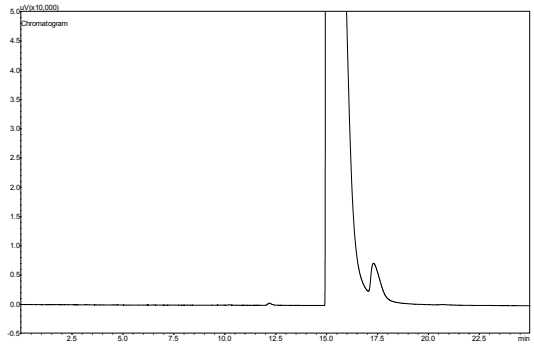

Figure I.235. Shimadzu G.C. 2010 FID chromatogram, experiment 37a.

Table I.236. Shimadzu G.C. 2014 TCD chromatogram, experiment 37a.

Component	Peak area
O_2	70109.7
COF_2	3530.4
CF_3COF	-
C_2F_4	-
c-C_3F_6	-
HFP	-
HFPO	-

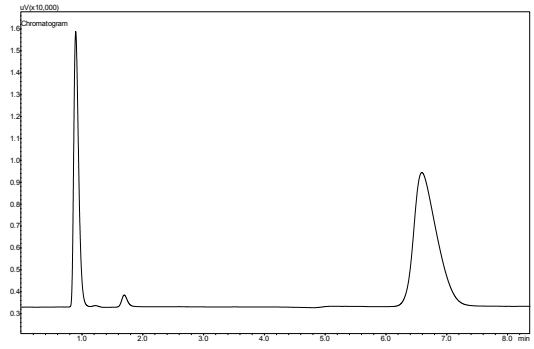

Figure I.236. Shimadzu G.C. 2014 TCD chromatogram, experiment 37a.

Table I.237. Shimadzu G.C. 2010 FID chromatogram, experiment 37b.

Component	Peak area
O_2	-
COF_2	-
CF_3COF	-
C_2F_4	951.3
c-C_3F_6	4823.5
HFP	6156835.8
HFPO	793175.1

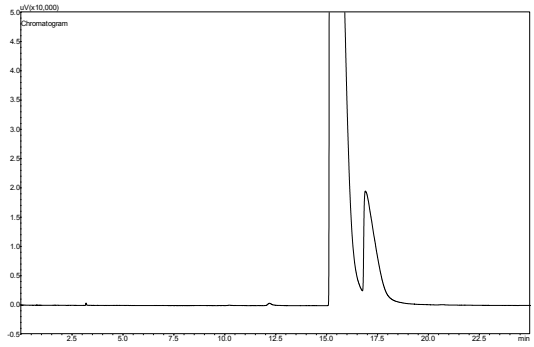

Figure I.237. Shimadzu G.C. 2010 FID chromatogram, experiment 37b.

Table I.238. Shimadzu G.C. 2014 TCD chromatogram, experiment 37b.

Component	Peak area
O_2	53340.5
COF_2	19303.9
CF_3COF	941.5
C_2F_4	-
c-C_3F_6	-
HFP	-
HFPO	-

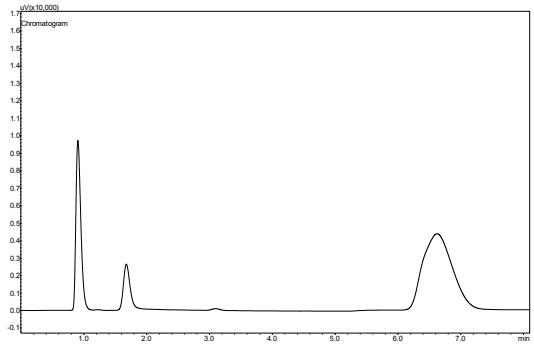

Figure I.238. Shimadzu G.C. 2014 TCD chromatogram, experiment 37b.

Table I.239. Shimadzu G.C. 2010 FID chromatogram, experiment 37c.

Component	Peak area
O_2	-
COF_2	-
CF_3COF	-
C_2F_4	71.3
c-C_3F_6	5541.9
HFP	25562.1
HFPO	849191.4

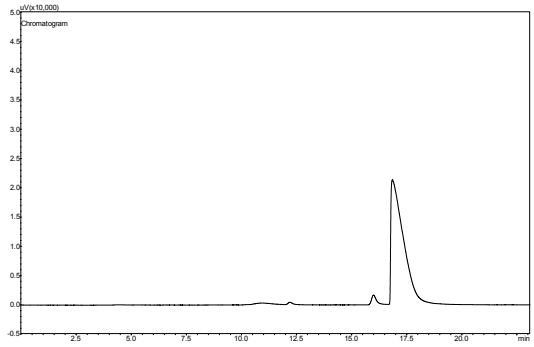

Figure I.239. Shimadzu G.C. 2010 FID chromatogram, experiment 37c.

Table I.240. Shimadzu G.C. 2014 TCD chromatogram, experiment 37c.

Component	Peak area
O_2	9706.1
COF_2	67059.9
CF_3COF	25831.6
C_2F_4	-
c-C_3F_6	-
HFP	-
HFPO	-

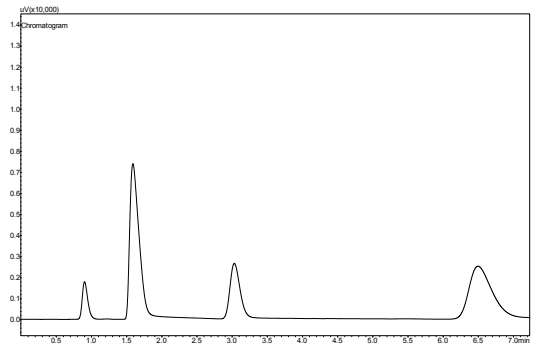

Figure I.240. Shimadzu G.C. 2014 TCD chromatogram, experiment 37c.

Table I.241. Shimadzu G.C. 2010 FID chromatogram, experiment 37d.

Component	Peak area
O_2	-
COF_2	-
CF_3COF	-
C_2F_4	94.6
c-C_3F_6	4982.4
HFP	10777.4
HFPO	763799.7

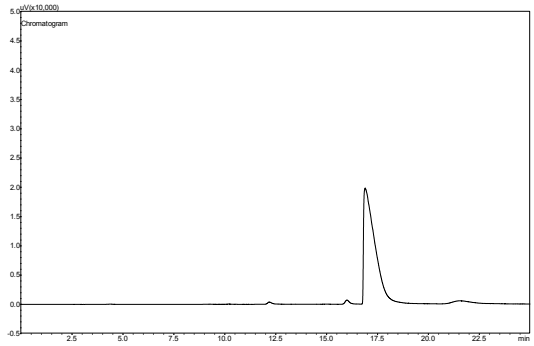

Figure I.241. Shimadzu G.C. 2010 FID chromatogram, experiment 37d.

Table I.242. Shimadzu G.C. 2014 TCD chromatogram, experiment 37d.

Component	Peak area
O_2	28261
COF_2	60750.6
CF_3COF	22303.8
C_2F_4	-
c-C_3F_6	-
HFP	-
HFPO	-

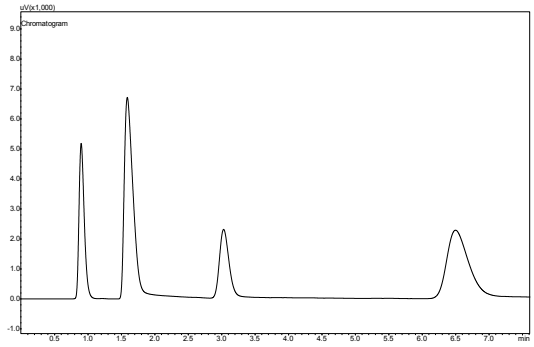

Figure I.242. Shimadzu G.C. 2014 TCD chromatogram, experiment 37d.

Table I.243. Shimadzu G.C. 2010 FID chromatogram, experiment 37e.

Component	Peak area
O_2	-
COF_2	-
CF_3COF	-
C_2F_4	806.5
c-C_3F_6	4251.2
HFP	5083822.8
HFPO	645974.8

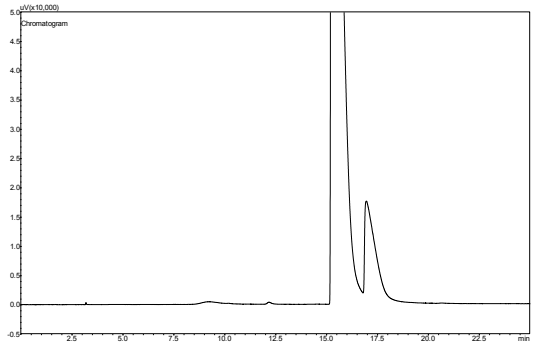

Figure I.243. Shimadzu G.C. 2010 FID chromatogram, experiment 37e.

Table I.244. Shimadzu G.C. 2014 TCD chromatogram, experiment 37e.

Component	Peak area
O_2	61954.4
COF_2	20828.1
CF_3COF	3741
C_2F_4	-
c-C_3F_6	-
HFP	-
HFPO	-

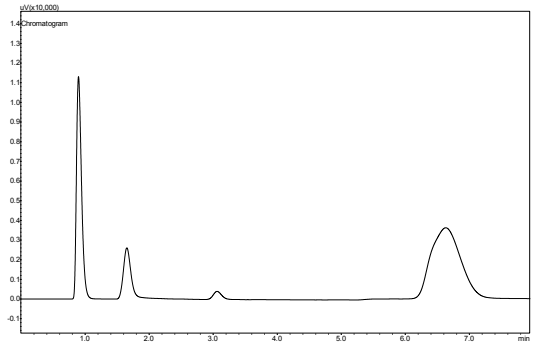

Figure I.244. Shimadzu G.C. 2014 TCD chromatogram, experiment 37e.

Table I.245. Shimadzu G.C. 2010 FID chromatogram, experiment 37f.

Component	Peak area
O_2	-
COF_2	-
CF_3COF	-
C_2F_4	44.3
c-C_3F_6	3739.7
HFP	8298084
HFPO	271683.6

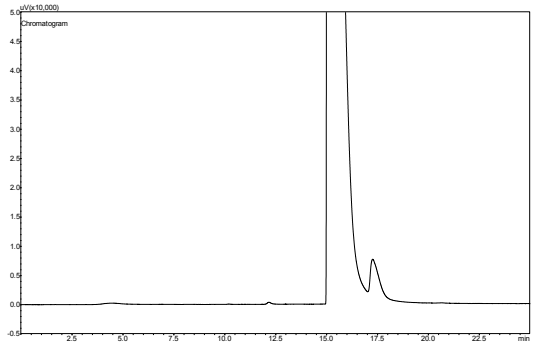

Figure I.245. Shimadzu G.C. 2010 FID chromatogram, experiment 37f.

Table I.246. Shimadzu G.C. 2014 TCD chromatogram, experiment 37f.

Component	Peak area
O_2	76682.1
COF_2	4788.5
CF_3COF	-
C_2F_4	-
c-C_3F_6	-
HFP	-
HFPO	-

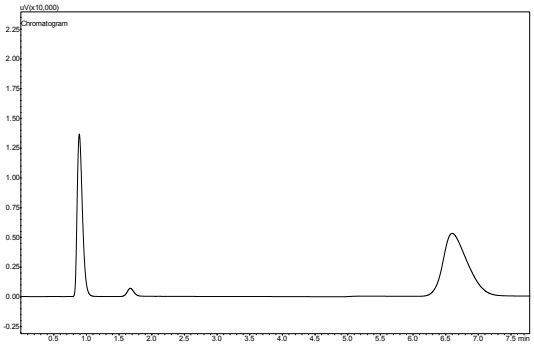

Figure I.246. Shimadzu G.C. 2014 TCD chromatogram, experiment 37f.

Table I.247. Shimadzu G.C. 2010 FID chromatogram, experiment 37g.

Component	Peak area
O_2	-
COF_2	-
CF_3COF	-
C_2F_4	79.6
c-C_3F_6	5046.5
HFP	10965748.4
HFPO	319402.1

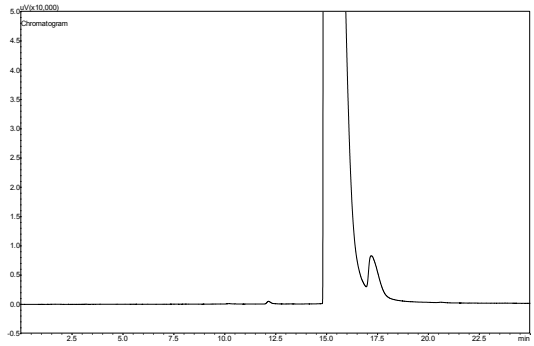

Figure I.247. Shimadzu G.C. 2010 FID chromatogram, experiment 37g.

Table I.248. Shimadzu G.C. 2014 TCD chromatogram, experiment 37g.

Component	Peak area
O_2	59782.9
COF_2	4848.6
CF_3COF	-
C_2F_4	-
c-C_3F_6	-
HFP	-
HFPO	-

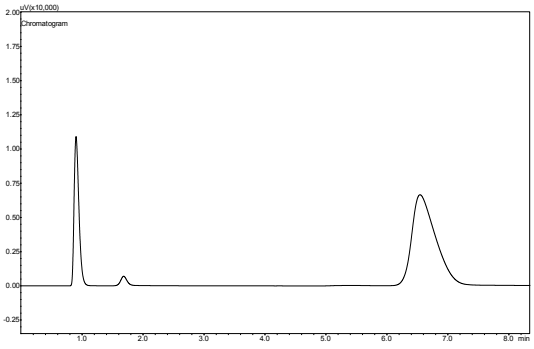

Figure I.248. Shimadzu G.C. 2014 TCD chromatogram, experiment 37g.

Table I.249. Shimadzu G.C. 2010 FID chromatogram, experiment 37h.

Component	Peak area
O_2	-
COF_2	-
CF_3COF	-
C_2F_4	1023.8
c-C_3F_6	5724.8
HFP	7477486.5
HFPO	836126.2

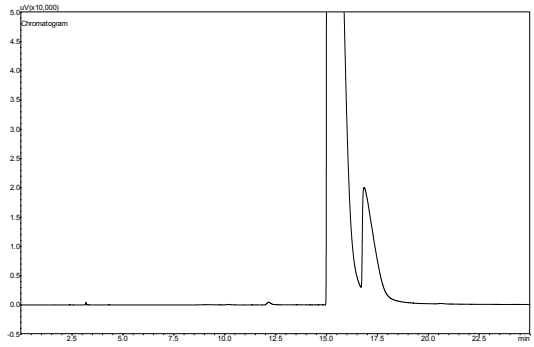

Figure I.249. Shimadzu G.C. 2010 FID chromatogram, experiment 37h.

Table I.250. Shimadzu G.C. 2014 TCD chromatogram, experiment 37h.

Component	Peak area
O_2	41746.8
COF_2	20745.6
CF_3COF	3956.8
C_2F_4	-
c-C_3F_6	-
HFP	-
HFPO	-

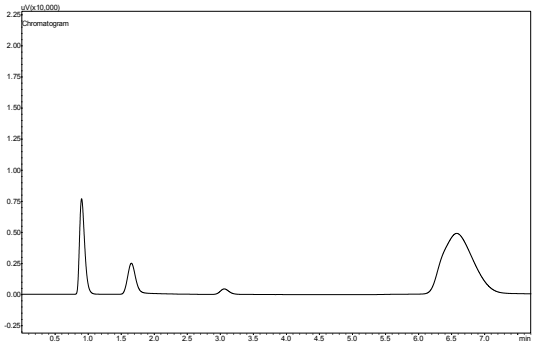

Figure I.250. Shimadzu G.C. 2014 TCD chromatogram, experiment 37h.

Table I.251. Shimadzu G.C. 2010 FID chromatogram, experiment 37i.

Component	Peak area
O_2	-
COF_2	-
CF_3COF	-
C_2F_4	51790
c-C_3F_6	11218.7
HFP	899999.2
HFPO	1029298.4

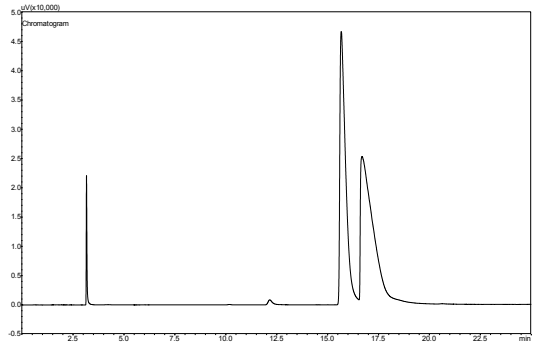

Figure I.251. Shimadzu G.C. 2010 FID chromatogram, experiment 37i.

Table I.252. Shimadzu G.C. 2014 TCD chromatogram, experiment 37i.

Component	Peak area
O_2	799.7
COF_2	64539.1
CF_3COF	26650.5
C_2F_4	-
c-C_3F_6	-
HFP	-
HFPO	-

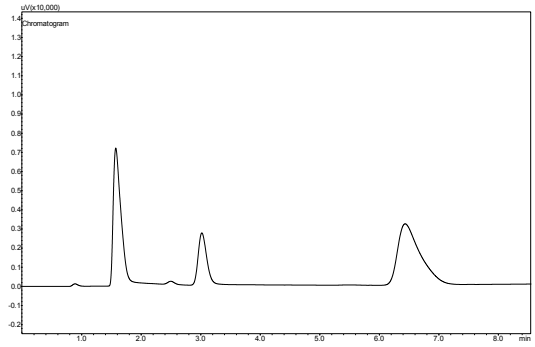

Figure I.252. Shimadzu G.C. 2014 TCD chromatogram, experiment 37i.

Table I.253. Shimadzu G.C. 2010 FID chromatogram, experiment 38a.

Component	Peak area
O_2	-
COF_2	-
CF_3COF	-
C_2F_4	185.5
c-C_3F_6	7299.5
HFP	13714491.1
HFPO	523428.1

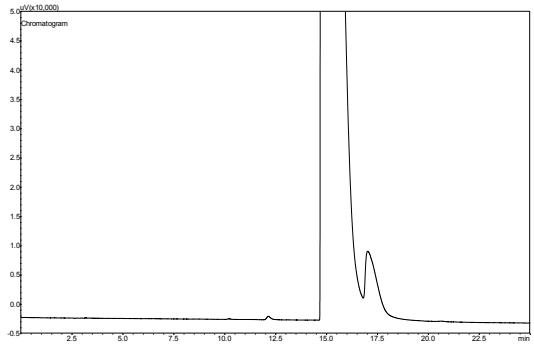

Figure I.253. Shimadzu G.C. 2010 FID chromatogram, experiment 38a.

Table I.254. Shimadzu G.C. 2014 TCD chromatogram, experiment 38a.

Component	Peak area
O_2	32075.8
COF_2	7690.4
CF_3COF	-
C_2F_4	-
c-C_3F_6	-
HFP	-
HFPO	-

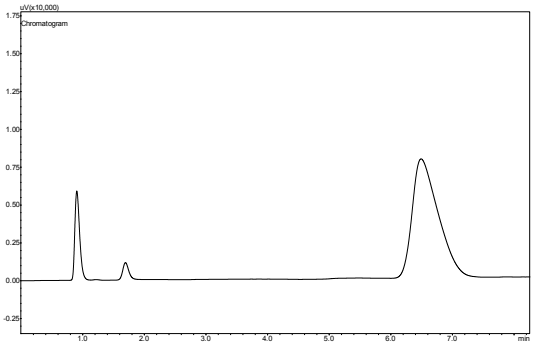

Figure I.254. Shimadzu G.C. 2014 TCD chromatogram, experiment 38a.

Table I.255. Shimadzu G.C. 2010 FID chromatogram, experiment 38b.

Component	Peak area
O_2	-
COF_2	-
CF_3COF	-
C_2F_4	7590.2
c-C_3F_6	8139.9
HFP	8552658.2
HFPO	1363133.5

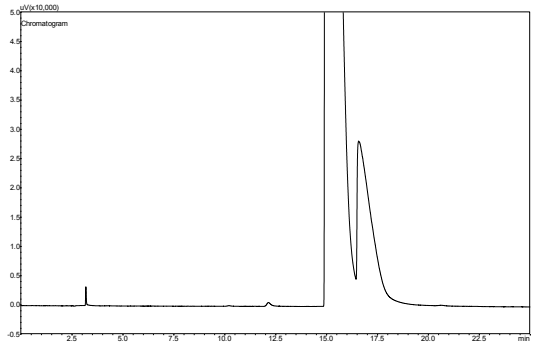

Figure I.255. Shimadzu G.C. 2010 FID chromatogram, experiment 38b.

Table I.256. Shimadzu G.C. 2014 TCD chromatogram, experiment 38b.

Component	Peak area
O_2	2094.8
COF_2	32814.7
CF_3COF	7788.9
C_2F_4	-
c-C_3F_6	-
HFP	-
HFPO	-

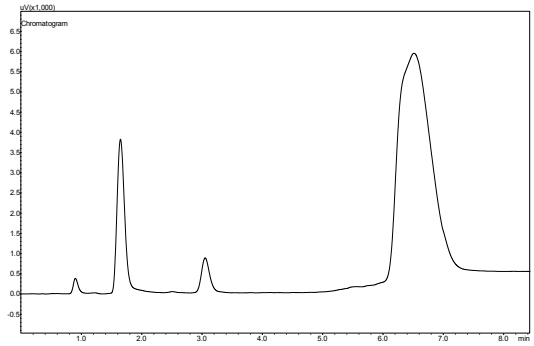

Figure I.256. Shimadzu G.C. 2014 TCD chromatogram, experiment 38b.

Table I.257. Shimadzu G.C. 2010 FID chromatogram, experiment 38c.

Component	Peak area
O_2	-
COF_2	-
CF_3COF	-
C_2F_4	123717
c-C_3F_6	46233
HFP	8249344.8
HFPO	1046754.3

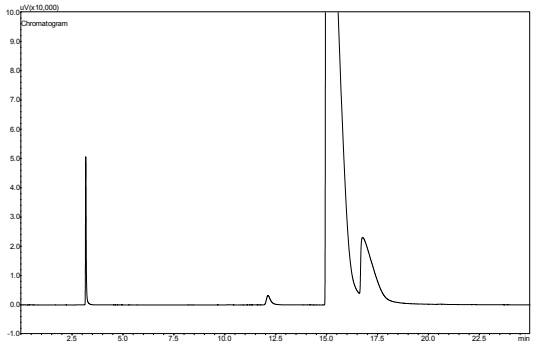

Figure I.257. Shimadzu G.C. 2010 FID chromatogram, experiment 38c.

Table I.258. Shimadzu G.C. 2014 TCD chromatogram, experiment 38c.

Component	Peak area
O_2	673.4
COF_2	35958
CF_3COF	15598.3
C_2F_4	-
c-C_3F_6	-
HFP	-
HFPO	-

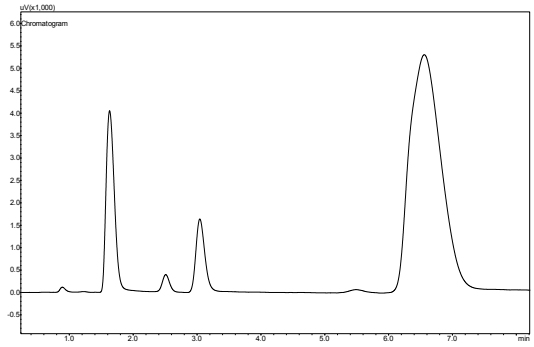

Figure I.258. Shimadzu G.C. 2014 TCD chromatogram, experiment 38c.

Table I.259. Shimadzu G.C. 2010 FID chromatogram, experiment 38d.

Component	Peak area
O_2	-
COF_2	-
CF_3COF	-
C_2F_4	112259.9
c-C_3F_6	40177.9
HFP	9535231.1
HFPO	1184836.3

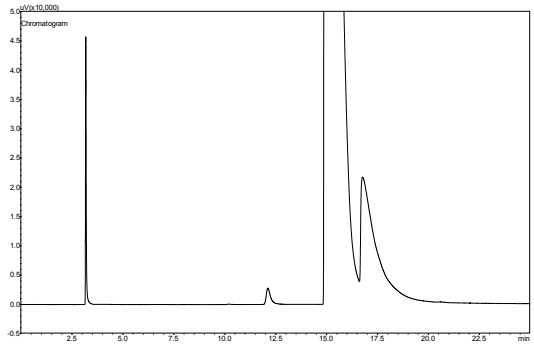

Figure I.259. Shimadzu G.C. 2010 FID chromatogram, experiment 38d.

Table I.260. Shimadzu G.C. 2014 TCD chromatogram, experiment 38d.

Component	Peak area
O_2	376
COF_2	32875.1
CF_3COF	14397.8
C_2F_4	-
c-C_3F_6	-
HFP	-
HFPO	-

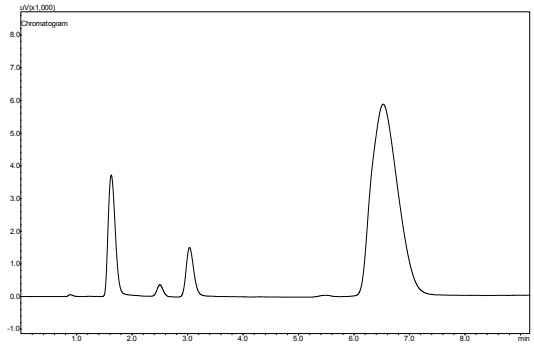

Figure I.260. Shimadzu G.C. 2014 TCD chromatogram, experiment 38d.

Table I.261. Shimadzu G.C. 2010 FID chromatogram, experiment 38e.

Component	Peak area
O_2	-
COF_2	-
CF_3COF	-
C_2F_4	20091
c-C_3F_6	7400.8
HFP	9693149.3
HFPO	1250735.1

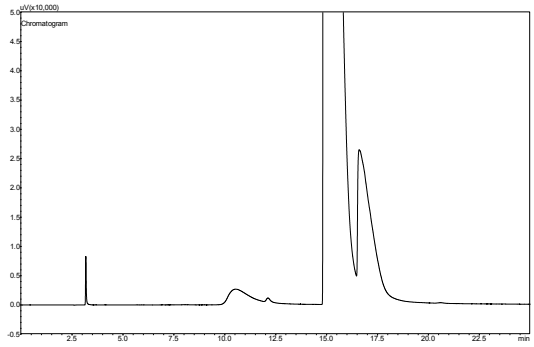

Figure I.261. Shimadzu G.C. 2010 FID chromatogram, experiment 38e.

Table I.262. Shimadzu G.C. 2014 TCD chromatogram, experiment 38e.

Component	Peak area
O_2	255.6
COF_2	31692
CF_3COF	9982.3
C_2F_4	-
c-C_3F_6	-
HFP	-
HFPO	-

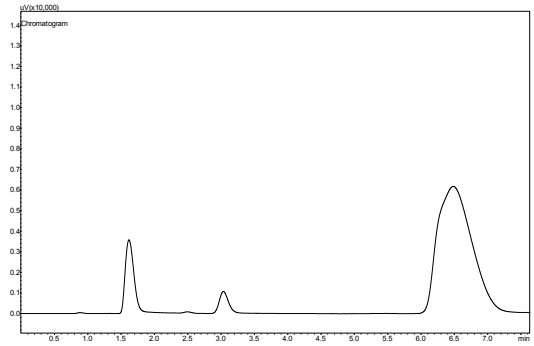

Figure I.262. Shimadzu G.C. 2014 TCD chromatogram, experiment 38e.

Table I.263. Shimadzu G.C. 2010 FID chromatogram, experiment 38f.

Component	Peak area
O_2	-
COF_2	-
CF_3COF	-
C_2F_4	707.6
c-C_3F_6	7418.3
HFP	12335546
HFPO	825191.8

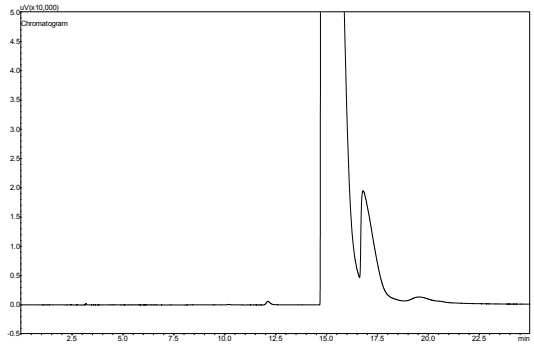

Figure I.263. Shimadzu G.C. 2010 FID chromatogram, experiment 38f.

Table I.264. Shimadzu G.C. 2014 TCD chromatogram, experiment 38f.

Component	Peak area
O_2	15723.8
COF_2	18183.5
CF_3COF	3187.5
C_2F_4	-
c-C_3F_6	-
HFP	-
HFPO	-

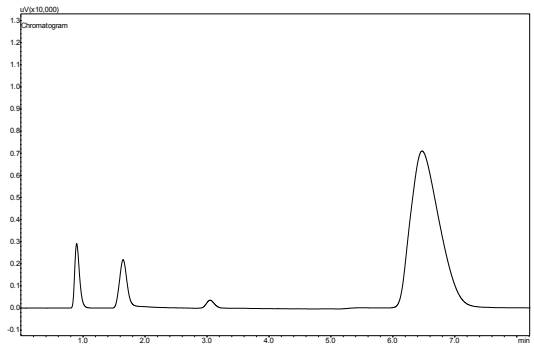

Figure I.264. Shimadzu G.C. 2014 TCD chromatogram, experiment 38f.

Table I.265. Shimadzu G.C. 2010 FID chromatogram, experiment 38g.

Component	Peak area
O_2	-
COF_2	-
CF_3COF	-
C_2F_4	100.8
c-C_3F_6	5710.2
HFP	11622407.2
HFPO	377400.2

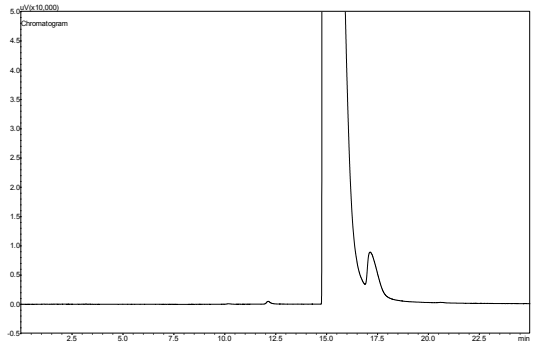

Figure I.265. Shimadzu G.C. 2010 FID chromatogram, experiment 38g.

Table I.266. Shimadzu G.C. 2014 TCD chromatogram, experiment 38g.

Component	Peak area
O_2	56190.5
COF_2	5682.6
CF_3COF	-
C_2F_4	-
c-C_3F_6	-
HFP	-
HFPO	-

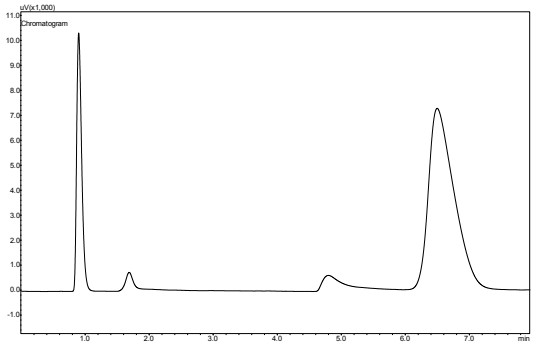

Figure I.266. Shimadzu G.C. 2014 TCD chromatogram, experiment 38g.

Table I.267. Shimadzu G.C. 2010 FID chromatogram, experiment 38h.

Component	Peak area
O_2	-
COF_2	-
CF_3COF	-
C_2F_4	1294.8
c-C_3F_6	6124.9
HFP	7294691.7
HFPO	1020814.2

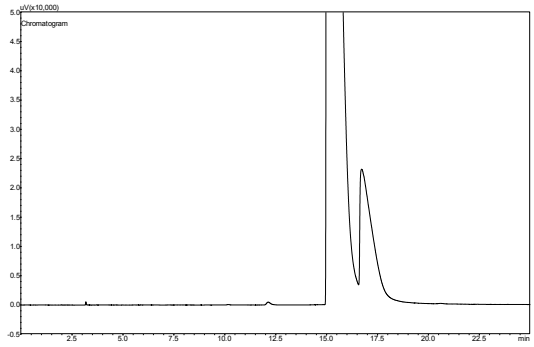

Figure I.267. Shimadzu G.C. 2010 FID chromatogram, experiment 38h.

Table I.268. Shimadzu G.C. 2014 TCD chromatogram, experiment 38h.

Component	Peak area
O_2	30115.1
COF_2	25176.6
CF_3COF	6431.9
C_2F_4	-
c-C_3F_6	-
HFP	-
HFPO	-

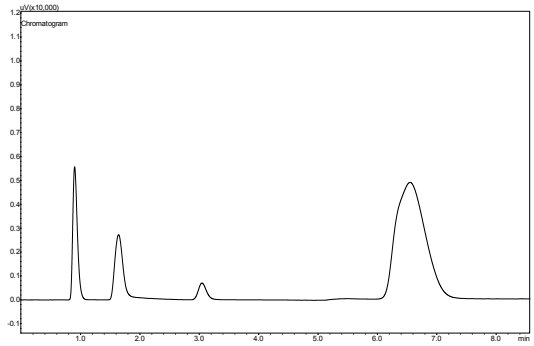

Figure I.268. Shimadzu G.C. 2014 TCD chromatogram, experiment 38h.

Table I.269. Shimadzu G.C. 2010 FID chromatogram, experiment 38i.

Component	Peak area
O_2	-
COF_2	-
CF_3COF	-
C_2F_4	91078.4
c-C_3F_6	22878.3
HFP	2531774.6
HFPO	1110093.3

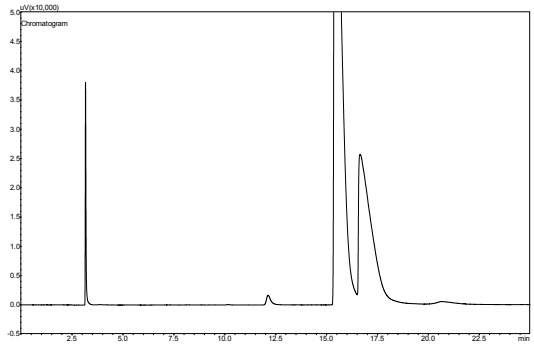

Figure I.269. Shimadzu G.C. 2010 FID chromatogram, experiment 38i.

Table I.270. Shimadzu G.C. 2014 TCD chromatogram, experiment 38i.

Component	Peak area
O_2	470.4
COF_2	57942.1
CF_3COF	24449.2
C_2F_4	-
c-C_3F_6	-
HFP	-
HFPO	-

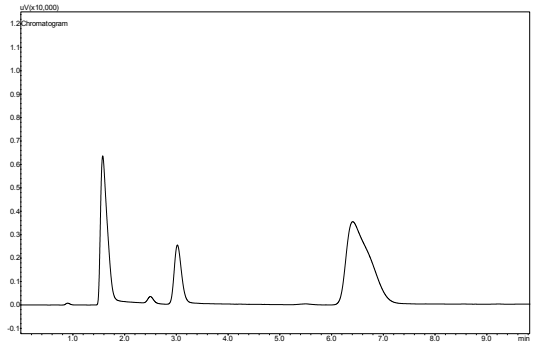

Figure I.270. Shimadzu G.C. 2014 TCD chromatogram, experiment 38i.

Table I.271. Shimadzu G.C. 2010 FID chromatogram, experiment 39a.

Component	Peak area
O_2	-
COF_2	-
CF_3COF	-
C_2F_4	46.6
c-C_3F_6	4843.7
HFP	10746670.3
HFPO	229647.9

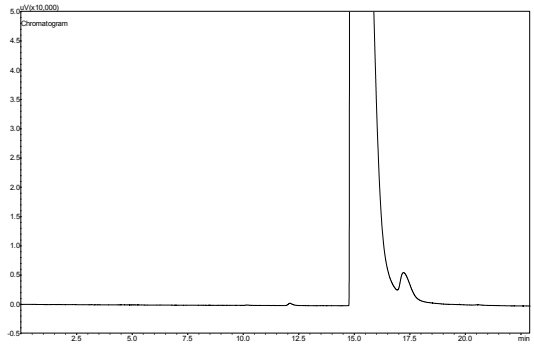

Figure I.271. Shimadzu G.C. 2010 FID chromatogram, experiment 39a.

Table I.272. Shimadzu G.C. 2014 TCD chromatogram, experiment 39a.

Component	Peak area
O_2	66356.7
COF_2	2366.4
CF_3COF	-
C_2F_4	-
c-C_3F_6	-
HFP	-
HFPO	-

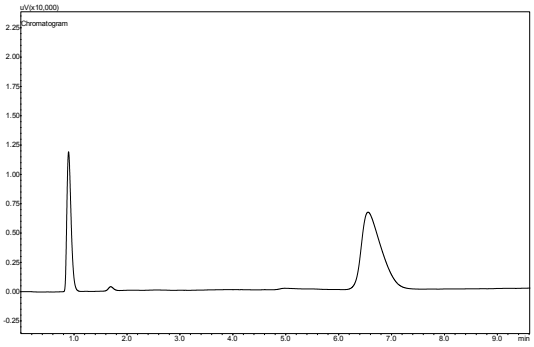

Figure I.272. Shimadzu G.C. 2014 TCD chromatogram, experiment 39a.

Table I.273. Shimadzu G.C. 2010 FID chromatogram, experiment 39b.

Component	Peak area
O_2	-
COF_2	-
CF_3COF	-
C_2F_4	718.1
c-C_3F_6	4973.8
HFP	8801058.9
HFPO	563728.1

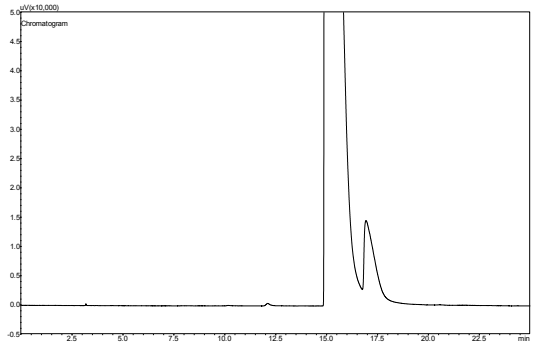

Figure I.273. Shimadzu G.C. 2010 FID chromatogram, experiment 39b.

Table I.274. Shimadzu G.C. 2014 TCD chromatogram, experiment 39b.

Component	Peak area
O_2	57939.9
COF_2	9448.4
CF_3COF	-
C_2F_4	-
c-C_3F_6	-
HFP	-
HFPO	-

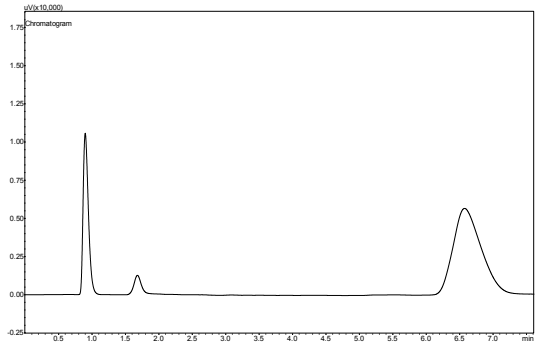

Figure I.274. Shimadzu G.C. 2014 TCD chromatogram, experiment 39b.

Table I.275. Shimadzu G.C. 2010 FID chromatogram, experiment 39c.

Component	Peak area
O_2	-
COF_2	-
CF_3COF	-
C_2F_4	104
c-C_3F_6	5896.8
HFP	44851.1
HFPO	991442.3

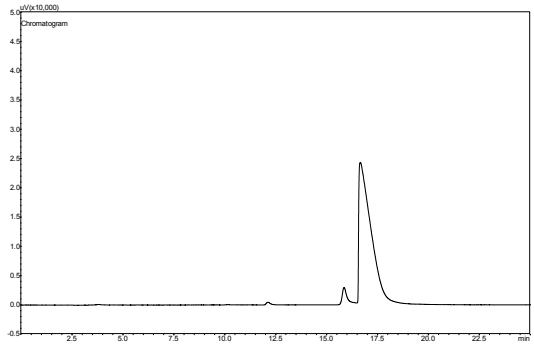

Figure I.275. Shimadzu G.C. 2010 FID chromatogram, experiment 39c.

Table I.276. Shimadzu G.C. 2014 TCD chromatogram, experiment 39c.

Component	Peak area
O_2	2166.5
COF_2	73716.2
CF_3COF	27308.8
C_2F_4	-
c-C_3F_6	-
HFP	-
HFPO	-

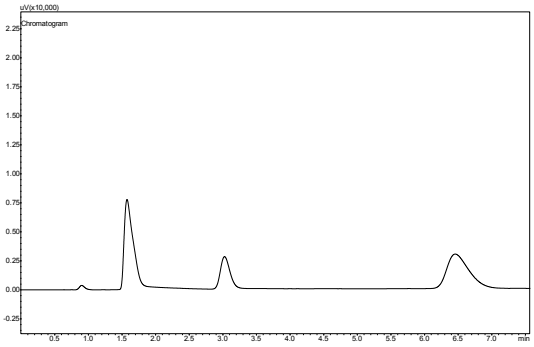

Figure I.276. Shimadzu G.C. 2014 TCD chromatogram, experiment 39c.

Table I.277. Shimadzu G.C. 2010 FID chromatogram, experiment 39d.

Component	Peak area
O_2	-
COF_2	-
CF_3COF	-
C_2F_4	59802.4
c-C_3F_6	13312.8
HFP	2075471
HFPO	1233934.4

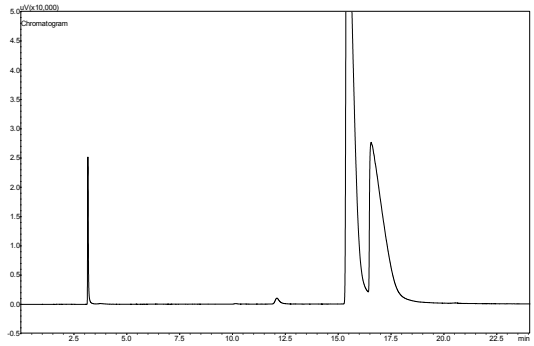

Figure I.277. Shimadzu G.C. 2010 FID chromatogram, experiment 39d.

Table I.278. Shimadzu G.C. 2014 TCD chromatogram, experiment 39d.

Component	Peak area
O_2	519.1
COF_2	61065
CF_3COF	24506.6
C_2F_4	-
c-C_3F_6	-
HFP	-
HFPO	-

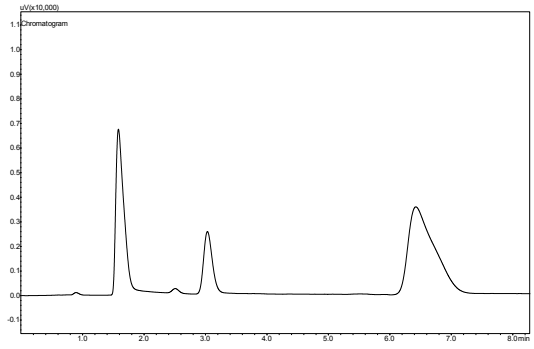

Figure I.278. Shimadzu G.C. 2014 TCD chromatogram, experiment 39d.

Table I.279. Shimadzu G.C. 2010 FID chromatogram, experiment 39e.

Component	Peak area
O_2	-
COF_2	-
CF_3COF	-
C_2F_4	1376.4
c-C_3F_6	5992.4
HFP	6549679.9
HFPO	954007.8

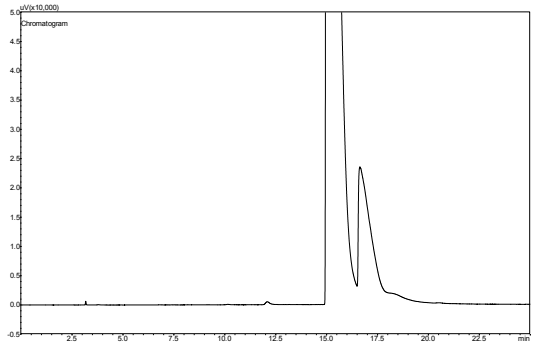

Figure I.279. Shimadzu G.C. 2010 FID chromatogram, experiment 39e.

Table I.280. Shimadzu G.C. 2014 TCD chromatogram, experiment 39e.

Component	Peak area
O_2	28589.2
COF_2	28459.4
CF_3COF	8881.7
C_2F_4	-
c-C_3F_6	-
HFP	-
HFPO	-

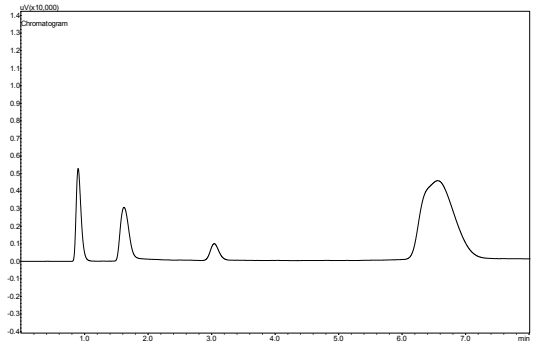

Figure I.280. Shimadzu G.C. 2014 TCD chromatogram, experiment 39e.

Table I.281. Shimadzu G.C. 2010 FID chromatogram, experiment 39f.

Component	Peak area
O_2	-
COF_2	-
CF_3COF	-
C_2F_4	86
c-C_3F_6	5469.4
HFP	11517617
HFPO	356651.8

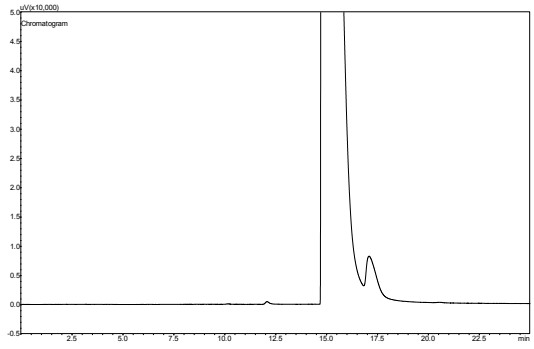

Figure I.281. Shimadzu G.C. 2010 FID chromatogram, experiment 39f.

Table I.282. Shimadzu G.C. 2014 TCD chromatogram, experiment 39f.

Component	Peak area
O_2	55190.5
COF_2	4583.4
CF_3COF	-
C_2F_4	-
c-C_3F_6	-
HFP	-
HFPO	-

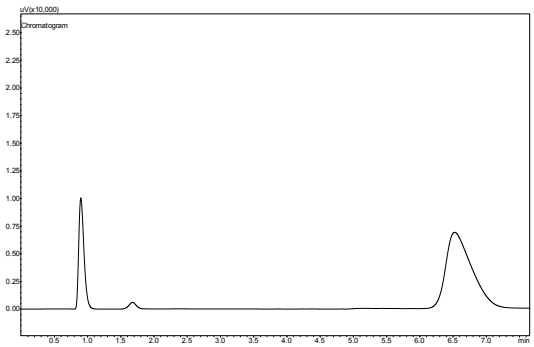

Figure I.282. Shimadzu G.C. 2014 TCD chromatogram, experiment 39f.

Table I.283. Shimadzu G.C. 2010 FID chromatogram, experiment 39g.

Component	Peak area
O_2	-
COF_2	-
CF_3COF	-
C_2F_4	121.7
c-C_3F_6	6309.8
HFP	12855789.4
HFPO	453829.3

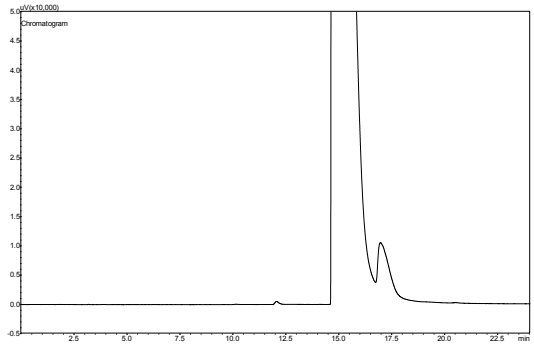

Figure I.283. Shimadzu G.C. 2010 FID chromatogram, experiment 39g.

Table I.284. Shimadzu G.C. 2014 TCD chromatogram, experiment 39g.

Component	Peak area
O_2	41822.7
COF_2	6378.6
CF_3COF	-
C_2F_4	-
c-C_3F_6	-
HFP	-
HFPO	-

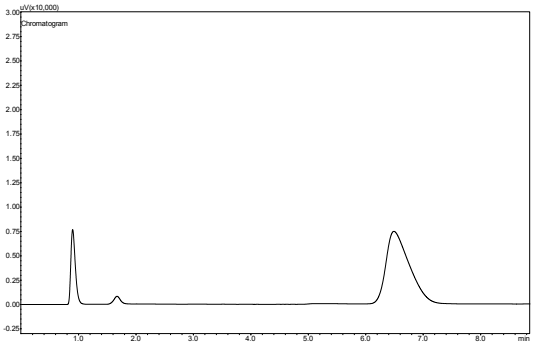

Figure I.284. Shimadzu G.C. 2014 TCD chromatogram, experiment 39g.

Table I.285. Shimadzu G.C. 2010 FID chromatogram, experiment 39h.

Component	Peak area
O_2	-
COF_2	-
CF_3COF	-
C_2F_4	1529.9
c-C_3F_6	7199.1
HFP	8754100.6
HFPO	1032708.7

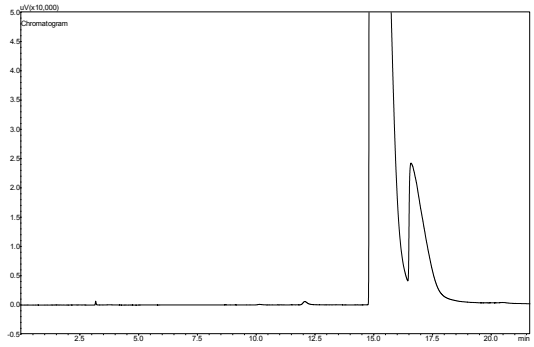

Figure I.285. Shimadzu G.C. 2010 FID chromatogram, experiment 39h.

Table I.286. Shimadzu G.C. 2014 TCD chromatogram, experiment 39h.

Component	Peak area
O_2	19643.8
COF_2	26561.8
CF_3COF	6218
C_2F_4	-
c-C_3F_6	-
HFP	-
HFPO	-

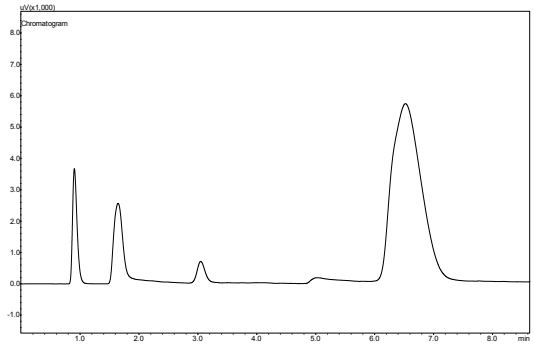

Figure I.286. Shimadzu G.C. 2014 TCD chromatogram, experiment 39h.

Table I.287. Shimadzu G.C. 2010 FID chromatogram, experiment 39i.

Component	Peak area
O_2	-
COF_2	-
CF_3COF	-
C_2F_4	101691.4
c-C_3F_6	28416.3
HFP	5608923.2
HFPO	1182386.2

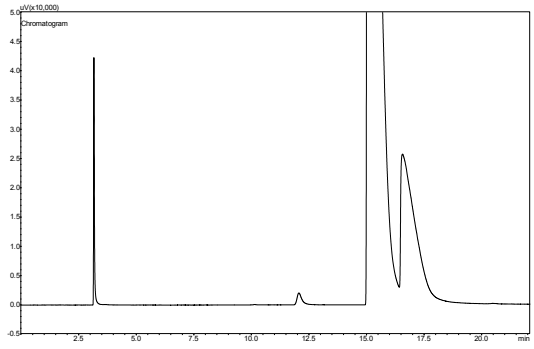

Figure I.287. Shimadzu G.C. 2010 FID chromatogram, experiment 39i.

Table I.288. Shimadzu G.C. 2014 TCD chromatogram, experiment 39i.

Component	Peak area
O_2	585.9
COF_2	46105.3
CF_3COF	19390.7
C_2F_4	-
c-C_3F_6	-
HFP	-
HFPO	-

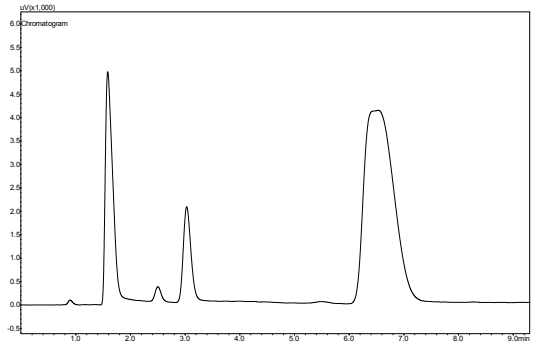

Figure I.288. Shimadzu G.C. 2014 TCD chromatogram, experiment 39i.

Table I.289. Shimadzu G.C. 2010 FID chromatogram, experiment 40a.

Component	Peak area
O_2	-
COF_2	-
CF_3COF	-
C_2F_4	-
c-C_3F_6	2840.7
HFP	7071973.2
HFPO	183601.5

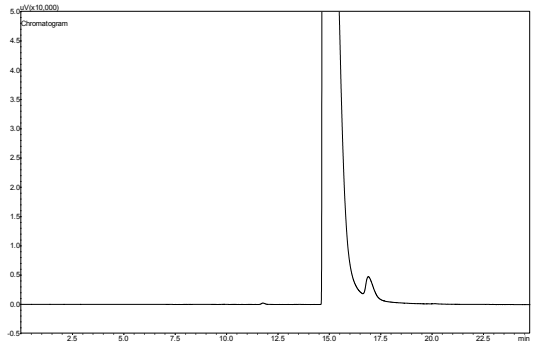

Figure I.289. Shimadzu G.C. 2010 FID chromatogram, experiment 40a.

Table I.290. Shimadzu G.C. 2014 TCD chromatogram, experiment 40a.

Component	Peak area
O_2	88566.7
COF_2	1859
CF_3COF	-
C_2F_4	-
c-C_3F_6	-
HFP	-
HFPO	-

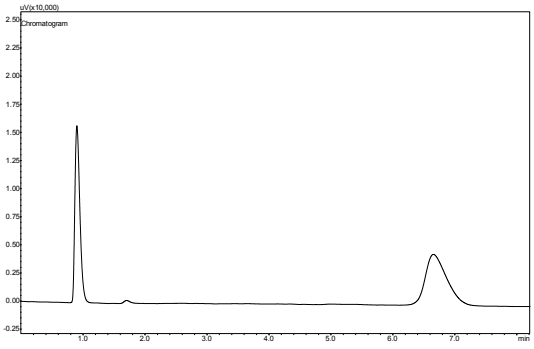

Figure I.290. Shimadzu G.C. 2014 TCD chromatogram, experiment 40a.

Table I.291. Shimadzu G.C. 2010 FID chromatogram, experiment 40b.

Component	Peak area
O_2	-
COF_2	-
CF_3COF	-
C_2F_4	659.4
c-C_3F_6	3329.4
HFP	5235896.3
HFPO	433035.1

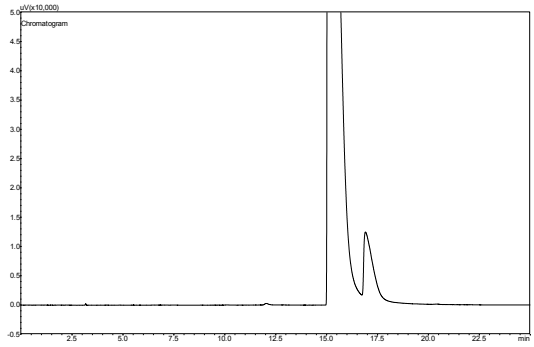

Figure I.291. Shimadzu G.C. 2010 FID chromatogram, experiment 40b.

Table I.292. Shimadzu G.C. 2014 TCD chromatogram, experiment 40b.

Component	Peak area
O_2	80666
COF_2	8403.7
CF_3COF	-
C_2F_4	-
c-C_3F_6	-
HFP	-
HFPO	-

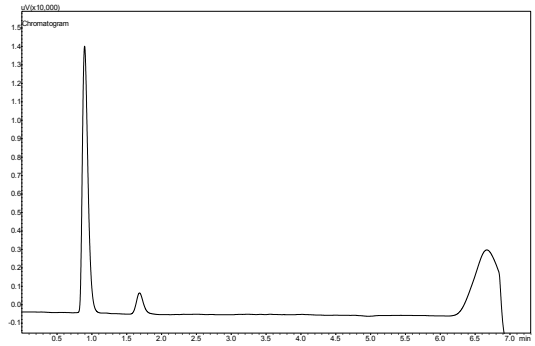

Figure I.292. Shimadzu G.C. 2014 TCD chromatogram, experiment 40b.

Table I.293. Shimadzu G.C. 2010 FID chromatogram, experiment 40c.

Component	Peak area
O_2	-
COF_2	-
CF_3COF	-
C_2F_4	205.5
c-C_3F_6	2901.8
HFP	26529.3
HFPO	533247.5

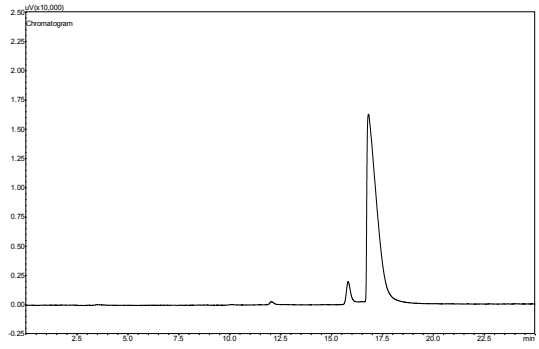

Figure I.293. Shimadzu G.C. 2010 FID chromatogram, experiment 40c.

Table I.294. Shimadzu G.C. 2014 TCD chromatogram, experiment 40c.

Component	Peak area
O_2	47418.1
COF_2	47313.5
CF_3COF	13948.1
C_2F_4	-
c-C_3F_6	-
HFP	-
HFPO	-

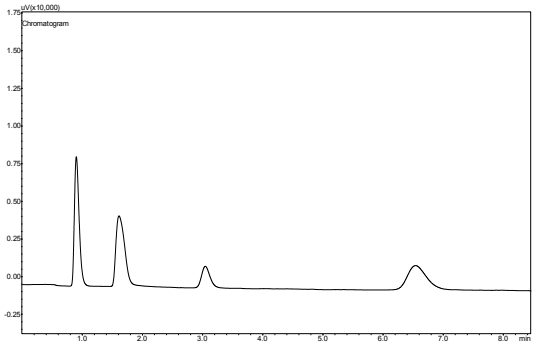

Figure I.294. Shimadzu G.C. 2014 TCD chromatogram, experiment 40c.

Table I.295. Shimadzu G.C. 2010 FID chromatogram, experiment 40d.

Component	Peak area
O_2	-
COF_2	-
CF_3COF	-
C_2F_4	303.4
c-C_3F_6	4014.8
HFP	11521.3
HFPO	626875.7

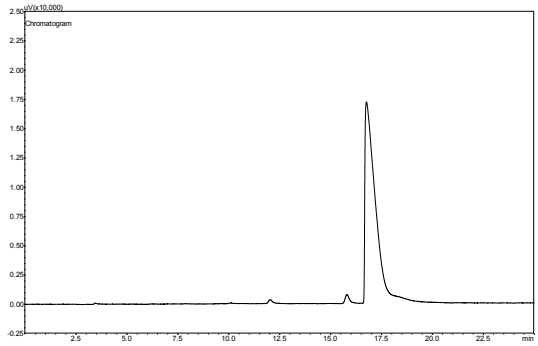

Figure I.295. Shimadzu G.C. 2010 FID chromatogram, experiment 40d.

Table I.296. Shimadzu G.C. 2014 TCD chromatogram, experiment 40d.

Component	Peak area
O_2	30954.4
COF_2	59260.6
CF_3COF	20595.2
C_2F_4	-
c-C_3F_6	-
HFP	-
HFPO	-

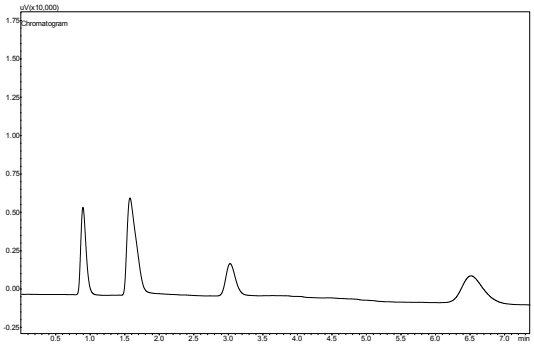

Figure I.296. Shimadzu G.C. 2014 TCD chromatogram, experiment 40d.

Table I.297. Shimadzu G.C. 2010 FID chromatogram, experiment 40e.

Component	Peak area
O_2	-
COF_2	-
CF_3COF	-
C_2F_4	869.8
c-C_3F_6	3923.2
HFP	2162181.9
HFPO	862166.9

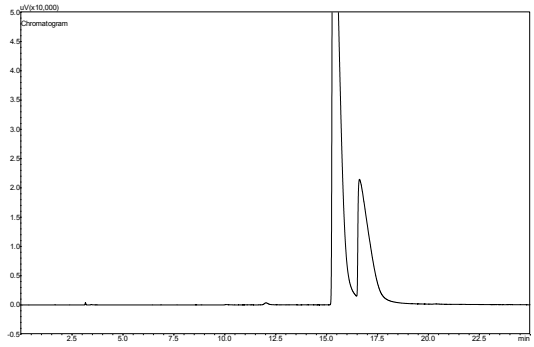

Figure I.297. Shimadzu G.C. 2010 FID chromatogram, experiment 40e.

Table I.298. Shimadzu G.C. 2014 TCD chromatogram, experiment 40e.

Component	Peak area
O_2	48653
COF_2	35863.8
CF_3COF	10528.6
C_2F_4	-
c-C_3F_6	-
HFP	-
HFPO	-

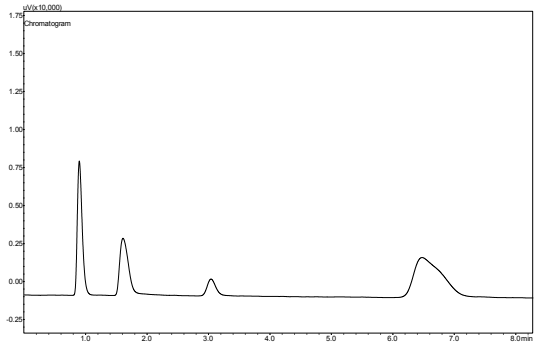

Figure I.298. Shimadzu G.C. 2014 TCD chromatogram, experiment 40e.

Table I.299. Shimadzu G.C. 2010 FID chromatogram, experiment 40f.

Component	Peak area
O_2	-
COF_2	-
CF_3COF	-
C_2F_4	84.6
c-C_3F_6	3697.9
HFP	7274603.5
HFPO	356526.4

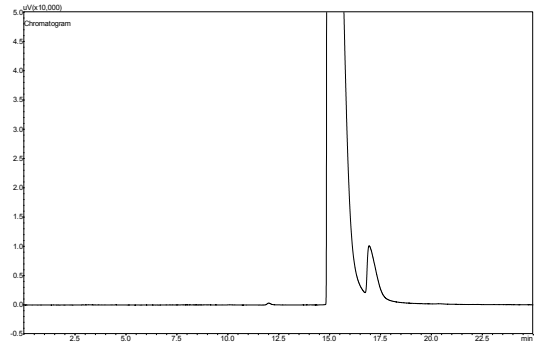

Figure I.299. Shimadzu G.C. 2010 FID chromatogram, experiment 40f.

Table I.300. Shimadzu G.C. 2014 TCD chromatogram, experiment 40f.

Component	Peak area
O_2	73864.1
COF_2	7642.3
CF_3COF	-
C_2F_4	-
c-C_3F_6	-
HFP	-
HFPO	-

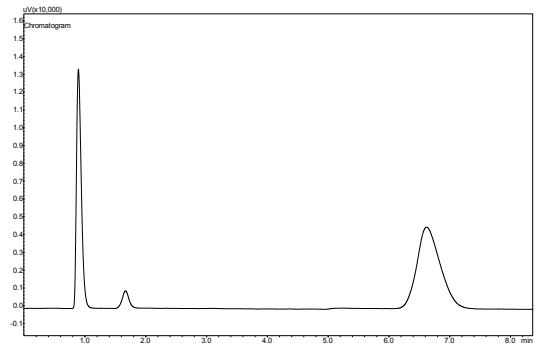

Figure I.300. Shimadzu G.C. 2014 TCD chromatogram, experiment 40f.

Table I.301. Shimadzu G.C. 2010 FID chromatogram, experiment 40g.

Component	Peak area
O_2	-
COF_2	-
CF_3COF	-
C_2F_4	96.3
c-C_3F_6	2416.5
HFP	6796146.9
HFPO	220146.9

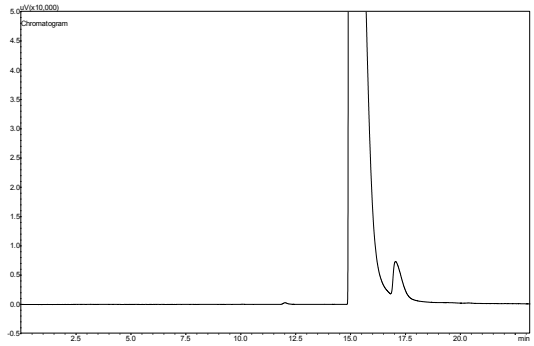

Figure I.301. Shimadzu G.C. 2010 FID chromatogram, experiment 40g.

Table I.302. Shimadzu G.C. 2014 TCD chromatogram, experiment 40g.

Component	Peak area
O_2	83295.4
COF_2	4456.3
CF_3COF	-
C_2F_4	-
c-C_3F_6	-
HFP	-
HFPO	-

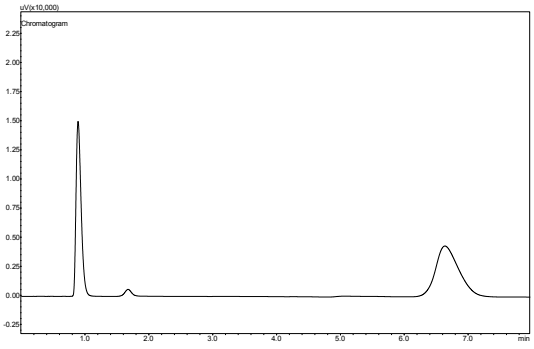

Figure I.302. Shimadzu G.C. 2014 TCD chromatogram, experiment 40g.

Table I.303. Shimadzu G.C. 2010 FID chromatogram, experiment 40h.

Component	Peak area
O_2	-
COF_2	-
CF_3COF	-
C_2F_4	734.8
c-C_3F_6	2836
HFP	3404759.6
HFPO	608979.1

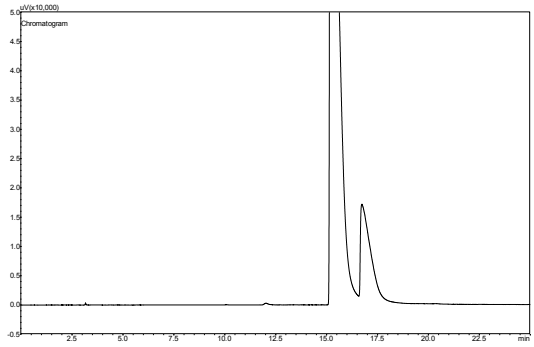

Figure I.303. Shimadzu G.C. 2010 FID chromatogram, experiment 40h.

Table I.304. Shimadzu G.C. 2014 TCD chromatogram, experiment 40h.

Component	Peak area
O_2	68521
COF_2	20351.6
CF_3COF	4022.6
C_2F_4	-
c-C_3F_6	-
HFP	-
HFPO	-

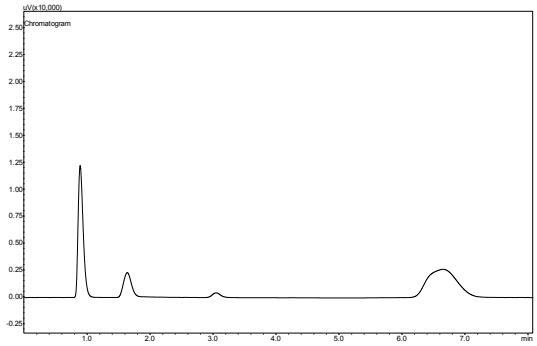

Figure I.304. Shimadzu G.C. 2014 TCD chromatogram, experiment 40h.

Table I.305. Shimadzu G.C. 2010 FID chromatogram, experiment 40i.

Component	Peak area
O_2	-
COF_2	-
CF_3COF	-
C_2F_4	811.1
c-C_3F_6	3506.3
HFP	36004
HFPO	491198.4

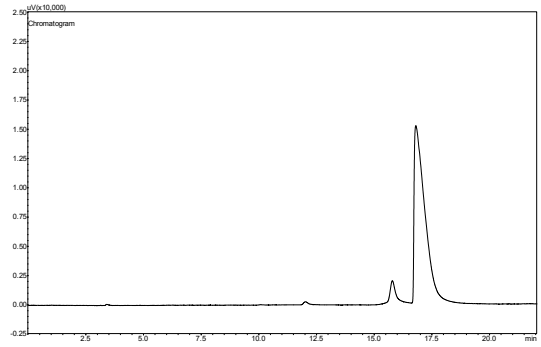

Figure I.305. Shimadzu G.C. 2010 FID chromatogram, experiment 40i.

Table I.306. Shimadzu G.C. 2014 TCD chromatogram, experiment 40i.

Component	Peak area
O_2	43448.1
COF_2	52872.5
CF_3COF	18256.4
C_2F_4	-
c-C_3F_6	-
HFP	-
HFPO	-

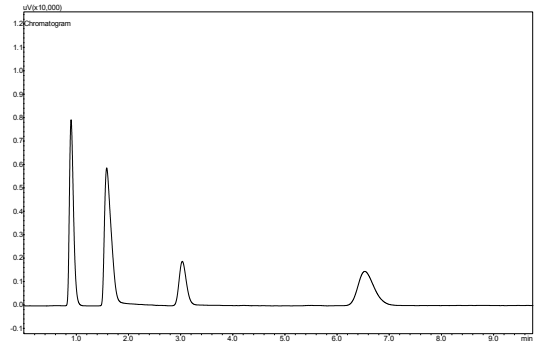

Figure I.306. Shimadzu G.C. 2014 TCD chromatogram, experiment 40i.

Table I.307. Shimadzu G.C. 2010 FID chromatogram, experiment 41a.

Component	Peak area
O_2	-
COF_2	-
CF_3COF	-
C_2F_4	189.2
c-C_3F_6	5944.6
HFP	10859236.6
HFPO	498878.5

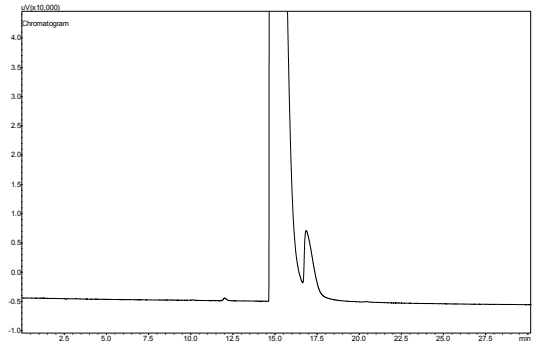

Figure I.307. Shimadzu G.C. 2010 FID chromatogram, experiment 41a.

Table I.308. Shimadzu G.C. 2010 FID chromatogram, experiment 41b.

Component	Peak area
O_2	-
COF_2	-
CF_3COF	-
C_2F_4	1643.5
c-C_3F_6	6954.1
HFP	4144973
HFPO	1336239.5

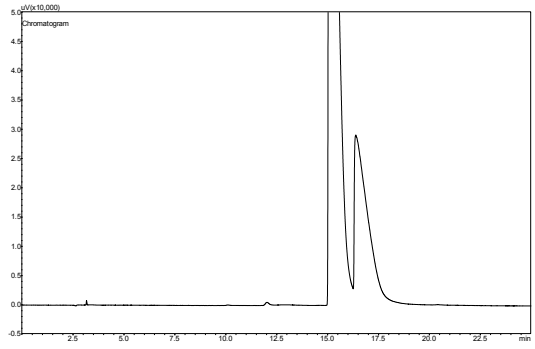

Figure I.308. Shimadzu G.C. 2010 FID chromatogram, experiment 41b.

Table I.309. Shimadzu G.C. 2010 FID chromatogram, experiment 41c.

Component	Peak area
O_2	-
COF_2	-
CF_3COF	-
C_2F_4	141443.3
c-C_3F_6	61027.9
HFP	2536109.6
HFPO	934175.5

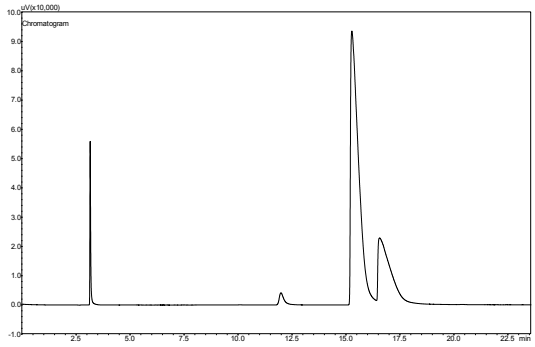

Figure I.309. Shimadzu G.C. 2010 FID chromatogram, experiment 41c.

Table I.310. Shimadzu G.C. 2014 TCD chromatogram, experiment 41d.

Component	Peak area
O_2	511.4
COF_2	71065.6
CF_3COF	27907.9
C_2F_4	-
c-C_3F_6	-
HFP	-
HFPO	-

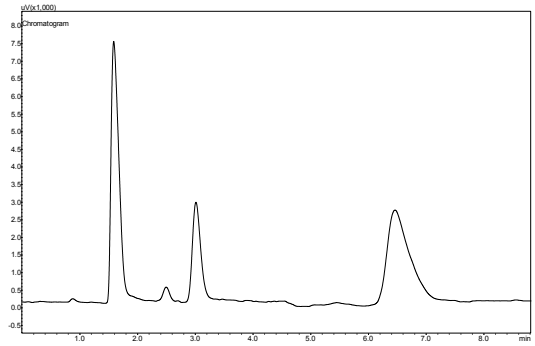

Figure I.310. Shimadzu G.C. 2014 TCD chromatogram, experiment 41d.

Table I.311. Shimadzu G.C. 2010 FID chromatogram, experiment 41e.

Component	Peak area
O_2	-
COF_2	-
CF_3COF	-
C_2F_4	4251.6
c-C_3F_6	7101.8
HFP	1493352
HFPO	1288536.2

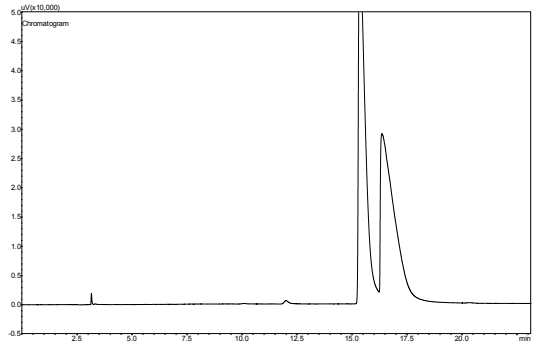

Figure I.311. Shimadzu G.C. 2010 FID chromatogram, experiment 41e.

Table I.312. Shimadzu G.C. 2014 TCD chromatogram, experiment 41e.

Component	Peak area
O_2	6595.7
COF_2	60790.4
CF_3COF	19819.6
C_2F_4	-
c-C_3F_6	-
HFP	-
HFPO	-

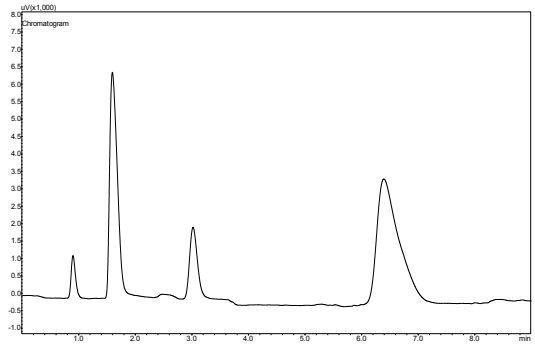

Figure I.312. Shimadzu G.C. 2014 TCD chromatogram, experiment 41e.

Table I.313. Shimadzu G.C. 2010 FID chromatogram, experiment 41f.

Component	Peak area
O_2	-
COF_2	-
CF_3COF	-
C_2F_4	554.2
c-C_3F_6	5801.4
HFP	7506366.1
HFPO	778268.5

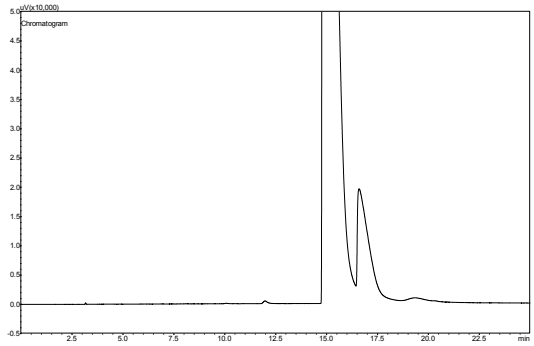

Figure I.313. Shimadzu G.C. 2010 FID chromatogram, experiment 41f.

Table I.314. Shimadzu G.C. 2014 TCD chromatogram, experiment 41f.

Component	Peak area
O_2	42421.3
COF_2	22008.8
CF_3COF	2724.3
C_2F_4	-
c-C_3F_6	-
HFP	-
HFPO	-

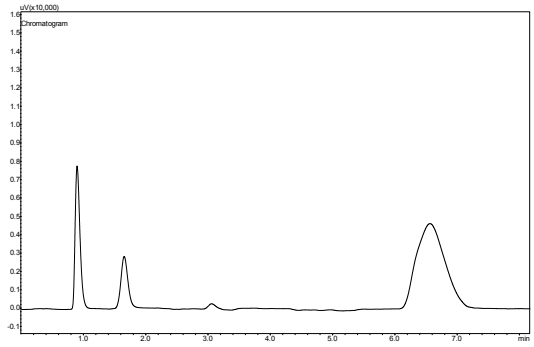

Figure I.314. Shimadzu G.C. 2014 TCD chromatogram, experiment 41f.

Table I.315. Shimadzu G.C. 2010 FID chromatogram, experiment 41g.

Component	Peak area
O_2	-
COF_2	-
CF_3COF	-
C_2F_4	147.7
c-C_3F_6	3797
HFP	8169290.8
HFPO	392749.6

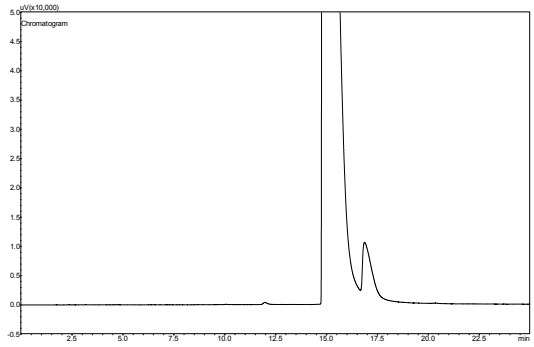

Figure I.315. Shimadzu G.C. 2010 FID chromatogram, experiment 41g.

Table I.316. Shimadzu G.C. 2014 TCD chromatogram, experiment 41g.

Component	Peak area
O_2	68941.6
COF_2	8175.8
CF_3COF	145.7
C_2F_4	-
c-C_3F_6	-
HFP	-
HFPO	-

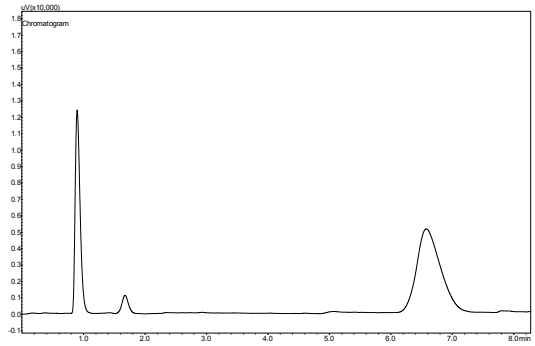

Figure I.316. Shimadzu G.C. 2014 TCD chromatogram, experiment 41g.

Table I.317. Shimadzu G.C. 2010 FID chromatogram, experiment 41h.

Component	Peak area
O_2	-
COF_2	-
CF_3COF	-
C_2F_4	1145
c-C_3F_6	4397.3
HFP	3457886.7
HFPO	872638.1

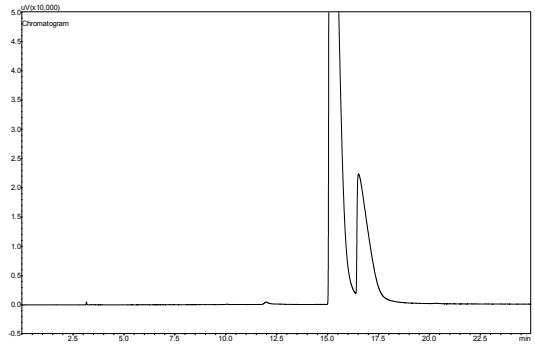

Figure I.317. Shimadzu G.C. 2010 FID chromatogram, experiment 41h.

Table I.318. Shimadzu G.C. 2014 TCD chromatogram, experiment 41h.

Component	Peak area
O_2	47410.1
COF_2	35084.7
CF_3COF	8296.2
C_2F_4	-
c-C_3F_6	-
HFP	-
HFPO	-

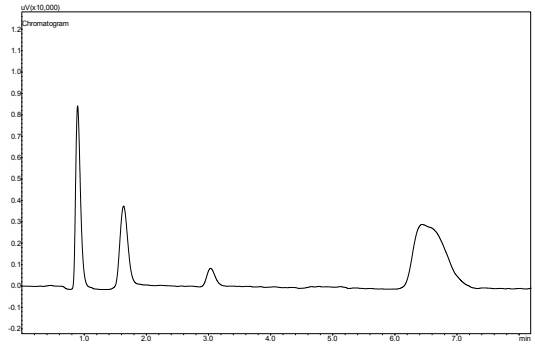

Figure I.318. Shimadzu G.C. 2014 TCD chromatogram, experiment 41h.

Table I.319. Shimadzu G.C. 2010 FID chromatogram, experiment 41i.

Component	Peak area
O_2	-
COF_2	-
CF_3COF	-
C_2F_4	735.4
c-C_3F_6	4287.5
HFP	41248.8
HFPO	647909.4

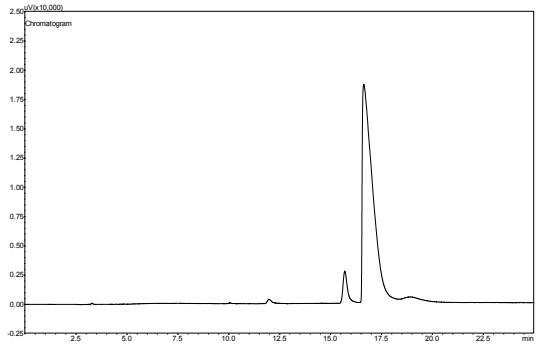

Figure I.319. Shimadzu G.C. 2010 FID chromatogram, experiment 41i.

Table I.320. Shimadzu G.C. 2014 TCD chromatogram, experiment 41i.

Component	Peak area
O_2	19261.6
COF_2	69093.6
CF_3COF	24320.9
C_2F_4	-
c-C_3F_6	-
HFP	-
HFPO	-

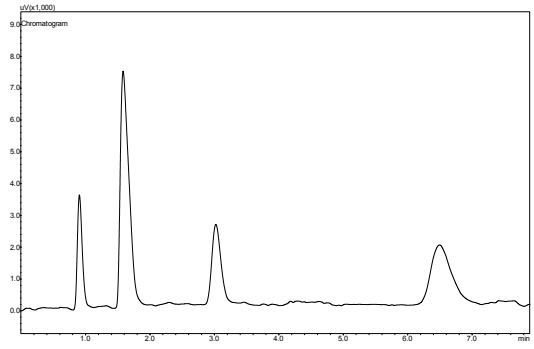

Figure I.320. Shimadzu G.C. 2014 TCD chromatogram, experiment 41i.

Table I.321. Shimadzu G.C. 2010 FID chromatogram, experiment 42a.

Component	Peak area
O_2	-
COF_2	-
CF_3COF	-
C_2F_4	112.9
c-C_3F_6	4776.7
HFP	10765616.4
HFPO	245480.8

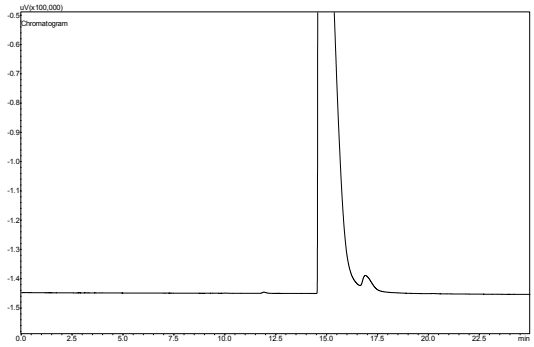

Figure I.321. Shimadzu G.C. 2010 FID chromatogram, experiment 42a.

Table I.322. Shimadzu G.C. 2014 TCD chromatogram, experiment 42a.

Component	Peak area
O_2	63843.6
COF_2	2928.3
CF_3COF	-
C_2F_4	-
c-C_3F_6	-
HFP	-
HFPO	-

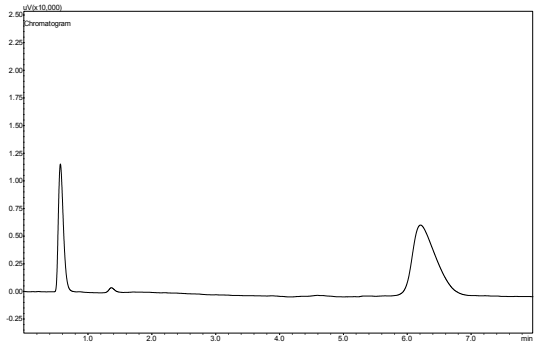

Figure I.322. Shimadzu G.C. 2014 TCD chromatogram, experiment 42a.

Table I.323. Shimadzu G.C. 2010 FID chromatogram, experiment 42b.

Component	Peak area
O_2	-
COF_2	-
CF_3COF	-
C_2F_4	859.3
c-C_3F_6	5301.9
HFP	7894236.9
HFPO	741091.7

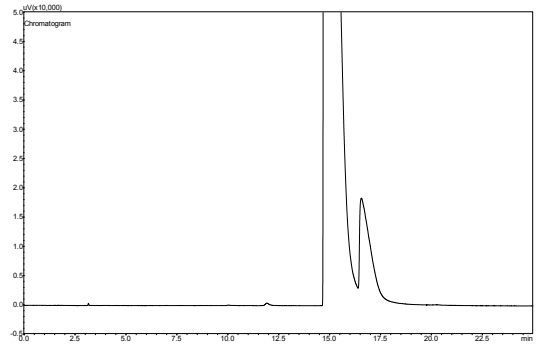

Figure I.323. Shimadzu G.C. 2010 FID chromatogram, experiment 42b.

Table I.324. Shimadzu G.C. 2014 TCD chromatogram, experiment 42b.

Component	Peak area
O_2	49618.8
COF_2	14373.2
CF_3COF	8549.9
C_2F_4	-
c-C_3F_6	-
HFP	-
HFPO	-

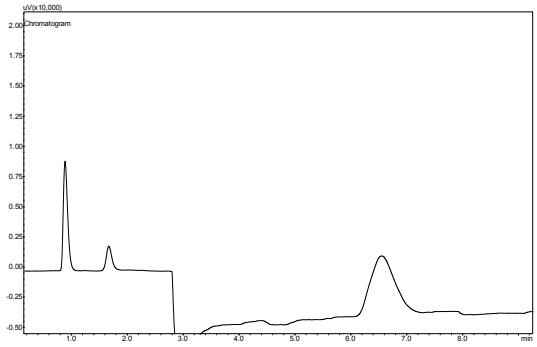

Figure I.324. Shimadzu G.C. 2014 TCD chromatogram, experiment 42b.

Table I.325. Shimadzu G.C. 2010 FID chromatogram, experiment 42c.

Component	Peak area
O_2	-
COF_2	-
CF_3COF	-
C_2F_4	33437
c-C_3F_6	7826.8
HFP	149443.5
HFPO	990940.7

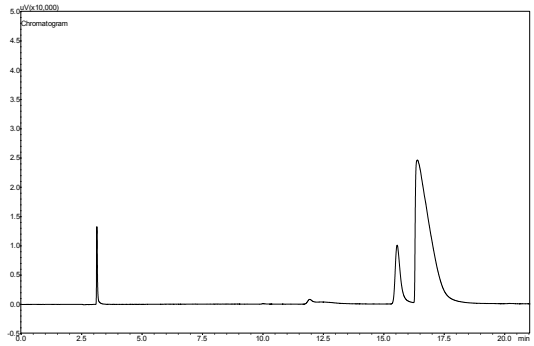

Figure I.325. Shimadzu G.C. 2010 FID chromatogram, experiment 42c.

Table I.326. Shimadzu G.C. 2014 TCD chromatogram, experiment 42c.

Component	Peak area
O_2	987.7
COF_2	72267
CF_3COF	22945.3
C_2F_4	-
c-C_3F_6	-
HFP	-
HFPO	-

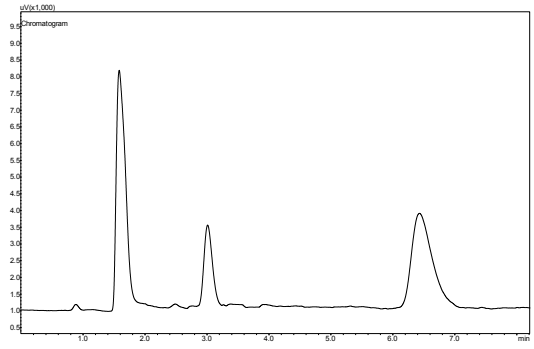

Figure I.326. Shimadzu G.C. 2014 TCD chromatogram, experiment 42c.

Table I.327. Shimadzu G.C. 2010 FID chromatogram, experiment 42d.

Component	Peak area
O_2	-
COF_2	-
CF_3COF	-
C_2F_4	144622.4
c-C_3F_6	66426.8
HFP	5146491.2
HFPO	904825.8

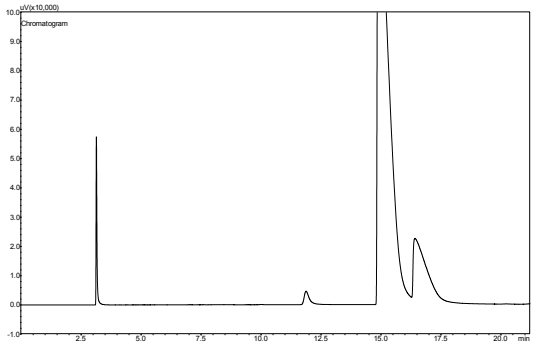

Figure I.327. Shimadzu G.C. 2010 FID chromatogram, experiment 42d.

Table I.328. Shimadzu G.C. 2014 TCD chromatogram, experiment 42d.

Component	Peak area
O_2	974
COF_2	48876.5
CF_3COF	20758.1
C_2F_4	-
c-C_3F_6	-
HFP	-
HFPO	-

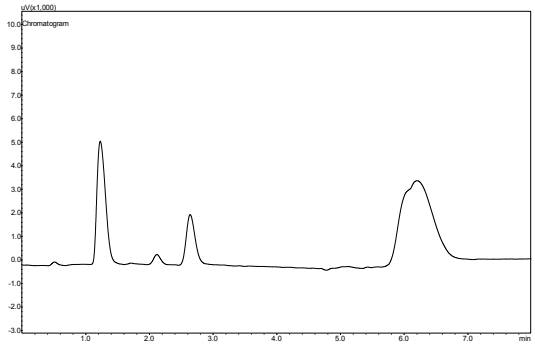

Figure I.328. Shimadzu G.C. 2014 TCD chromatogram, experiment 42d.

Table I.329. Shimadzu G.C. 2010 FID chromatogram, experiment 42e.

Component	Peak area
O_2	-
COF_2	-
CF_3COF	-
C_2F_4	36286.9
c-C_3F_6	11401.6
HFP	5765346.5
HFPO	1341545.1

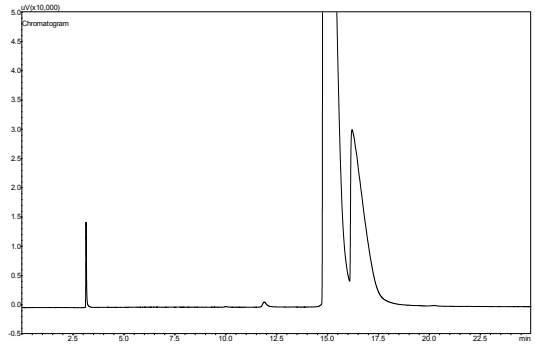

Figure I.329. Shimadzu G.C. 2010 FID chromatogram, experiment 42e.

Table I.330. Shimadzu G.C. 2014 TCD chromatogram, experiment 42e.

Component	Peak area
O_2	706.6
COF_2	44677.8
CF_3COF	14812.5
C_2F_4	-
c-C_3F_6	-
HFP	-
HFPO	-

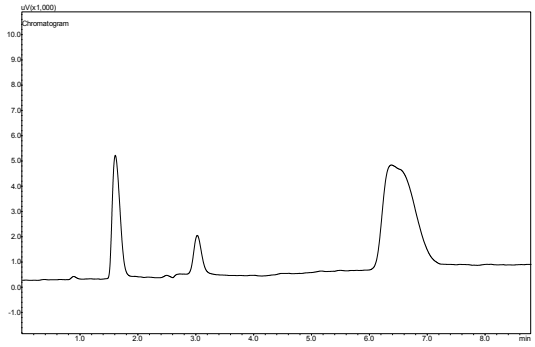

Figure I.330. Shimadzu G.C. 2014 TCD chromatogram, experiment 42e.

Table I.331. Shimadzu G.C. 2010 FID chromatogram, experiment 42f.

Component	Peak area
O_2	-
COF_2	-
CF_3COF	-
C_2F_4	730.4
c-C_3F_6	7452.4
HFP	9232038.6
HFPO	1059379.9

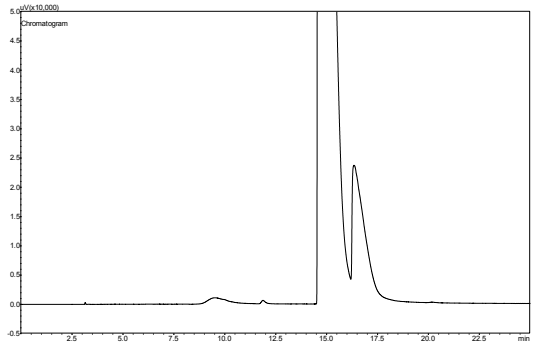

Figure I.331. Shimadzu G.C. 2010 FID chromatogram, experiment 42f.

Table I.332. Shimadzu G.C. 2014 TCD chromatogram, experiment 42f.

Component	Peak area
O_2	19688.6
COF_2	25595.8
CF_3COF	5139.4
C_2F_4	-
c-C_3F_6	-
HFP	-
HFPO	-

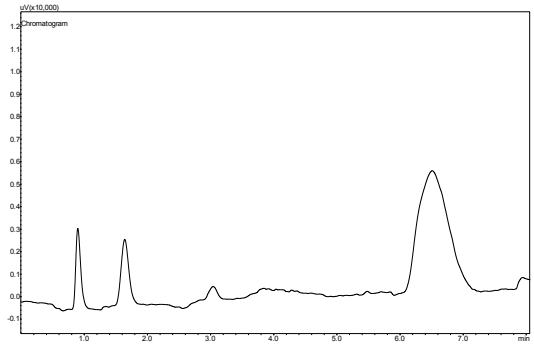

Figure I.332. Shimadzu G.C. 2014 TCD chromatogram, experiment 42f.

Table I.333. Shimadzu G.C. 2010 FID chromatogram, experiment 42g.

Component	Peak area
O_2	-
COF_2	-
CF_3COF	-
C_2F_4	384.1
c-C_3F_6	7746.5
HFP	11563199.8
HFPO	855679.3

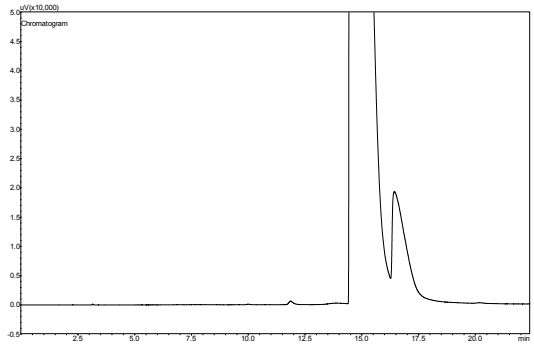

Figure I.333. Shimadzu G.C. 2010 FID chromatogram, experiment 42g.

Table I.334. Shimadzu G.C. 2010 FID chromatogram, experiment 42h.

Component	Peak area
O_2	-
COF_2	-
CF_3COF	-
C_2F_4	14334.4
c-C_3F_6	8303.8
HFP	7447398.8
HFPO	1481803.7

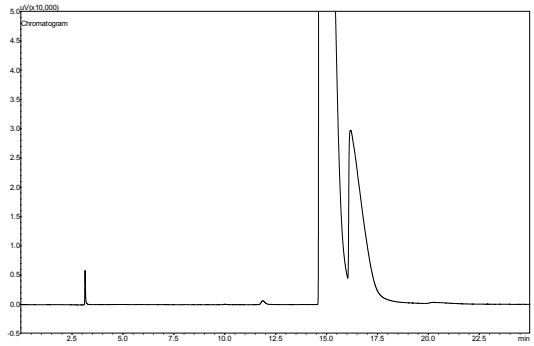

Figure I.334. Shimadzu G.C. 2010 FID chromatogram, experiment 42h.

Table I.335. Shimadzu G.C. 2014 TCD chromatogram, experiment 42h.

Component	Peak area
O_2	22818.2
COF_2	15060
CF_3COF	754.9
C_2F_4	-
c-C_3F_6	-
HFP	-
HFPO	-

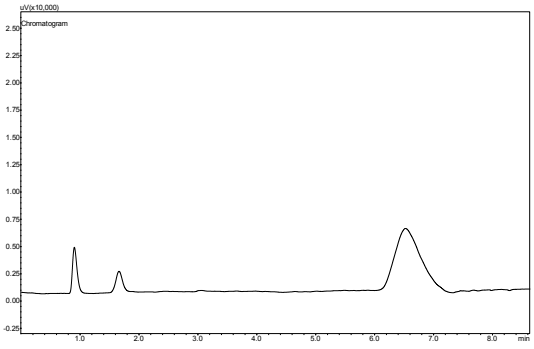

Figure I.335. Shimadzu G.C. 2014 TCD chromatogram, experiment 42h.

Table I.336. Shimadzu G.C. 2010 FID chromatogram, experiment 42i.

Component	Peak area
O_2	-
COF_2	-
CF_3COF	-
C_2F_4	133983
c-C_3F_6	53168.4
HFP	7248150.1
HFPO	989151

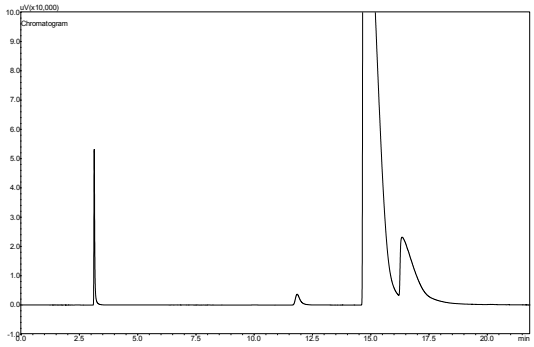

Figure I.336. Shimadzu G.C. 2010 FID chromatogram, experiment 42i.

Table I.337. Shimadzu G.C. 2014 TCD chromatogram, experiment 42i.

Component	Peak area
O_2	352.5
COF_2	38094.2
CF_3COF	16304.6
C_2F_4	-
c-C_3F_6	-
HFP	-
HFPO	-

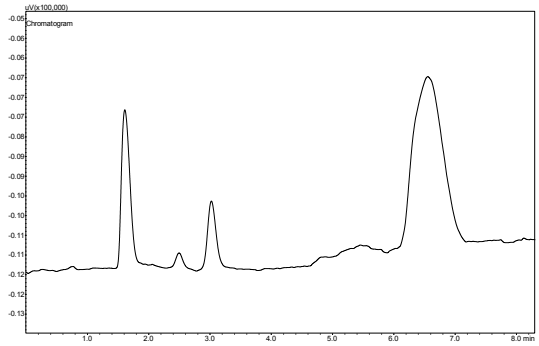

Figure I.337. Shimadzu G.C. 2014 TCD chromatogram, experiment 42i.

Table I.338. Shimadzu G.C. 2010 FID chromatogram, experiment 43a.

Component	Peak area
O_2	-
COF_2	-
CF_3COF	-
C_2F_4	118.5
c-C_3F_6	7497.5
HFP	14703135.8
HFPO	392921.6

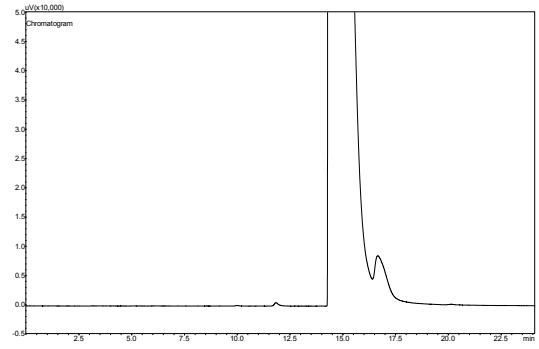

Figure I.338. Shimadzu G.C. 2010 FID chromatogram, experiment 43a.

Table I.339. Shimadzu G.C. 2014 TCD chromatogram, experiment 43a.

Component	Peak area
O_2	35029.7
COF_2	3428.9
CF_3COF	-
C_2F_4	-
c-C_3F_6	-
HFP	-
HFPO	-

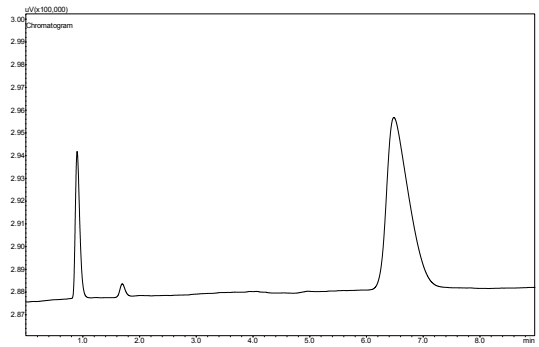

Figure I.339. Shimadzu G.C. 2014 TCD chromatogram, experiment 43a.

Table I.340. Shimadzu G.C. 2010 FID chromatogram, experiment 43b.

Component	Peak area
O_2	-
COF_2	-
CF_3COF	-
C_2F_4	1501.1
c-C_3F_6	7686.6
HFP	10697358.9
HFPO	1106644.1

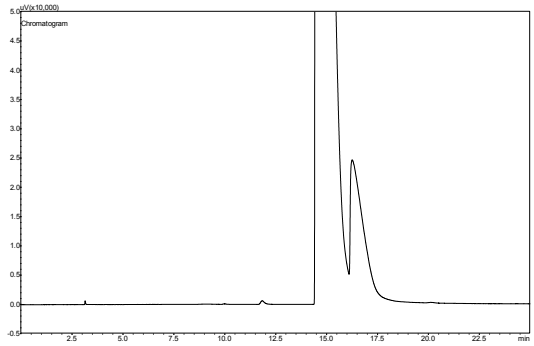

Figure I.340. Shimadzu G.C. 2010 FID chromatogram, experiment 43b.

Table I.341. Shimadzu G.C. 2014 TCD chromatogram, experiment 43b.

Component	Peak area
O_2	27781.3
COF_2	21134.9
CF_3COF	-
C_2F_4	-
c-C_3F_6	-
HFP	-
HFPO	-

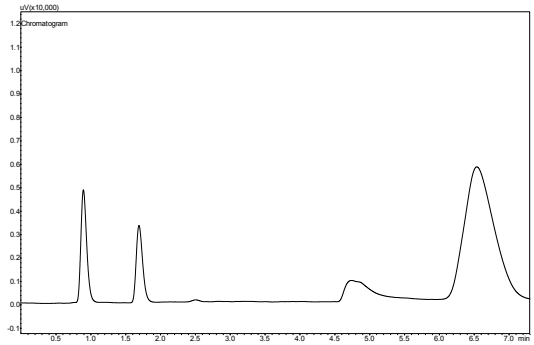

Figure I.341. Shimadzu G.C. 2014 TCD chromatogram, experiment 43b.

Table I.342. Shimadzu G.C. 2010 FID chromatogram, experiment 43c.

Component	Peak area
O_2	-
COF_2	-
CF_3COF	-
C_2F_4	102725.7
c-C_3F_6	31365.9
HFP	8089385.6
HFPO	1093723.2

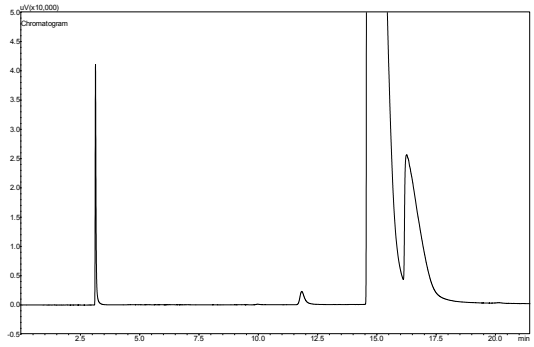

Figure I.342. Shimadzu G.C. 2010 FID chromatogram, experiment 43c.

Table I.343. Shimadzu G.C. 2014 TCD chromatogram, experiment 43c.

Component	Peak area
O_2	646
COF_2	36590.2
CF_3COF	12436.1
C_2F_4	-
c-C_3F_6	-
HFP	-
HFPO	-

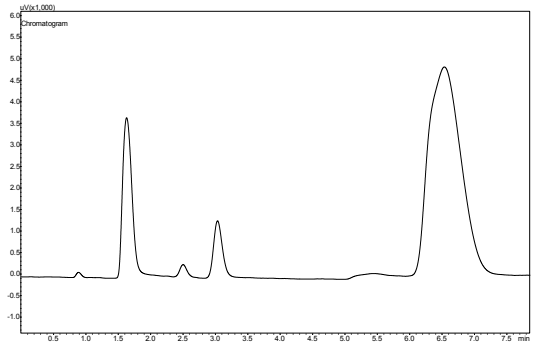

Figure I.343. Shimadzu G.C. 2014 TCD chromatogram, experiment 43c.

Table I.344. Shimadzu G.C. 2010 FID chromatogram, experiment 43d.

Component	Peak area
O_2	-
COF_2	-
CF_3COF	-
C_2F_4	95504.7
c-C_3F_6	29291.7
HFP	10643736.2
HFPO	1002192.3

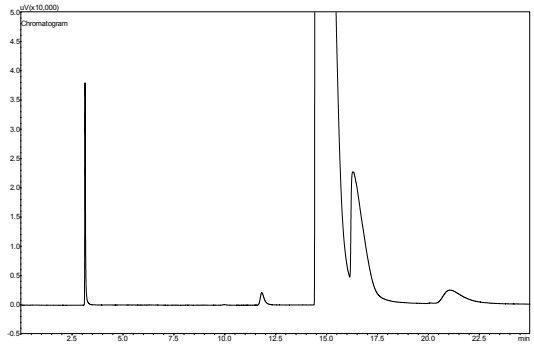

Figure I.344. Shimadzu G.C. 2010 FID chromatogram, experiment 43d.

Table I.345. Shimadzu G.C. 2014 TCD chromatogram, experiment 43d.

Component	Peak area
O_2	652.4
COF_2	29620.3
CF_3COF	7427.1
C_2F_4	-
c-C_3F_6	-
HFP	-
HFPO	-

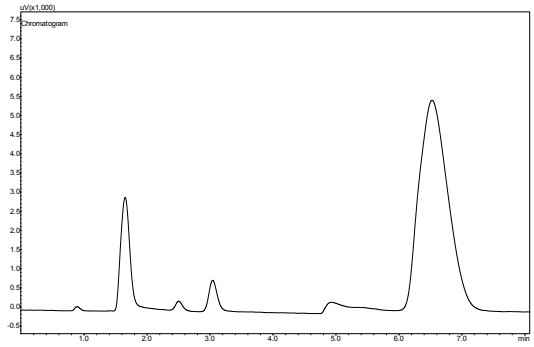

Figure I.345. Shimadzu G.C. 2014 TCD chromatogram, experiment 43d.

Table I.346. Shimadzu G.C. 2010 FID chromatogram, experiment 43e.

Component	Peak area
O_2	-
COF_2	-
CF_3COF	-
C_2F_4	12430.5
c-C_3F_6	8977
HFP	11020861.1
HFPO	1277180.2

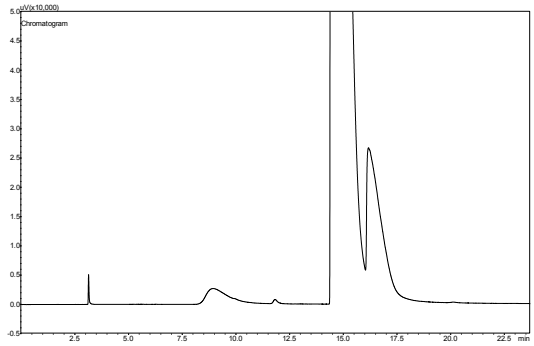

Figure I.346. Shimadzu G.C. 2010 FID chromatogram, experiment 43e.

Table I.347. Shimadzu G.C. 2014 TCD chromatogram, experiment 43e.

Component	Peak area
O_2	746.9
COF_2	30755.2
CF_3COF	2658.1
C_2F_4	-
c-C_3F_6	-
HFP	-
HFPO	-

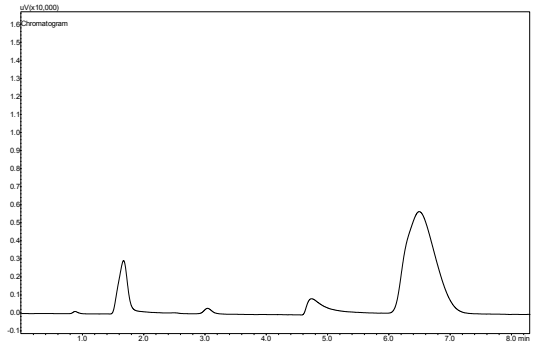

Figure I.347. Shimadzu G.C. 2014 TCD chromatogram, experiment 43e.

Table I.348. Shimadzu G.C. 2010 FID chromatogram, experiment 43f.

Component	Peak area
O_2	-
COF_2	-
CF_3COF	-
C_2F_4	346.6
c-C_3F_6	8135.7
HFP	14051427.2
HFPO	682949.5

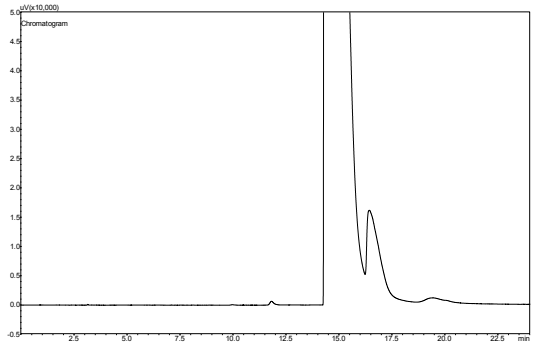

Figure I.348. Shimadzu G.C. 2010 FID chromatogram, experiment 43f.

Table I.349. Shimadzu G.C. 2014 TCD chromatogram, experiment 43f.

Component	Peak area
O_2	17148.6
COF_2	12842.9
CF_3COF	458.5
C_2F_4	-
c-C_3F_6	-
HFP	-
HFPO	-

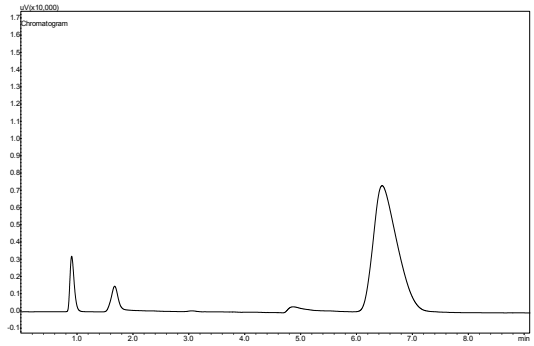

Figure I.349. Shimadzu G.C. 2014 TCD chromatogram, experiment 43f.

Table I.350. Shimadzu G.C. 2010 FID chromatogram, experiment 43g.

Component	Peak area
O_2	-
COF_2	-
CF_3COF	-
C_2F_4	226.4
c-C_3F_6	3872.9
HFP	8057875.3
HFPO	459647.1

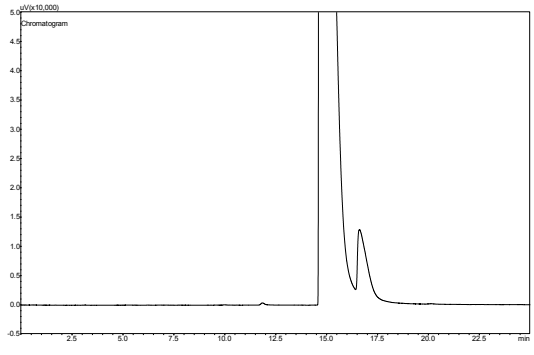

Figure I.350. Shimadzu G.C. 2010 FID chromatogram, experiment 43g.

Table I.351. Shimadzu G.C. 2014 TCD chromatogram, experiment 43g.

Component	Peak area
O_2	66900.8
COF_2	8508.7
CF_3COF	123.2
C_2F_4	-
c-C_3F_6	-
HFP	-
HFPO	-

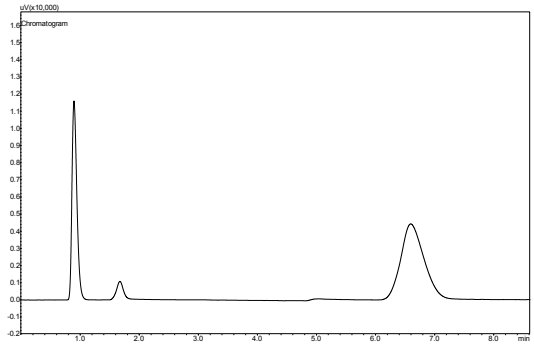

Figure I.351. Shimadzu G.C. 2014 TCD chromatogram, experiment 43g.

Table I.352. Shimadzu G.C. 2010 FID chromatogram, experiment 43h.

Component	Peak area
O_2	-
COF_2	-
CF_3COF	-
C_2F_4	1184.5
c-C_3F_6	5247.5
HFP	2285044.1
HFPO	940740

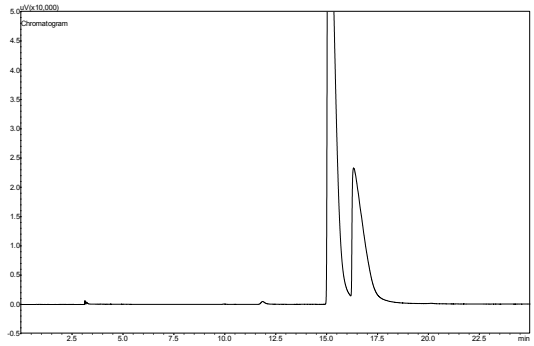

Figure I.352. Shimadzu G.C. 2010 FID chromatogram, experiment 43h.

Table I.353. Shimadzu G.C. 2014 TCD chromatogram, experiment 43h.

Component	Peak area
O_2	41367.4
COF_2	35503.7
CF_3COF	10274.5
C_2F_4	-
c-C_3F_6	-
HFP	-
HFPO	-

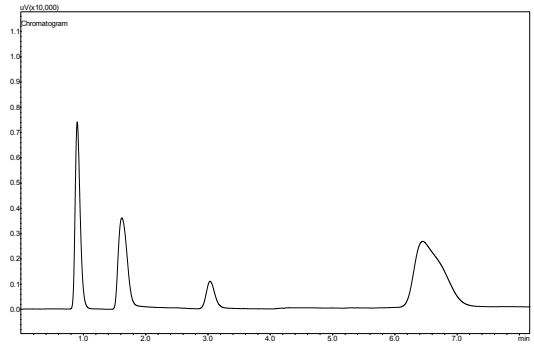

Figure I.353. Shimadzu G.C. 2014 TCD chromatogram, experiment 43h.

Table I.354. Shimadzu G.C. 2010 FID chromatogram, experiment 43i.

Component	Peak area
O_2	-
COF_2	-
CF_3COF	-
C_2F_4	3305.9
c-C_3F_6	4312
HFP	35586.6
HFPO	566102.1

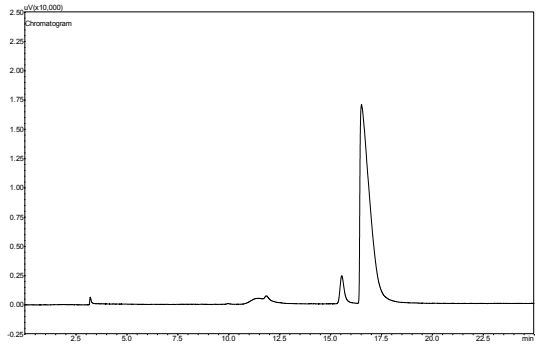

Figure I.354. Shimadzu G.C. 2010 FID chromatogram, experiment 43i.

Table I.355. Shimadzu G.C. 2014 TCD chromatogram, experiment 43i.

Component	Peak area
O_2	19707.8
COF_2	67341.7
CF_3COF	23836.2
C_2F_4	-
c-C_3F_6	-
HFP	-
HFPO	-

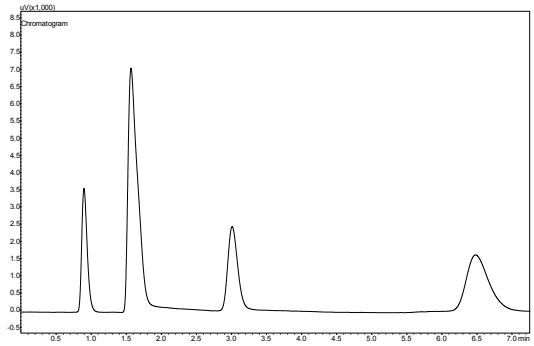

Figure I.355. Shimadzu G.C. 2014 TCD chromatogram, experiment 43i.

Table I.356. Shimadzu G.C. 2010 FID chromatogram, experiment 44a.

Component	Peak area
O_2	-
COF_2	-
CF_3COF	-
C_2F_4	-
c-C_3F_6	5907.4
HFP	12746764.8
HFPO	339432.9

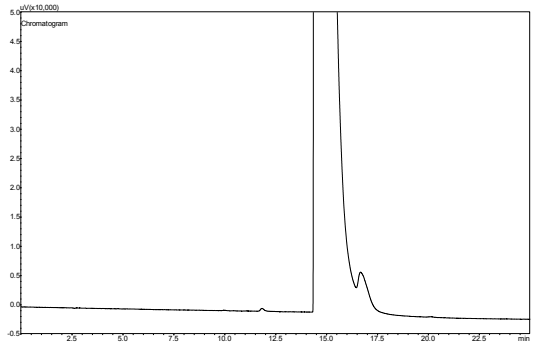

Figure I.356. Shimadzu G.C. 2010 FID chromatogram, experiment 44a.

Table I.357. Shimadzu G.C. 2010 FID chromatogram, experiment 44b.

Component	Peak area
O_2	-
COF_2	-
CF_3COF	-
C_2F_4	881.9
c-C_3F_6	6081.8
HFP	10325688.9
HFPO	756540.4

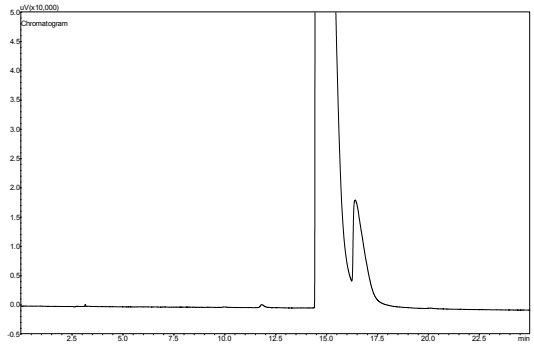

Figure I.357. Shimadzu G.C. 2010 FID chromatogram, experiment 44b.

Table I.358. Shimadzu G.C. 2010 FID chromatogram, experiment 44c.

Component	Peak area
O_2	-
COF_2	-
CF_3COF	-
C_2F_4	80567
c-C_3F_6	19779.5
HFP	3777230.9
HFPO	1183708.9

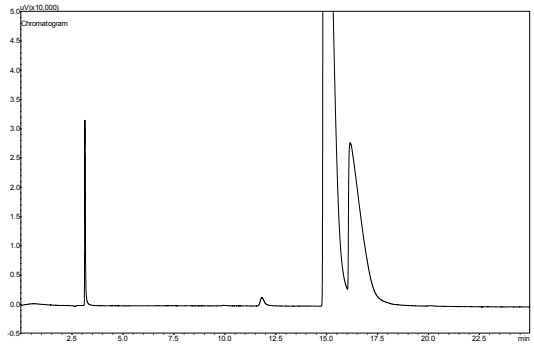

Figure I.358. Shimadzu G.C. 2010 FID chromatogram, experiment 44c.

Table I.359. Shimadzu G.C. 2010 FID chromatogram, experiment 44d.

Component	Peak area
O_2	-
COF_2	-
CF_3COF	-
C_2F_4	160397
c-C_3F_6	84407.7
HFP	3227331.4
HFPO	805572.8

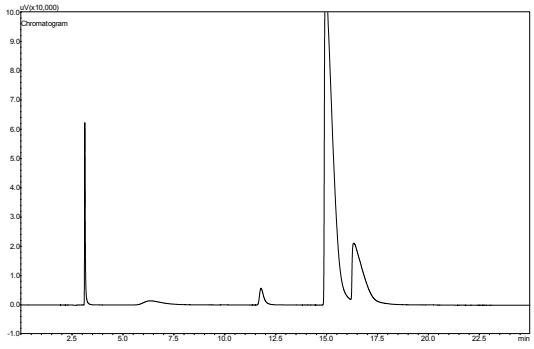

Figure I.359. Shimadzu G.C. 2010 FID chromatogram, experiment 44d.

Table I.360. Shimadzu G.C. 2010 FID chromatogram, experiment 44e.

Component	Peak area
O_2	-
COF_2	-
CF_3COF	-
C_2F_4	56469.9
c-C_3F_6	16713.8
HFP	3483796.6
HFPO	1296702.5

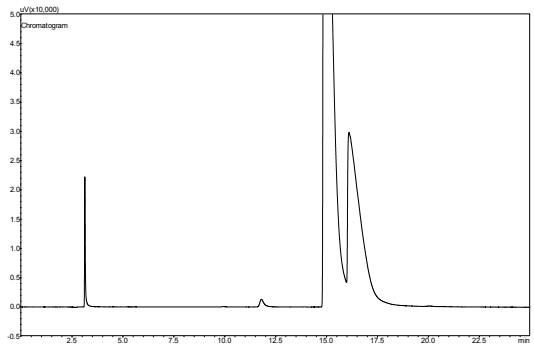

Figure I.360. Shimadzu G.C. 2010 FID chromatogram, experiment 44e.

Table I.361. Shimadzu G.C. 2010 FID chromatogram, experiment 44f.

Component	Peak area
O_2	-
COF_2	-
CF_3COF	-
C_2F_4	1958
c-C_3F_6	6738.7
HFP	5854212
HFPO	1206760.8

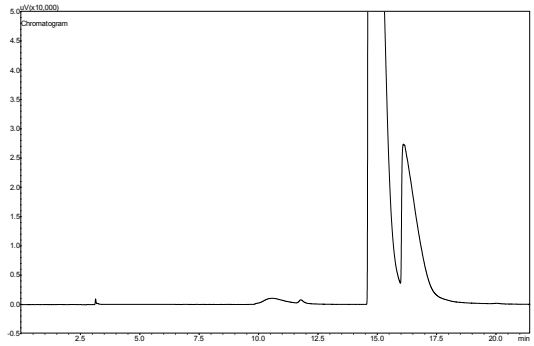

Figure I.361. Shimadzu G.C. 2010 FID chromatogram, experiment 44f.

Table I.362. Shimadzu G.C. 2010 FID chromatogram, experiment 44g.

Component	Peak area
O_2	-
COF_2	-
CF_3COF	-
C_2F_4	676.9
c-C_3F_6	5307.5
HFP	5785560.1
HFPO	845944.2

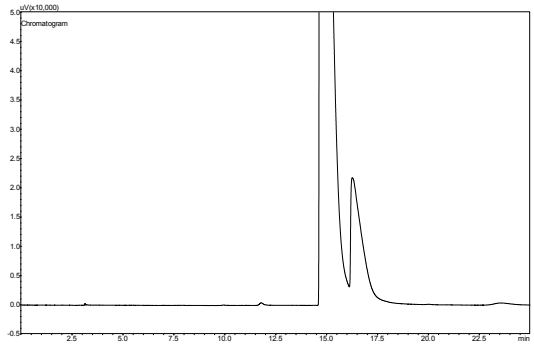

Figure I.362. Shimadzu G.C. 2010 FID chromatogram, experiment 44g.

Table I.363. Shimadzu G.C. 2010 FID chromatogram, experiment 44h.

Component	Peak area
O_2	-
COF_2	-
CF_3COF	-
C_2F_4	391.5
c-C_3F_6	5790.4
HFP	593810.1
HFPO	955129.2

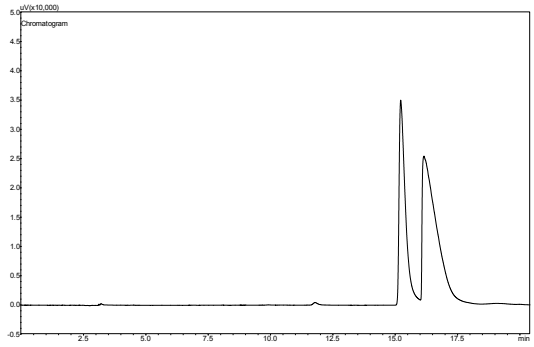

Figure I.363. Shimadzu G.C. 2010 FID chromatogram, experiment 44h.

Table I.364. Shimadzu G.C. 2010 FID chromatogram, experiment 44i.

Component	Peak area
O_2	-
COF_2	-
CF_3COF	-
C_2F_4	1549.5
c-C_3F_6	5309.6
HFP	52182.7
HFPO	661170

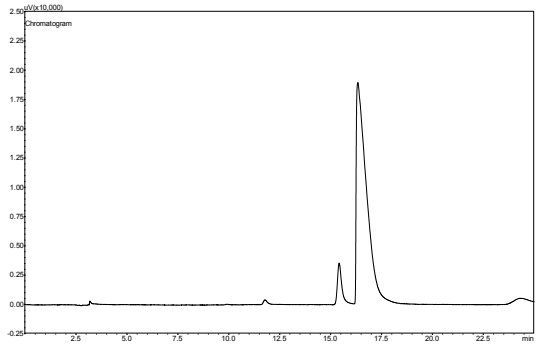

Figure I.364. Shimadzu G.C. 2010 FID chromatogram, experiment 44i.

Table I.365. Shimadzu G.C. 2010 FID chromatogram, experiment 45a.

Component	Peak area
O_2	-
COF_2	-
CF_3COF	-
C_2F_4	-
c-C_3F_6	4578.4
HFP	11466006.5
HFPO	222584.2

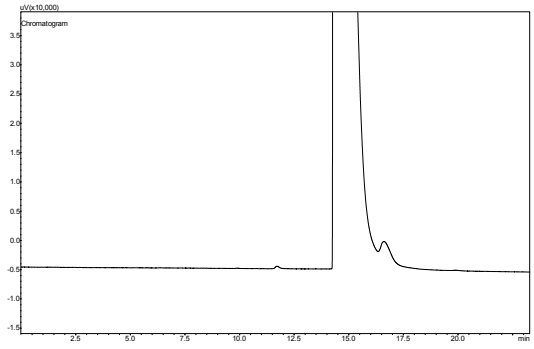

Figure I.365. Shimadzu G.C. 2010 FID chromatogram, experiment 45a.

Table I.366. Shimadzu G.C. 2010 FID chromatogram, experiment 45b.

Component	Peak area
O_2	-
COF_2	-
CF_3COF	-
C_2F_4	582.6
c-C_3F_6	5320.1
HFP	10258183.1
HFPO	512906.8

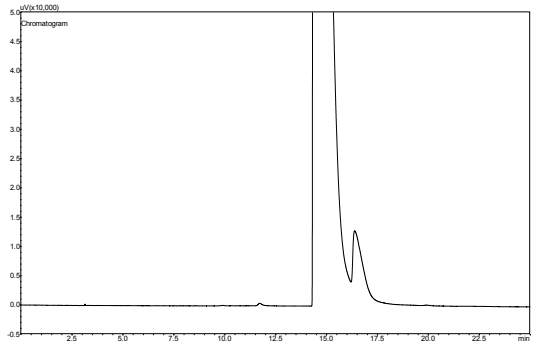

Figure I.366. Shimadzu G.C. 2010 FID chromatogram, experiment 45b.

Table I.367. Shimadzu G.C. 2010 FID chromatogram, experiment 45c.

Component	Peak area
O_2	-
COF_2	-
CF_3COF	-
C_2F_4	3566.1
c-C_3F_6	6788.3
HFP	1277626.1
HFPO	1199623.4

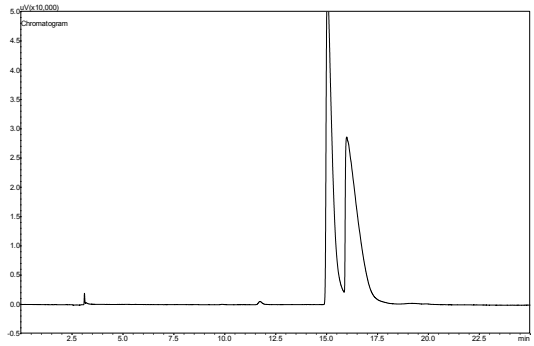

Figure I.367. Shimadzu G.C. 2010 FID chromatogram, experiment 45c.

Table I.368. Shimadzu G.C. 2010 FID chromatogram, experiment 45d.

Component	Peak area
O_2	-
COF_2	-
CF_3COF	-
C_2F_4	1526
c-C_3F_6	4133.8
HFP	101669
HFPO	550113.5

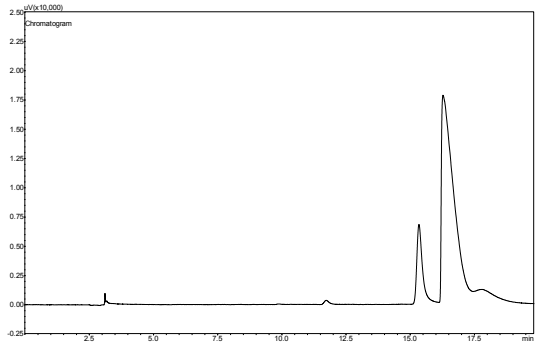

Figure I.368. Shimadzu G.C. 2010 FID chromatogram, experiment 45d.

Table I.369. Shimadzu G.C. 2010 FID chromatogram, experiment 45e.

Component	Peak area
O_2	-
COF_2	-
CF_3COF	-
C_2F_4	557.4
c-C_3F_6	3571.7
HFP	2039241.1
HFPO	703191.9

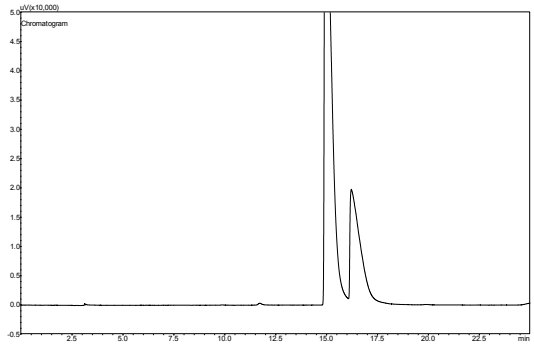

Figure I.369. Shimadzu G.C. 2010 FID chromatogram, experiment 45e.

Table I.370. Shimadzu G.C. 2010 FID chromatogram, experiment 45f.

Component	Peak area
O_2	-
COF_2	-
CF_3COF	-
C_2F_4	108.9
c-C_3F_6	2995.3
HFP	6717110.5
HFPO	290300.3

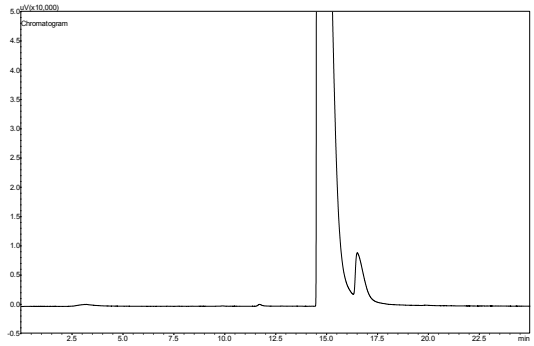

Figure I.370. Shimadzu G.C. 2010 FID chromatogram, experiment 45f.

Table I.371. Shimadzu G.C. 2010 FID chromatogram, experiment 45g.

Component	Peak area
O_2	-
COF_2	-
CF_3COF	-
C_2F_4	362.3
c-C_3F_6	5465.2
HFP	6534096.2
HFPO	970347.7

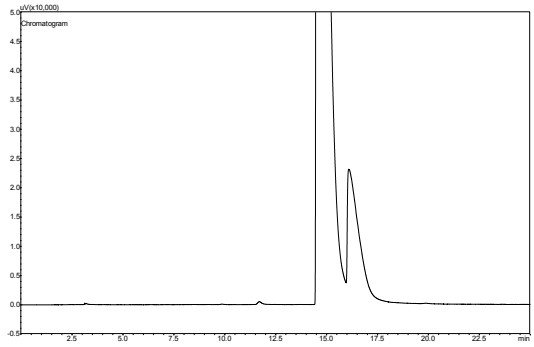

Figure I.371. Shimadzu G.C. 2010 FID chromatogram, experiment 45g.

Table I.372. Shimadzu G.C. 2010 FID chromatogram, experiment 45h.

Component	Peak area
O_2	-
COF_2	-
CF_3COF	-
C_2F_4	26134.5
c-C_3F_6	7567.4
HFP	1082584.7
HFPO	1155555.9

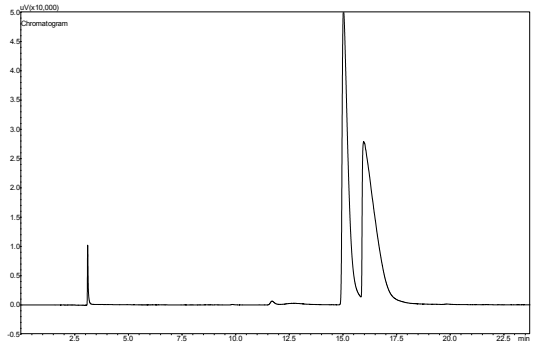

Figure I.372. Shimadzu G.C. 2010 FID chromatogram, experiment 45h.

Table I.373. Shimadzu G.C. 2010 FID chromatogram, experiment 45i.

Component	Peak area
O_2	-
COF_2	-
CF_3COF	-
C_2F_4	144787.5
c-C_3F_6	77154.7
HFP	1154774.8
HFPO	713240.8

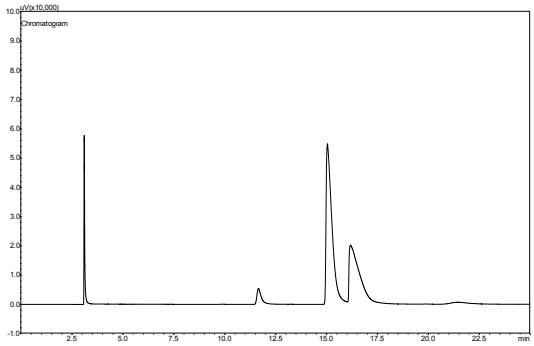

Figure I.373. Shimadzu G.C. 2010 FID chromatogram, experiment 45i.

Table I.374. Shimadzu G.C. 2010 FID chromatogram, Au/Al_2O_3 catalyst experiment 1.

Component	Peak area
O_2	-
COF_2	-
CF_3COF	-
C_2F_4	-
c-C_3F_6	4689.8
HFP	11919913.7
HFPO	-

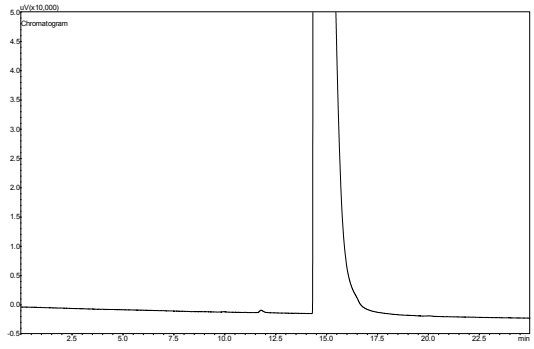

Figure I.374. Shimadzu G.C. 2010 FID chromatogram, Au/Al_2O_3 catalyst experiment 1.

Table I.375. Shimadzu G.C. 2014 TCD chromatogram, Au/Al_2O_3 catalyst experiment 1.

Component	Peak area
O_2	73687.4
COF_2	-
CF_3COF	-
C_2F_4	-
c-C_3F_6	-
HFP	-
HFPO	-

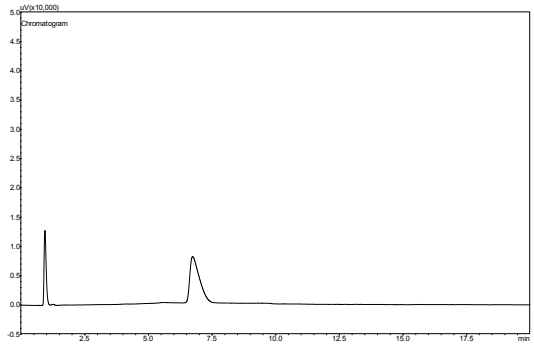

Figure I.375. Shimadzu G.C. 2014 TCD chromatogram, Au/Al_2O_3 catalyst experiment 1.

Table I.376. Shimadzu G.C. 2010 FID chromatogram, Au/Al_2O_3 catalyst experiment 2.

Component	Peak area
O_2	-
COF_2	-
CF_3COF	-
C_2F_4	-
c-C_3F_6	4638.4
HFP	11950442.2
HFPO	-

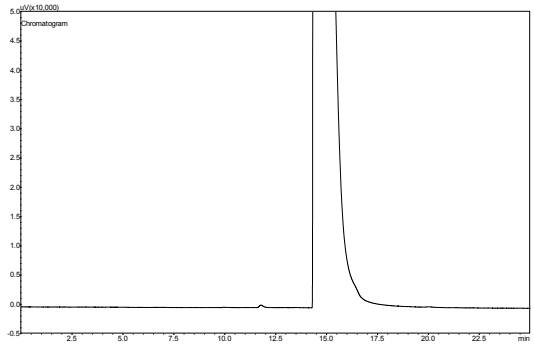

Figure I.376. Shimadzu G.C. 2010 FID chromatogram, Au/Al_2O_3 catalyst experiment 1.

Table I.377. Shimadzu G.C. 2014 TCD chromatogram, Au/Al_2O_3 catalyst experiment 2.

Component	Peak area
O_2	71734.3
COF_2	-
CF_3COF	-
C_2F_4	-
c-C_3F_6	-
HFP	-
HFPO	-

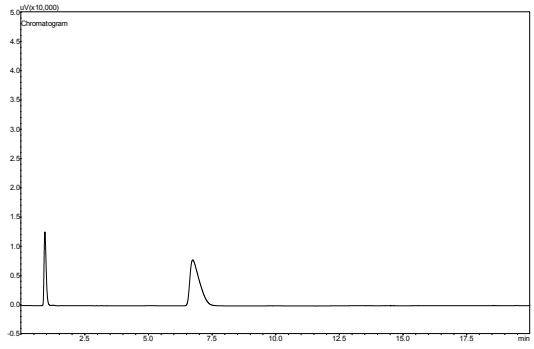

Figure I.377. Shimadzu G.C. 2014 TCD chromatogram, Au/Al_2O_3 catalyst experiment 2.

Table I.378. Shimadzu G.C. 2010 FID chromatogram, Au/Al_2O_3 catalyst experiment 3.

Component	Peak area
O_2	-
COF_2	-
CF_3COF	-
C_2F_4	-
c-C_3F_6	4754.6
HFP	11902751.9
HFPO	-

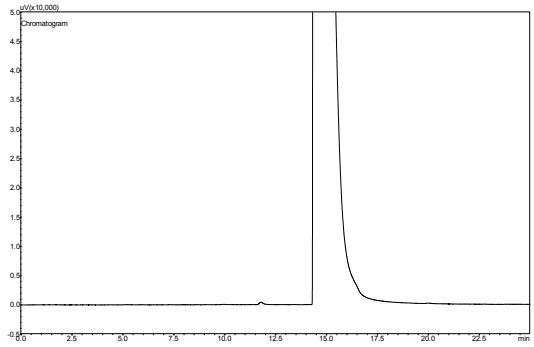

Figure I.378. Shimadzu G.C. 2010 FID chromatogram, Au/Al_2O_3 catalyst experiment 3.

Table I.379. Shimadzu G.C. 2014 TCD chromatogram, Au/Al_2O_3 catalyst experiment 3.

Component	Peak area
O_2	70746.8
COF_2	-
CF_3COF	-
C_2F_4	-
c-C_3F_6	-
HFP	-
HFPO	-

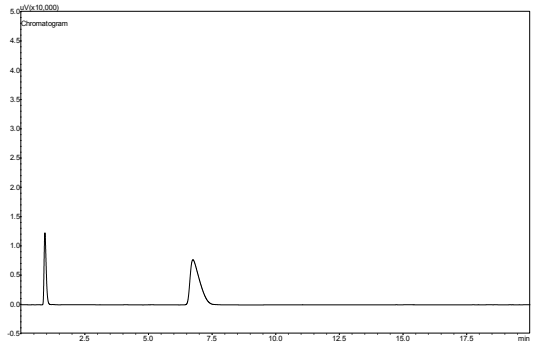

Figure I.379. Shimadzu G.C. 2014 TCD chromatogram, Au/Al_2O_3 catalyst experiment 3.

Table I.380. Shimadzu G.C. 2010 FID chromatogram, Au/Al_2O_3 catalyst experiment 4.

Component	Peak area
O_2	-
COF_2	-
CF_3COF	-
C_2F_4	-
c-C_3F_6	2609.4
HFP	8214972.3
HFPO	-

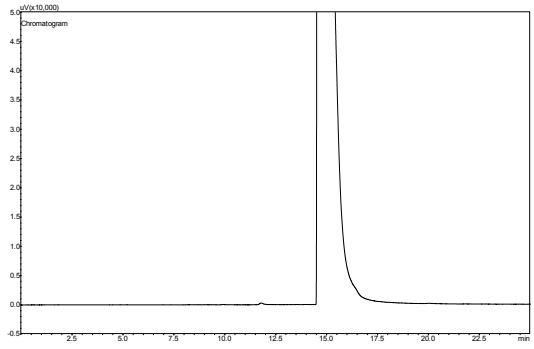

Figure I.380. Shimadzu G.C. 2010 FID chromatogram, Au/Al_2O_3 catalyst experiment 4.

Table I.381. Shimadzu G.C. 2014 TCD chromatogram, Au/Al_2O_3 catalyst experiment 4.

Component	Peak area
O_2	92978.9
COF_2	-
CF_3COF	-
C_2F_4	-
c-C_3F_6	-
HFP	-
HFPO	-

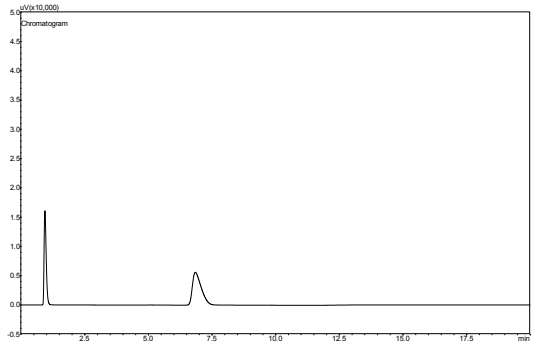

Figure I.381. Shimadzu G.C. 2014 TCD chromatogram, Au/Al_2O_3 catalyst experiment 4.

Table I.382. Shimadzu G.C. 2010 FID chromatogram, Au/Al_2O_3 catalyst experiment 5.

Component	Peak area
O_2	-
COF_2	-
CF_3COF	-
C_2F_4	-
c-C_3F_6	6038
HFP	14157719.3
HFPO	-

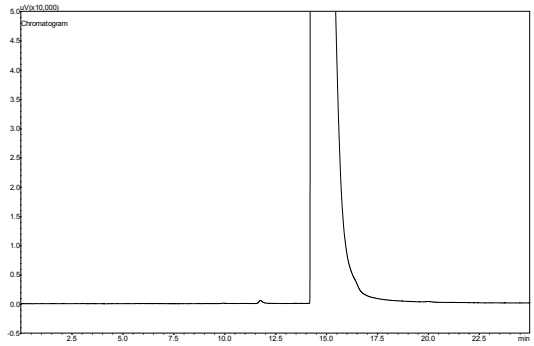

Figure I.382. Shimadzu G.C. 2010 FID chromatogram, Au/Al_2O_3 catalyst experiment 5.

Table I.383. Shimadzu G.C. 2014 TCD chromatogram, Au/Al_2O_3 catalyst experiment 5.

Component	Peak area
O_2	55713.4
COF_2	-
CF_3COF	-
C_2F_4	-
c-C_3F_6	-
HFP	-
HFPO	-

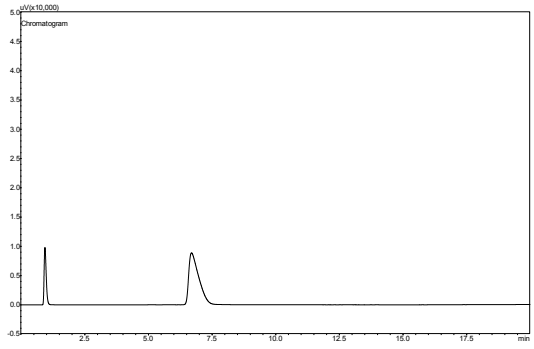

Figure I.383. Shimadzu G.C. 2014 TCD chromatogram, Au/Al_2O_3 catalyst experiment 5.

Table I.384. Shimadzu G.C. 2010 FID chromatogram, Au/Al_2O_3 catalyst experiment 6.

Component	Peak area
O_2	-
COF_2	-
CF_3COF	-
C_2F_4	-
c-C_3F_6	5341.6
HFP	12931006.7
HFPO	-

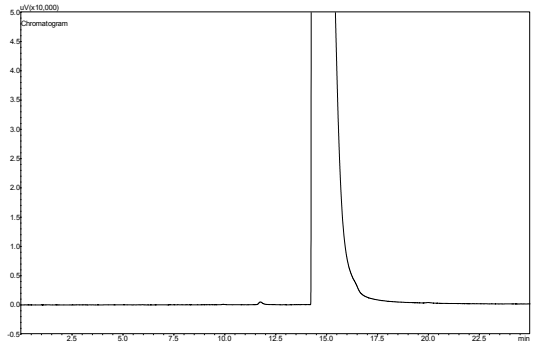

Figure I.384. Shimadzu G.C. 2010 FID chromatogram, Au/Al_2O_3 catalyst experiment 6.

Table I.385. Shimadzu G.C. 2014 TCD chromatogram, Au/Al_2O_3 catalyst experiment 6.

Component	Peak area
O_2	63384.5
COF_2	-
CF_3COF	-
C_2F_4	-
c-C_3F_6	-
HFP	-
HFPO	-

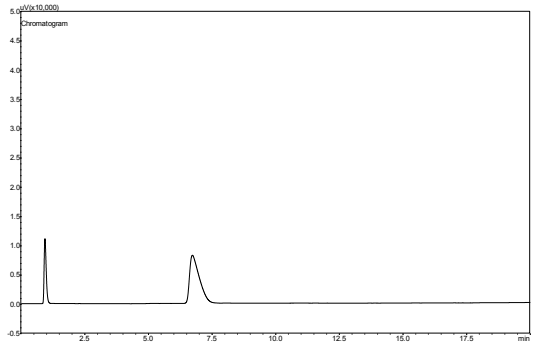

Figure I.385. Shimadzu G.C. 2014 TCD chromatogram, Au/Al_2O_3 catalyst experiment 6.

Table I.386. Shimadzu G.C. 2010 FID chromatogram, Au/Al_2O_3 catalyst experiment 7.

Component	Peak area
O_2	-
COF_2	-
CF_3COF	-
C_2F_4	-
c-C_3F_6	4832.5
HFP	11464304.8
HFPO	-

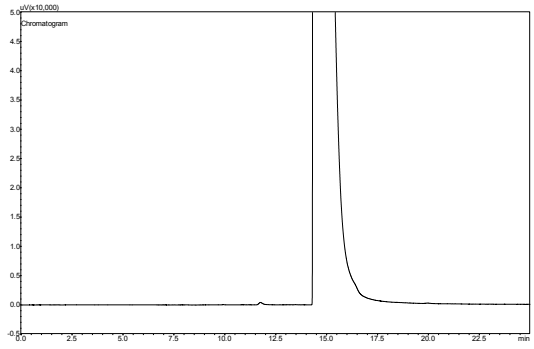

Figure I.386. Shimadzu G.C. 2010 FID chromatogram, Au/Al_2O_3 catalyst experiment 7.

Table I.387. Shimadzu G.C. 2014 TCD chromatogram, Au/Al_2O_3 catalyst experiment 7.

Component	Peak area
O_2	73342.4
COF_2	-
CF_3COF	-
C_2F_4	-
c-C_3F_6	-
HFP	-
HFPO	-

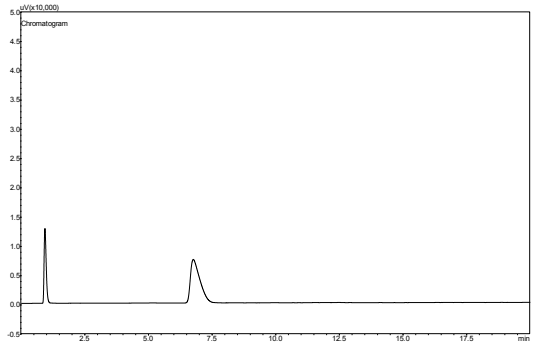

Figure I.387. Shimadzu G.C. 2014 TCD chromatogram, Au/Al_2O_3 catalyst experiment 7.

Table I.388. Shimadzu G.C. 2010 FID chromatogram, Au/Al_2O_3 catalyst experiment 8.

Component	Peak area
O_2	-
COF_2	-
CF_3COF	-
C_2F_4	-
c-C_3F_6	4714.9
HFP	11770742.2
HFPO	-

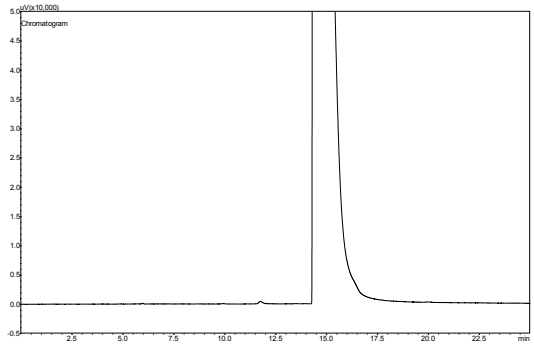

Figure I.388. Shimadzu G.C. 2010 FID chromatogram, Au/Al_2O_3 catalyst experiment 8.

Table I.389. Shimadzu G.C. 2014 TCD chromatogram, Au/Al_2O_3 catalyst experiment 8.

Component	Peak area
O_2	70920.9
COF_2	404
CF_3COF	-
C_2F_4	-
c-C_3F_6	-
HFP	-
HFPO	-

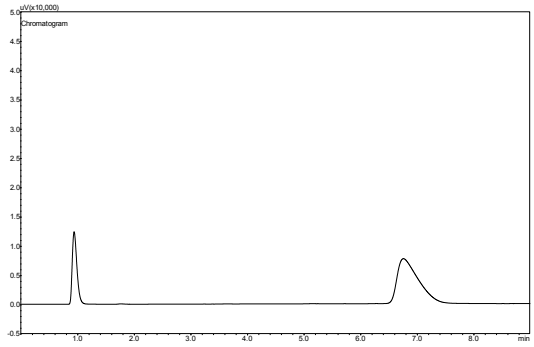

Figure I.389. Shimadzu G.C. 2014 TCD chromatogram, Au/Al_2O_3 catalyst experiment 8.

Table I.390. Shimadzu G.C. 2010 FID chromatogram, Au/ZnO catalyst experiment 1.

Component	Peak area
O_2	-
COF_2	-
CF_3COF	-
C_3F_8	-
c-C_3F_6	7189.4
HFP	16485079.5
HFPO	-

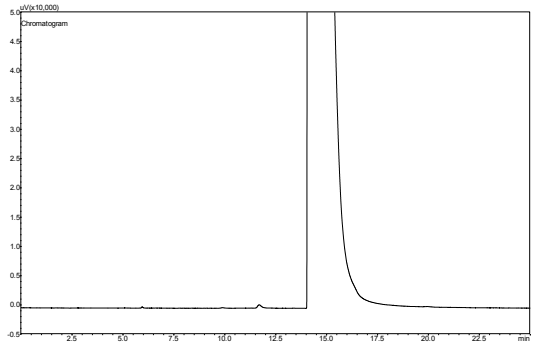

Figure I.390. Shimadzu G.C. 2010 FID chromatogram, Au/ZnO catalyst experiment 1.

Table I.391. Shimadzu G.C. 2014 TCD chromatogram, Au/ZnO catalyst experiment 1.

Component	Peak area
O_2	65632.2
COF_2	1861.4
CF_3COF	-
C_2F_4	-
c-C_3F_6	-
HFP	-
HFPO	-

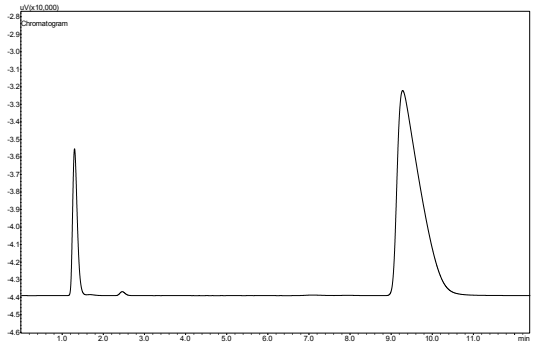

Figure I.391. Shimadzu G.C. 2014 TCD chromatogram, Au/ZnO catalyst experiment 1.

Table I.392. Shimadzu G.C. 2010 FID chromatogram, Au/ZnO catalyst experiment 2.

Component	Peak area
O_2	-
COF_2	-
CF_3COF	-
C_3F_8	2686.2
c-C_3F_6	6862.4
HFP	16133605.3
HFPO	-

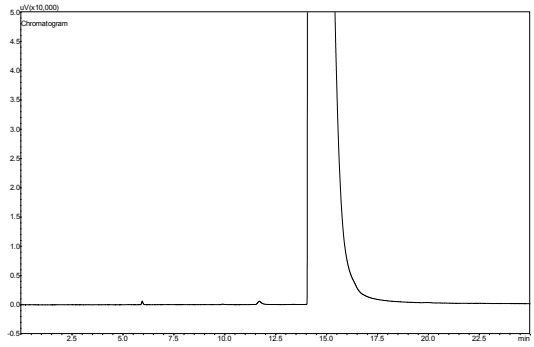

Figure I.392. Shimadzu G.C. 2010 FID chromatogram, Au/ZnO catalyst experiment 2.

Table I.393. Shimadzu G.C. 2014 TCD chromatogram, Au/ZnO catalyst experiment 2.

Component	Peak area
O_2	68229.8
COF_2	1601.1
CF_3COF	-
C_2F_4	-
c-C_3F_6	-
HFP	-
HFPO	-

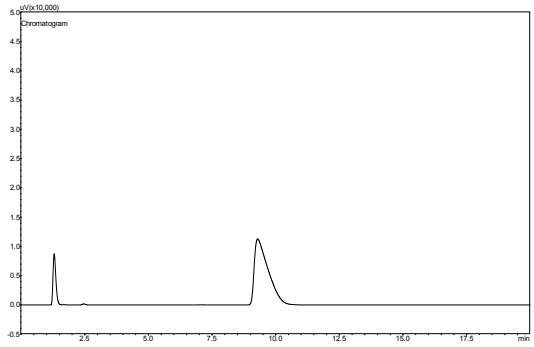

Figure I.393. Shimadzu G.C. 2014 TCD chromatogram, Au/ZnO catalyst experiment 2.

Table I.394. Shimadzu G.C. 2010 FID chromatogram, Au/ZnO catalyst experiment 3.

Component	Peak area
O_2	-
COF_2	-
CF_3COF	-
C_3F_8	3051.9
c-C_3F_6	6347.7
HFP	16460957
HFPO	-

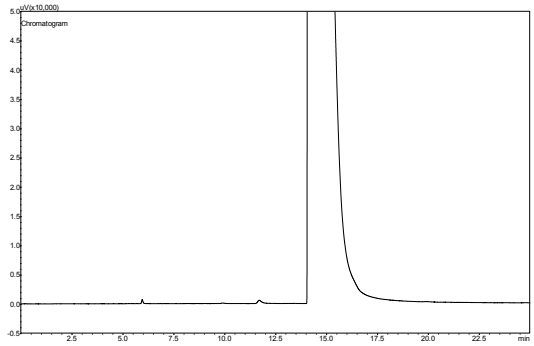

Figure I.394. Shimadzu G.C. 2010 FID chromatogram, Au/ZnO catalyst experiment 3.

Table I.395. Shimadzu G.C. 2014 TCD chromatogram, Au/ZnO catalyst experiment 3.

Component	Peak area
O_2	63009.6
COF_2	2274.5
CF_3COF	-
C_2F_4	-
c-C_3F_6	-
HFP	-
HFPO	-

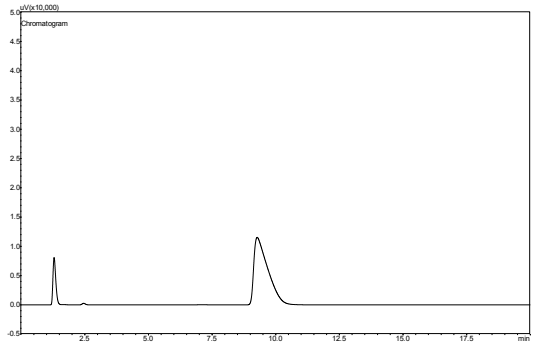

Figure I.395. Shimadzu G.C. 2014 TCD chromatogram, Au/ZnO catalyst experiment 3.

Table I.396. Shimadzu G.C. 2010 FID chromatogram, Au/ZnO catalyst experiment 4.

Component	Peak area
O_2	-
COF_2	-
CF_3COF	-
C_3F_8	971.3
c-C_3F_6	4059.1
HFP	10540398.5
HFPO	-

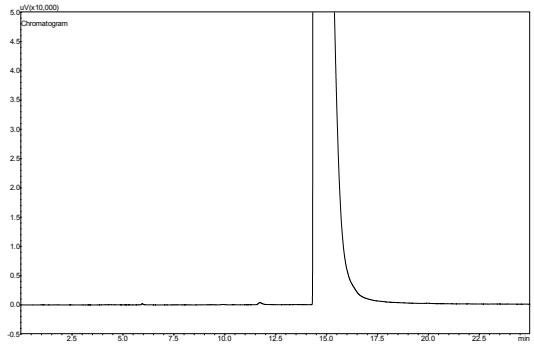

Figure I.396. Shimadzu G.C. 2010 FID chromatogram, Au/ZnO catalyst experiment 4.

Table I.397. Shimadzu G.C. 2014 TCD chromatogram, Au/ZnO catalyst experiment 4.

Component	Peak area
O_2	126874.6
COF_2	1345.4
CF_3COF	-
C_2F_4	-
c-C_3F_6	-
HFP	-
HFPO	-

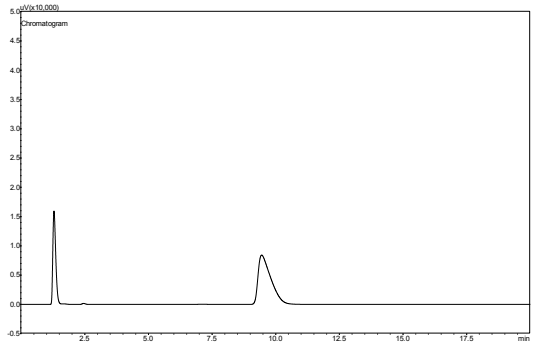

Figure I.397. Shimadzu G.C. 2014 TCD chromatogram, Au/ZnO catalyst experiment 4.

Table I.398. Shimadzu G.C. 2010 FID chromatogram, Au/ZnO catalyst experiment 5.

Component	Peak area
O_2	-
COF_2	-
CF_3COF	-
C_3F_8	897.9
c-C_3F_6	3409.6
HFP	10212355.7
HFPO	-

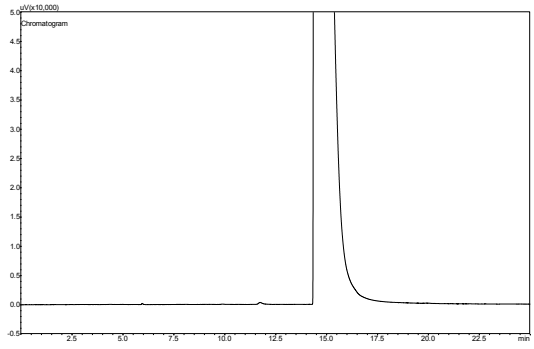

Figure I.398. Shimadzu G.C. 2010 FID chromatogram, Au/ZnO catalyst experiment 5.

Table I.399. Shimadzu G.C. 2014 TCD chromatogram, Au/ZnO catalyst experiment 5.

Component	Peak area
O_2	130908.5
COF_2	2288.4
CF_3COF	-
C_2F_4	-
c-C_3F_6	-
HFP	-
HFPO	-

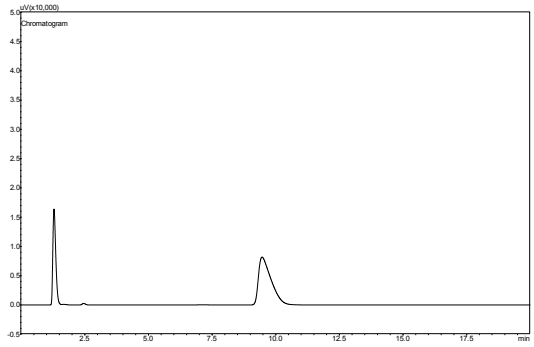

Figure I.399. Shimadzu G.C. 2014 TCD chromatogram, Au/ZnO catalyst experiment 5.

Table I.400. Shimadzu G.C. 2010 FID chromatogram, CuO/SiO_2 catalyst experiment 1.

Component	Peak area
O_2	-
COF_2	-
CF_3COF	-
C_2F_4	-
c-C_3F_6	5075.5
HFP	12773619
HFPO	-

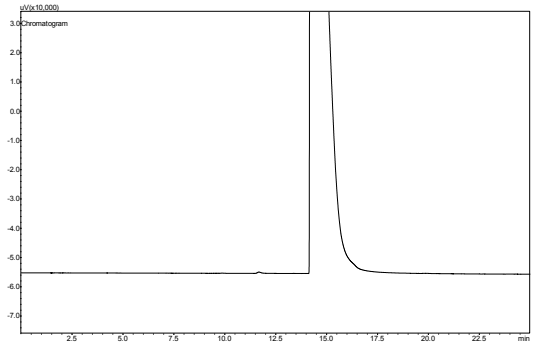

Figure I.400. Shimadzu G.C. 2010 FID chromatogram, CuO/SiO_2 catalyst experiment 1.

Table I.401. Shimadzu G.C. 2014 TCD chromatogram, CuO/SiO_2 catalyst experiment 1.

Component	Peak area
O_2	107175.1
COF_2	227.4
CF_3COF	-
C_2F_4	-
c-C_3F_6	-
HFP	-
HFPO	-

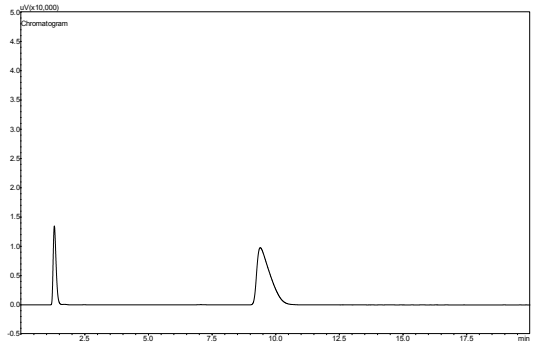

Figure I.401. Shimadzu G.C. 2014 TCD chromatogram, CuO/SiO_2 catalyst experiment 1.

Table I.402. Shimadzu G.C. 2010 FID chromatogram, CuO/SiO_2 catalyst experiment 2.

Component	Peak area
O_2	-
COF_2	-
CF_3COF	-
C_2F_4	-
c-C_3F_6	5149.5
HFP	12650378
HFPO	-

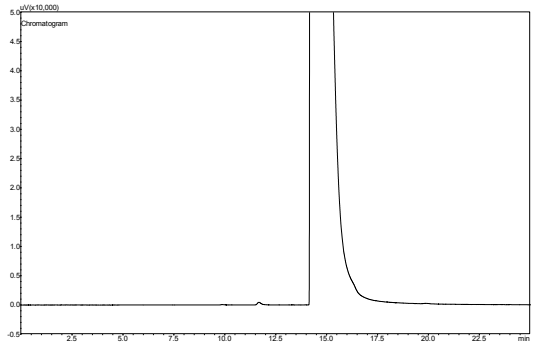

Figure I.402. Shimadzu G.C. 2010 FID chromatogram, CuO/SiO_2 catalyst experiment 2.

Table I.403. Shimadzu G.C. 2014 TCD chromatogram, CuO/SiO_2 catalyst experiment 2.

Component	Peak area
O_2	105543.6
COF_2	457.1
CF_3COF	-
C_2F_4	-
c-C_3F_6	-
HFP	-
HFPO	-

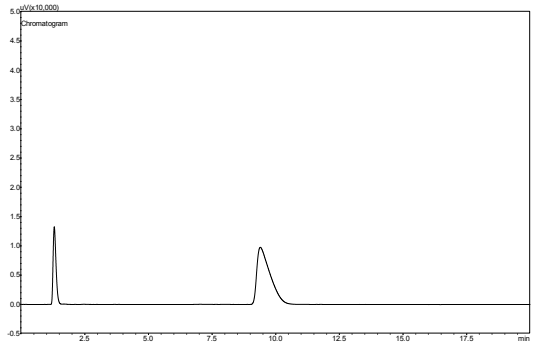

Figure I.403. Shimadzu G.C. 2014 TCD chromatogram, CuO/SiO_2 catalyst experiment 2.

Table I.404. Shimadzu G.C. 2010 FID chromatogram, CuO/SiO_2 catalyst experiment 3.

Component	Peak area
O_2	-
COF_2	-
CF_3COF	-
C_2F_4	-
c-C_3F_6	4965.3
HFP	12616230
HFPO	-

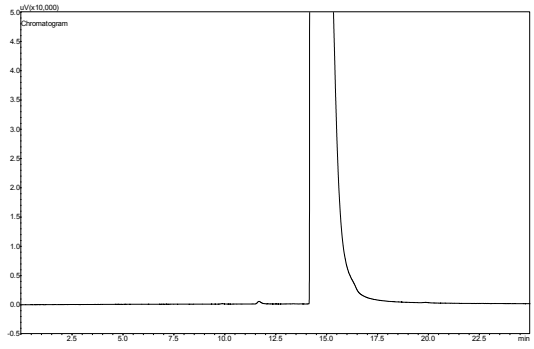

Figure I.404. Shimadzu G.C. 2010 FID chromatogram, CuO/SiO_2 catalyst experiment 3.

Table I.405. Shimadzu G.C. 2014 TCD chromatogram, CuO/SiO_2 catalyst experiment 3.

Component	Peak area
O_2	108335.1
COF_2	978.2
CF_3COF	-
C_2F_4	-
c-C_3F_6	-
HFP	-
HFPO	-

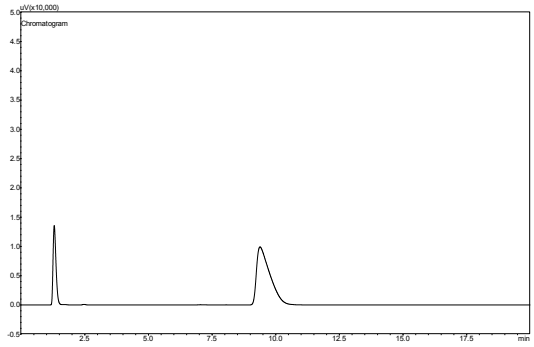

Figure I.405. Shimadzu G.C. 2014 TCD chromatogram, CuO/SiO_2 catalyst experiment 3.

Table I.406. Shimadzu G.C. 2010 FID chromatogram, CuO/SiO_2 catalyst experiment 4.

Component	Peak area
O_2	-
COF_2	-
CF_3COF	-
C_2F_4	-
c-C_3F_6	3335.3
HFP	9665715
HFPO	-

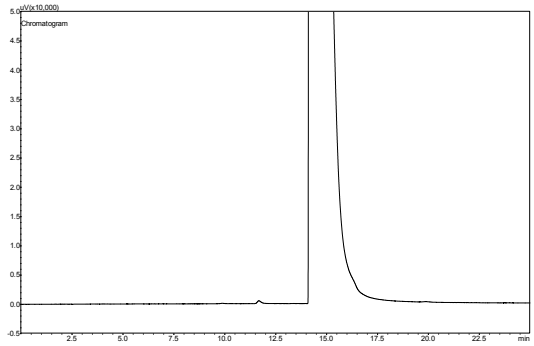

Figure I.406. Shimadzu G.C. 2010 FID chromatogram, CuO/SiO_2 catalyst experiment 4.

Table I.407. Shimadzu G.C. 2014 TCD chromatogram, CuO/SiO_2 catalyst experiment 4.

Component	Peak area
O_2	140232.5
COF_2	579
CF_3COF	-
C_2F_4	-
c-C_3F_6	-
HFP	-
HFPO	-

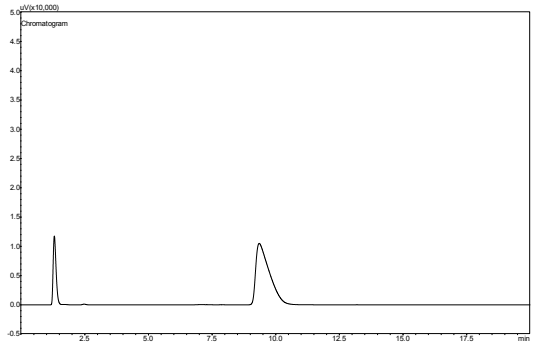

Figure I.407. Shimadzu G.C. 2014 TCD chromatogram, CuO/SiO_2 catalyst experiment 4.

Table I.408. Shimadzu G.C. 2010 FID chromatogram, CuO/SiO_2 catalyst experiment 5.

Component	Peak area
O_2	-
COF_2	-
CF_3COF	-
C_2F_4	94229.4
c-C_3F_6	1635.4
HFP	8475911
HFPO	43336.6

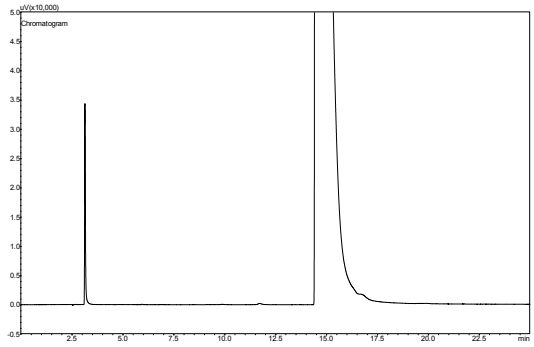

Figure I.408. Shimadzu G.C. 2010 FID chromatogram, CuO/SiO_2 catalyst experiment 5.

Table I.409. Shimadzu G.C. 2014 TCD chromatogram, CuO/SiO_2 catalyst experiment 5.

Component	Peak area
O_2	56041.6
COF_2	69001.7
CF_3COF	-
C_2F_4	-
c-C_3F_6	-
HFP	-
HFPO	-

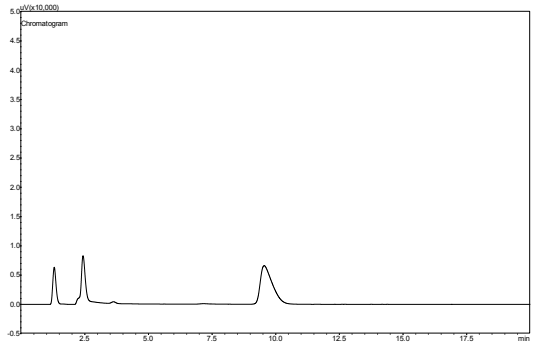

Figure I.409. Shimadzu G.C. 2014 TCD chromatogram, CuO/SiO_2 catalyst experiment 5.

Table I.410. Shimadzu G.C. 2010 FID chromatogram, CuO/SiO_2 catalyst experiment 6.

Component	Peak area
O_2	-
COF_2	-
CF_3COF	-
C_2F_4	-
c-C_3F_6	5956.4
HFP	15278209
HFPO	-

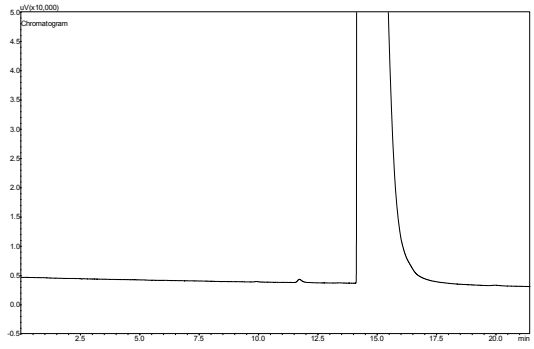

Figure I.410. Shimadzu G.C. 2010 FID chromatogram, CuO/SiO_2 catalyst experiment 6.

Table I.411. Shimadzu G.C. 2014 TCD chromatogram, CuO/SiO_2 catalyst experiment 6.

Component	Peak area
O_2	77762.9
COF_2	607.4
CF_3COF	-
C_2F_4	-
c-C_3F_6	-
HFP	-
HFPO	-

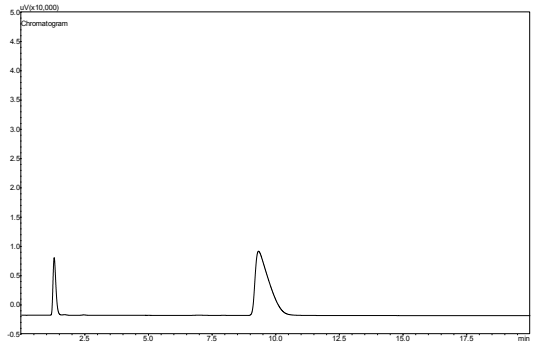

Figure I.411. Shimadzu G.C. 2014 TCD chromatogram, CuO/SiO_2 catalyst experiment 6.

Table I.412. Shimadzu G.C. 2010 FID chromatogram, CuO/SiO_2 catalyst experiment 7.

Component	Peak area
O_2	-
COF_2	-
CF_3COF	-
C_2F_4	-
c-C_3F_6	6764.1
HFP	15402247
HFPO	-

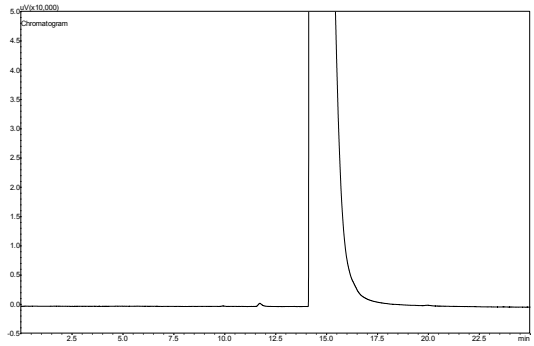

Figure I.412. Shimadzu G.C. 2010 FID chromatogram, CuO/SiO_2 catalyst experiment 7.

Table I.413. Shimadzu G.C. 2014 TCD chromatogram, CuO/SiO_2 catalyst experiment 7.

Component	Peak area
O_2	76501.3
COF_2	910.8
CF_3COF	-
C_2F_4	-
c-C_3F_6	-
HFP	-
HFPO	-

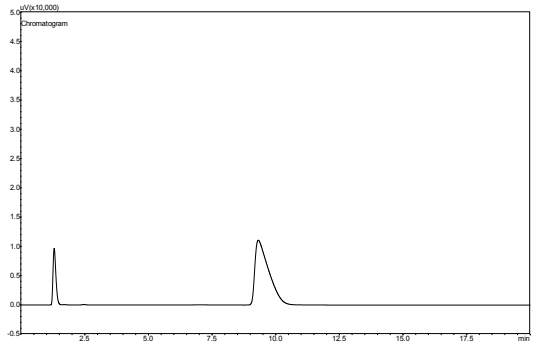

Figure I.413. Shimadzu G.C. 2014 TCD chromatogram, CuO/SiO_2 catalyst experiment 7.

Table I.414. Shimadzu G.C. 2010 FID chromatogram, CuO/SiO_2 catalyst experiment 8.

Component	Peak area
O_2	-
COF_2	-
CF_3COF	-
C_2F_4	-
c-C_3F_6	6495.3
HFP	15379545
HFPO	-

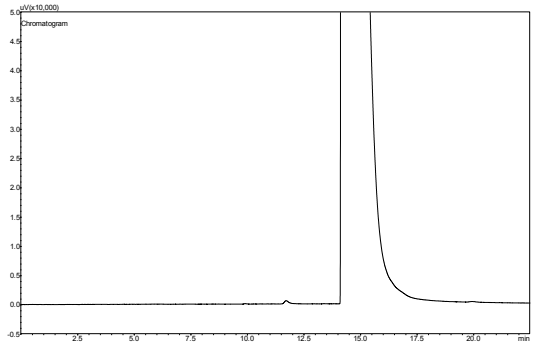

Figure I.414. Shimadzu G.C. 2010 FID chromatogram, CuO/SiO_2 catalyst experiment 8.

Table I.415. Shimadzu G.C. 2014 TCD chromatogram, CuO/SiO_2 catalyst experiment 8.

Component	Peak area
O_2	55742.2
COF_2	45.3
CF_3COF	-
C_2F_4	-
c-C_3F_6	-
HFP	-
HFPO	-

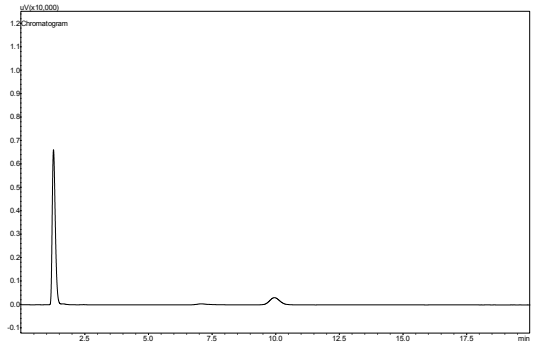

Figure I.415. Shimadzu G.C. 2014 TCD chromatogram, CuO/SiO_2 catalyst experiment 8.

Table I.416. Shimadzu G.C. 2010 FID chromatogram, CuO/SiO_2 catalyst experiment 9.

Component	Peak area
O_2	-
COF_2	-
CF_3COF	-
C_2F_4	-
c-C_3F_6	6779.7
HFP	15970205
HFPO	-

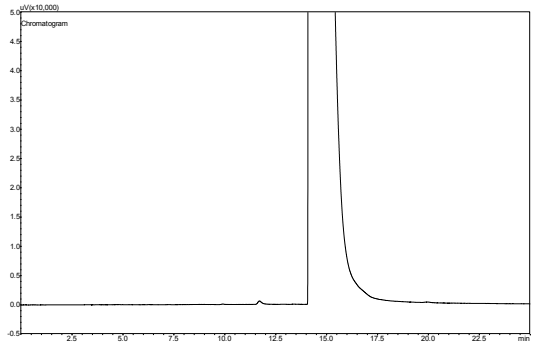

Figure I.416. Shimadzu G.C. 2010 FID chromatogram, CuO/SiO_2 catalyst experiment 9.

Table I.417. Shimadzu G.C. 2014 TCD chromatogram, CuO/SiO_2 catalyst experiment 9.

Component	Peak area
O_2	67415.4
COF_2	1035.4
CF_3COF	-
C_2F_4	-
c-C_3F_6	-
HFP	-
HFPO	-

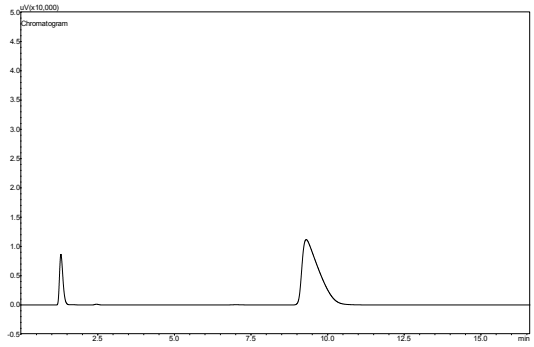

Figure I.417. Shimadzu G.C. 2014 TCD chromatogram, CuO/SiO_2 catalyst experiment 9.

Table I.418. Shimadzu G.C. 2010 FID chromatogram, CuO/SiO_2 catalyst experiment 10.

Component	Peak area
O_2	-
COF_2	-
CF_3COF	-
C_2F_4	109024.1
c-C_3F_6	1768.6
HFP	7287715
HFPO	25381.9

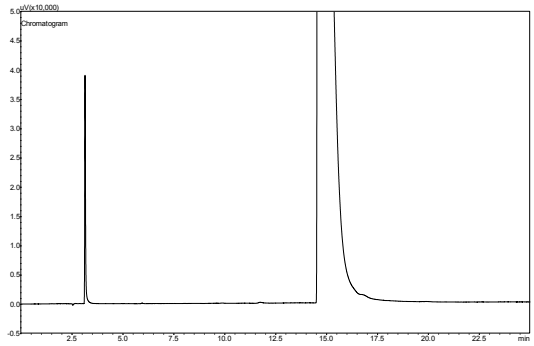

Figure I.418. Shimadzu G.C. 2010 FID chromatogram, CuO/SiO_2 catalyst experiment 10.

Table I.419. Shimadzu G.C. 2014 TCD chromatogram, CuO/SiO_2 catalyst experiment 10.

Component	Peak area
O_2	31854.4
COF_2	89227.2
CF_3COF	-
C_2F_4	-
c-C_3F_6	-
HFP	-
HFPO	-

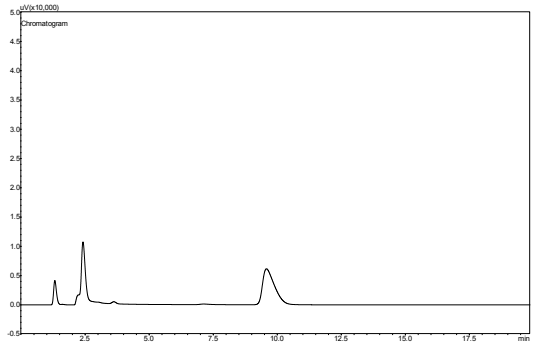

Figure I.419. Shimadzu G.C. 2014 TCD chromatogram, CuO/SiO_2 catalyst experiment 10.

Table I.420. Shimadzu G.C. 2010 FID chromatogram, Cs-CuO/SiO_2 catalyst experiment 1.

Component	Peak area
O_2	-
COF_2	-
CF_3COF	-
C_2F_4	-
c-C_3F_6	7039.2
HFP	16449838
HFPO	-

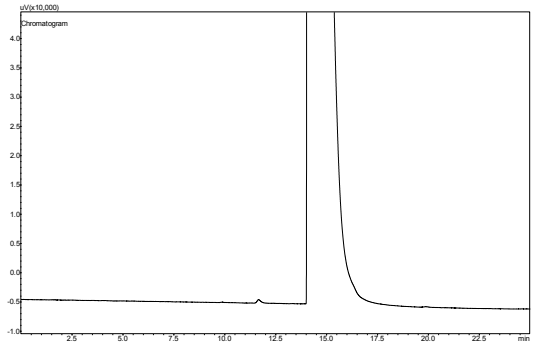

Figure I.420. Shimadzu G.C. 2010 FID chromatogram, Cs-CuO/SiO_2 catalyst experiment 1.

Table I.421. Shimadzu G.C. 2014 TCD chromatogram, Cs-CuO/SiO_2 catalyst experiment 1.

Component	Peak area
O_2	65417.6
COF_2	176.8
CF_3COF	-
C_2F_4	-
c-C_3F_6	-
HFP	-
HFPO	-

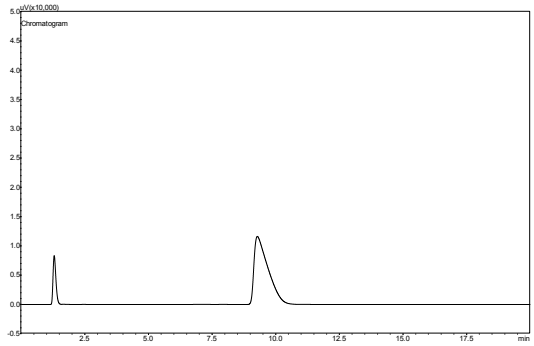

Figure I.421. Shimadzu G.C. 2014 TCD chromatogram, Cs-CuO/SiO_2 catalyst experiment 1.

Table I.422. Shimadzu G.C. 2010 FID chromatogram, Cs-CuO/SiO_2 catalyst experiment 2.

Component	Peak area
O_2	-
COF_2	-
CF_3COF	-
C_2F_4	-
c-C_3F_6	6930.4
HFP	16564542
HFPO	-

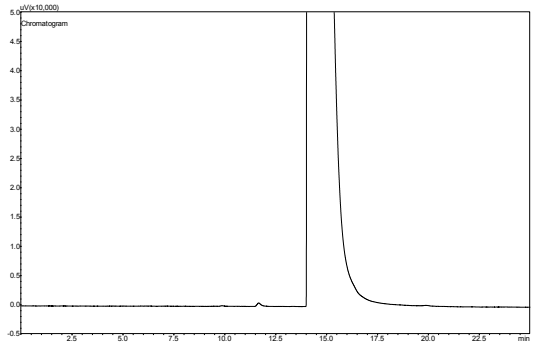

Figure I.422. Shimadzu G.C. 2010 FID chromatogram, Cs-CuO/SiO_2 catalyst experiment 2.

Table I.423. Shimadzu G.C. 2014 TCD chromatogram, Cs-CuO/SiO_2 catalyst experiment 2.

Component	Peak area
O_2	64157
COF_2	611.4
CF_3COF	-
C_2F_4	-
c-C_3F_6	-
HFP	-
HFPO	-

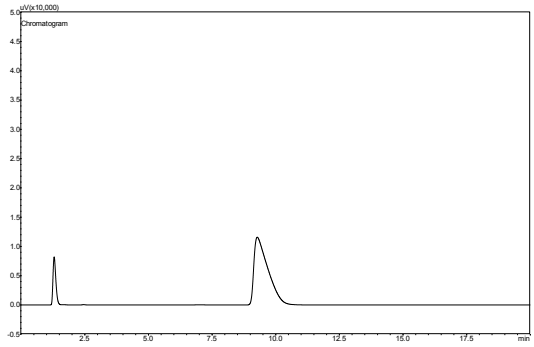

Figure I.423. Shimadzu G.C. 2014 TCD chromatogram, Cs-CuO/SiO_2 catalyst experiment 2.

Table I.424. Shimadzu G.C. 2010 FID chromatogram, Cs-CuO/SiO_2 catalyst experiment 3.

Component	Peak area
O_2	-
COF_2	-
CF_3COF	-
C_2F_4	-
c-C_3F_6	7072.5
HFP	16484263
HFPO	-

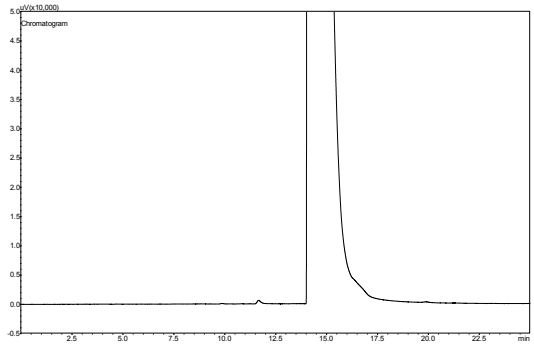

Figure I.424. Shimadzu G.C. 2010 FID chromatogram, Cs-CuO/SiO_2 catalyst experiment 3.

Table I.425. Shimadzu G.C. 2014 TCD chromatogram, Cs-CuO/SiO_2 catalyst experiment 3.

Component	Peak area
O_2	71540.8
COF_2	1979.1
CF_3COF	-
C_2F_4	-
c-C_3F_6	-
HFP	-
HFPO	-

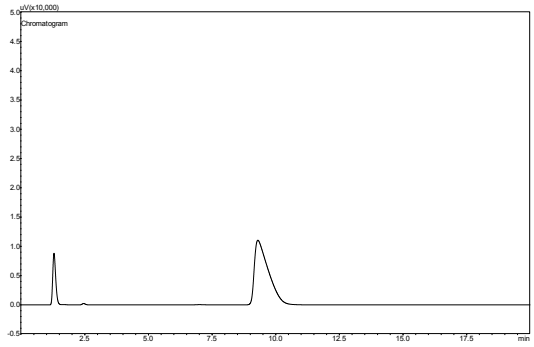

Figure I.425. Shimadzu G.C. 2014 TCD chromatogram, Cs-CuO/SiO_2 catalyst experiment 3.

Table I.426. Shimadzu G.C. 2010 FID chromatogram, Cs-CuO/SiO_2 catalyst experiment 4.

Component	Peak area
O_2	-
COF_2	-
CF_3COF	-
C_2F_4	-
c-C_3F_6	6757
HFP	16420244
HFPO	97892.2

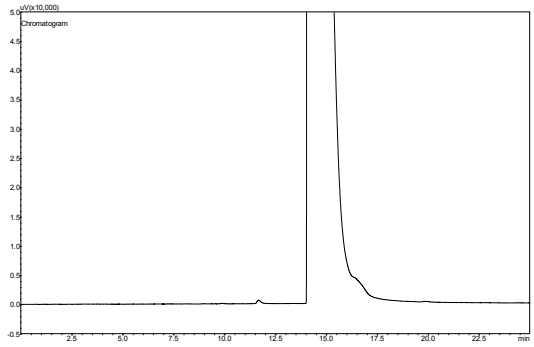

Figure I.426. Shimadzu G.C. 2010 FID chromatogram, Cs-CuO/SiO_2 catalyst experiment 4.

Table I.427. Shimadzu G.C. 2014 TCD chromatogram, Cs-CuO/SiO_2 catalyst experiment 4.

Component	Peak area
O_2	66333.6
COF_2	2585.2
CF_3COF	-
C_2F_4	-
c-C_3F_6	-
HFP	-
HFPO	-

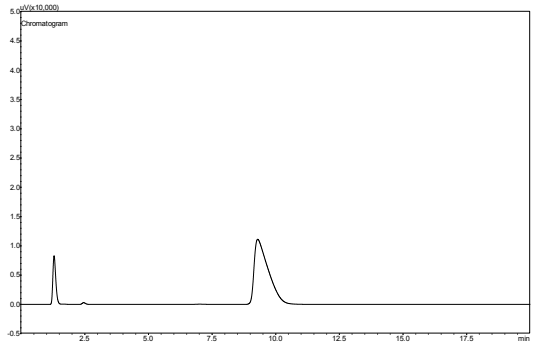

Figure I.427. Shimadzu G.C. 2014 TCD chromatogram, Cs-CuO/SiO_2 catalyst experiment 4.

Table I.428. Shimadzu G.C. 2010 FID chromatogram, Cs-CuO/SiO_2 catalyst experiment 5.

Component	Peak area
O_2	-
COF_2	-
CF_3COF	-
C_2F_4	-
c-C_3F_6	7563.4
HFP	18105450
HFPO	-

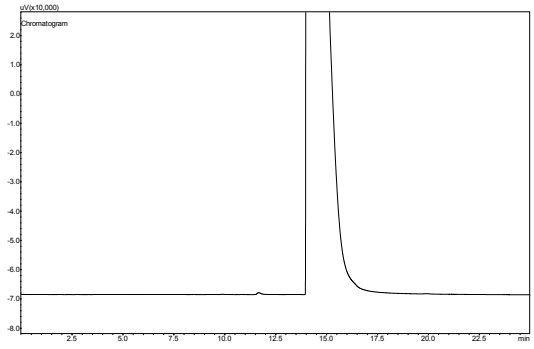

Figure I.428. Shimadzu G.C. 2010 FID chromatogram, Cs-CuO/SiO_2 catalyst experiment 5.

Table I.429. Shimadzu G.C. 2014 TCD chromatogram, Cs-CuO/SiO_2 catalyst experiment 5.

Component	Peak area
O_2	46465.9
COF_2	352.7
CF_3COF	-
C_2F_4	-
c-C_3F_6	-
HFP	-
HFPO	-

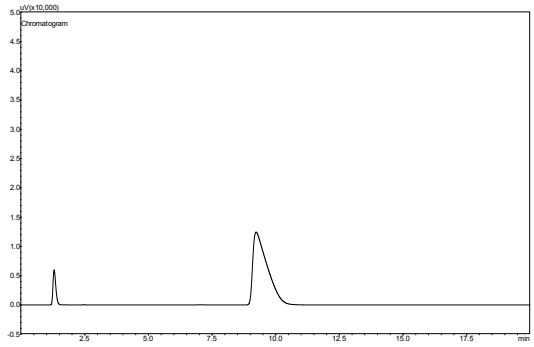

Figure I.429. Shimadzu G.C. 2014 TCD chromatogram, Cs-CuO/SiO_2 catalyst experiment 5.

Table I.430. Shimadzu G.C. 2010 FID chromatogram, Cs-CuO/SiO_2 catalyst experiment 6.

Component	Peak area
O_2	-
COF_2	-
CF_3COF	-
C_2F_4	-
c-C_3F_6	6505.9
HFP	17606153
HFPO	-

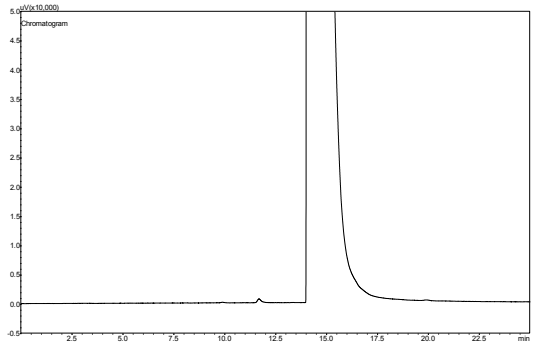

Figure I.430. Shimadzu G.C. 2010 FID chromatogram, Cs-CuO/SiO_2 catalyst experiment 6.

Table I.431. Shimadzu G.C. 2014 TCD chromatogram, Cs-CuO/SiO_2 catalyst experiment 6.

Component	Peak area
O_2	52039.1
COF_2	975.9
CF_3COF	-
C_2F_4	-
c-C_3F_6	-
HFP	-
HFPO	-

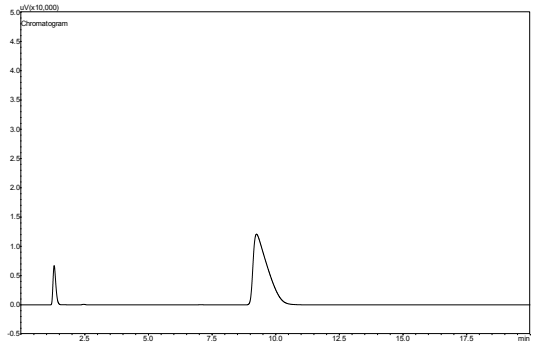

Figure I.431. Shimadzu G.C. 2014 TCD chromatogram, Cs-CuO/SiO_2 catalyst experiment 6.

Table I.432. Shimadzu G.C. 2010 FID chromatogram, Cs-CuO/SiO_2 catalyst experiment 7.

Component	Peak area
O_2	-
COF_2	-
CF_3COF	-
C_2F_4	-
c-C_3F_6	6967.1
HFP	17404101
HFPO	-

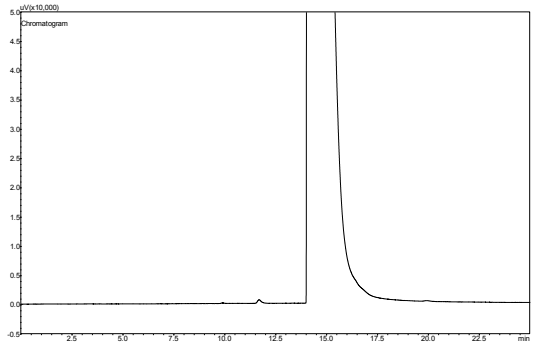

Figure I.432. Shimadzu G.C. 2010 FID chromatogram, Cs-CuO/SiO_2 catalyst experiment 7.

Table I.433. Shimadzu G.C. 2014 TCD chromatogram, Cs-CuO/SiO_2 catalyst experiment 7.

Component	Peak area
O_2	94051.6
COF_2	1040
CF_3COF	-
C_2F_4	-
c-C_3F_6	-
HFP	-
HFPO	-

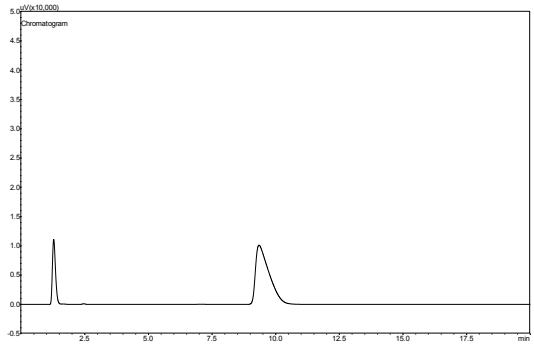

Figure I.433. Shimadzu G.C. 2014 TCD chromatogram, Cs-CuO/SiO_2 catalyst experiment 7.

Table I.434. Shimadzu G.C. 2010 FID chromatogram, Cs-CuO/SiO_2 catalyst experiment 8.

Component	Peak area
O_2	-
COF_2	-
CF_3COF	-
C_2F_4	-
c-C_3F_6	7810
HFP	18202850
HFPO	-

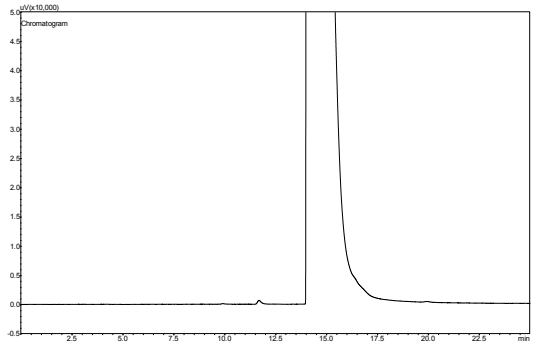

Figure I.434. Shimadzu G.C. 2010 FID chromatogram, Cs-CuO/SiO_2 catalyst experiment 8.

Table I.435. Shimadzu G.C. 2014 TCD chromatogram, Cs-CuO/SiO_2 catalyst experiment 8.

Component	Peak area
O_2	76960.1
COF_2	1131.4
CF_3COF	-
C_2F_4	-
c-C_3F_6	-
HFP	-
HFPO	-

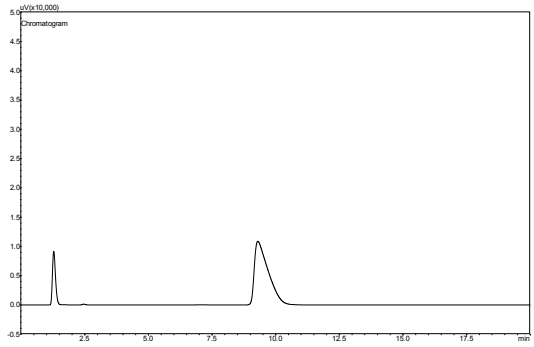

Figure I.435. Shimadzu G.C. 2014 TCD chromatogram, Cs-CuO/SiO_2 catalyst experiment 8.

Table I.436. Shimadzu G.C. 2010 FID chromatogram, Cs-CuO/SiO_2 catalyst experiment 9.

Component	Peak area
O_2	-
COF_2	-
CF_3COF	-
C_2F_4	-
c-C_3F_6	7278.8
HFP	15642783
HFPO	-

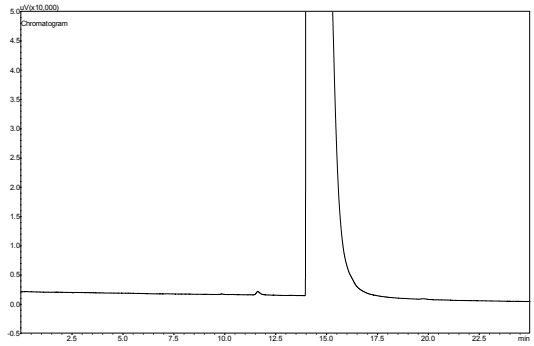

Figure I.436. Shimadzu G.C. 2010 FID chromatogram, Cs-CuO/SiO_2 catalyst experiment 9.

Table I.437. Shimadzu G.C. 2014 TCD chromatogram, Cs-CuO/SiO_2 catalyst experiment 9.

Component	Peak area
O_2	77010.6
COF_2	1972.2
CF_3COF	-
C_2F_4	-
c-C_3F_6	-
HFP	-
HFPO	-

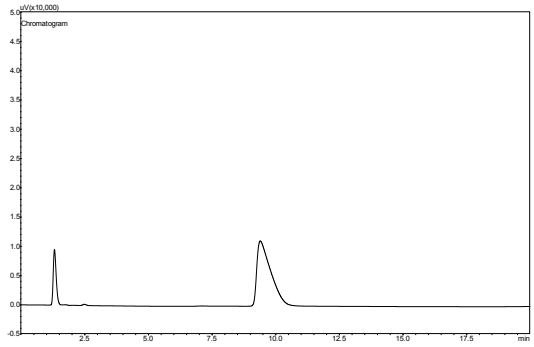

Figure I.437. Shimadzu G.C. 2014 TCD chromatogram, Cs-CuO/SiO_2 catalyst experiment 9.

Table I.438. Shimadzu G.C. 2010 FID chromatogram, Cs-CuO/SiO_2 catalyst experiment 10.

Component	Peak area
O_2	-
COF_2	-
CF_3COF	-
C_2F_4	-
c-C_3F_6	7039.2
HFP	16010766
HFPO	85767.5

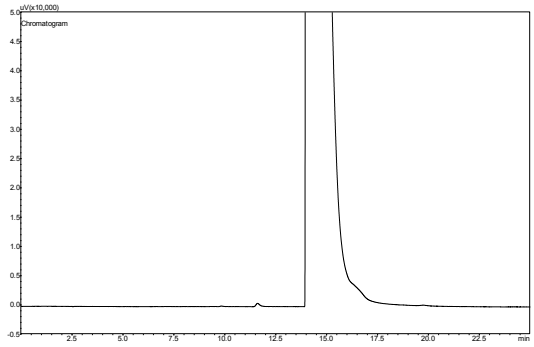

Figure I.438. Shimadzu G.C. 2010 FID chromatogram, Cs-CuO/SiO_2 catalyst experiment 10.

Table I.439. Shimadzu G.C. 2014 TCD chromatogram, Cs-CuO/SiO_2 catalyst experiment 10.

Component	Peak area
O_2	66426.6
COF_2	4529.5
CF_3COF	-
C_2F_4	-
c-C_3F_6	-
HFP	-
HFPO	-

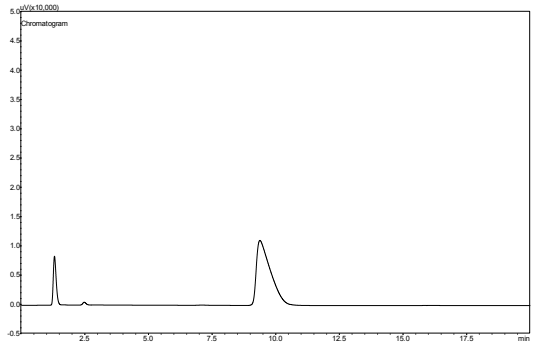

Figure I.439. Shimadzu G.C. 2014 TCD chromatogram, Cs-CuO/SiO_2 catalyst experiment 10.

Table I.440. Shimadzu G.C. 2010 FID chromatogram, Cs-CuO/SiO_2 catalyst experiment 11.

Component	Peak area
O_2	-
COF_2	-
CF_3COF	-
C_2F_4	-
c-C_3F_6	4477.6
HFP	10831147
HFPO	80999

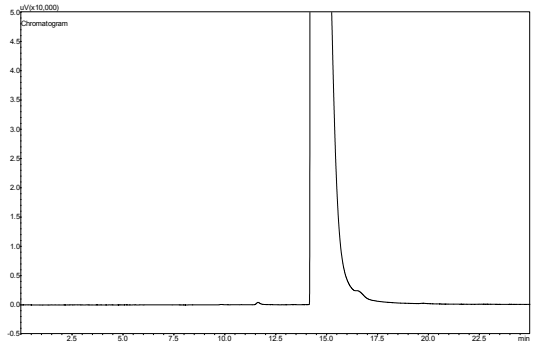

Figure I.440. Shimadzu G.C. 2010 FID chromatogram, Cs-CuO/SiO_2 catalyst experiment 11.

Table I.441. Shimadzu G.C. 2014 TCD chromatogram, Cs-CuO/SiO_2 catalyst experiment 11.

Component	Peak area
O_2	124005.5
COF_2	2494.8
CF_3COF	-
C_2F_4	-
c-C_3F_6	-
HFP	-
HFPO	-

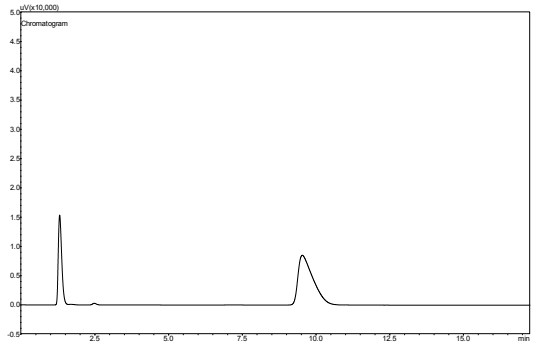

Figure I.441. Shimadzu G.C. 2014 TCD chromatogram, Cs-CuO/SiO_2 catalyst experiment 11.

Table I.442. Shimadzu G.C. 2010 FID chromatogram, Cs-CuO/SiO_2 catalyst experiment 12.

Component	Peak area
O_2	-
COF_2	-
CF_3COF	-
C_2F_4	-
c-C_3F_6	6940.7
HFP	16509730
HFPO	182405

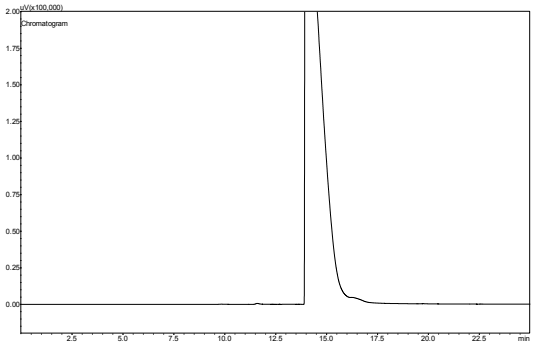

Figure I.442. Shimadzu G.C. 2010 FID chromatogram, Cs-CuO/SiO_2 catalyst experiment 12.

Table I.443. Shimadzu G.C. 2014 TCD chromatogram, Cs-CuO/SiO_2 catalyst experiment 12.

Component	Peak area
O_2	63356.8
COF_2	5451.4
CF_3COF	-
C_2F_4	-
c-C_3F_6	-
HFP	-
HFPO	-

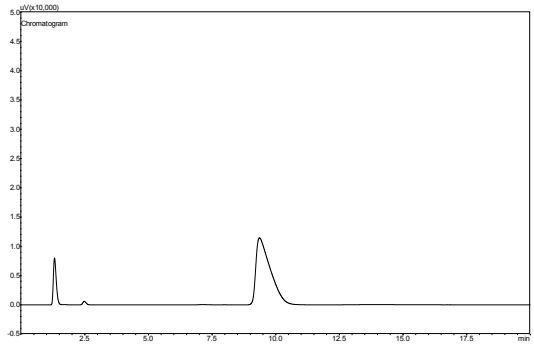

Figure I.443. Shimadzu G.C. 2014 TCD chromatogram, Cs-CuO/SiO_2 catalyst experiment 12.

Table I.444. Shimadzu G.C. 2010 FID chromatogram, Cs-CuO/SiO_2 catalyst experiment 13.

Component	Peak area
O_2	-
COF_2	-
CF_3COF	-
C_2F_4	-
c-C_3F_6	3898.9
HFP	10614397
HFPO	105637.4

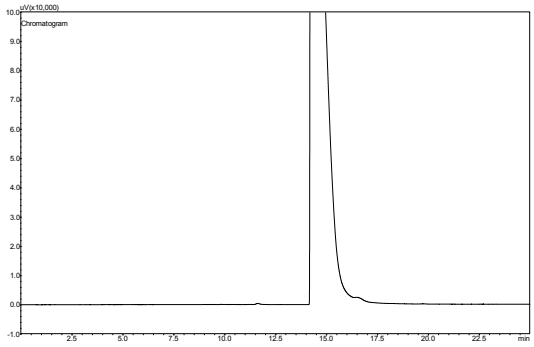

Figure I.444. Shimadzu G.C. 2010 FID chromatogram, Cs-CuO/SiO_2 catalyst experiment 13.

Table I.445. Shimadzu G.C. 2014 TCD chromatogram, Cs-CuO/SiO_2 catalyst experiment 13.

Component	Peak area
O_2	127032.3
COF_2	2397.6
CF_3COF	-
C_2F_4	-
c-C_3F_6	-
HFP	-
HFPO	-

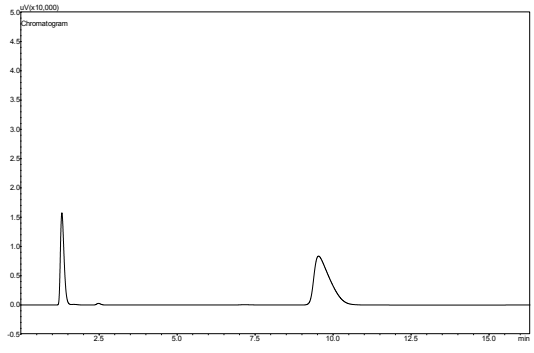

Figure I.445. Shimadzu G.C. 2014 TCD chromatogram, Cs-CuO/SiO_2 catalyst experiment 13.